AN AMMONIA-BASED CHEMISORPTION HEAT PUMP FOR COLD CLIMATE: EXPERIMENTS AND MODELING FOR PERFORMANCE ANALYSIS AND DESIGN OPTIMIZATION

by

Zhiyao Yang

A Dissertation

Submitted to the Faculty of Purdue University

In Partial Fulfillment of the Requirements for the degree of

Doctor of Philosophy

Lyles School of Civil Engineering

West Lafayette, Indiana

August 2020

THE PURDUE UNIVERSITY GRADUATE SCHOOL

STATEMENT OF COMMITTEE APPROVAL

Dr. Ming Qu, Chair

School of Civil Engineering

Dr. Eckhard Groll

School of Mechanical Engineering

Dr. Travis Horton

School of Civil Engineering

Dr. Kyle Gluesenkamp

Oak Ridge National Laboratory

Approved by:

Dr. Ming Qu

ACKNOWLEDGEMENT

This thesis is an outcome of my work at Purdue University and at the Oak Ridge National Laboratory. In putting together the pieces of this thesis work over the last three years as a PhD student—as well as the five more years before that, I have benefited tremendously from the support of my advisor Professor Ming Qu. Thank you for expecting the best from me and showing me that it's dedication and hard work that takes one to where he wishes to be. I also would like to express my deep gratitude to Dr. Kyle Gluesenkamp as my committee and host at the ORNL. I learned a lot from the initiative and methodological approach towards challenges of various sorts as well as the inspiration from numerous leadership examples. I am also very appreciative of the valuable time and advices of Prof. Groll and Prof. Horton as my committee.

I would also like to acknowledge the following people: my parents for their unconditional love and support; J for everything; Shuo and Shan for offering me a place to call home and sharing with me the happiness of the amazing growing up of little Winston; Handsome Fei and Yixuan Sun for the comradeship and late nights at Hicks and (sometimes very early morning) at CoRec, reminding me every time of why I love being at school; Liang Shi, Feng Wu, and Xiaoli Liu for sharing the mid-night grinding in the office and talks around the hearth; Xiaobing Liu and Shuai Li for the company and example of dedicated scholarship; Vishal Sharma, Juncheng Zhu, Yuki Chen, Weining Wang for the encouragement that picked me up from the bottom; Joseph Rendall, Cheng-min Yang, and James for the inspiring discussions and office/lab companionship late into Friday evenings; I also want to thank Viral Patel and Tony "the magician" Gehl for keeping the testbench alive; Corey Blackman from SaltX and Ingemar Hallin from HeatAmp for providing valuable information on the current prototype system and the improved new design, as well as offering helpful discussion on the experiment; Dr. Michel van der Pal for the insight in LiCl ammoniate reactions; Prof. Jun Chen and Mingkan Zhang for the expert advice on simulation; Navin Kumar, Tugba Turnaoglu, and other members on TeamG for the energetic discussions every two weeks; and other colleagues at ORNL, as well as the administrative staffs at both Purdue and ORNL for making the unique joint-program experience possible and memorable.

TABLE OF CONTENTS

LIST OF TABLES

LIST OF FIGURES

ABSTRACT

Space and water heating contribute over 50% of all the residential building energy consumption and are especially major energy consumers in the cold climates. Meanwhile, conventional furnaces and boilers with energy efficiency limited to below 100% dominate the residential heating in the cold climate, and the electric vapor-compression heat pump capacity and efficiency decline drastically at low ambient temperatures. Thermally driven ammonia-based chemical adsorption (chemisorption) heat pump (CSHP) systems utilize the reversible chemical reaction between the ammonia vapor and solid sorbent to generate heat pumping effect, which can provide heating with much higher energy efficiency than existing cold-climate heating technologies. Despite the significant potential of energy efficiency improvement from existing technologies, most studies in the literature on chemisorption heat pump systems focus on adopting the technology for refrigeration and energy storage applications, with very limited investigations available for using the technology for producing heating in cold climates.

This thesis study is thus conducted to characterize the operation behavior and performance of a CSHP system under cold ambient conditions and further identify optimal design and control for such systems to achieve high performance. In this study, both experimental and modelling approaches are pursued to investigate a CSHP heating system from the perspective of the sorption material using the multiple-stage LiCl-ammonia reactions, to the novel adsorber component with hybrid heat pipe heat exchanger, and finally to the performance of the complete heat pump system. The experimental studies are based on a prototype CSHP system tested to identify the chemical kinetics of the sorption material, as well as the transient performance of the adsorber and the system. The calibrated chemical kinetics are then used in the development of a transient adsorber model to analyze the operation and improve design of the adsorber. The heating COP of the prototype system was measured to be 0.75-1.16 under ambient temperatures of 8-20°C. Finally, a dynamic system model is developed based on the dynamic models of the adsorber and other components in the system. The system model is validated against the experimental data and used to analyze the detailed energy flow and operation dynamic. Based on the inefficiencies revealed by the simulation of the current prototype system, an improved system design with reduced thermal

mass and heat loss is introduced. Simulation of the improved system results in heating COP of 1.17 to 1.23 under -13.9°C to 8.3°C ambient, respectively.

1. INTRODUCTION

1.1 Heating in Cold Climate

Residential buildings accounted for 21.8% of total energy consumption in the United States [1]. Among all end-uses in residential buildings as shown in Figure 1, space and water heating are the major energy consumers, especially in cold climates where heating is in high demand. According to the Residential Energy Consumption Survey (RECS) conducted by the U.S. Energy Information Agency (EIA) in 2015 [2], space and water heating consumed over 60% of household site energy nationwide and almost three quarters of household site energy in cold and very cold climates as shown in Figure 1.

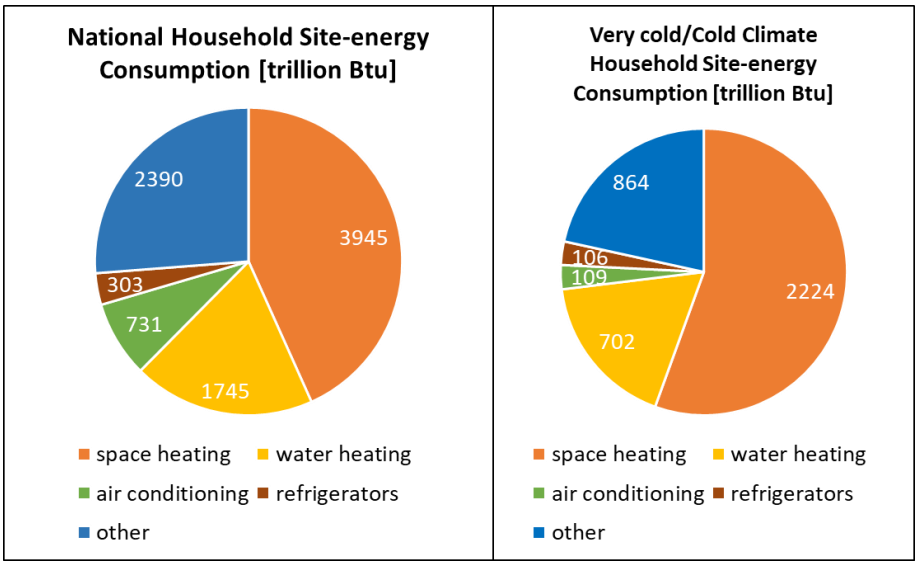

Figure 1 Breakdown of residential site-energy consumption

Figure 2 shows the main heating equipment and energy source by climate region from the same EIA report[2]. Over 80% of the 42 million households in cold and very cold climates in the country acquire heating by combustion of natural gas and other fuels, leaving less than 20% of them relying on electric-resistance or electric-driven heat pumps for heating purposes.

Therefore, developing highly efficient heating equipment especially for cold climates has significant energy saving potential. However, existing heating systems that are used in low-ambient conditions have seen major obstacles in improving their energy efficiency.

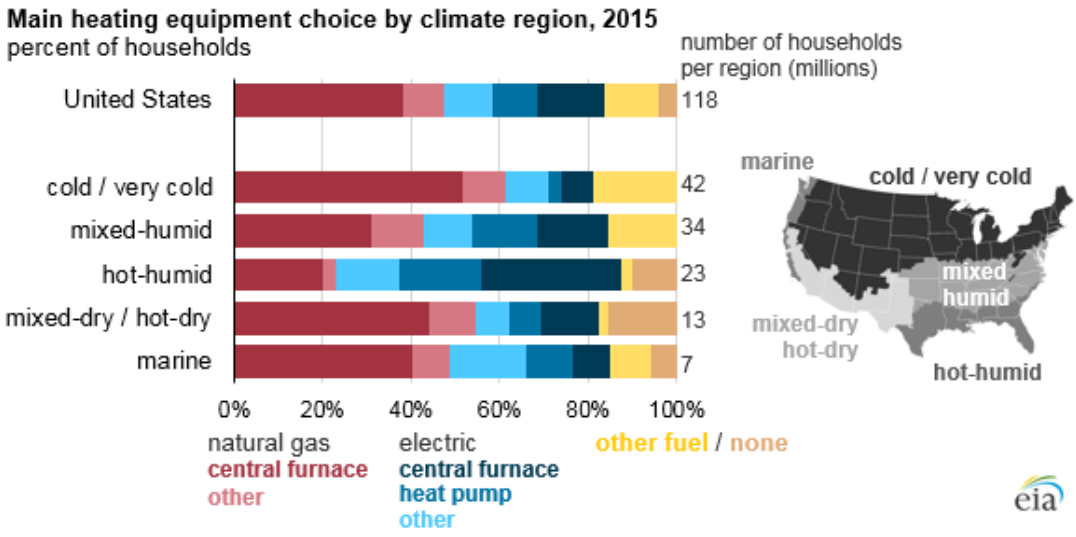

Figure 2 Heating equipment choice by climate region

1.2 State-of-the-art of Cold-climate Heating Technologies

As shown in Figure 2, the predominant heating equipment in cold climate is fuel-combustion furnaces; electric-driven vapor-compression heat pumps have limited applications in the cold climate zone; there are still some electric resistant heating systems operational especially in older buildings; in addition, there are several thermally-driven heat pump systems under lab research and development for the heating applications as well.

1.2.1 Conventional Fuel-combustion Furnaces

Fuel-combustion heating systems convert the chemical energy in fuel such as natural gas and propane into thermal energy in the hot flue gas to heat up water or air. The energy efficiency of the fuel-combustion systems is often represented by the Annualized Fuel Utilization Efficiency (AFUE) defined as the ratio of seasonal heat supply over the energy of total gas consumption.

The typical AFUE for non-condensing furnaces where the hot flue gas does not reach its dew point temperature during heating of domestic air or water is around 80% [3, 4], while the rest of the energy is vented out with the warm exhaust flue and the water vapor in it. If extra heat exchange and heated medium circulation is added, the water content in the flue gas can condensate and the associated energy recovered. The typical AFUE of condensing furnaces is around 92-95%, while the additional circulation of heated medium introduces parasitic electric load [5]. As the result, the

primary energy coefficient of performance (COP_{PE}) of non-condensing and condensing furnaces are around 80% and 85%, respectively [5].

The heat supply of fuel-combustion furnaces is insensitive to the ambient temperatures, and therefore they are the system of choice for households in cold and very cold climates. Meanwhile, as a highly mature technology, fuel-combustion furnaces are approaching their theoretical energy efficiency of 100% with very limited potential for further efficiency improvement.

1.2.2 Electric-driven Vapor-compression Heat Pumps

Based on the low-temperature heat source, the electric-driven vapor compression heat pumps can be categorized into air-source and ground-source systems.

1.2.2.1 Air-source Vapor Compression Heat Pumps

Air-source vapor-compression heat pumps extract heat from the ambient air and supply it to the end uses. They are widely used in mild climate where the ambient temperature is relatively high during heating seasons, which results in typical heating COP of above 5 [6]. However, their efficiency and heating capacity decrease drastically as the ambient temperature drops due to the reduced volumetric efficiency of the compressor and decreased refrigerant density at the compressor inlet [7].

Several researches and developments have been carried out to achieve a high heating COP and capacity under low ambient temperature.

- Two-stage compression cycle were proposed to reduce the compression ratio of each stage and improve heating capacity and efficiency, and the tested and simulated heating COP was about 2.1 at -30°C [8]and 3.0 at -20°C [7, 9].

- Vapor compression using scroll compressors was able to alleviate the unfavorable high compression ratio, and the performance of a system adding a flash tank and two-stage throttling was tested by Ma et al. [10] with COP above 2.0 at -17°C. Another scroll compressor heat pump using vapor injection to achieve multi-stage compression was tested by Bach et al. [11] and achieved COP of 2.2 at -17.8°C ambient.

- System with tandem compressors allows the compressors to operate at higher discharge temperatures and higher capacity under low ambient. And a tandem-compressor system

was simulated and field-tested by Shen et al. [12, 13] to achieve COP of 3.0 at -12°C and 2.5 at -20°C.

- Studies were also carried out on improving the low-ambient system performance using refrigerant mixtures with favorable properties under large temperature lift [14]. The performance of a heat pump system using a R32-CO_2 mixture as the refrigerant was simulated and compared with the dominant low-temperature refrigerant R410A. The mixture refrigerant system achieved COP above 3.0 at -20°C.

1.2.2.2 Ground-source Vapor Compression Heat Pumps

Instead of trying to improve efficiency under large temperature lifts like air-source heat pumps, ground-source (also referred to as geothermal-) heat pumps avoid extreme cold temperature by taking heat from the ground. Ground-source vapor compression heat pumps extract heat from bore-hole heat exchangers that are buried underneath the ground. Since the soil temperature is generally steady year-round and much higher than the cold ambient air temperature, the ground-source heat pumps usually have higher heating COP compared with the air-source ones, as pointed out in literature [15-17], for a residential system the COP of 3.4 to 4 can be achieved. However, the high installation cost of drilling boreholes as well as the limitation of ground conditions resulted in limited deployment of ground-source heat pumps [8].

1.2.3 Other Cold-climate Heating Technologies

Apart from fuel-combustion furnaces and electric-driven vapor-compression heat pumps, cold-climate heating systems have also been developed using vapor-sorption cycle and gas cycle.

- Ammonia-based absorption: Garrabrant et al. [5] developed and tested prototypes of gas-fired ammonia-water absorption heat pump for cold climates. The absorption system demonstrated gas COP of above 1.2 at -14°C ambient. The system used the simplest single-effect configuration and low capacity (22 kW) to reduce the equipment cost. Meanwhile, the system prototype faces challenges of the cost and system complexity associated with the specialized components such as the ammonia solution pump, rectifier.

- Gas engine-driven vapor compression: Heat engine-driven vapor compression systems have been built and tested for heat pumping applications at around freezing temperatures in literature [18-20] with gas COP of around 1.6. However, few existing studies reported performance of gas engine heat pumps below freezing temperatures. Furthermore, the complexity and maintenance requirement introduced by using natural gas engine in the heat pump system are likely to lead to a higher premium and operating cost.

- Gas cycle: Yang et al. [21] simulated the performance of an electric-driven air (reversed Brayton) cycle heat pump for cold climate water heating. By using air as the working fluid in a semi-open configuration, the air-cycle system had more stable COP under different ambient temperatures, and it eliminated the performance reduction associated with frosting. The air-cycle system achieved the highest COP of 2.5 under ambient of -7°C and heating temperature of 60°C and demonstrated a higher instantaneous heating capacity compared with a trans-critical CO_2 cycle and a conventional heat pump water heater running on R134a.

To sum up as in Table 1, heat pump technology is required to provide heating under cold ambient conditions with efficiencies surpassing the limit of conventional gas furnaces. For vapor compression heat pumps system powered by either electricity or gas engine, the major challenge towards high efficiency is the high compression ratio under large temperature lift in cold climate which drastically reduces the system efficiency. The temperature lift can be reduced by using geothermal instead of ambient air as the low-temperature heat source, although the geothermal heat pumps require a high installation premium and suitable ground conditions. The thermally driven absorption heat pumps with ammonia as the refrigerant demonstrated high performance under low ambient and large temperature lift. On the other hand, the residential-sized ammonia-water absorption systems require special components such as small ammonia solution heat pump and rectifier, which adds considerably to the system complexity, maintenance requirement, as well as cost.

Table 1 Comparison of existing cold-climate heating technologies

	Gas Furnace	**Electric-driven Heat Pump**		**Gas-driven Heat Pump**	
		Air Source	**Geo. Source**	**Gas Engine**	**NH_3 Abs.**
Primary Energy COP [a]	0.80 – 0.85	0.8 – 0.9	1.1 – 1.3	1.4 – 1.8	1.5 – 1.7
System Complexity	Simple	Simple	Complex	Complex	Complex
Moving Parts	Blower	Electric compressor	Compressor, pump	Gas engine – compressor	Ammonia solution pump
Initial Cost	Inexpensive	Inexpensive	Expensive (borehole)	Expensive (engine)	Expensive (rectifier & NH_3 solution pump)

[a] *primary energy conversion ratio: electricity = 3.165, natural gas = 1.0 [22]*

Therefore, a thermally driven sorption heat pump with a simple configuration and capable of producing high-efficiency heating under low temperature conditions is highly desired to meet the need of next-generation heating systems for cold climates.

1.3 Chemisorption Heat Pump Systems

Gas-fired chemical adsorption (chemisorption) heat pumps using ammonia as the refrigerant have the potential to provide space and water heating in cold climate with high energy efficiency. In a chemisorption heat pump (CSHP), ammonia vapor is adsorbed or desorbed by the solid sorbent through reversible chemical reactions, and the associated reaction heat is used for extracting heat from the cold ambient air and supplying heat to the end-use. With the heat pumping effect and high chemical adsorption capacity, the energy efficiency of CSHP can exceed the thermodynamic limit of gas-fired furnaces; on the other hand, with consistent equilibrium of chemical adsorption, the performance and efficiency of CSHP are much more sustained compared with the drastic efficiency decline of vapor compression heat pumps as the ambient temperature drops below freezing.

Chemisorption heat pumps used to suffer low COP and capacity due to the limitation of the sorbent materials. Before the composite sorbent was first introduced by Mauran et al. [23], the sorbent salt was prepared as small grains and filled loosely in the adsorber. During adsorption reaction the salt grains agglomerates and swells, which severely reduces the heat and mass transfer within the agglomerated bulk and reduces the system performance. With the recent researches in composite sorbent materials where the salt is hosted in porous matrix materials with highly enhanced thermal conductivity and permeability such as expanded graphite, the critical limitations of salt agglomeration and low heat and mass transfer performance were significantly mitigated, enabling competitive chemisorption heat pump system to be built for various applications.

Many recent research and development of chemisorption systems aimed at applying the technology for refrigeration and thermal energy storage driven by low-grade heat such as solar and industrial waste heat. However, the consistent high sorption capacity of chemisorption reactions also grants the technology great potentials to provide highly effective and efficient heat pumping under low ambient temperatures. However, only limited studies were found in literature investigating the performance of CSHP in low-ambient heating applications including the thermodynamic modelling in [24, 25] and the tri-generation system studied in [26]. As calculated by Pons et al. [24] for heating applications under -15°C ambient and producing heating at 50°C, single- and double-effect chemisorption heat pumps were able to achieve thermal COP of above 1.2. Yang et al [25] calculated the primary energy COP of chemisorption heat pumps operating at below -20°C to be around 1.1 for single-effect cycles and 1.2 for double-effect cycles. Such performance offers energy efficiency improvement of around 30% compared with the market-dominating furnaces and electric heat pumps as shown in Figure 3 from [25]. CSHP requires much less system complexity and specialized components compared with absorption and gas engine heat pumps, and therefore it offers higher reliability at a lower premium and operation cost.

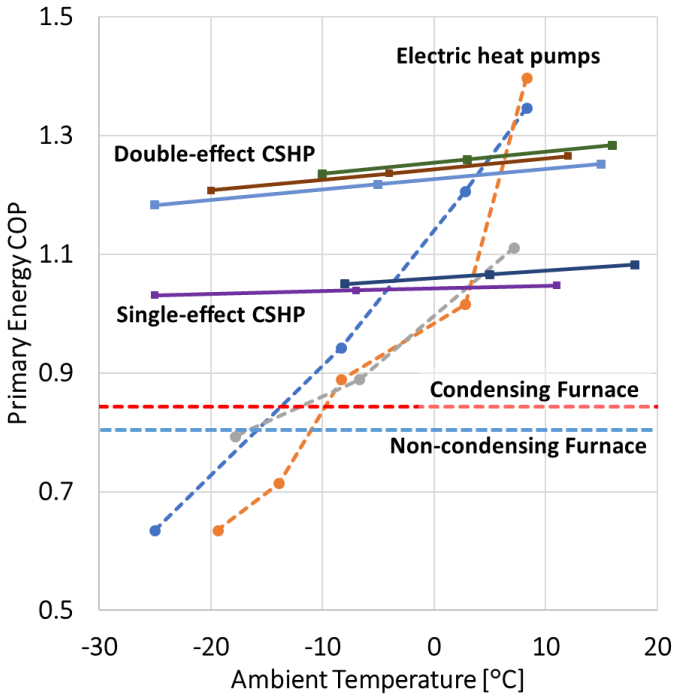

Figure 3 Comparison of primary energy COP between cold-climate heating technologies

Therefore, investigating the performance of chemisorption heat pumping system through experimental testing and validated models are of critical value to evaluate the performance of CSHP and identify possible improvement specifically for cold-climate heating applications.

1.4 Organization of the Dissertation Document

The chapters of this dissertation document are arranged as follows: chapter two summarizes the state-of-the-art of chemisorption heat pump technology from the literature and points out the research gaps to be addressed; chapter three introduces the objectives and methodologies of the current thesis research; chapter four to chapter six describes in detail the research approaches and results of experimental and modelling studies in current thesis research; chapter seven summarizes the achievement in this thesis study and lists the plan for future work; chapter eight lists the existing and planned publications stemmed from this thesis study.

2. LITERATURE REVIEW

In this chapter, the state-of-the-art of chemisorption heat pump technology is presented by first introducing the basic principles of the technology before summarizing the published studies on the material, component, and system of the chemisorption heat pumps in the literature.

The review includes studies of chemisorption systems specifically capable of extracting heat from low low-temperature heat sources, i.e. heat pumping in cold-climate conditions and refrigeration at low temperatures. While the heating applications aim at rejecting heat at a high capacity and at a high temperature, the refrigeration applications usually focus on utilizing low-temperature heat source to drive the system cycle. Nevertheless, the studies on chemisorption refrigeration systems can provide unique insights for the chemisorption heat pumping applications due to the similar operating conditions, and therefore they are included in this review as well.

Part of this chapter is based on the paper published in the journal Applied Thermal Engineering by the author titled "Ammonia-Based Chemisorption Heat Pumps for Cold-Climate Heating Applications: A Comprehensive Review" [27]. Furthermore, based on the summarized information in the literature review, a thermodynamic analysis on choosing the working pair and cycle configuration for cold-climate heating application is also published by the author in the journal Energy [28]. Both Applied Thermal Engineering and Energy journals are published by the publisher Elsevier.

2.1 Basic Principles of Chemisorption Heat Pump Technology

2.1.1 Chemisorption Reaction and Sorbent Material

Ammonia-based chemisorption heat pump systems are based on the reversible chemical reactions between the solid sorbent salt and the ammonia vapor. In such a reaction, neutral ammonia molecule is adsorbed by the sorbent salt by donating a pair of electrons to the metal ion in the sorbent salt and forms a coordinate covalent bond. The bonding energy is released during the synthesis of the complex compound. On the other hand, when the compound is heated at a high temperature, it decomposes as the bond is broken with the external heat input, and ammonia molecule is desorbed from the sorbent [29]. The coordinate covalent bonds are much stronger than

the van der Waals interaction that dominates the physical adsorption phenomena, yet they are not as strong as the covalent or ionic bonds within molecules. Thus, the chemisorption reactions have higher energy density than physical adsorption, and yet they are reversible under a moderate change in temperature and pressure. Ammonia molecule can form complex compound with salt of both main group metals (e.g. Li, Ca, Na) and transition metals (e.g. Co, Mn, Ni) [30], and metal halide salts (e.g. $CaCl_2$, NaBr) are the most commonly used sorbent for ammonia-based chemisorption reactions. Depending on the vacant electric orbits available in the metal ion, different numbers of ammonia molecules can bond to one metal ion and lead to different sorption capacities between salts. For example, one mole of $NiCl_2$ and $CaCl_2$ can form complex compound with at most 6 and 8 moles of NH_3, respectively, corresponding to maximum sorption capacity of 0.79 and 1.22 kg/kg salt.

The equilibrium vapor pressure of a chemisorption reaction (P_{eq}) is mono variant as a function of only the sorbent temperature (T_s). It can be expressed by the van't Hoff equation (Equation 1) and illustrated as a tilted straight line on the Clapeyron chart as in Figure 4 (a), with the slope and y-intersection of the line corresponding to the reaction enthalpy and entropy (ΔH in and ΔS in Equation 1) over the gas constant (R in Equation 1). The ammonia vapor-liquid equilibrium is also a line with a flatter slope on the Clapeyron chart located to the left of the reaction equilibrium line, as the equilibrium vapor pressure of pure ammonia liquid is always higher than that of the sorbents, and the heat of ammonia vaporization is lower than the heat of chemisorption reaction.

$$\ln(P_{eq}) = \frac{-\Delta H}{R \cdot T_s} + \frac{\Delta S}{R} \qquad \text{Equation 1}$$

Besides the salt's adsorption capacity and feasible operating conditions, the performance of the chemisorption system is also significantly influenced by the heat and mass transfer within the sorbent. Conventional pure halide salts are usually available in granular form with very limited heat and mass transfer rate. For example, the thermal conductivity of granular $CaCl_2$ and its ammoniates ranges between 0.0065-0.145 W/m-K [31, 32]. Moreover, the swelling and agglomeration of the bulk salt during adsorption deteriorates the sorption capacity and vapor transfer across the sorbent [33]. Therefore, composite sorbent material consists of salt and highly conductive porous materials such as activated carbon and graphite were developed. The composite

sorbents demonstrated significant improvement of the sorbent heat and mass transfer performance (e.g. 1.7-17.4 W/m-K for expanded graphite-$CaCl_2$ composite sorbent [34, 35]) while also eliminating the mass transfer deterioration due to agglomeration.

2.1.2 Component and System

In an ammonia-based CSHP system, the thermal effects of chemisorption reaction and ammonia phase change are applied to produce useful heating in sorbent- and ammonia-containing heat exchangers under different temperatures and pressures. Figure 4 illustrates the schematic and working procedure of a basic CSHP cycle with a sorbent-containing adsorber and a heat exchanger acting as a condenser or an evaporator. The CSHP cycles between the desorption and adsorption modes. In the desorption mode, heat from a high-temperature source, Q_{des}, is supplied to the adsorber. The ammonia-salt compound is heated and starts to decompose, releasing ammonia vapor. The ammonia vapor flows into the condenser to be cooled by the medium-temperature heat sink and condense, releasing heat, Q_{cond}. The desorption mode ends with the sorbent in the adsorber exhausted of ammonia and the ammonia accumulating in liquid phase in the condenser. The adsorption mode then starts by cooling the dry sorbent in the adsorber. The adsorber pressure decreases to below the ammonia-containing heat exchanger (acting as evaporator) and drives evaporation of the liquid ammonia, which continuously extracts heat, Q_{evap}, from the low-temperature heat source. The ammonia vapor flows into the adsorber and bonds with the sorbent, releasing heat, Q_{ads}, to the medium-temperature heat sink. The adsorption mode ends upon exhaustion of ammonia in the evaporator, and the system switches back to the desorption mode for continued operation.

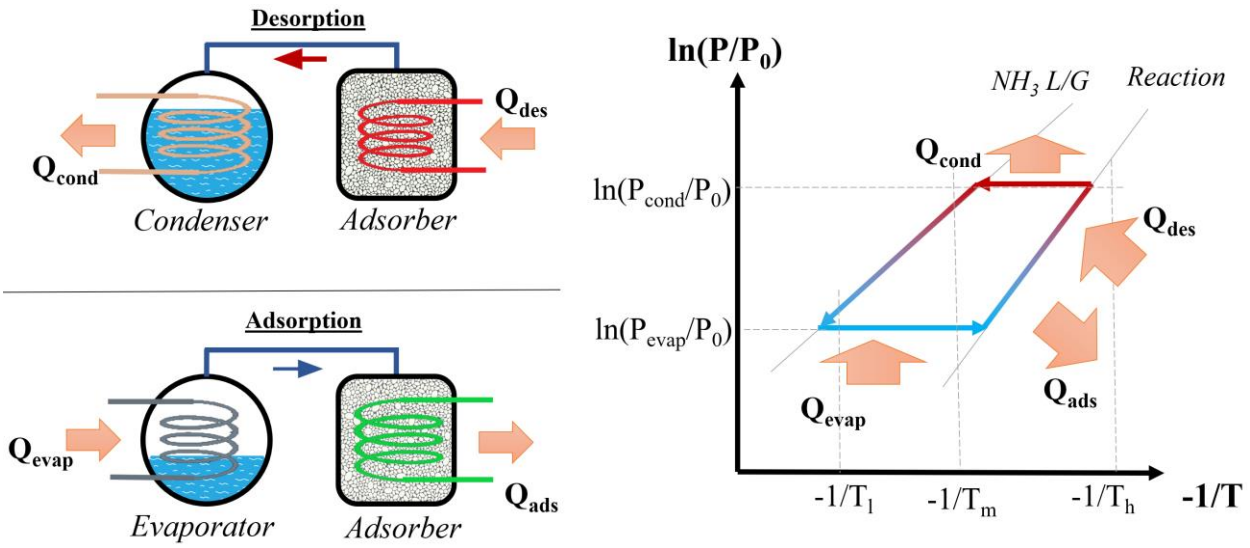

Figure 4 Working principle on the Clapeyron chart (right) and schematic diagram (left) of a chemisorption system

In the basic chemisorption heat pump cycle, the heat input to the system (Q_{in}) is the desorption heat (i.e. Q_{des}), and the useful heat output (Q_{ht}) is the heat output in the condenser and adsorber at the heat supply temperature (i.e., Q_{cond} and Q_{ads}). The system performance of the CSHP can be evaluated by two parameters: (1) the COP as the ratio of useful heating produced over the high-temperature heat input in, and (2) the specific heating power (SHP) as the ratio of heating output over the system mass (m_{sys}) averaged over the time lapse of a complete desorption-adsorption cycle (t_{cyc}).

Equation 2

$$COP_{ht} = \frac{Q_{ht}}{Q_{in}} = \frac{Q_{cond} + Q_{ads}}{Q_{des}}$$

Equation 3

$$SHP = \frac{1}{t_{cyc}} \cdot \frac{Q_{ht}}{m_{sys}}$$

2.2 Chemisorption Reaction and Material

The viability and performance of the CSHPs are largely determined by the properties of the sorbent salt, where a suitable equilibrium and large sorption capacity are preferred. A sorption material has suitable equilibrium means that when the material is at the driving heat temperature, the

saturation temperature corresponding to the equilibrium vapor pressure of the material is above the heat rejection temperature; meanwhile, when the material is at the heat rejection temperature, the saturation temperature corresponding to the equilibrium vapor pressure of the material is below the cold ambient temperature. As the result, the sorption material can support continuous ammonia condensation and evaporation. An ideal chemisorption reaction adsorbs a large amount of ammonia to extract heat under freezing temperatures and reject heat at a high temperature through ammonia condensation and adsorption reaction.

In practical operations, the CSHP performance is also significantly affected by the heat and mass transfer rate in the sorbent, as well as the extent of reaction completion. Therefore, the sorbent salts in CSHP systems were often combined with thermally conductive porous matrix materials to enhance heat and mass transfer performance. This section summarizes the sorbent salt and matrix materials commonly used in published studies.

In this section, the sorbent salt and matrix materials commonly used in existing studies of chemisorption refrigeration and heat pumping systems are described.

2.2.1 Sorbent Salts and Chemisorption Reactions

In an ammonia-based chemisorption reaction, a neutral ammonia molecule is adsorbed by the sorbent salt by donating a pair of electrons to the metal ion in the sorbent salt and forming a complex compound with coordinate covalent bond while releasing the bonding energy as heat. On the other hand, when the compound is heated at a high temperature, the bond is broken and ammonia is desorbed from the sorbent [29]. A generic reaction formula between ammonia and metal chloride (MCl_x) can be written as Eq. (4) [36]. In the reaction formula, M is the metal in the sorbent salt capable of bonding with ammonia molecules and forming complex compounds. $MCl_x \cdot n_1 NH_3$ and $MCl_x \cdot (n_1 - n_2) NH_3$ are both solid-phase ammoniate compounds. n_2 is the mole of ammonia that reacts with each mole of ammoniate salt. The reaction can be simply denoted as $MCl_x \cdot n_1/(n_1 - n_2)$. The reaction in the forward direction, i.e. decomposition of $MCl_x \cdot n_1 NH_3$ requires heat input; on the other hand, the reaction in the backward direction, i.e. the synthesis of $MCl_x \cdot n_1 NH_3$ releases heat.

$$MCl_x \cdot n_1 NH_3(s) \leftrightarrow MCl_x \cdot (n_1 - n_2) NH_3(s) + n_2 NH_3(g)\ . \tag{4}$$

Ammonia molecules can form complex compounds with salts of both main group metals (e.g., Li, Ca, and Na) and transition metals (e.g., Co, Mn, and Ni) [30], and metal halide salts (e.g., $CaCl_2$ and NaBr) are the most commonly used sorbent for ammonia-based chemisorption reactions. The number of ammonia molecules bonded to one metal ion is determined by the type of metal ion, as well as the chemisorption reaction equilibrium, which also leads to different sorption capacities between salts. For example, one mole Ni^{2+} and Ca^{2+} in $NiCl_2$ and $CaCl_2$ can bond with six and eight moles of NH_3, which corresponds on a mass basis to maximum sorption capacities of 0.79 kg/kg and 1.22 kg/kg of salt, respectively. Some salts have only one stable complex compound corresponding to one reaction, such as $BaCl_2$-8/0; other salts can form multiple stable compounds at different temperatures and pressures, such as $CaCl_2$-8/4 and $CaCl_2$-4/2.

The equilibrium vapor pressure of a chemisorption reaction is usually considered mono-variant as a function of the sorbent temperature expressed by the van 't Hoff equation (Eq. (4)). The coefficients in Eq. (4), ΔH and ΔS, are often associated to the reaction enthalpy and entropy per mole of NH_3 under the standard state, albeit they are usually derived from the linear equilibrium curve (e.g. in [37-39]) instead of directly measured. R is the gas constant of 8.314 J/(mol·K), T_s is the sorbent temperature in Kelvin, K_p is the equilibrium constant of the reaction, P_{eq} is the equilibrium vapor pressure in Pascal. The reference pressure P_0 in chemical reactions is usually defined as 1 bar, 1 atm, or 100 kPa [40-43]. However, the reference pressure was assumed to be 1 Pa for the equilibrium of ammonia chemisorption reactions reported in [44, 45] and listed in Table 2. The different values adopted for the reference pressure will not affect the value of the reaction enthalpy obtained from linear fitting but will lead to an offset to the value of the reaction entropy.

$$\ln\left(\frac{P_{eq}}{P_0}\right) = \ln(K_p) = \frac{-\Delta H}{R \cdot T_s} + \frac{\Delta S}{R} \tag{5}$$

The reaction equilibrium can be illustrated as straight lines on the Clapeyron diagram, as shown in Figure 5. The vapor-liquid equilibrium of pure ammonia is shown in the left of the chart, and the lines to the right of the ammonia equilibrium represent the vapor-solid equilibria of 66 chemisorption reactions between ammonia and halide salts/compounds. The reaction enthalpy and entropy of these reaction were collected from [44-46]. 14 commonly used reactions are highlighted with bold lines in Figure 5 including $CaCl_2$-8/4 [47], $BaCl_2$-8/0 [24, 47], $MnCl_2$-6/2 [24, 48], $SrCl_2$-

8/1 [24], $NiCl_2$-6/2 [24, 47], NH_4Cl-3/0 [48], LiCl [49], and NaBr-5.25/0 [50]. These reactions are popular choices in chemisorption systems [44, 51-53] for cold-climate heating applications.

Table 2. Summary of chemisorption reactions between ammonia and metal halide salts ordered by the equilibrium temperature when the pressure is 40 kPa. The labels correspond to the order of the equilibrium lines on Figure 2 from left to right.

Label	Reaction	Label	Reaction	Label	Reaction	Label	Reaction
1	$CuCl_2$-10/6	18	NaI-4.5/0	35	LiCl-1/0	52	$NiBr_2$-6/2
2	$ZnCl_2$-10/6	19	$SrCl_2$-8/1	36	$FeCl_2$-6/2	53	$CaCl_2$-1/0
3	$SnCl_2$-9/4	20	$BaBr_2$-8/4	37	SrI_2-6/2	54	NiI_2-6/2
4	KI-4/1	21	$CaCl_2$-4/2	38	$MnBr_2$-6/2	55	$MnCl_2$-2/1
5	LiBr-5/4	22	$BaBr_2$-4/2	39	$CuCl_2$-3.3/2	56	$MgCl_2$-2/1
6	NH_4Cl-3/0	23	$ZnCl_2$-6/4	40	BaI_2-2/0	57	$FeCl_2$-2/1
7	$PbCl_2$-8/3.25	24	LiCl-3/2	41	$CoCl_2$-6/2	58	$CoCl_2$-2/1
8	CaI_2-8/6	25	$PbCl_2$-2/1.5	42	$PbCl_2$-1/0	59	$NiCl_2$-2/1
9	NaBr-5.25/0	26	$SrBr_2$-8/2	43	$MgCl_2$-6/2	60	$ZnCl_2$-2/1
10	$PbBr_2$-5.5/3	27	BaI_2-6/4	44	$FeBr_2$-6/2	61	$MnCl_2$-1/0
11	LiCl-4/3	28	$PbCl_2$-1.5/1	45	CaI_2-6/2	62	$FeCl_2$-1/0
12	$SnCl_2$-4/2.5	29	BaI_2-4/2	46	$CoBr_2$-6/2	63	$MgCl_2$-1/0
13	$BaCl_2$-8/0	30	LiCl-2/1	47	$CaCl_2$-2/1	64	$CoCl_2$-1/0
14	$PbCl_2$-3.25/2	31	$MnCl_2$-6/2	48	$NiCl_2$-6/2	65	$NiCl_2$-1/0
15	$PbBr_2$-3/2	32	$CaBr_2$-6/2	49	MnI_2-6/2	66	$ZnCl_2$-1/0
16	PbI_2-5/2	33	$ZnCl_2$-4/2	50	FeI_2-6/2		
17	$CaCl_2$-8/4	34	$CuCl_2$-5/3.3	51	$MgBr_2$-6/2		

Table 3. Summary of the sorption capacity, reaction enthalpy and entropy of chemisorption reactions between ammonia and metal halide salts.

Salt	Molar mass [g/mol]	Reaction	Specific sorption cap. [kg/kg salt]	Reaction enthalpy [J/mol]	Reaction entropy [J/(mol·K)]	Reaction	Specific sorption cap. [kg/kg salt]	Reaction enthalpy [J/mol]	Reaction entropy [J/(mol·K)]
LiCl	42.3	4-3	0.401	36828	224.6	2-1	0.401	48128	230.6
		3-2	0.401	44780	229.8	1-0	0.401	51894	234.4
NH_4Cl	53.4	3-0	0.955	29433	207.9	—	—	—	—
$CoCl_2$	94.3	6-2	0.721	53987	228.1	1-0	0.18	88303	232.8
		2-1	0.18	78134	232.17	—	—	—	—
$MgCl_2$	95.1	6-2	0.715	55661	230.63	1-0	0.179	87048	230.88
		2-1	0.179	74911	230.3	—	—	—	—
$CaCl_2$	110.8	8-4	0.614	41013	230.3	2-1	0.153	63193	237.34
		4-2	0.307	42269	229.92	1-0	0.153	69052	234.14
$MnCl_2$	125.7	6-2	0.541	47416	228.07	1-0	0.135	84202	233.18
		2-1	0.135	71019	232.35	—	—	—	—
$FeCl_2$	126.6	6-2	0.537	51266	227.99	1-0	0.134	86880	233.01
		2-1	0.134	76167	231.91	—	—	—	—
$NiCl_2$	129.5	6-2	0.525	59218	227.75	1-0	0.131	89810	233.01
		2-1	0.131	79515	232.17	—	—	—	—
$CuCl_2$	134.5	10-6	0.506	31387	227.72	3.3-2	0.164	56497	237.22
		5-3.3	0.215	50241	230.75	—	—	—	—
$ZnCl_2$	136.2	10-6	0.499	29588	219.23	2-1	0.125	80352	229.72
		6-4	0.25	44779	230.24	1-0	0.125	104625	227.79
		4-2	0.25	49467	230.24	—	—	—	—
$SrCl_2$	158.4	8-1	0.751	41432	228.8	—	—	—	—
$SnCl_2$	189.6	9-4	0.448	31806	224.86	4-2.5	0.134	38920	229.82
$BaCl_2$	208.2	8-0	0.653	38250	227.25	—	—	—	—
$PbCl_2$	278	8-3.25	0.29	34317	223.76	1.5-1	0.031	47290	232.5
		3.25-2	0.076	39339	230.27	1-0	0.061	55660	231.04
		2-1.5	0.031	46035	230.89	—	—	—	—
LiBr	86.8	5-4	0.196	33689	225.9	—	—	—	—
NaBr	102.9	5.25-0	0.867	35363	225.2	—	—	—	—
$MgBr_2$	184.1	6-2	0.369	63612	230.2	—	—	—	—
$CaBr_2$	199.8	6-2	0.34	48965	230.4	—	—	—	—
$MnBr_2$	214.7	6-2	0.317	53066	228.3	—	—	—	—
$FeBr_2$	215.6	6-2	0.315	55828	228.1	—	—	—	—
$NiBr_2$	218.5	6-2	0.311	64240	227.2	—	—	—	—
$CoBr_2$	218.7	6-2	0.311	58590	227.5	—	—	—	—

Table 3 continued

$SrBr_2$	247.4	8-2	0.412	45617	229.3	—	—	—	—
$BaBr_2$	297.1	8-4	0.229	41850	229.8	4-2	0.114	42687	230.7
$PbBr_2$	367	5.5-3	0.116	37665	229.4	3-2	0.046	39758	229.4
NaI	149.9	4.5-0	0.51	39339	224.5	—	—	—	—
KI	166	4-1	0.307	32015	219.8	—	—	—	—
CaI_2	293.8	8-6	0.115	35991	229.3	6-2	0.231	58590	231
MnI_2	308.7	6-2	0.22	59301	227.4	—	—	—	—
FeI_2	309.6	6-2	0.22	60683	227.5	—	—	—	—
NiI_2	312.5	6-2	0.218	65453	224.1	—	—	—	—
SrI_2	341.4	6-2	0.2	52731	230.5	—	—	—	—
BaI_2	391.1	6-4	0.087	46454	231.6	4-2	0.087	47291	230.3
		2-0	0.087	56079	235	—	—	—	—
PbI_2	461	5-2	0.111	40595	229.1	—	—	—	—

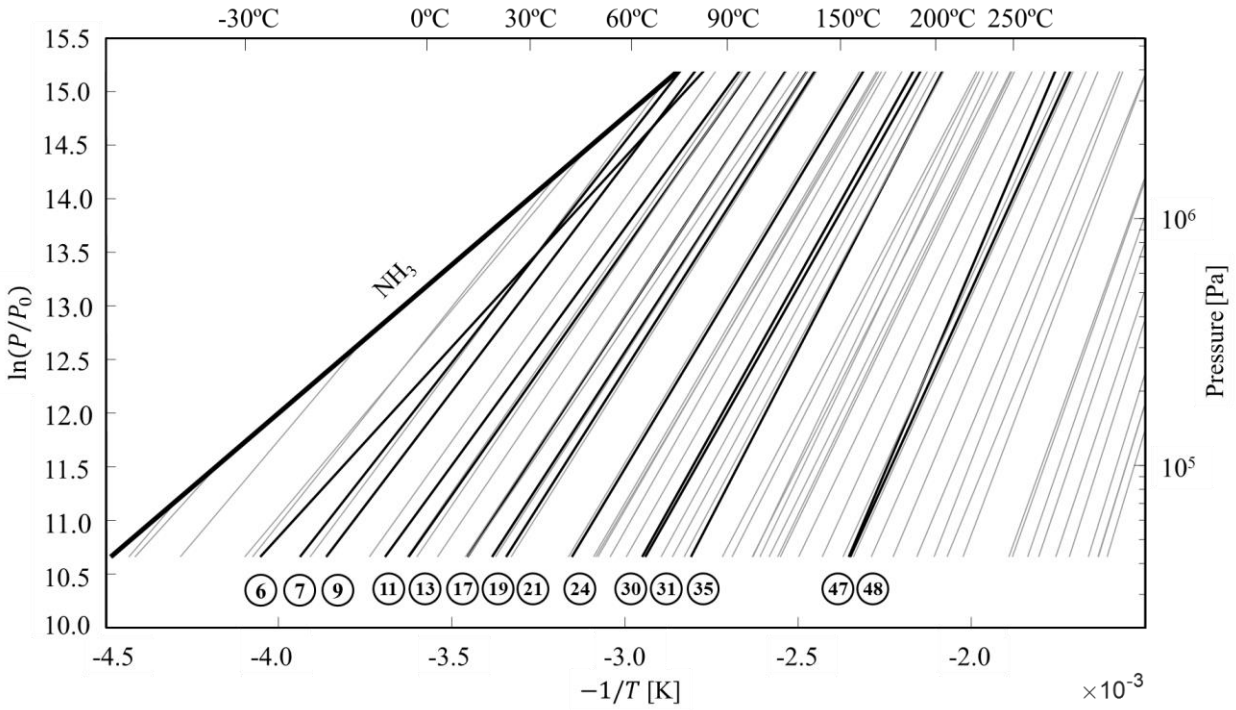

Figure 5. Ammonia-based chemisorption reaction equilibrium on the Clapeyron chart. The labels of all lines from left to right are listed in Table 1.

The reactions are used in CSHP systems in two different arrangements: (1) conventional adsorption coupling the adsorption/desorption reactions with evaporation and condensation of pure ammonia such as the basic cycle in Figure 4, and (2) resorption [54, 55] where two different ammoniate compounds are coupled to extract heat with the desorption reaction of the low-temperature salt and supply heat with the adsorption reaction of both the high-temperature and low-temperature salts.

The viability of a reaction for the cold-climate heating application is determined by its equilibrium pressure relative to the ammonia pressure under the cold ambient and the hot heat source. The low-temperature heat extraction—either through ammonia evaporation or desorption reaction—happens toward the left of Figure 5 with a low vapor pressure; on the other hand, the heat rejection through ammonia condensation or adsorption reaction needs to happen at a sufficiently high temperature toward the right of Figure 5 with a high vapor pressure. Moreover, a deviation from the equilibrium is necessary for the chemical reaction to occur [44, 51]; therefore, the desorption equilibrium pressure needs to be higher than the pressure around the ammoniate compound, and vice versa for adsorption. Such temperature or pressure deviation is often referred to as the equilibrium drop and indicates the driving force of the chemisorption reactions [44].

2.2.1.1 Salts for Conventional Adsorption Configuration

While all the 66 available reactions can be coupled with ammonia condensation and evaporation to form a chemisorption heat pump cycle, only a few of them have been selected for real system development. These commonly used reactions usually have high maximum ammonia sorption capacities, while also being able to operate under the desired conditions. In refrigeration applications, when ammonia is evaporating at low temperature (e.g. 0~-15°C), the adsorption reaction needs to disperse heat at a temperature higher than the medium heat sink (e.g. 30°C); on the other hand, when the ammonia-rich salt is heated by high-temperature heat source and decomposes, the corresponding ammonia condensation needs to reject heat at a temperature higher than the medium heat sink. For cold-climate heat pumping applications, the medium heat sink temperature is around 50°C.

Based on these typical operating conditions, the maximum sorption capacity and minimum desorption temperatures of all available reactions are plotted and compared in Figure 6 (a) and (b)

for medium-temperature heat sink of 30°C and 50°C, and evaporation temperature of 0°C and 15°C, respectively. Reactions based on the same salt such as LiCl-4/3 and LiCl-3/2 can form multiple-stage reactions with sufficiently high heat source temperature for the high-temperature reaction, while the low-temperature reaction can occur under the medium-temperature heat sink. The sorption capacity of such multiple-stage reactions is the sum of each stage's capacity. The ideal reaction(s) should provide a high maximum sorption capacity under a relatively low desorption temperature. In Figure 6 such reaction(s) are located towards the top left corner.

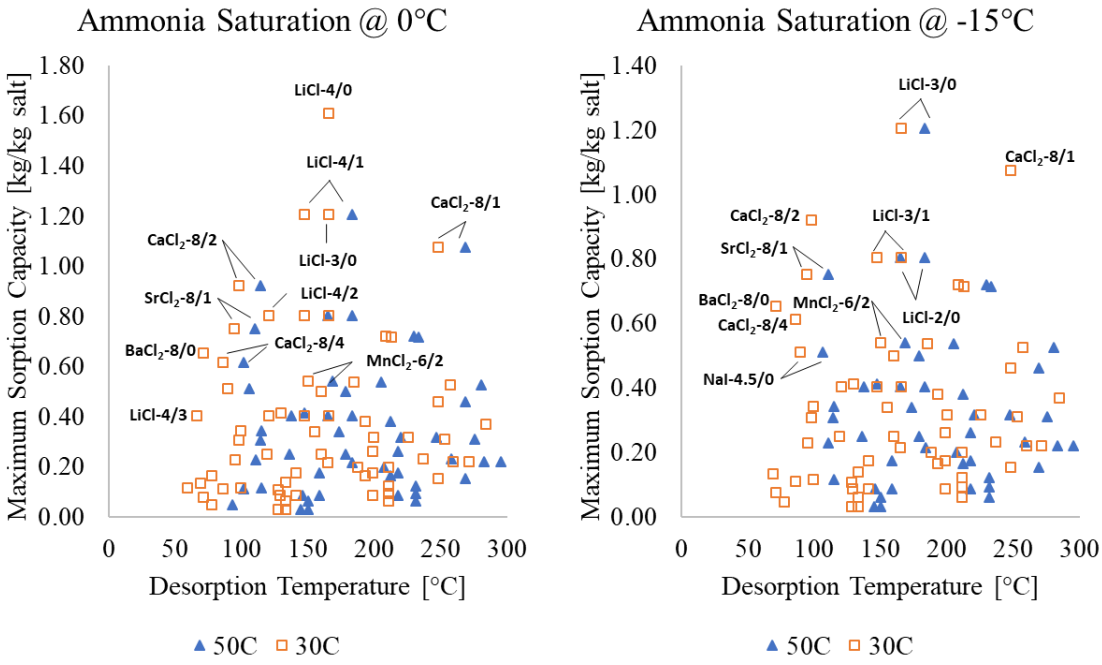

Figure 6 Maximum sorption capacity and desorption temperature of metal halide salts corrosponding to 0°C and -15°C ammonia saturation pressure

The reactions to the left can be driven with low-temperature heat sources such as solar heat, and therefore $BaCl_2$-8/0 was used by Le Pierres et al. [56], Li et al. [57], and Rivera et al. [58] to utilize low-temperature solar heat (<80°C) and produce refrigeration; Jiang et al. [35] and Hu et al. [59] used $BaCl_2$-8/0 driven by the adsorption heat of high stage in a two-stage freezer. Other low-temperature reactions such as NaBr-5.25/0, NH_4Cl-3/0, LiCl-4/3, and were also tested for freezing applications by Jiang et al. [35], Oliveira et al. [50], and Kiplagat et al. [60]. With heat rejection temperature of 30°C, NH_4Cl-3/0 and NaBr-5.25/0 is not able to operate below freezing, but under lower heat rejection temperature such as 20°C in

With higher heat source temperature, $SrCl_2$-8/1 was used in multiple refrigeration systems either directly driven with below 100°C heat source [61], or as the high stage salt in two stage systems [35, 59]. $CaCl_2$ has four ammoniate reactions and is the most used salt in ammonia-based chemisorption systems. $CaCl_2$-8/4 and $CaCl_2$-4/2 require similar heat source temperature around 100°C under typical condensing temperature as well as rejection temperature of around 40°C and 50°C, and therefore they are often preferred given sufficient heat source [35, 59, 62-70]. If heat source of above 150-180°C is available, the $CaCl_2$ based reactions can proceed to higher-stage ($CaCl_2$-2/1) [71, 72], and other high-temperature reactions such as $MnCl_2$-6/2 were used in deep freezing applications in [73] and refrigeration-power cogeneration in [74]. For these reactions, the heat rejection temperature during adsorption are typically above 50°C and can be used for heating applications.

Figure 6 also shows with above 150°C heat source temperature, multiple reactions based on LiCl can provide considerably higher sorption capacity compared with all other available reaction due to the lightness of the LiCl molecule. Such feature can be useful for heat pumping applications where the heat source is usually gas-fired and adequate to enable these reactions. However, LiCl ammoniate reactions are not as extensive used in published studies as other high-capacity salts. It was experimentally tested for solar-driven ice making application [60] with only one stage (4/3) due to the limited heat source temperature. Therefore, a chemisorption heating system with sufficiently high-temperature heat source to utilize multiple stages of LiCl-based reaction with high sorption capacity can potentially achieve high system performance compared with other potential salts.

2.2.1.2 Salts for Resorption Configuration

In resorption configuration, the system pressure is determined by both high temperature salt (HTS) and low temperature salt (LTS). When extracting heat from low temperature heat source, the pressure of LTS under low temperature needs to be higher than the pressure of HTS at heat rejection temperature; meanwhile, the HTS equilibrium pressure should be sufficiently high so that the mass transfer is not to significantly hindered as discovered by [65]. Therefore, suitable LTS for the cold operation such as NH_4Cl-3/0 [48, 75] and NaBr-5.25/0 [50] usually locate in the very left of Figure 5. Although the reaction heat of NH_4Cl salt with ammonia is lower than other salts, it has the advantage of low mass density and inexpensive price. $BaCl_2$-8/0 were also used as

the LTS for applications with higher refrigeration temperature [65, 76]. $PbCl_2$-8/3.25 was used by Lepinesse et al. [77] as the LTS in a resorption cold box storage. Goetz et al. [76] also considered using the $PbCl_2$ reaction as LTS, but they pointed out the equilibrium line of $PbCl_2$-8/3.25 is close to the ammonia vapor-liquid line and the system risks condensation in the adsorber during desorption phase. The HTS in resorption systems needs to provide sufficient heat rejection temperature at very low pressure, and therefore they often have medium to high operation temperatures to the right in Figure 5: $NiCl_2$-6/2 [76] and $MnCl_2$-6/2 [48, 65, 70, 75, 77] are often used as HTS.

2.2.1.3 Challenges in Chemisorption Reaction and Sorbent Salt

2.2.1.3.1 Resorption Low-Operating-Pressure Limit

A heating system based on the resorption configuration theoretically has a higher COP than the adsorption configuration under the same operating conditions as simulated by Goetz et al. and Wang et al. [51, 65]. Meanwhile, unlike the adsorption configuration that nearly always operates above atmospheric pressure, the pressure during the LTS desorption in resorption is usually below atmospheric pressure. Such low pressure was found to limit the sorption reaction rate in some studies [65, 76]. Wang et al. [65] tested a $BaCl_2$-$MnCl_2$ resorption system cooling at −5°C, and only 0.33 kg/kg sorption capacity was observed in 20 min of adsorption compared with the theoretical sorption capacity of 0.65 kg/kg. The difference was attributed to the very low pressure (<0.03 MPa) during LTS desorption, which limited the vapor transfer in the sorbent and slowed down the reaction rate. A similar conclusion was drawn by Goetz et al. from detailed simulation that the vapor diffusion in the sorbent at low operating pressures was very limited, reducing the equilibrium drop and the reaction rate [51]. Bao et al. [75] tested a resorption cold box with NH_4Cl/$MnCl_2$ cooling to −25°C. After 3 h, the adsorption reaction progressed to only 31% with 0.29 kg/kg sorption capacity compared with the theoretical 0.9 kg/kg. In contrast, Bao et al. [78] tested resorption refrigeration using the same $MnCl_2$-NH_4Cl pair cooling at −5°C and rejecting heat at 30°C, and a sorption capacity of more than 80% was observed. On the other hand, resorption systems operating around 0.1 MPa were reported by Xu et al. and Jiang et al. [48, 70] with relatively high completion. Goetz et al. [51] set a pressure limit of 0.1 bar for resorption cycle models.

2.2.1.3.2 Hysteresis

As described in the van 't Hoff equation (Equation 1]), the equilibrium vapor pressure of chemisorption reactions is generally considered monovariant as the function of only the sorbent temperature. However, the bivariant behavior, or hysteresis, of the equilibrium of some ammonia-metal halide chemisorption working pairs was identified by Goetz and Marty [79], where the decomposition of ammoniate $MnCl_2$ took a higher temperature to occur than the synthesis reaction under the same pressure. The hysteresis effect of ammonia-halide salt reactions was also reported for $MnCl_2$ [77], $CoCl_2$ [80, 81], $BaCl_2$ [82], LiCl [49], $CaCl_2$ [83], NH_4Cl [83], and $FeCl_2$ [84].

Wu et al. [85] measured the hysteresis of ammoniate $SrCl_2$ adsorption and desorption, where the $SrCl_2$ salt was embedded in porous expanded graphite and kept at 0.615 MPa while its temperature varied between 65°C and 90°C to trigger desorption and adsorption reactions. As shown in Figure 7, when the temperature increases from 65°C, the reactions of $SrCl_2$-8/2 and $SrCl_2$-2/1 start in the desorption direction at ~73°C and 92°C, respectively. However, when the temperature decreases from 95°C, the adsorption-direction reactions start at ~74°C and 70°C, respectively. As highlighted in the figure, there is a 3°C and 18°C difference between equilibrium of the adsorption and desorption of the same reaction.

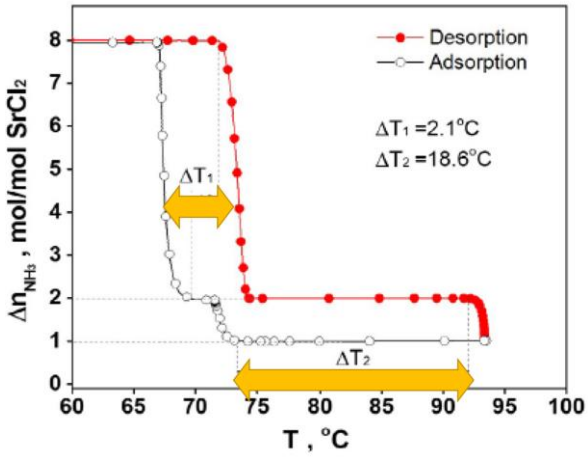

Figure 7. Hysteresis of ammoniate $SrCl_2$ plotted by Wu et al. [85].

Trudel et al. [86] observed a similar behavior when measuring the equilibrium of $CoCl_2$-6/2 reaction. Both Zhong et al. and Trudel et al. attributed the hysteresis to the solid phase change and expansion-contraction of the salt crystal during synthesis-decomposition reactions. The additional

energy required for desorption was connected to the work of expansion of the crystal lattice during adsorption.

Though the hysteresis phenomenon is not yet fully understood, studies have been carried out to model [83] and mitigate [87, 88] the hysteresis effect using a mixture of sorbents NH_4Cl, $CaCl_2$, and $MnCl_2$ with an identified optimal mixing portion for refrigeration operation.

Table 4 lists the reactions used in cold-climate CSHP heating systems in the literature.

Table 4. Summary of chemisorption reactions used in existing cold-climate chemisorption heat pump heating systems.

Salt	Reaction	Max. sorption capacity [kg/kg salt]	Actual sorption capacity [kg/kg salt]	Operating temperatures [°C]	Reference
$CaCl_2$	8/2	0.919	0.6	120/50/−18	Vasiliev 2001 (exp) [47]
$SrCl_2$	8/1	0.751	—	135/55/5	Pons 1999 (sim) [24]
			—	180/55/−15	Pons 1999 (sim) [24]
$MnCl_2$	6/2	0.541	—	240/55/−15	Pons 1999 (sim) [24]
$NiCl_2$	6/2	0.525	—	300/55/−15	Pons 1999 (sim) [24]
NH_4Cl (LTS)	3/0	0.953	0.743	140/70–80/−5–5	Xu 2011 (exp) [48]
$BaCl_2$ (LTS)	8/0	0.654	—	231/50/0	Vasiliev 2001 (exp) [47]
NaBr (LTS)	5.25/0	0.866	—	165/50/−5	Oliveira 2009 (exp) [50]
$MnCl_2$ (HTS)	6/2	0.541	0.332	140/80/−	Xu 2011 (exp) [48]
			—	150/55/5	Pons 1999 (sim) [24]
			—	245/55/5	Pons 1999 (sim) [24]
			—	165/50/−5	Oliveira 2009 (exp) [50]
$NiCl_2$ (HTS)	6/2	0.525	—	240/50/0	Vasiliev 2001 (exp) [47]

2.2.2 Porous Matrix Material

Besides the salt's adsorption capacity and feasible operating temperature and pressure, the performance of the chemisorption system is also significantly influenced by the heat and mass transfer within the sorbent. Conventional pure halide salts are usually available in granular form with limited heat and mass transfer rates. For example, the thermal conductivity of granular $CaCl_2$ and its ammoniates ranges between 0.0065 W/(m·K) and 0.145 W/(m·K) [32, 53]. Moreover, the swelling and agglomeration of the bulk salt during adsorption deteriorates the sorption capacity and vapor transfer across the sorbent [33]. Therefore, composite sorbent materials were developed

that consist of salt and highly conductive porous materials such as activated carbon (AC) and graphite. The composite sorbents demonstrated significant improvement of the sorbent heat and mass transfer performance (e.g., 1.7–17.4 W/(m·K) for expanded graphite-$CaCl_2$ composite sorbent [34, 35]) while also eliminating the mass transfer deterioration due to agglomeration.

Under proper temperatures and pressures, the sorbent salts can react with ammonia vapor upon contact. However, the salt grains have very poor heat and mass transfer performances, and they tend to agglomerate together and create a large nonporous bulk during adsorption, preventing the center salts from reacting with ammonia and reducing the adsorption capacity [23, 89]. The salt grains also swell during adsorption, which could potentially damage the confinement of the heat exchanger.

Porous matrix materials were thus introduced to overcome the issues of the salt grain. The porous matrix materials offer large surface area to host sorbent salts as sites for the vapor-solid reaction. Matrix materials such as expanded graphite have a high thermal conductivity that allows fast heat propagation through the bulk sorbent. The porous matrix also helps mitigate the performance deterioration of ammoniate salt agglomeration and swelling. The composites of the porous matrix and salt during adsorption/desorption reactions are illustrated in Figure 8.

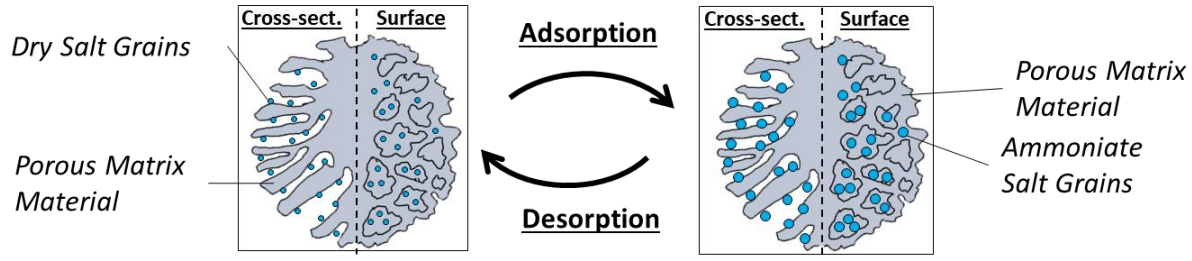

Figure 8. Salt-matrix composite in adsorption and desorption reactions.

The key parameters for a matrix material are therefore its porosity, permeability, and thermal conductivity. The most common porous matrix materials studied and applied in chemisorption systems are expanded graphite (EG) [23, 34, 35, 50, 56, 59, 62, 63, 73, 75, 76, 78, 90-100], AC [33, 64, 69, 71, 72], AC fiber (ACF) [47, 101-105], and other materials including multiwall carbon nanotube (MWCNT) [106, 107] and expanded vermiculite (EVM) [82]. The proper mass ratio

between the salt and matrix material, the composite density, and the direction of consolidation also affect the heat and mass transfer performance of the porous matrix.

2.2.2.1 Expanded Graphite

EG, also referred to as expanded natural graphite (ENG), is prepared by electrochemically and chemically treating (oxidizing) natural graphite to force apart the crystal lattice and create abundant micropores for salt impregnation and channels for vapor transfer. The salt can be embedded into the pores of EG by (1) mixing EG with a salty solution, (2) drying the composite, and (3) compressing the composite as shown in Figure 9. This impregnation procedure is also used in graphite [35, 93] and other composite sorbent preparations.

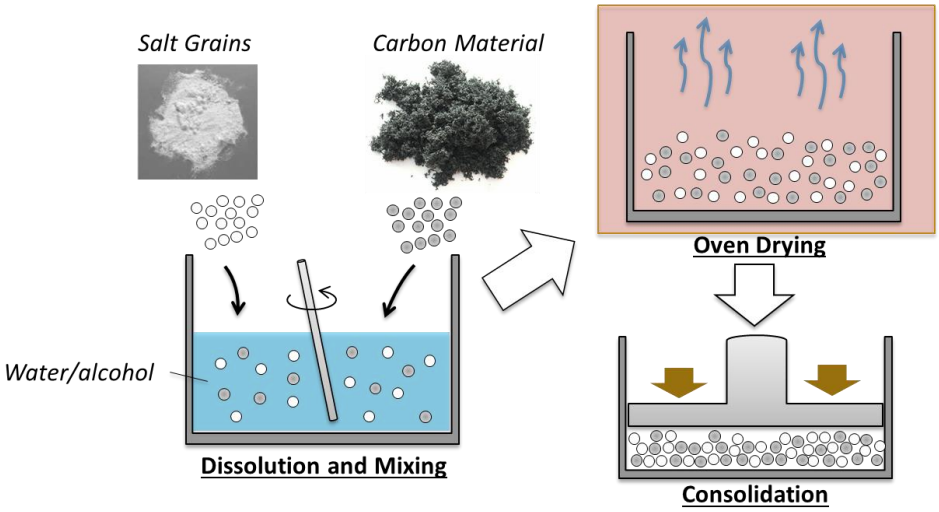

Figure 9. Steps of preparing consolidated salt composite sorbent.

The interconnected flake structure of EG provides high thermal conductivity (4–40 W/m·K) and high gas permeability (10^{-14}–10^{-12} m^2) [108] while the creases of the flakes provide a large surface area to host ammoniate salt. Wang et al. [96] also measured the thermal conductivity of EG without salt to be ~1.7 to 4 W/(m·K).

One of the early EG-based composites, IMPEX, was developed at CNRS-IMP in France and has thermal conductivities as high as 4 to 40 W/(m·K) [23, 90]. The thermal conductivity of the EG-salt composite sorbent is strongly related to the EG/salt ratio and its density after consolidation. Han et al. [91] reported that the effective thermal conductivity of $CaCl_2$ ammoniates increased

with a higher EG ratio, higher density, and more ammonia in the compound. Jiang et al. [92] measured the thermal conductivity of the $SrCl_2$-EG compound ranging from 0.44 W/m·K (500 kg/m^3) to almost 2.94 W/m·K (800 kg/m^3). Wang et al. [93] measured the thermal conductivity of $CaCl_2$-EG composite to be ~7.02–9.2 W/(m·K) at densities of 1,100–1,300 kg/m^3.

Gas permeability, on the other hand, declines with increasing density. Tian et al. [34] reported a decrease of permeability of $CaCl_2$-EG compound from 3.16×10^{-11} m^2 to 8.61×10^{-13} m^2 when the density increased from 400 kg/m^3 to 550 kg/m^3. Han and Lee. [109] measured the permeability of EG composites of $CaCl_2$, $MnCl_2$, and $BaCl_2$ at different densities, EG/salt ratios, and ammoniate states and found a similar trend.

Because EG is inexpensive and the process to embed salt into it is mature, it has been widely used as the matrix material for a variety of sorbent salts in numerous chemisorption systems [34, 35, 50, 56, 59, 62, 63, 73, 75, 76, 78, 92, 94-96].

To further enhance the heat transfer performance of ENG, Wang et al. [97] introduced ENG treated with sulfuric acid (ENG-TSA): the sulfuric acid is first intercalated in the graphite flakes; then, the graphite is exfoliated by heating in a flame to form ENG with densities as low as 5–6 kg/m^3 compared with the normal ENG density of 20–50 kg/m^3 [34]. The sulfuric acid treatment improved the thermal conductivity of the ENG-TSA up to 15.4 W/(m·K) for Jiang et al. [35], and 337 W/(m·K) for Wang et al. [97]. ENG-TSA was further used by Jiang et al. [98, 99] in several experimental tests in which the effect of higher heat transfer capacity was investigated. Zhao et al. [100] reported 45 times higher conductivity and 50% volumetric cooling power enhancement by using the ENG-TSA composite over granular AC for the ammonia-AC physical adsorption system.

Figure 10 shows the scanning electron microscopy (SEM) picture of EG and ENG-TSA from Zhao et al. [100].

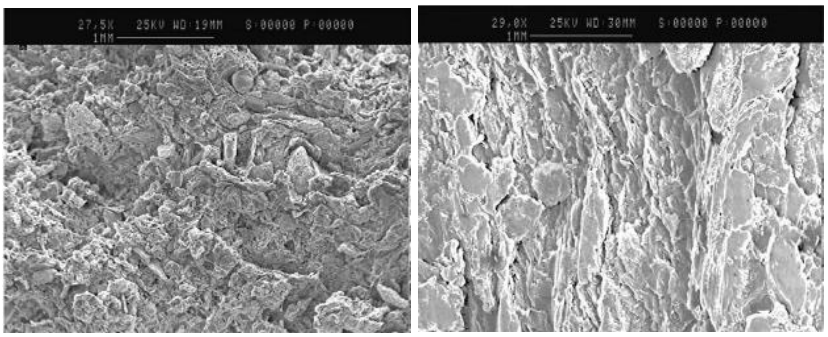

Figure 10. Scanning electron microscopy of expanded graphite (left) and expanded graphite treated with sulfuric acid (right) [100].

For both EG and ENG-TSA, the direction of consolidation compression in the matrix-salt composite significant influences the composite heat and mass transfer performance. The thermal conductivity and permeability of EG [96] and ENG-TSA [97] parallel (disk) and perpendicular (plate) to the direction of compression were measured. Both studies used consolidated graphite without salt embedment, and the results are shown in Table 5. The disk thermal conductivity has a plateau with the increasing density after compression compared with the monotonic increase in plates. The plates of both matrices showed higher thermal conductivity than the disks at similar densities as the microlayers after compression in the plates follow the heat transfer direction [97]. The permeability decreased with higher density as compression reduced pore size and interconnection of pores [96]. As the result, compression perpendicular to the heat and mass transfer direction led to a higher transfer rate, while a higher compression density generally improved thermal conduction but reduced mass diffusion in the sorbent.

Table 5. Anisotropic conductivity and permeability test; illustration generated according to [96, 97].

Sample	**Compression direction***	**Dominant micro-layer direction***	**Expanded graphite [96]**		**Expanded natural graphite treated with sulfuric acid [97]**	
			Thermal conductivity [W/(m·K)]	**Permeability [$\times 10^{-12}$ m^2]**	**Thermal conductivity [W/(m·K)]**	**Permeability [$\times 10^{-16}$ m^2]**
Disk	Parallel	Perpendicular	1.2–1.8	1.9–2.1	<8.9	0.15–11.2
Plate	Perpendicular	Parallel	1.5–4.1	4.5–8.8	<337	1.64–117

*directions relative to the heat/mass transfer direction

The limitation of a chemisorption reaction under low operation pressures presented in Section 3.1.2 was also discussed in the studies of the EG-salt composite sorbents from the matrix material perspective. Lu et al. [90] analyzed the reaction progression of $MnCl_2$ in an EG composite with a validated detailed model and concluded that when constraint pressure gets below 1 bar (0.1 MPa), the sorbent permeability great influences the reaction completion. Because the sorbent permeability decreases with higher density after consolidation, Han et al. [109] suggested using a sorbent with a density below 200 kg/m^3 for low-pressure (i.e., low-temperature) applications to avoid a significantly reduced mass transfer rate. Moreover, Lu and Mazet [110] compared the modeled and measured reaction progression and suggested that the composite permeability varies with the progression of the chemisorption reaction.

2.2.2.2 Activated Carbon

AC is produced from natural materials such as acorn and coconut shells. A typical preparation process starts with crushing and sieving the raw material to control the particle dimension; then, the particles are chemically activated by immersion in salt solutions before being heat-treated at high temperatures; finally, the remaining salt in the particles are rinsed off with acid and distilled water and dried [111]. Such preparation procedure results in a highly porous surface structure, as shown in Figure 11 from Saka [111]. The AC can then be impregnated with sorbent salt to form a consolidated composite through a similar process as described for EG-salt composites.

The AC-salt composites were used in a series of studies on a chemisorption ice making system [64, 69, 71] and a refrigeration system [72] and demonstrated improved sorption performance. Because AC can physically adsorb vapor ammonia as well, using AC as the matrix material for composite sorbent can increase the sorption capacity [33]. However, the thermal conductivity of AC (0.35–0.4 W/(m·K) for granular AC [112]) is considerably lower than EG because of the lack of interconnected plate structure; therefore, composite sorbents using AC are less seen in recent literatures.

Figure 11 illustrates the SEM picture of the microstructure of AC from Saka [111].

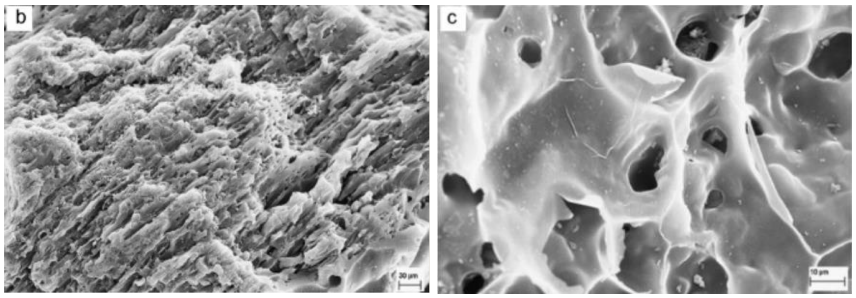

Figure 11. Scanning electron microscopy picture of activated carbon at a scale of 30 µm (left) and 10 µm (right) [111].

2.2.2.3 Activated Carbon Fiber

Carbon fibers (CFs) are fiber-shaped materials containing more than 92% carbon content in a non-graphitic state with a diameter of 5–10 µm [113]. ACFs are prepared from general-purpose CFs by heat treatment to achieve high porosity and well-defined porous structure [114, 115]. The specific surface area of ACFs can be ~2,000 m^2/g [113], making them good candidates to host large amounts of salt for composite sorbent materials.

A single CF has a very high thermal conductivity of 150–1,100 W/m·K [101]. Dellero et al. [101] developed and tested an ACF-$MnCl_2$ composite of the impregnated carbon fiber (ICF) and the graphite fiber intercalation (GFIC). The ICF was prepared by immersing CF in an alcoholic solution of $MnCl_2$ before heating and vaporizing the alcohol to let the salt adhere to the fiber surface. The GFIC was prepared by intercalation of $MnCl_2$ salt into the graphitized fibers. The intercalation process involves impregnating sulfuric and nitric acid in graphite fiber and heating it to a high temperature before impregnating the $MnCl_2$ salt in between the graphite layers. Both ACF-$MnCl_2$ composite sorbents improved in reaction kinetics compared with granular $MnCl_2$. However, it was found that the salt in ICF adhered less to the fiber after a few cycles, and the preparation time was quite long.

The ICF, which has a simpler preparation, was further studied by Dellero and Touzain [102] to improve the transfer performance through compression and fiber arrangement in the adsorber. By balancing the thermal conductivity and permeability, an optimal composite density of ~700 kg/m^3 was identified to achieve the shortest reaction time. Furthermore, because the thermal conductivity

along the fiber is 10 times higher than that across the fiber, the influence of fiber disposition on the reaction rate was studied. The long (30 cm) fibers winding around the adsorber led to a slower reaction compared with short (3 cm) fibers lying radially in the direction of heat transfer.

Vasiliev et al. introduced a $CaCl_2$-ACF composite sorbent using a special type of CF named "Busofit" that has a thermal conductivity of 0.2 W/(m·K) [103]. Later, Vasiliev et al. developed ACF-$NiCl_2$ and ACF-$BaCl_2$ for a multi-salt space cooling system [47]. The ACF provided a uniform distribution of thin (2–3 μm) films of salt on the porous host material surface [104]. Aristov et al. developed a $CaCl_2$-ACF Busofit composite for cooling applications and reported a composite thermal conductivity of 0.2–0.4 W/(m·K) [105]. The SEM of ACF and ACF-salt composite from [116] is illustrated in Figure 12.

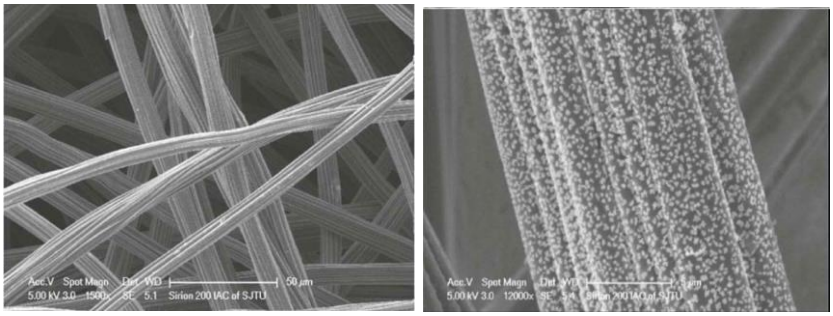

Figure 12. Scanning electron microscopy of activated carbon fiber (left) and activated carbon fiber–$CaCl_2$ composite sorbent (right) [116].

2.2.2.4 Other Matrix Materials

Other matrix materials include carbon nanotubes (CNTs) and expanded vermiculite (EVM). CNTs are molecules of carbon with a cylindrical nanostructure. The high thermal conductivity (W/(m·K)) of CNT makes it a good candidate for composite matrix material with enhanced heat transfer performance. Yan et al. [106, 107] prepared a composite sorbent made of $CaCl_2$ and multi-wall carbon nanotubes (MWCNT) for its macro-porous structure. The MWCNT had an average diameter of 10 nm and length of 10 μm and a specific surface area of 200 m^2/g. The thermal conductivity of MWCNT was 750 W/(m·K) in array form and 15–25 W/(m·K) in film form. The composite was prepared by impregnating the salt into the MWCNT in aqueous solution before drying in the oven. The thermal conductivity of the composite was 1.52 W/(m·K) compared with

the granular $CaCl_2$ thermal conductivity of 0.17 W/(m·K). Moreover, the MWCNT proved to prevent salt agglomeration during adsorption. SEM pictures of the MWCNT from Yan et al. [106] are shown in Figure 13.

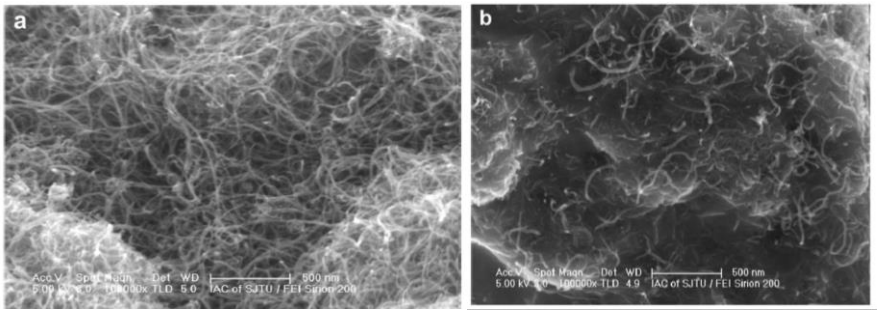

Figure 13. Scanning electron microscopy of multiwall carbon nanotube (left) and multiwall carbon nanotube–$CaCl_2$ composite sorbent (right) [106].

EVM is made by heat-treatment of natural vermiculite, a hydrous phyllosilicate mineral. EVM has a flake structure like expanded graphite, but its thermal conductivity is considerably lower. Zhong et al. [82] prepared EVM with grain sizes of 2–3 mm by immersing EVM with aqueous solution of $BaCl_2$ before drying it under 200°C for 5 h. The composite was then used to test an isothermal adsorption and desorption process. SEM pictures of EVM from Zhang et al. [117] are shown in Figure 14.

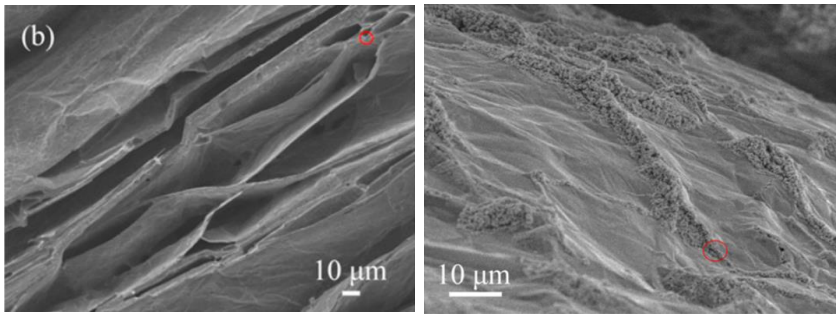

Figure 14. Scanning electron microscopy of expanded vermiculite (left) and expanded vermiculite impregnated with $SrBr_2$ salt (right) [117].

Table 6 compare the thermal conductivity and permeability of granular salt, AC, and composite sorbents using EG and ENG-TSA matrixes. Because of the lack of thermal conductivity and permeability data reported in the literature, ACF, CNT, and EVM composites are not plotted in Figure 15. The granular salt in Figure 15 was measured by Jiang et al. [99] for $CaCl_2$, which

demonstrated very low permeability due to agglomeration. The only known AC data with both thermal conductivity and permeability measurements is from Critoph et al. for consolidated AC sorbent without salt embedment [118].

Compared with granular salt, AC had a higher permeability but lower thermal conductivity. Most data points in Figure 15 and Figure 15. Comparison of thermal conductivity and permeability of composite sorbents. AC = activated carbon; EG = expanded graphite; ENG-TSA = expanded natural graphite treated with sulfuric acid.

Table 6 are EG and ENG-TSA since they have been extensively investigated with both the thermal conductivity and permeability reported in multiple papers. The permeability of a composite sorbent using EG was measured to be one to four orders of magnitude higher than granular salt [34, 92, 109, 119]. The thermal conductivity of EG composites was about 1–3 W/(m·K) [34, 92, 109] and 10–26 W/(m·K) [119]. The ENG-TSA composites generally have thermal conductivities of more than 10 W/(m·K) and slightly lower permeabilities than EG [98, 99]. Figure 15. Comparison of thermal conductivity and permeability of composite sorbents. AC = activated carbon; EG = expanded graphite; ENG-TSA = expanded natural graphite treated with sulfuric acid.

Table 6 shows that the thermal conductivities and permeabilities of the graphite composites are related to their density, salt/matrix mass ratio, sorption quantity, and the consolidation direction. Though the thermal conductivity generally improves with the density as shown by Tian et al., Jiang et al., and Han et al. [34, 99, 119], the permeability suffers with increasing density with narrower vapor transfer channels shown in the same literature. Unlike granular salt where the agglomeration improves thermal conduction, more salt in the composite leads to lower conductivity and slightly higher permeability [34, 98, 99, 119]. As reported by Han et al. [119], the sorption capacity affects the permeability considerably because of the significant change in molecular volume during the chemisorption reaction, while it has little influence on the thermal conductivity.

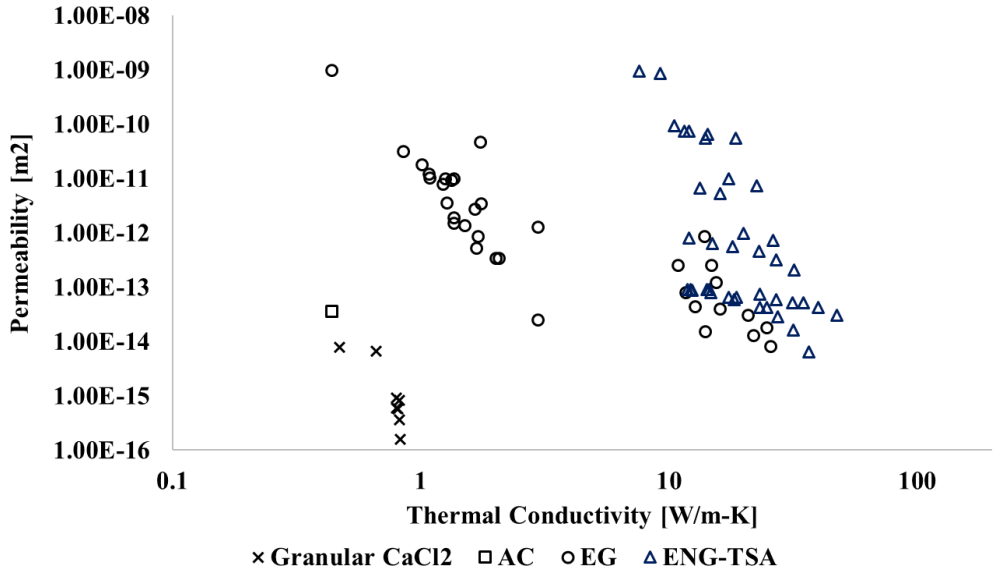

Figure 15. Comparison of thermal conductivity and permeability of composite sorbents. AC = activated carbon; EG = expanded graphite; ENG-TSA = expanded natural graphite treated with sulfuric acid.

Table 6. Thermal conductivity and permeability of composite sorbents.

Reference	**Salt/matrix**	**Salt mass ratio**	**Density [kg/m^3]**	**Sorption quantity [mol/mol]**	**Conductivity [W/(m·K)]**	**Permeability [m^2]**
Jiang 2014 [99]	$CaCl_2$ granular	—	—	1	0.47	7.78×10^{-15}
			—	2	0.66	6.55×10^{-15}
			—	3	0.8	9.26×10^{-16}
			—	4	0.82	8.18×10^{-16}
			—	5	0.8	5.87×10^{-16}
			—	6	0.81	5.78×10^{-16}
			—	7	0.82	3.65×10^{-16}
			—	8	0.83	1.56×10^{-16}
Critoph 2004 [118]	AC	—	—	—	0.44	3.60×10^{-14}
Tian 2012 [34]	$CaCl_2$ EG	50%	450	—	1.66	2.73×10^{-12}
		67%		—	1.23	7.85×10^{-12}
		75%		—	1.09	1.02×10^{-11}
		80%		—	1.01	1.76×10^{-11}
		83%		—	0.85	3.16×10^{-11}
		50%	550	—	1.7	8.61×10^{-13}
		67%		—	1.51	1.36×10^{-12}
		75%		—	1.36	1.90×10^{-12}
		80%		—	1.28	3.58×10^{-12}
		83%		—	1.08	1.19×10^{-11}
Han 2000 [119]	$MnCl_2$ EG	50%	100	6	14.8	2.50×10^{-13}
		50%		2	13.9	8.60×10^{-13}
		30%		6	11.7	8.00×10^{-14}
		30%		2	10.9	2.50×10^{-13}
		50%	150	6	16.1	4.00×10^{-14}
		50%		2	15.5	1.20×10^{-13}
		50%		6	14	1.50×10^{-14}
		50%		2	12.8	4.30×10^{-14}

Table 6 continued

		50%	200	6	21.9	1.30×10^{-14}
		50%		2	20.8	3.00×10^{-14}
		50%	250	6	25.6	8.10×10^{-15}
		50%		2	24.7	1.80×10^{-14}
Jiang 2016 [98][a]	NH_4Cl ENG-TSA	50%	400	—	34.9	5.14×10^{-14}
		67%		—	27.4	2.87×10^{-14}
		75%		—	18.7	6.45×10^{-14}
		80%		—	14.7	8.00×10^{-14}
		83%		—	12.4	8.67×10^{-14}
	$MnCl_2$ ENG-TSA	50%		—	36.6	6.47×10^{-15}
		67%		—	24.8	4.25×10^{-14}
		75%		—	18.3	5.95×10^{-14}
		80%		—	14.5	8.94×10^{-14}
		83%		—	11.9	8.96×10^{-14}
	$CaCl_2$ ENG-TSA	50%		—	31.7	1.63×10^{-14}
		67%		—	23.3	4.24×10^{-14}
		75%		—	17.4	6.45×10^{-14}
		80%		—	14.2	8.94×10^{-14}
		83%		—	12.2	8.96×10^{-14}
Jiang 2014 [99][a]	$CaCl_2$ ENG-TSA	50%	300	—	23.2	7.34×10^{-14}
			350	—	27.1	5.96×10^{-14}
			400	—	31.5	5.20×10^{-14}
			450	—	40	4.23×10^{-14}
			500	—	47.5	3.05×10^{-14}
		67%	300	—	15	6.34×10^{-13}
			350	—	18	5.54×10^{-13}
			400	—	23	4.52×10^{-13}
			450	—	27	3.14×10^{-13}
			500	—	32	2.05×10^{-13}
		75%	300	—	12	8.05×10^{-13}
			350	—	13.3	6.64×10^{-12}
			400	—	16.1	5.20×10^{-12}
			450	—	20	9.66×10^{-13}
			500	—	26.3	7.34×10^{-13}
		80%	300	—	10.5	9.25×10^{-11}
			350	—	12	7.32×10^{-11}
			400	—	14	5.52×10^{-11}
			450	—	17.4	9.84×10^{-12}
			500	—	22.6	7.34×10^{-12}
		83%	300	—	7.6	9.31×10^{-10}
			350	—	9.2	8.51×10^{-10}
			400	—	11.5	7.52×10^{-11}
			450	—	14.3	6.56×10^{-11}
			500	—	18.5	5.42×10^{-11}

[a] data digitized from plot

2.3 Components

The major components in CSHP systems are heat-exchanging vessels, including adsorbers, condensers, and evaporators. An adsorber is a sorbent-containing heat exchanger that allows heat to be transferred between the sorbent and an external heat transfer fluid (HTF) such as water, steam, oil, and others. The condenser and evaporator provide a heat exchange surface for the condensation or evaporation of ammonia and transfer the phase-change heat to the external HTF. The heating/cooling power of the CSHP system depends on effectively providing heat to or extracting heat from the sorbent or the refrigerant. Furthermore, as suggested by Li et al. and Zhu et al. [120, 121], the extra heat associated with the thermal mass of the heat exchangers has significant impact on the CSHP system COP. Therefore, numerous studies have been carried out to improve the design of the adsorber and condenser/evaporator (C/E) to enhance heat transfer performance and reduce the mass of metallic heat exchangers.

2.3.1 Adsorber

In a CSHP system, the sorbent-containing adsorber is the most important component, as it provides heat exchange surfaces for the solid sorbent and heat transfer fluid. The design of the adsorber also determines the length of the ammonia vapor transfer path and the subsequent vapor mass flow rate. Figure 16 is a schematic of general heat and mass transfer in the adsorber. Heat from the HTF transfers through the heat exchanger wall that is in contact with the sorbent block. Meanwhile, ammonia vapor diffuses in the sorbent and flows in and out of the block across openings not in contact with the heat exchanger wall.

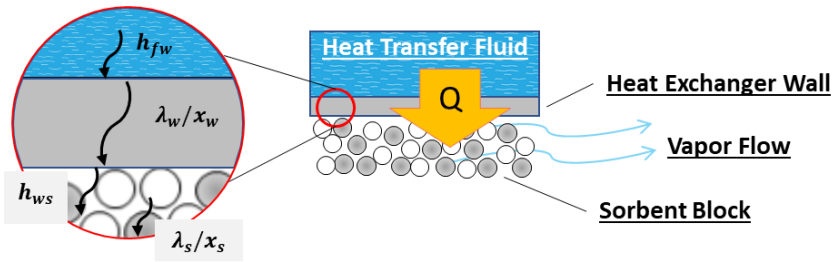

Figure 16. General heat and mass transfer in the adsorber.

The overall heat transfer resistance between the external HTF and the sorbent can be expressed in (6) as the sum of resistance between the heat exchanger wall and the HTF and the sorbent, the

conduction resistance across the heat exchanger wall, and the conduction resistance within the sorbent block.

$$\frac{1}{(UA)_{overall}} = \frac{1}{h_{fw} \cdot A_{fw}} + \frac{1}{h_{ws} \cdot A_{ws}} + \frac{x_w}{\lambda_w \cdot A_w} + \frac{x_s}{\lambda_s \cdot A_s}. \quad (6)$$

In (6), $(UA)_{overall}$ is the overall thermal conductance between the HTF and the sorbent, h_{fw} and h_{ws} are the heat transfer coefficients on the HTF-wall and sorbent-wall surface, A_{fw} and A_{ws} are the heat exchange surfaces on each side, and x_w and λ_w are the thickness and thermal conductivity of the heat exchanger wall, λ_s is the thermal conductivity, x_s is the mean heat transfer path length (average distance of sorbent to the heat exchanger wall), and A_s is the mean heat transfer cross section area (the average cross-sectional area perpendicular to the heat transfer direction). Based on Equation (5), the heat transfer through the adsorber heat exchanger can be improve with larger heat exchange areas, higher heat transfer coefficients, and thinner wall and sorbent mean thicknesses. The increase of the heat exchange area could lead to a decrease of the sorbent thickness and an increase of sorbent cross section area, reducing the heat transfer path length and could affect the mass transfer path length.

To accommodate the incompatibility of ammonia refrigerant with copper, adsorbers and ammonia piping are usually built with stainless steel [55, 122] or aluminum [69]. The salt stays in solid phase in the matrix during operation and therefore poses no corrosion threat to the component materials. The heat transfer resistance across the heat exchanger wall is usually small, and the reduction of metal mass by using thinner heat exchanger walls is limited because the walls need to sustain the pressure difference between the ammonia and HTF loop.

This section presents the designs to improve the heat and mass transfer in the chemisorption adsorbers. Since the consolidated composite sorbents do not experience swelling and expansion during adsorption, the enhancement designs proposed in physical adsorption adsorbers using adsorbents of similar form factors (e.g. consolidated porous material such as activate carbon) in [118, 123-125] are also included. These physisorption adsorber designs could provide beneficial reference for designing high-performance chemisorption adsorbers, but they have not been proven on chemisorption systems. In general, two approaches have been followed to enhance adsorber heat transfer in the literature: (1) increase the heat transfer area (A_{fw} and A_{ws}) by using an

extended exchange surface such as a finned tube and flat plate, and (2) improve the heat transfer coefficients (h_{fw} and h_{ws}) at the heat exchanger surface by using heat pipe.

2.3.1.1 Increasing Adsorber Heat Exchanger Surface Area

2.3.1.1.1 Chemisorption Adsorbers

Adsorbers in early CSHP studies [79, 126] used a simple annular design in which the sorbent is molded into an annular shape and placed in a cylindrical adsorber shell as in . The sorbent transfers heat with the external HTF through the adsorber shell, and the ammonia vapor flows across the sorbent to the vapor channel in the center. Wrapped electric heating coil [79] and a water/oil bath [35, 55] were used to maintain the sorbent temperature.

Finned tube heat exchangers are inexpensive to manufacture and provide a large heat exchange surface area; therefore, they are also popular choices for adsorbers, usually with a cylindrical pressure vessel as the shell with multiple tube-and-fin heat exchangers inside, as shown in Figure 17. Thin fins are crossed by several tubes or welded on individual tubes to increase the heat transfer surface. The sorbent material is filled around the tube and between the fins, and the heat transfer fluid flows in the tube. This type of adsorber was used in a few experimental studies [61, 68, 127, 128], and the systems using the shell-and-tube adsorbers achieved 115–245 W/kg system specific cooling power (SCP) . The chemical adsorbent needs to be filled between the fins and often covered with wire mesh to secure the sorbent while allowing the ammonia vapor to pass through [61].

2.3.1.1.2 Physisorption Adsorbers

Improvement of the annular design was proposed in physical adsorption systems. To increase the heat transfer area of the annular adsorbers, fins were added inside the adsorber. Critoph et al. built and tested an annular adsorber where the monolithic carbon powder and thin aluminum plates were compressed to form a compact plate-fin structure in close contact with the stainless steel cylinder wall for enhanced heat transfer (Figure 17) [129, 130]. SCP of 218 W/kg based on the carbon adsorbent mass was achieved using this type of adsorber. Tube-fin heat exchanger design was also used in physical adsorption systems such as [131]. Plate heat exchangers were used in a few physical adsorption systems. A serpentine-shaped plate heat exchanger was built by Tchernev et al. [125, 132] from folded 0.1 mm thin metal foil with pumped heat transfer fluid flowing inside

the plates for a high heat transfer rate (Figure 19, left). Critoph and Metcalf [118] developed a detailed simulation model for a plate-type adsorber (Figure 19, right). Thin carbon plates were bonded on the space between stainless steel heat exchanger plates, with small gaps between the carbon plates to allow free flow of ammonia vapor. The thickness and dimensions of the carbon plates were optimized using the model for a high SCP and COP.

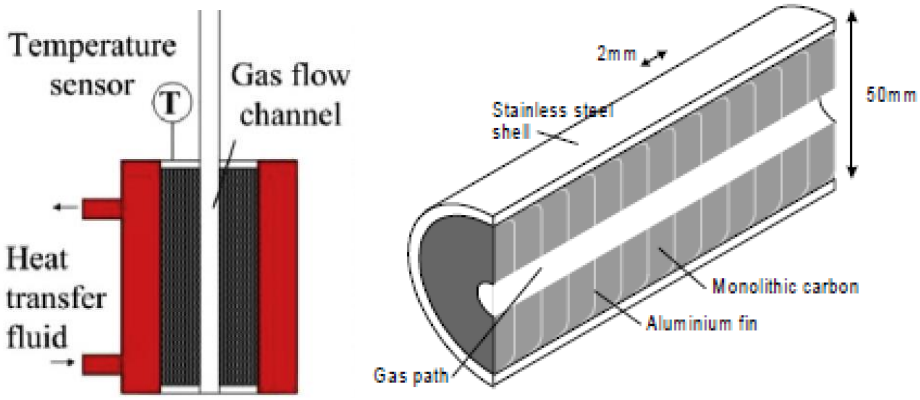

Figure 17. Annular adsorbers without fins (left [35]) and with fins (right [130]).

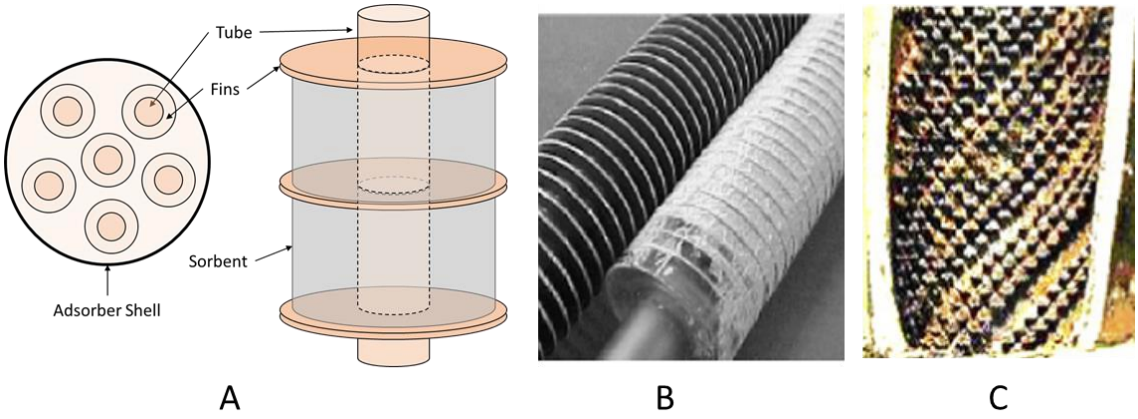

Figure 18. Tube-fin-type adsorber. A—schematic; B—sorbent-filled tube-fin heat exchanger [131]; C—3D fins inside tube (Lu et al. [69]).

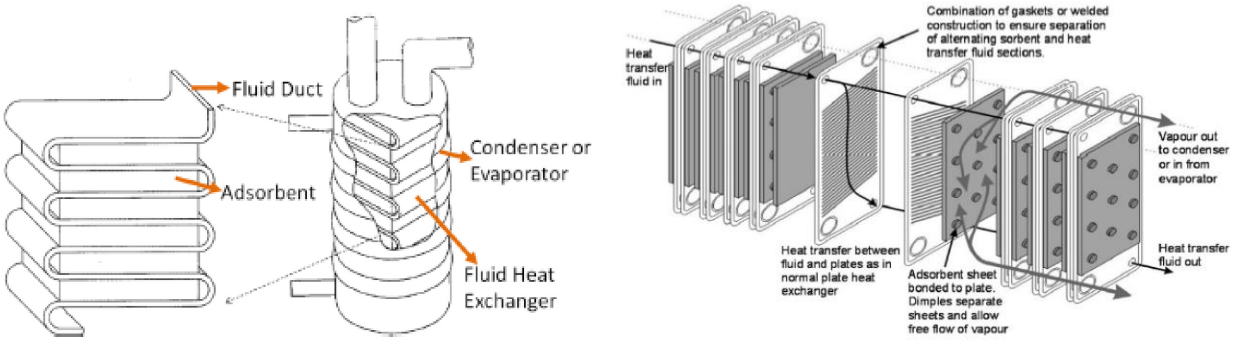

Figure 19. Flat-plate adsorber design by Tchernev et al. (left [125, 132]) and Critoph and Metcalf (right [118]).

2.3.1.2 Enhancing Adsorber Heat Transfer

Apart from increasing the heat transfer surface area of the adsorber heat exchanger, heat pipes using two-phase heat transfer principles were also used in CSHP adsorbers to provide high heat transfer capacity. Critoph [133] discussed the pros and cons of using heat pipe versus pumped HTF in the adsorber. The benefit of using pumped HTF is that the pumping pressure can be controlled to equalize the pressure on both sides of the heat exchanger, allowing thin heat exchanger walls. On the other hand, adding a pump reduces the system's reliability and simplicity. In contrast, a thermosyphon heat pipe can operate without a pump and achieve a high heat transfer rate. The major drawback of a heat pipe in an adsorber is that the large pressure difference usually leads to thick heat pipe walls and thus, large thermal mass. Since the adsorber needs to be heated during desorption and cooled during adsorption, different heat pipe designs were implemented to provide the alternating heating and cooling: reversable heat pipe, hybrid heat pipe/HTF, and multiple heat pipe designs.

2.3.1.2.1 Chemisorption Adsorber

The design of reversable heat pipes switching the hot and cold ends of the heat pipe was used in several CSHP systems. Vasiliev et al. [104] built a heat pipe adsorber with horizontally installed heat pipes to allow two-way heat transfer. Heating elements at the outer end of the heat pipe generated steam to heat the adsorber in the heating phase; in the cooling phase, cold water passes through the outer end of the heat pipe and the induced evaporative cooling in the adsorber. Split-type heat pipes were used in a series of studies using CSHP to make ice for a fishing boat [33, 66, 71, 72, 134]. The steam heat pipes were used to transfer heat from the diesel engine exhaust gas to

the sorbent for desorption with an average heat transfer coefficient of 155.8 W/m^2·K. Finned tube adsorbers in these systems were then cooled by evaporating liquid water in the heat pipe at low pressure during adsorption. The liquid level and pressure in the heat pipe between two operating modes was controlled by a pump. Depending on the temperatures of the available heat and selected sorbent salt, the use of methanol and water as the heat pipe medium was discussed [122].

The hybrid heat pipe/HTF design uses the heat pipe effect for heating and a circulating HTF for cooling the adsorber. Li et al. [68] pointed out that the split-type heat pipes involved significant steam pressure difference between heating and cooling modes and that the heat pipe pressure was very low during cooling. Instead, pumped water was proposed for cooling to operate at more stable pressures. The hybrid heat pipe/circulated HTF design was also used by Alyousef et al. [135] with a valved heat pipe for transferring solar heat to the adsorbers for desorption, and circulating cooling water in a separate loop for cooling the adsorber.

In addition to heat pipe designs, Lu et al. [69] used heat exchange tubes with internal 3-D fins as shown in Figure 17 to further enhance the heat transfer between the HTF and the heat exchanger wall. On the other side of the heat exchanger wall, the chemisorption sorbents need to be prefabricated into disks or blocks and inserted into the heat exchanger. Therefore, good contact is needed to reduce the heat resistance on the sorbent-metal surface. Even though the consolidated composite sorbent is considered to eliminate the swelling effect during adsorption, Lu et al. [110] reported that the heat transfer coefficients at the sorbent heat exchanger varied between 40 W/m^2·K and 3,000 W/m^2·K during adsorption and attributed it to the expansion and contraction of the sorbent block.

2.3.1.2.2 Physisorption Adsorber

In addition to the two heat pipe designs, multiple heat pipe design using separate heat pipes operating at different temperature ranges for heating and cooling was proposed for physical adsorption systems. Critoph et al. [136] contrived an adsorption refrigerator using two sets of heat pipes with water and pentane outside a circular adsorber to transfer heat from the heat source to support desorption. In a different design, Critoph built an aluminum circular adsorber with a steam heat pipe in the center for heating and an R22 heat pipe surrounding the sorbent for cooling [137].

To enhance the heat transfer between the sorbent and the heat exchanger walls in the physical adsorption systems, sorbents such as zeolites were directly coated on the surface of the heat exchanger [138-140] to reduce the contact heat resistance between the sorbent and the heat exchanger walls.

Table 7 provides a summary of different adsorber designs in literature.

Table 7. Summary of adsorber designs and performances.

Reference	Adsorption type	Heat exchanger	Heat transfer method	Average heat transfer coefficient [W/m^2·K]	
				Heating	Cooling
[55]	Chemical	Tubular shell	Circulated oil	—	—
[64]	Chemical	Finned tube	Reversable steam heat pipe	150–200 ([141])	
[122]	Chemical	Finned tube	Reversable steam heat pipe	109.3	105.1
[122]	Chemical	Finned tube	Reversable methanol heat pipe	90.1	84.8
[104]	Chemical	Finned tube	Reversable steam/HFC heat pipe	—	
[69]	Chemical	Finned tube with inner 3D fins	Steam heat pipe	204.9	208.8
[68]	Chemical	Finned tube	Hybrid steam heat pipe (H)/pumped water (C)	745.4 ([141])	832.6 ([141])
[135]	Chemical	Finned tube	Hybrid steam heat pipe (H)/pumped water (C)	—	—
[137]	Physical	Finned tubular shell	Separate steam (H)/R22 (C) heat pipe	—	—

2.3.2 Condenser/evaporator and Integrated Component Design

Compared with the adsorbers where designs considerations encompass the sorbent and the external heat source, the condenser/evaporator (C/E) operates under a simpler premise. With adequate heat transfer surface between ammonia phase change and the pumped HTF, the novel designs of the C/E focus on reducing the thermal mass and vapor transfer path. Furthermore, integrated designs

combining the adsorber and C/E into a single vessel for modular system capable of continuous operation have also been investigated.

The separate condenser and evaporator in [68] were integrated into a connected component with the condensate flows from the top condenser down into the evaporator/reservoir, and the ammonia vapor in and out the component shares one passage, reducing the thermal mass compared with using two separate vessels.

Further integration of the C/E combines it with the adsorber to create even more compact component with less thermal mass and short vapor transfer path between the sorbent and the condensing/evaporating surface. Iammak et al. [142] integrated the adsorber, condenser, evaporator, and liquid refrigerant reservoir in one annular tube as shown in Figure 20. The refrigerant vapor condenses when cooled in the condenser, and the condensate accumulates in the evaporator/reservoir at the bottom. When the adsorber section is cooled, the liquid refrigerant vaporizes and flows upward into the adsorber.

Jaehnig et al. [143] integrated the C/E under the adsorber by separating the cylindrical vessel into two compartments. The whole system was packed in a single pressure vessel where the water-silica gel working pair is used for thermal storage. The liquid level in the C/E is controlled to avoid emersion of HX and improve heat transfer.

Tchernev [125, 132] integrated the adsorber with the condenser/evaporator by using the cylindrical wall of the adsorber as the heat transfer surface of refrigerant condensation to reduce the vapor transport resistance between the adsorbent and the condenser/evaporator, as well as to eliminate the need for a separate condenser/evaporator component.

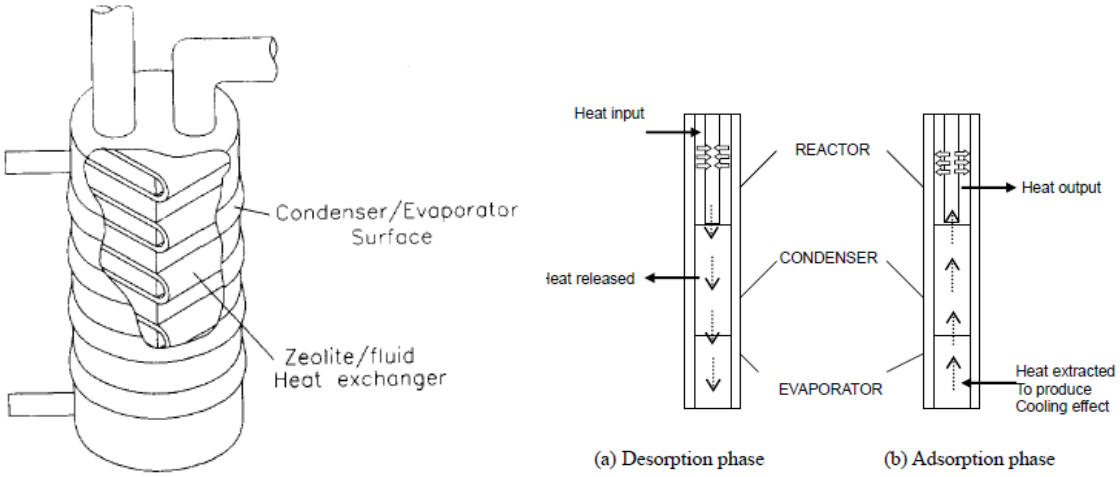

Figure 20 Compact condenser-evaporator design (left drawing referred to [125], right drawing referred to [142])

2.4 Cycle and System

Although enhancing the heat and mass transfer in the sorbent material and heat-exchanging components can improve system performance with faster and more complete reactions, the thermodynamic performance of a CSHP system is largely determined by its cycle configuration. Based on the heat source of the chemisorption reactions in the systems, CSHP cycles can be categorized into single-effect, double-effect, and other configurations. By arranging the chemisorption reactions in adsorption or resorption arrangements, numerous cycle configurations have been investigated for CSHP applications by simulation [24] and experiment [47, 48, 50]. This section summarizes the configuration and performance of these CSHP cycles and systems.

2.4.1 Single-effect Cycles

Single-effect CSHP cycles take external high-temperature heat directly for desorption heat in all adsorbers. Depending on the how the chemisorption reactions in the adsorber(s) are arranged, single-effect systems can be further categorized into combined condenser-evaporator (SCCE), separate condenser and evaporator (SSCE), and resorption (SRES). Figure 21 shows the generic operation of single-effect cycles. For SCCE and SSCE cycles, pure ammonia is the low-temperature (LT) material and salt is the medium-temperature (MT) material. Similarly, for SRES cycles, the LT is the LTS, and MT is the HTS. At high pressure, MT takes in high-temperature

heat from the heat source and desorbs to give off ammonia. The high-pressure ammonia vapor is condensed (in SCCE/SSCE) or adsorbed (in SRES) and rejects useful heat. Once the system gets to low pressure, useful heat is extracted from the MT and the system starts to adsorb vapor ammonia. The ammonia in LT is released, taking in LT heat from the cold ambient.

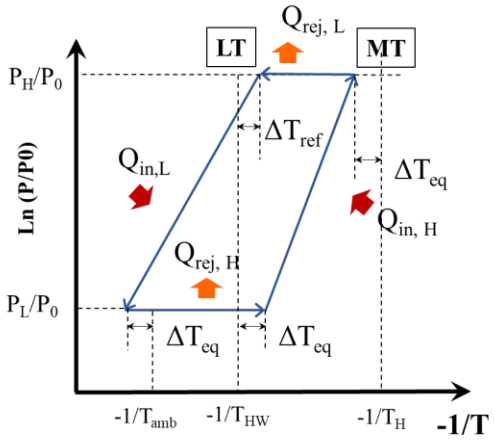

Figure 21. Clapeyron chart of typical single-effect cycles

2.4.2. Single-Effect Combined Condenser-Evaporator and Single-Effect Separate Condenser and Evaporator Cycles

SCCE is the most basic chemisorption cycle, described in Figure 4 as an adsorber coupling with a single phase-change heat exchanger alternately acting as the condenser and the evaporator under high and low pressures. SCCE has been studied for chemisorption cooling applications [50, 51, 57, 68, 73] with a cooling COP of ~0.3. The low COP was attributed to the heat loss caused by the temperature swing of the sorbent and the heat exchanger metal, which reduced the COP by 10–20% [44]. Therefore, few SCCE cycles were used for cold-climate heating in which the temperature swing heat loss could be exacerbated by the large temperature lift.

The SSCE configuration, as shown in Figure 22, avoids repeated heating and cooling of the combined C/E during the operating cycle switches by using separate and dedicated heat exchangers for condensation and evaporation. Although the two adsorbers are alternately heated and cooled by external heat, the hot ammonia vapor always condenses in the condenser, and the liquid ammonia always vaporizes to take in LT heat in the evaporator. Thus, the SSCE cycle avoids the

heat losses and the associated COP reduction in the repeated heating and cooling of the condenser and evaporator.

The ideal COP of SCCE and SSCE cycles according to Equation 2) are shown in Eq. (6) assuming $Q_{des} = Q_{ads}$ [121]. Since the reaction heat of desorption and adsorption reactions are similar, and both are about twice the vaporization heat of ammonia [44, 51], the ideal heating COP of SSCE and SCCE is 1.5 [51].

$$COP_{ht,SSCE/SCCE} = \frac{Q_{ht}}{Q_{in}} \approx \frac{Q_{cond}+Q_{ads}}{Q_{des}} = 1 + \frac{H_{fg,NH3}}{\Delta H_{reaction}}. \quad (7)$$

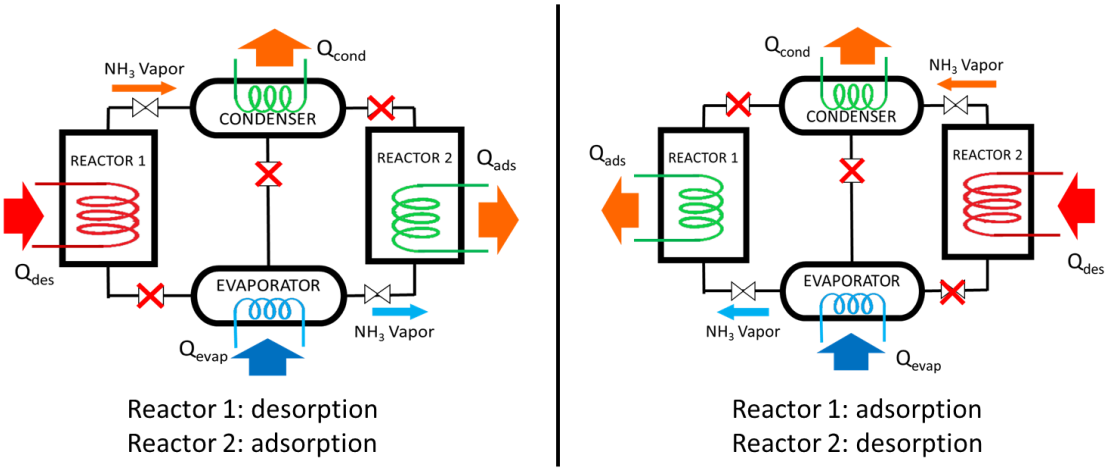

Figure 22. Typical configuration and operating modes of a single-effect separate condenser-evaporator cycle.

Pons et al. used an analytical model developed by Stitou et el. [36] that was verified against an established phenomenological model and validated with experimental data to simulate CSHP heating systems in an SSCE configuration based on a $SrCl_2$-8/1 reaction [24]. The heating COP was between 1.31–1.35 at a heating temperature of 40°C and between 1.21–1.23 at a heating temperature of 55°C. The SHP at 40°C was ~450 W/kg and below 300 W/kg at 55°C. The low ambient temperature of −15°C required a high heat input temperature of 170–185°C, compared with a 135°C heat source for 5°C ambient. Vasiliev et al. [47] built and tested an SSCE system based on $CaCl_2$ reactions and an ACF Busofit matrix and reported heating COP of 1.43 under 50°C heating and −18°C evaporation.

It is worth mentioning that type-II heat pump (heat transformers) can also be assembled in SCCE [144] and SSCE [145] configurations and used for heating in cold climate. The "Heat from Cold" cycles introduced in uses methanol instead of ammonia as the refrigerant, and elevates heat from the ambient of 2-20°C up to 35-50°C with typical COPs below 1.0 [144, 145]. These new cycles have the potential to be applied using ammonia as the refrigerant.

2.4.3. Single-Effect Resorption Cycle

The SRES direct couples two different chemisorption reactions where the system extracts heat from the LT ambient through the desorption reaction of LTS and supplies heat via the adsorption reactions of both LTS and HTS at high temperatures (Figure 23). The ideal COP of a SRES cycle according to Equation 2) is calculated in Eq. (7) with all heat input and output based on chemisorption reaction heat [44, 51] [121]; the ideal heating COP of SRES is 2.0 [51].

$$COP_{ht,SRES} = \frac{Q_{ht}}{Q_{in}} = \frac{Q_{ads,HTS}+Q_{ads,LTS}}{Q_{des,HTS}} \approx 1 + \frac{\Delta H_{LTS}}{\Delta H_{HTS}}. \quad (8)$$

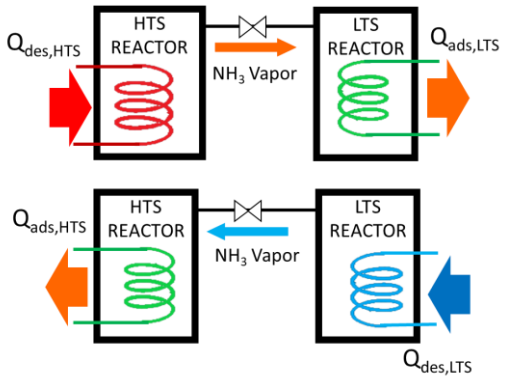

Figure 23. Single-effect resorption cycle.

SRES cycles have been studied to produce high-temperature heating under subfreezing ambient conditions. However, because of the temperature and operating pressure limits on LTS, the minimum ambient temperature for resorption systems is usually above −10°C. Oliveira [146] calculated the heating COP of SRES using thermodynamic property data of several working pairs. For $CaCl_2$-$MgCl_2$ and $ZnCl_2$-$NiCl_2$ pairs, the heating COP was 1.75 and 1.79, respectively. For

$CaCl_2$-$CoCl_2$ working pair with simultaneous cooling at 5°C and heating at 65-75°C, the calculated cooling COP was 1.0 and heating COP was 2.9~3.3 depending on the heat source temperature.

Pons et al. [24] simulated an SRES system using $MnCl_2$-$BaCl_2$ as the working pair, and the system supplying 40–55°C heat under 5°C ambient achieved a COP above 1.52 and an SHP of 370 W/kg. Vasiliev et al. [47] tested a resorption system using $NiCl_2$ as the HTS and $MnCl_2$ as the LTS. The system produced 50°C heating and cooling at 0°C with a heating COP of 1.44 and an SHP of 350 W/kg. Xu et al. [48] tested $MnCl_2$-NH_4Cl resorption systems for heating above 70°C with only the HTS adsorption reaction, while the LTS desorption took heat from the 0°C ambient. With cycle times of more than 6 h, the chemisorption reactions approached completion, and the heating COPs with only HTS adsorption heat were above 0.92. Oliveira et al. [50] conducted similar tests with an $MnCl_2$-NaBr pair with HTS adsorption producing heat at 55°C, and the heating COP was 0.9.

2.5 Double-Effect Cycles

When salts with different operating temperatures are used with ammonia condensing and evaporating, a double-effect system can be formed by directing the adsorption heat of HTS to drive the desorption reaction of the medium-temperature salt (MTS), thereby reducing the heat demand from a high-temperature heat source and improving system COP. Double-effect cycles involve three different reactive materials; thus, their generic operations can be described on the Clapeyron chart, as in Figure 24, with LT representing the ammonia in adsorption cycles and the LTS in resorption cycles, with the other two equilibrium lines representing two different salts.

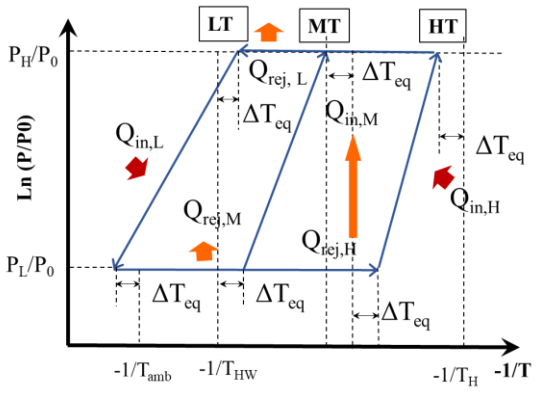

Figure 24. Clapeyron chart of typical double-effect cycles.

Figure 24 illustrates the generic operation of double-effect cycles. The HTS and MTS in double-effect cycles operate in opposite phases; that is, when the HTS desorbs ammonia by the heat from a high-temperature heat source, the MTS absorbs ammonia either from evaporation or desorption of LTS. Once the operating modes of the two salts are switched, the adsorption heat of the HTS, which is at higher temperature than the desorption threshold of the MTS, is used to directly drive ammonia out of the MTS.

Therefore, with the same HTS desorption heat input from the heat source, double-effect cycles can produce heating with condensation and adsorption in multiple components, leading to an elevated thermal COP. The ideal heating COP of the double-effect separate condenser-evaporator (DSCE) and double-effect resorption (DRES) are calculated in Eq. (8) and Eq. (9) [121]:

$$COP_{ht,DSCE} = \frac{Q_{ht}}{Q_{in}} = \frac{Q_{cond,HTS}+Q_{cond,MTS}+Q_{ads,MTS}}{Q_{des,HTS}} \approx 1 + \frac{2 \cdot H_{fg}}{\Delta H_{HTS}}. \quad (9)$$

$$COP_{ht,DRES} = \frac{Q_{ht}}{Q_{in}} = \frac{Q_{ads,MTS}+Q_{ads,LTS-HTS}+Q_{ads,LTS-MTS}}{Q_{des,HTS}} \approx 1 + \frac{2 \cdot \Delta H_{LTS}}{\Delta H_{HTS}}. \quad (10)$$

However, because of the added system complexity, most studies on multiple-effect cycles are via the simulation approach, with only a few physical systems constructed and tested. The configuration of the double-effect corresponding cycles of DSCE and DRES are shown in Figure 25.

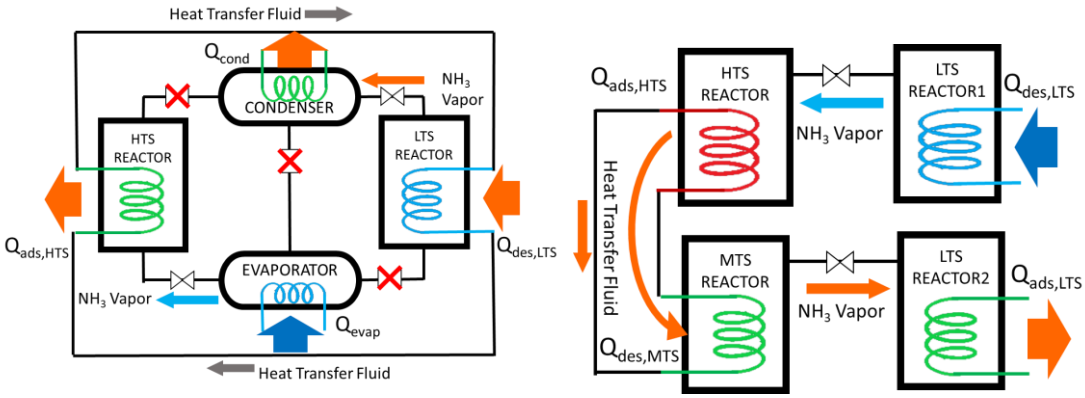

Figure 25. Configuration and operation of double-effect separate condenser-evaporator (left) and double-effect resorption (right).

Oliveira [146]calculated the heating COP of 2.27 for a DSCE system based on thermodynamic properties of CaCl2-FeCl2 working pair under supplying heat of 75-90°C and ambient of 25°C. Pons et al. [24] simulated the performance of a DSCE heat pump system using $MnCl_2$ as the MTS and $NiCl_2$ as the HTS. The system required a heat source above 280°C and achieved heating COP above 1.43. The temperatures of the heat rejection and cold ambient had little impact on the heating COP, while the colder ambient of −15°C compared with 5°C reduced the SHP from above 300 W/kg to 140 W/kg. The SHP is about half of the SSCE system simulated under the −15°C ambient conditions.

A DRES heat pump was also simulated by Pons et al. [24] for producing heating under 5°C ambient temperature. The DRES heat pump used $NiCl_2$, $MnCl_2$, and $BaCl_2$ as the HTS, MTS, and LTS and achieved a heating COP of above 1.9. The SHP was also about half compared with SRES systems operating under similar conditions.

The simulation and experimental studies on the CSHP heating systems are listed in Table 8 and Table 9.

Table 8. Simulation studies of chemisorption heat pump heating systems by Pons et al. [24].

Configuration	Salt	Temp [°C]	Temp lift [°C]	COP	SHP [W/kg]
SSCE	$SrCl_2$	135/40/5	35	1.35	450
		170/40/−15	55	1.23	290
		135/55/5	60	1.31	430
		185/55/−15	70	1.21	290
SRES	$MnCl_2/BaCl_2$	130/40/5	35	1.55	380
		150/55/5	60	1.52	370
DSCE	$MnCl_2$-$NiCl_2$	280/40/5	35	1.45	350
		285/40/−15	55	1.44	140
		295/55/5	60	1.45	320
		290/55/−15	70	1.43	140
DRES	$MnCl_2$-$NiCl_2/BaCl_2$	230/40/5	35	1.92	220
		250/55/5	60	1.90	210

Table 9. Experimental studies of chemisorption heat pump heating systems.

Reference	Configuration	Salt	Temp [°C]	Temp lift [°C]	COP	SHP [W/kg]
Vasiliev 2001 [47]	SSCE	$CaCl_2$	120/50/−18	68	1.43	850
	SRES	$NiCl_2/BaCl_2$	140/50/0	50	1.44	—
Xu 2011 [48]	SRES	$MnCl_2/NH_4Cl$	140/75/0	75	0.95[a]	35
			145/75/0	75	0.95[a]	36
			140/80/0	80	0.92[a]	24
			140/70/−5	75	0.95[a]	29
			145/80/5	85	0.95[a]	35
			140/80/0	80 (11 h)	0.96[a]	16
			140/70/−5	75 (10 h)	0.95[a]	18
Oliveira 2009 [50]	SRES	$MnCl_2/NaBr$	165/50/−5	55	0.90[a]	—

[a] Considering only high-temperature salt adsorption heat

The comparisons of COP and SHP in different studies are shown in Figure 26. For ambient temperatures below −10°C, only conventional adsorption configurations (i.e., SSCE and DSCE) are viable, with double-effect systems having a higher COP. At a higher ambient temperature around 0°C, resorption configurations (i.e., SRES and DRES) become available and achieve higher COP than adsorption configurations. The SHP, on the other hand, is affected by the temperature lift defined as the temperature difference between heat rejection and cold ambient. Generally, single-effect systems have higher SHPs than double-effect systems. The two adsorption systems (SSCE and DSCE) with a dip in SHP at 55°C and 70°C were simulated under −15°C, indicating that the SHP was also affected by the ambient temperature.

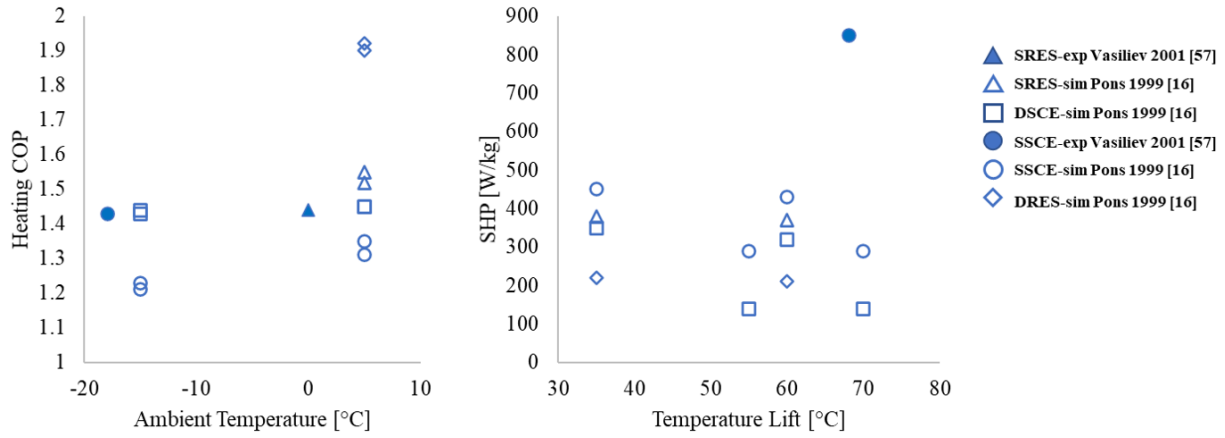

Figure 26. Coefficient of performance (COP; left) and specific heating power (SHP; right) of chemisorption heat pump heating systems under different ambient temperatures and temperature lifts.

2.6 Research Gap and Contribution of This Study

The research gap for cold-climate chemisorption heat pump technology can be summarized at three levels: material, component, and system.

On the material level, most of the existing studies of chemisorption reaction and materials focus on the salts suitable for refrigeration or heat transformation applications, i.e. the well-studied salts works well at either absorbing heat at low temperature and releasing heat at room temperature, or absorbing heat at room temperature and releasing heat at a very high temperature. Either of these are typical operating condition for cold-climate heating applications, which requires heat absorption at low temperature and release at high temperature. Therefore, multiple-stage reactions using the same salt across a wide temperature range with significantly higher specific sorption capacity are preferred for the heating application. Compared with widely studied CaCl2-8/4/2 reactions, the LiCl-3/2/1/0 reactions can achieve lower evaporating temperature, has higher specific sorption capacity, but it has not been studied thoroughly, especially for the heating application. This study characterizes the chemical kinetic properties of the LiCl-based reactions with a series of specially designed experimental tests, and further investigates the transient behavior and performance of the LiCl-based system via both experiment and dynamic simulation. The methodology of identifying the chemical equilibrium and kinetic coefficients from test data

as well as the identified values in this study provide reference for future studies on this material. The measured and tested system operation of such as system fill the blank of LiCl-based system performance in the literature.

On the component level, a novel adsorber based on a hybrid heat pipe plate heat exchanger is used in this study. Unlike conventional adsorbers with annular or tube/tube-fin heat exchangers, this new adsorber combines the benefit of plate heat exchanger and heat-pipe phase-change heat transfer for heat supply, while the heat extraction is done by switching to circulating water mode. Despite all the theoretical advantages of the plate heat pipe heat exchanger, few studies were found to report the performance of such design. In this work the actual performance of this novel adsorber is experimentally measured under different ambient temperature, heat input rate, heat pipe temperature, etc. for operating with chemisorption working pairs. Furthermore, a detailed dynamic model is developed and validated to describe the heat and mass transfer and chemical reaction in the adsorber as well as the interaction with the heat pipe steam. Parametric analysis was conducted using the model to identify optimal design parameters for the adsorber. The detailed dynamic adsorber model also offers a great tool to further investigate different design factors on the performance.

On the system level: the performance of a CSHP system in cold-climate heating application has been modeled by several paper in the literature with promising COP, but the actual performance was not confirmed with experimental measurement. This study assembles a complete CSHP heating cycle and conducted multiple tests to measure the operation and performance. The dynamic system model is developed to extend the operating and design conditions to very low ambient temperature. The measured and simulated results points to the optimal design and control parameters. Furthermore, the configuration of paring the adsorber with a combined condenser-evaporator which also works are the reservoir for the condensed ammonia liquid was much less studied in the literature especially via experiment. By using the test data and validated system dynamic model, the operation, performance, and potential improvement of the combined condenser-evaporator configuration can be identified and adding to the limited published results.

3. RESEARCH OBJECTIVES AND METHODOLOGY

3.1 Research Objectives and Approach

The goal of this thesis study is to enhance the understanding of the multi-stage LiCl-ammonia chemisorption reactions and the dynamic of heat pump systems based on the reactions; identify optimal design and develop strategies to improve the performance for cold-climate heating applications.

The goal is accomplished through modeling and experimental approaches on three levels:

- Material level: experimentally test and identify chemical equilibrium and kinetic parameters of the multi-stage LiCl-ammonia reactions.
- Component level: develop and validate dynamic model based on fundamental transfer equations and chemical kinetics, identify optimal component design.
- System level: experimentally measure the system performance, develop, and validate dynamic system model to analyze energy flow and simulate system performance under cold climate conditions, identify optimal system design and strategy for COP improvement.

3.2 Thesis Organization

Following the objectives of the study, the organization of the thesis study is illustrated in Figure 27.

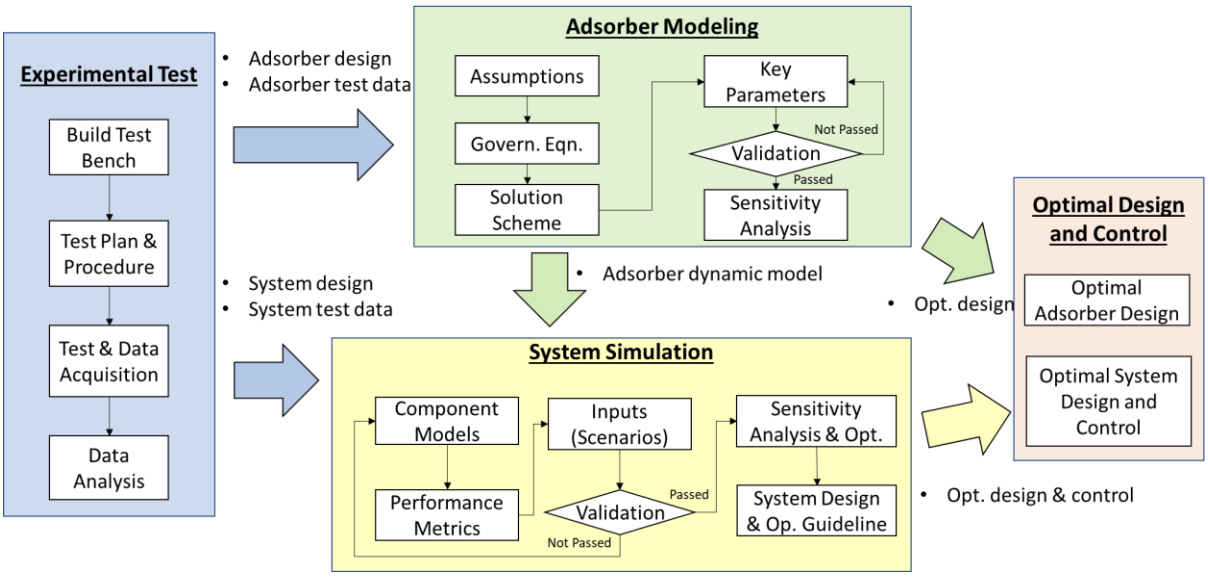

Figure 27 organization of the thesis study

The following chapters will describe the experimental and modelling works that have been carried out to achieve the research objectives. Chapter four will introduce the experimental test of the prototype CSHP system. The prototype assembly as well as the test bench and apparatus will be described, followed by test result and data analysis. Chapter five will focus on development of the transient adsorber model. The finite-difference method is applied to simulate the time-dependent heat and mass transfer inside the sorbent block in the adsorber, coupled with the progression of the chemisorption reaction. The assumptions, governing equations, solving scheme, and results of the adsorber model will be introduced. The key chemical equilibrium and kinetic coefficients are fitted using experiment data. The adsorber model will be validated against test data and used to analyze the impact of design parameters. Chapter six will introduce the transient system model developed based on the dynamic models of the adsorber as well as the other components in the system. The governing equations of key components are described, followed with validation and simulation results. Chapter seven summarizes the key findings and achievement in this thesis study, and lists the future work recommended to further the study. Chapter eight lists publications and publication plans based on the thesis research. Finally, all the references in the document can be found at the end of document.

4. EXPERIMENTAL TEST

4.1 Test Goal

The goals of experimentally test include:

(1) Experimentally investigate the performance of a prototype CSHP system.
(2) Calibrate the component parameters for component and system model development and validation.

The experimental tests were carried out on a prototype CSHP at ORNL. In this chapter, the test setup is first introduced, followed by the test design and performance metrics, and finally the test results are presented and analyzed.

4.2 Test Setup

The test setup includes (1) the CSHP prototype, (2) the hydronic system, and (3) the DAQ and control system. Figure 28 illustrates the test setup in the environmental chamber at ORNL. The packaged CSHP prototype is located to the left, and the hydronic system kart is to the right carrying the heat transfer fluid (HTF) pumps, flow meters, heat exchangers, and motorized valves. The fan coil for exchanging heat between the HTF and the chamber air is connected to the hydronic kart and located next to it. The National Instrument DAQ modules and chassis along with the power supply and safety switches of the entire testbench are mounted at the front of the hydronic kart.

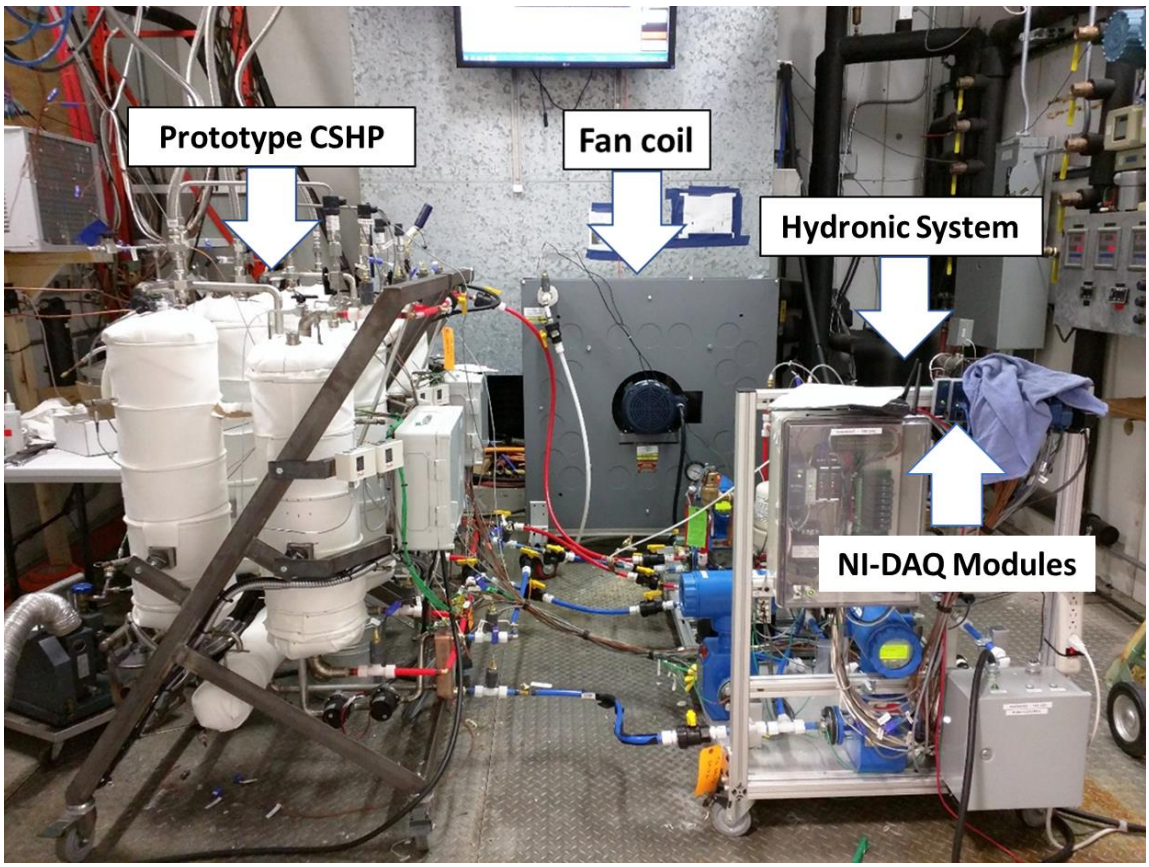

Figure 28 experimental setup in the environmental chamber at ORNL

4.2.1 CSHP Prototype

The CSHP prototype includes two identical sorption modules. Each sorption module comprises two pairs of adsorber-condenser/evaporators and a hybrid heat pipe system as shown in Figure 29. The adsorbers and condenser/evaporators are plate-shell heat exchangers enclosed in stainless-steel pressure vessels. The hybrid heat pipe system includes a gas-fired steam generator, water pumps, a water tank, and a heat exchanger. The heat exchangers in the two adsorbers in the same module are connected to the hybrid heat pipe system located at the bottom of the sorption module. The heat exchanger in the condenser-evaporators are plumbed to the hydronic system. The adsorber contains the sorbent salt in between the heat exchanger plates. The adsorber and the condenser-evaporator are connected via an open vapor channel. The materials and masses of different parts in the CSHP system are listed in Table 10.

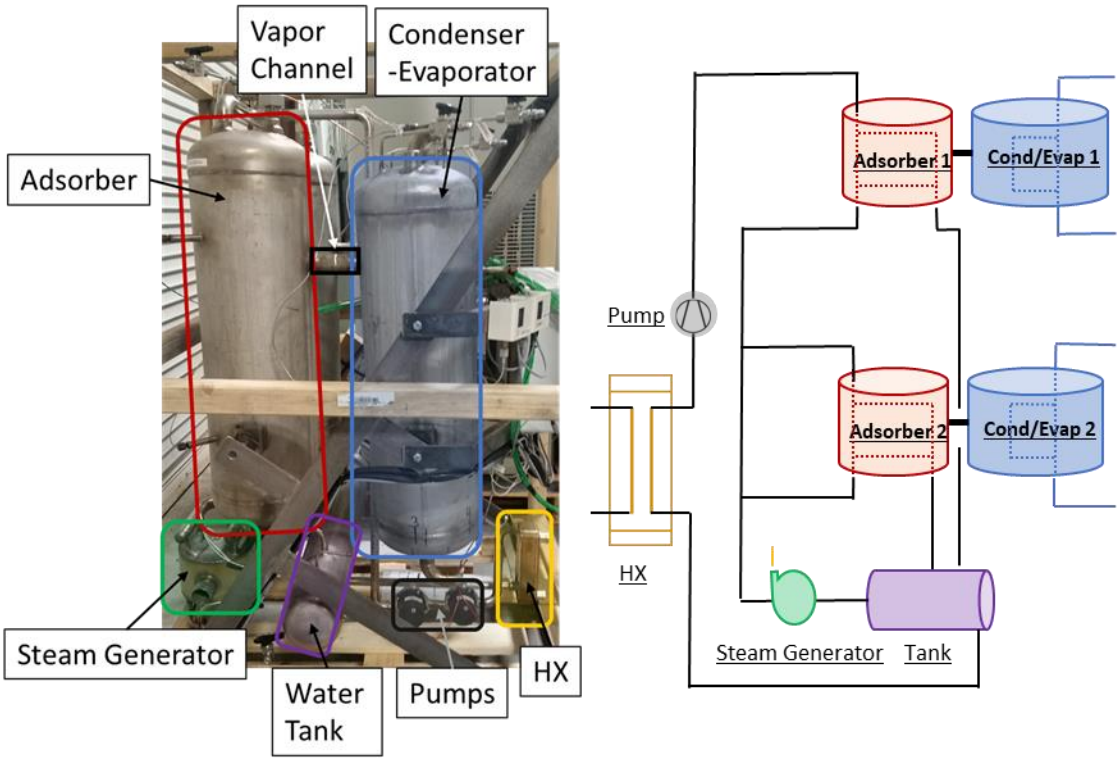

Figure 29 Photograph (left) and schematic (right) of one sorption module in the CSHP prototype

Table 10 Material, mass, and thermal mass of the components in the CSHP prototype (2 sorption modules)

Component	Material	Mass [kg]	Specific heat [kJ/kg-K]	Thermal mass [kJ/K]
Sorbent	Salt-in-carbon matrix	8.8	1.5	13.2
Refrigerant	Ammonia	8.4	4.8	40.32
Adsorber HX	Stainless steel	32	0.5	16
Adsorber Shell	Stainless steel	96	0.5	48
CE HX	Stainless steel	32	0.5	16
CE shell	Stainless steel	96	0.5	48
Heat pipe fluid	Water	16	4.18	66.88

The CSHP operates in two alternating modes: desorption and sorption. In desorption mode, the hybrid heat pipe operates as a conventional heat pipe with natural gas combusted in the steam generator (burner) to boil water from the water tank and generate steam; the steam flows into the heat exchange plates in the adsorbers and condenses; the salt in the adsorber is heated and releases ammonia vapor which flows into the condenser-evaporator and condenses to finally providing heat

to the end use; the steam condensate in the adsorber plates accumulates and flows by gravity into the water tank at the bottom.

The sorption mode starts with ammonia condensed in the condenser-evaporator and the salt in the adsorbers hot and “dry”. The burner is shut off, and the water pump is turned on to flood the steam channels in the adsorber heat exchange plates and circulate water between the adsorber and the heat exchanger; the salt is cooled by the circulating water and absorbs ammonia vapor, driving the liquid ammonia in the condenser-evaporator to evaporate and extract heat from cold ambient; The circulating water passes the sensible and absorption heat from the salt to the heat exchanger to provide heat to the end use. The system can switch back to desorption mode once the liquid ammonia in the condenser-evaporator is exhausted.

4.2.2 Hydronic System

As shown in Figure 30, the hydronic system consists of four heat exchangers (HX), two HTF pumps, check valves to switch between loops, as well as motorized and solenoid valves to modulate the pump flow directions and flow rates. The hydronic system can be divided into two loops: condenser-evaporator loop and heat load loop.

The heat load loop runs through three HX and is also plumbed to the hybrid heat pipe in the CSHP prototype. The heat load HX simulates the heat load of the residential building by transferring heat from the CSHP-generated hot HTF to the city water. In desorption mode, valve-6 is closed, and valve-4 is open to direct the flow through the HX-1 and the HX-2. The HX-1 recovers heat from the flue generated by the burner during natural gas combustion. The HX-2 connects the heat load loop and the condenser-evaporator loop and operates during desorption mode of the CSHP system to pass the heat generated in the condenser-evaporator to the heat load. In sorption mode, valve-4 is closed, and valve-6 is open, and the flow is circulated between the hybrid heat pipe in the CSHP and the heat load HX. The flow rate of this loop is modulated by valve-5 directly after the pump.

The condenser-evaporator loop circulates HTF between the condenser-evaporators in the prototype CSHP system and the HX-2 in desorption mode and the fan coil in sorption mode. In desorption mode, valve-1 is open, and valve-2 is closed, and the condensing heat is transferred from the condenser through the HX-2 and eventually to the heat load HX. When the CSHP system is in sorption mode, velve-1 is closed, and valve-2 is opened. The HTF flows between the

condenser-evaporator and the fan-coil to extract heat form the chamber air. The flow rate of this loop is modulated by valve-3 on the by-pass line of the pump.

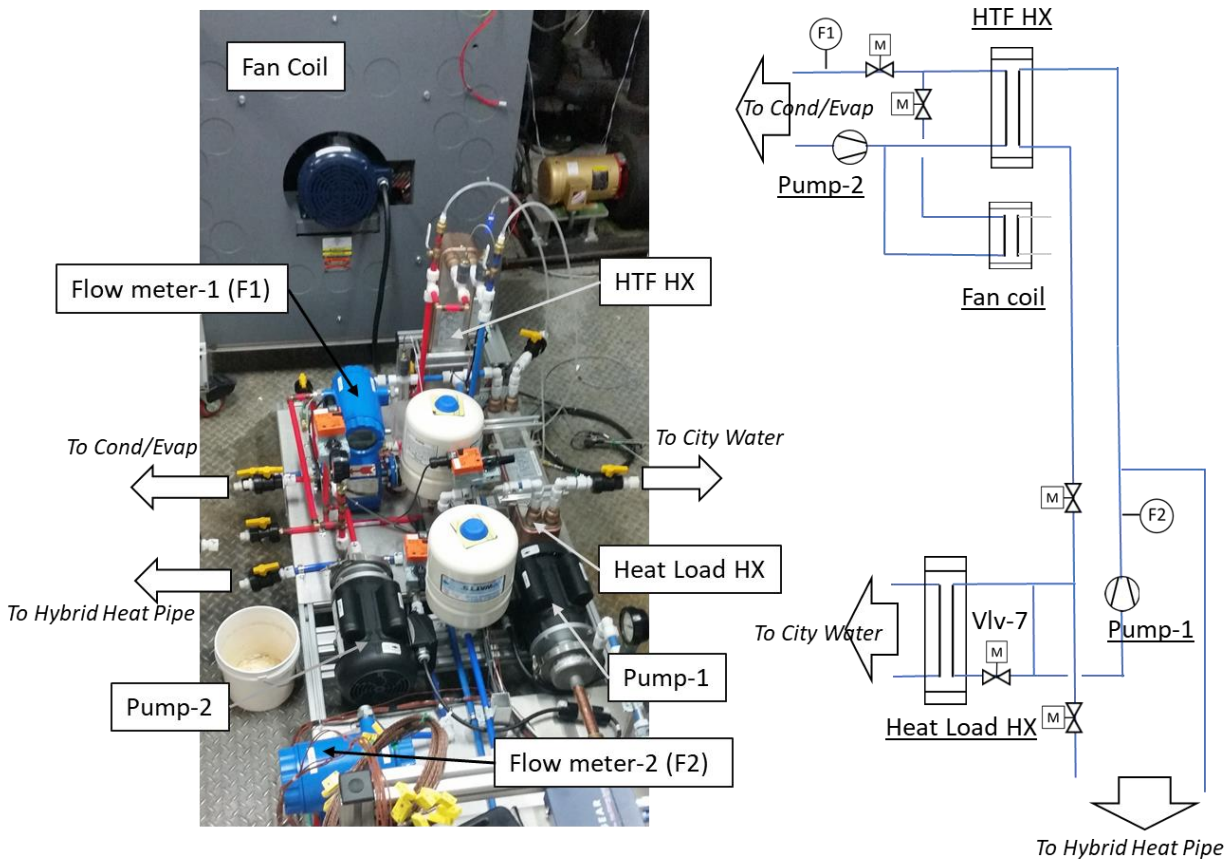

Figure 30 picture and schematic of the hydronic system

4.2.3 Setups and P&ID

The prototype CSHP system was tested in three setup configurations under different operating conditions and controls. The P&ID of each of the four configurations and their testing purposes are briefly described below.

- Setup #1

Setup #1 was designed to investigate individual adsorber-condenser/evaporator pairs in the sorption module to acquire component-level data. The P&ID of Setup #1 as in Figure 31 includes one sorption module and the hydronic system with three heat exchangers. Setup #1 was operated at room temperature (23^{o}C).

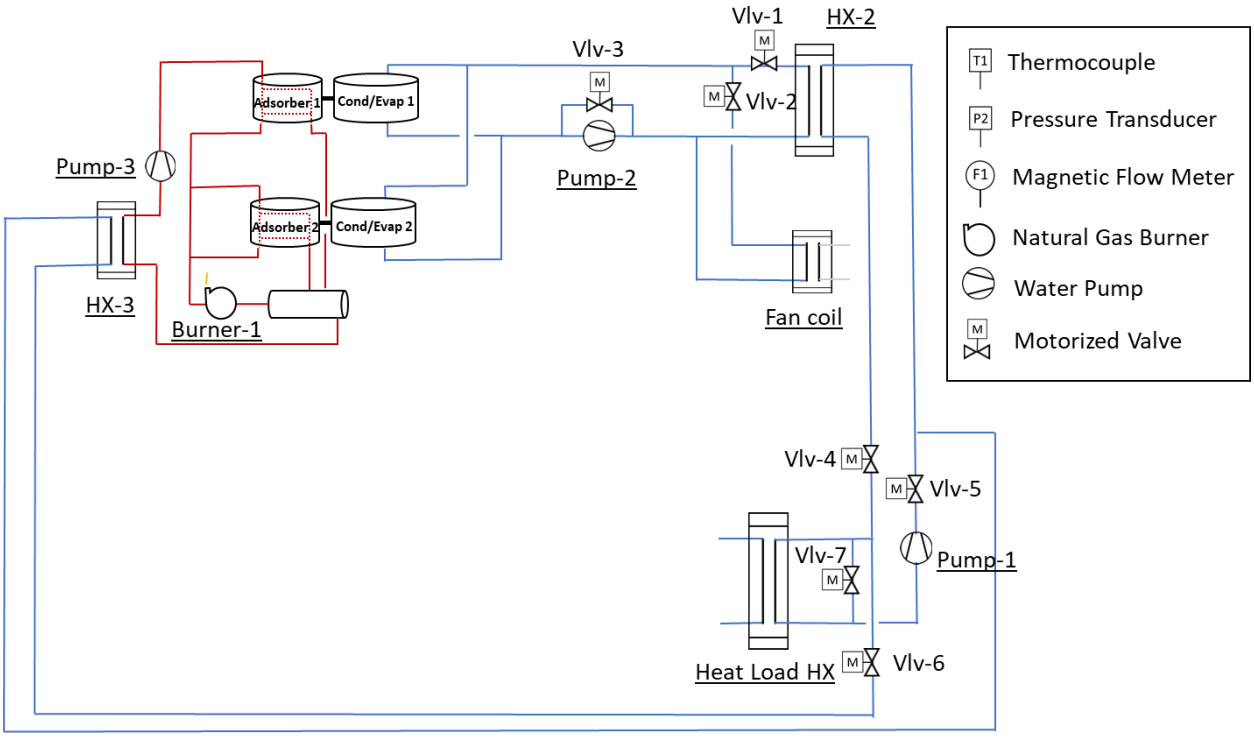

Figure 31 P&ID of setup #1

- Setup #2

Setup #2 as in Figure 32 added a flue gas heat exchanger to the hydronic system to recover the heat from the combustion flue gas and to pre-heat the pump-2 loop HTF at the start of the desorption mode. Setup #2 was operated at room temperature (23^{o}C).

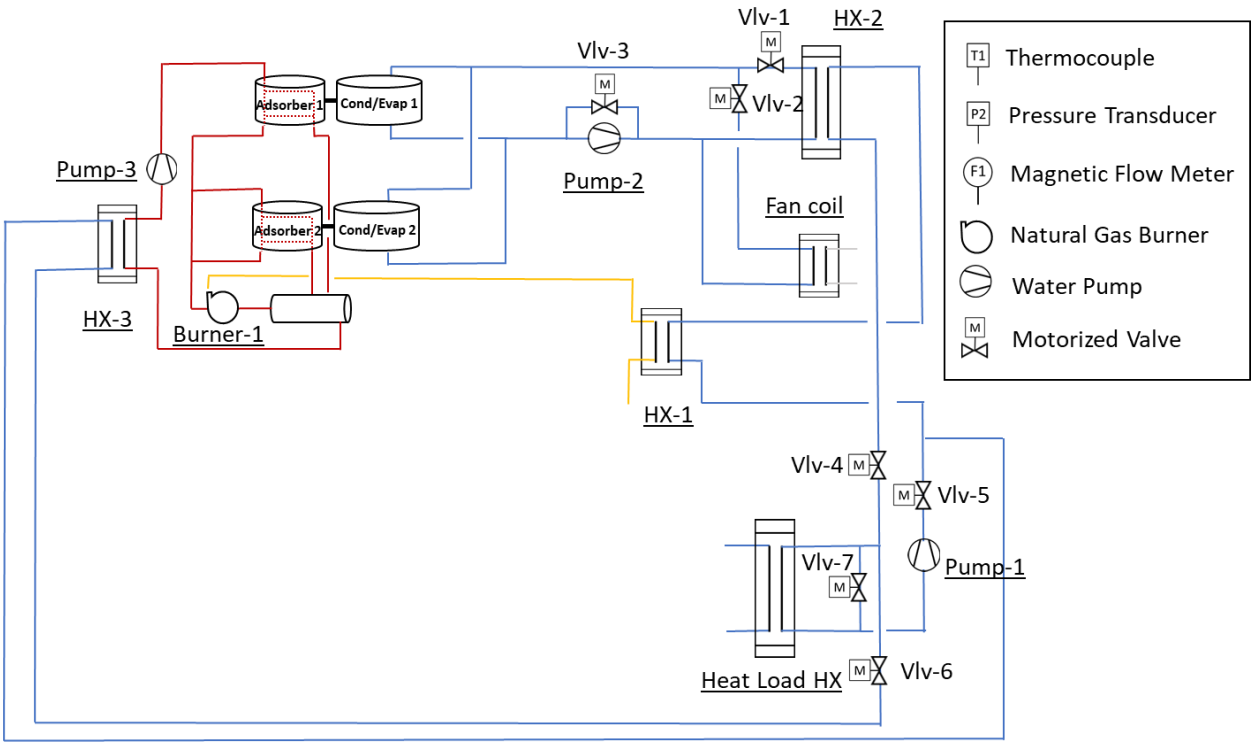

Figure 32 P&ID of setup #2

- Setup #3

Setup #3 as in Figure 33 includes two sorption modules with both plumbed to the hydronic system in parallel. Setup #3 is the baseline setup for cycle performance and was tested under cold temperature (8^{o}C).

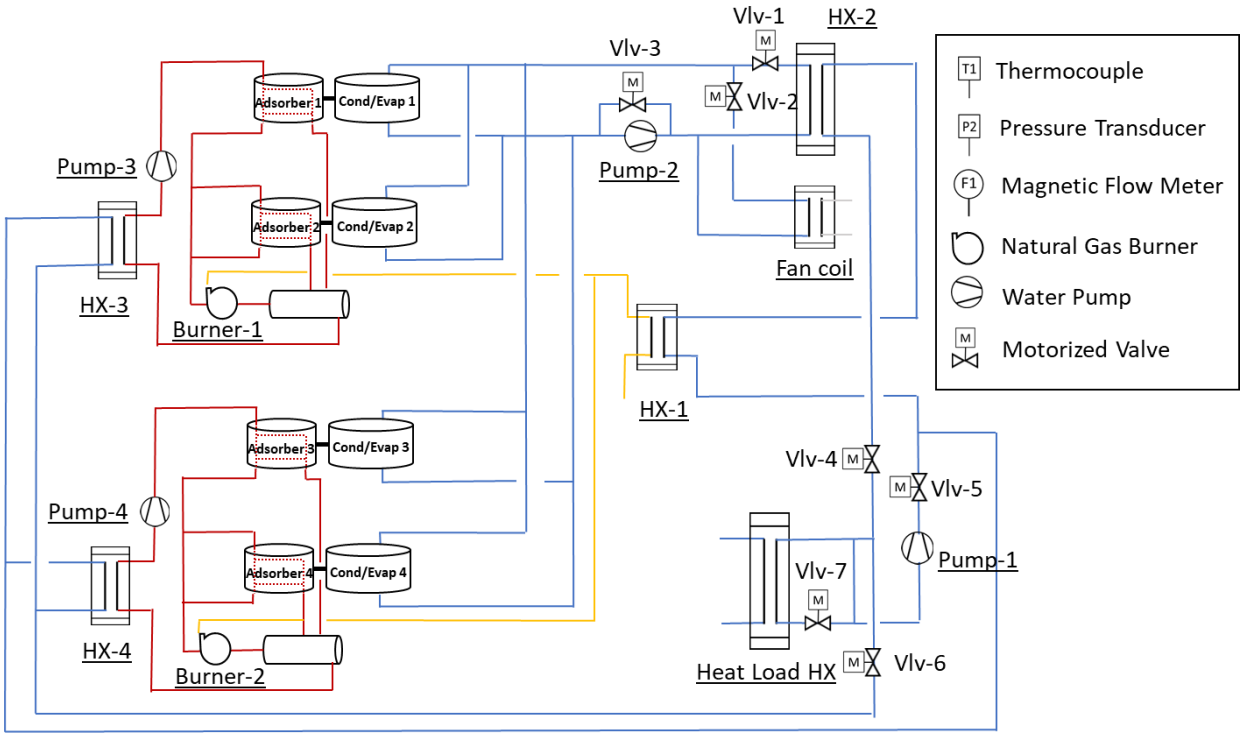

Figure 33 P&ID of setup #3

4.2.4 Data Acquisition (DAQ) System

Various sensors are mounted on the prototype system to measure the temperatures at different state points, pressures in each sorption module and heat pipe, flow rates of liquid as well as natural gas stream, and status of the ambient air. Most of the temperature measurements are thermal couples, and 6 RTDs are used to measure the key temperatures that are used to calculate the heat flux for performance evaluation. The locations of the sensors are indicated in Figure 34 and the summary of different types of sensors installed on the prototype are listed in Table 11.

Table 11 summary of sensors installed on the CSHP prototype testbench

Measurement	Sensor type	Model	Count	Accuracy
Temperature	Thermocouple	Omega TMQSS	32	±0.5°C
	Thermistor	Vaisala HMP-60	2	±0.6°C
	RTD	Omega P-M-1	6	±0.08°C
Mass flow rate	Magnetic	Tek-Trol Tek-Flux	3	±0.5%
Volume flow rate	Pulse counter	Campbell Scientific	1	±1%
Ammonia Pressure	Transducer	Wika S-10	4	±10.34 kPa
Steam pressure	Transducer	Omega PX419	2	±2.76 kPa
Relative humidity	Thermistor	Vaisala HMP-60	2	±3%

Besides the sensors listed above, additional sensors were installed for safety protection (e.g. to make sure operation stays below the pre-set maximum temperature/pressure in streams as well as vessels), and they are not shown in the schematics. Furthermore, mechanical burst disks are installed in both the ammonia vessels and steam heat pipes as the last-resort safety insurance in case of over-pressure. Once burst, the hot steam will be vented into buckets near the prototype, while the ammonia will be directly vented outside of the building.

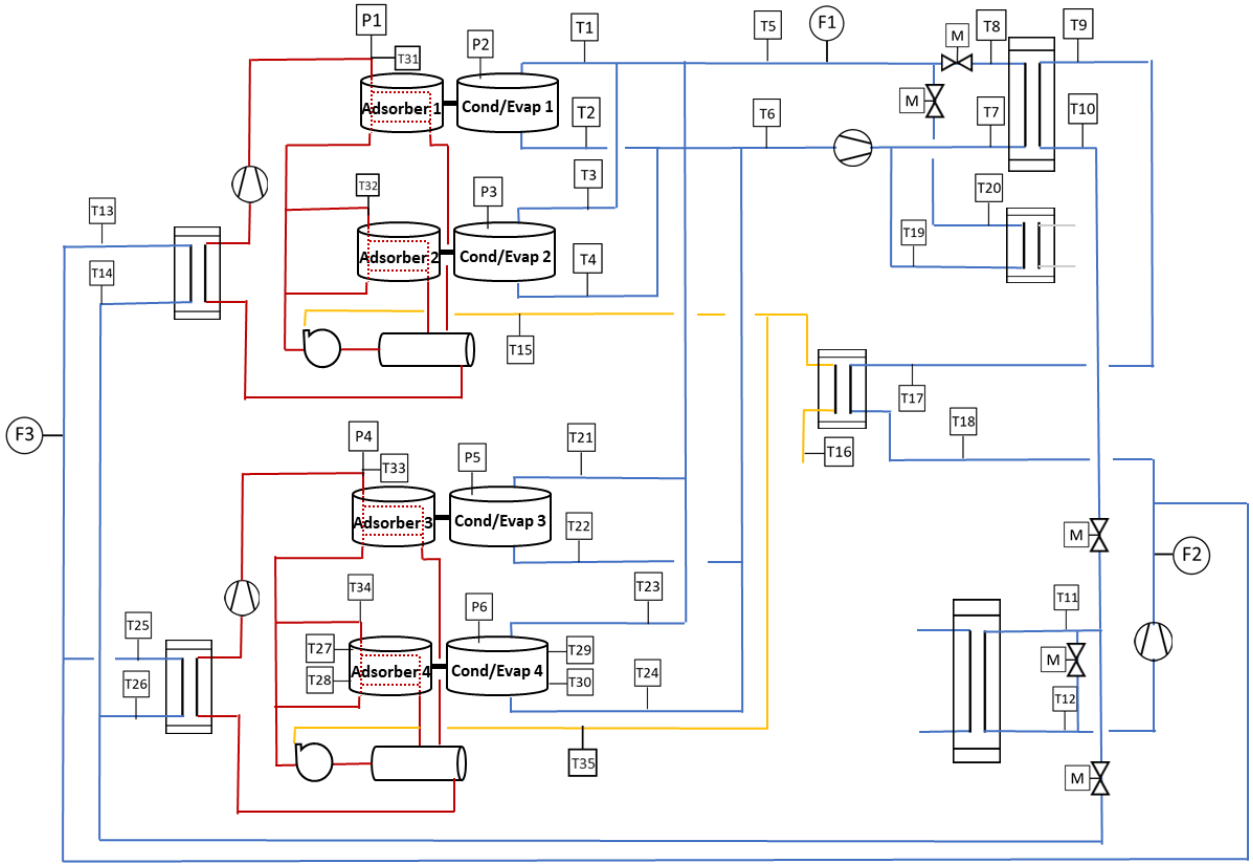

Figure 34 Sensor locations in the test bench

All the sensors are wired to 8 National Instrument (NI) modules (3 NI-9214 TC temperature input modules, 1 NI-9226 RTD temperature input module, 1 NI-9207 pressure and flow rate input module, 2 NI-9401 digital output module, and 1 NI-9265 analog output module) on an NI chassis (NI-cDAQ 9189) and recorded in the LabVIEW program during operation. The LabVIEW system also outputs control signals to modulate and switch valves in the hydronic system. Figure 35 shows the screenshot of the main control panel of the LabVIEW program with real-time readings of key sensors as well as control buttons and dials for valves, pumps, and burners. Each of the two sorption modules is controlled by a Raspberry Pi (RPi) with the manufacture-tuned control logic. The LabVIEW program communicates with the RPi via ethernet, reads measured data on the sorption modules, and commands the operation of the burners and heat pipe pumps via the RPi.

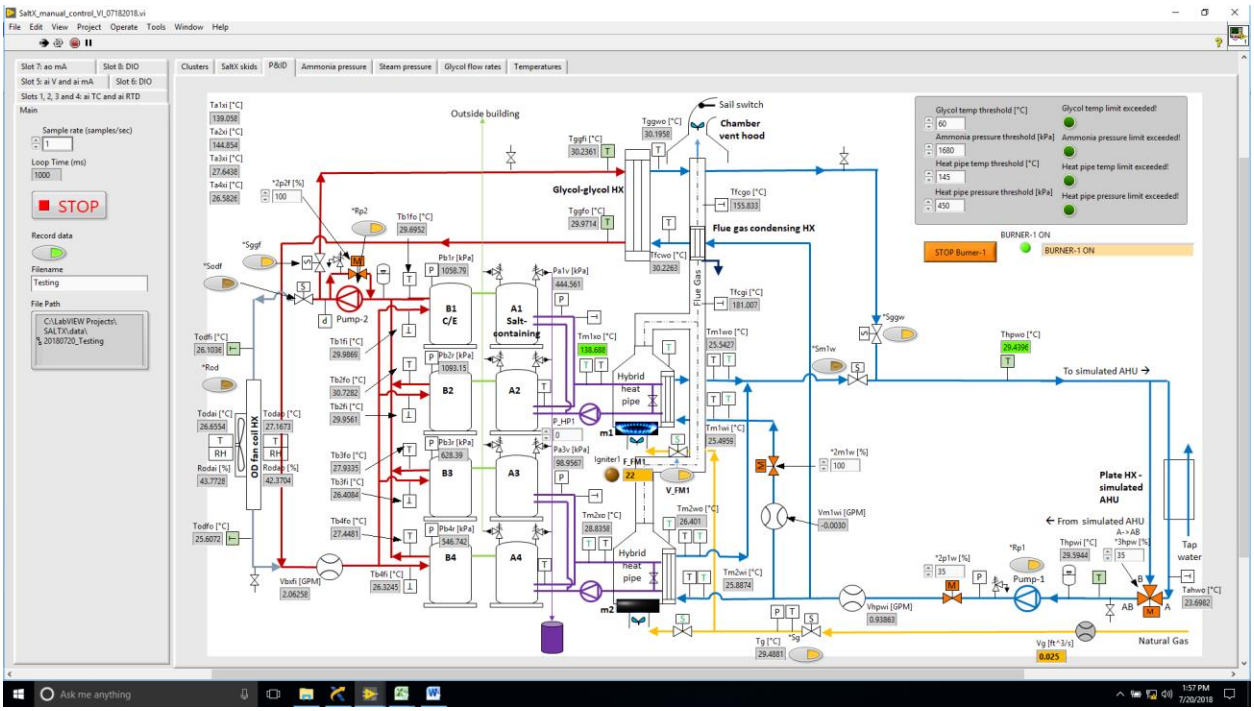

Figure 35 Screenshot of the NI LabVIEW DAQ and control program interface

The detailed temperature and pressure sensors list corresponding to Figure 34 are listed below. The three mass flow rate meters for the HTF are all inline to water pipes.

Table 12 Summary of temperature sensors

Sensor Numbering	**Internal/external**	**medium**	**Type**	**accuracy**
T1-T10, T13, T14, T17, T18, T21-T26	Internal	water	TC	0.5^0C
T15, T16, T35	Internal	flue	TC	0.5^0C
T11, T12, T19, T20	Internal	water	RTD	0.08^0C
T27, T28	Internal	salt	TC	0.5^0C
T29, T30	External	HX shell	TC	0.5^0C
T31-T34	External	steam/water	TC	0.5^0C

Table 13 summary of pressure sensors

Sensor	Location	Medium	Accuracy
P1	inside heat pipe-1	steam/water	2.76 kPa
P2	inside condenser-1	ammonia	10.34 kPa
P3	inside condenser-2	ammonia	10.34 kPa
P4	inside heat pipe-2	steam/water	2.76 kPa
P5	inside condenser-3	ammonia	10.34 kPa
P6	inside condenser-4	ammonia	10.34 kPa

4.3 Operation Procedure and Performance Metrics

With the multiple controlled component (pumps, burners, valves) the cyclic operation of the CSHP prototype along with the hydronic system is described below. The performance metrics of the tested system are formulated using the measurements taken from the system.

4.3.1 Operation Procedure

The operation procedure during the performance tests are illustrated using setup #3 as the example with desorption mode in Figure 36 and sorption mode in Figure 37. The illustrations of operation procedure of the other setups can be found in the appendix of this chapter. The active parts of the system are highlighted in both figures. Pump-1 and Pump-2 are turned on in both modes to drive the HTF loops carrying heat to the heat load HX and the condenser-evaporators. The flow rate of the heat load loop driven by Pump-1 is regulated with a motorized valve (valve-5) directly after the pump. The flow rate of the condenser-evaporator loop driven by Pump-2 is regulated with a motorized valve (valve-3) on the by-pass line parallel to the pump. A motorized valve (valve-7) controls the hot water flow rate that goes through the heat load HX to exchange heat with the cool city water, which therefore regulates the heating load of the HX or the hot water return temperature.

In the desorption mode, Burner-1 and Burner-2 are both turned on and supply heat to the adsorbers, driving ammonia out of the sorbent salt to condense in the condenser-evaporators. With valve-1 open and valve-2 closed, the HTF in the condenser-evaporator loop carries the condensation heat to HX-2. Meanwhile in the heat load loop, valve-4 is open, and valve-6 is closed to direct the heat

from HX-2 to the load HX. The heat in the flue gas from the two burners is recovered into the heat load loop through HX-1. At the start of the desorption mode the condensers are below the heat supply temperature, and the heat from the flue gas is transferred via HX-2 to pre-heat the condensers. Once the condensation and the flue gas heat up the condensers to the heat supply temperature, the heat flow direction in HX-2 is reversed so that heat is transferred from the condensers to the heat load loop.

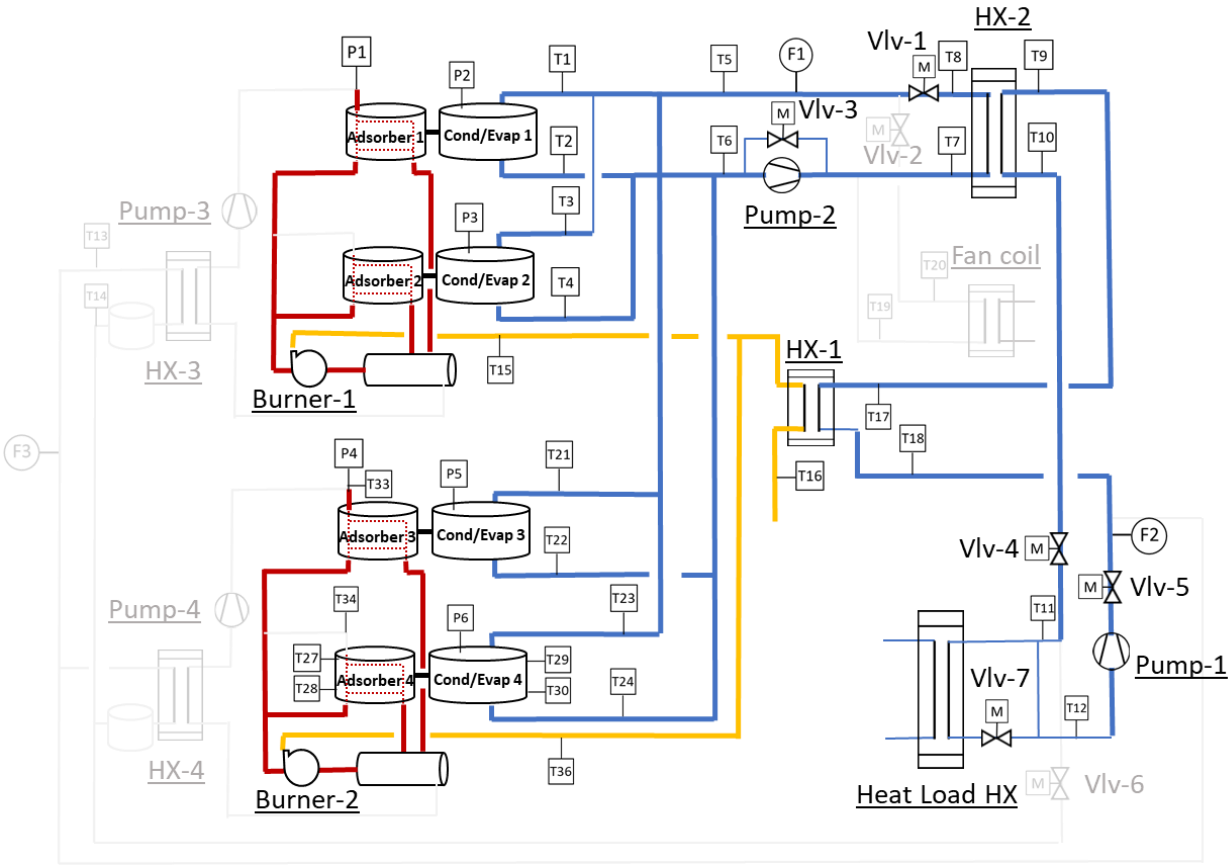

Figure 36 Active part of the system in desorption mode

In the sorption mode, the two burners are turned off and the pump-3 and pump-4 are turned on to circulate water in the heat pipe and draw heat from the adsorbers and supply it to HX-3 and HX-4. Valve-4 is now closed and valve-6 open to pass the heat from HX-3 and HX-4 to the heat load HX. Once the hot and “dry” sorbent salt is cooled, it starts to react with ammonia vapor and drive evaporation in the condenser-evaporator. The condenser-evaporator loop is directed towards the fan coil with valve-1 closed and valve-2 open, which allows low-temperature heat be extracted

from the ambient through the fan coil and supplied to the condenser-evaporator to support continuous evaporation.

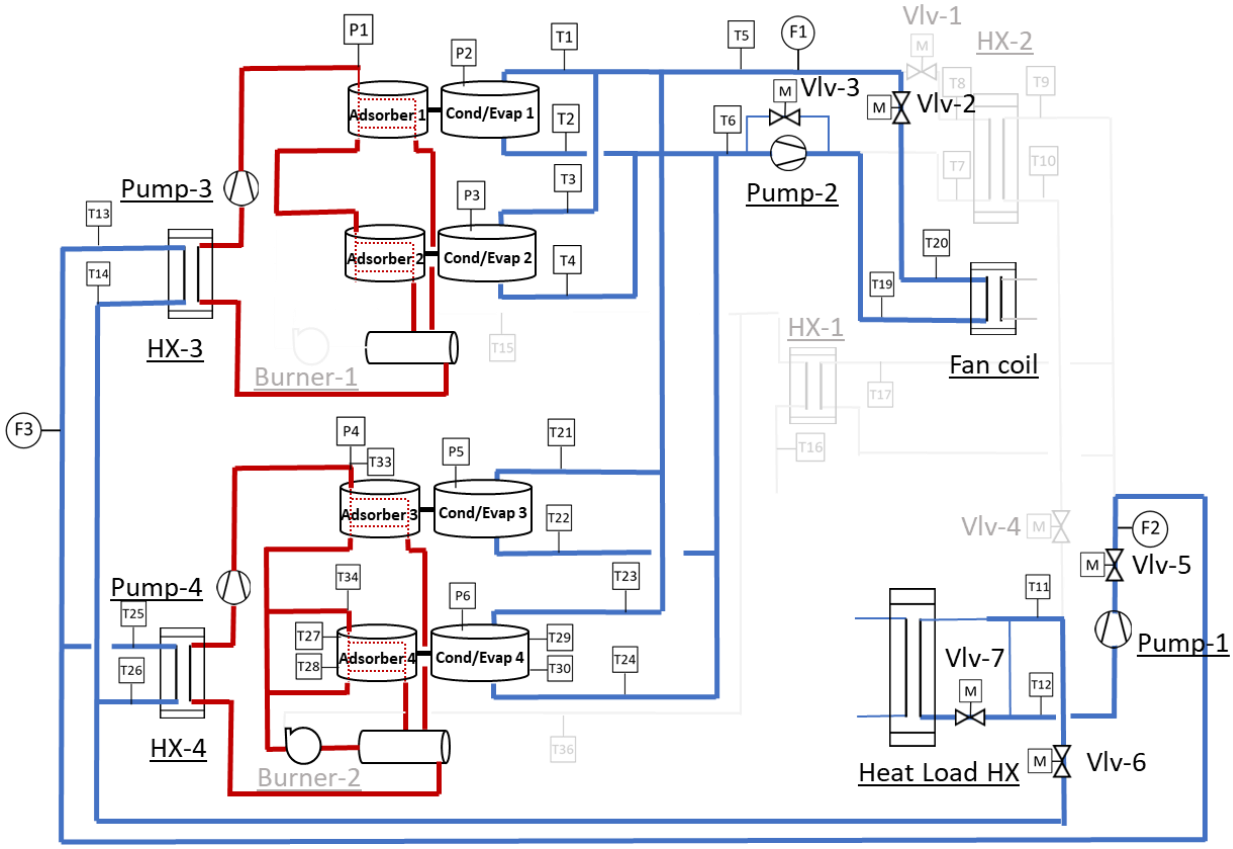

Figure 37 Active part of the system in sorption mode

4.3.2 Performance Metrics

The performance of the system is evaluated by the heating coefficient of performance (COP) and the specific heating power (SHP). The COP indicates the energy efficiency of the system, i.e. how much heat can be supplied under a given heat input over an entire desorption-sorption cycle. The SHP is the average heating power per unit mass of the sorbent salt throughout the entire operation period.

Both the COP and the SHP are calculated from the heat load of the heat exchangers in the system, which are the time-integral of the instant heat flow based on the temperature and flow rate measurements of the heat transfer fluids. The correlations of the key heat flows and the measurements from the testbench are listed below for desorption and sorption modes:

Desorption-condensation:

$$\dot{Q}_{cond} = F1 \cdot Cp_{HTF} \cdot (T6 - T5) \quad \text{Equation 11}$$

$$\dot{Q}_{HX-1} = F1 \cdot Cp_{HTF} \cdot (T17 - T18) \quad \text{Equation 12}$$

Sorption-evaporation:

$$\dot{Q}_{ads} = \dot{Q}_{HX-3} + \dot{Q}_{HX-4} = F3 \cdot Cp_{HTF} \cdot (T14 - T13) + (F2 - F3) \cdot Cp_{HTF} \cdot (T26 - T25) \quad \text{Equation 13}$$

For the condensers in the desorption mode, the heat flow starts towards the condensers due to their lower temperature than the target heat supply temperature, until later it reverses to out towards the heat load loop when the condensers are warmed up. The energy input to the condensers are also counted as energy input to the system from gas. The heating COP of the CSHP cycle is defined as the ratio of the total heat supplied to the heat load over the heat entering the adsorber:

$$COP_{cyc} = \frac{Q_{out,cyc}}{Q_{in,cyc}} = \frac{Q_{cond,out} + Q_{ads}}{Q_{des} + Q_{cond,in}} \quad \text{Equation 14}$$

$Q_{cond,in}$ and $Q_{cond,out}$ are the heat input and output of condenser during desorption mode; Q_{ads} is the heat output of the reactor during sorption mode; and Q_{des} is the heat entering the adsorber through the heat pipe during the desorption mode. Q_{cond} and Q_{ads} can be calculated by integrating the measured heat flow. Q_{des} is correlated to the natural gas combustion rate in the burner, which is explained in detail in the Appendix.

The SHP of the CSHP cycle indicates the average cyclic heating power generated by a unit mass of sorbent salt and is defined as equation (5). t_{cyc} is the total operation time for one complete desorption-sorption cycle. m_{salt} is the mass of the sorbent salt.

$$SHP = \frac{Q_{out,cyc}}{t_{cyc} \cdot m_{salt}}$$ Equation 15

4.4 Test Program and Test Results

4.4.1 Test Program

Table 14 lists the operating conditions and controls of the experimental tests, which are categorized based on their purposes. The base case to evaluate the system rating performance was tested using setup #3 under 8°C ambient based on the AHRI standard 210/240 [147] rating condition for air-source heat pumps. Following the base case, multiple test runs were carried out, and their results are compared to investigate the impact of key operating conditions and controls on the system performance. The groups of test runs are listed in Table 14 with regard to the initial (cold-start) and normal cycles, ambient temperature, heat rejection temperature, and burner firing rate.

Table 14 test program of the prototype CSHP system

Goal	Run	Insulation	Cycle type	Natural gas firing rate	Ambient temp. [°C]	Target water return temp. (T12) [°C]	Target water supply temp. (T11) [°C]
Base case	BC	Yes	Normal	High	~8*	45	50
Impact of heat rejection temp. (HT)	HT-L	No	Initial	High	~22	35	40
	HT-M	No	Initial	High	~22	40	45
	HT-H	No	Initial	High	~22	45	50
Impact of NG firing rate (FR)	FR-L	Yes	Initial	Low	~8	45	50
	FR-H	Yes	Initial	High	~8	45	50

Table 14 continued

Impact of initial or normal cycle (IN)	**IN-I1**	**Yes**	**Initial**	**Low**	**~8**	**45**	**50**
	IN-N1	Yes	Normal	Low	~8	45	50
	IN-I2	Yes	Initial	Low	~22	45	50
	IN-N2	Yes	Normal	Low	~22	45	50
Impact of ambient temp. (AT)	AT-H1	Yes	Initial	Low	~22	45	50
	AT-L1	Yes	Initial	Low	~8	45	50
	AT-H2	Yes	Normal	Low	~22	45	50
	AT-L2	Yes	Normal	Low	~8	45	50

**rating condition (outdoor air temperature) for air-source heat pump according to AHRI standard 210/240*

The switching between the desorption and the sorption operation modes was controlled by monitoring the minimum heating output. During the desorption mode, the condensation heat supplied through the condenser declines towards the end of the desorption-condensation process, and once a preset threshold is reached and the system turn to sorption mode. Similarly, with the cooling down of the sorbent in the sorption mode, the heating power continues to decline until the system is switched to desorption mode again. In all the tests, the minimum heating output was set to 1kW per sorption module, i.e. 1kW for setup #1 and setup #2 with one sorption module, and 2kW for setup #3 which runs two sorption modules simultaneously.

The HTF flow rates in the condenser loop and the heat load loop were 0.13kg/s and 0.18kg/s for setup #1 and #2 where the system is running on one sorption module. The flow rates are increased to 0.2kg/s and 0.18kg/s for the two sorption modules in setup #3.

4.4.2 Test Result Summary

Some test runs in Table 14 can be used for more than one purposes and reveal the impact of different parameters when compared with various other runs. As a result, 10 test runs were carried out in this study to fulfill the 18-run list in Table 14. The list of the conducted test runs, and their corresponding run numbers are listed in Table 15 by the setup and test dates. The recorded measured parameters and calculated results include the ambient temperature, hot water (HW) return and supply temperatures, desorption and sorption cycle time, average natural gas (NG) firing

rate when the burner(s) are on, total NG consumption, heat of desorption, condensation, adsorption, the total useful heat produced, average heat production power, specific heating power (SHP), and the COP.

Table 15 Summary of test results by test runs

Run	Setup	Date	Cycle type	Insulation	T_{amb} [°C]	HW return temp. (T12) [°C]	HW supply temp. (T11) [°C]	Des. mode time [min]	Sorp. mode time [min]	Tot. cycle time [min]	Avg. NG firing rate [cfm]	Total NG usage [cf]	Q_{des} [kJ]	$Q_{cond,in}$ [kJ]	$Q_{cond,out}$ [kJ]	Q_{ads} [kJ]	Q_{in} [kJ]	Q_{out} [kJ]	Avg. heating power [kW]	SHP [W/kg]	COP [-]
HT-L	#1	9/5/18	Initial	No	23.4	35.3	41.9	87.5	59.5	147.0	0.53	39.44	24967	0	5066	15468	24967	20534	2.33	529.5	0.82
HT-M		9/7/18	Initial	No	24.4	40.7	44.8	89.7	86.5	176.2	0.60	44.39	28100	0	4213	16846	28100	21059	1.99	452.3	0.75
HT-H	#2	10/24/18	Initial	No	23.5	44.5	49.3	79.4	59.5	138.9	0.61	42.72	27043	708	3950	14391	27751	18341	2.09	475.0	0.66
IS-N2			Normal	No	30.2	45.0	50.7	76.6	60.9	137.5	0.54	38.21	24187	881	4426	15372	25068	19798	2.30	522.7	0.79
AT-H1, IN-I2		10/29/18	Initial	Yes	25.1	44.3	50.0	99.1	57.8	156.9	0.46	36.20	22916	796	4109	18560	23712	22669	2.33	529.5	0.96
AT-H2, IN-N2			Normal	Yes	30.0	44.1	50.2	90.0	51.1	141.1	0.45	29.88	18913	530	4042	18570	19443	22612	2.60	590.9	1.16
AT-L1, FR-L, IN-I1	#3	11/02/18	Initial	Yes	8.0	43.6	48.2	83.9	62.1	146.0	0.91	70.19	44428	863	4667	29617	45291	34284	3.77	428.4	0.76
IN-N1			Normal	Yes	7.9	44.4	49.7	66.0	58.1	124.1	0.92	50.74	32119	1229	2619	28119	33348	30738	3.91	444.3	0.92
FR-H		11/14/18	Initial	Yes	7.9	44.3	49.4	61.6	59.5	121.1	1.12	62.92	39830	1430	4576	27209	41260	31785	4.18	475.0	0.77
BC, AT-L2			Normal	Yes	8.0	45.5	50.9	66.0	58.2	124.2	0.99	51.48	32585	1840	4056	27828	34425	31884	3.99	453.4	0.93

4.4.3 Base Case (BC) Performance Results

The test to evaluate the system heating performance under cold ambient was carried out using setup #3 in a psychrometric chamber. The chamber was pre-conditioned and kept at 8°C (47°F) according to the rating condition of air-source heat pumps by AHRI standard 210/240. According to the test program in Table 14, the hot water return temperature was set to 45°C, and the target hot water supply temperature was 50°C. The two burners (burner-1 and burner-2) and pumps (pump-3 and pump-4) in the two sorption modules in setup #3 were controlled separately to synchronize temperatures of the steam or water in the heat pipes. The base case cycle is a normal cycle, that is, it follows previous cycles with the components and materials in the system already warmed up. The difference between initial (cold-start) cycles and normal cycles is discussed in more details in the later parametric study section.

The key operation parameters of the base case are illustrated in Figure 38 to Figure 40. To filter out the temperature fluctuation due to the closed heat load loop, the HTF temperatures in Figure 39 and Figure 40 are moving average of 10 seconds. The heat flow fluctuation due to the heat pipe response is also filtered by taking the moving average of 2 minute.

As shown in Figure 38, the desorption mode follows four stages after the burners are turned on: the first stage is to pre-heat the salt from about 50°C up to the desorption equilibrium temperature of about 90°C. No desorption of ammonia from the sorbent occurs before the salt reaches the equilibrium temperature, which corresponds to the saturation temperature in the condenser. The second stage starts as the salt temperature exceeds the equilibrium and starts desorbing ammonia. The endothermic desorption process took significant amount of heat, and therefore the salt temperature increase rate dropped upon the start of the desorption. The desorbed ammonia vapor condenses in the condenser/evaporator to pre-heat the heat exchanger metal up to the heat supply temperature of 50°C. During the first two stages, the CSHP takes in the natural gas combustion heat through the heat pipe; meanwhile it does not reject heat to outside the system.

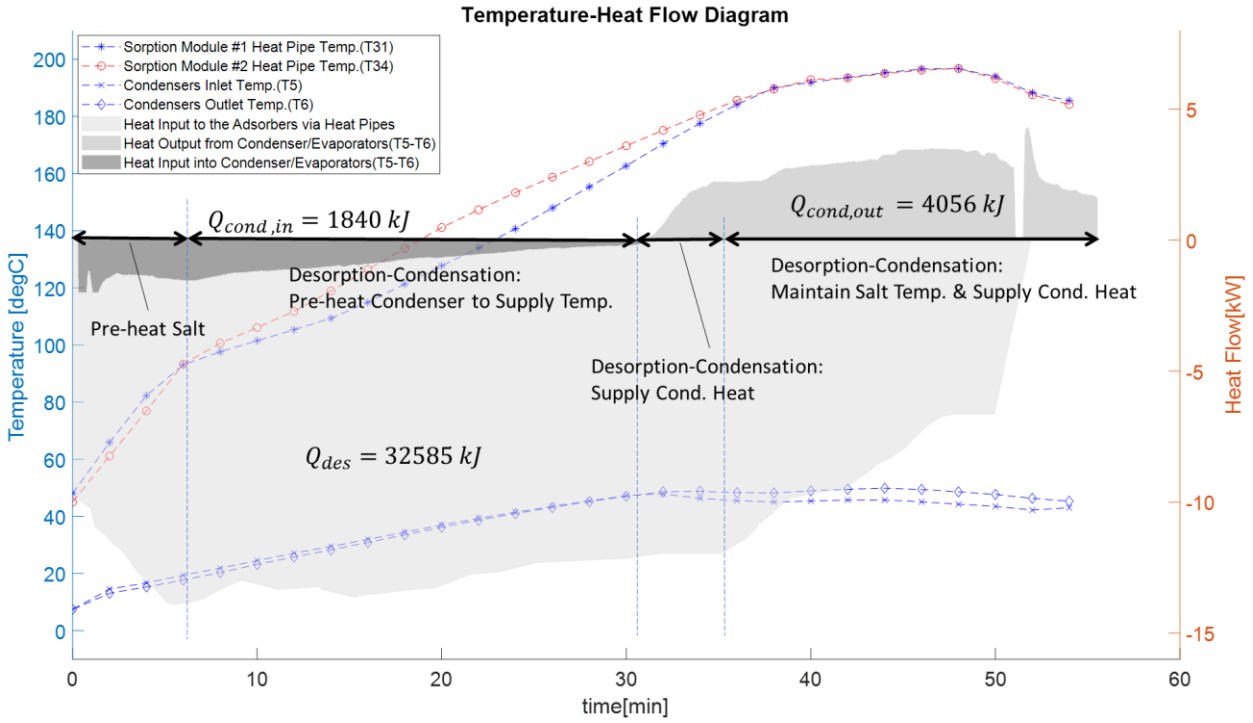

Figure 38 BC desorption mode temperatures and heat flow

The third stage begins when the condenser reaches the target heat supply temperature and starts to produce useful heat to the condenser/evaporator HTF loop. Then once the salt temperature approaches the safety limit of 200°C, the last desorption stage starts, and the burner power is gradually reduced to maintain the high salt temperature and support continued desorption and condensation. Eventually, the burner reaches the turndown limit and shuts off, and the condensing heat rejection declines as the ammonia in the salt is exhausted. The desorption mode terminates when the condensing heat rejection rate drops below the preset minimum heating power, which is 2 kW for the BC cycle.

The heat input to the adsorber in the desorption mode is generated by combusting natural gas in the boiler and supplied to the adsorber through the heat pipe, which is correlated to the measured natural gas input and a constant boiler steam generation efficiency (see appendix for the detailed calculation). Meanwhile, heat from the flue gas from HX-1 is added to the system to pre-heat the condenser. The heat output in the desorption mode is through the condenser HTF loop, which is calculated based on the measured HTF inlet and outlet temperatures and flow rate.

In the measured BC cycle, 32585 kJ of heat was supplied to the adsorber to heat up the salt to about 200°C and support desorption of ammonia for condensation. An additional 1840 kJ of heat was recovered from the flue gas and supplied to the condenser at stage 1 and 2 of the desorption mode. As a result, both the adsorber and the condenser got heated up, and the condenser supplied 4056 kJ of heat at around 50°C to the heat load lop during stage 3 and 4 of the desorption mode through the condenser HTF loop.

The sorption mode starts with the water circulating pumps of the heat pipe systems (pump-3 and pump-4) being turned on. The circulating water flows through the adsorber heat exchangers and transfers heat from the hot sorbent to the HTF in the heat load loop. As shown in Figure 39, the sorption mode has two stages. In the first stage, the circulated water cools the sorbent salt to below the sorption equilibrium temperature and drives the sorption reaction. The salt bonds with the ammonia vapor, and the reduction of vapor pressure in turn drives evaporation of the liquid ammonia accumulated in the condenser-evaporator. The evaporation takes heat from the condenser/evaporator, pre-cooling it down to the cold ambient temperature. The evaporated ammonia vapor continuously re-combines with the salt and releasing large amount of sorption heat in the process.

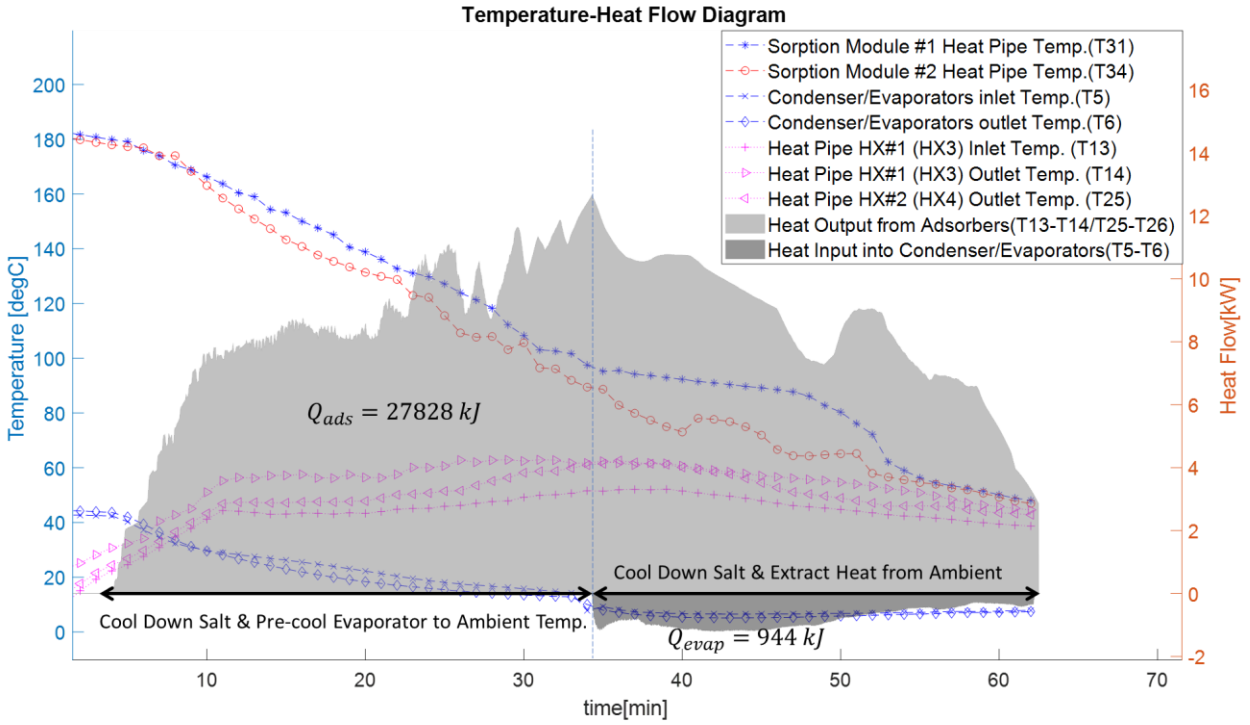

Figure 39 BC sorption mode time series plot of temperature and heat flow

The second stage of sorption mode starts when the condenser/evaporator is colder than the ambient, and the system starts to extract heat from the ambient air through the fan-coil unit through the condenser/evaporator HTF loop. The salt continues being cooled and supplying its sensible heat along with the sorption heat to the end-use. The heating power produced by circulating water in the adsorber starts high and fluctuating when the salt is very hot (e.g. >100°C) and the sorption-evaporation process is strong. This power declines quickly once the salt is cooled towards the heat supply temperature of 50°C, and the liquid ammonia in the evaporator is exhausted. The sorption mode terminates when the minimum heating power threshold is reached.

The overall cycle operation is illustrated in Figure 40 combining Figure 38 and Figure 39. The desorption mode consumes a significant amount of heat (Q_{des} and $Q_{cond,in}$) to heat the salt in the adsorbers and the heat exchanger metal in the condenser/evaporators. As the salt temperature (using the heat pipe temperature as the proxy) rises, ammonia is desorbed from the salt and condenses in the condenser/evaporators to also heats up the heat exchanger metal. Eventually the condenser/evaporators reach the heat supply temperature and supplies heat to the end use at the target temperature of 50°C ($Q_{cond,out}$). The high-temperature heat input into the system stops once

the boiler is turned off, and heat flow in the adsorber reverses as a significant amount of heat (Q_{ads}) is produced by cooling the hot salt. The sorption-evaporation proceeds with temperature decrease in both the adsorber and the condenser/evaporator. Low-temperature heat starts to flow into the system at later stage of the sorption mode when the evaporator temperature is lower than the cold ambient. At the end of the sorption mode, the components in the system resumes their initial temperature with heat supply temperature of 50°C in the adsorber and around ambient temperature of 8°C in the condenser/evaporator.

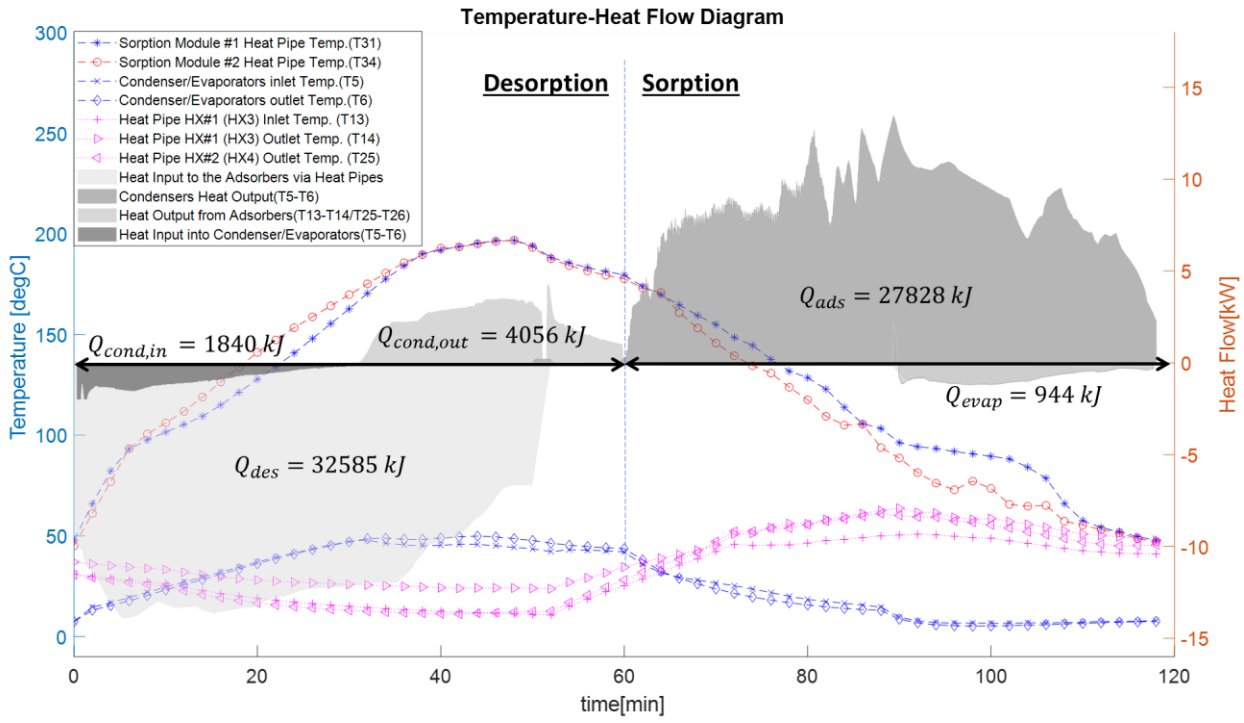

Figure 40 BC overall time series plot of temperature and heat flow

The cumulative high-temperature heat input and useful heat output in the BC cycle are illustrated in Figure 41. Unlike heating systems such as furnaces and conventional heat pumps that directly convert the energy input (fuel, electricity, etc.) to thermal energy and output the heat instantly, there is a considerable lag between the energy input to the CSHP system and the heat output. The temporal difference between heat input and heat output is an inherent feature of adsorption heat pump systems, where the alternating thermal-chemical energy conversions act in the place of mechanical compressors. Much of the significant heat input to the CSHP system in the desorption mode is used to desorb ammonia from the salt and is thus converted to chemical potential. The

conversion (desorption) process also generates heat at the target supply temperature via condensation. The rest of the heat input is stored as the sensible heat of various components and materials in the system as both the adsorber and the condenser/evaporator temperature rises. Most of the heat output occurs when the system is switched to the sorption mode, where both the sensible heat in the materials and the chemical potential of the sorbent-ammonia working pair are supplied as heat to the end use.

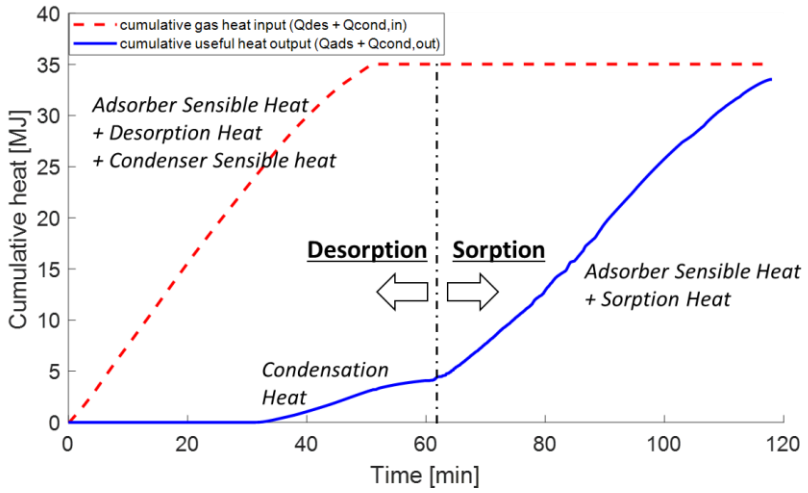

Figure 41 Cumulative heat input and useful heat output of the BC

Based on the cycle cumulative heat flow and Equation (4) and (5), the COP of the BC cycle is 0.922, the average heating power is 3.99kW. Based on the 8.4 kg sorbent in the system, the SHP is 453.4 W/kg. The one-minute average of key temperatures, HTF flow rates, and heat flows of the base case are listed in Table 16.

Table 16 Key operation and performance parameters of the BC

Time [min]	T31 [°C]	T34 [°C]	T5 [°C]	T6 [°C]	T13 [°C]	T14 [°C]	T25 [°C]	T26 [°C]	T11 [°C]	T12 [°C]	F1 [kg/s]	F2 [kg/s]	F3 [kg/s]	NG rate [cfm]	Qdes [kW]	Cumulative Qin [kJ]	Qads [kW]	Qcond [kW]	Qevap [kW]	Cumulative Qout [kJ]
1	53.3	51.3	14.9	9.8	36.1	40.2	37.1	36.7	18.3	18.7	0.162	0.225	0.000	0.763	8.3	495.1	0.0	0.0	0.0	0.0
2	62.1	62.0	14.6	12.7	34.2	39.8	36.6	34.4	13.6	13.8	0.231	0.239	0.000	0.840	9.1	1040.1	0.0	0.0	0.0	0.0
3	70.3	70.9	15.0	13.6	32.6	38.8	35.8	32.4	14.0	14.1	0.230	0.234	0.000	0.957	10.4	1661.2	0.0	0.0	0.0	0.0
4	78.6	79.6	16.2	14.8	31.2	37.6	34.8	30.7	15.1	15.1	0.228	0.226	0.000	1.000	10.8	2310.0	0.0	0.0	0.0	0.0
5	86.3	87.5	17.4	15.9	29.9	36.4	33.9	29.1	16.2	16.2	0.225	0.220	0.000	1.102	11.9	3025.0	0.0	0.0	0.0	0.0
6	91.7	92.8	18.8	17.2	28.7	35.3	33.1	27.7	17.4	17.4	0.221	0.214	0.000	1.120	12.1	3751.7	0.0	0.0	0.0	0.0
7	94.2	95.0	20.1	18.4	27.6	34.3	32.4	26.4	18.7	18.6	0.217	0.208	0.000	1.108	12.0	4470.4	0.0	0.0	0.0	0.0
8	96.5	97.2	21.3	19.7	26.6	33.4	31.7	25.1	19.9	19.8	0.213	0.203	0.000	1.100	11.9	5184.1	0.0	0.0	0.0	0.0
9	98.7	99.4	22.6	21.2	25.6	32.6	31.2	24.0	21.2	21.1	0.210	0.199	0.000	1.065	11.5	5875.3	0.0	0.0	0.0	0.0
10	100.6	101.4	23.9	22.5	24.7	31.9	30.6	22.9	22.6	22.4	0.207	0.197	0.000	1.060	11.5	6563.1	0.0	0.0	0.0	0.0
11	102.5	103.3	25.2	23.9	23.9	31.2	30.0	21.9	23.9	23.7	0.205	0.194	0.000	1.097	11.9	7274.6	0.0	0.0	0.0	0.0
12	104.5	105.3	26.5	25.2	23.1	30.5	29.5	21.0	25.2	25.0	0.203	0.194	0.000	1.100	11.9	7988.3	0.0	0.0	0.0	0.0
13	106.3	107.2	27.8	26.5	22.4	30.0	29.0	20.1	26.4	26.3	0.202	0.191	0.000	1.100	11.9	8702.0	0.0	0.0	0.0	0.0
14	108.3	109.3	29.0	27.7	21.7	29.5	28.6	19.4	27.7	27.5	0.200	0.190	0.000	1.100	11.9	9415.7	0.0	0.0	0.0	0.0
15	110.7	111.8	30.1	29.0	21.1	29.0	28.2	18.7	28.9	28.7	0.199	0.191	0.000	1.142	12.3	10156.5	0.0	0.0	0.0	0.0
16	113.5	114.8	31.4	30.3	20.5	28.6	27.8	18.0	30.1	29.9	0.197	0.191	0.000	1.140	12.3	10896.2	0.0	0.0	0.0	0.0
17	116.6	117.9	32.6	31.6	19.9	28.2	27.5	17.4	31.4	31.2	0.196	0.191	0.000	1.140	12.3	11635.8	0.0	0.0	0.0	0.0
18	119.8	121.3	33.9	32.9	19.4	27.9	27.2	16.9	32.7	32.5	0.195	0.191	0.000	1.140	12.3	12375.5	0.0	0.0	0.0	0.0
19	123.0	124.6	35.1	34.3	18.9	27.6	26.9	16.3	34.0	33.7	0.194	0.191	0.000	1.140	12.3	13115.1	0.0	0.0	0.0	0.0
20	126.2	127.8	36.4	35.6	18.4	27.4	26.7	15.8	35.3	35.0	0.194	0.191	0.000	1.140	12.3	13854.8	0.0	0.0	0.0	0.0
21	129.3	131.1	37.7	36.9	17.9	27.2	26.5	15.4	36.5	36.3	0.193	0.191	0.000	1.120	12.1	14581.5	0.0	0.0	0.0	0.0
22	132.5	134.2	38.8	38.1	17.5	27.0	26.3	14.9	37.7	37.5	0.193	0.190	0.000	1.100	11.9	15295.2	0.0	0.0	0.0	0.0
23	135.7	137.6	39.9	39.3	17.1	26.8	26.1	14.5	38.9	38.6	0.192	0.188	0.000	1.100	11.9	16008.9	0.0	0.0	0.0	0.0
24	139.1	141.0	41.0	40.4	16.6	26.6	25.8	14.2	40.0	39.7	0.191	0.188	0.000	1.100	11.9	16722.6	0.0	0.0	0.0	0.0
25	142.7	144.7	42.0	41.6	16.2	26.5	25.6	13.8	41.1	40.8	0.191	0.188	0.000	1.082	11.7	17424.6	0.0	0.0	0.0	0.0
26	146.3	148.4	43.1	42.7	15.9	26.4	25.5	13.5	42.2	41.9	0.191	0.189	0.000	1.080	11.7	18125.4	0.0	0.0	0.0	0.0
27	150.0	152.1	44.1	43.7	15.5	26.2	25.3	13.2	43.2	42.9	0.191	0.188	0.000	1.080	11.7	18826.1	0.0	0.0	0.0	0.0
28	153.6	155.8	45.0	44.7	15.1	26.1	25.2	12.9	44.2	43.9	0.191	0.188	0.000	1.080	11.7	19526.8	0.0	0.0	0.0	0.0
29	157.3	159.6	45.9	45.7	14.8	26.0	25.0	12.7	45.1	44.8	0.190	0.188	0.000	1.080	11.7	20227.6	0.0	0.0	0.0	0.0
30	161.0	163.4	46.9	46.6	14.5	25.9	24.8	12.5	46.0	45.7	0.190	0.189	0.000	1.080	11.7	20928.3	0.0	0.0	0.0	0.0
31	164.8	167.2	47.7	47.5	14.2	25.8	24.6	12.2	46.8	46.6	0.189	0.189	0.000	1.080	11.7	21629.0	0.0	0.0	0.0	0.0
32	168.7	171.2	48.0	48.3	13.9	25.6	24.5	12.0	46.5	47.4	0.189	0.188	0.000	1.080	11.7	22329.7	0.0	0.3	0.0	14.6
33	172.4	174.9	47.4	48.8	13.7	25.5	24.3	11.9	45.2	47.8	0.189	0.188	0.000	1.080	11.7	23030.5	0.0	1.1	0.0	75.1
34	176.0	178.5	46.6	48.9	13.5	25.4	24.2	11.8	44.2	47.8	0.189	0.188	0.000	1.080	11.7	23731.2	0.0	1.8	0.0	174.9
35	179.3	181.8	46.0	48.7	13.3	25.1	24.0	11.7	43.5	47.5	0.189	0.188	0.000	1.080	11.7	24431.9	0.0	2.1	0.0	292.5
36	182.6	185.1	45.6	48.4	13.1	24.9	23.8	11.6	43.2	47.2	0.190	0.188	0.000	1.080	11.7	25132.7	0.0	2.2	0.0	415.2
37	185.8	188.3	45.4	48.2	12.9	24.7	23.6	11.5	43.0	47.0	0.189	0.189	0.000	1.011	10.9	25788.4	0.0	2.2	0.0	538.6
38	188.8	191.3	45.1	48.1	12.7	24.4	23.4	11.4	42.8	46.9	0.189	0.188	0.000	0.972	10.5	26419.1	0.0	2.3	0.0	667.6
39	190.5	192.7	45.1	48.5	12.5	24.2	23.2	11.3	43.0	47.0	0.189	0.188	0.000	0.897	9.7	27001.1	0.0	2.7	0.0	815.6
40	191.4	193.5	45.3	48.8	12.4	24.0	23.1	11.2	43.2	47.3	0.189	0.188	0.000	0.880	9.5	27572.0	0.0	2.8	0.0	969.7
41	192.3	194.2	45.4	49.1	12.2	23.8	22.9	11.1	43.5	47.6	0.189	0.188	0.000	0.865	9.4	28133.1	0.0	2.9	0.0	1127.9
42	193.2	195.1	45.6	49.4	12.0	23.6	22.7	11.0	43.7	47.8	0.190	0.188	0.000	0.860	9.3	28691.0	0.0	2.9	0.0	1290.2

Table 16 continued

43	**194.3**	**196.1**	**45.8**	**49.6**	**11.9**	**23.5**	**22.6**	**10.9**	**43.9**	**48.1**	**0.189**	**0.188**	**0.000**	**0.829**	**9.0**	**29229.1**	**0.0**	**3.0**	**0.0**	**1456.0**
44	194.9	196.7	45.9	49.8	11.7	23.3	22.4	10.8	43.9	48.3	0.189	0.188	0.000	0.775	8.4	29732.0	0.0	3.1	0.0	1627.9
45	195.6	197.3	45.6	49.8	11.6	23.2	22.3	10.7	43.5	48.2	0.190	0.188	0.000	0.743	8.0	30214.1	0.0	3.3	0.0	1810.9
46	196.3	197.9	45.2	49.6	11.5	23.1	22.2	10.7	43.2	48.1	0.190	0.188	0.000	0.695	7.5	30665.0	0.0	3.4	0.0	2001.2
47	196.5	198.0	44.9	49.3	11.3	22.9	22.1	10.6	43.0	47.8	0.190	0.188	0.000	0.619	6.7	31066.6	0.0	3.5	0.0	2192.9
48	196.5	197.9	44.4	48.8	11.2	22.8	22.0	10.5	42.7	47.4	0.190	0.189	0.000	0.600	6.5	31455.9	0.0	3.5	0.0	2384.2
49	197.0	198.4	44.1	48.4	11.1	22.7	21.9	10.4	42.4	47.0	0.189	0.188	0.000	0.600	6.5	31845.2	0.0	3.4	0.0	2572.2
50	195.9	196.9	43.8	47.9	11.0	22.5	21.7	10.4	42.6	46.6	0.189	0.188	0.000	0.600	6.5	32234.5	0.0	3.3	0.0	2754.1
51	192.0	192.3	43.5	47.3	10.8	22.7	21.6	10.6	42.7	46.1	0.188	0.188	0.000	0.540	5.8	32584.9	0.0	3.0	0.0	2918.2
52	189.1	189.5	42.2	46.7	10.2	28.6	17.8	18.2	42.1	44.5	0.100	0.166	0.000	0.000	0.0	32584.9	0.0	2.0	0.0	3028.1
53	187.4	187.8	43.0	45.9	10.2	27.1	19.8	16.1	43.0	44.8	0.202	0.203	0.000	0.000	0.0	32584.9	0.0	2.4	0.0	3162.6
54	186.1	186.5	43.1	45.5	10.2	26.1	19.7	15.5	43.0	44.5	0.202	0.198	0.000	0.000	0.0	32584.9	0.0	2.0	0.0	3274.5
55	184.9	185.3	43.0	45.1	10.1	25.2	19.5	15.0	42.9	44.2	0.201	0.195	0.000	0.000	0.0	32584.9	0.0	1.8	0.0	3375.2
56	183.7	184.1	42.9	44.8	10.1	24.4	19.2	14.6	42.9	44.0	0.199	0.193	0.000	0.000	0.0	32584.9	0.0	1.6	0.0	3464.4
57	182.7	183.0	42.7	44.5	10.0	23.6	19.0	14.1	42.9	43.7	0.198	0.192	0.000	0.000	0.0	32584.9	0.0	1.4	0.0	3544.2
58	181.7	182.1	42.7	44.2	10.0	23.0	18.9	13.7	42.9	43.5	0.197	0.190	0.000	0.000	0.0	32584.9	0.0	1.3	0.0	3614.8
59	180.8	181.2	42.5	44.0	10.0	22.4	18.7	13.3	42.8	43.2	0.196	0.190	0.000	0.000	0.0	32584.9	0.0	1.2	0.0	3678.3
60	179.9	180.3	42.4	43.7	9.9	21.9	18.6	12.9	42.7	43.0	0.160	0.190	0.000	0.000	0.0	32584.9	0.0	0.9	0.0	3726.1
61	179.2	179.6	40.3	42.1	16.3	24.2	22.7	19.3	37.8	37.9	0.000	0.194	0.029	0.000	0.0	32584.9	0.0	0.0	0.0	3726.1
62	176.1	175.7	37.2	39.4	40.2	51.6	41.7	39.9	42.7	42.4	0.000	0.221	0.102	0.000	0.0	32584.9	4.0	0.0	0.0	3963.2
63	173.7	173.7	34.5	36.5	49.0	52.3	49.0	49.4	48.9	50.7	0.000	0.252	0.117	0.000	0.0	32584.9	1.8	0.0	0.0	4069.5
64	171.4	169.5	32.4	33.6	43.2	52.1	43.3	44.1	43.3	47.4	0.000	0.265	0.123	0.000	0.0	32584.9	4.8	0.0	0.0	4357.9
65	168.1	166.8	31.0	31.3	45.2	57.3	45.5	47.7	45.7	51.1	0.000	0.274	0.126	0.000	0.0	32584.9	7.4	0.0	0.0	4804.0
66	166.1	165.7	29.8	29.6	42.2	49.5	42.1	45.6	42.1	47.3	0.000	0.278	0.127	0.000	0.0	32584.9	5.8	0.0	0.0	5151.8
67	163.5	163.0	29.0	28.2	44.5	55.4	44.5	47.8	44.7	50.4	0.000	0.281	0.130	0.000	0.0	32584.9	7.6	0.0	0.0	5608.3
68	160.8	160.3	28.2	26.7	43.4	53.3	43.7	47.1	43.7	49.7	0.000	0.282	0.130	0.000	0.0	32584.9	7.2	0.0	0.0	6042.5
69	158.6	158.2	27.6	25.4	43.2	51.6	43.2	47.6	43.3	49.0	0.000	0.282	0.130	0.000	0.0	32584.9	7.0	0.0	0.0	6464.9
70	155.7	155.5	26.9	24.2	44.6	54.3	44.7	49.0	44.6	51.2	0.000	0.282	0.130	0.000	0.0	32584.9	7.7	0.0	0.0	6927.9
71	153.3	152.7	26.3	23.0	43.5	54.3	43.6	47.5	43.6	50.1	0.000	0.282	0.130	0.000	0.0	32584.9	8.0	0.0	0.0	7406.9
72	150.3	149.2	25.6	21.9	44.1	55.5	44.3	48.3	44.4	51.0	0.000	0.281	0.130	0.000	0.0	32584.9	8.4	0.0	0.0	7908.8
73	147.3	145.7	24.8	20.9	44.8	55.4	44.7	49.0	44.7	51.8	0.000	0.282	0.130	0.000	0.0	32584.9	8.1	0.0	0.0	8396.6
74	145.3	144.4	24.0	20.0	43.0	51.8	43.0	46.9	43.0	49.0	0.000	0.281	0.130	0.000	0.0	32584.9	6.9	0.0	0.0	8812.2
75	141.1	140.9	23.1	19.1	43.6	56.1	43.7	47.2	43.8	50.6	0.000	0.282	0.130	0.000	0.0	32584.9	8.6	0.0	0.0	9330.7
76	138.5	137.3	22.2	18.4	43.6	54.1	43.6	47.4	43.6	50.0	0.000	0.281	0.129	0.000	0.0	32584.9	7.8	0.0	0.0	9798.0
77	135.8	133.7	21.3	17.7	43.0	53.7	43.1	47.2	43.1	49.6	0.000	0.281	0.130	0.000	0.0	32584.9	8.0	0.0	0.0	10279.9
78	132.7	130.9	20.4	17.1	43.2	52.8	43.5	50.4	43.6	50.4	0.000	0.281	0.130	0.000	0.0	32584.9	9.2	0.0	0.0	10832.9
79	131.5	129.6	19.5	16.5	46.8	55.9	46.8	53.2	46.8	54.4	0.000	0.280	0.129	0.000	0.0	32584.9	8.6	0.0	0.0	11346.9
80	129.7	127.6	18.8	16.0	43.7	52.6	43.8	52.3	43.9	51.1	0.000	0.279	0.129	0.000	0.0	32584.9	9.7	0.0	0.0	11926.7
81	125.5	125.4	18.1	15.4	48.3	55.0	48.6	61.1	48.8	57.8	0.000	0.279	0.128	0.000	0.0	32584.9	11.0	0.0	0.0	12586.8
82	123.8	122.6	17.6	15.0	50.3	58.4	50.5	60.9	50.6	59.0	0.000	0.281	0.130	0.000	0.0	32584.9	10.5	0.0	0.0	13217.1
83	121.5	119.8	17.1	14.5	47.4	55.4	47.3	50.7	47.2	53.0	0.000	0.282	0.130	0.000	0.0	32584.9	6.2	0.0	0.0	13588.9
84	117.6	110.1	16.7	14.1	44.4	60.5	44.7	51.9	44.9	54.2	0.000	0.282	0.130	0.000	0.0	32584.9	12.7	0.0	0.0	14350.5
85	111.4	108.9	16.3	13.8	50.6	58.4	50.5	54.0	50.5	56.5	0.000	0.282	0.131	0.000	0.0	32584.9	6.2	0.0	0.0	14724.1
86	108.4	101.2	15.9	13.5	46.7	65.4	47.0	49.2	47.1	55.9	0.000	0.282	0.131	0.000	0.0	32584.9	11.1	0.0	0.0	15391.2

Table 16 continued

87	**103.3**	**96.1**	**15.4**	**13.3**	**51.6**	**64.1**	**52.0**	**62.6**	**52.3**	**62.1**	**0.000**	**0.283**	**0.131**	**0.000**	**0.0**	**32584.9**	**12.9**	**0.0**	**0.0**	**16164.2**
88	102.7	100.5	14.8	13.1	51.9	52.4	51.8	65.0	51.8	58.9	0.000	0.282	0.131	0.000	0.0	32584.9	8.2	0.0	0.0	16655.7
89	101.9	96.9	14.3	12.8	49.7	58.7	49.9	62.0	50.0	59.4	0.000	0.283	0.131	0.000	0.0	32584.9	12.1	0.0	0.0	17380.4
90	97.6	91.7	10.0	10.5	54.7	66.8	55.0	65.2	55.3	65.0	0.142	0.283	0.131	0.000	0.0	32584.9	12.5	0.0	0.6	18127.6
91	95.5	90.3	9.2	8.0	55.4	66.2	55.6	64.4	55.7	64.7	0.201	0.283	0.131	0.000	0.0	32584.9	11.0	0.0	-1.0	18788.9
92	95.3	89.6	8.1	7.1	53.7	63.3	53.8	62.4	53.9	62.3	0.202	0.283	0.131	0.000	0.0	32584.9	10.2	0.0	-0.9	19402.2
93	94.1	88.5	7.4	6.4	52.3	61.6	52.4	60.9	52.5	60.8	0.201	0.282	0.130	0.000	0.0	32584.9	10.1	0.0	-0.8	20005.9
94	93.7	87.6	7.1	5.9	51.4	60.6	51.5	60.2	51.6	59.8	0.201	0.282	0.131	0.000	0.0	32584.9	10.1	0.0	-1.0	20609.5
95	92.9	86.9	6.9	5.6	50.9	59.9	51.0	60.1	51.1	59.4	0.201	0.282	0.130	0.000	0.0	32584.9	10.3	0.0	-1.0	21225.5
96	92.3	86.7	6.7	5.4	51.4	60.2	51.5	61.3	51.7	60.1	0.201	0.283	0.130	0.000	0.0	32584.9	10.5	0.0	-1.1	21857.5
97	91.5	86.2	6.6	5.3	51.2	60.0	51.3	60.2	51.4	59.5	0.201	0.282	0.131	0.000	0.0	32584.9	10.0	0.0	-1.1	22458.4
98	91.0	85.7	6.6	5.2	50.5	59.3	50.6	59.0	50.7	58.6	0.201	0.282	0.130	0.000	0.0	32584.9	9.7	0.0	-1.2	23040.0
99	90.4	85.2	6.6	5.2	49.8	58.7	49.9	57.8	49.9	57.7	0.201	0.282	0.130	0.000	0.0	32584.9	9.4	0.0	-1.2	23605.5
100	89.8	84.6	6.6	5.2	48.9	57.9	49.0	56.4	49.1	56.6	0.201	0.283	0.131	0.000	0.0	32584.9	9.2	0.0	-1.2	24156.3
101	89.2	84.1	6.6	5.2	48.1	57.1	48.2	55.1	48.3	55.6	0.201	0.282	0.131	0.000	0.0	32584.9	8.9	0.0	-1.2	24688.2
102	88.5	83.3	6.6	5.3	47.3	56.4	47.4	53.9	47.4	54.5	0.201	0.282	0.130	0.000	0.0	32584.9	8.7	0.0	-1.1	25207.4
103	87.6	82.2	6.6	5.4	46.6	55.5	46.6	52.7	46.7	53.6	0.200	0.282	0.130	0.000	0.0	32584.9	8.3	0.0	-1.0	25707.0
104	85.8	80.6	6.7	5.5	44.4	53.9	44.3	46.1	44.3	49.7	0.200	0.281	0.130	0.000	0.0	32584.9	6.0	0.0	-1.0	26069.0
105	82.7	76.7	6.8	5.7	41.7	53.0	41.7	43.5	41.7	47.5	0.199	0.281	0.129	0.000	0.0	32584.9	7.0	0.0	-0.9	26486.6
106	80.0	72.2	6.8	5.8	42.1	56.1	42.2	43.3	42.3	48.7	0.199	0.281	0.130	0.000	0.0	32584.9	7.9	0.0	-0.8	26961.5
107	76.2	67.9	6.8	6.0	42.9	55.8	43.1	46.7	43.1	50.1	0.199	0.281	0.130	0.000	0.0	32584.9	8.9	0.0	-0.7	27494.2
108	71.5	60.2	6.9	6.1	45.6	55.5	45.8	52.1	45.9	53.0	0.198	0.282	0.130	0.000	0.0	32584.9	9.0	0.0	-0.6	28031.8
109	62.4	56.4	7.0	6.3	45.5	54.4	45.6	51.2	45.6	52.2	0.197	0.281	0.130	0.000	0.0	32584.9	8.1	0.0	-0.6	28516.3
110	59.0	54.0	7.1	6.4	44.0	52.1	44.0	48.5	44.0	49.9	0.197	0.281	0.130	0.000	0.0	32584.9	6.9	0.0	-0.5	28930.2
111	56.4	52.0	7.1	6.6	42.4	50.6	42.4	46.9	42.4	48.3	0.196	0.281	0.129	0.000	0.0	32584.9	7.0	0.0	-0.5	29348.3
112	54.6	50.3	7.3	6.8	40.9	48.8	40.9	44.9	40.9	46.3	0.196	0.281	0.129	0.000	0.0	32584.9	6.5	0.0	-0.5	29737.5
113	53.4	48.4	7.5	7.0	39.5	46.8	39.5	44.0	39.5	44.8	0.195	0.280	0.129	0.000	0.0	32584.9	6.5	0.0	-0.5	30127.8
114	52.5	47.8	7.5	7.1	40.0	46.5	40.1	45.8	40.1	45.7	0.195	0.275	0.127	0.000	0.0	32584.9	6.6	0.0	-0.3	30526.1
115	51.5	46.4	7.5	7.1	38.8	45.0	38.8	44.0	38.8	44.1	0.194	0.256	0.118	0.000	0.0	32584.9	5.7	0.0	-0.3	30869.2
116	50.1	44.9	7.6	7.2	37.6	43.5	37.7	42.5	37.6	42.6	0.194	0.240	0.111	0.000	0.0	32584.9	5.1	0.0	-0.3	31176.0
117	48.9	43.8	7.8	7.3	37.5	42.8	37.7	41.7	37.7	41.8	0.194	0.228	0.105	0.000	0.0	32584.9	4.2	0.0	-0.4	31426.0
118	48.1	43.5	7.9	7.5	39.1	43.0	39.4	42.0	39.5	41.9	0.136	0.163	0.075	0.000	0.0	32584.9	2.2	0.0	-0.3	31557.5

4.4.4 Parametric Studies

4.4.4.1 Ambient Temperature

The impact of the ambient temperature on the system performance was investigated by comparing the test results under two different ambient temperatures as listed in Table 17. The AT-H1 and AT-H2 tests were conducted under high ambient temperatures of 25°C and 30C, respectively. AT-H1 test is an initial cycle using setup #2, where the system cold-started from 25°C. AT-H2 is a normal cycle using setup #2, and the system was already warmed up following the previous sorption-evaporation mode. The AT-L1 and AT-L2 tests were both using setup #3 conducted under low ambient temperature of 8°C with AT-L1 the initial cycle and AT-L2 the normal cycle. Therefore, the impact of different ambient temperatures can be observed by comparing the performances of AT-H1 and AT-L1, as well as AT-H2 and AT-L2.

Table 17 Performance comparison of test runs under different ambient temperatures

Run	**AT-H1**	**AT-L1**	**AT-H2**	**AT-L2**
Setup	#2	#3	#2	#3
Insulation	Yes	Yes	Yes	Yes
Cycle Type	Cold-start	Cold-start	Pre-heated	Pre-heated
T_{amb} [°C]	25.1	8	30	8
HW Return Temp. (T12) [°C]	44.3	43.6	44.1	45.5
HW Supply Temp. (T11) [°C]	50	48.2	50.2	50.9
Des. Mode Time [min]	99.1	83.9	90	66
Sorp. Mode Time [min]	57.8	62.1	51.1	58.2
Tot. Cycle Time [min]	156.9	146	141.1	124.2
Avg. Ng Firing Rate [cfm]	0.46	0.91	0.45	0.99
Total Ng Usage [cf]	36.2	70.19	29.88	51.48
Q_{des} [kJ]	22916	44428	18913	32585
$Q_{cond,In}$ [kJ]	796	863	530	1840
$Q_{cond,Out}$ [kJ]	4109	4667	4042	4056
Q_{ads} [kJ]	18560	29617	18570	27828
Q_{in} [kJ]	23712	45291	19443	34425
Q_{out} [kJ]	22669	34284	22612	31884
Q_{des}/Q_{ads}	1.500	1.234	1.142	1.171
$Q_{cond,net}/Q_{ads}$	0.128	0.181	0.063	0.080
Avg. Heating Power [kW]	2.33	3.77	2.6	3.99
SHP [W/kg]	529.5	428.4	590.9	453.4
COP [-]	0.96	0.76	1.16	0.93

To compare the heat production and energy consumption of setup #2 with one sorption module and setup #3 with two sorption modules, the desorption and condensation heat in each test are normalized based on the adsorption heat of that test to eliminate the difference of system sizes.

The adsorption heat is chosen as the basis because all adsorption processes start at the sorbent at about 200°C and ends with sorbent at about 50°C regardless of the ambient temperature. The desorption heat inputs and condensation heat outputs compared with the adsorption heat output for the four tests are also listed in Table 17. The desorption heat input is considerably lower for high-ambient-temperature cases. Between initial (cold-start) cycles of AT-H1 and AT-L1, a higher starting temperature leads to lower energy needed to heat up the adsorber thermal mass. Normal (pre-heated) cycles of AT-H2 and AT-L2 show higher COP compared with the cold-start cycles under the same ambient temperature as the thermal masses of the adsorber has already been warmed up, and thus the heat input is used more effectively to generate useful heating. The comparison is illustrated in Figure 42.

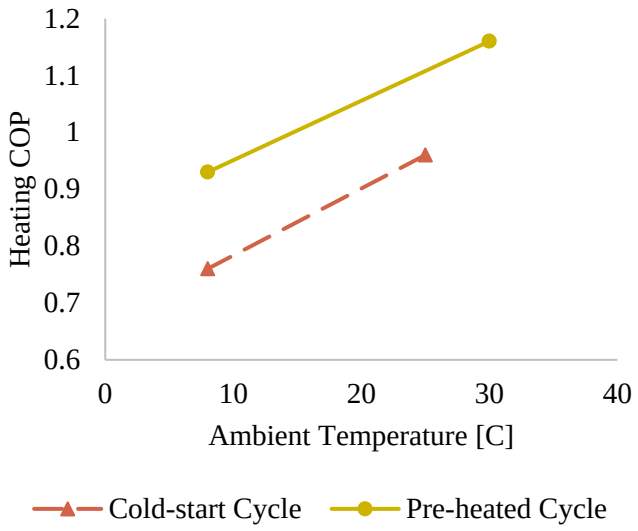

Figure 42 Measured system COP under different ambient temperatures

Meanwhile, the condensation heat output is lower for low-ambient-temperature cases largely due to the increased temperature swing that the thermal mass of condensers experience in a cycle. The evaporation temperature is much lower under cold ambient conditions, and therefore the condensers in AT-L1 and AT-L2 started at a much lower temperature than the high-ambient cases and required more energy to be heated up to the heat-supply temperature.

Comparing the initial and normal cycles under cold ambient, the cold-start cycle takes more desorption heat while also producing slightly more in condensation. The former is due to the much larger temperature lift in the adsorber for cold-start and for a cycle following a sorption process.

The latter can be attributed to the condenser/evaporator temperature at the start of the normal cycle being lower than the ambient due to evaporation. The impact of initial/normal cycles will be discussed in later sections in more detail. Here the comparisons are mostly focused within the same cycle type.

Due to the increased desorption heat input and reduced condensation heat output, the system COPs under low ambient temperatures are lower than those at high ambient temperatures. With similar cycle times, the specific heating power (SHP) also see a decrease at the low ambient temperature. In comparison, a conventional vapor compression heat pump can achieve electric COP above 4.0 at 25°C ambient, while at 8°C the electric COP drops to below 3.0 ([148]). When converted to source energy using the factors in [22], the source energy COP (comparable with gas COP) of electric heat pumps are about 1.7 under 25°C and about 0.95 under 8°C.

4.4.4.2 Heat Rejection Temperature

The impact of the heat rejection temperature was investigated by comparing three cycle operations that produces heat at different temperature levels with a similar temperature lift. The heat rejection temperatures of HT-L, HT-M, and HT-H are 40°C, 45°C, and 50°C, and the temperature difference of the hot water supply and demand were 5°C for all three cases. The ambient temperature of all three cases were about 23°C. HT-L and HT-M were using setup #1 and HT-H was using setup #2, all of which had one sorption module. The test results of the test runs with the three different heat rejection temperatures a summarized in Table 18 and illustrated in Figure 43.

Table 18 Performance comparison of tests with different heat rejection temperatures

Run	HT-L	HT-M	HT-H
Setup	#1	#1	#2
Insulation	No	No	No
Cycle Type	Initial	Initial	Initial
T_{amb} [°C]	23.4	24.4	23.5
HW Return Temp. (T12) [°C]	35.3	40.7	44.5
HW Supply Temp. (T11) [°C]	41.9	44.8	49.3
Des. Mode Time [min]	87.5	89.7	79.4
Sorp. Mode Time [min]	59.5	86.5	59.5
Tot. Cycle Time [min]	147.0	176.2	138.9
Avg. Ng Firing Rate [cfm]	0.53	0.6	0.61
Total Ng Usage [cf]	39.44	44.39	42.72
Q_{des} [kJ]	24967	28100	27043
$Q_{cond,In}$ [kJ]	0	0	708
$Q_{cond,Out}$ [kJ]	5066	4213	3950
Q_{ads} [kJ]	15468	16846	14391
Q_{in} [kJ]	24967	28100	27751
Q_{out} [kJ]	20534	21059	18341
Avg. Heating Power [kW]	2.33	1.99	2.09
SHP [W/kg]	529.5	452.3	475
COP [-]	0.82	0.75	0.66

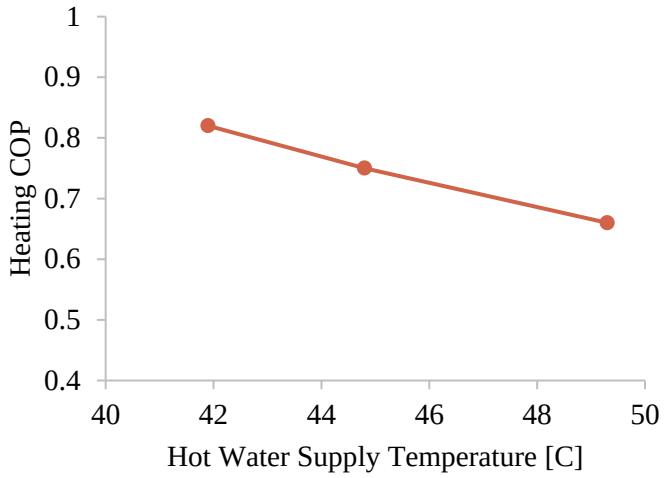

Figure 43 Heating COP under different hot water supply temperatures

The condensation heat outputs decrease with the increase of the heat rejection temperature. On the other hand, the desorption heat input of three cases were similar, with HT-L about 11% lower than the other two due to slightly lower firing rate. The adsorption heat outputs of the three cases were similar as well. As a result, the COP drops from 0.82 to 0.65 as the heat rejection temperature increases from 40°C to 50°C. The increase of the condensation heat output can be attributed to the

lower heat supply temperature, which in turn required less condensation heat for heating up the condenser/evaporator thermal mass.

4.4.4.3 Burner Firing Rate

The impact of the burner firing rate was investigated by comparing two tests: FR-L and FR-H. As shown in Table 19 and illustrated in Figure 44, the two cases were operated under the same ambient temperature, with similar hot water inlet return temperatures. FR-L had an average natural gas consumption rate of 0.91 cfm during burner operation; FR-H operated at a 23% higher average rate of 1.12 cfm. Based on the correlation of natural gas consumption and heat input to the adsorber via the heat pipe (see appendix), the average heat input of the two cases were 16.0kW and 19.7kW.

Table 19 Performance comparison of tests under different burner firing rates

Run	FR-L	FR-H
Setup	#3	#3
Insulation	Yes	Yes
Cycle Type	Initial	Initial
T_{amb} [°C]	7.9	8
HW Return Temp. (T12) [°C]	44.3	43.6
HW Supply Temp. (T11) [°C]	49.4	48.2
Des. Mode Time [min]	61.6	83.9
Sorp. Mode Time [min]	59.5	62.1
Tot. Cycle Time [min]	121.1	146
Avg. Ng Firing Rate [cfm]	1.12	0.91
Total Ng Usage [cf]	62.92	70.19
Q_{des} [kJ]	39830	44428
$Q_{cond,In}$ [kJ]	1430	863
$Q_{cond,Out}$ [kJ]	4576	4667
Q_{ads} [kJ]	27209	29617
Q_{in} [kJ]	41260	45291
Q_{out} [kJ]	31785	34284
Avg. Heating Power [kW]	4.18	3.77
SHP [W/kg]	475	428.4
COP [-]	0.77	0.76

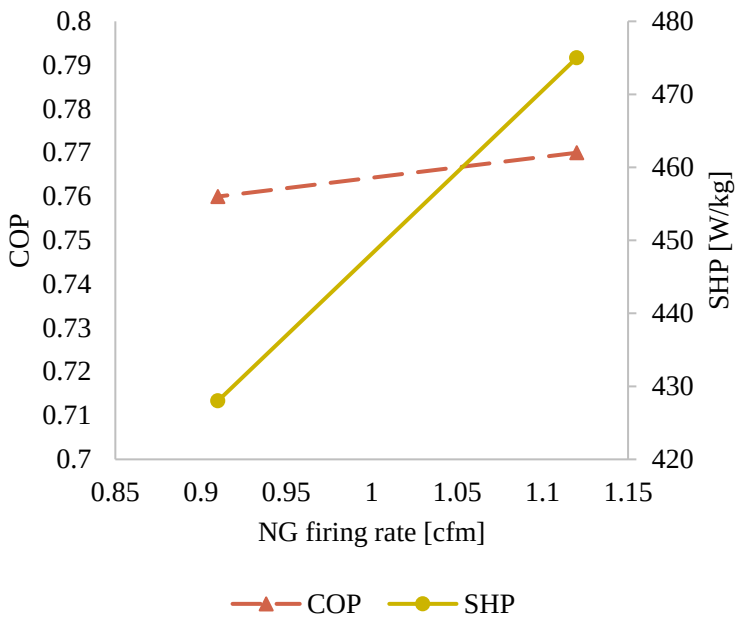

Figure 44 COP and SHP under different firing rate

As described in the operation procedure, the cyclic mode-switching was controlled by the minimum heat production rate. Therefore, FR-H with the higher heat input rate reached exhaustion of ammonia in the adsorber faster, and thus the desorption mode lasted for only 61.6 min before the system was switched to the sorption mode. The desorption mode for FR-L, in contrast, lasted for 20 min or 34% longer due to the slower input of heat into the adsorber. Meanwhile, the sorption mode of the two cycles took similar amount of time. Thus, the overall shortened cycle time for the higher-firing-rate case overwhelmed the slight increase of condensation and sorption heat output from more complete desorption, and therefore the average heating power of FR-H is 10% higher than that of FR-L.

On the other hand, the COP difference between the two cases is not significant. To exhaust the same amount of ammonia in the adsorber towards the minimum heat rejection rate, a similar amount of heat is needed. The total heat input can be achieved with either a higher input rate and a shorter cycle time, as in the case of FR-H; or a lower input rate and a longer cycle time, as in the case of FR-L. The slight increase of heat input as well as heat output in both condensation and sorption under a lower firing rate as shown by comparing FR-L and FR-H indicates a more complete desorption process at a slower heating rate. With 4598 kJ or 11% more heat input, the longer cycle got 22% more condensing heat and 9% more sorption heat, or a total of 3071 kJ in

return. As the result, within the heat input rate of these two cases, the trade-off of a higher cyclic total heat output and a higher average heat output rate does not affect the COP much.

4.4.4.4 Initial cycle vs. normal cycle

The differences between an initial (cold-start) cycle and a normal cycle were investigated by comparing two pairs of cycles of each type. IN-I1 and IN-N1 (also as the BC cycle) were setup #3 tested under 8°C ambient temperature. IN-I2 and IN-N2 were setup #2 systems tested under 25°C and 30°C.

Table 20 Performance comparison of tests of different cycle types

Run	IN-I1	IN-N1	IN-I2	IN-N2
Setup	#3	#3	#2	#2
Insulation	Yes	Yes	Yes	Yes
Cycle Type	Initial	Normal	Initial	Normal
T_{amb} [°C]	8	7.9	25.1	30
HW Return Temp. (T12) [°C]	43.6	44.4	44.3	44.1
HW Supply Temp. (T11) [°C]	48.2	49.7	50	50.2
Des. Mode Time [min]	83.9	66	99.1	90
Sorp. Mode Time [min]	62.1	58.1	57.8	51.1
Tot. Cycle Time [min]	146	124.1	156.9	141.1
Avg. Ng Firing Rate [cfm]	0.91	0.92	0.46	0.45
Total Ng Usage [cf]	70.19	50.74	36.2	29.88
Q_{des} [kJ]	44428	32119	22916	18913
$Q_{cond,In}$ [kJ]	863	1229	796	530
$Q_{cond,Out}$ [kJ]	4667	2619	4109	4042
Q_{ads} [kJ]	29617	28119	18560	18570
Q_{in} [kJ]	45291	33348	23712	19443
Q_{out} [kJ]	34284	30738	22669	22612
Avg. Heating Power [kW]	3.77	3.91	2.33	2.6
SHP [W/kg]	428.4	444.3	529.5	590.9
COP [-]	0.76	0.92	0.96	1.16

As shown in Table 20, the most important difference of the two type of cycles is with the required heat input and condensation heat output. As analyzed with the AT-L1 and AT-L2 cycle, the energy input required to heat the adsorber up to the desorption temperatures is more significant for cold-start cycles. This is again manifested by comparing the cyclic energy changes of thermal masses in the two types of cycles in Table 21 and Table 22. The initial heat-up of the adsorber and the condenser takes about 20% of the total heat input into the system, with the heat pipe water, the adsorber shell, and the ammonia in the sorbent the major contributors.

Table 21 Cyclic energy change of thermal masses in an initial (IN-I1) cycle

Component/material	Thermal mass [kJ/K]	Starting temperature [C]	Ending temperature [C]	Change in energy [kJ]	% of Qdes
Sorbent/salt + carbon	13.2	7.9	45.8	500.28	1.13
Ammonia	40.32	7.9	45.8	1528.13	3.44
Adsorber HX/SS	16	7.9	45.8	606.40	1.36
Adsorber Shell/SS	48	7.9	79.5	3436.80	7.74
CE HX/SS	16	8.0	7.8	-3.20	-0.01
CE shell/SS	48	8.0	11.9	187.20	0.42
Water in heat pipe	66.88	7.9	45.8	2534.75	5.71
Total				8790.36	19.79

In contrast, the temperatures of each component and material in the system at the start of the normal cycle is close to their temperatures at the end of the cycle, and therefore the heat loss associated with heating up the thermal masses from the ambient temperature, especially those in the adsorber, is eliminated. The heat-up energy only takes less than 0.4% of the total heat input. As a result, the COP of the normal cycle is 23% higher than the initial cycle under the same operating condition.

Table 22 Cyclic energy change of thermal masses in a normal (IN-N1) cycle

Component/material	Thermal mass [kJ/K]	Starting temperature [C]	Ending temperature [C]	Change in energy [kJ]	% of Qdes
Sorbent/salt + carbon	6.6	45.9	46.6	4.6	0.014
Ammonia	20.16	45.9	46.6	14.1	0.043
Adsorber HX/SS	8	45.9	46.6	5.6	0.017
Adsorber Shell/SS	24	79.4	81.4	48.0	0.147
CE HX/SS	8	7.8	7.7	-0.8	-0.002
CE shell/SS	24	10.3	11.5	28.8	0.088
Hot water	33.44	45.9	46.6	23.4	0.072
Total				123.7	0.380

5. ADSORBER MODELLING

In this chapter, the dynamic model of the salt-containing adsorber is introduced. First, the geometry of the modelled control volume is described, followed by general model assumption. Then the governing equations describing the transient heat and mass transfer as well as chemical reaction in the modelled control volume are derived from fundamental correlations. To solve the governing differential equations, finite-difference method is applied to discretize the equations for numerical solution. Finally, the results of the adsorber model are illustrated, and the adsorber performance characteristic under different design parameters and operating conditions are discussed.

5.1 Adsorber Component Geometry

As shown in the schematic of the adsorber in Figure 45, the adsorber is built around a stack of salt matrix – heat pipe plates, with steam/water connection of the heat pipe plates to the burner or reservoir tank, and ammonia vapor connection to the condenser/evaporator.

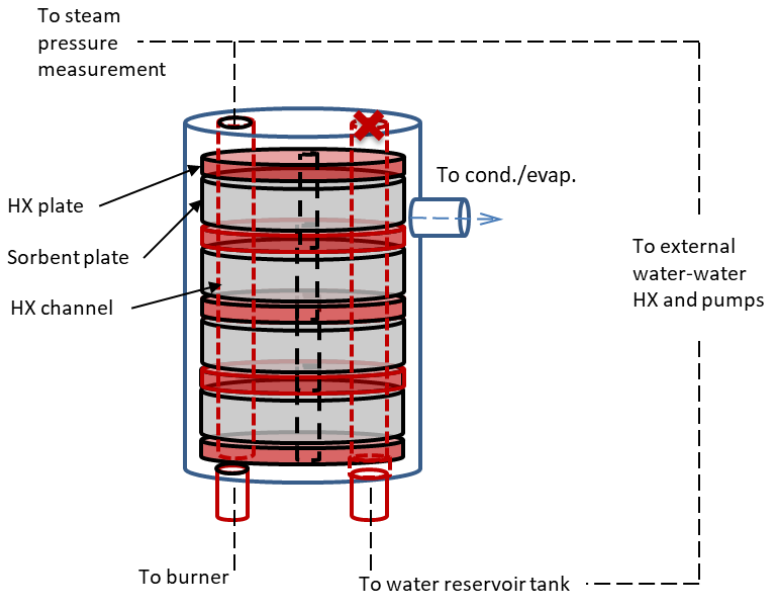

Figure 45 schematic of the adsorber

The CAD drawing of the adsorber in the prototype system is shown in Figure 46. There are 56 composite sorbent disks in the adsorber between the heat exchanger plates. Each of the sorbent disk has an outer diameter of 150 mm and a thickness of 10 mm.

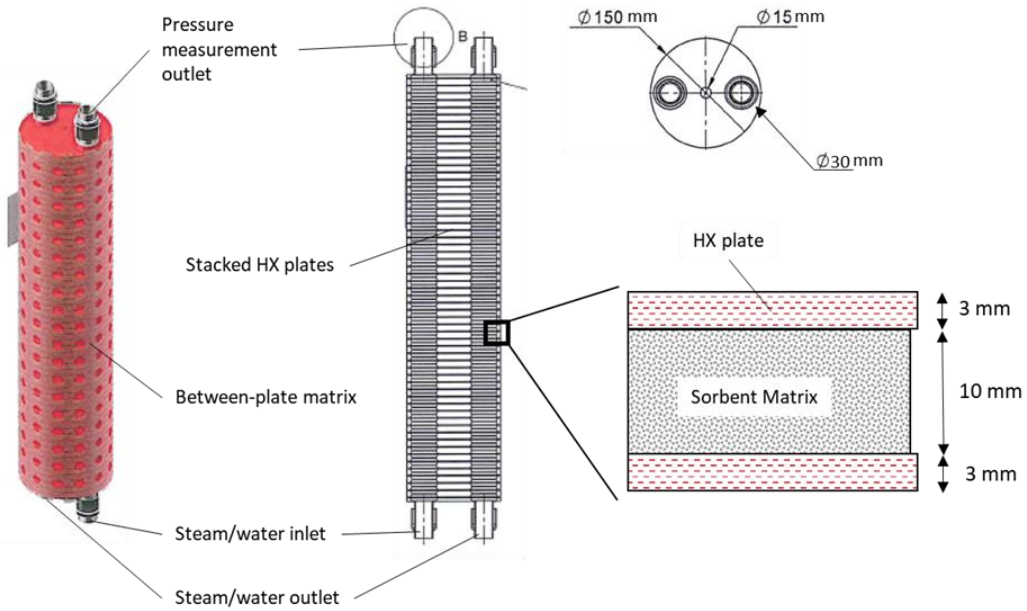

Figure 46 schematic and dimension of the adsorber heat exchanger and the sorbent matrix

There is a hollow center through all the salt and heat pipe plates from top to bottom, providing extra passage for ammonia vapor to flow in and out of the salt in the center of the plate. Each piece of the salt plate contains around 1 mole or 42g of LiCl salt, which is impregnated in the porous carbon matrix material.

During operation, the heat pipe plates conducts heat to or from the salt plates, leading to the endo- or exothermic chemical reaction between the salt and ammonia vapor to occur. The pores where salt grains reside are inter-connected to allow ammonia vapor to flow into and through for reaching the salt. With the proceeding of the reaction, the molar concentration in the local pore changes, creating a driving force for the ammonia vapor in the local pore to flow.

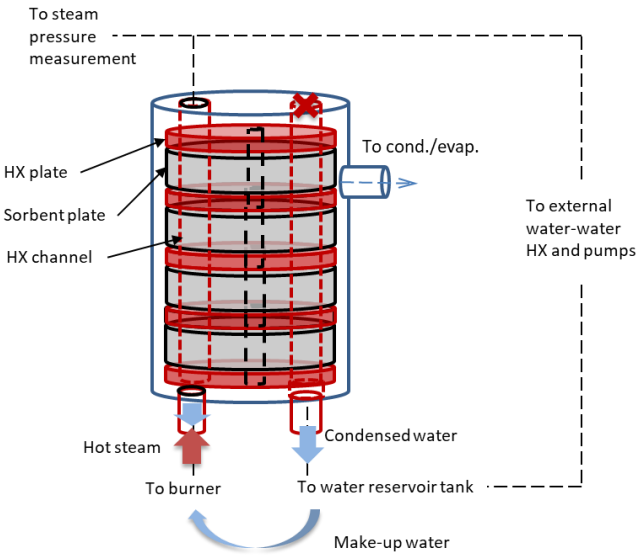

Figure 47 schematic illustration of the adsorber in desorption mode

During desorption mode as shown in Figure 47, the ammonia vapor accumulated in the interior of the salt plate eventually arrives at the inner or external perimeter of the salt plate and gets released into the adsorber chamber. During sorption mode as in Figure 48, ammonia vapor from evaporator seeps into the salt plates from the perimeter to get adsorbed by the dry salts.

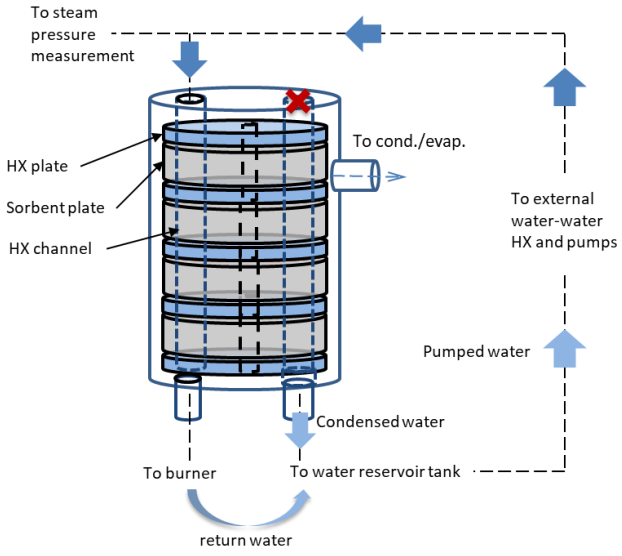

Figure 48 schematic illustration of adsorber in sorption model

In addition to the sorbent disks, the envelope shell of the adsorber vessel is also exchanging heat with the heat pipe and the ambient and is included in the adsorber dynamic model. For the shell,

the temperature of the steam or water in the heat pipe is used to calculate their heat exchange with the heat pipe (Q_{shell}). Meanwhile, since the shell is exposed to the ambient, its heat loss via convection and radiation heat transfer is calculated based on the temperatures of the shell and the surrounding ambient.

5.2 Sorbent Model Description

5.2.1 Differential Control Volume

The coupled heat mass transfer and chemical reaction cannot be analytically studied. Instead, these transient processes in the adsorber are numerically investigated in detail by dividing the salt into differential control volumes (c.v.). The governing equation of the processed in a differential c.v. can be derived and solved, and eventually the status of the entire adsorber can be described as the summation of the differential c.v.

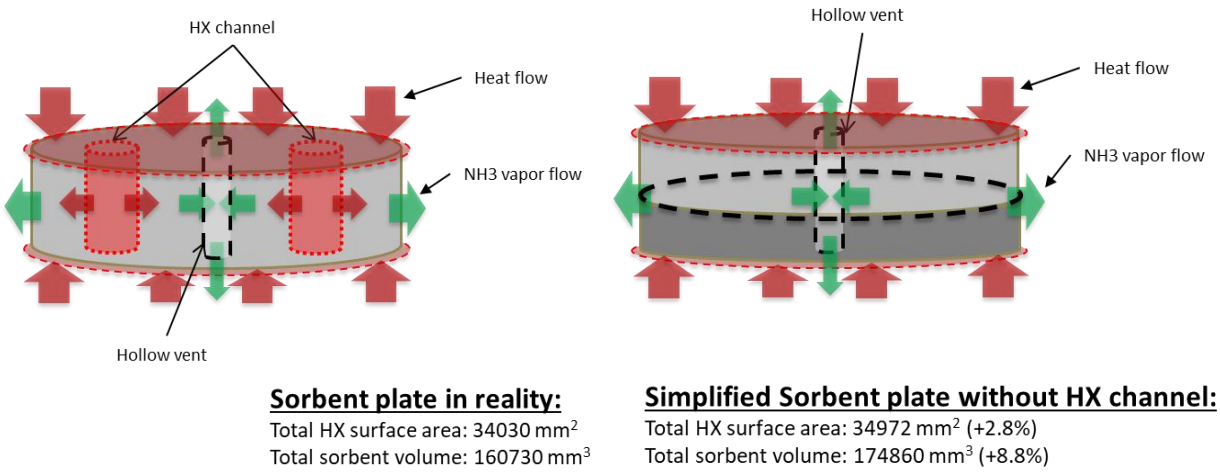

Figure 49 simplification of the sorbent disk geometry

In the actual adsorber heat exchanger there are two vertical pipes going through all the salt and heat pipe disks as the steam flow channel. To simplify calculation, both the sorbent disk and the heat pipe plates in the model are solid with only the center ammonia vent. Such simplification leads to 2.8% of total heat exchange surface area increase, and 8.8% sorbent volume increase compared with the actual dimensions as illustrated in Figure 49. With the effective diameter of the steam flow channel large sufficiently large, all the heat pipe plates are assumed to share the same steam pressure. The condensation heat transfer onto the heat pipe plate surface above the salt (roof)

and below the salt (ceiling) are calculated using empirically fitted correlation of Nusselt number for upward and downward flat disks.

The salt disk is a typical cylindrical geometry that can be divided into differential "rings" as shown in Figure 50. The cross-section of the ring is rectangular, and by using a cylindrical coordination $z - r$ the differential c.v. can be described as below:

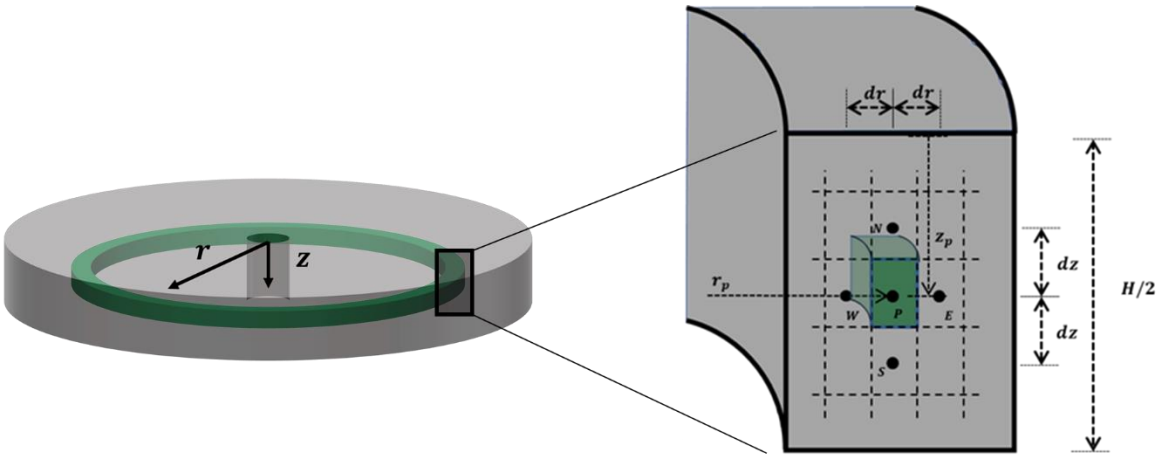

Figure 50 control volume division of the salt disk

c.v. P is a representative c.v., with the adjacent c.v. termed east/west/north/south. The distance between the center of adjacent c.v. in the radial direction is defined as dr, and in the vertical direction as dz. Obviously, the dimensions of the c.v. are determined by the number of c.v. created as well as the absolute radius from the c.v. center to the center line of the cylinder.

5.2.2 Key Assumptions

To describe the transient processes in the salt disk, following simplifying assumptions are made:

- The disk geometry is simplified as solid disk with a center vent.
- Uniform steam pressure across all heat pipe plates and the steam is at saturation state.
- Uniform ammonia pressure across the adsorber.
- Neglect convection and radiation heat transfer between the ammonia vapor and the sorbent.

Therefore, only one disk needs to be modeled to be representative of all the sorbent disks in the adsorber, and the overall adsorber performance can be calculated based on the modeled disk operation parameters.

5.2.3 Governing Equations

5.2.3.1 Heat Transfer and Energy Balance

In a c.v. the energy balance equation can be written as:

$$\Delta Q_{int} = \dot{Q}_z + \dot{Q}_r + \dot{S}_{chem} \quad \text{Equation 16}$$

Where ΔQ_{int} is the change of internal energy, $\dot{Q}_z$ is the net heat inflow in vertical direction, $\dot{Q}_r$ is the net heat inflow in radial direction, and $\dot{S}_{chem}$ is the reaction heat.

For heat transfer between adjacent c.v., Fourier's law applies:

$$\dot{q} = -K \cdot \nabla T \quad \text{Equation 17}$$

For the net inflow in vertical direction:

$$\dot{Q}_z = \dot{Q}_n - \dot{Q}_s = \frac{d\dot{q}_z \cdot A_z}{dz} \cdot dz = \frac{\partial}{\partial z}\left(K_T \cdot \frac{\partial T}{\partial z} \cdot r \cdot 2\pi \cdot dr\right) \cdot dz = K_T \cdot \frac{\partial^2 T}{\partial z^2} \cdot dr \cdot r \cdot 2\pi \cdot dz \quad \text{Equation 18}$$

Where K_T is the thermal conductivity, and $\dot{Q}_n$ and $\dot{Q}_s$ are heat conduction with the two vertically adjacent c.v. A_z is the top-bottom surface area of the c.v.

Similarly, for heat conduction in radial direction:

$$\dot{Q}_r = \dot{Q}_e - \dot{Q}_w = \frac{d\dot{q}_r \cdot A_r}{dr} \cdot dr = \frac{\partial}{\partial r}\left(K_T \cdot \frac{\partial T}{\partial r} \cdot r \cdot 2\pi \cdot dz\right) \cdot dr \quad \text{Equation 19}$$

$$= K_T \cdot \frac{\partial^2 T}{\partial r^2} \cdot dz \cdot r \cdot 2\pi \cdot dr + K_T \cdot \frac{\partial T}{\partial r} \cdot dz \cdot 2\pi \cdot dr$$

$\dot{Q}_e$ and $\dot{Q}_w$ are heat conduction with the two radially adjacent c.v. A_r is the radial surface area of the c.v. And finally, for chemical reaction heat in the c.v.:

$$\dot{S}_{chem} = S_{v,q} \cdot V = \Sigma \frac{dN_{NH3,i} \cdot \Delta H_{r,i}}{dt} \cdot n_{salt} \cdot dz \cdot dr \cdot r \cdot 2\pi \quad \text{Equation 20}$$

Where $N_{NH3,i}$ is the ammonia change associated with reaction, $\Delta H_{r,i}$ is the reaction heat, and n_{salt} is the volumetric mole density of salt in the c.v.

The change of internal energy can be expressed with specific heat as:

$$\Delta Q_{int} = \rho \cdot Cp \cdot \frac{\partial T}{\partial t} \cdot dz \cdot r \cdot 2\pi \cdot dr \quad \text{Equation 21}$$

Where ρ and Cp are the apparent density and specific heat of the c.v. Substitute Eqn. (15-18) into Eqn. (13) and cancel out the volume of the c.v., the energy balance governing equation is:

$$\rho \cdot Cp \cdot \frac{\partial T}{\partial t} = K_T \cdot \left(\frac{\partial^2 T}{\partial z^2} + \frac{\partial^2 T}{\partial r^2} + \frac{1}{r} \cdot \frac{\partial T}{\partial r} \right) + S_{v,q} \quad \text{Equation 22}$$

5.2.3.2 Mass Transfer and Local Ammonia Vapor Mass Balance

Like heat conduction between adjacent c.v., ammonia vapor in the interconnected pores flows across the boundary of c.v. through diffusion driven by the molar concentration difference. The mass balance is:

$$\Delta N = J_z + J_r + J_{chem}$$ Equation 23

Where N is the total amount of ammonia vapor in the pores of the c.v., J_z is net mass inflow flux in the vertical direction, J_r for radial direction, and J_{chem} is the ammonia vapor change due to chemical reaction. According to Fick's first law the diffusion the molar flow flux can expressed as:

$$J = D \cdot \nabla n$$ Equation 24

D is the diffusivity and n is the volumetric molar density. For diffusion Darcy's law can be used to calculate the diffusivity based on permeability:

$$u = -\frac{K_M}{\mu} \cdot \nabla P$$ Equation 25

u is the Darcy velocity caused by the pressure difference, K_M the permeability of the porous material, and μ the dynamic viscosity of the fluid. By associating the flow velocity and the flux, the molar flow flux using the Darcy's law is:

$$J = u \cdot n_{tot} = -\frac{K_M}{\mu} \cdot \nabla P \cdot \frac{P_p}{R \cdot T_p} \cdot \varphi$$ Equation 26

Where φ is the porosity and R the gas constant. Eqn. (23) can be derived from below using the porosity definition:

$$\frac{P_p}{R \cdot T_p} = n_{pore} = \frac{N}{V_{pore}} = \frac{N}{V_{tot}} \cdot \frac{1}{\varphi} = \frac{n_{tot}}{\varphi}$$ Equation 27

Therefore, the diffusivity of slip flow can be written as:

$$D = -\frac{K_M}{\mu} \cdot P_p \cdot \varphi$$ Equation 28

With the diffusivity, the net inflow fluxes in both vertical and radial direction can be written as Eqn. (25) and (26):

$$J_z = J_n - J_s = \frac{\partial}{\partial z}\left(D \cdot \frac{\partial n}{\partial z} \cdot r \cdot 2\pi \cdot dr\right) \cdot dz$$

$$= D \cdot \frac{\partial^2 n}{\partial z^2} \cdot dr \cdot r \cdot 2\pi \cdot dz$$ Equation 29

$$J_r = J_e - J_w = \frac{\partial}{\partial r}\left(D \cdot \frac{\partial n}{\partial r} \cdot r \cdot 2\pi \cdot dz\right) \cdot dr$$

$$= D \cdot \left(\frac{\partial^2 n}{\partial r^2} \cdot r \cdot 1 \cdot dz + \frac{\partial n}{\partial r} \cdot dz \cdot 2\pi\right) \cdot dr$$ Equation 30

Finally, for chemical reaction the ammonia generation flux is:

$$J_{chem} = S_{v,n} \cdot V = \Sigma \frac{dN_{NH3,i}}{dt} \cdot n_{salt} \cdot dz \cdot dr \cdot r \cdot 2\pi$$ Equation 31

Substituting Eqn. (25-27) into Eqn. (20) and cancelling out volume term we have:

$$\frac{\partial n}{\partial t} = D \cdot \left(\frac{\partial^2 n}{\partial z^2} + \frac{\partial^2 n}{\partial r^2} + \frac{1}{r} \cdot \frac{\partial n}{\partial r} \right) + S_{v,q}$$ Equation 32

5.2.3.3 Chemical Reaction

The chemical reactions used in the studied system are:

$$LiCl \cdot 3NH_3(s) \rightarrow LiCl \cdot 2NH_3(s) + NH_3(g)$$

$$LiCl \cdot 2NH_3(s) \rightarrow LiCl \cdot 1NH_3(s) + NH_3(g)$$

$$LiCl \cdot 1NH_3(s) \rightarrow LiCl(s) + NH_3(g)$$

The equilibrium state of each chemisorption reaction can be described using the van't Hoff equations:

$$ln\left(P_{eq}/P_0\right) = -\frac{\Delta H_r}{RT_{salt}} + \frac{\Delta S_r}{R}$$ Equation 33

With ΔH_r and ΔS_r the enthalpy and entropy change associated with the reaction. The reaction kinetics of chemisorption reaction is expressed in Eqn. (30) as the change rate of the reaction progression.

$$\frac{dX}{dt} = (1 - X)^n \cdot s \cdot exp\left(\frac{E_a}{RT}\right) \cdot ln\left(\frac{P_{eq}(T_{salt})}{P_{local}}\right)$$ Equation 34

The n in Eqn. (30) is the pseudo-order of the reaction and is experimentally determined. X is the reaction progression defined as in Eqn. (31), where γ is the stochastic ratio of the reaction product and the reactant. In the case of the reaction used in this study, the stochastic ratio is 1:1.

$$X = \frac{\gamma \cdot N_{product,t}}{N_{reactant,0}} = \frac{\gamma \cdot N_{product,t}}{\gamma \cdot N_{product,t} + N_{reactant,t}} = \frac{N_{LiCl\cdot(n-1)NH_3}}{N_{LiCl\cdot nNH_3} + N_{LiCl\cdot(n-1)NH_3}} = \frac{N_{NH_3}}{N_{LiCl\cdot nNH_3} + N_{LiCl\cdot(n-1)NH_3}}$$ Equation 35

The second term in Eqn. (30) is the Arrhenius term $Ar = s \cdot \exp\left(\frac{E_a}{RT}\right)$ describing the influence of temperature on the reaction rate. In the Arrhenius term s is the pre-exponential constant determined from experiment data, and E_a is the effective activation energy associated to the reaction. Although the Arrhenius term is a function of the salt temperature, it was deemed as constants in literature for desorption and adsorption assuming the effect of temperature variation during the process is neglectable. In this study the Arrhenius terms are deemed as constants that are curve-fitted from specially contrived experimental tests to acquire them.

Taking time derivative of Eqn. (31), the ammonia generation rate can be correlated to the chemical reaction rate in Eqn. (32):

$$\frac{dN_{NH3,i}}{dt} = \frac{dX_i}{dt} \cdot \left(N_{LiCl\cdot iNH3} + N_{LiCl\cdot(i-1)NH3}\right)$$ Equation 36

5.2.4 Discretization and Solving Scheme

To solve the spatial differential equations (heat and mass transfer) numerically, the differential equations need to be discretized over the simulated control volume (half plate). Meanwhile, since there is also a temporal derivative in both the energy and substance balance equations, different approaches can be used to discretize the time-derivative terms over the simulation time step and calculate the next moment values based on the previous moment values.

5.2.4.1 Explicit Approach

The explicit approach assumes all target values (temperature in energy equation and molar density in substance equation) remains at the previous values until the end of a time step. Therefore, the heat and mass transfer are calculated based on the previous moment target values.

Discretize both the first and second order spatial derivatives using central-difference method to achieve second-order truncating error; discretize the first order temporal derivatives using forward-difference method with first-order truncating error. Then the energy and substance balance equations (Equation 33 and Equation 34)can be written as below with explicit discretization approach:

$$\frac{1}{\alpha}\cdot\frac{T_{r,z}^{1}-T_{r,z}^{0}}{\Delta t}=\frac{T_{r,z+1}^{0}+T_{r,z-1}^{0}-2T_{r,z}^{0}}{(\Delta z)^{2}}+\frac{T_{r+1,z}^{0}+T_{r-1,z}^{0}-2T_{r,z}^{0}}{(\Delta r)^{2}}+\frac{T_{r+1,z}^{0}-T_{r-1,z}^{0}}{2\Delta r\cdot r}+\frac{1}{K_{T}}\cdot S_{v,q} \quad \text{Equation 37}$$

$$\frac{n_{r,z}^{1}-n_{r,z}^{0}}{\Delta t}=\mathrm{D}\cdot\left(\frac{n_{r,z+1}^{0}+n_{r,z-1}^{0}-2n_{r,z}^{0}}{(\Delta z)^{2}}+\frac{n_{r+1,z}^{0}+n_{r-1,z}^{0}-2n_{r,z}^{0}}{(\Delta r)^{2}}+\frac{n_{r+1,z}^{0}-n_{r-1,z}^{0}}{2\Delta r\cdot r}\right)+S_{v,n} \quad \text{Equation 38}$$

$T_{r,z}$ and $n_{r,z}$ are the temperature and molar density of DCV at the r^{th} radial and z^{th} vertical position; Δz and Δr are the height and radial width of the DCV; the relative locations of adjacent c.v. are noted with subscript, under the same cylindrical coordination introduced. Superscript 0 and 1 means the previous-moment and current-moment values.

In Equation 37 and Equation 38, all but one current-moment values are known, and therefore the equations can be directly solved with previous-moment values. The advantage of the explicit approach is simplicity in implementation. On the other hand, it also has the risk of introducing numeric oscillation that might cause the solution to diverge [149]. Therefore, criteria for selecting the cell size (Δz, Δr) as well as the time step (Δt) need to be applied to ensure stability of explicitly solved equation.

$$1 - \frac{2\alpha\Delta t}{(\Delta z)^2} - \frac{2\alpha\Delta t}{(\Delta r)^2} > 0, \Delta t < \frac{1}{2\alpha} \cdot \left(\frac{1}{(\Delta z)^2} + \frac{1}{(\Delta r)^2}\right)$$

Equation 39

$$1 - \frac{2D\Delta t}{(\Delta z)^2} - \frac{2D\Delta t}{(\Delta r)^2} > 0, \Delta t < \frac{1}{2D} \cdot \left(\frac{1}{(\Delta z)^2} + \frac{1}{(\Delta r)^2}\right)$$

Equation 40

The actual time step used in simulation needs to be smaller than the minimum of the two. When the DCV is small, as implied in these two equations, the maximum time step could be very small, leading to many computation steps and long computation time. For instance, dividing a sorbent plate of 1 cm thick and 15 / 1.5 cm of outer and inner radii into 3 vertical by 5 radial DCVs and with representative diffusivities, the stability criterion for energy equation requires the time step to be smaller than 0.0914 s, while that for the substance balance equation is 7.5e-5 s, which is not practical for simulation of cycles with time span of over 1-2 hours.

5.2.4.2 Implicit Approach

Another approach to solve the discretized differential equation is the implicit approach. Instead of correlating the current-moment parameter to that of adjacent DCVs in the previous-moment, the implicit approach assumes the changes of target values (temperature, molar density) due to transfer phenomena occur at the start of the time step. Therefore, the spatial transfer in the balance equations instead correlates $T_{r,z}^1$ and $n_{r,z}^1$ directly with the current-moment values at adjacent DCVs, leaving the only known in the equation to be the previous-moment temperature and molar density at the target DCV. Following the implicit approach, the energy and substance balance equations Equation 41 and Equation 42 are again discretized with central-difference in space and forward-difference in time into:

$$\frac{1}{\alpha}\cdot\frac{T_{r,z}^{1}-T_{r,z}^{0}}{\Delta t}=\frac{T_{r,z+1}^{1}+T_{r,z-1}^{1}-2T_{r,z}^{1}}{(\Delta z)^{2}}+\frac{T_{r+1,z}^{1}+T_{r-1,z}^{1}-2T_{r,z}^{1}}{(\Delta r)^{2}}+\frac{T_{r+1,z}^{1}-T_{r-1,z}^{1}}{2\Delta r\cdot r}+\frac{1}{K}\cdot S_{v,q}^{1}$$ Equation 41

$$\frac{n_{r,z}^{1}-n_{r,z}^{0}}{\Delta t\cdot D}=\frac{n_{r,z+1}^{1}+n_{r,z-1}^{1}-2n_{r,z}^{1}}{(\Delta z)^{2}}+\frac{n_{r+1,z}^{1}+n_{r-1,z}^{1}-2n_{r,z}^{1}}{(\Delta r)^{2}}+\frac{n_{r+1,z}^{1}-n_{r-1,z}^{1}}{2\Delta r\cdot r}+\frac{1}{D}\cdot S_{v,n}$$ Equation 42

Equation 41 and Equation 42 can be re-arranged so that the current-moment values are at the left-hand side and the previous-moment values as well as the source terms are at the right-hand side:

$$\left(\frac{1}{\Delta t\alpha}+\frac{2}{\Delta z^{2}}+\frac{2}{\Delta r^{2}}\right)T_{r,z}^{1}-\frac{1}{\Delta z^{2}}T_{r,z+1}^{1}-\frac{1}{\Delta z^{2}}T_{r,z-1}^{1}-\left(\frac{1}{\Delta r^{2}}+\frac{1}{2r\Delta r}\right)T_{r+1,z}^{1}-\left(\frac{1}{\Delta r^{2}}-\frac{1}{2r\Delta r}\right)T_{r-1,z}^{1}=\frac{1}{K}\cdot S_{v,q}^{1}+\frac{1}{\Delta t\alpha}T_{r,z}^{0}$$ Equation 43

$$\left(\frac{1}{\Delta tD}+\frac{2}{\Delta z^{2}}+\frac{2}{\Delta r^{2}}\right)n_{r,z}^{1}-\frac{1}{\Delta z^{2}}n_{r,z+1}^{1}-\frac{1}{\Delta z^{2}}n_{r,z-1}^{1}-\left(\frac{1}{\Delta r^{2}}+\frac{1}{2r\Delta r}\right)n_{r+1,z}^{1}-\left(\frac{1}{\Delta r^{2}}-\frac{1}{2r\Delta r}\right)n_{r-1,z}^{1}=\frac{1}{D}\cdot S_{v,n}^{1}+\frac{1}{\Delta tD}n_{r,z}^{0}$$ Equation 44

Then the Equation 43 and Equation 44 of all DCVs form a system of linear equations of the current-moment temperatures and molar densities that can be solved numerically for all the current values and source terms. The system of equations built from Eqn. (30) is explained in the following. First,

create a matrix with z rows and r columns corresponding to the discretization scheme, and fill the matrix with the current-moment temperatures at each corresponding DCV as T; rearrange the matrix into a 1-D array $\boldsymbol{x}$:

$$\{T\} = \begin{pmatrix} T_{r1,z1} & T_{r2,z1} & \cdots & T_{rn,z1} \\ T_{r1,z2} & T_{r2,z2} & \cdots & T_{rn,z2} \\ \vdots & \vdots & \vdots & \vdots \\ T_{r1,zm} & T_{r2,zm} & \cdots & T_{rn,zm} \end{pmatrix}_{m \times n} , \boldsymbol{x} = \begin{pmatrix} T^1_{r1,z1} \\ T^1_{r2,z1} \\ \vdots \\ T^1_{rn,z1} \\ T^1_{r1,z2} \\ \vdots \\ T^1_{rn,zm} \end{pmatrix} \quad \text{Equation 45}$$

Similarly build the 1-D array $\boldsymbol{b}$ of previous-moment values and source terms corresponding to each DCV:

$$\boldsymbol{b} = \begin{pmatrix} S^1_{v,q,r1,z1} + \dfrac{1}{\Delta t \alpha} T^0_{r1,z1} \\ S^1_{v,q,r2,z1} + \dfrac{1}{\Delta t \alpha} T^0_{r2,z1} \\ \vdots \\ S^1_{v,q,rn,z1} + \dfrac{1}{\Delta t \alpha} T^0_{rn,z1} \\ S^1_{v,q,r1,z2} + \dfrac{1}{\Delta t \alpha} T^0_{r1,z2} \\ \vdots \\ S^1_{v,q,rn,zm} + \dfrac{1}{\Delta t \alpha} T^0_{rn,zm} \end{pmatrix} \quad \text{Equation 46}$$

Let:

$$a = \frac{1}{\Delta t \alpha} + \frac{2}{\Delta z^2} + \frac{2}{\Delta r^2} \quad \text{Equation 47}$$

$$b = c = -\frac{1}{\Delta z^2} \quad \text{Equation 48}$$

$$d = \frac{-1}{\Delta r^2} + \frac{-1}{2r\Delta r}$$ Equation 49

$$e = \frac{-1}{\Delta r^2} + \frac{1}{2r\Delta r}$$ Equation 50

Then the left-hand side of Equation 43 becomes:

$$a \cdot T^1_{r,z} + b \cdot T^1_{r,z+1} + c \cdot T^1_{r,z-1} + d \cdot T^1_{r+1,z} + e \cdot T^1_{r-1,z}$$ Equation 51

The operator matrix A is built as:

$$A = \begin{pmatrix} a_{r1,z1} & d_{r1,z1} & 0 & 0 & \dots & 0 & 0 & 0 & b_{r1,z1} & 0 & 0 & \dots & 0 & 0 & 0 \\ e_{r2,z1} & a_{r2,z1} & d_{r2,z1} & 0 & \dots & 0 & 0 & 0 & 0 & b_{r2,z1} & 0 & \dots & 0 & 0 & 0 \\ 0 & e_{r3,z1} & a_{r3,z1} & d_{r3,z1} & \dots & 0 & 0 & 0 & 0 & 0 & b_{r3,z1} & \dots & 0 & 0 & 0 \\ \vdots & \vdots & \vdots & \vdots & \dots & \vdots & \vdots & \vdots & \vdots & \vdots & \vdots & \dots & \vdots & \vdots & \vdots \\ 0 & 0 & 0 & 0 & \dots & e_{rn-1,z1} & a_{rn-1,z1} & d_{rn-1,z1} & 0 & 0 & 0 & \dots & 0 & 0 & 0 \\ 0 & 0 & 0 & 0 & \dots & 0 & e_{rn,z1} & a_{rn,z1} & 0 & 0 & 0 & \dots & 0 & 0 & 0 \\ c_{r1,z2} & 0 & 0 & 0 & \dots & 0 & 0 & 0 & a_{r1,z2} & d_{r1,z2} & 0 & \dots & 0 & 0 & 0 \\ 0 & c_{r2,z2} & 0 & 0 & \dots & 0 & 0 & 0 & e_{r2,z2} & a_{r2,z2} & d_{r2,z2} & \dots & 0 & 0 & 0 \\ \vdots & \vdots & \vdots & \vdots & \dots & \vdots & \vdots & \vdots & \vdots & \vdots & \vdots & \dots & \vdots & \vdots & \vdots \\ 0 & 0 & 0 & 0 & \dots & 0 & 0 & 0 & 0 & c_{rn-1,zm} & 0 & \dots & e_{rn-1,zm} & a_{rn-1,zm} & d_{rn-1,zm} \\ 0 & 0 & 0 & 0 & \dots & 0 & 0 & 0 & 0 & 0 & c_{rn,zm} & \dots & 0 & e_{rn,zm} & a_{rn,zm} \end{pmatrix}_{(n \times m)}$$ Equation 52

With each DCV having a corresponding $a \sim e$ values in the operator matrix. A has five diagonals of elements, each corresponding to the coefficient of current-moment temperatures in the re-arranged left-hand side above.

Finally, the system of equations can be written and solved as Equation 53:

$$A \cdot \boldsymbol{x} = \boldsymbol{b} \rightarrow \boldsymbol{x} = A^{-1} \cdot \boldsymbol{b}$$ Equation 53

The same operator matrix can be used for the substance balance equation (Equation 44), with the unknown array and the known/source term array written as below and solved similarly with Equation 44:

$$\boldsymbol{x} = \begin{pmatrix} n^1_{r1,z1} \\ n^1_{r2,z1} \\ \vdots \\ n^1_{rn,z1} \\ n^1_{r1,z2} \\ \vdots \\ n^1_{rn,zm} \end{pmatrix}, \boldsymbol{b} = \begin{pmatrix} S^1_{v,n,r1,z1} + \dfrac{1}{\Delta tD} n^0_{r1,z1} \\ S^1_{v,n,r2,z1} + \dfrac{1}{\Delta tD} n^0_{r2,z1} \\ \vdots \\ S^1_{v,n,rn,z1} + \dfrac{1}{\Delta tD} n^0_{rn,z1} \\ S^1_{v,n,r1,z2} + \dfrac{1}{\Delta tD} n^0_{r1,z2} \\ \vdots \\ S^1_{v,n,rn,zm} + \dfrac{1}{\Delta tD} n^0_{rn,zm} \end{pmatrix} \qquad \text{Equation 54}$$

The implicit approach guarantees solution stability with the cost of additional equation system solving in implementation [149]. Therefore, the implicit approach is implemented in the MATLAB code for solving the differential equations.

There are other approaches to discretize the temporal differential equations besides the explicit and implicit approaches. The Crank-Nicolson (C-N) approach discretizes the temporal term at the half time step between previous and current moment using central-difference method and results in an improved second-order truncate error in the temporal domain. Meanwhile, although mathematically guaranteed stable, C-N approach has the risk of coming up with results that are not physically feasible, and therefore its time step also needs to be constrained, albeit with much looser limit [149].

5.2.5 Boundary Conditions

The previous section gives the general equations of energy and substance balance in a typical DCV inside the sorbent plate. However, the transfer conditions are different for DCVs at the boundary of the plate, and therefore special treatments need to be applied in the system of equations for those DCVs.

5.2.5.1 Heat Transfer

All heat and mass transfer and chemical reaction in the c.v. inside the salt plate can be described using the general governing equations listed above. Meanwhile, for those c.v. located at the boundary of the plate, i.e. the top/bottom and inner/outer perimeter, they are subjected to different conditions than the inside c.v.

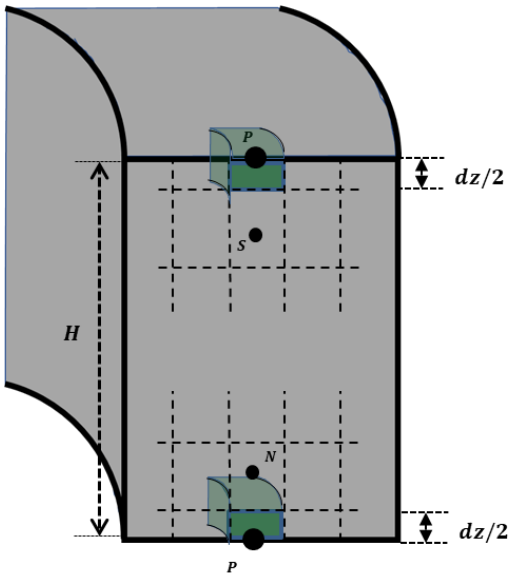

Figure 51 Upper and lower boundary c.v. in the salt disk

For heat transfer at the top and bottom layer shown in Figure 51, half c.v.'s are used to be in direct contact with the heat pipe metal. Therefore, instead of heat conduction with the same medium previously described by the thermal conductivity K_T, the heat flow is described with a heat transfer coefficient h_{HP}, and the corresponding terms in the discretized equation are changed to:

$$\frac{T^0_{r,z+1} + T^0_{r,z-1} - 2T^0_{r,z}}{(\Delta z)^2} \rightarrow \frac{T^0_{r,z+1} - T^0_{r,z}}{(\Delta z)^2} + 2\frac{T_{HP} - T^0_{r,z}}{(\Delta z)^2} \qquad \text{Equation 55}$$

Where T_{steam} is the temperature of the steam in the heat pipe.

The overall heat transfer coefficient between the boundary layer sorbent and the steam/water in the heat pipe is a combination of the condensation (steam) or convection (water) on the heat pipe inner side and the heat conduction through the heat pipe wall. For the heat pipe wall to the top of

the sorbent disk, the Nusselt number for the film condensation heat transfer on upward horizontal disk described in Bejan 1991 [150] is used. For the bottom heat pipe wall, the Nusselt number for laminar film condensation heat transfer on downward horizontal plate described in Gerstmann and Griffith 1967 [151] is used.

$$Nu_{top} = 1.368 \cdot \left[\frac{D^3 \cdot g \cdot h'_{fg} \cdot (\rho_l - \rho_v)}{k_l \cdot \nu_l \cdot (T_{sat} - T_w)}\right]^{\frac{1}{5}}$$ Equation 56

$$h_{HP,cond,top} = Nu_{top} * \frac{k_l}{D}$$ Equation 57

$$Ra_{bottom} = \frac{g \cdot \rho \cdot (\rho_l - \rho_v) \cdot h_{fg}}{\mu_l \cdot (T_s - T_w) \cdot k_l} \cdot \left(\frac{\sigma}{g \cdot (\rho_l - \rho_v)}\right)^{\frac{3}{2}}$$ Equation 58

$$Nu_{bottom} = 0.81 \cdot (Ra_{bottom})^{0.193}$$ Equation 59

$$h_{HP,cond,bottom} = Nu_{bottom} * \frac{k_l}{\left(\frac{\sigma}{g \cdot (\rho_l - \rho_v)}\right)^{\frac{1}{2}}}$$ Equation 60

The heat conduction through the stainless-steel heat pipe wall is:

$$h_{cond} = \lambda_{SS}/x_{wall}$$ Equation 61

During sorption mode when liquid water is circulated in the heat pipe, the convective heat transfer coefficient is set to $h_{HP,conv} = 3000W/(m^2 \cdot K)$. Then the overall heat transfer coefficient between the sorbent and the heat pipe medium is:

$$h_{HP} = 1/(\frac{1}{h_{HP,cond/conv}} + \frac{1}{h_{cond}}) \quad \text{Equation 62}$$

In the radial direction it was assumed that there is no heat transfer between the solid sorbent and the free vapor in the adsorber chamber as shown in Figure 52.

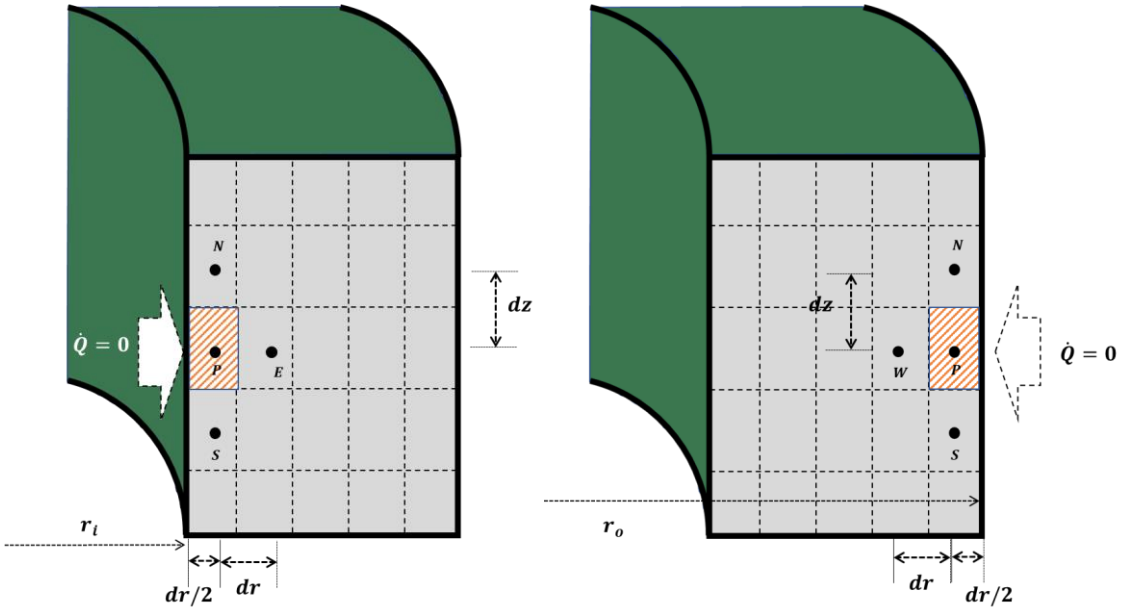

Figure 52 heat transfer at radial boundaries

Therefore, the DCVs at the inner and outer rim layer has only two-point heat transfer with the adjacent DCV in the sorbent plate. Their energy balance equations become:

$$\frac{1}{\alpha} \cdot \frac{T_{r,z}^1 - T_{r,z}^0}{\Delta t} = \frac{T_{r,z+1}^1 + T_{r,z-1}^1 - 2T_{r,z}^1}{(\Delta z)^2} + \frac{T_{r+1,z}^1 - T_{r,z}^1}{(\Delta r)^2} + \frac{1}{K} \cdot S_{v,q}^1 \quad \text{Equation 63}$$

$$\frac{1}{\alpha}\cdot\frac{T_{r,z}^{1}-T_{r,z}^{0}}{\Delta t}=\frac{T_{r,z+1}^{1}+T_{r,z-1}^{1}-2T_{r,z}^{1}}{(\Delta z)^{2}}+\frac{T_{r-1,z}^{1}-T_{r,z}^{1}}{(\Delta r)^{2}}+\frac{1}{K}\cdot S_{v,q}^{1}$$ Equation 64

For the "corner" DCVs at the intersection of top/bottom and inner/outer rims, the treatments of both vertical and radial boundaries are applied:

$$\frac{1}{\alpha}\cdot\frac{T_{r,z}^{1}-T_{r,z}^{0}}{\Delta t}=\frac{T_{r,z+1}^{1}-T_{r,z}^{1}}{(\Delta z)^{2}}+\frac{\boldsymbol{T_{HP}}-T_{r,z}^{1}}{\Delta z}+\frac{T_{r+1,z}^{1}-T_{r,z}^{1}}{(\Delta r)^{2}}+\frac{1}{K}\cdot S_{v,q}^{1}$$ Equation 65

$$\frac{1}{\alpha}\cdot\frac{T_{r,z}^{1}-T_{r,z}^{0}}{\Delta t}=\frac{T_{r,z+1}^{1}-T_{r,z}^{1}}{(\Delta z)^{2}}+\frac{\boldsymbol{T_{HP}}-T_{r,z}^{1}}{\Delta z}+\frac{T_{r-1,z}^{1}-T_{r,z}^{1}}{(\Delta r)^{2}}+\frac{1}{K}\cdot S_{v,q}^{1}$$ Equation 66

$$\frac{1}{\alpha}\cdot\frac{T_{r,z}^{1}-T_{r,z}^{0}}{\Delta t}=\frac{T_{r,z-1}^{1}-T_{r,z}^{1}}{(\Delta z)^{2}}+\frac{T_{r+1,z}^{1}-T_{r,z}^{1}}{(\Delta r)^{2}}+\frac{1}{K}\cdot S_{v,q}^{1}$$ Equation 67

$$\frac{1}{\alpha}\cdot\frac{T_{r,z}^{1}-T_{r,z}^{0}}{\Delta t}=\frac{T_{r,z-1}^{1}-T_{r,z}^{1}}{(\Delta z)^{2}}+\frac{T_{r-1,z}^{1}-T_{r,z}^{1}}{(\Delta r)^{2}}+\frac{1}{K}\cdot S_{v,q}^{1}$$ Equation 68

Equation 52~Equation 68 lead to different values of $a\sim e$ in the operator matrix A.

5.2.5.2 Mass transfer

In the vertical direction, the two boundary surfaces see no vapor flow across, and therefore the mass transfer of DCVs on these two layers is only two-point transfer with the inner adjacent DCV, as shown in Figure 53.

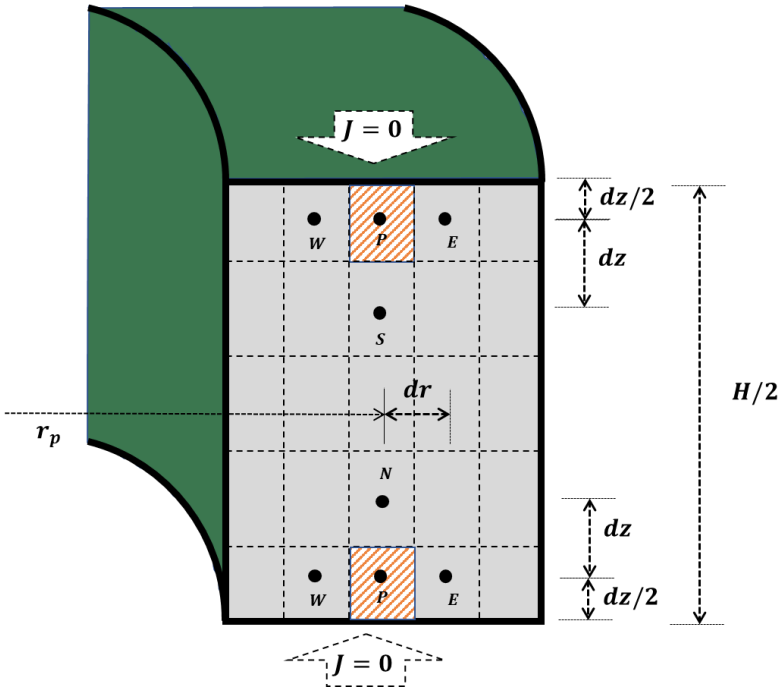

Figure 53 mass transfer at vertical boundaries

Their implicitly discretized substance balance Equation 42 becomes Equation 69 for top and Equation 70 for bottom layer DCVs:

$$\frac{n_{r,z}^{1}-n_{r,z}^{0}}{\Delta t\cdot D}=\frac{n_{r,z+1}^{1}-n_{r,z}^{1}}{(\Delta z)^{2}}+\frac{n_{r+1,z}^{1}+n_{r-1,z}^{1}-2n_{r,z}^{1}}{(\Delta r)^{2}}+\frac{n_{r+1,z}^{1}-n_{r-1,z}^{1}}{2\Delta r\cdot r}+\frac{1}{D}\cdot S_{v,n} \quad \text{Equation 69}$$

$$\frac{n_{r,z}^1 - n_{r,z}^0}{\Delta t \cdot D} = \frac{n_{r,z-1}^1 - n_{r,z}^1}{(\Delta z)^2} + \frac{n_{r+1,z}^1 + n_{r-1,z}^1 - 2n_{r,z}^1}{(\Delta r)^2} + \frac{n_{r+1,z}^1 - n_{r-1,z}^1}{2\Delta r \cdot r} + \frac{1}{D} \cdot S_{v,n} \quad \text{Equation 70}$$

In the radial direction, the inner and outer perimeter of the sorbent plate is open to the free vapor in the adsorber chamber. It is assumed that the free vapor adjacent to the perimeter DCVs have the same temperature as the DCVs, and that the apparent vapor pressure of the free vapor in the adsorber are the same (P_{cons}) as in Figure 54. Therefore, the diffusion between the perimeter DCV and the free vapor can be expressed given the constraint vapor pressure and the DCV sorbent temperature.

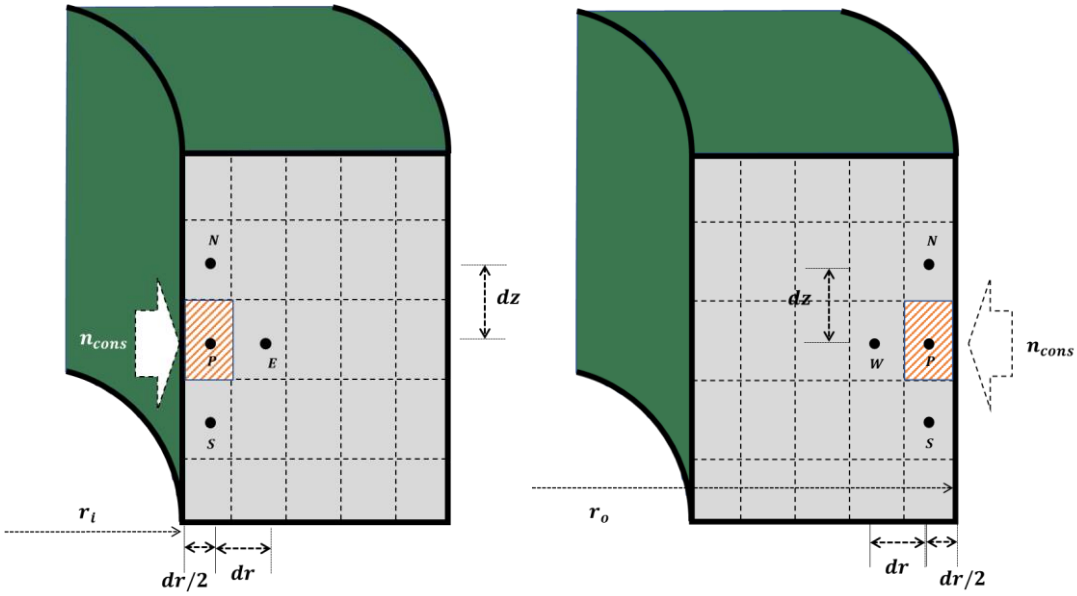

Figure 54 mass transfer at radial boundaries

The molar density of the free vapor adjacent to the DCV is calculated using Equation 71, and the substance balance equations for inner and outer perimeters become Equation 72-Equation 73:

$$\boldsymbol{n_{cons}} = \frac{\boldsymbol{P_{cons}}}{R \cdot T_{r,z}}$$ Equation 71

$$\frac{n_{r,z}^1 - n_{r,z}^0}{\Delta t \cdot D} = \frac{n_{r,z+1}^1 + n_{r,z-1}^1 - 2n_{r,z}^1}{(\Delta z)^2} + \frac{n_{r+1,z}^1 - n_{r,z}^1}{(\Delta r)^2} + \frac{\boldsymbol{n_{cons}} - n_{r,z}^1}{\Delta r \cdot \Delta r/2} + \frac{1}{D} \cdot S_{v,n}$$ Equation 72

$$\frac{n_{r,z}^1 - n_{r,z}^0}{\Delta t \cdot D} = \frac{n_{r,z+1}^1 + n_{r,z-1}^1 - 2n_{r,z}^1}{(\Delta z)^2} + \frac{n_{r-1,z}^1 - n_{r,z}^1}{(\Delta r)^2} + \frac{\boldsymbol{n_{cons}} - n_{r,z}^1}{\Delta r \cdot \Delta r/2} + \frac{1}{D} \cdot S_{v,n}$$ Equation 73

5.3 Calibration of Chemical Equilibrium and Kinetic Coefficients

5.3.1 Test Setup to Acquire Calibration Data

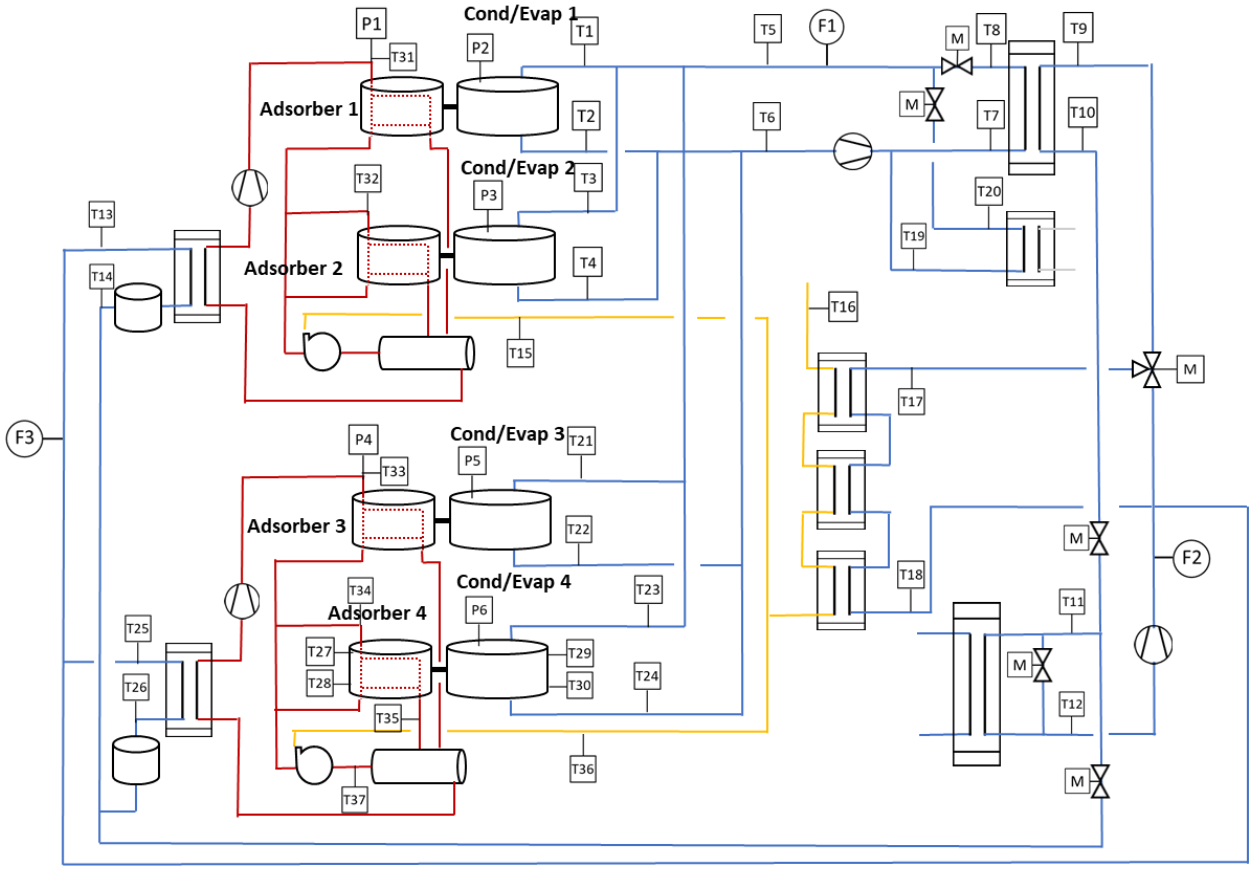

Figure 55 Test setup to calibrate chemical kinetic coefficients

The test setup to acquire the calibration data is shown in Figure 55. The system was operated with low burner and pump setting to slow down the heating and cooling process of the sorbent salt, so that the different chemical reaction stages can be separated and individually studied.

5.3.2 Calibrating the Chemical Equilibrium Coefficients

The chemical equilibrium equation is written as:

$$\ln\left(\frac{P_{eq}}{P_0}\right) = -\frac{\Delta H}{R \cdot T_{salt}} + \frac{\Delta S}{R} \qquad \text{Equation 74}$$

Ideally the two coefficients in the equation ΔH and ΔS correspond to the enthalpy and entropy of the reaction. Collins and Cameron 1928 [152] observed LiCl-4, LiCl-3, and LiCl-1 complexes. Bevers et al. 2006 [38] had the same observation. Van der Pal et al. 2010 [153] observed an intermediate phase of LiCl-2 under higher ammonia pressure (5.5 bar instead of 3 bar). Collins and Cameron used pressure scan at constant temperature. Bevers et al. 2006 used a differential scanning calorimeter (DSC) to for temperature scan under constant pressure. Van der Pal et al. used temperature scan for high and low temperature reactions (1/0 and 4/3) and applied both temperature and pressure scans to medium temperature reaction. In this work we observed three stages of reactions, i.e. LiCl-3/2, LiCl-2/1, and LiCl-1/0. The equilibrium of the LiCl-3/2 reaction is fitted using test date since the test results contradict with the equilibrium data reported in the literature. The equilibrium reported for LiCl-2/1 also varies a lot in the literature and therefore is fitted using test data in this study. The equilibrium LiCl-1/0 reaction reported from different data sources matches well, and therefore is directly used in this study. Table 23 lists the summary.

Table 23 Chemical equilibrium coefficients for LiCl ammonia reactions

Reaction	**ΔH [J/mol]**	**ΔS [J/mol.K]**	**Reference**
LiCl 4→3	36792	126.60	Bevers 2006[38]
	37461	128.90	Van der Pal 2010[153]
LiCl 3→4	30431	109.44	Bevers 2006[38]
	30859	110.80	Van der Pal 2010[153]
LiCl 3→1	49098	146.58	Bevers 2006[38]
	55267	163.90	Van der Pal 2010[153]
LiCl 1→3	43681	132.62	Bevers 2006[38]
	45822	138.36	Van der Pal 2010[153]
LiCl 3→2	62534	184	Van der Pal 2010[153]
	44780	113.97*	Berthiaud 2007 [154]
	54433	161.8*	This work
LiCl 2→3	75629	222	Van der Pal 2010[153]
	44780	113.97*	Berthiaud 2007[154]
LiCl 2→1	18935	64	Van der Pal 2010[153]
	48128	134.77*	Berthiaud 2007[154]
	47894	131.77*	This work
LiCl 1→2	22415	74	Van der Pal 2010[153]
	48128	134.77*	Berthiaud 2007[154]
LiCl 1→0	60494	159.43	Bevers 2006[38]
	49338	133.46	Van der Pal 2010[153]
	51894	138.57*	SaltX measurement
LiCl 0→1	40470	114.76	Bevers 2006[38]
	41298	117.05	Van der Pal 2010[153]

**This work uses 1 Pa as the reference pressure. To convert to 1 atm reference pressure in the literature the offset is ln(101325)*8.314=95.828.*

Fitting the equilibrium equation requires accurate account of P_{eq} and T_{salt}. Data is available from performance tests and contrived tests. The value of P_{eq} can be identified at the observed starting point of the reaction where it exceeds the measured chamber pressure. Then P_{eq} stays above the chamber pressure for continuous reaction, which is used as an inequality condition to the fitting optimization. The T_{salt} was directly measured during the four contrived tests. The ideal start-up process is shown in Figure 56:

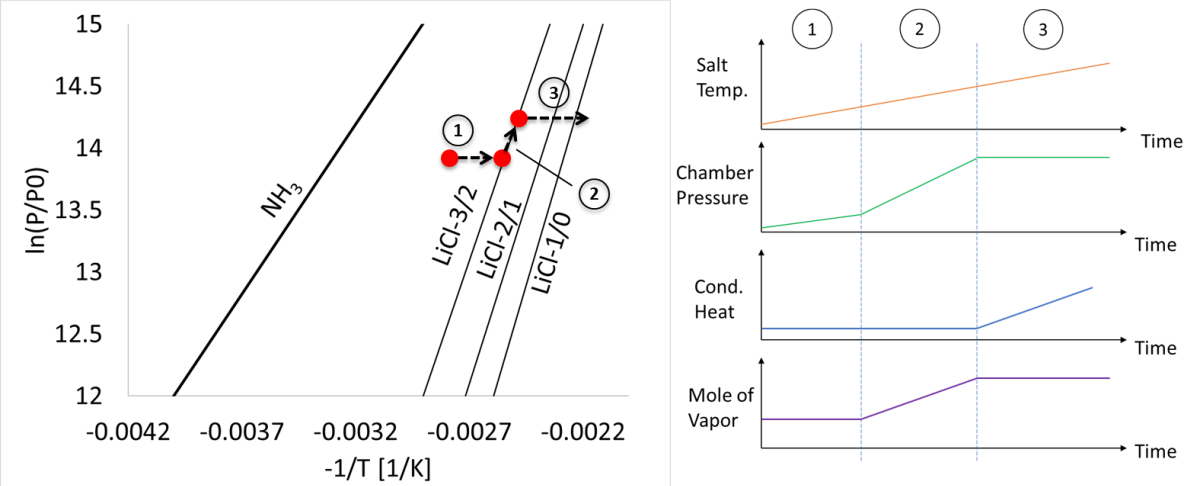

Figure 56 Progression of key parameters during an ideal desorption mode startup

As the salt is heated up, the ammonia vapor in the chamber is heated up as well. During stage #1, the chamber pressure increases slowly due to the heating-up, and no ammonia is generated from the salt. Stage #2 starts when the reaction equilibrium pressure exceeds the chamber pressure, and additional ammonia is released into the chamber to quickly push up the pressure. The molarity of vapor increases as well. Stage #3 starts when the chamber pressure passes the saturation pressure in the condenser and turns stable, while heat flow can be observed in the condenser. The starting point of the reaction can be identified as the turning point of the chamber pressure and the vapor molarity as the operation switch from stage #1 to stage #2.

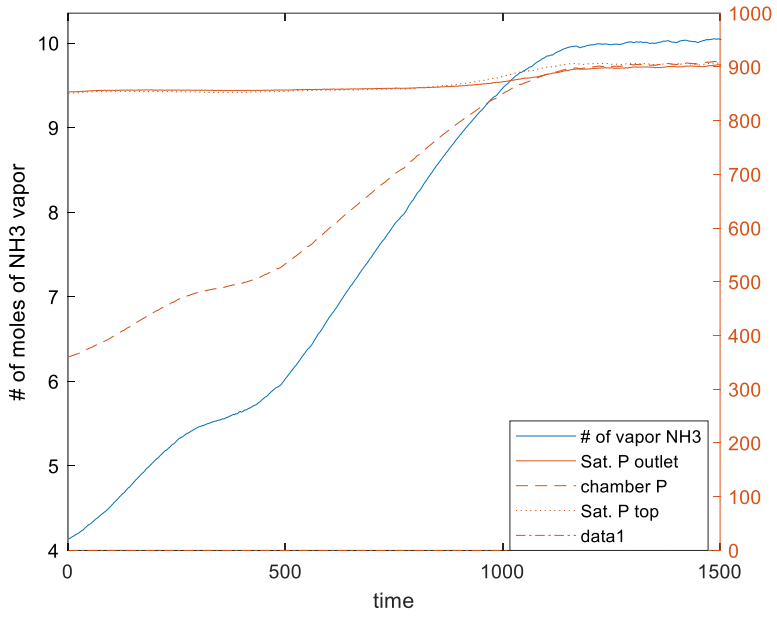

Figure 57 Measured reaction starting stage on 8/28/2019

Figure 57 shows the data from 8/28/2019, the pressures and the molarity of vapor ammonia. The turning point is around 460 s. The corresponding salt temperature and pressure are 94.49 C and 515.8 kPa. The cumulative heat in the condenser HX from the turning point to the starting point of condensation (1100 s) is 58.4 kJ. Mere sensible heat of ammonia vapor is not enough to explain such heat, especially the increasing heat flow after 800 s (49.6 kJ). One possible explanation is capillary condensation in the porous matrix in the condenser HX leading to a lower saturation point. Similar identification was done for the test data from the other three days as in Table 24.

Table 24 salt temperature and ammonia pressure at the transition point of first stage reaction

Date	**Module#**	**Transition time [s]**	**Salt temperature @transition [C]**	**Pressure @transition [kPa]**
8/20/19	4	3000	94.5	507.1
8/23/19	4	2130	94.3	507.5
8/27/19	4	-*	96.5*	558.7*
8/28/19	4	460	94.5	515.8

**reaction already started when data was recorded, no transition identified. Equilibrium point is below the data starting point*

Fitting is carried out for the two equilibrium coefficients so that the equilibrium pressure curve (1) crosses the reaction start point identified above, and (2) stays above the chamber pressure after the

reaction start point. Based on data from the four contrived tests, the optimized result of ΔH and ΔS are 54433 J^1mol^{-1} and 257.7 $J^1mol^{-1}K^{-1}$.

The calibration for the second desorption reaction equilibrium coefficients was based on the transition point observed at the end of the first stage reaction. The reversal of flow occurred only on 8/28/19 at around 146.4°C and 894 kPa and 150°C and 888 kPa. The actual equilibrium point should be slightly before the first point as the 1st stage was still going, and the same goes for the second point. 8/23/19 has an almost-zero point corresponding to 147.2°C and 882 kPa. Assuming the equilibrium line passes that point, the relationship of dH and dS is established, and the values identified as 47894 J^1mol^{-1} and 227.6 $J^1mol^{-1}K^{-1}$. For the last desorption reaction and the other three sorption reactions, the experimental data was not sufficient to carry out calibration as accurate as the first desorption reaction. Fortunately, the data reported in the literature from difference sources for those four reactions are in reasonably good agreement, and therefore they are directly used in this study.

5.3.3 Calibrating the Chemical Kinetic Coefficients

Lebrun 1990 summarized the studies on the model for chemical kinetics. In a general rate of chemical reaction as below, the specific rate $k(P,T)$ represents the influence of the reaction equilibrium, and $f(X)$ represents the reactivity.

$$v = \frac{dX}{dt} = k(P,T) \cdot f(X) \qquad \text{Equation 75}$$

Spinner and Rheault (1985) [155] reviewed kinetic models for the specific rate and identified the equation proposed by Tykodi (1967, 1979) [156, 157]to be the most suitable (Lebrun 1990)[158]. The chemical kinetic equation is as below. The deviation from equilibrium is logarithmic ratio of equilibrium pressure and the reaction site, if porous reactants such as graphite can guarantee sufficient mass transfer and the limiting factor is the reaction rate instead of the mass transfer in vapor or through sorbent.

$$\frac{dX}{dt} = (1-X)^n \cdot s \cdot exp\left(\frac{-E}{R \cdot T_{salt}}\right) \cdot ln\left(\frac{P_{eq}(T_{salt})}{P_{local}}\right) \quad \text{Equation 76}$$

With n, s, E the coefficients. Despite the physical meaning behind the coefficients, e.g. E is the activation energy of the reaction, these values are fitted empirically. In addition to the equation form shown in Eq. (76), several other kinetic equation forms were found to lead to good fitting results in the literature as well. An et al. 2020 [159] used an exponential kinetic equation as in Eq. (77), which doesn't deal with driving force reversal properly:

$$\frac{dX}{dt} = (1-X)^n \cdot K \cdot \exp\left(m \cdot \frac{P_{eq} - P_c}{P_c}\right) \quad \text{Equation 77}$$

Instead, when Peq=Pc, the reaction rate should be zero. Adjustment is made in this study:

$$\frac{dX}{dt} = (1-X)^n \cdot K \cdot \left(\exp\left(m \cdot \frac{P_{eq} - P_c}{P_c}\right) - 1\right) \quad \text{Equation 78}$$

The experimental data used to fit the equilibrium and kinetic correlations is based on special tests with controlled constant salt temperature and ammonia pressure to calibrate these values for each reaction stage as shown in Figure 58. The salt temperature was carefully controlled between the equilibrium temperatures of two reactions for as long as possible to exhaust the ammonia corresponding to that stage. The heat flow in the condenser-evaporator side is recorded for calculating the ammonia flow from the phase change heat.

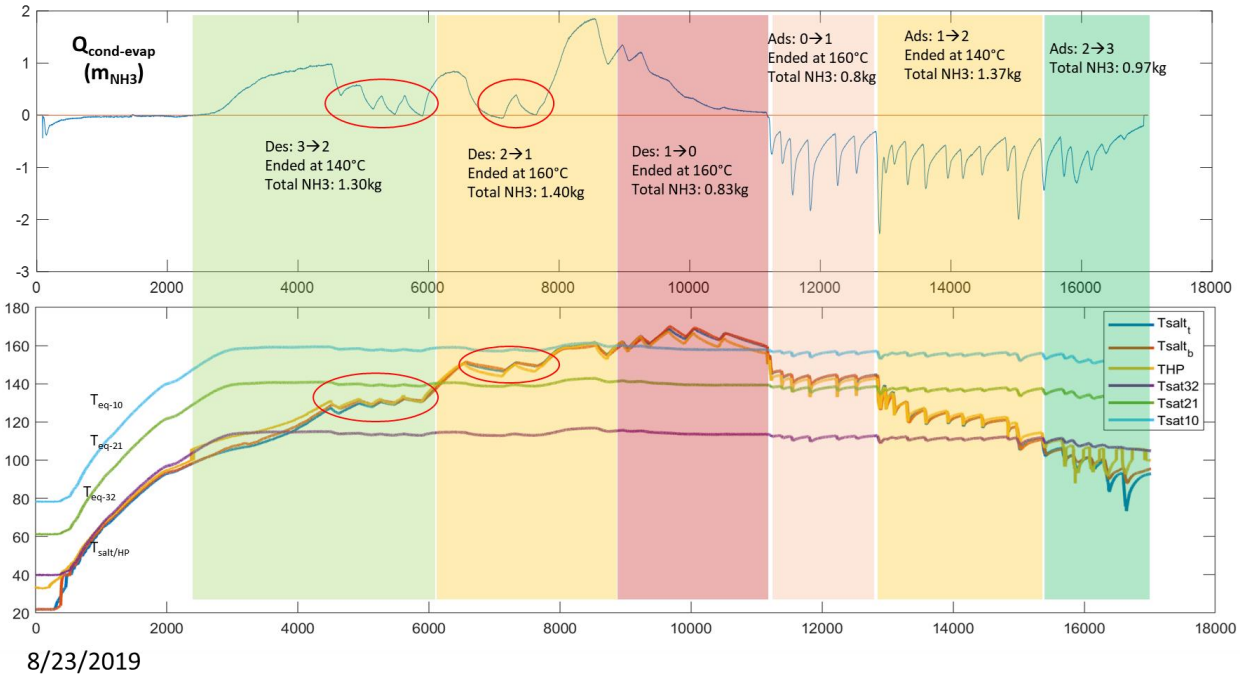

Figure 58 Result of specially designed test for chemical parameter calibration

The reaction progression and reaction rate are both calculated from the measured condensing heat output:

$$\frac{dX}{dt} = \frac{d(\frac{N_{NH3,cond}}{N_{NH3,tot}})}{dt} = \frac{1}{m_{NH3,tot}} \cdot \frac{dm_{NH3,cond}}{dt} = \frac{1}{m_{NH3,tot}} \cdot \frac{d\left(\frac{Q_{CW}}{h_{fg,NH3}}\right)}{dt} = \frac{\dot{Q}_{CW}}{m_{NH3,tot} \cdot h_{fg,NH3}} \quad \text{Equation 79}$$

$$X = \int_{t=0}^{t=n} \frac{dX}{dt} \cdot dt = \frac{Q_{CW}}{m_{NH3,tot} \cdot h_{fg,NH3}} \quad \text{Equation 80}$$

The influence of sensible heat of ammonia vapor can be corrected out of the condensing heat by adjusting the h_{fg}:

$$\dot{Q}_{CW} = m_{NH3} \cdot h_{fg} + m_{NH3} \cdot Cp_{vap} \cdot \Delta T_{NH3} = m_{CW} \cdot Cp_{CW} \cdot \Delta T_{CW} \quad \text{Equation 81}$$

$$m_{NH3} = \frac{\dot{Q}_{CW}}{h_{fg} + Cp_{vap} \cdot \Delta T_{NH3}}$$ Equation 82

The adjusted h_{fg} depends on the vapor temperature difference, which is within the temperature difference between the salt and the condensing water inlet. In this study, correction is applied assuming the vapor temperature changes from the average salt temperature to the mean temperature of condenser cooling water inlet and outlet. The condenser heat output is calculated using the temperatures and flow rate of the cooling water going through the two sorption modules.

$$\dot{Q}_{CW} = Cp_{CW} \cdot \dot{m}_{CW} \cdot \left(T_{CW,out} - T_{CW,in}\right)$$ Equation 83

Meanwhile, since the temperature of the salt is relatively constant during such test period, the temperature gradient within the entire salt stack is neglected, and the mean temperature measured in the salt and the heat pipe during the selected period is used as the salt temperature.

Using the time-series $\frac{dX}{dt}$ and X data for each reaction stage calculated from the measured condenser-evaporator heat flow, the optimal combination of the coefficients k, n, and m in Eq. (78) can be identified using the non-linear curve fit routine "lsqcurvefit" in MATLAB. The fitting of the first-stage reaction using the test data from four different days are listed in Table 25:

Table 25 kinetic fitting coefficients for stage 1

date	**time**	**mNH3 (m0)**	**N**	**K**	**M**	**R^2**	**RMSE**
8/20/19	4200-6610	0.7362	6.5	0.0014	3.64	0.9617	1.17e-5
8/23/19	3800-5900	0.7287	7.1	0.0021	3.25	0.9646	1.27e-5
8/27/19	500-6500	0.7278	6.8	0.0011	3.72	0.9363	2.89e-5
8/28/19	1500-3500	0.7742	6.8	0.0020	3.72	0.9139	2.27e-5
7/20/18	4750-5450	0.71	6.7	0.0012	3.30	0.9234	1.05e-5
Avg.			6.78	0.00156	3.526		

The calibrated equilibrium and fitted kinetic coefficients of the 1st stage is used to calculate the ammonia flow associated with that stage of reaction, which is later subtracted from the total ammonia flow to get the value for the next stage reaction. Following the same approach and using the equilibrium previously identified, the kinetic coefficients for the rest of the reaction stages were identified. The only exception is the last sorption stage, where the ammonia low was not accurately reflected by the measured evaporator heat flow in all test data. For that stage, nominal values in the same order of magnitude as the identified coefficients are used in the model.

The result of the calculated ammonia flow associated with each reaction stage compared with the total ammonia flow calculated from the measured condenser heat flow during desorption is illustrated below in Figure 59.

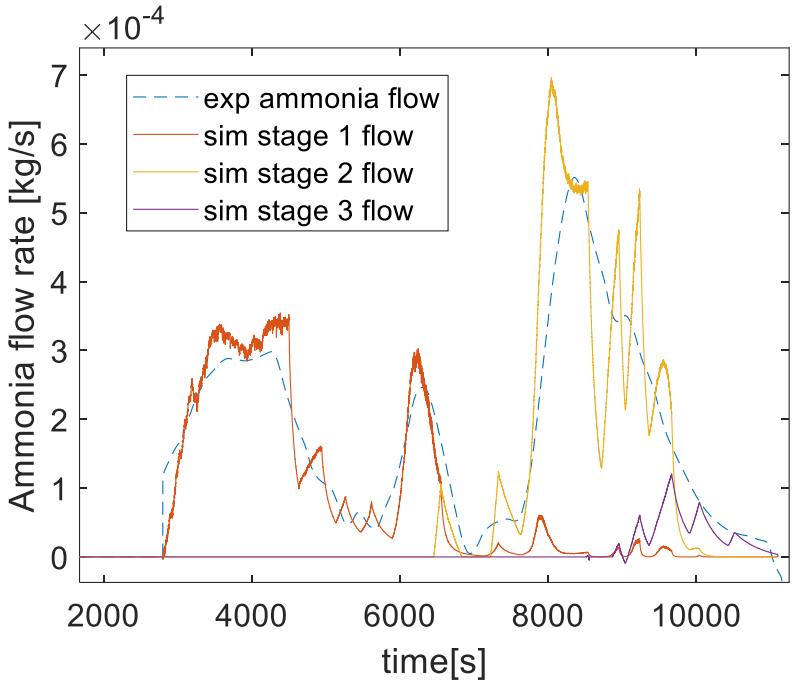

Figure 59 comparison of calculated ammonia flow based on fitted coefficients and measured heat flow

Table 26 lists the final calibrated chemical equilibrium and kinetic coefficients, with the first two desorption equilibrium fitted, and the third desorption equilibrium taken from the literature. The sorption reaction equilibrium uses the corresponding desorption reaction equilibrium assuming no hysteresis. The kinetic last sorption reaction (LiCl-2→3) was not fitted because the current testbench was not able to capture the ammonia evaporation during that stage.

Table 26 Calibrated chemical equilibrium and kinetic coefficients

Reaction	Equilibrium			Kinetics (exponential correlation)			
	Source	dH	dS	Source	n	K (x10^4)	m
LiCl-3/2	Fitted from test data	54433	257.6	Fitted from test data	6.8	16	3.53
LiCl-2/1	Fitted from test data	47894	227.6	Fitted form test data	1.8	5.6	3.15
LiCl-1/0	Pal 2010, Bevers 2006	50616	231.3	Fitted form test data	3.8	5.8	2.44
LiCl-0/1	Assuming no hysteresis	50616	231.3	Fitted from test data	1.15	18.9	4.86
LiCl-1/2	Assuming no hysteresis	47894	227.6	Fitted from test data	0.49	7.8	3.12
LiCl-2/3	Assuming no hysteresis	54433	257.6	Not enough data for fitting	3*	5*	3*

**nominal values in the same magnitude as the fitted coefficients*

5.4 Model Validation

The validation is carried out by comparing the ammonia flow calculated from the measured condenser-evaporator heat flux and the ammonia flow simulated by the dynamic model. The experimental data of configuration #1 with only skid #1 operational is used. The thermodynamic and transfer properties of the sorbent salt are provided by the manufacturer. Due to the incomplete evaporation heat recorded from the evaporator heat flux, the validation only takes data for the desorption reaction stages and the first two sorption stages. The measured steam temperature and the ammonia chamber pressure from the test data are used as the input to the adsorber model. The validation calculations start by setting the temperature, pressure, and composition of the sorbent salt to the initial condition of the test data and run the simulation.

The ammonia vapor flow into and out of the adsorber is used as the indicator of the adsorber operation and performance. The ammonia flow is calculated based on the heat flow at the condenser-evaporator water side:

$$\dot{Q}_{cond} = \dot{m}_{NH3} \times h_{fg,NH3} = \dot{m}_{cw} \times Cp_{cw} \times (T_{w,o} - T_{w,i}) \quad \text{Equation 84}$$

The comparison for the four days' test are shown in Figure 60 to Figure 63.

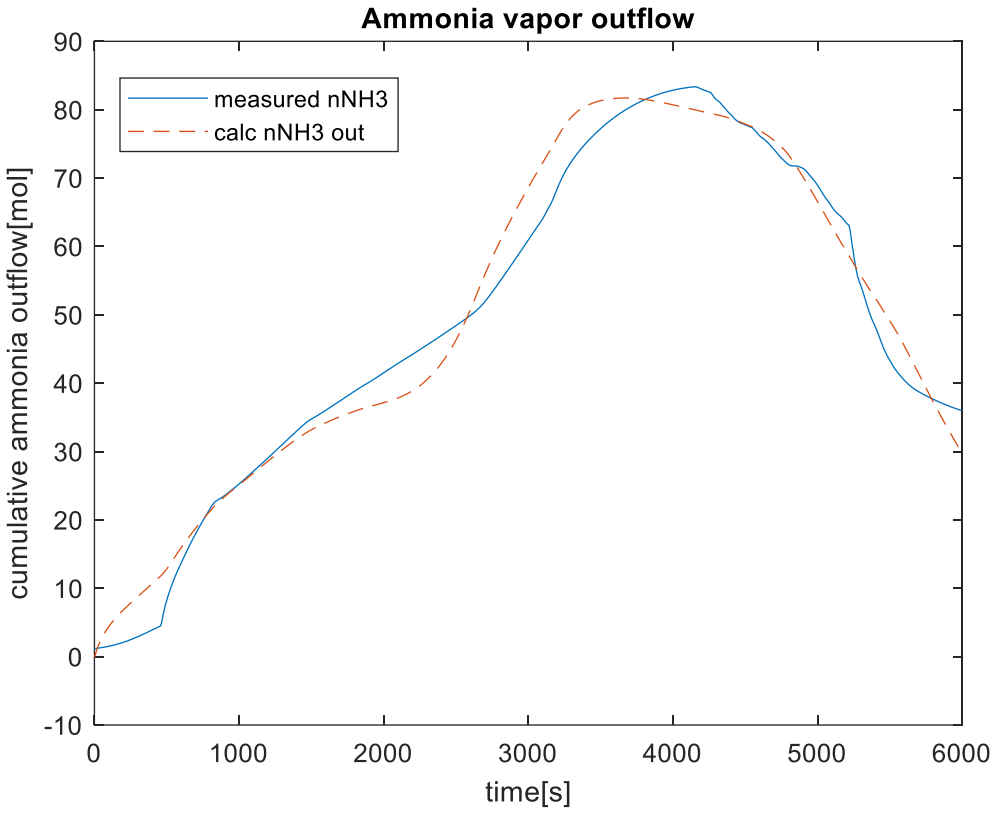

Figure 60 comparison of adsorber ammonia flow using 8/15 data

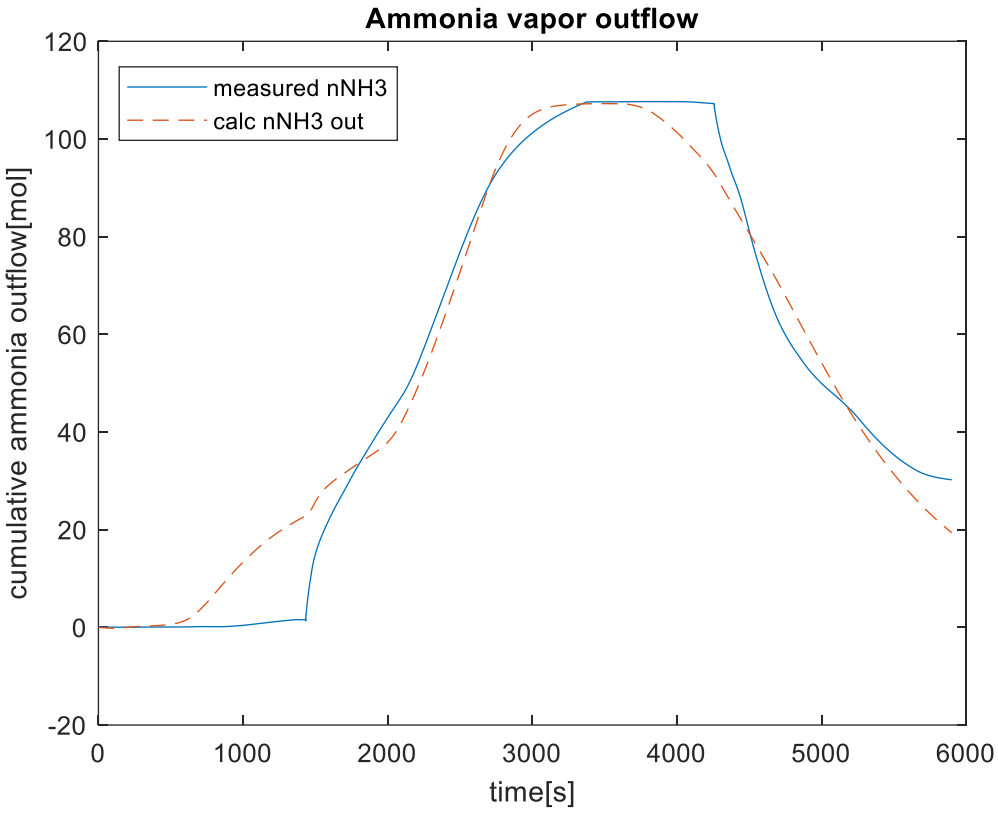

Figure 61 comparison of adsorber ammonia flow using 8/27 data

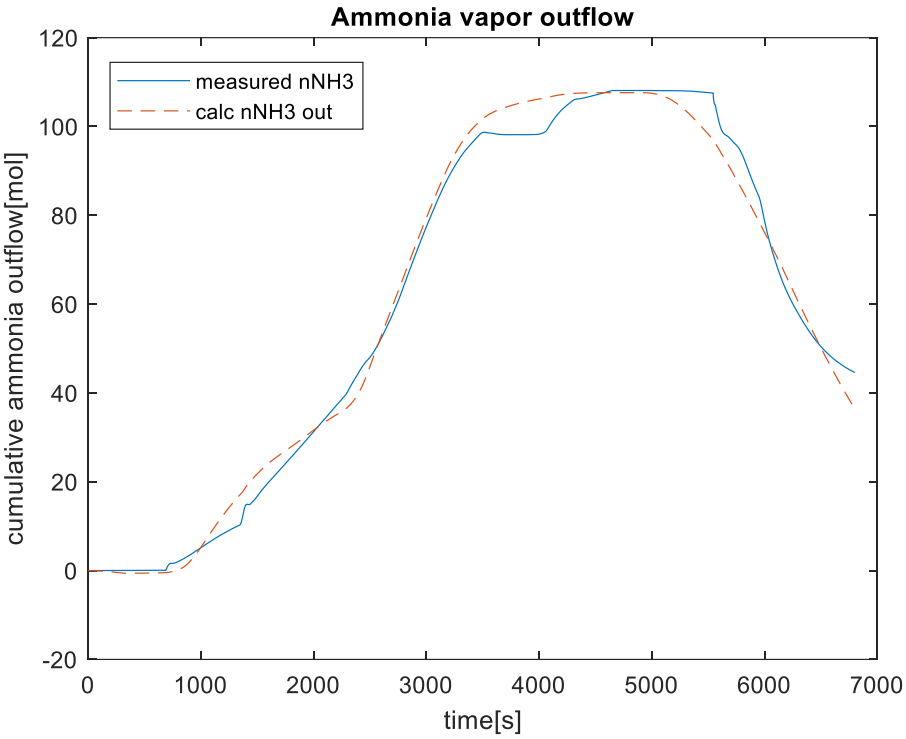

Figure 62 comparison of adsorber ammonia flow using 9/5 data

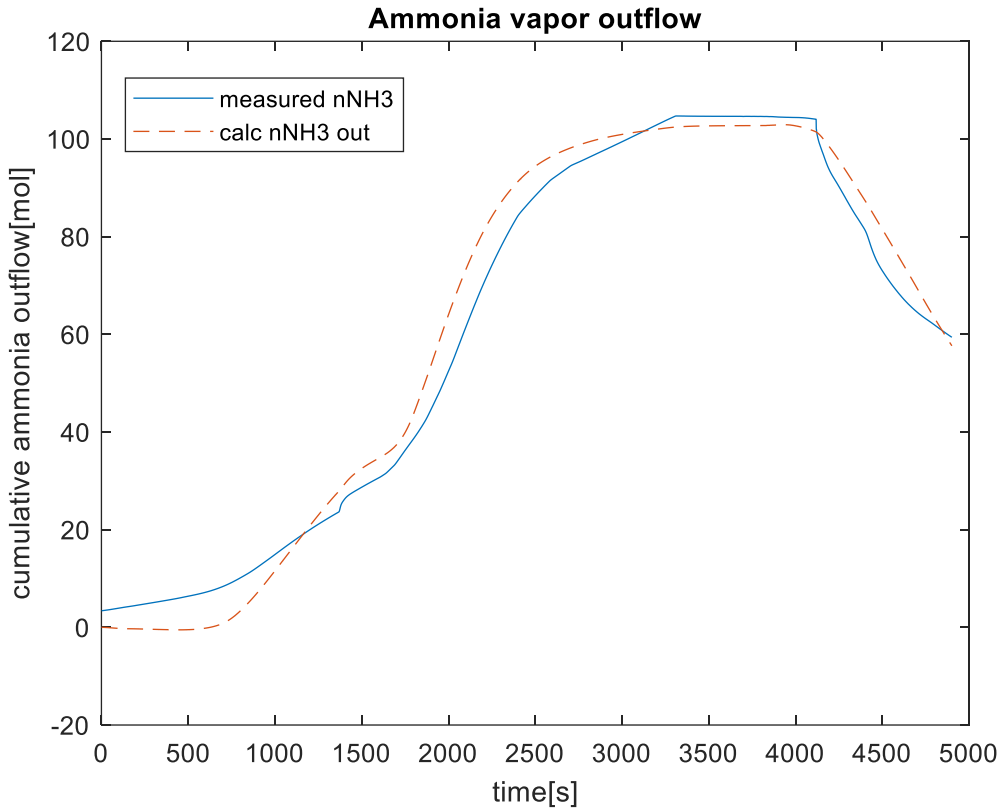

Figure 63 comparison of adsorber ammonia flow using 9/7 data

Table 27 compares the cumulative ammonia vapor flow from the adsorber calculated by the adsorber model and that calculated from measured heat flow in the condenser-evaporator. The high R^2 and relatively low RMSE value indicates that the adsorber model with the calibrated chemical coefficients can accurately simulate the operation of the adsorber component throughout the desorption and sorption cycle.

Table 27 comparison of calculated and measured ammonia vapor flow from adsorber

Date	R^2	RMSE	RMSE% of maximum
8/15/2018	0.9761	3.7749	3%
8/27/2018	0.9662	7.0378	6%
9/5/2018	0.9909	3.8223	3%
9/7/2018	0.9821	5.4033	4%

5.5 Parametric Study

With both the geometry of the sorbent disk and the sorbent properties taken into account, the adsorber model can be used to study the sensitivity of the ammonia desorption and sorption

performance to these parameters to identify possible pathway for improvement of the adsorber and sorbent design. In this parametric study section, only one of these parameters is changed at a time to investigate its effect on the adsorber performance. The boundary conditions applied to the adsorber model are the steam temperature and the ammonia chamber pressure. In the desorption mode, the steam temperature is always 2°C higher than the average salt temperature. In the sorption mode, the heat pipe is filled with circulated water at 1°C lower than the average salt temperature. The ammonia pressure is fixed at the saturation pressure of 40°C

5.5.1 Sorbent Disk Thickness

The original thickness of the sorbent disk is 10 mm with 56 disks and 57 heat pipe plates in the adsorber. With thicker sorbent disks, the heat exchanger would require less plates to hold the same amount of sorbent in the container, while also offering less heat transfer area between the heat pipe medium and the salt sorbent.

Figure 64 shows the comparison of the cumulative ammonia outflow between sorbent disk thickness of 5mm, 10mm, and 15mm. The thin-disk scenario has the highest cumulative outflow with the same boundary conditions thanks to the short heat transfer path length and thorough heating. The thickest disk at 20 mm is twice as thick as the original salt disk, and its longer heat transfer path length leads to slower heating of the salt, which eventually leads to about 13% less ammonia desorption.

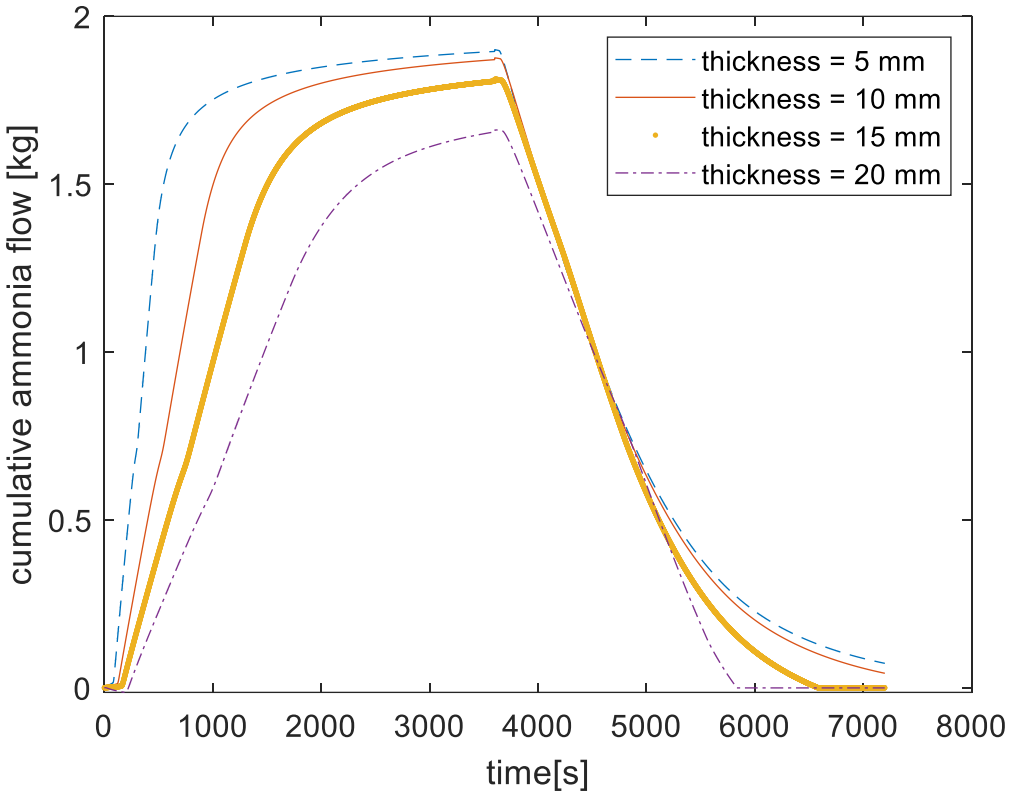

Figure 64 cumulative ammonia flow under different sorbent disk thicknesses

Figure 65 shows the comparison of the salt state progression in the disks. With thin thickness, the heat propagation across the salt disk is faster than in thick disks, and therefore the salt is more thoroughly heated and cooled, leading to faster overall ammonia generation and sorption rates and consequently higher cumulative ammonia flow.

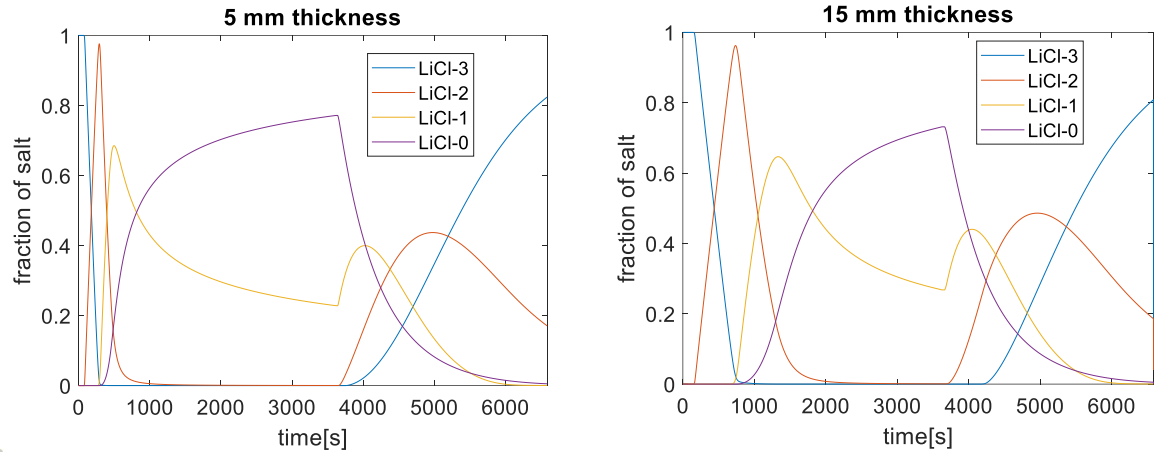

Figure 65 comparison of salt state progression in 5mm and 15mm thick disks

5.5.2 Sorbent Porosity

A higher porosity is usually from the loose arrangement of the sorbent material, while a low porosity indicates the sorbent been compressed and compacted. The thermal conductivity and permeability of the sorbent material are also affected by the compactness of the sorbent material. However, due to the lack of measured data for the sorbent material under difference levels of compactness, this study uses the range of thermal conductivity and permeability of the expanded graphite from the literature to qualitatively investigate the impact of the sorbent porosity on the adsorber performance due to the heat and mass transfer property change.

Figure 66 shows the cumulative ammonia flow under porosity of the sorbent from 0.2 to 0.7. The impact of the lowering the porosity is not manifested until the porosity get below 0.3, and when the porosity is 0.2 the ammonia sorption capacity is considerably reduced.

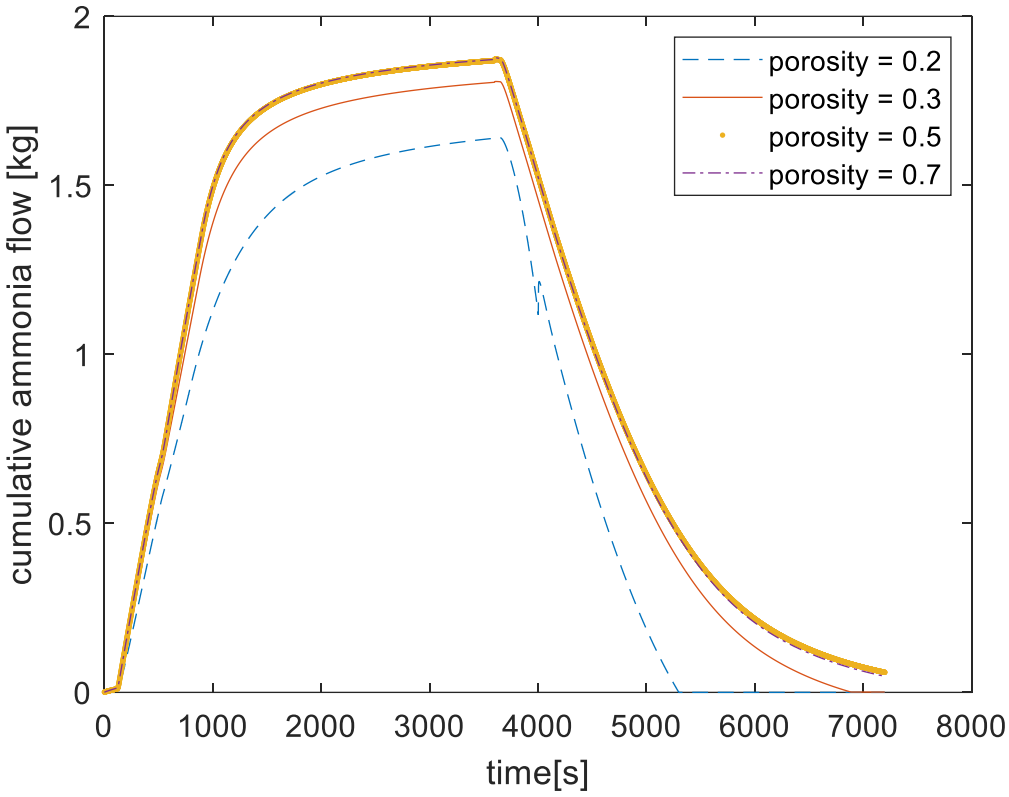

Figure 66 ammonia sorption under different porosity of the salt disk

5.6 Discussion and Conclusion

In this chapter the dynamic model for the chemisorption adsorber is developed, validated, and used to investigate the influence of the adsorber design parameters on the component performance. The dynamic adsorber model is centered around the heat and mass transfer as well as the chemical reaction inside the sorbent salt disk, which is modelled using the finite-difference method. The coefficients for the chemical equilibrium and the semi-empirical chemical kinetic equations are identified for the multiple-stage reactions involved in the adsorber operation. Using the calibrated parameters, the adsorber model is validated by comparing the simulated ammonia generation and sorption and those values calculated from experimental test results. The dynamic adsorber model can capture the transient adsorber operation under varying operating conditions, and therefore it can be used in the dynamic system simulation in the next chapter.

The chemical reaction coefficients are important parameters in the simulation. The identification of chemical equilibrium and kinetic coefficients can be found in several recent published studies. However, for multiple-stage reactions such as the LiCl-3/2/1/0 used in this study, the separation of the reaction stages is very important during the measuring test for both equilibrium and kinetic coefficients. Furthermore, there are several semi-empirical equation forms reported in the literature for the chemical kinetics, and this study used a modified exponential equation.

The parametric study results show the effect of adding the heat transfer area by using thinner sorbent disks. Doubling the current thickness leads to about 13% loss in ammonia sorption and desorption capacity under similar operating conditions. On the other hand, doubling the number of heat pipe plates and halving the sorbent disk thickness leads to faster sorption and desorption rate with limited increase of the total sorption capacity. The thickness of 15 mm is recommended for requiring less heat exchanger surface and thermal mass while not compromising the heat transfer performance.

The compactness of the sorbent disk is an important parameter that affects the porosity, thermal conductivity, and permeability of the sorbent. The parametric calculation using expanded graphite properties shows that there is a lower threshold for the porosity after which the adsorber performance is considerably affected. The porosity of below 0.3 leads to considerable performance decline, and therefore the optimal porosity of the sorbent is around 0.3.

6. SYSTEM MODELLING

The goal of the system modeling is to develop and validate a dynamic system model capable of accurately simulating the transient evolution of the system operation and calculate the overall system performance under various operating conditions and control strategies. The system model is used to extend the investigation of system performance under low ambient temperatures and to identify improvement method by studying the energy flow during operation.

In this chapter, the configuration and measured operation of the CSHP system are first introduced. Then the heat transfer and thermodynamic governing equations for each key component in the system are described. The system model is assembled with the key component models and validated by comparing the simulation results with the test data. Finally, simulations results are presented and discussed to study the system performance under various operating conditions and to identify further improvement of the system operation and control.

6.1 System Configuration and Operation Data Used for Model Validation.

The system under investigation is one of the four adsorber-condenser/evaporator modules in the same configuration as the experiment configuration #3 introduced in Chapter 4. The tested system consists of an adsorber and a combined condenser-evaporator. The heat exchanger in the adsorber is a hybrid heat pipe which includes a natural gas burner for steam generation, as well as a reservoir water tank and water pump for heat transfer via water circulation. The heat pipe system is also connected to a plate-type heat exchanger to pass the heat from circulated water to the external heat transfer fluids (cooling water). The adsorber and the condenser-evaporator are two connected vessels filled with ammonia vapor, and there is no check valve between them. The investigated adsorber-condenser/evaporator module is one of the two modules served by the same hybrid heat pipe.

To capture the change of energy in the heat pipe as well as the thermal masses in the component shells, the water reservoir tank, and the natural gas burner during the transient operation, several additional temperature sensors are installed as well. The configuration and sensors of the simulated

system are illustrated in Figure 67. The sensors measuring key system operating parameters are listed in Table 28.

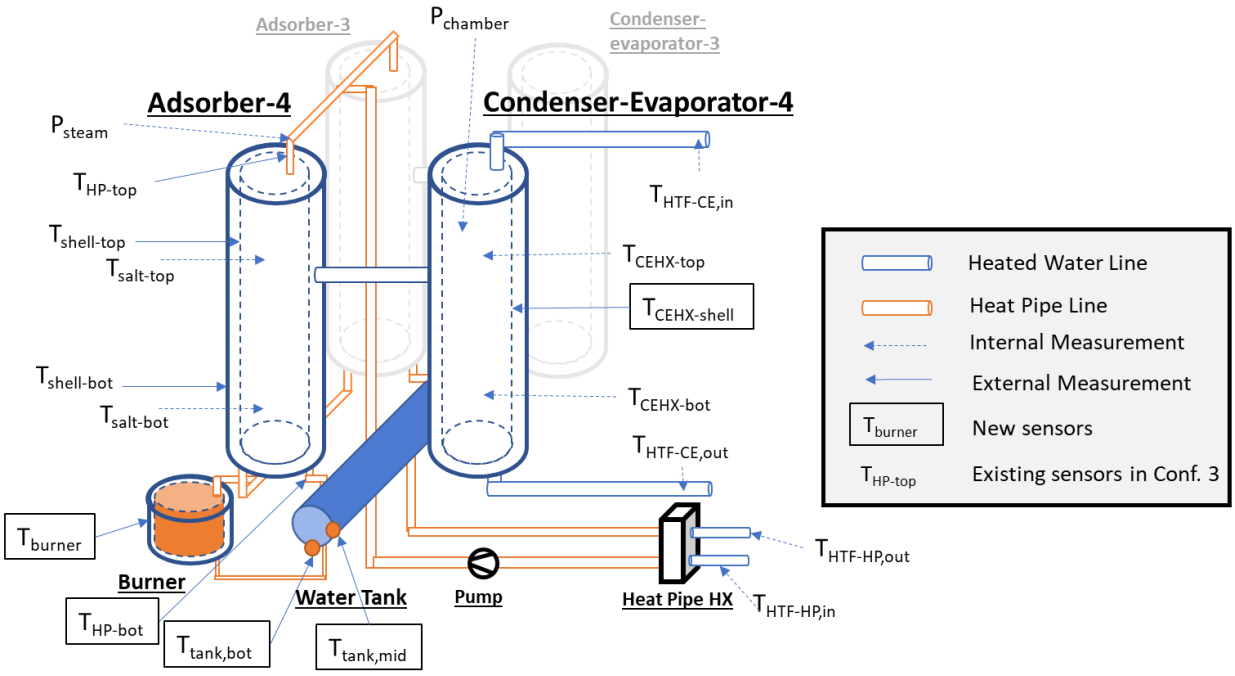

Figure 67 System configuration and additional sensor location

Table 28 Sensors in the tested system

Name	Sensor	Internal /external	Location	Medium	Parameter
$T_{HP,top}$	Thermocouple	External	Top of the heat pipe	Stainless steel	Heat pipe external temperature
$T_{shell,top}$	Thermocouple	External	Top ¼ of the adsorber vessel	Stainless steel	Shell temperature
$T_{shell,bot}$	Thermocouple	External	Bottom ¼ of the adsorber vessel	Stainless steel	Shell temperature
$T_{salt,top}$	Thermocouple	Internal	Top ¼ of the adsorber heat exchanger stack	Sorbent salt	Salt temperature
$T_{salt,bot}$	Thermocouple	Internal	Bottom ¼ of the adsorber heat exchanger stack	Sorbent salt	Salt temperature
T_{burner}	Thermocouple	External	Outside burner envelope	Stainless steel	Burner shell temperature
$T_{HP,bot}$	Thermocouple	External	Bottom of adsorber heat pipe return to the water tank	Stainless steel	Heat pipe external temperature
$T_{tank,bot}$	Thermocouple	External	Bottom of the water tank shell	Stainless steel	Water temperature
$T_{tank,mid}$	Thermocouple	External	Middle level of the water tank shell	Stainless steel	Water temperature
$T_{HTF,HP,in}$	RTD	Internal	In the HTF flow into the heat pipe HX	Water	HTF inlet temperature during sorption mode

Table 28 continued

$T_{HTF,HP,out}$	RTD	Internal	In the HTF low out of the heat pipe HX	Water	HTF outlet temperature during sorption mode
$T_{HTF,CE,out}$	RTD	Internal	In the HTF flow out of the condenser-evaporator	Water	HTF outlet temperature during desorption mode
$T_{HTF,CE,in}$	RTD	Internal	In the HTF flow into the condenser-evaporator	Water	HTF inlet temperature during desorption mode
$T_{CEHX,shell}$	Thermocouple	External	On the condenser-evaporator vessel wall in the middle	Stainless steel	Condenser-evaporator shell temperature
$T_{CEHX,top}$	Thermocouple	Internal	Top ¼ inside the condenser-evaporator heat exchanger	Ammonia	Heat exchanger (and ammonia condensate) temperature
$T_{CEHX,bot}$	Thermocouple	Internal	Bottom ¼ inside the condenser-evaporator heat exchanger	Ammonia	Heat exchanger (and ammonia condensate) temperature
P_{steam}	Pressure transducer	Internal	Top of the heat pipe	Water/steam	Heat pipe steam pressure
$P_{chamber}$	Pressure transducer	Internal	Top of the condenser-evaporator vessel	Ammonia	Sorption module ammonia pressure

Experimental test of the above configuration was carried out on 6/7/2019 in an unconditioned environment chamber. The ambient temperature was around 20°C. The target heat supply temperature (cooling water temperature leaving the heat pump system) was set to be 43°C.

The operation started with the desorption mode where the burner was turned on to generate steam for the hybrid heat pipe. The steam condensed in the heat pipe heat exchanger in the adsorber to heat up the salt, driving ammonia out of the salt. With an increasing amount of ammonia released by the salt, ammonia started to condense in the condenser-evaporator heat exchanger (CEHX) and raised the temperature of the CEHX. Meanwhile, the pump on the cooling water line through the CEHX was kept off until the temperature of the CEHX reached the target supply temperature. Once the temperature of CEHX reached the supply temperature, cooling water was pump through the CEHX to extract the ammonia condensation heat until the ammonia in the salt was exhausted and the desorption mode is ended by turning off the burner and the cooling water circulation through the CEHX.

The sorption mode following the end of the desorption model started with the pump in the hybrid heat pump turned on to circulate water in the heat pipe to draw heat from the hot salt in the adsorbers. The cooling water was pumped through the heat pipe HX to extract the sorption heat from the circulated water in the heat pipe. Upon cooling the hot and "dry" sorbent salt, ammonia vapor started to be absorbed by the salt, lowering the ammonia vapor pressure in the adsorber-CE chamber, which further drove the liquid ammonia condensate in the CEHX to evaporate. The evaporation absorbed heat and cooled the thermal mass of the CEHX until its temperature went below the ambient temperature when the external HTF was once again circulated through the

CEHX to supply extra heat for evaporation. The sorption mode ended when the liquid ammonia in the CEHX all evaporated and the temperature of the hot water supply through the heat pipe HX drops below the target value.

The operating temperatures of the salt and supplied hot water, as well as the energy input and output to the system are summarized in Table 29 and illustrated in Figure 68. Like the experimental study in Chapter 4, the heat input during the desorption mode by the steam generation of the burner is estimated by the measured natural gas flow and the empirically calibrated steam generation thermal efficiency. The details of the estimation process can be found in the appendix in Chapter 4.

Table 29 Key operating condition and performance summary for test on 6/7/2019

T_{amb} [°C]	HW return temp. [°C]	HW supply temp. [°C]	Des. mode time [min]	Sorp. mode time [min]	Tot. cycle time [min]	Q_{des} [kJ]	Q_{cond} [kJ]	Q_{ads} [kJ]	Q_{evap} [kJ]	Q_{in} [kJ]	Q_{out} [kJ]	Avg. heating power [kW]	COP [-]
21.4	35.3	43.9	83.4	73.1	156.5	8909	1377	6732	817	9726	8109	0.817	0.91

As shown in Figure 68, the desorption mode started with heat input into the adsorber for desorption (Q_{des}) from the natural gas burner. The heat pipe temperature increased steadily with the continual steam generation in the burner. Meanwhile, the condenser HTF outlet remained at the room temperature as the HTF pump was not turned on at first. Once the CEHX temperature reached the target heating supply temperature of 43.9°C, the condenser side HTF pump was turned on, and condensing heat was supplied at the desired temperature. The desorption mode ended when the burner was turned down as eventually off to maintain the heat pipe temperature around the maximum operating temperature of 200°C. A total of 8909kJ heat was supplied to the system via steam generation during the desorption mode. The condensing heat output was turned off at the same time with the heat supplied summed up to 1377kJ at above 43.9°C.

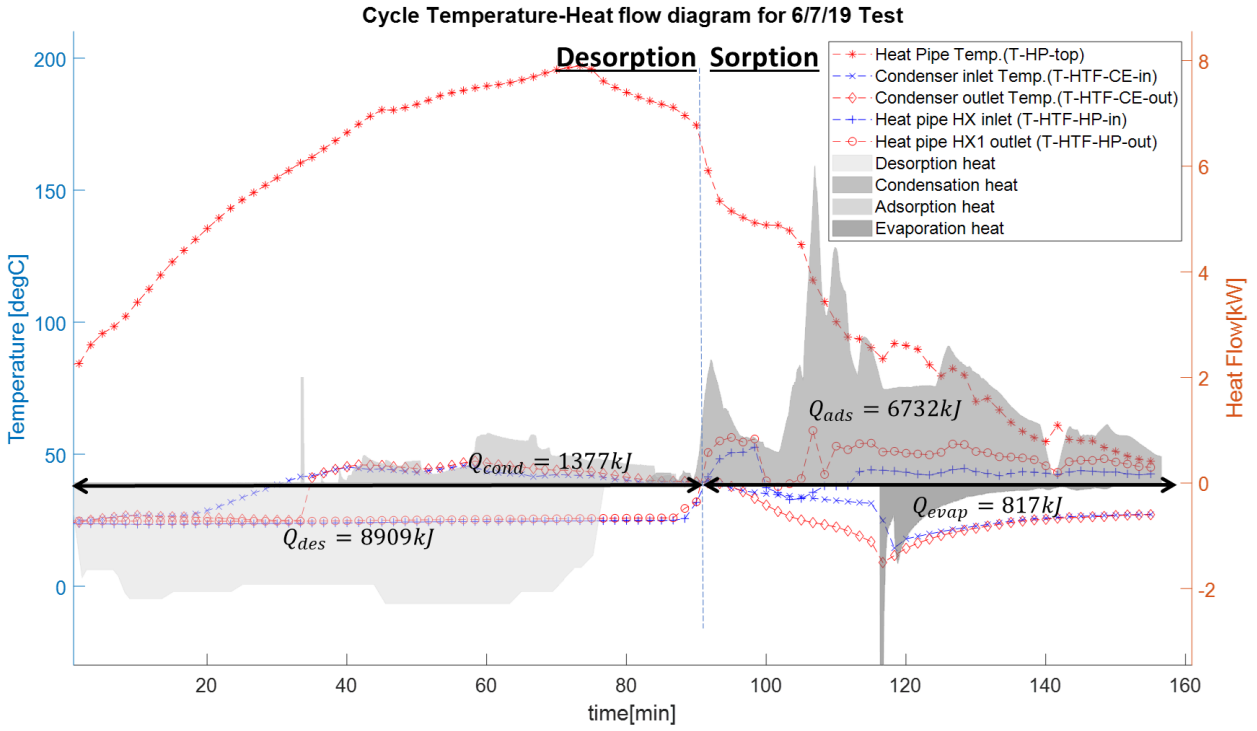

Figure 68 Time-series of key operating temperature and heat flow for 6/7/2019 test

The sorption mode started with the heat pipe pump turned on and heat extracted from the hot salt, leading to drastic drop of the heat pipe temperature. The water circulated in the heat pipe passed the heat to the cooling water side via the heat pipe HX, leading to the HTF temperature at the heat pipe HX outlet increasing quickly past the target heating temperature. Meanwhile, the HTF pump at the condenser-evaporator side was kept off to let the evaporation cool the thermal mass of the C-E first. Once the CEHX is cooled to below the ambient temperature, the CE side pump was turned on, and the HTF supplies ambient-temperature heat to support the continual evaporation. The sorption mode was eventually ended when the salt temperature dropped to around the heating supply temperature, when the heat pipe water circulation and cooling water pump were both turned off. The heat supply by cooling the salt during the sorption mode added up to 6732kJ, and the total heat input at the ambient temperature in the evaporator was 817kJ.

Based on the system heat input and output measured during the operation, the average heating power of this single adsorber-condenser/evaporator module was 0.817kW, and the heating COP is 0.91. The total heat input is 1617kJ higher than the total heat output, and this difference can be

attributed to the increase of the temperature in the thermal masses in various components in the system. These operation data and system performance are later used to calibrate parameters in the key component models described below, and further used to validate the complete system model.

6.2 Key System Component Models

As shown in the system configuration in Figure 67, the CSHP system comprises several interconnected components, and each component undergoes transient operation with the varying system energy input and output during desorption and sorption modes. Therefore, to accurately capture the dynamic behavior of the system, transient models for the key system components are first developed.

The system dynamic model is consisted of three key components: the salt-containing adsorber, the hybrid heat pipe which includes the burner, the reservoir water tank, and the heat pipe heat exchanger, and the combined condenser-evaporator. Each component model is developed independently. Figure 69 and Figure 70 illustrate the data flow of the three component models interaction during desorption and sorption mode.

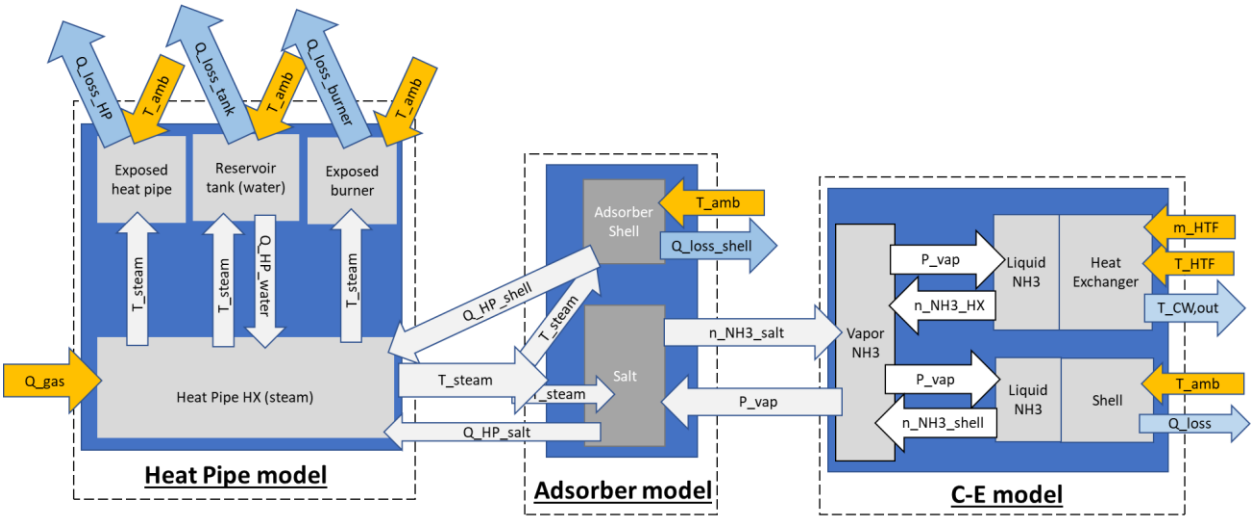

Figure 69 Structure and data flow of the system dynamic model (in desorption mode)

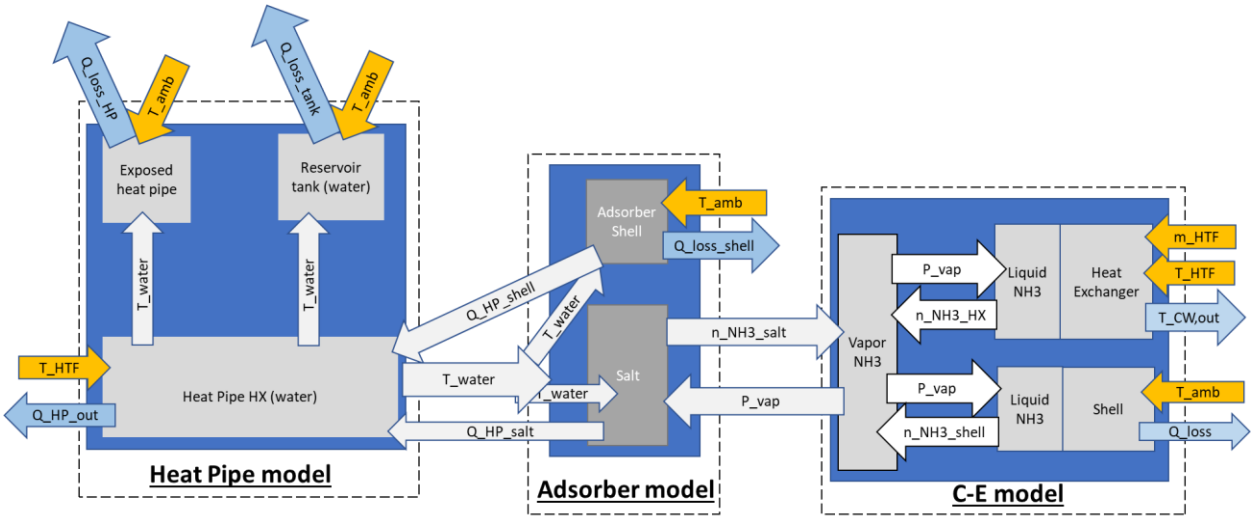

Figure 70 Structure and data flow of the system model (in sorption mode)

The arrows in the two figures indicates the data flow into and out of each component model. The colored arrows such as Q_{gas} and T_{amb} for the gas heat input and the ambient temperature are given by the operating condition. The greyed arrows such as T_{steam} and P_{vap} indicating the heat pipe steam temperature and ammonia vapor pressure are intermediate parameters between the three key components. These intermediate parameters are calculation results of one component and is used as the calculation input of another component.

6.2.1 Dynamic Model of Adsorber

The dynamic model of the adsorber has been introduced in detail in Chapter 5. The data flow of the adsorber model is illustrated in Figure 71. Inside the adsorber, the salt is subjected to the ammonia vapor pressure in the chamber of both the adsorber and the condenser-evaporator. With the heat pipe temperature supplied by the hybrid heat pipe model and the ammonia vapor pressure supplied by the condenser-evaporator model, the sorbent dynamic model can calculate the heat exchange with the heat pipe medium ($Q_{HP \rightarrow salt}$) and the total amount of ammonia released/absorbed by the salt (n_{NH_3}), which are in turn passed to the heat pipe model and the condenser-evaporator model as their calculation inputs.

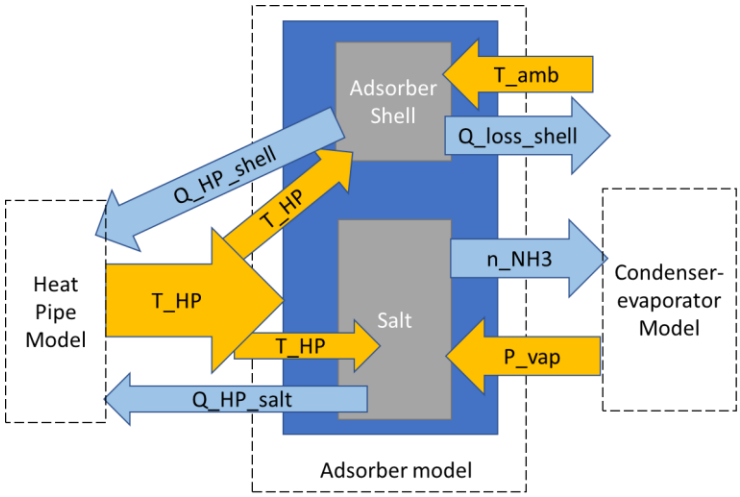

Figure 71 Structure and data flow in the adsorber model

In addition to the transient sorbent salt conditions, i.e. its temperature and the remaining amount of ammonia absorbed by it, the adsorber model also keeps track of the temperature of the adsorber shell thermal mass. The change of energy in them are calculated for every time step.

6.2.2 Dynamic Models for the Hybrid Heat Pipe

The hybrid heat pipe comprises the heat pipe heat exchanger connected to the sorbent salt and shell of the adsorber, the natural gas boiler, the water reservoir tank, and the heat pipe heat exchanger connected to the cooling water loop. These sub-components operate differently in the desorption and sorption modes, leading to different energy conservation equations.

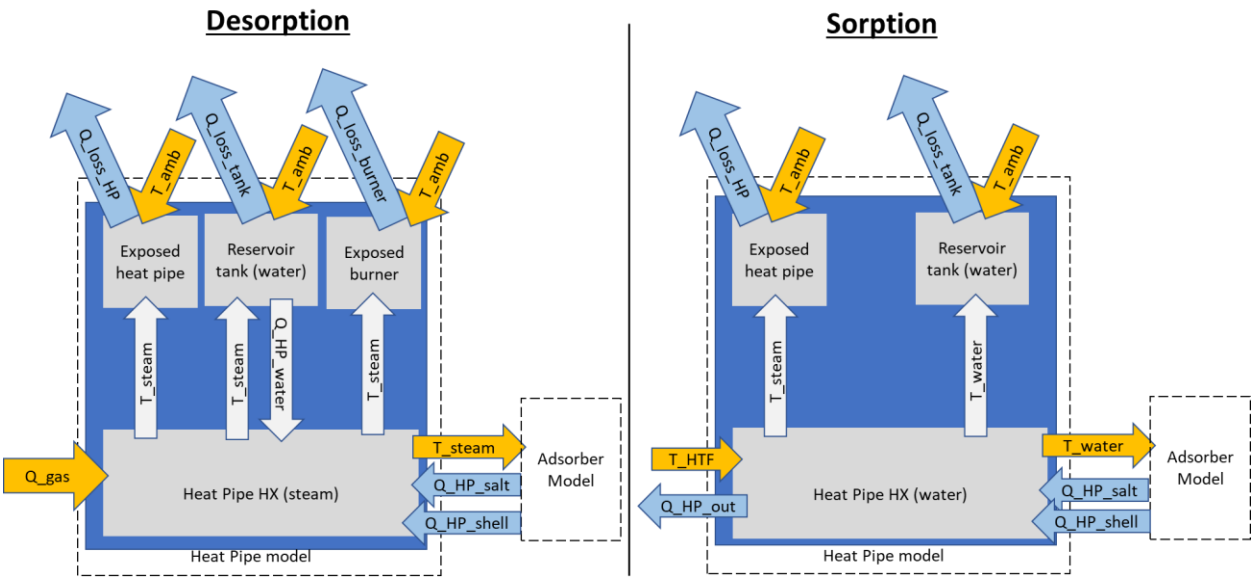

Figure 72 Structure and data flow of the hybrid heat pipe model

In the desorption mode, steam is generated by combusting natural gas to boil water in the burner. The steam fills all the empty volume of the heat pipe and thus is assumed to be at a uniform saturation state across the entire heat pipe. Based on the steam temperature, the heat transfer between the heat pipe and the adsorber salt and shell, as well as the heat loss through the heat pipe and burner exposed to the ambient can be calculated. Meanwhile, the majority of the 4kg of water in the system stays in the liquid form inside the reservoir tank. During desorption mode the water in the reservoir tank is in contact with the hot steam while also receiving hot condensate return from the heat pipe to replenish the water boiled in the burner. The water is likely to be stratified in the tank. However, due to lack of temperature sensor in the reservoir tank (one on the middle-height), the water temperature is assumed to be uniform to simplify calculation. The heat exchange between the liquid water and the steam can be simplified into a UA-type heat transfer problem. Similarly, the heat transfer between the heat pipe and the adsorber shell is also simplified into a UA-type heat transfer problem with uniform-temperature assumption applied also to the adsorber shell.

$$\dot{Q}_{HP\to water} = (T_{steam} - T_{water}) \times UA_{HP\to water}$$ Equation 85

$$\dot{Q}_{HP\to shell} = (T_{steam} - T_{shell}) \times UA_{HP\to shell}$$ Equation 86

With the measured steam and water temperature, the $UA_{HP\to water}$ is calibrated to be 0.01 kW/K. Based on the water temperature, the heat loss of the reservoir tank can then be calculated. The exposed heat pipe and the reservoir tank are both horizontal cylinders, and their convective and radiation heat exchange with the ambient can be calculated as below. Similarly, the $UA_{HP\to shell}$ is identified to be 0.006 kW/K to make the shell temperature match the experimental measurement. The heat loss through the burner, which can be deemed as a vertical cylinder, can be calculated using the same equations for the adsorber shell with the dimension of the burner and the steam temperature.

$$Ra = \frac{g\beta L^3 \Delta T \cdot Pr}{v^2}$$ Equation 87

$$Nu = \left(0.6 + \frac{0.387 \cdot Ra^{\frac{1}{6}}}{\left[1 + \left(\frac{0.559}{Pr}\right)^{\frac{9}{16}}\right]^{\frac{8}{27}}} \right)^2$$ Equation 88

$$Q_{conv} = Nu \cdot \frac{K}{L} \cdot A \cdot \Delta T$$ Equation 89

$$\dot{Q}_{rad} = A \cdot \varepsilon \cdot \sigma \cdot (T^4 - T^4)$$ Equation 90

For the steam in the heat pipe heat exchanger, the energy conservation equation is below. With the saturation assumption, both the specific enthalpy and the mass of the steam in the fix-volume heat pipe are functions of the steam temperature. Therefore, the steam temperature becomes the only variable in the equation and can be determined by solving the energy balance equation of the steam for each time step. The volume of the heat pipe is estimated to be 3.2L based on the dimensions of the heat pipe heat exchanger inside the adsorber as well as the part of heat pipe outside the adsorber.

$$\frac{d(\mathrm{H_{steam}} \times m_{steam})}{dt} = \dot{Q}_{gas} + \dot{Q}_{HP\rightarrow salt} + \dot{Q}_{HP\rightarrow shell} + \dot{Q}_{loss,HP} + \dot{Q}_{loss,burner} + \dot{Q}_{HP\rightarrow water} \quad \text{Equation 91}$$

$$H_{steam} \times m_{steam} = f(T_{steam}) = H_{sat,steam}(T_{steam}) \times \frac{V_{HP}}{v_{sat,steam}(T_{steam})} \quad \text{Equation 92}$$

In the sorption model, the burner is turned off and the water in the reservoir tank is circulated through the heat pipe plates and tubes. The heated water is brought in contact with the external heat transfer fluid (HTF) to release the heat to the end-use. Due to the lack of temperature sensors across the heat pipe and the fast dynamic of the heat transfer between the hot salt, the circulated water, and the external HTF, the temperature of the liquid water is assumed to be uniform throughout the heat pipe and the water tank. As a result, the heat transfer between the heat pipe and other parts of the system can be written as a function of the water temperature, and thus the water temperature can be determined by solving the energy balance equation. And the heat transfer between the heat pipe water and the external HTF described with the UA-LMTD method.

$$Cp \cdot m_{water} \cdot \frac{d\mathrm{T_{water}}}{dt} = \dot{Q}_{HP\rightarrow salt} + \dot{Q}_{HP\rightarrow shell} + \dot{Q}_{loss,HP} + \dot{Q}_{HP\rightarrow out} \quad \text{Equation 93}$$

6.2.3 Dynamic Model for the Condenser-evaporator

The condenser-evaporator (C-E) model describes the state of the ammonia in the empty volume of the sorption module as well on the heat exchanger and shell of the C-E vessel. The ammonia vapor

is subjected to the ammonia release and absorption via the chemisorption reaction in the adsorber as well as the phase change on the C-E heat exchanger and shell. The C-E is also a reservoir of the condensed liquid ammonia, and depending on the location of condensation, the accumulated liquid is associated with either the heat exchanger or the shell. The C-E model is linked to the adsorber model with the ammonia vapor pressure and flow associated with the chemical reaction with the salt.

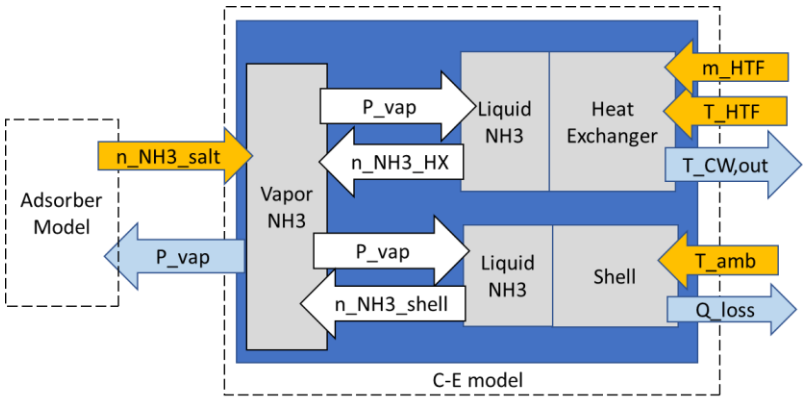

Figure 73 Structure and data flow of the condenser-evaporator model

The state of the ammonia vapor is calculated using the ideal gas law. The number of moles in vapor (n_{vap}) is calculated by the mass balance between the vapor ammonia change associated with the chemisorption reaction and the phase change as below. The temperature of the vapor ammonia (T_{vap}) is calculated by the energy balance equation of the vapor ammonia as below under the assumption that the heat transfer between the ammonia vapor and the adsorber salt and shell are negligible, and that only condensation and evaporation heat transfer occurs between the vapor and the C-E heat exchanger and shell. The fixed empty volume of the adsorber-condenser/evaporator chamber is estimated to be 42.1L based on the dimension of the adsorber and C-E vessels as well as the internal heat exchanger dimensions.

$$P_{vap} \cdot V_{chamber} = n_{vap} \cdot R \cdot T_{vap} \quad \text{Equation 94}$$

$$\frac{dn_{vap}}{dt} = \dot{n}_{NH_3,HX} + \dot{n}_{NH_3,shell} + \dot{n}_{NH_3,salt} \quad \text{Equation 95}$$

In the energy balance equation, when the ammonia vapor flow is towards salt (i.e. sorption reaction) or liquid ammonia (i.e. condensation), the exiting energy is calculated using the ammonia temperature. Otherwise the entering energy with the ammonia vapor inflow is calculated using the temperature of the corresponding sources.

$$\dot{Q}_{vap,HX} = Cp_{vap} \cdot M_{NH_3} \cdot \dot{n}_{NH_3,HX} \cdot T_{CE,HX}, \dot{n}_{NH_3,HX} > 0$$
$$\dot{Q}_{vap,HX} = Cp_{vap} \cdot M_{NH_3} \cdot \dot{n}_{NH_3,HX} \cdot T_{vap}, \dot{n}_{NH_3,HX} < 0$$ Equation 96

$$\dot{Q}_{vap,shell} = Cp_{vap} \cdot M_{NH_3} \cdot \dot{n}_{NH_3,shell} \cdot T_{CE,shell}, \dot{n}_{NH_3,shell} > 0$$
$$\dot{Q}_{vap,shell} = Cp_{vap} \cdot M_{NH_3} \cdot \dot{n}_{NH_3,shell} \cdot T_{vap}, \dot{n}_{NH_3,shell} < 0$$ Equation 97

$$\dot{Q}_{vap,salt} = Cp_{vap} \cdot M_{NH_3} \cdot \dot{n}_{NH_3,salt} \cdot T_{salt}, \dot{n}_{NH_3,salt} > 0$$
$$\dot{Q}_{vap,salt} = Cp_{vap} \cdot M_{NH_3} \cdot \dot{n}_{NH_3,salt} \cdot T_{vap}, \dot{n}_{NH_3,salt} < 0$$ Equation 98

$$\frac{d(T_{vap} \cdot n_{vap})}{dt} \cdot Cp_{vap} \cdot M_{NH_3} = \dot{Q}_{vap,HX} + \dot{Q}_{vap,shell} + \dot{Q}_{vap,salt}$$ Equation 99

While the ammonia in-flow from the salt is calculated by the adsorber model, the ammonia condensation on the CEHX and the shell is calculated based on the condensation heat transfer model. The temperature of the ammonia vapor in the heat transfer calculation is the saturation temperature corresponding to its pressure to account for the superheated condition.

$$h_{fg,NH_3} \cdot M_{NH_3} \cdot \dot{n}_{NH_3,HX} = hA_{CEHX} \cdot \left(T_{vap,sat} - T_{CE,HX}\right)$$ Equation 100

$$h_{fg,NH_3} \cdot M_{NH_3} \cdot \dot{n}_{NH_3,shell} = hA_{CE,shell} \cdot \left(T_{vap,sat} - T_{CE,shell}\right)$$ Equation 101

Since the CEHX is a combination of a multi-stack flat-plate heat exchanger and carbon porous matrix, its condensation heat transfer coefficient and surface area cannot be directly measured. Instead, in the current model, their product (hA_{CEHX}) is calibrated to be 5kW/K and 0.5kW/K using the experimental data for condensation and evaporation, separately. The similar is done for the phase change heat transfer with the shell, and the $hA_{CE,shell}$ for condensation and evaporation are 0.5kW/K and 0.05kW/K.

6.3 System Model Validation

With the individual component model developed above, the system dynamic model can be assembled. The structure and data flow between the components in the system model are illustrated in Figure 69 and Figure 70. For each time step, the system model is calculated starting from the heat pipe and propagating to the adsorber and finally the condenser-evaporator. For example, in desorption mode, the heat pipe model takes the current combustion heat input as well as the previous-step energy flow to the salt and shell of the adsorber to calculate the steam temperature along with the heat transfer to the water and loss to the ambient for the current time step. Then the adsorber model takes the steam temperature and chamber ammonia pressure from the previous step and calculates the energy and ammonia sorption associated with the chemical reaction. Finally the condenser-evaporator model updates the current chamber ammonia pressure based on the previous time-step ammonia in-flow from the salt as well as the ammonia condensation on the CEHX and shell, along with the heat output in the cooling water loop and heat loss to the ambient.

The system model is used to simulate the operation of the one adsorber-condenser/evaporator module on 6/7/2019. The model takes the time-series data of the measured natural gas input, hot water return temperature and flow rate, as well as the ambient temperature as the simulation input, and set the temperatures and pressures of each system to correspond to the beginning of the test as the initial value. The calculated key temperatures and energy flow are compared with the experiment measurement below to validate the system model.

Figure 74 illustrates the comparison of the calculated and measured ammonia chamber pressure and heat pipe steam and water temperature. The hot water supply temperature in the test and simulation are compared in Figure 75. The simulation results generally show good agreement with

the measured values. For the ammonia chamber pressure between 90 and 140 min, the simulated value is higher than the measurement. This can be explained by the significant temperature fluctuation at the beginning of the sorption mode when water in the reservoir tank was first pumped into the adsorber to extract heat from the hot salt. The model assumes the temperature of the entire water body is uniform and calculates the heat flux into the water using that temperature. To compensate for the over-estimated temperature difference between the salt and the water, the model turns on the water pumping intermittently at the beginning stage. As the combining result of the two factors, at the beginning of water circulation, the model overestimates the temperature change of the water body (Figure 75) and underestimates the ammonia pressure change (Figure 74).

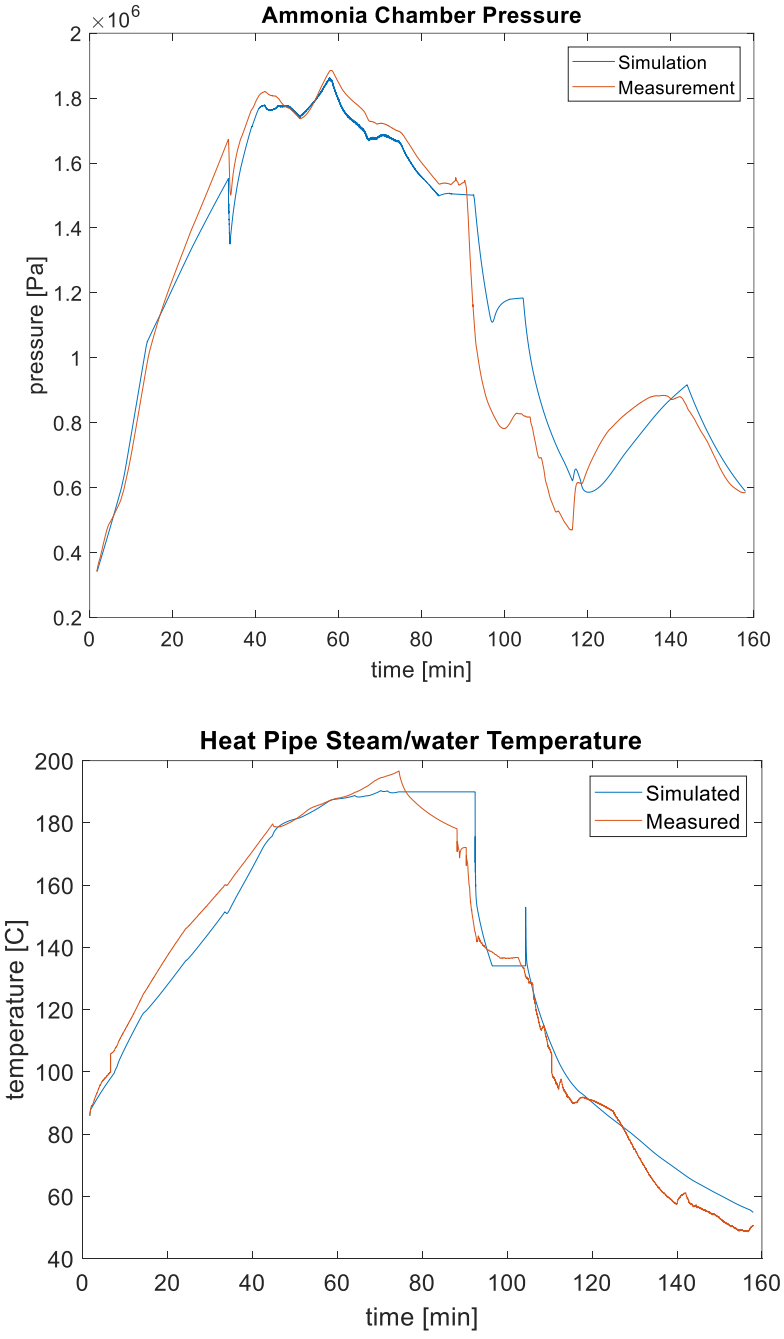

Figure 74 Comparison of simulation and test ammonia pressure (top) and steam/water temperature in the heat pipe (bottom)

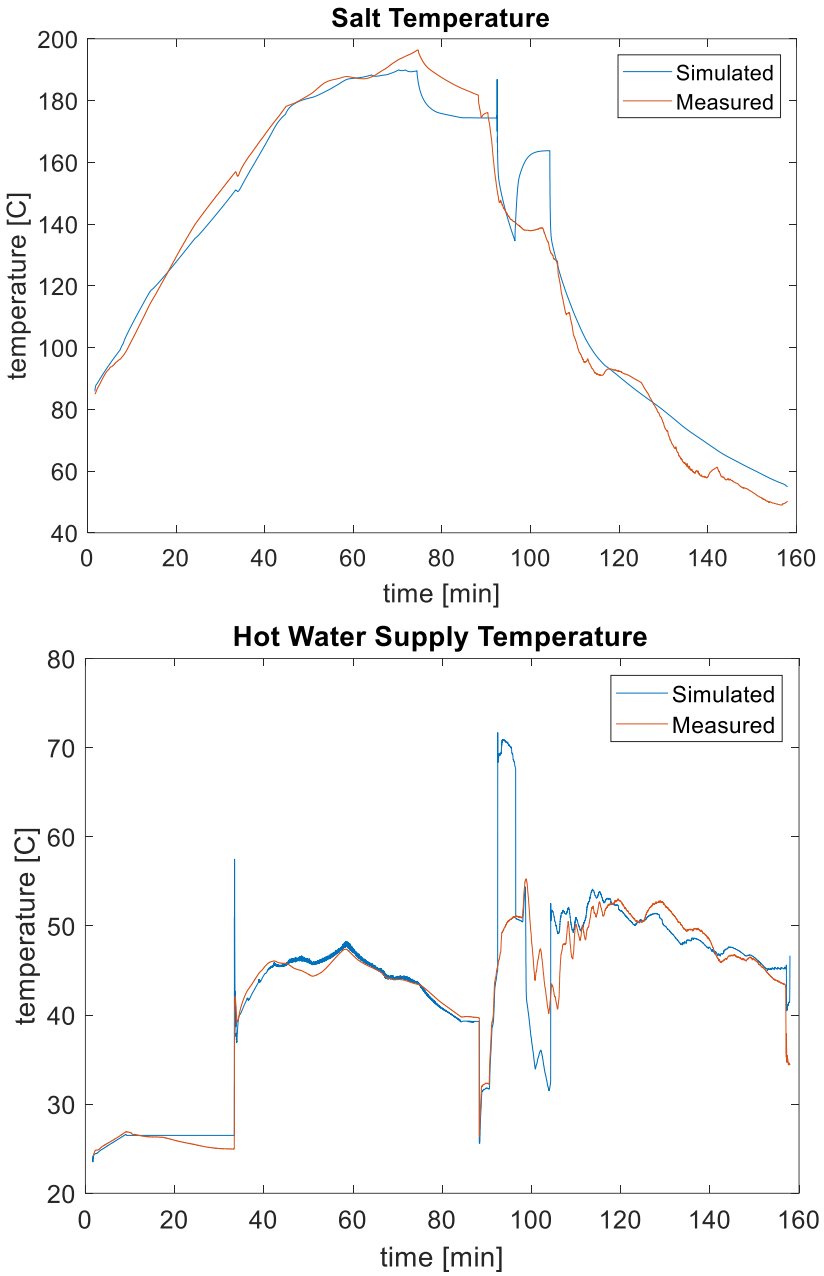

Figure 75 Comparison of simulation and test salt temperature (top) and hot water supply temperature (bottom)

Nevertheless, such difference does not lead to considerable error in predicting the key operating parameters after the beginning of the sorption mode. More importantly, the accuracy for system overall performance prediction is not affected by the simplification in the heat pipe water circulation, as is shown in Table 30 for key energy flow during the system operation. The overestimation of the evaporation heat is further discussed in the discussion section.

Table 30 Comparison of simulation and experiment system overall performance

PARAMETER	Q_{DES} [KJ]	Q_{COND} [KJ]	Q_{ADS} [KJ]	Q_{EVAP} [KJ]	$Q_{IN,TOT}$ [KJ]	$Q_{OUT,TOT}$ [KJ]	COP [-]
EXPERIMENT	8909	1377	6732	817	9726	8109	0.91
MODEL	8909	1206	6653	1187	10096	7859	0.88
ERROR	0	-13%	-1.2%	+45%	+3.8%	-3.1%	-3.3%

To further analyze the system operation given the detailed information from the validated system model, the energy flow is further categorized into in-flow, storage, and outflow as listed in

Table 31. Most of the heat input into the system is from the natural gas combustion at high temperature compared with the heat inflow at the cold ambient temperature. The heat loss during heat inflow is around 7% of the total heat input. The heat that enters the system during the desorption mode is mostly stored in the form of the chemical potential and heat in the salt ($Q_{in-salt}$) and the sensible heat of various other thermal masses in the system (Q_{in-TM}). The heat that enters the system during the sorption mode is transferred in the system in the form of the vaporization heat of ammonia (Q_{in-NH3}). Finally, most of the stored heat is supplied to the end use or lost to the ambient. The heat outflow during the sorption mode comes from both the hot thermal mass (Q_{out-TM}) and the sensible and chemical heat of the salt ($Q_{out-salt}$). The condensation heat of the ammonia is released during the desorption mode.

Table 31 Energy flow breakdown of the simulated results, also illustrated in Figure 76

	INFLOW			STORAGE			OUTFLOW			
	Q_{in-NG}	$Q_{in-Evap}$	$Q_{in-loss}$	Q_{in-TM}	$Q_{in-salt}$	Q_{in-NH3}	Q_{out-TM}	$Q_{out-loss}$	$Q_{out-salt}$	$Q_{out-Cond}$
HEAT [KJ]	8909	1187	727	3670	4521	1606	2211	794	4342	1206
%TOTAL	88.2	11.8	-7.2	39.2	48.2	12.6	25.8	9.3	50.8	14.1

As shown in the table, the heat associated with the essential phenomenon of the CSHP, i.e. the chemisorption reaction in the salt, is only less than half in both the heat input and output. Therefore, only less than half of the total input heat is amplified by the theoretical ammonia-based chemisorption cycle COP of about 1.5, while over half of the input heat is merely temporarily stored as sensible heat in the thermal masses before passes on to the end use or lost to the ambient.

The overall system energy flow is illustrated in the Sankey diagram in Figure 76.

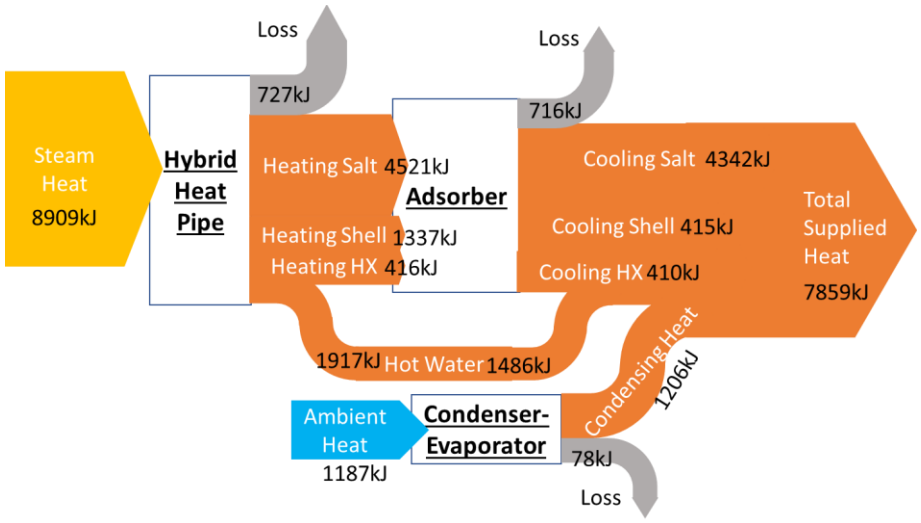

Figure 76 Simulated overall system energy flow corresponding in

Table 31

6.4 System Performance Simulation

6.4.1 Baseline System

The baseline system consist of a single adsorber-C/E module is simulated under the rating condition for heat pump systems according to the ANSI-Z21.40.4 [160] for gas-fired air-source heat pumps for heating with ambient temperature of -8.3°C. The hot water return temperature is 43.3°C/110°F and the supply is 48.9°C/120°F. The hot water flow rate is fixed at 0.06kg/s. The HTF temperature entering the C-E during sorption mode is 10°C below the ambient temperature to emulate a typical fan-coil. The low-temperature HTF is 40% aqueous ethylene glycol solution with freezing point of -23.5°C. The average properties between -20°C and 50°C are used. The density is 1070 kg/m3, and the specific heat is 3.63 kJ/kg.C. The HTF flow rate is fixed at 0.07kg/s. The burner gas input is fixed at 2kW during desorption mode, with steam generation effectiveness at 65%. Table 32 lists the design parameters and the boundary and initial conditions for the baseline system.

Table 32 Design Parameter and Boundary Conditions for the Baseline System

Design Parameter	Value	Boundary & Initial Conditions	Value
Salt mass [kg]	2.2	Ambient temperature [°C]	-8.3
Ammonia mass [kg]	2.1	Hot water return temperature [°C]	43.3
Adsorber shell mass [kg]	24	Hot water supply temperature [°C]	48.9
Adsorber HX mass [kg]	8	Hot water flow rate [kg/s]	0.06
Condenser-evaporator UA [W/°C]	800	Evaporator HTF flow rate [kg/s]	0.07
Burner steam generation input [kW]	3	Temperature diff. between ambient and evaporator water inlet [°C]	10
Fiberglass insulation thickness [in]	3	Insulation conductance [W/m2-K]	0.52
Mode switch threshold [kW]	0.1		

The simulated time-series of the system heat input and output for two consecutive cycles under the baseline case condition is illustrated in Figure 77. The natural gas heat input was sustained until the salt temperature approaches the safety limit of 200°C, when it is turned down gradually. The condensing heat output starts once the condenser HX temperature exceeds the target hot water supply temperature, about in the middle of the desorption mode. The desorption mode is terminated when the condensing heat output drops below 0.1 kW. Upon switching to the sorption

mode, the burner is turned off the heat output is by cooling the salt in the adsorber, until the heating power drops below the threshold.

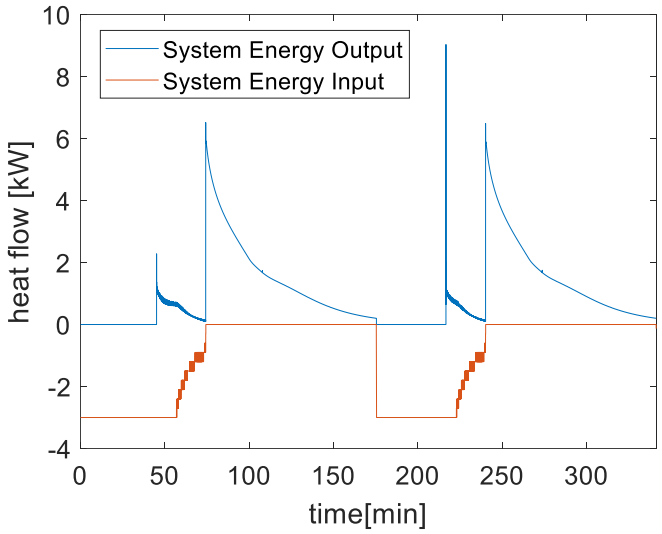

Figure 77 Time-series of the system heat input and output during two consecutive cycles simulated under -8.3°C ambient and low insulation

The key temperature and heat flow of the baseline system simulation are listed in Table 33. The temperature of both the heat exchanger and the shell of the condenser-evaporator is lower than the ambient temperature, and therefore more condensing heat is consumed in the pre-heated cycle. On the other hand, the thermal masses such as the adsorber shell are heated up during the cold-start cycle and therefore consumes much less heat to heat up in the pre-heated cycle. Meanwhile, the higher average temperature of these thermal masses also leads to an increase of the heat loss to the ambient. The combined result of above changes between the cold-start and pre-heated cycles is that the latter has a higher heating COP, which can be representative to the continued operation of the system.

Table 33 Simulation results of baseline system

CYCLE	Q_{DES} [KJ]	Q_{COND} [KJ]	Q_{ADS} [KJ]	Q_{EVAP} [KJ]	$Q_{TM,IN}$ [KJ]	Q_{LOSS} [KJ]	$Q_{OUT,TOT}$ [KJ]	COP [-]	P_{AVG} [W]
COLD-START	12555	488	8546	264	2212	1573	9034	0.72	885
PRE-HEATED	11097	182	8941	288	391	1871	9123	0.82	883
CHANGE	-1458	-306	+395	+24	-1821	+298	+89	+0.1	-2
CHANGE%	-11.6%	-62.7%	+4.6%	+9.1%	-82.3%	+18.9%	+1.0%	+14%	-0.2%

6.4.2 Parametric Study

Based on the baseline case, the investigation of the system performance is extended into different ambient temperatures, levels of insulation, for both cold-start and pre-heated scenarios. The cold-climate ambient temperatures of 8.3°C, -8.3°C, and -13.9°C are selected based on ANSI standard Z21.40.4 for gas-fired air-source heat pumps [160]. Two typical fiberglass insulation are investigated: 3-inch R11 batted fiberglass, and 5-inch R21 high-density batted fiberglass. Their corresponding heat conductance are 0.52W/m2.K and 0.27W/m2.K.

The simulated performances of the system under these operating conditions are listed in Table 34. The heating COP are plotted in Figure 78. In general, the system heating COP decreases with lower ambient temperatures and low insulation level. Like the baseline case, the pre-heated cycles always have higher COP than the corresponding cold-start cycle due to the reduced temperature swing of most thermal masses in the system. The reduction of the condensing heating output is more pronounced in the low-ambient-temperature scenarios since the temperature swing of the CE thermal mass is considerably higher. In the extreme case of -13.9°C ambient with low insulation, the system is not able to finish the pre-heated cycle since the ammonia condensing heat is not enough to heat the condenser HX up to the target hot water supply temperature. In another word, the heat pumping effect of the CSHP system dwindles quickly as the ambient temperature gets low.

Table 34 Summary of the key performances of the parametric simulations

T_{amb} [C]	Insulation conductance [W/m2.K]	Cycle type	Q_{des} [kJ]	Q_{cond} [kJ]	Q_{ads} [kJ]	Q_{evap} [kJ]	Q_{TM} [kJ]	Q_{loss} [kJ]	COP [-]
8.3	0.52	cold-start	12222	829	8746	677	1859	1465	0.78
	0.52	pre-heated	10551	625	8747	621	335	1465	0.89
	0.27	cold-start	11799	881	9470	728	1856	320	0.88
	0.27	pre-heated	10104	674	9465	661	265	361	1.00
-8.3	0.52	cold-start	12555	488	8546	264	2212	1573	0.72
	0.52	pre-heated	11097	182	8941	288	391	1871	0.82
	0.27	cold-start	12135	581	9352	324	2188	338	0.82
	0.27	pre-heated	10107	347	9373	291	304	374	0.96
-13.9	0.52	cold-start	12648	373	8510	159	2295	1629	0.70
	0.52	pre-heated	*	*	*	*	*	*	*
	0.27	cold-start	12171	444	9327	192	2248	344	0.80
	0.27	pre-heated	11085	177	10338	209	239	540	0.95

**the cycle was not able to continue as no condensing heat output at the supply temperature was achieved.*

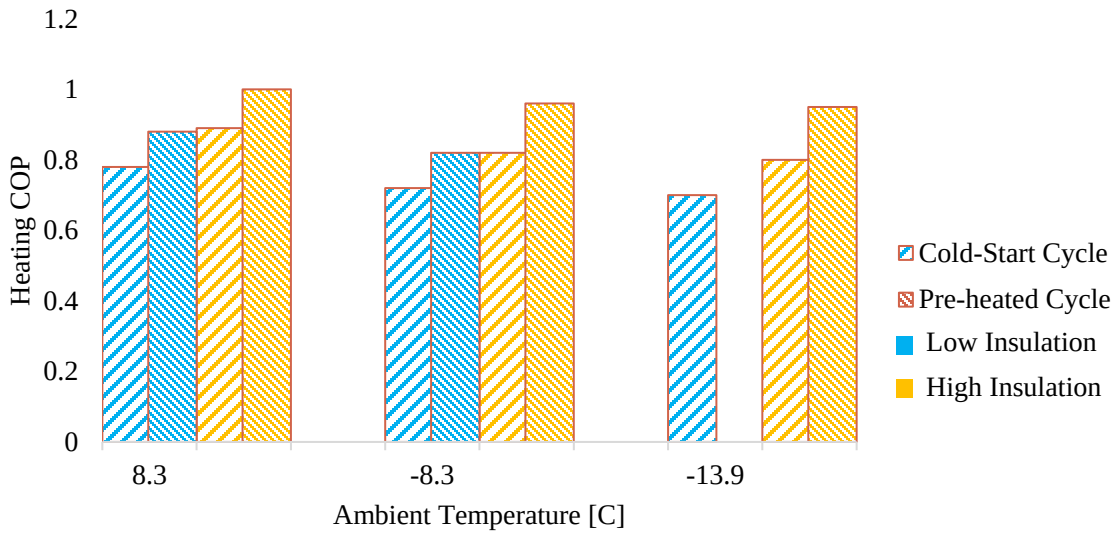

Figure 78 Heating COP for parametric runs

The effect of adding insulation is significant especially at low ambient temperature. By replacing the default R11 fiberglass with R21 fiberglass, the heat loss can be reduced by almost 80% and improving the overall COP by 13-18%. Despite the reduced heating output at the condenser, the pre-heated cycle COP is always higher than the cold-start cycles as the former requires less heat input to drive the operation thanks to the pre-heated thermal masses.

The parametric study shows the system's sustained COP of above 0.95 even at -13.9°C with sufficient insulation. On the other hand, the reduced condensing heat output at low temperatures

considerably hampers the heat pumping effect of the CSHP system, therefore limiting the system COP below 1.0. To approach the theoretical heating COP of above 1.0, the future system needs to reduce the heat consumption by the thermal masses under large temperature swings, as well as to reduce heat loss during the long operating period.

6.5 Discussions

The baseline case simulation and the parametric study have revealed the system performance under typical operating conditions. Further analysis of the results leads to following discussions on discoveries and possible future improvement of the system.

6.5.1. Issues with the Combined Condenser-evaporator

The current system uses a combined condenser-evaporator to exchange the phase-change heat of ammonia with external heat sources and to store the condensed liquid ammonia. Although using the dual-purpose heat exchanger reduces the total number of components in the system and thus makes the system more compact, it also leads to issues that limits the system performance.

6.5.1.1 Non-useful Condensation on the Shell

Since the CE shell is also in constant contact with the ammonia vapor, a considerable amount of condensation happens on the shell. Figure 79 shows the cumulative amount of ammonia liquid on the CEHX and CE shell calculated by the system model. Of the maximum 1.2 kg ammonia released from the salt during desorption mode, over 0.2 kg or 17% condensed on the CE shell.

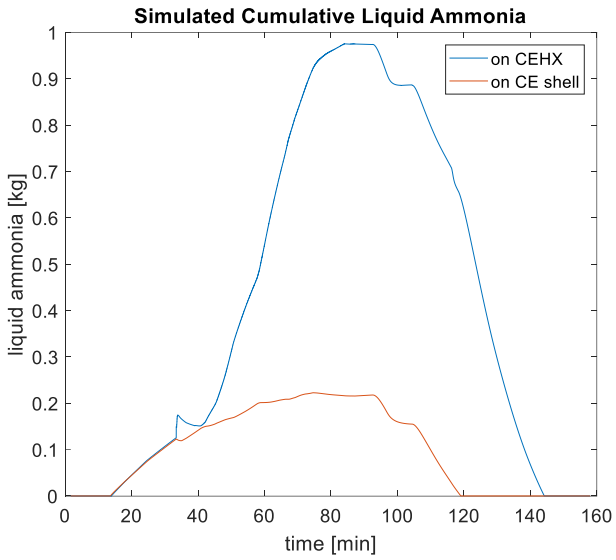

Figure 79 cumulative liquid ammonia on CEHX and CE shell under baseline case condition

The condensation on the CE shell reduces the heating output during desorption mode with less condensing heat extracted by the hot water through the CEHX. As shown in the parametric study under extremely low ambient temperature (-13.9C) and with insufficient insulation, the reduction of condensation on the CEHX could disable the condensing heat output and further reduces the system performance. To mitigate such negative effect, the CE vessel needs to be heavily insulated to avoid the shell temperature drop below the HX temperature. Another way to solve the issue is to collect and supply the heat of condensation on the shell as useful heating output by surrounding the vessel of condensation with medium to be heated, such as wrapping the vessel with external heat exchanger for heating, or emerging the vessel in a hot water tank.

6.5.1.2 Liquid Ammonia Accumulation on the Shell

Although the model accounts for the ammonia condensation on the condenser heat exchanger as well as on the shell, it assumes all the condensate stays on the surface of condensation, where it absorbs heat once the system is switched to the sorption-evaporation mode. However, the open-disk design of the condenser heat exchanger makes it possible for the ammonia condensed on the CEHX to outflow the loose carbon matrix between the CEHX disks and accumulate at the bottom of the CE shell. Such movement of the liquid ammonia increases the amount of liquid ammonia on the shell and reduces the liquid ammonia on the CEHX at the beginning of the sorption mode. As the result, the CEHX sees less heat input during the sorption mode, while the shell has more

heat taken from it in sorption mode due to evaporation than the condensation heat it gets during the desorption mode. This can further leads to cold-spot at the bottom of the shell, which makes it easier for more ammonia vapor to condense on the shell in the next desorption-condensing cycle, as illustrated in Figure 80.

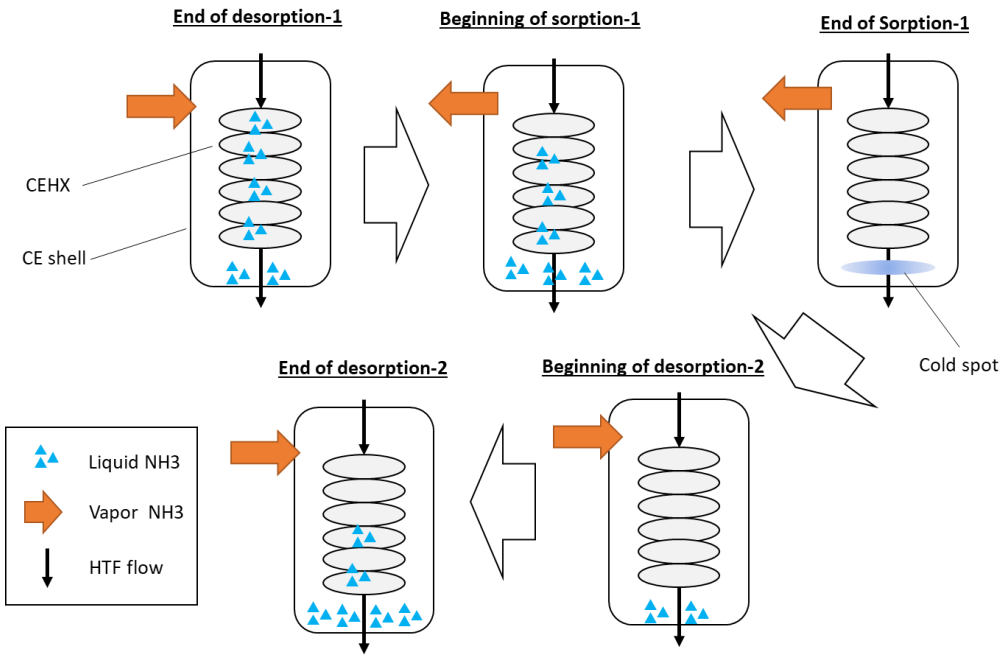

Figure 80 Migration and accumulation of liquid ammonia on the shell

Such hypothesis of the liquid ammonia migration is supported by the observed discrepancy between the condensing heat and the evaporation heat on the CEHX, as well as the difference between the simulated and measured evaporation heat. In Chapter 4, the evaporation heat measured during the sorption mode is significantly lower (often about half) than their previous condensation stage in most of the tests. In the system model validation (section 6.3.) the calculated evaporation heat is 45% higher than the experimentally measured value. Since the measurement can only capture the evaporation of liquid ammonia on the CEHX, it suggests the amount of liquid ammonia condensed on the CEHX is higher than the liquid ammonia evaporated from the CEHX.

6.5.1.3 Thermal Mass

The thermal mass of the condenser-evaporator undergoes significant temperature swing between the desorption-condensing and the sorption-evaporating mode, especially under low ambient

temperatures. The heat needed to heat up and cool down this thermal mass is supplied by the ammonia phase change, and therefore it reduces the amount of useful heat generated as well as reducing the amount of low-temperature ambient heat entering the system. In the current design as measured in [161], the mass of the CEHX and CE shell is significant compared with the ammonia. Depending on the ambient temperature, the heat involved in the CE thermal mass temperature swing takes 60%~100% of the total condensing/evaporating heat. If the condenser and the evaporator are separated, they do not have to operate between two temperatures, and therefore eliminates the loss of useful heat production.

6.5.2. Output Fluctuation: Need a Buffer Tank

As shown in Figure 77, the system heating output is always transient during operation. Generally, the desorption model has a lower heating power at the condenser side compared with the heat produced at the adsorber in the sorption mode. Within the desorption and sorption mode, the heating output is also affected by the changing temperature of system thermal masses and chemical reaction rate. Moreover, there is an intermediate period during the starting stage of the desorption mode when the condenser temperature is yet not high enough for heating output. These transient behavior of the system heating output calls for a buffer tank to smoothen the overall system heating output.

6.5.3. Fuel Combustion Heat Recovery and Gas COP

The overall system gas COP can be defined as the ratio of the total heat output and the total gas heat input. The heat generated by combusting the natural gas is split into two parts: the heat transferred through the hybrid heat pipe into the CSHP system and the heat carried away in the hot flue gas leaving the burner.

$$Q_{CSHP,out} = COP_{CSHP} \times Q_{CSHP,in} = COP_{CSHP} \times \left(Q_{gas,in} \times \eta_{steam,gen}\right) \quad \text{Equation 102}$$

$$Q_{flue,out} = Q_{flue} \times \eta_{flue,recov} = Q_{gas,in} \times \left(1 - \eta_{steam,gen}\right) \times \eta_{flue,recov} \quad \text{Equation 103}$$

$$COP_{gas} = \frac{Q_{out}}{Q_{gas,in}} = \frac{Q_{CSHP,out} + Q_{flue,out}}{Q_{gas,in}} = COP_{CSHP} \times \eta_{steam,gen} + \eta_{flue,recov} \times \left(1 - \eta_{steam,gen}\right) \quad \text{Equation 104}$$

The above equations show that improving the heating COP of the CSHP is only affecting the heat pump amplification effect on the part of the heat that reaches the salt in the adsorber. To maximize the system gas efficiency, improvement needs to be implemented on the steam generation efficiency of the burner as well as the flue gas heat recovery.

6.5.4. An Improved System Design

To overcome the issues with the combined condenser-evaporator and considerable loss of heating capacity and efficiency discussed above, an improved design was conceived by SaltX/HeatAmp for the future systems. The adsorber and much of the heat pipe system is placed in a hot-water buffer tank. The shell of the adsorber is used as the condensing surface of the vapor ammonia during desorption-condensation mode, where the condensation heat is transferred to the surrounding water. The condensate liquid ammonia flows down the adsorber shell and accumulates in the evaporator outside the buffer tank. During sorption-evaporation mode, the liquid ammonia evaporates and re-combines with the sorbent in the adsorber, transferring the reaction heat to the pumped water in the heat pipe and eventually heating the water in the buffer tank.

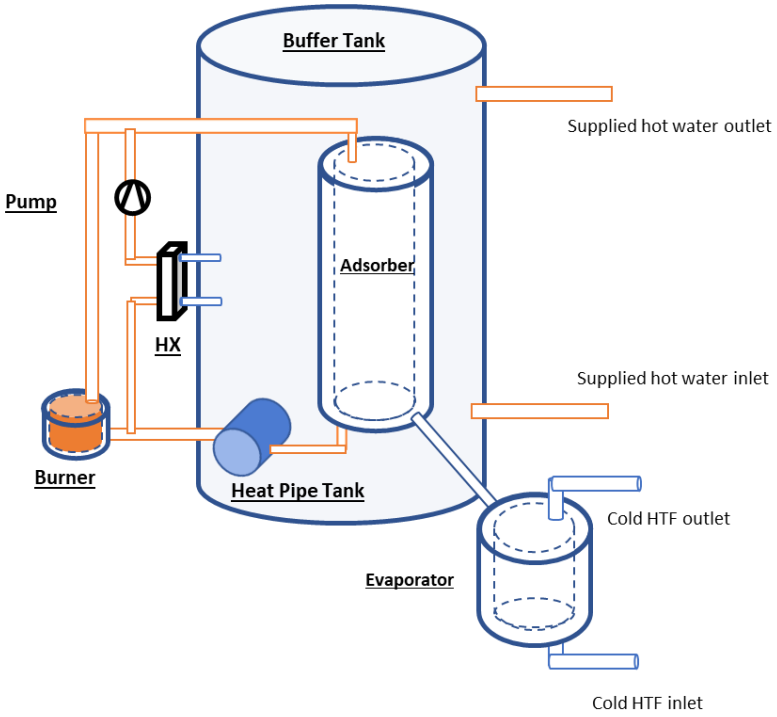

Figure 81 Schematic of the improved system design

The improved design separates the condenser and evaporator to avoid the temperature swing of the metal thermal masses; it mitigates the heat loss to the ambient by enclosing the hot parts of the system in the buffer tank; and it better harvest the condensation heat for water heating by using the adsorber shell as the condensing surface.

The last desorption stage of LiCl-NH3 reaction happens at around 190°C, which is close to the upper temperature limit of around 210°C of the current welded stainless-steel steam heat pipe for transferring heat from the high-temperature source to the salt. To increase the reaction rate of the last desorption stage and accelerate the system operation for a higher heating power, the temperature limit of the heat pipe in the improved design is raised to 250°C. In real systems, this temperature might require changing the heating method from the current steam heat pipe to flue-gas direct heat.

Using the same component dimensions, the system model is used to calculate the performance of such an improved system. The energy flow breakdown of the system operating under 8.3°C is summarized in Table 35 and shown in Figure 82. The heating COP of the improved system is 1.23. Compared with the previous prototype, the improved design significantly reduces the heat loss and

increases the heating output associated with the condensation. The heat retention in the thermal masses is also considerably reduced with the separate condenser-evaporator design.

Table 35 Energy breakdown of the improved system under 8.3°C

	INFLOW			STORAGE			OUTFLOW			
	$Q_{in\text{-}NG}$	$Q_{in\text{-}Evap}$	$Q_{in\text{-}loss}$	$Q_{in\text{-}TM}$	$Q_{in\text{-}salt}$	$Q_{in\text{-}NH3}$	$Q_{out\text{-}TM}$	$Q_{out\text{-}loss}$	$Q_{out\text{-}salt}$	$Q_{out\text{-}Cond}$
HEAT [KJ]	8508	2466	289	1520	6678	2466	1487	118	6466	2480
%TOTAL	77.5	22.5	-2	14.3	62.6	23.1	14.1	1.1	61.3	23.5

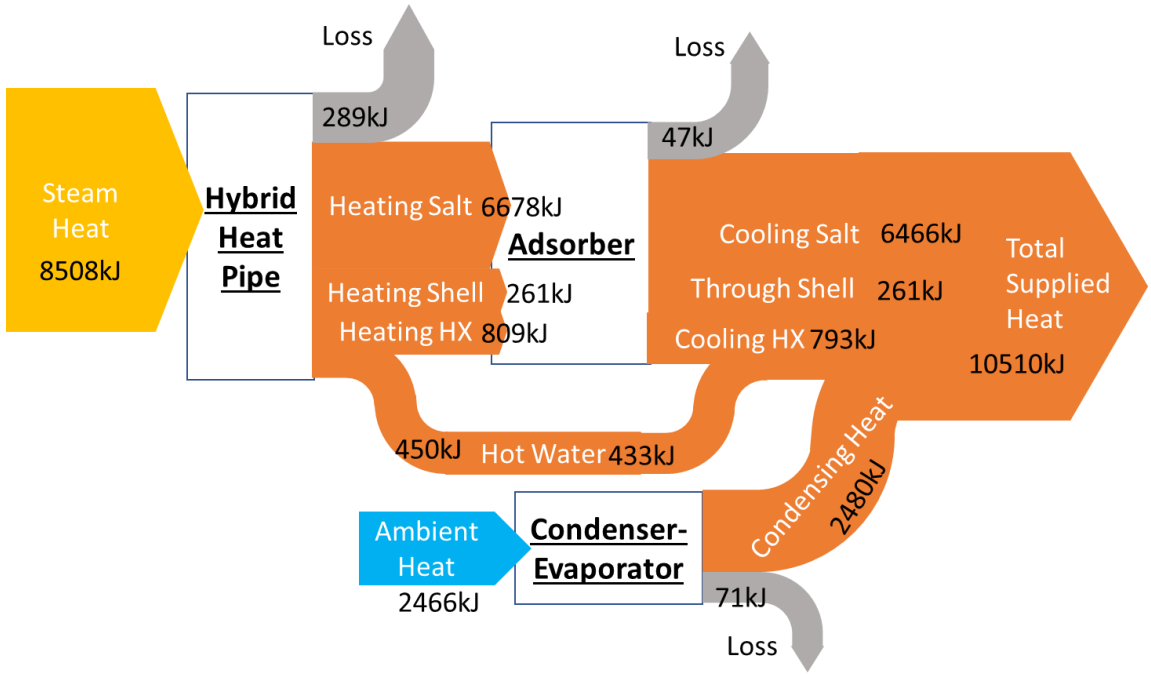

Figure 82 Energy flow of the improved system design operating at 8.3°C

The comparison of heating COP with the current prototype system under the three ambient temperatures as shown in Figure 83. The improved design demonstrates significant increase of heating COP in all scenarios and maintains high heating COP of around 1.2 down to -13.9°C ambient.

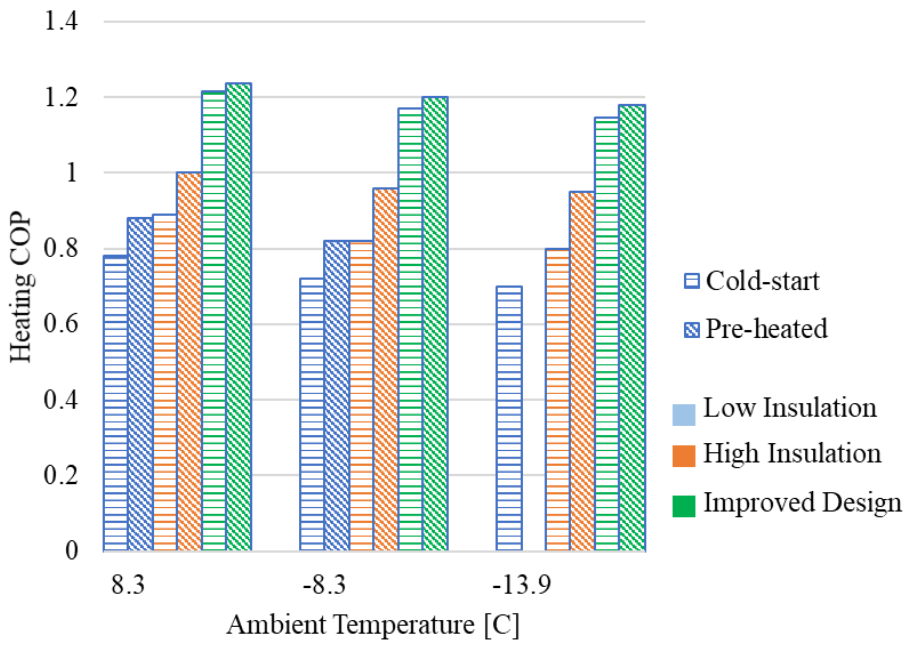

Figure 83 Performance comparison of the improved design under cold-climate heating conditions

To further improve the system heating COP, the heat retention in the thermal mass of the system need to be further reduced. This can be achieved by using working pairs with lower operating temperature and pressure (e.g. $CaCl_2$). Due to the high operating temperature (>200°C) and corresponding high steam pressure (>1500kPa), a closed hybrid heat pipe system with considerable metal mass needs to be used. The thermal mass of the salt and adsorber heat exchanger also undergoes significant temperature swing and requires considerable amount of heat from the heat source to raise the reaction temperature. In contrast, for a working pair with a lower operating temperature range, the heat required to raise the temperature of exchanger metal and sorbent is reduced. Furthermore, at lower steam pressure, the closed hybrid heat pipe system can be replaced with an open water boiling/circulation system to further reduce the number of component and thermal mass in the system for higher heating performance.

6.5.5. Improving the Model Accuracy

The following assumptions were made in the system dynamic model to simplify the calculation. The simulation accuracy can be further improved in the future by describing and calibrating the dynamic spatial gradient of these parameters. The uniform temperature assumptions were applied in (1) ammonia vapor, (2) heat pipe steam, (3) heat pipe water, and (4) adsorber and condenser-evaporator shell.

6.6. Conclusion

This chapter developed and validated a dynamic model for the CSHP system. The models for each key component are first introduced and calibrated to capture the transient temperature, pressure, and energy change during the operation. Then the component models are assembled into an integrated system model and used to simulate the system operation on 6/7/2019. The simulation results were compared with the measured values for the period of operation and showed good match. The overall system performances of the tested and simulated operation were compared as well. The differences of the total amount of heat input and output are below 4%. The difference in measured and calculated condensing heat and evaporation heat was attributed to the likely movement of the condensate liquid ammonia, and the effect of such difference on the system performance is small.

With the validated system model, a baseline case under the rating condition for air source heat pump was simulated and analyzed. Parametric analysis was carried out to investigate the system performance under cold-climate ambient conditions and with different levels of insulation. The system COP only drops slightly as the ambient temperature drops. However, due to the significant thermal mass in the current system design, the system heating COP is below 1.0. The results of the parametric study point to several possible approaches to improve the system performance especially for cold-ambient operations. Among them are using separate condenser and evaporator, collect and supply the condensation on the condenser shell, and integrate the system with a buffer tank for smooth operation. Based on the findings in the baseline and parametric simulation, an improved system design is proposed to improve the system heating COP by reducing the thermal mass and heat loss. Simulation predicts the heating COP of the improved system to be considerably higher than the current prototype at 1.17-1.23 under ambient temperature of 8.3°C to -13.9°C. The

improved system simulation also points to direction for further system improvement by applying working pairs with lower operating temperature range that allows simplified system configuration and reduces thermal mass heat loss.

7. CONCLUSION AND FUTURE WORK

Space and water heating are major contributors to the energy consumption in residential buildings in the U.S., especially in the cold climates where heating is at high demand. However, the existing heating technologies, available on the market, i.e. fuel-combusting furnaces, and electric-driven heat pumps, face significant challenges improving their energy efficiency under low ambient temperatures. Ammonia-based chemisorption heat pumps have great potential of producing heating with much higher energy efficiency than conventional systems. However, through a comprehensive literature review of the chemisorption technology for below-freezing operating conditions, only limited studies were found focusing on adopting CSHP in cold-climate heating applications in literature.

This thesis study is an important step towards understanding the dynamic behavior of the CSHP systems in general and the LiCl-based working pair in particular under the cold-climate heating scenario. The developed methodology and findings through experimental and simulation study lays the foundation of improving the CSHP technology to become a viable and competitive option to break through the long-standing barrier of high-efficiency residential heating in cold climates. The findings can be categorized into material, component, and system levels:

- Material level: a methodology to identify the chemical reaction equilibrium and kinetic coefficients was developed, with dedicated tests carried out to measure the salt sorption behavior under controlled temperature and pressure conditions. The chemical equilibrium and kinetic coefficients for multiple-stage reaction between LiCl and NH_3 are fitted from the test results.

- Component level: the experimental performance of a novel adsorber using hybrid heat pipe plate heat exchanger was measured and analyzed. Based on fundamental heat and mass transfer and chemical kinetics, a high-fidelity dynamic model using the finite-difference method for the adsorber was developed and validated. Further study on the optimization of adsorber design parameters including the dimension of the disk and the compactness of the sorbent was conducted using the adsorber model.

- System level: experimental tests were carried out on a lab-scale gas-fired CSHP heating system with comprehensive data acquisition and dynamic control was under various operating conditions and control strategies. The CSHP prototype system achieved heating COP of 0.8-1.16 producing hot water at around 45°C under ambient temperature of 8-20°C. A system-level dynamic model including multiple components was developed and validated. Simulation of the performance of the CSHP system under the cold-climate rating (-8.3°C) and extreme cold conditions (-13.9°C) calculated the heating COP of the current prototype system to be around 0.7-0.95. The system dynamic model was also used to investigate the impact of other design parameters such as insulation as well as the cause of the limited performance in the current prototype system. A new system design was introduced by SaltX/HeatAmp to improve on the inefficiencies revealed by the current system simulation by enclosing the high-temperature components in a buffer tank and separates the condenser and evaporator. Simulation of the improved system resulted in heating COP of 1.17-1.23 at temperatures of 8.3°C to -13.9°C. The suggestions for future development were provided based on the analysis.

To further study and improve the technology, these future works are recommended:

- Material level: the thermophysical as well as thermochemical properties of the ammoniate LiCl salt is calling for comprehensive study to characterize the key parameters such as thermal conductivity, permeability, specific heat, and porosity under different reaction state (i.e. with different amount of ammonia attached to the salt) and different compactness (density). The likely expansion and foaming of the salt during sorption reactions needs to be carefully studied and considered for performance prediction as well as safety. The chemical equilibrium and kinetic of the salt-matrix composite sorbent need to be characterized with more accurate and precisely controlled experiment, especially for the three sorption stages. Chemical equilibrium and kinetics of other high-sorption-capacity working pairs with lower operating temperature range

such as $CaCl_2$ needs to be identified and used to predict their performance under the improved system design.

- Component level: more comprehensive measurement around the novel hybrid heat pipe adsorber is desired to confirm the influence of the irregular geometry (e.g. non-concentric vertical pipes through disks) on the temperature gradient. Compared with the current single pressure measurement on the steam side and two thermocouples on different levels and depth in the salt, a more systematic scheme of temperature measurement can help capture more useful details during the dynamic operation and calibrate the model to accurately describe the strongly transient process of pumping water through the hot heat pipe. Hardware-wise, the issue with significant pressure swing in the heat pipe needs to be properly addressed. During our own tests, the steam system burst multiple times at the transition from desorption to sorption mode when the heat pipe pressure plummeted from 1500 kPa to lower than 100 kPa. Designs such as pressuring the heat pipe during water circulation should be considered. Although an optimal spacing between the heat pipe plates is identified in this study, a more systematic optimization should be carried out consider more factors such as difficulty and cost of manufacturing.

- System level: A prototype system using the improved system design using LiCl and selected salt can be manufactured and tested to confirm its heating COP of around 1.2 under cold-climate operating conditions. On the other hand, once the thermochemical properties of alternative low-temperature high-capacity working pair are available, the system model should be used to predict the performance and select the best-performing working pair to replace the current LiCl. Furthermore, the integration of the adsorber and the buffer tank warrants conjugated dynamic simulation to determine the optimal sizing and operating control of the combined system.

8. PUBLICATIONS

Some of the progress and findings of this thesis research have been published and presented in peer-reviewed conferences. The published journal papers are also attached in the appendix.

Journal:

Title	Status	Journal	Ref.
Yang, Z., Qu, M., Gluesenkamp, K. (2020). Design screening and analysis of gas-fired ammonia-based chemisorption heat pumps for space heating in cold climate. *Energy, 118213.*	Published	Energy	[28]
Yang, Z., Qu, M., Gluesenkamp, K. (2019). Ammonia-based Chemisorption Heat Pumps for Cold-climate Heating Applications: A Comprehensive Review. *Applied Thermal Engineering, 115674.*	Published	Applied Thermal Engineering	[27]
Blackman, C., Gluesenkamp, K. R., Malhotra, M., & **Yang, Z.** (2019). Study of optimal sizing for residential sorption heat pump system. Applied Thermal Engineering, 150, 421-432.	Published	Applied Thermal Engineering	[162]
Gluesenkamp, K., Frazzica, A., Velte, A., Metcalf, S, **Yang, Z.,** Rouhani, M., Blackman. C., Qu, M., Laurenz, E., Rivero-Pacho, A., Hinmers, S., Critoph, R., Bahrami, M., Füldner, G., Hallin, I. (2020). Experimentally Measured Thermal Masses of Adsorption Heat Exchangers. *Energies*, 13, 1150; doi:10.3390/en13051150	Published	Energies	[161]
Zhu, C., Gluesenkamp, K. R., **Yang, Z.,** & Blackman, C. (2019). Unified thermodynamic model to calculate COP of diverse sorption heat pump cycles: Adsorption, absorption, resorption, and multistep crystalline reactions. International journal of refrigeration, 99, 382-392.	Published	International Journal of Refrigeration	[121]
Qu, M., Liu, X., **Yang, Z.** , Wu, F. , Shi, L. , Liu, X., Zhang, T., Liu, X., Jiang, Y., H. Yin, (2018) Energy-saving Technologies for Building Heating, Ventilation, and Air Conditioning Systems, *Annual Review of Heat Transfer (Technologies for Energy Efficient Buildings),* Begell House, Inc, 147-204.	Published	Annual Review of Heat Transfer	[163]
Performance Optimization of a Chemisorption Adsorber Using Dynamic Modeling of Heat Mass Transfer and Chemical Kinetics	Planned	IJR/ATE (target)	N/A
Simulation of Chemisorption Heat Pump and Its Optimization for High Seasonal Heating Performance	Planned	IJR/ATE/BE (target)	N/A

Conferences:

Status	Conference	Title
Presented	International Conference of Air Conditioning and Refrigeration 2018	Model-Based Performance Comparison of Ammonia Chemisorption Heat Pumps for Cold Climate with Different Working Pairs and Cycle Configurations
Presented	ASHRAE annual conference 2019	Optimization of a Chemisorption Heat Pump with Buffer Tank for Residential Heating Applications
Presented	IMPRES conference 2019	Chemisorption Heat Pump for Cold Climate Heating Applications
Presented	ASHRAE winter conference 2020	Dynamic Modelling and Performance Evaluation of a Chemisorption Heat Pump for Cold Climate
Accepted	IEA Heat Pump Conference 2021	Dynamic Modelling and Design Optimization of a Heat-Pipe-Integrated Chemisorption Adsorber
Accepted	SimBuild Conference 2020	Seasonal Performance of a Chemisorption Heat Pump System

APPENDIX A. OPERATION SCHEMATICS OF SETUP #1 AND #2

The schematics of the active loops during desorption and sorption mode using setup #1 and #2 are illustrated in Figure 84 to Figure 87. The control of the burner, pumps, and valves are similar as the operating procedure of setup #3, with only one sorption module.

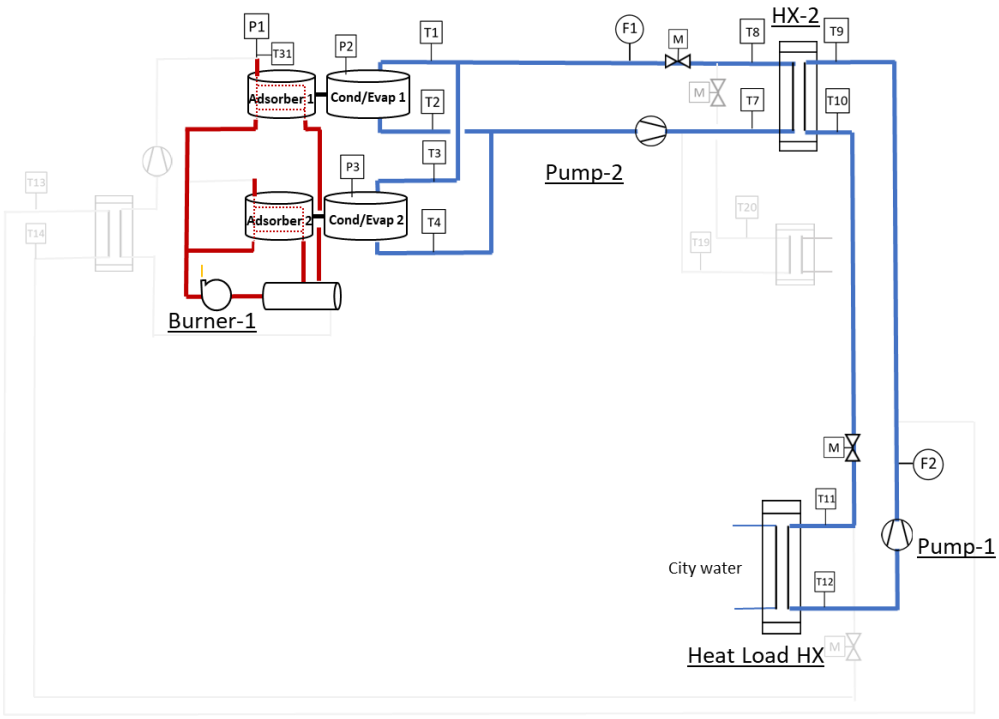

Figure 84 desorption mode of setup #1

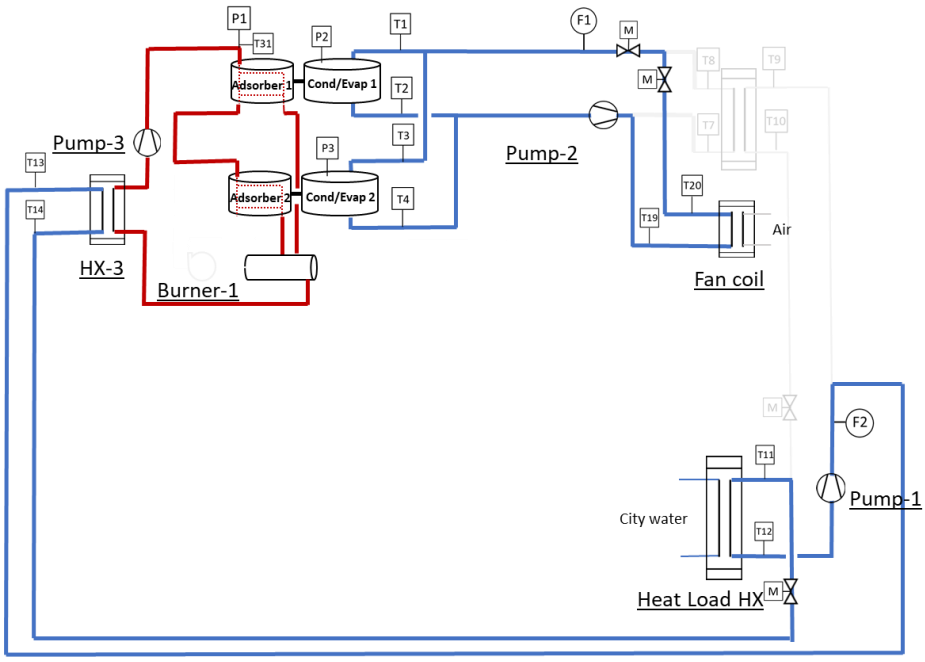

Figure 85 sorption mode of setup #1

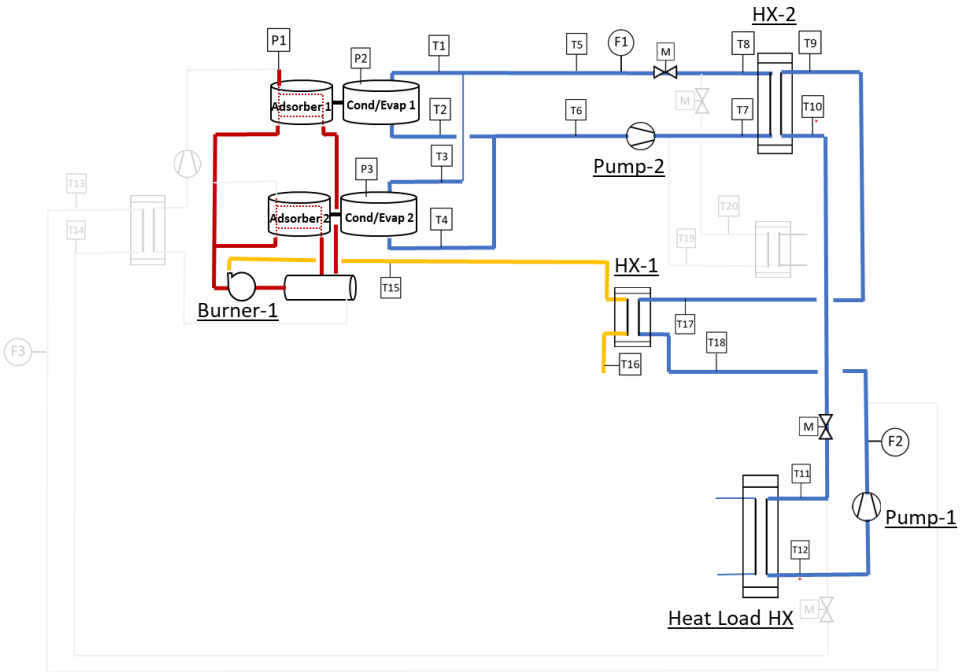

Figure 86 desorption mode of setup #2

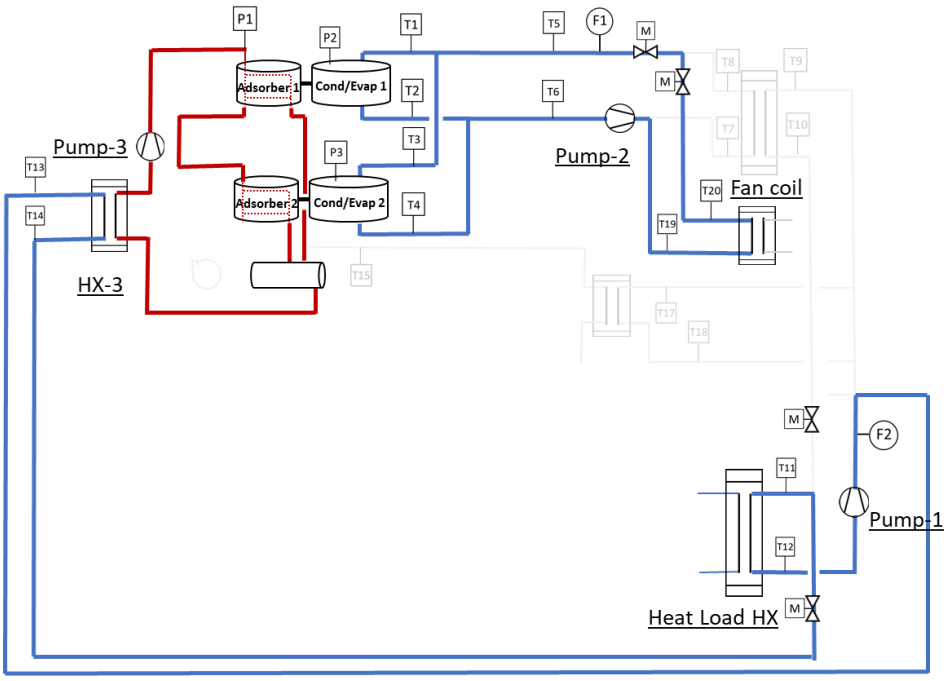

Figure 87 sorption mode of setup #2

APPENDIX B. BURNER COMBUSTION ESTIMATION

- Burner Energy Conversion and Heat Transfer

The gas analyzer and flue gas temperature/heat capacity measurement are used here to determine the burner combustion efficiency and the effectiveness of transferring the combustion heat from the flame to the heat pipe to generate steam.

Combustion of the main component of natural gas (methane, CH_4) with excessive air is expressed below:

$$CH_4 + (1+\lambda)\cdot 2(O_2 + 3.76N_2) \rightarrow CO_2 + 2H_2O + 7.52(1+\lambda)N_2 + 2\lambda O_2 \quad \text{Equation 105}$$

In Eqn. (1) λ is the excess air ratio based on with theoretical amount of air for stoichiometric combustion. In stoichiometric combustion $\lambda = 0$. The theoretical heat generation from combustion is calculated as the difference of the summed enthalpy of formation of all reactants and products.

The measured flue gas content for burner-1 is shown below. The measurement was taken under 20% blower setting and steady combustion, and the excess air ratio measured (95.4%) is used as the representative value for combustion of this burner.

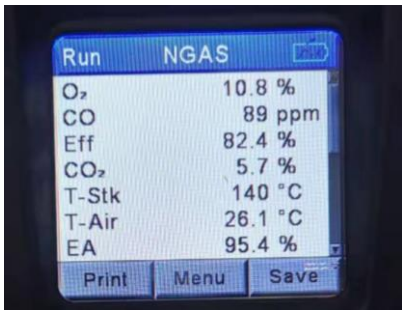

Figure 88 Reading from flue gas analyzer

With the measured λ, the amount of reactant and product can be determined, and the heat generated from combustion can be calculated as the difference of formation enthalpies of the reactant (hf_r^0) and product (hf_p^0) as in Eqn. (2):

$$Q_{combution} = \sum N_p \cdot hf_p^0 - \sum N_r \cdot hf_r^0 \qquad \text{Equation 106}$$

The number of mole and enthalpy of all participants in the reaction per mole of methane are listed below:

Table 36 formation enthalpy of combustion reactants and products

	Substance	**Mole**	$\boldsymbol{hf^0}$ **[kJ/kmol]**
Reactants	Methane (CH4)	1	-74850
	Oxygen (O2)	3.908	0
	Nitrogen (N2)	14.69	0
Products	Carbon dioxide (CO2)	1	-393520
	Water vapor (H2O (g))	2	-241820
	Nitrogen (N2)	14.69	0
	Oxygen (O2)	1.908	0

$$Q_{combustion} = \left[1[kmol] \times (-393520)[\frac{kJ}{kmol}] + 2[kmol] \times (-241820)[\frac{kJ}{kmol}] + 14.69[kmol] \times 0[\frac{kJ}{kmol}] + 1.908[kmol] \times 0[\frac{kJ}{kmol}]\right]$$
$$- \left[1[kmol] \times (-74850)\left[\frac{kJ}{kmol}\right] + 3.908[kmol] \times 0\left[\frac{kJ}{kmol}\right] + 14.69[kmol] \times 0\left[\frac{kJ}{kmol}\right]\right]$$
$$= 802310\left[\frac{kJ}{kmol\ CH_4}\right] \sim 50144\left[\frac{kJ}{kg\ CH_4}\right]$$

Since the formation enthalpy of water vapor is used, above calculation assumes water in vapor phase. Assume all contents start and end at 25 °C [1], the combustion heat is the low heating value (LHV) of methane.

The adiabatic flame temperature (T_{AF}) of the combustion assumes the products (flue gas) are generated at the same temperature of the reactants, and all the combustion heat is used to increase the flue gas temperature. T_{AF} is calculated for natural gas combustion in this burner assuming no work or heat transfer from the flue gas to the surroundings. The heat capacity of the flue gas is the weighted average value of all its components between 300 K and 2300 K, the heat capacity of each component at the two temperatures can be found in the appendix. The reactant temperature is set at 25°C.

Table 37 Mass and specific heat of flue gas components

Gas	**Mass per kg CH4 [kg]**	**Cp [kJ/kg-K]**
O2	3.816	1.0594
N2	31.225	0.9634
CO2	2.750	1.1169
H2O	2.250	2.4492

[1] Standard enthalpy of formation corresponds to 1bar, no temperature requirement

The effective heat capacity of the flue gas is 1.067 kJ/kg-K, and the flue gas mass per kg CH_4 is 40.04 kg. The adiabatic flame temperature is:

$$T_{AF} = T_{ref} + \frac{Q_{cv}}{Cp \cdot m_{flue}} = 25[^0C + \frac{50144\left[\frac{kJ}{kg\ CH_4}\right]}{40.04\left[\frac{kg}{kg\ CH_4}\right] \times 1.0666\left[\frac{kJ}{kg\ ^0C}\right]} = 1174[^0C]$$

- Heat Flow into the Adsorber

In reality, the combustion heat is split between the steam generation and the exhaust flue gas, and therefore the flue gas temperature leaving at the burner exit is much lower than the adiabatic flame temperature, and such difference can be used to estimate the heat consumed by the steam generation.

The flue gas temperature leaving the burner was around 315 ºC when the combustion is stable as shown below. The average natural gas flow rate during the same period was around 0.56 cfm. With typical natural gas density of 0.8 kg/m^3, the mass flow rate was 0.0002643 kg/s. With LHV the total chemical energy input via the natural gas is 13.2 kW.

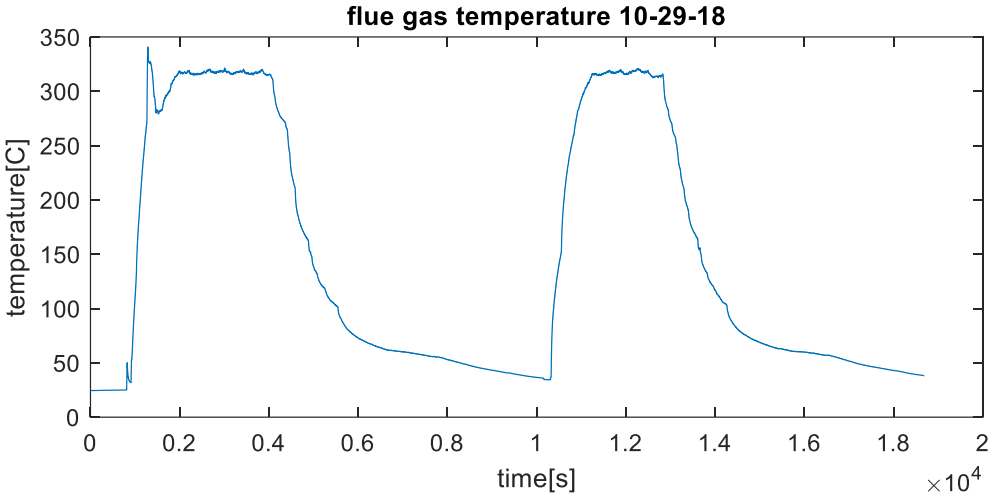

Based on the difference between adiabatic flame temperature and the exhaust flue gas temperature, assuming no heat loss in the burner and the flue duct (insulation was installed before the test), the heat to the adsorber is expressed in Eqn. (3):

$$Q_{ads} = Q_{heat} - Q_{exh} = \dot{m}_{flue} \cdot \left(T_{AF} \cdot Cp_{AF} - T_{flue} \cdot Cp_{flue}\right) \quad \text{Equation 107}$$

Plugging in the flow rates and temperatures:

$$Q_{ads} = 40.04\left[\frac{kg}{kg\ CH_4}\right] \times 0.0002643\left[\frac{kg\ CH_4}{s}\right] \times (1056 - 315)[^0C \times 1.0666\left[\frac{kJ}{kg \cdot ^0 C}\right]$$
$$= 8.36\ [kW]$$

During the steady operation, 8.36 kW, or 63% of the total chemical energy put into the burner is used to generate steam in the heat pipe.

The proportion of the combustion heat going into the heat pipe and eventually reaching the adsorber was verified by manufacture test as well. The tests resulted in the efficiency of 65-67%.

- Correlating Natural Gas Flow Rate with Burner Blower Setting

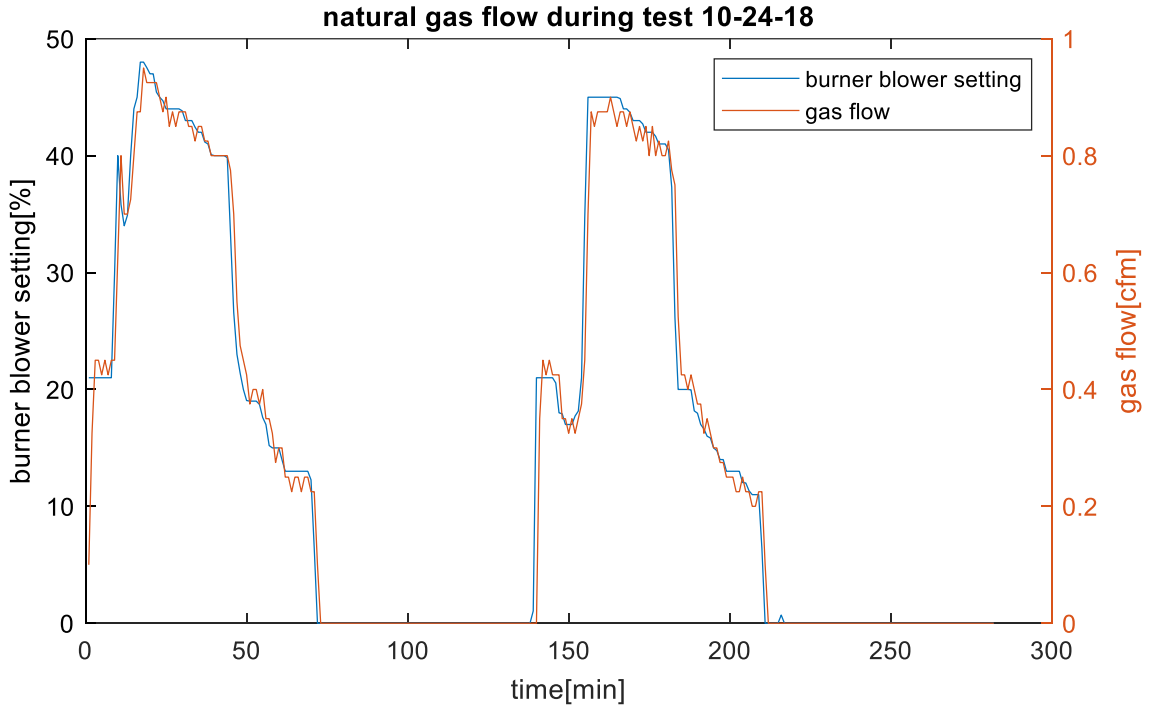

The correlation between the blower setting and the gas flow is for each percent of blower setting the corresponding natural gas flow rate is 0.02 cfm. With the steady ratio, the natural gas flow information of tests prior of 10/24/18 can be inferred from the blower setting – and their gas heat input be estimated with good accuracy. This correlation between the natural gas flow rate and the blower setting is verified with data from 9/21 and 10/29 tests as well.

For burner #2 serving sorption module #3 and #4, the natural gas flow rate is also correlated to the burner blower setting using the test data of 6/26/2019 as shown in the figure below. For each

percent of blower setting, the corresponding natural gas flow rate is 0.025 cfm when the setting is above 11%, and 0.04 cfm when the setting is below 11%.

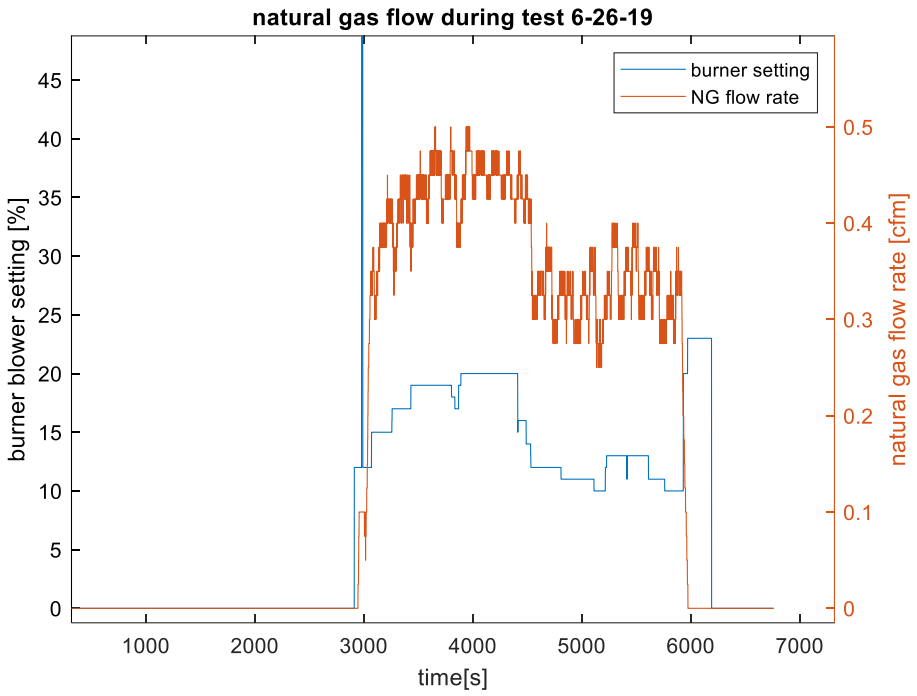

APPENDIX C. MATLAB SOURCE CODE OF SYSTEM AND ADSORBER DYNAMIC MODEL

The MATLAB code for system dynamic model is consisted of one main file and several supporting files containing subroutines for a specific function used in the main file.

```
% system_constInput.m
% author: Zhiyao Yang
% last modified: 7/20/20

tic
clear
%% global parameters
global K_MT K_HT phi rho_matrix zElement rElement dz dr
r_cv;
global dt R;

close all

n_module = 1;

%% simulation control
dt = 1;
timeTot = 28000;%60*75; %s, total time simulated after
initial condition
i_end = round(timeTot/dt);%total number of operation time

cycleCount = 3;
startTime = 1;
opTime = startTime:startTime+timeTot-1;

%% operating conditions
T_amb = 8.3;%C
Qburn = 3;%kW, constant gas input
T_HW_i = 43.3;%C, hot water return temperature
T_HW_o_set = 48.9;%C, threshold hot water supply
m_HW = 0.06;%kg/s, hot water flow rate
T_EW_i = T_amb - 10;%C, fan coil water return temperature
m_EW = 0.07;%kg/s, EG flow rate
k_insulation = 0.27;%W/m2.K, 3-inch R11: 0.52. 5-inch R21:
0.27
rat = 0.2; %with insulation

%% system dimensions

% constants and fixed properties of materials
sigma_rad = 5.67e-8;%W/m2.K4, S-B constant
R = 8.314;                %gas constant
g = 9.81;
epsilon_SS = 0.85;%emissivity of stainless steel
```

```
Cp_matrix_min = 1.5;%kJ/kg-K, minimum specific heat, from
pure salt+matrix
hfg_NH3=1350;
Cp_SS = 0.46;%kJ/kg-K
Cp_water = 4.18;
% CP_HTF = Cp_water;
Cp_HTF = 3.63;% 40% ethylene glycol
Cp_NH3_l = 4.2;%kJ/kg.K, ammonia liquid
Cp_NH3_g = 2.8;%kJ/kg.K, ammonia gas
rho_SS = 800;%kg/m3
k_SS = 16.3e-3; %kW/m.K, stainless steel 304 (Perry's
handbook)

% vessel sizes
m_HX = 8;%kg
m_shell = 24;%kg
M_mat = 1.2;%kg, total matrix mass
M_salt_tot = 2.2;%kg, total salt mass, more than 1:3 to NH3
M_NH3_tot = 2.1;%kg, total ammonia mass
m_water = 4;%kg, reservoir tank water serving one adsorber

H_shell = 0.8;%m, height of the adsorber shell
A_shell = 0.5;%m2, surface area of the adsorber shell
D_tank = 0.114;%m, diameter of tank
L_tank = 0.724;%m, length
A_tank = 3.14*D_tank*L_tank;%m2, surface area of tank
m_tank = 3.14/4*(D_tank^2-(D_tank-0.008)^2)*L_tank*rho_SS;
H_burner = 0.2;%m, height of the adsorber shell
A_burner = 0.19;%m2, surface area of the adsorber shell
D_HP = 0.03;%m, diameter of heat pipe
L_HP = 0.75;%m, length
A_HP = 3.14*D_HP*L_HP;%m2
x_HP = 1e-3; %m, thickness of the heat pipe wall
D_chamber = 0.2;%m, diameter of adsorber and condenser
shell
V_equip = .8*.03^2*3.14/4*2+56*(.15^2-.015^2)*.003*3.14/4;
V_chamber = (H_shell*D_chamber^2*3.14/4-V_equip)*2;%m3

% salt disk dimension
n_plate = n_module*56;%-, number of salt plates
r_plate_i = 0.015/2;%m, inner radius of plate (hollow)
r_plate_o = 0.15/2;%m, outer radius of plate
z_plate = 0.01;%m, thickness of plate
```

```
A_plate = 3.14 * (r_plate_o^2 - r_plate_i^2);%m2, area of
plate
V_plate = z_plate * A_plate;%m3, volume of a plate

% property of the salt matrix
K_HT = 1e-3; %kW/m-K, thermal conductivity
K_MT = 1e-13;%m2, permeability, later should be fitted to
X_tot
phi = 0.7;%-, porosity, later should be fiited to X_tot
rho_matrix = (M_salt_tot + M_mat)/n_plate/V_plate;

% fixed heat transfer coefficients
U_wall = k_SS/x_HP; %kW/m2.K, heat pipe disk conduction U
value
UA_HP_shell = 0.006;%kW/K
UA_HP_water = 0.01;
UA_HP_out = 0.05;%kW/K
UA_HTF_CE_shell = 0.1;
UA_HTF_CE_HX = 0.3;
hA_NH3_HX_cond=10;%kW/K, condensation/evaporation HT coeff.
at CEHX
hA_NH3_shell_cond=0.5;%kW/K, condensation/evaporation HT
coeff. at CE shell
hA_NH3_HX_evap=0.1;%kW/K, condensation/evaporation HT
coeff. at CEHX
hA_NH3_shell_evap=0.05;%kW/K, condensation/evaporation HT
coeff. at CE shell

%chemical reaction enthalpy
delta_H32 = 44780/1000;     %kJ/mol
delta_H21 = 48128/1000;
delta_H10 = 51894/1000;
delta_S32 = 257.6;

%% salt disk simulation control
zElement = 30;%number of differential c.v. in z direction
rElement = 10;%number of differential c.v. in r direction
dz = z_plate / zElement;%m, height of a diff. c.v.
dr = (r_plate_o-r_plate_i)/rElement;%m, depth of a diff.
c.v.
r_cv = r_plate_i+(0.5+(0:rElement-1))*dr;%m, middle line
radius of c.v.
V_cv_r = dr*r_cv*dz*2*3.14;%m3, c.v. volume
```

```
%% initial condition
T_salt_0 = T_amb + 273;

%mol, initial mole number of salt in each state
P_init = 3.5e5;%Pa
Nnh3_tot = M_NH3_tot/17*1000;
Ns_tot = Nnh3_tot / 3;
Ns0=[Ns_tot/n_plate,0,0,0];
n_NH3_local_0 = P_init*phi/R/T_salt_0;
%mol/m3, initial ammonia vapor mole density w.r.t total
c.v. volume


%% allocate matrix/vector for
% the parameters are stored in matrix formatting as:
% row - runs
% column - [ [dr of 1st (top) plane] [dr of 2nd plane] ...
[dr of bottom
% plane]

% key parameters
T_salt = zeros(i_end,zElement*rElement);
Q_HP_salt_top = zeros(i_end,rElement);
Q_HP_salt_bot = zeros(i_end,rElement);
Ns_3 = zeros(i_end,zElement*rElement);%mol/m3, vol. mol.
density of LiCl-3NH3
Ns_2 = zeros(i_end,zElement*rElement);%mol/m3, vol. mol.
density of LiCl-2NH3
Ns_1 = zeros(i_end,zElement*rElement);%mol/m3, vol. mol.
density of LiCl-1NH3
Ns_0 = zeros(i_end,zElement*rElement);%mol/m3, vol. mol.
density of pure LiCl
n_NH3_local = zeros(i_end,zElement*rElement);%mol/m3, vol.
mol. density of NH3 w.r.t total c.v. volume
dN_NH3_out = zeros(i_end,zElement*2);%mol, ammonia vapor
crossing the inner/outer primeter\
T_CE_HX = zeros(i_end,1);
T_CE_shell = zeros(i_end,1);
m_NH3_CE_HX = zeros(i_end,1);
m_NH3_CE_shell = zeros(i_end,1);
T_HTF_CE_i = zeros(i_end,1);
T_HTF_CE_o = zeros(i_end,1);
T_HTF_HP_o = ones(i_end,1)*T_HW_i;
```

```
P_NH3_CE_HX = zeros(i_end,1);
P_NH3_CE_shell = zeros(i_end,1);

% monitored parameters
U_ceil_cond = zeros(i_end,1);
U_floor_cond = zeros(i_end,1);
U_ceil = zeros(i_end,1);
U_floor = zeros(i_end,1);
P_local = zeros(i_end,zElement*rElement);
dN_g_32 = zeros(i_end,zElement*rElement);
dN_g_21 = zeros(i_end,zElement*rElement);
dN_g_10 = zeros(i_end,zElement*rElement);
Q_chem = zeros(i_end,zElement*rElement);
dN_NH3_chem = zeros(i_end,zElement*rElement);
dtsalt = zeros(i_end,zElement*rElement);
nsum = zeros(i_end,3);%used to store total ammonia changes
T_shell = zeros(i_end,1);
Q_HP_shell = zeros(i_end,1);
Q_shell_loss = zeros(i_end,1);
T_water = zeros(i_end,1);
Q_tank_loss = zeros(i_end,1);
Q_HP_water = zeros(i_end,1);
Q_HP_loss = zeros(i_end,1);
Q_burner_loss = zeros(i_end,1);
Q_hp_net = zeros(i_end,1);
Q_HP_salt = zeros(i_end,1);
T_steam = zeros(i_end,1);
Q_HTF_CE_shell = zeros(i_end,1);
Q_HTF_CE_HX = zeros(i_end,1);
P_chamber = zeros(i_end,1);
Q_HP_out = zeros(i_end,1);
Q_CondEvap_CE_HX = zeros(i_end,1);
Q_CondEvap_CE_shell = zeros(i_end,1);
n_NH3_chamber = zeros(i_end,1);
T_NH3_vap = zeros(i_end,1);
dm_NH3_CE_HX = zeros(i_end,1);
dm_NH3_CE_shell = zeros(i_end,1);
m_HTF_CE = zeros(i_end,1);
Qgen = zeros(i_end,1);


% initial values
T_salt(1,:) = T_amb+273;
T_steam(1) = max([T_amb,1]);
```

```
T_water(1) = max([T_amb,1]);
T_HTF_CE_o(1) = T_HW_i;
T_CE_HX(1) = T_amb;
T_CE_shell(1) = T_amb;
T_NH3_vap(1) = T_amb;
T_shell(1) = T_amb;

P_chamber(1) = P_init;
P_local(1,:) = P_init;
P_NH3_CE_HX(1) = Psat_NH3_Tk(T_amb+273);
P_NH3_CE_shell(1) = Psat_NH3_Tk(T_amb+273);
n_NH3_local(1,:) = ones(1,zElement*rElement)*n_NH3_local_0;
n_NH3_chamber(1) =
P_chamber(1)*V_chamber/R/(T_NH3_vap(1)+273);


% assign amount of salt to each volume
% use reshape(A',[],1) to convert matrix into 1d array
V_cv_mat = ones(zElement,1)*V_cv_r;
V_cv_vec = reshape(V_cv_mat',1,[]);
Ns_3(1,:) = Ns0(1)/V_plate*V_cv_vec;
Ns_2(1,:) = Ns0(2)/V_plate*V_cv_vec;
Ns_1(1,:) = Ns0(3)/V_plate*V_cv_vec;
Ns_0(1,:) = Ns0(4)/V_plate*V_cv_vec;
m_mat_vec = M_mat/n_plate/V_plate*V_cv_vec;%kg, matrix mass
in each c.v.

mode_des = true;
mode_des_pumpon = false;
mode_sorp_pumpon = false;
%% solution
tic
hwait = waitbar(0,'calculating');
set(findobj(hwait,'type','patch'),'edgecolor','k','facecolo
r','b');
i=1;
i_cycle = 1;
while(i_cycle<cycleCount+1&&i<i_end)

    % ================== chamber ammonia pressure
========================
    P_chamber(i) =
n_NH3_chamber(i)*R*(T_NH3_vap(i)+273)/V_chamber;
```

```
    % ========================== end of chamber pressure
==================


    % ======================== salt model
================================
    % ======================== heat pipe HT coefficient
====================
    if(~mode_des)
        %sorption mode: heat pipe filled with water

        U_fconv = 3;%kW/m2.K, forced convection between
liquid and metal plate
        U_ceil(i) = 1/(1/U_wall+1/U_fconv);
        U_floor(i) = 1/(1/U_wall+1/U_fconv);

    else
        ttsteam = T_steam(i);
        delta_T_steam_HP = 2;%tsteam+273-T_salt(i,1);

        % get properties
        % property of the steam-heat pipe (implement
property subroutines)
        hfg_water = steamlookup(ttsteam,'hfg');%kJ/kg.K,
steam vaporization heat
        rho_v = 1/steamlookup(ttsteam,'vg');%saturated
steam density
        rho_l = 1/steamlookup(ttsteam,'vl');%water density
        cp_l = steamlookup(ttsteam,'cpl');%specific heat
        k_l = steamlookup(ttsteam,'kl');%thermal
conductivity
        mu_l = steamlookup(ttsteam,'mul');%dynamic
viscosity
        nu_l = steamlookup(ttsteam,'nul');%kinematic
viscosity
        sigma_l = steamlookup(ttsteam,'sigmal');%surface
tension
        % bottom (ceiling): Gerstmann and Griffith
        Ra=(g*rho_l*(rho_l-
rho_v)*hfg_water)/(mu_l*delta_T_steam_HP*k_l)...
        *(sigma_l/g/(rho_l-rho_v))^(3/2);
        Nu_ceil=0.81*Ra^0.193;
        h_ceil=Nu_ceil*k_l/(sigma_l/g/(rho_l-rho_v))^.5;
        U_ceil_cond(i) = h_ceil/1000;
```

```
        % top (floor): Bejan
        Nu_floor =
1.368*((2*r_plate_o)^3*(hfg_water+3/8*cp_l*delta_T_steam_HP
)...
            *g*(rho_l-
rho_v)/k_l/nu_l*delta_T_steam_HP)^(1/5);
        h_floor = Nu_floor*k_l/(2*r_plate_o);
        U_floor_cond(i) = h_floor/1000;

        U_ceil(i) = 1/(1/U_wall+1/U_ceil_cond(i));
        U_floor(i) = 1/(1/U_wall+1/U_floor_cond(i));

    end
    T_HP_c = T_steam(i);
    T_HP_k = T_HP_c + 273;

    % ===== salt model: chemical reaction and heat-mass
transfer ==========
    % Chemical kinetic calculate ammonia generation
    [dN_g_32(i+1,:),dN_g_21(i+1,:),dN_g_10(i+1,:)] =
calcChem(i,...
        T_salt(i,:), P_local(i,:), Ns_3(i,:), Ns_2(i,:),
Ns_1(i,:), Ns_0(i,:));
    Ns_3(i+1,:) = Ns_3(i,:) - dN_g_32(i+1,:);
    Ns_2(i+1,:) = Ns_2(i,:) + dN_g_32(i+1,:) -
dN_g_21(i+1,:);
    Ns_1(i+1,:) = Ns_1(i,:) + dN_g_21(i+1,:) -
dN_g_10(i+1,:);
    Ns_0(i+1,:) = Ns_0(i,:) + dN_g_10(i+1,:);
    dN_NH3_chem(i+1,:) = dN_g_32(i+1,:) + dN_g_21(i+1,:) +
dN_g_10(i+1,:);
    Q_chem(i+1,:) = - (dN_g_32(i+1,:) * delta_H32 +
dN_g_21(i+1,:) ...
        * delta_H21 + dN_g_10(i+1,:) * delta_H10);

    % Mass transfer calculate local volumetric vapor
ammonia mole density

[n_NH3_local(i+1,:),P_local(i+1,:),dN_NH3_out(i+1,:),nsum(i
+1,:)]...
        = calcMbal(i+1, T_salt(i,:),n_NH3_local(i,:),...

P_chamber(i),P_local(i,:),dN_NH3_chem(i,:),V_cv_vec);
```

```
    % Heat transfer calculate salt temperature and heat
transfer with HP

[T_salt(i+1,:),dtsalt(i+1,:),Q_HP_salt_top(i+1,:),Q_HP_salt
_bot(i+1,:)] =...
        calcEbal_v2_wholeDisk(i, Q_chem(i,:), T_salt(i,:),
T_HP_k,...
        U_ceil(i), U_floor(i), Ns_3(i,:), Ns_2(i,:),
Ns_1(i,:), Ns_0(i,:),V_cv_vec,m_mat_vec);


Q_HP_salt(i)=n_plate*(sum(Q_HP_salt_bot(i,:))+sum(Q_HP_salt
_top(i,:)));
    % ==================== end of salt model
==============================



    % ========= heat pipe system: calculate steam/water
temperature =======
    if(mode_des)
        % heat pipe filled with steam
        % Actively heated by burner, search for Tsteam to
balance net
        % heat of Qgen and Qsalt with thermal masses and
heat losses

        if(T_steam(i)>205)
            Qgen(i)=0;
        else
            Qgen(i)=Qburn;
        end
        Q_hp_net(i) = Qgen(i)-Q_HP_salt(i);
        tsat0 = T_steam(i);
        fun = @(x)Q_hp_net(i)-
calcQwater(x,T_water(i),UA_HP_water)...
            -calcQshell(x,T_shell(i),UA_HP_shell)-
calcQhploss(x,T_amb,rat)...
            -calcQburnerloss(x,T_amb,rat)-
calcQsteam(x,tsat0)-calcQhx(x,tsat0);
        options = optimset('Display','off');
        res=fsolve(fun,tsat0,options);
        T_steam(i+1) = res;
```

```
        Q_HP_loss(i) = calcQhploss(T_HP_c,T_amb,rat);
        Q_burner_loss(i) =
calcQburnerloss(T_HP_c,T_amb,rat);

        % calculate shell
        % heat transfer with heat pipe
        Q_HP_shell(i) = (T_HP_c-T_shell(i))*UA_HP_shell;
        % heat loss to air

Q_shell_loss(i)=calcQshellloss(T_shell(i),T_amb,rat);
        % energy balance
        T_shell(i+1)=T_shell(i)+(Q_HP_shell(i)-
Q_shell_loss(i))/Cp_SS/m_shell;

        % calculate water and tank (assuming same, uniform
temperature)
        % heat transfer with steam
        Q_HP_water(i) = (T_HP_c-T_water(i))*UA_HP_water;
        % heat loss through tank to air
        Q_tank_loss(i) =
calcQtankloss(T_water(i),T_amb,rat);
        % energy balance
        T_water(i+1) = T_water(i)+(Q_HP_water(i)-
Q_tank_loss(i))...
            /(m_water*Cp_water+m_tank*Cp_SS);
    else
        % heat pipe filled with water (actively circulated,
deemed as
        % uniform temperature lumped body for
simplification) search for
        % Twater to balance net heat of Qout and Qsalt

        DT_HPHX_avg=T_water(i)-(T_HW_i+T_HTF_HP_o(i))/2;
        Q_HP_out(i) = DT_HPHX_avg*UA_HP_out;
        Q_hp_net(i) = -Q_HP_salt(i)-Q_HP_out(i);
        T_HTF_HP_o(i+1) =
T_HW_i+Q_HP_out(i)/(Cp_water*m_HW);

        twater0 = T_water(i);
        fun = @(x)Q_hp_net(i)-
calcQshell(x,T_shell(i),UA_HP_shell)...
            -calcQhploss(x,T_amb,rat)-
calcQtankloss(x,T_amb,rat)...
```

```
            -m_water*(steamlookup(x,'hl')-
steamlookup(twater0,'hl'))...
            -calcEHX(x,twater0);
        options = optimset('Display','off');
        res=fsolve(fun,twater0,options);
        T_water(i+1) = res;

        Q_HP_loss(i) = calcQhploss(T_HP_c,T_amb,rat);
        Q_burner_loss(i) = 0;

        % calculate shell
        % heat transfer with heat pipe
        Q_HP_shell(i) = (T_HP_c-T_shell(i))*UA_HP_shell;
        % heat loss to air

Q_shell_loss(i)=calcQshellloss(T_shell(i),T_amb,rat);
        % energy balance
        T_shell(i+1)=T_shell(i)+(Q_HP_shell(i)-
Q_shell_loss(i))/Cp_SS/m_shell;

        % calculate water and tank (assuming same, uniform
temperature)
        % heat transfer with steam
        Q_HP_water(i) = 0;
        % heat loss through tank to air
        Q_tank_loss(i) =
calcQtankloss(T_water(i),T_amb,rat);

        T_steam(i+1) = (T_water(i)+2*(T_salt(i,1)-273))/3;
    end

    % ====================== end of heat pipe model
=======================



    % ========== condenser/evaporator: calculate NH3
pressure =============
    % phase change and heat flow in ammonia side

    tsat_vap = ammonialookup(P_chamber(i),'t');

    if(P_chamber(i)>P_NH3_CE_HX(i))
        % condensing on HX
```

```
        Q_CondEvap_CE_HX(i) = (tsat_vap-
T_CE_HX(i))*hA_NH3_HX_cond;
        dm_NH3_CE_HX(i)=Q_CondEvap_CE_HX(i)/hfg_NH3;
        m_NH3_CE_HX(i+1) = m_NH3_CE_HX(i)+dm_NH3_CE_HX(i);

    elseif(P_chamber(i)<P_NH3_CE_HX(i)&&m_NH3_CE_HX(i)>0)
        % evaporate on HX

        Q_CondEvap_CE_HX(i) = (tsat_vap-
T_CE_HX(i))*hA_NH3_HX_evap;
        dm_NH3_CE_HX(i)=Q_CondEvap_CE_HX(i)/hfg_NH3;

        % in case liquid NH3 is exhausted in the current
run

m_NH3_CE_HX(i+1)=max([0,m_NH3_CE_HX(i)+dm_NH3_CE_HX(i)]);
        dm_NH3_CE_HX(i) = m_NH3_CE_HX(i+1)-m_NH3_CE_HX(i);
        Q_CondEvap_CE_HX(i) = dm_NH3_CE_HX(i)*hfg_NH3;

    else
        % dry HX with low P_chamber: no HX
        m_NH3_CE_HX(i+1)=0;
        Q_CondEvap_CE_HX(i)=0;
        dm_NH3_CE_HX(i) = 0;
    end

    if(P_chamber(i)>P_NH3_CE_shell(i))
        % condensing on shell

        Q_CondEvap_CE_shell(i) = (tsat_vap-
T_CE_shell(i))*hA_NH3_shell_cond;
        dm_NH3_CE_shell(i)=Q_CondEvap_CE_shell(i)/hfg_NH3;
        m_NH3_CE_shell(i+1) =
m_NH3_CE_shell(i)+dm_NH3_CE_shell(i);


elseif(P_chamber(i)<P_NH3_CE_shell(i)||m_NH3_CE_shell(i)>0)
        % condensing on shell
        Q_CondEvap_CE_shell(i) = (tsat_vap-
T_CE_shell(i))*hA_NH3_shell_evap;
        dm_NH3_CE_shell(i)=Q_CondEvap_CE_shell(i)/hfg_NH3;
```

```
        % in case liquid NH3 is exhausted in the current
run

m_NH3_CE_shell(i+1)=max([0,m_NH3_CE_shell(i)+dm_NH3_CE_shel
l(i)]);
        dm_NH3_CE_shell(i) = m_NH3_CE_shell(i+1)-
m_NH3_CE_shell(i);
        Q_CondEvap_CE_shell(i) =
dm_NH3_CE_shell(i)*hfg_NH3;

    else
        % dry shell with low P_chamber: no HX
        m_NH3_CE_shell(i+1)=0;
        Q_CondEvap_CE_shell(i)=0;
        dm_NH3_CE_shell(i) = 0;
    end

    % mode control:
    % mode_des + T_CE_HX > T_HW_o_set: pump on, using
T_HW_i, m_HW
    % ~mode_des + T_CE_HX < T_EW_i: pump on, using T_EW_i,
m_EW
    % else: pump off
    if(T_CE_HX(i)>T_HW_o_set+2&&mode_des)
        mode_des_pumpon = true;
    end
    if(T_CE_HX(i)<T_EW_i-2&&~mode_des)
        mode_sorp_pumpon = true;
    end
    if(mode_des_pumpon||mode_sorp_pumpon)
        if(mode_des_pumpon)
            T_HTF_CE_i(i) = T_HW_i;
            m_HTF_CE(i) = m_HW;
            diff=0.1;
        else
            T_HTF_CE_i(i) = T_EW_i;
            m_HTF_CE(i) = m_EW;
            diff=-0.1;
        end

        tfo0 = T_HTF_CE_i(i)+diff;
        fun = @(x)UA_HTF_CE_HX*(T_CE_HX(i)-
(T_HTF_CE_i(i)+x)/2)...
```

```
            +UA_HTF_CE_shell*(T_CE_shell(i)-
(T_HTF_CE_i(i)+x)/2)...
            -Cp_HTF*m_HTF_CE(i)*(x-T_HTF_CE_i(i));
        options = optimset('Display','off');
        res=fsolve(fun,tfo0,options);
        T_HTF_CE_o(i+1) = res;

        DT_CEHX_avg = T_CE_HX(i)-
(T_HTF_CE_i(i)+T_HTF_CE_o(i))/2;
        Q_HTF_CE_HX(i) = UA_HTF_CE_HX*DT_CEHX_avg;
        DT_CEshell_avg = T_CE_shell(i)-
(T_HTF_CE_i(i)+T_HTF_CE_o(i))/2;
        Q_HTF_CE_shell(i) = UA_HTF_CE_shell*DT_CEshell_avg;

        TM_CE_water = 0;
    else
        % no HTF flow in the CE
        m_HTF_CE(i) = 0;
        T_HTF_CE_o(i+1)=T_HTF_CE_o(i);
        Q_HTF_CE_HX(i) = 0;
        Q_HTF_CE_shell(i) = 0;

        TM_CE_water = 0.0021*Cp_water*1000;%retained water
thermal mass

    end
    % CE shell and liq ammonia temperature
    T_CE_shell(i+1) = T_CE_shell(i) +
(Q_CondEvap_CE_shell(i)-Q_HTF_CE_shell(i)...
        -calcQshellloss(T_CE_shell(i),T_amb,rat))...

/(m_shell*Cp_SS+m_NH3_CE_shell(i)*calcCpNH3(T_CE_shell(i)))
;

    % CE HX and liq ammonia temperature
    T_CE_HX(i+1) = T_CE_HX(i) + (Q_CondEvap_CE_HX(i)-
Q_HTF_CE_HX(i))...

/(m_HX*Cp_SS+m_NH3_CE_HX(i)*calcCpNH3(T_CE_HX(i))+TM_CE_wat
er);
    % update corresponding saturation pressure
    P_NH3_CE_HX(i+1) = Psat_NH3_Tk(T_CE_HX(i+1)+273);%Pa
    P_NH3_CE_shell(i+1) =
Psat_NH3_Tk(T_CE_shell(i+1)+273);%Pa
```

```
    % ====================== end of condenser-evaporator
model ============

    % ====================== vapor in empty volume
========================

    % update mole of vapor
    dn_adsorber = sum(dN_NH3_out(i,:))*n_plate;
    dn_condenser =
(dm_NH3_CE_HX(i)+dm_NH3_CE_shell(i))*1000/17;
    n_NH3_chamber(i+1) = n_NH3_chamber(i)+ dn_adsorber -
dn_condenser;

    % update temperature of vapor
    qnh3_inflow=0;
    Ts_avg=mean(T_salt(i,rElement-
1:rElement:rElement*zElement-1)-273);
    if(dn_adsorber>0)

qnh3_inflow=qnh3_inflow+dn_adsorber*Cp_NH3_g*Ts_avg;
    else

qnh3_inflow=qnh3_inflow+dn_adsorber*Cp_NH3_g*T_NH3_vap(i);
    end
    if(dm_NH3_CE_HX(i)>0)
        qnh3_inflow=qnh3_inflow-
dm_NH3_CE_HX(i)*1000/17*Cp_NH3_g*T_NH3_vap(i);
    else
        qnh3_inflow=qnh3_inflow-
dm_NH3_CE_HX(i)*1000/17*Cp_NH3_g*T_CE_HX(i);
    end
    if(dm_NH3_CE_shell(i)>0)
        qnh3_inflow=qnh3_inflow-
dm_NH3_CE_shell(i)*1000/17*Cp_NH3_g*T_NH3_vap(i);
    else
        qnh3_inflow=qnh3_inflow-
dm_NH3_CE_shell(i)*1000/17*Cp_NH3_g*T_CE_shell(i);
    end

T_NH3_vap(i+1)=(T_NH3_vap(i)*n_NH3_chamber(i)*Cp_NH3_g+qnh3
_inflow)...
        /(n_NH3_chamber(i+1)*Cp_NH3_g);
```

```
    % ====================== end of vapor in empty volume
=================


if(i>20&&mode_des_pumpon&&m_NH3_CE_HX(i)>0.8&&Q_HTF_CE_HX(i
)<0.1)
        i
        db='switch to sorption mode'
        mode_des_pumpon = false;
        mode_des = false;

elseif(i>20&&mode_sorp_pumpon&&m_NH3_CE_HX(i)<0.1&&Q_HP_out
(i)<0.2)
        i
        db='switch to desorption mode'
        mode_sorp_pumpon = false;
        mode_des = true;
        i_cycle = i_cycle + 1;
    end

    rg=1:i;
    % update iteration parameters
    i=i+1;
    waitbar(i/i_end,hwait,[num2str(i),'/',num2str(i_end)]);
end
close(hwait)
toc
%% plot results

Q_loss_tot=(Q_HP_loss+Q_tank_loss+Q_shell_loss+Q_burner_los
s);


++++++++++++++++++++++++++++++++++++++++++++++++++++++++++++++++++++++++++++++++

++++++++++++++++++++++++++++++++++++++++++++++++++++++++++++++++++++++++++++++++

++++++++++++++++++++++++++++++++++++++++++++++++++++++++++++++++++++++++++++++++

% calcChem.m
% author: Zhiyao Yang
% last modified: 5/10/20

function [dN32, dN21, dN10] = calcChem(i, T_salt, P_local,
N3, N2, N1, N0)
```

```
    %constants
    global zElement rElement;
    R = 8.314;
    dt = 1;
    delta_H32 = 54433;     %J/mol, need to be converted to
kJ/kg for energy calculation
    delta_H21 = 47894;
    delta_H10 = 50616;
    delta_S32 = 257.6;
    delta_S21 = 227.6;
    delta_S10 = 231.3;

    nc32=6.78;
    kc32=0.00156;
    mc32=3.526;
    nc21=1.77;
    kc21=0.00056;
    mc21=3.15;
    nc10=3.8;
    kc10=0.00058;
    mc10=2.44;

    nc23=1;
    kc23=0.001;
    mc23=3;

    nc12=0.49;
    kc12=1.5e-3;
    mc12=3.12;
    nc01=1.15;
    kc01=18.9e-4;
    mc01=4.86;

    ncv= zElement*rElement;     %number of differentical
C.V.

    % (1) equilibrium pressure of reactions
    peq_32 = exp(-
delta_H32./(R.*(T_salt))+delta_S32/R); %Pa
    peq_21 = exp(-
delta_H21./(R.*(T_salt))+delta_S21/R); %Pa
    peq_10 = exp(-
delta_H10./(R.*(T_salt))+delta_S10/R); %Pa
    % (2) current reaction progression X based on molSalt
```

```
    X32 = N2./(N3+N2);
    X32(isnan(X32))=0;
    X32(isinf(X32))=0;
    X21 = N1./(N2+N1);
    X21(isnan(X21))=0;
    X21(isinf(X21))=0;
    X10 = N0./(N1+N0);
    X10(isnan(X10))=0;
    X10(isinf(X10))=0;

    % (3) reaction rate
    dX32dt=zeros(1,ncv);
    dX32dt_des=(1-X32).^nc32.*kc32.*(exp(mc32*(peq_32-
P_local)./P_local)-1);
    dX32dt_ads=X32.^nc23.*kc23.*(exp(mc23*(peq_32-
P_local)./P_local)-1);
    dX32dt(peq_32>P_local)=dX32dt_des(peq_32>P_local);
    dX32dt(peq_32<P_local)=dX32dt_ads(peq_32<P_local);
    dX32dt(isnan(dX32dt))=0;
    dX32dt(isinf(dX32dt))=0;

    dX21dt=zeros(1,ncv);
    dX21dt_des=(1-X21).^nc21.*kc21.*(exp(mc21*(peq_21-
P_local)./P_local)-1);
    dX21dt_ads=X21.^nc12.*kc12.*(exp(mc12*(peq_21-
P_local)./P_local)-1);
    dX21dt(peq_21>P_local)=dX21dt_des(peq_21>P_local);
    dX21dt(peq_21<P_local)=dX21dt_ads(peq_21<P_local);
    dX21dt(isnan(dX21dt))=0;
    dX21dt(isinf(dX21dt))=0;

    dX10dt=zeros(1,ncv);
    dX10dt_des=(1-X10).^nc10.*kc10.*(exp(mc10*(peq_10-
P_local)./P_local)-1);
    dX10dt_ads=X10.^nc01.*kc01.*(exp(mc01*(peq_10-
P_local)./P_local)-1);
    dX10dt(peq_10>P_local)=dX10dt_des(peq_10>P_local);
    dX10dt(peq_10<P_local)=dX10dt_ads(peq_10<P_local);
    dX10dt(isnan(dX10dt))=0;
    dX10dt(isinf(dX10dt))=0;


    % (4) update reaction progression
    dX32 = dX32dt * dt;
```

```
    X32=X32+dX32;
    dX32(X32>1)=dX32(X32>1)-(X32(X32>1)-1);
    X32(X32>1)=1;
    dX32(X32<0)=dX32(X32<0)-X32(X32<0);
    X32(X32<0)=0;

    dX21 = dX21dt * dt;
    X21=X21+dX21;
    dX21(X21>1)=dX21(X21>1)-X21(X21>1)-1;
    X21(X21>1)=1;
    dX21(X21<0)=dX21(X21<0)-X21(X21<0);
    X21(X21<0)=0;

    dX10 = dX10dt * dt;
    X10=X10+dX10;
    dX10(X10>1)=dX10(X10>1)-X10(X10>1)-1;
    X10(X10>1)=1;
    dX10(X10<0)=dX10(X10<0)-X10(X10<0);
    X10(X10<0)=0;

    % (5) update amount of salt in each state

    dN32 = (N3+N2) .* real(dX32);
    dN21 = (N1+N2) .* real(dX21);
    dN10 = (N1+N0) .* real(dX10);

end

++++++++++++++++++++++++++++++++++++++++++++++++++++++++++++++++++++++++++++++++++++

++++++++++++++++++++++++++++++++++++++++++++++++++++++++++++++++++++++++++++++++++++

++++++++++++++++++++++++++++++++++++++++++++++++++++++++++++++++++++++++++++++++++++

% calcMbal.m
% author: Zhiyao Yang
% last modified: 6/5/20
% solving the discretized heat equation using fully
implicit approach
% (0) prepare properties
% (1) construct operator matrix and source term vector
% (2) use Ax=B --> x = A\B to solve current moment cell
mole density
% (3) further calculate P_local and dn_NH3_out
% last modified: 5/9/19
```

```
function [n_NH3_local_new, P_local_new, dN_NH3_out, s] =
calcMbal(i, T_salt,n_NH3_local,P_c,P_local,dN_chem,vcv)

    run = i;
    %constants
    global zElement rElement phi K_MT dz dr r_cv;
    R = 8.314;
    dt = 1;
    tsalt = T_salt;
    n0 = n_NH3_local;
    Svn = dN_chem./vcv;

    mu_NH3 = calcMuNH3(T_salt);

    % (0) calculate the diffusivity
    D = K_MT ./ mu_NH3 .* P_local * phi;
    pos_peri_in = 1:rElement:(zElement-1)*rElement+1;
    pos_peri_out = rElement:rElement:zElement*rElement;
    a_peri_in = (r_cv(1)-dr/2)*2*3.14*dz;
    a_peri_out = (r_cv(rElement)+dr/2)*2*3.14*dz;
    nnh3_cons = [P_c*phi/R./tsalt(pos_peri_in),
P_c*phi/R./tsalt(pos_peri_out)];%inner/outer perimeter

    % (1) construct operator matrix "A" and source term
vector "B"
        % (1-1) operator matrix "A"
    a0 =
ones(zElement*rElement,1)'.*(1/dt./D+2/dz^2+2/dr^2);%genera
l coefficient for target cell temperature

    pos = 1:rElement:rElement*(zElement-1)+1;

a0(pos)=ones(zElement,1)'.*(1/dt./D(pos)+3/dr^2+2/dz^2);%ad
just inner perimeter rim for external radial MT
    pos = rElement:rElement:rElement*zElement;

a0(pos)=ones(zElement,1)'.*(1/dt./D(pos)+3/dr^2+2/dz^2);%ad
just outer perimeter rim for no external radial MT

    pos = 1:rElement;
    a0(pos) =
ones(rElement,1)'.*(1/dt./D(pos)+1/dz^2+2/dr^2);%adjust top
row for no MT
```

```
    a0(1) = 1/dt./D(1)+1/dz^2+3/dr^2;%adjust top inner
corner
    a0(rElement) = 1/dt./D(rElement)+1/dz^2+3/dr^2;%adjust
top outer corner

    pos = (zElement-1)*rElement+1:zElement*rElement;
    a0(pos) =
ones(rElement,1)'.*(1/dt./D(pos)+1/dz^2+2/dr^2);%adjust
bottom row for no MT
    a0((zElement-1)*rElement+1) = 1/dt./D((zElement-
1)*rElement+1)+1/dz^2+3/dr^2;%adjust for bottom inner
corner
    a0(rElement*zElement) =
1/dt./D(rElement*zElement)+1/dz^2+3/dr^2;%adjust for bottom
outer corner
    Aa = diag(a0);

    b0 = ones((zElement-1)*rElement,1)*(-1)/dz^2;%for next-
row vertical MT
    Ab = diag(b0,rElement);

    c0 = ones((zElement-1)*rElement,1)*(-1)/dz^2;%for
previous-row vertical MT
    Ac = diag(c0,-rElement);

    drcv0 = [r_cv(1:rElement-1),0];%for next-column radial
MT
    drcv = zeros(rElement*zElement,1)';
    for i = 1:zElement
        drcv(1+(i-1)*rElement:rElement+(i-1)*rElement) =
drcv0;
    end
    drcv(rElement*zElement)=[];
    d0 = -1/dr^2 - 1/2/dr./drcv;
    d0(1:rElement:rElement*(zElement-1)+1)=-1/dr^2;%adjust
for inner perimeter less internal MT
    Ad = diag(d0,1);
    Ad(isinf(Ad)) = 0;

    ercv0 = [r_cv(2:rElement), 0];%for previous-column
radial MT
    ercv = zeros(rElement*zElement,1)';
    for i = 1:zElement
```

```
        ercv(1+(i-1)*rElement:rElement+(i-1)*rElement) =
ercv0;
    end
    ercv(rElement*zElement)=[];
    e0 = -1/dr^2 + 1/2/dr./ercv;
    e0(rElement-1:rElement:rElement*zElement-1)=-
1/dr^2;%adjust for outer perimeter less internal MT
    Ae = diag(e0,-1);
    Ae(isinf(Ae)) = 0;

    sz=-1/dr^2;
    ddr = Ad+Ae;
    ddr(ddr~=0)=ddr(ddr~=0)-sz;

    A = Aa + Ab + Ac + Ad + Ae;
        % (1-2) source term vector "B"
    B = (Svn./D + 1/dt./D.*n0)';%including chemical
reaction generation and mass inertia from last step

B(pos_peri_in)=B(pos_peri_in)+2*nnh3_cons(1:zElement)'/dr^2
;%add inner perimeter boundary condition: MT with chamber

B(pos_peri_out)=B(pos_peri_out)+2*nnh3_cons(zElement+1:2*zE
lement)'/dr^2;%add inner perimeter boundary condition: MT
with chamber

    % (2) calculate new temperature "x"
    x = A\B;
    nnh3_new = x';
    n_NH3_local_new = nnh3_new;
    dn_NH3_local = nnh3_new-n0;


    % (3) calculate local pressure and ammoina out flow
    P_local_new = n_NH3_local_new*R.*tsalt/phi;
    nnh3_new_peri =
[nnh3_new(pos_peri_in),nnh3_new(pos_peri_out)];
    D_cons = [D(pos_peri_in),D(pos_peri_out)];
    a_cons = [ones(zElement,1)'.*a_peri_in,
ones(zElement,1)'.*a_peri_out];
    dN_NH3_out = (nnh3_new_peri -
nnh3_cons).*D_cons*2/dr.*a_cons;
```

```
    sumdnch = sum(dN_chem);
    sumdnn = sum(sum(dn_NH3_local.*vcv));
    sumdno = sum(sum(dN_NH3_out));

    s=[sumdnch,sumdnn,sumdno];

%     if(true)%rem(run,2)==0)
%
%         pcons=P_c
%         pl=reshape(P_local_new,[rElement,zElement])'
%         n0=reshape(n0,[rElement,zElement])'
%         nn=reshape(nnh3_new,[rElement,zElement])'
%         dn=reshape(dn_NH3_local,[rElement,zElement])'
%         nc=reshape(nnh3_cons,[zElement,2])
%         dnch=reshape(Svn,[rElement,zElement])'
%
dno=reshape(dN_NH3_out./[vcv(pos_peri_in),vcv(pos_peri_out)
],[zElement,2])
%         dNch=reshape(dN_chem,[rElement,zElement])'
%         sumNch=sum(sum(dN_chem))
%         dNo=reshape(dN_NH3_out,[zElement,2])
%         sumNo=sum(sum(dN_NH3_out))
%
%
%         deb='wait n'' check';
%
%     end
end
```

```
++++++++++++++++++++++++++++++++++++++++++++++++++++++++++++++++++++++++++++++++++++++++
++++++++++++++++++++++++++++++++++++++++++++++++++++++++++++++++++++++++++++++++++++++++
++++++++++++++++++++++++++++++++++++++++++++++++++++++++++++++++++++++++++++++++++++++++
```

```
% calcEbal_v2_wholeDisk.m
% author: Zhiyao Yang
% last modified: 6/10/20
% solving the discretized heat equation using fully
implicit approach
% (0) prepare properties
% (1) construct operator matrix and source term vector
```

```
% (2) use Ax=B --> x = A\B to solve current moment cell
temperatures
% (3) further calculate q_hp
% last modified: 5/9/19

function [T_salt_new, dtsalt, Q_hp_salt_top, Q_hp_salt_bot]
= calcEbal_v2_wholeDisk(i, Q_chem, T_salt, T_steam, U_bot,
U_top, ns3, ns2, ns1, ns0,vcv, m_mat_vec)

    global zElement rElement K_HT dz dr r_cv;

    dt = 1;

    tsalt_0 = T_salt;
    Svq = Q_chem./vcv;

    % (0) calculate X and Cp and rho
    Cp_s = calcCps(ns3,ns2,ns1,ns0,vcv,m_mat_vec);
    rho_s = calcRho(ns3,ns2,ns1,ns0,vcv,m_mat_vec);
    alpha_s = K_HT./(rho_s.*Cp_s);

    % (1) construct operator matrix "A" and source term
vector "B"
        % (1-1) operator matrix "A"
    a0 =
ones(zElement*rElement,1)'.*(1/dt./alpha_s+2/dz^2+2/dr^2);%
general coefficient for target cell temperature

    pos = 1:rElement:rElement*(zElement-1)+1;%adjust inner
perimeter rim for no external radial HT

a0(pos)=ones(zElement,1)'.*(1/dt./alpha_s(pos)+1/dr^2+2/dz^
2);
    pos = rElement:rElement:rElement*zElement;%adjust outer
perimeter rim for no external radial HT

a0(pos)=ones(zElement,1)'.*(1/dt./alpha_s(pos)+1/dr^2+2/dz^
2);

    pos_topLayer = 1:rElement;%adjust top row for HT with
HP
    a0(pos_topLayer) =
ones(rElement,1)'.*(1/dt./alpha_s(pos_topLayer)/2+1/dz^2+1/
dz*U_top/K_HT+2/dr^2);%adjust top row for HT with HP
```

```
    a0(1) =
1/dt./alpha_s(1)/2+1/dz^2+1/dz*U_top/K_HT+1/dr^2;%adjust
top inner corner
    a0(rElement) =
1/dt./alpha_s(rElement)/2+1/dz^2+1/dz*U_top/K_HT+1/dr^2;%ad
just top outer corner

    pos_botLayer = (zElement-
1)*rElement+1:zElement*rElement;%adjust bottom row for no
HT
    a0(pos_botLayer) =
ones(rElement,1)'.*(1/dt./alpha_s(pos_botLayer)/2+1/dz^2+1/
dz*U_bot/K_HT+2/dr^2);
    a0((zElement-1)*rElement+1) = 1/dt./alpha_s((zElement-
1)*rElement+1)/2+1/dz^2+1/dz*U_bot/K_HT+1/dr^2;%adjust for
bottom inner corner
    a0(rElement*zElement) =
1/dt./alpha_s(rElement*zElement)/2+1/dz^2+1/dz*U_bot/K_HT+1
/dr^2;%adjust for bottom outer corner

    Aa = diag(a0);

    b0 = ones((zElement-1)*rElement,1)*(-1)/dz^2;%for next-
row vertical HT
%     b0(1:rElement) = -1/dz^2;%adjust for top layer HT
    Ab = diag(b0,rElement);

    c0 = ones((zElement-1)*rElement,1)*(-1)/dz^2;%for
previous-row vertical HT
%     c0((zElement-2)*rElement+1:(zElement-1)*rElement)=-
1/dz^2;%adjust for bottom layer HT
    Ac = diag(c0,-rElement);

    drcv0 = [r_cv(1:rElement-1),0];%for next-column radial
HT
    drcv = zeros(rElement*zElement,1)';
    for i = 1:zElement
        drcv(1+(i-1)*rElement:rElement+(i-1)*rElement) =
drcv0;
    end
    drcv(rElement*zElement)=[];
    d0 = -1/dr^2 - 1/2/dr./drcv;
    d0(1:rElement:rElement*(zElement-1)+1)=-1/dr^2;%adjust
for inner perimeter no HT
```

```
    Ad = diag(d0,1);
    Ad(isinf(Ad)) = 0;

    ercv0 = [r_cv(2:rElement), 0];%for previous-column
radial HT
    ercv = zeros(rElement*zElement,1)';
    for i = 1:zElement
        ercv(1+(i-1)*rElement:rElement+(i-1)*rElement) =
ercv0;
    end
    ercv(rElement*zElement)=[];
    e0 = -1/dr^2 + 1/2/dr./ercv;
    e0(rElement-1:rElement:rElement*zElement-1)=-
1/dr^2;%adjust for outer perimeter no HT
    Ae = diag(e0,-1);
    Ae(isinf(Ae)) = 0;

    sz=-1/dr^2;
    ddr = Ad+Ae;
    ddr(ddr~=0)=ddr(ddr~=0)-sz;

    A = Aa + Ab + Ac + Ad + Ae;
        % (1-2) source term vector "B"
    B = (Svq/K_HT + 1/dt./alpha_s.*tsalt_0)';%including
chemical reaction heat and heat inertia from last step
    B(pos_topLayer)=B(pos_topLayer)-
(1/dt./alpha_s(pos_topLayer).*tsalt_0(pos_topLayer))'/2+U_t
op/K_HT/dz*T_steam*ones(rElement,1);%add top layer boundary
condition: HT with HP
    B(pos_botLayer)=B(pos_botLayer)-
(1/dt./alpha_s(pos_botLayer).*tsalt_0(pos_botLayer))'/2+U_b
ot/K_HT/dz*T_steam*ones(rElement,1);%add bottom layer
boundary condition: HT with HP


    % (2) calculate new temperature "x"
    x = A\B;
    T_salt_new = x';
    dtsalt = T_salt_new - tsalt_0;

    % (3) calculate Qhp
    Q_hp_salt_top = (T_steam-
T_salt_new(pos_topLayer))*U_top.*r_cv*dr*2*3.14*dt;
```

```
    Q_hp_salt_bot = (T_steam-
T_salt_new(pos_botLayer))*U_bot.*r_cv*dr*2*3.14*dt;

%     if(Svq<0)
%
%         sumqsaltbot =
sum(Q_hp_salt_bot)*56+sum(Q_hp_salt_top)*56
%         sumqchem=sum(Svq)*56
%         T_steam
%         tsalt_avg=mean(T_salt_new)
%         tsalt_avg_0 = mean(tsalt_0)
%         deb='wait n'' check'
%     end
end
```

```
++++++++++++++++++++++++++++++++++++++++++++++++++++++++++++++++++++++++++++++++
++++++++++++++++++++++++++++++++++++++++++++++++++++++++++++++++++++++++++++++++
++++++++++++++++++++++++++++++++++++++++++++++++++++++++++++++++++++++++++++++++
```

```
% adsorber_withHP_parametric.m
% author: Zhiyao Yang
% last modified: 7/20/20

tic
clear
%% global parameters
global K_MT K_HT phi rho_matrix zElement rElement dz dr
r_cv dt R;

close all

% time boundary

cycle_time = 60*120-1; %s, desorption/adsorption split
evenly
dt = 1;
timeTot = cycle_time; %s, total simulation time, evenly
split between desorption and adsorption
i_end =round(timeTot/dt);%total number of operation time

Pc_c=Psat_NH3_Tk(44+273);
```

```
Pc_e=Psat_NH3_Tk(40+273);

m_HX = 8;%kg
m_shell = 24;%kg
Cp_SS = 0.46;%kJ/kg-K
Cp_water = 4.18;
rho_SS = 800;%kg/m3
x_HP = 1e-3; %m, thickness of the heat pipe wall

%property constants
molarMass_NH3 = 17;      %g/mol
molarMass_LiCl = 42.4;   %g/mol
R = 8.314;               %gas constant
g = 9.81;
k_ss = 16.3e-3; %kW/m.K, stainless steel 304 (Perry's
handbook)
U_wall = k_ss/x_HP;

%% design parameters & properties
% design geometry parameters
n_plate = 56;%-, number of salt plates
r_plate_i = 0.015/2;%m, inner radius of plate (hollow)
r_plate_o = 0.15/2;%m, outer radius of plate
z_plate = .56/n_plate;%0.01;%m, thickness of plate
A_plate = 3.14 * (r_plate_o^2 - r_plate_i^2);%m2, area of
plate
V_plate = z_plate * A_plate;%m3, volume of a plate
M_mat = 1.2;%kg, total matrix mass
M_salt_tot = 2.2;%kg, total salt mass, more than 1:3 to NH3


% property of the salt matrix
phi = 0.2;%-, porosity, later should be fiited to X_tot
K_HT = 1e-3; %kW/m-K, thermal conductivity
K_MT = 10^(1+log(phi/2))*1e-13;%m2, permeability, later
should be fitted to X_tot
rho_matrix = (M_salt_tot + M_mat)/n_plate/V_plate;%kg/m3,
density, calculated from salt+matrix mass and salt plate
volume

% property of ammonia
mu_NH3_min = calcMuNH3(50+273.15);%Pa-s, dynamic viscosity
of vapor ammonia @ 100C, use EES to fit to T & P
```

```
%chemical reaction enthalpy
delta_H32 = 44780/1000;     %kJ/mol
delta_H21 = 48128/1000;
delta_H10 = 51894/1000;


%boundary properties for time step calculation
Cp_matrix_min = 1.5;%kJ/kg-K, minimum specific heat, from
pure salt+matrix
alpha_max = K_HT/rho_matrix/Cp_matrix_min;%kJ/m3-K, maximum
thermal diffusivity
P_max = 2e6; %Pa, maximum ammonia pressure
D_max = K_MT/mu_NH3_min*P_max*phi;%m2/s, maximum
diffusivity, H2 in clay: 1e-9
%% simulation control
% timeStep = 1;%s
zElement = 30;%number of differential c.v. in z direction
rElement = 10;%number of differential c.v. in r direction
dz = z_plate / zElement;%m, height of a diff. c.v.
dr = (r_plate_o-r_plate_i)/rElement;%m, depth of a diff.
c.v.
r_cv = r_plate_i+(0.5+(0:rElement-1))*dr;%m, middle line
radius of c.v.
V_cv_r = dr*r_cv*dz*2*3.14;%m3, c.v. volume

%% boundary conditions
T_salt_0 = 45+273;

%mol, initial mole number of salt in each state
Nnh3_tot = 2.1/17*1000;
Ns_tot = Nnh3_tot / 3;
Ns0=[Ns_tot/n_plate,0,0,0];
n_NH3_local_0 = Pc_c*phi/R/T_salt_0;%mol/m3, initial
ammonia vapor mole density w.r.t total c.v. volume


%% allocate matrix/vector for
% the parameters are stored in matrix formatting as:
% row - runs
% column - [ [dr of 1st (top) plane] [dr of 2nd plane] ...
[dr of bottom
% plane]

% key parameters
```

```
% T_steam_vec = zeros(i_end,1);
% P_constraint_vec = zeros(i_end,1);
T_salt = zeros(i_end,zElement*rElement);
Q_HP_salt_top = zeros(i_end,rElement);
Q_HP_salt_bot = zeros(i_end,rElement);
Ns_3 = zeros(i_end,zElement*rElement);%mol/m3, vol. mol.
density of LiCl-3NH3
Ns_2 = zeros(i_end,zElement*rElement);%mol/m3, vol. mol.
density of LiCl-2NH3
Ns_1 = zeros(i_end,zElement*rElement);%mol/m3, vol. mol.
density of LiCl-1NH3
Ns_0 = zeros(i_end,zElement*rElement);%mol/m3, vol. mol.
density of pure LiCl
n_NH3_local = zeros(i_end,zElement*rElement);%mol/m3, vol.
mol. density of NH3 w.r.t total c.v. volume
dN_NH3_out = zeros(i_end,zElement*2);%mol, ammonia vapor
crossing the inner/outer primeter\

% monitored parameters
U_ceil_cond = zeros(i_end,1);
U_floor_cond = zeros(i_end,1);
U_ceil = zeros(i_end,1);
U_floor = zeros(i_end,1);
P_local = zeros(i_end,zElement*rElement);
dN_g_32 = zeros(i_end,zElement*rElement);
dN_g_21 = zeros(i_end,zElement*rElement);
dN_g_10 = zeros(i_end,zElement*rElement);
Q_chem = zeros(i_end,zElement*rElement);
dN_NH3_chem = zeros(i_end,zElement*rElement);
dtsalt = zeros(i_end,zElement*rElement);
nsum = zeros(i_end,3);%used to store total ammonia changes
Q_HP_salt = zeros(i_end,1);
tsat_sim = zeros(i_end,1);
T_HP_vec = zeros(i_end,1);
X_tot = zeros(i_end,1);
n_NH3_CE = zeros(i_end,1);

% initial values
T_salt(1,:) = T_salt_0-0.1;
P_local(1,:) = Pc_c;
n_NH3_local(1,:) = ones(1,zElement*rElement)*n_NH3_local_0;
tsat_sim(1) = 45+273;

% assign amount of salt to each volume
```

```
% use reshape(A',[],1) to convert matrix into 1d array
V_cv_mat = ones(zElement,1)*V_cv_r;
V_cv_vec = reshape(V_cv_mat',1,[]);
Ns_3(1,:) = Ns0(1)/V_plate*V_cv_vec;
Ns_2(1,:) = Ns0(2)/V_plate*V_cv_vec;
Ns_1(1,:) = Ns0(3)/V_plate*V_cv_vec;
Ns_0(1,:) = Ns0(4)/V_plate*V_cv_vec;
m_mat_vec = M_mat/n_plate/V_plate*V_cv_vec;%kg, matrix mass
in each c.v.

dt_HP = 2;
T_HP_lim_des = 205+273;
T_HP_lim_ads = 55 + 273;
%% calculation
%desorption
i=1;
i_des = i
% db = 'desorption'
hwait = waitbar(0,'calculating');
set(findobj(hwait,'type','patch'),'edgecolor','k','facecolo
r','b');
dn_out = 1;
while(dn_out>0.0005&&i<i_end/2)
    tsalt_avg = T_salt(i,1);
    T_HP = min([tsalt_avg+dt_HP,T_HP_lim_des]);
    T_HP_vec(i) = T_HP;

    %calculate ammonia generation of each reaction stage
using chemical
    %kinetics
    [dN_g_32(i+1,:),dN_g_21(i+1,:),dN_g_10(i+1,:)] =
calcChem(i,...
        T_salt(i,:), P_local(i,:), Ns_3(i,:), Ns_2(i,:),
Ns_1(i,:), Ns_0(i,:));
    Ns_3(i+1,:) = Ns_3(i,:) - dN_g_32(i+1,:);
    Ns_2(i+1,:) = Ns_2(i,:) + dN_g_32(i+1,:) -
dN_g_21(i+1,:);
    Ns_1(i+1,:) = Ns_1(i,:) + dN_g_21(i+1,:) -
dN_g_10(i+1,:);
    Ns_0(i+1,:) = Ns_0(i,:) + dN_g_10(i+1,:);
    dN_NH3_chem(i+1,:) = dN_g_32(i+1,:) + dN_g_21(i+1,:) +
dN_g_10(i+1,:);
    Q_chem(i+1,:) = - (dN_g_32(i+1,:) * delta_H32 +
dN_g_21(i+1,:) ...
```

```
        * delta_H21 + dN_g_10(i+1,:) * delta_H10);

    X_tot(i,:) =
(sum(Ns_2(i,:))+sum(Ns_1(i,:))*2+sum(Ns_0(i,:))*3)./Ns_tot/
3;

    % Mass transfer calculate local volumetric vapor
ammonia mole density

[n_NH3_local(i+1,:),P_local(i+1,:),dN_NH3_out(i+1,:),nsum(i
+1,:)]...
        = calcMbal(i+1, T_salt(i,:),n_NH3_local(i,:),...
        Pc_c,P_local(i,:),dN_NH3_chem(i,:),V_cv_vec);


    % Heat transfer of the steam -> heat pipe wall -> salt:
HT resistance
    % assuming the thermal mass of the heat pipe wall can
be neglected
    ttsteam = T_HP-273;
    delta_T_steam_HP = 2;%tsteam+273-T_salt(i,1);

    % get properties
    % property of the steam-heat pipe (implement property
subroutines)
    hfg_water = steamlookup(ttsteam,'hfg');%kJ/kg.K, steam
vaporization heat
    rho_v = 1/steamlookup(ttsteam,'vg');%saturated steam
density
    rho_l = 1/steamlookup(ttsteam,'vl');%water density
    cp_l = steamlookup(ttsteam,'cpl');%specific heat
    k_l = steamlookup(ttsteam,'kl');%thermal conductivity
    mu_l = steamlookup(ttsteam,'mul');%dynamic viscosity
    nu_l = steamlookup(ttsteam,'nul');%kinematic viscosity
    sigma_l = steamlookup(ttsteam,'sigmal');%surface
tension
    % bottom (ceiling): Gerstmann and Griffith
    Ra=(g*rho_l*(rho_l-
rho_v)*hfg_water)/(mu_l*delta_T_steam_HP*k_l)...
    *(sigma_l/g/(rho_l-rho_v))^(3/2);
    Nu_ceil=0.81*Ra^0.193;
    h_ceil=Nu_ceil*k_l/(sigma_l/g/(rho_l-rho_v))^.5;
    U_ceil_cond(i) = h_ceil/1000;
    % top (floor): Bejan
```

```
    Nu_floor =
1.368*((2*r_plate_o)^3*(hfg_water+3/8*cp_l*delta_T_steam_HP
)...
        *g*(rho_l-rho_v)/k_l/nu_l*delta_T_steam_HP)^(1/5);
    h_floor = Nu_floor*k_l/(2*r_plate_o);
    U_floor_cond(i) = h_floor/1000;

    U_ceil(i) = 1/(1/U_wall+1/U_ceil_cond(i));
    U_floor(i) = 1/(1/U_wall+1/U_floor_cond(i));


    % Heat transfer calculate salt temperature using energy
balance

[T_salt(i+1,:),dtsalt(i+1,:),Q_HP_salt_top(i+1,:),Q_HP_salt
_bot(i+1,:)] =...
        calcEbal_v2_wholeDisk(i, Q_chem(i,:), T_salt(i,:),
T_HP,...
        U_ceil(i), U_floor(i), Ns_3(i,:), Ns_2(i,:),
Ns_1(i,:), Ns_0(i,:),V_cv_vec,m_mat_vec);


Q_HP_salt(i)=n_plate*(sum(Q_HP_salt_bot(i,:))+sum(Q_HP_salt
_top(i,:)));
        n_NH3_CE(i+1) =
n_NH3_CE(i)+sum(dN_NH3_out(i,:))*n_plate;

    i=i+1;
    waitbar(i/i_end,hwait,[num2str(i),'/',num2str(i_end)]);
end

%adsorption
i_ads = i
% db = 'adsorption'
while(i<i_end+1&&n_NH3_CE(i-1)>0)
    tsalt_avg = T_salt(i,1);
    T_HP = max([tsalt_avg-dt_HP/2,T_HP_lim_ads]);
    T_HP_vec(i) = T_HP;

    %calculate ammonia generation of each reaction stage
using chemical
    %kinetics
    [dN_g_32(i+1,:),dN_g_21(i+1,:),dN_g_10(i+1,:)] =
calcChem(i,...
```

```
        T_salt(i,:), P_local(i,:), Ns_3(i,:), Ns_2(i,:),
Ns_1(i,:), Ns_0(i,:));
    Ns_3(i+1,:) = Ns_3(i,:) - dN_g_32(i+1,:);
    Ns_2(i+1,:) = Ns_2(i,:) + dN_g_32(i+1,:) -
dN_g_21(i+1,:);
    Ns_1(i+1,:) = Ns_1(i,:) + dN_g_21(i+1,:) -
dN_g_10(i+1,:);
    Ns_0(i+1,:) = Ns_0(i,:) + dN_g_10(i+1,:);
    dN_NH3_chem(i+1,:) = dN_g_32(i+1,:) + dN_g_21(i+1,:) +
dN_g_10(i+1,:);
    Q_chem(i+1,:) = - (dN_g_32(i+1,:) * delta_H32 +
dN_g_21(i+1,:) ...
        * delta_H21 + dN_g_10(i+1,:) * delta_H10);

    X_tot(i,:) =
(sum(Ns_2(i,:))+sum(Ns_1(i,:))*2+sum(Ns_0(i,:))*3)./Ns_tot/
3;

    % Mass transfer calculate local volumetric vapor
ammonia mole density

[n_NH3_local(i+1,:),P_local(i+1,:),dN_NH3_out(i+1,:),nsum(i
+1,:)]...
        = calcMbal(i+1, T_salt(i,:),n_NH3_local(i,:),...
        Pc_e,P_local(i,:),dN_NH3_chem(i,:),V_cv_vec);


    % Heat transfer of the steam -> heat pipe wall -> salt:
HT resistance
    % assuming the thermal mass of the heat pipe wall can
be neglected
    ttsteam = T_HP-273;
    delta_T_steam_HP = 2;%tsteam+273-T_salt(i,1);

    U_fconv = 3;%kW/m2.K, forced convection between liquid
and metal plate
    U_ceil(i) = 1/(1/U_wall+1/U_fconv);
    U_floor(i) = 1/(1/U_wall+1/U_fconv);


    % Heat transfer calculate salt temperature using energy
balance
```

```
[T_salt(i+1,:),dtsalt(i+1,:),Q_HP_salt_top(i+1,:),Q_HP_salt
_bot(i+1,:)] =...
        calcEbal_v2_wholeDisk(i, Q_chem(i,:), T_salt(i,:),
T_HP,...
        U_ceil(i), U_floor(i), Ns_3(i,:), Ns_2(i,:),
Ns_1(i,:), Ns_0(i,:),V_cv_vec,m_mat_vec);


Q_HP_salt(i)=n_plate*(sum(Q_HP_salt_bot(i,:))+sum(Q_HP_salt
_top(i,:)));

    n_NH3_CE(i) = n_NH3_CE(i-
1)+sum(dN_NH3_out(i,:))*n_plate;

    i=i+1;
    waitbar(i/i_end,hwait,[num2str(i),'/',num2str(i_end)]);
end
close(hwait)
toc
```

APPENDIX D. PUBLISHED JOURNAL PAPER

Applied Thermal Engineering 179 (2020) 115674

Contents lists available at ScienceDirect

Applied Thermal Engineering

journal homepage: www.elsevier.com/locate/apthermeng

Ammonia-based chemisorption heat pumps for cold-climate heating applications: A comprehensive review☆

Zhiyao Yang[a], Ming Qu[a], Kyle R. Gluesenkamp[b,*]

[a] Purdue University, Lyle School of Civil Engineering, West Lafayette, IN 47906, USA
[b] Oak Ridge National Laboratory, 1 Bethel Valley Rd., Oak Ridge, TN 37831, USA

HIGHLIGHTS

- New Clapeyron diagram compares 66 chemisorption working pairs.
- Innovative developments are reviewed for materials, components, and system designs.
- Research priorities are matching salts to applications and reducing thermal mass.
- Hysteresis and reaction heat of sorbent salts significantly affect performance.

ARTICLE INFO

Keywords:
Chemisorption
Ammonia
Heat pump
Adsorption
Cold climate
Ammoniated salts

ABSTRACT

This article reviews the state of the art of chemisorption heat pumps that use ammonia as the refrigerant for cold-climate heating applications. In such a system, ammonia vapor is adsorbed by the solid salt through reversible chemisorption reactions, and the thermal effect of the reaction and ammonia phase change is used to extract heat from a cold environment and supply heat to a warm environment. With the high latent heat and low boiling point of ammonia as a low-temperature refrigerant and the high sorption capacity of ammonia-based chemisorption reactions, chemisorption heat pumps have the potential to produce high-efficiency heating, particularly for cold climates. This review first briefly introduces the basics of ammonia-based chemisorption heat pump systems. Then, the latest development of sorbent materials, including ammoniate salts and heat-conductive porous matrix materials, are summarized with the focus on low-temperature heating conditions. The design of system components, as well as cycle configurations, in the literature are summarized. This review concludes with highlights of recent developments on these topics and suggestions of areas for further research.

1. Introduction

Buildings are responsible for around 40% of the total energy consumption in the United States and Europe [1,2]. To reduce this consumption and the associated greenhouse gas emissions, the energy efficiencies of heating, ventilation, and air conditioning (HVAC) systems in buildings are constantly improved with advances in existing technologies and development of novel systems. Among building HVAC applications, space and water heating are the major energy consumers [3]. For example, in 2015, space and water heating accounted for 6.0 EJ

Abbreviations: AC, activated carbon; ACF, activated carbon fiber; C/E, condenser/evaporator; CF, carbon fiber; CNT, carbon nanotube; COP, coefficient of performance; CSHP, chemisorption heat pump; DRES, double-effect resorption; DSCE, double-effect separate condenser-evaporator; EG, expanded graphite; ENG, expanded natural graphite; ENG-TSA, expanded natural graphite treated with sulfuric acid; EVM, expanded vermiculite; GFIC, graphite fiber intercalation; HTF, heat transfer fluid; HTS, high-temperature salt; HVAC, heating, ventilation, and air conditioning; ICF, impregnated carbon fiber; LT, low temperature; LTS, low-temperature salt; MT, medium temperature; MTS, medium-temperature salt; MWCNT, multiwall carbon nanotube; SCCE, single-effect combined condenser-evaporator; SCP, specific cooling power; SEM, scanning electron microscopy; SHP, specific heating power; SRES, single-effect resorption; SSCE, single-effect separate condenser and evaporator

* Corresponding author.
E-mail addresses: yang573@purdue.edu (Z. Yang), mqu@purdue.edu (M. Qu), gluesenkampk@ornl.gov (K.R. Gluesenkamp).

https://doi.org/10.1016/j.applthermaleng.2020.115674
Received 24 January 2020; Received in revised form 26 June 2020; Accepted 27 June 2020
Available online 03 July 2020
1359-4311/

Nomenclature

A	heat transfer area
ΔH	reaction enthalpy
ΔS	reaction entropy
h	heat transfer coefficient
MCl_x	metal chloride
n	stoichiometric coefficient of ammonia
P	vapor pressure
Q	heat flow
R	gas constant
T	temperature
t	time
UA	product of heat transfer coefficient and heat transfer area
x	thickness of heat exchanger wall

Subscripts

ads	adsorbing
cond	condensing
cyc	cycle
des	desorbing
evap	evaporating
eq	equilibrium
fg	vaporization heat
fw	between heat transfer fluid and heat exchanger wall
ht	heating
in	Input
ref	refrigeration
s	sorbent
sys	system
w	heat exchanger wall
ws	between heat exchanger wall and sorbent

of energy, or more than 62% of the total residential on-site energy consumption in US households. In cold-climate regions, heating energy consumption was 3.09 EJ, or 73% of the total energy [4]. Meanwhile, improving the efficiencies of existing heating systems has been particularly difficult. Electric-driven vapor-compression heat pumps can achieve high heating efficiencies in mild climates [5], but their performance declines considerably in cold climates because of the large compression ratio and high discharge temperature needed to produce heating under freezing ambient conditions [6–10]. More than 80% of the heating systems in cold-climate residential buildings in the United States are fuel-combusting furnaces and boilers [4]. The thermal efficiency of typical off-the-shelf condensing gas boilers is above 95%, which already approaches the theoretical thermal efficiency limit of 100%.

Thermally driven vapor-sorption heat pumps are a promising alternative to vapor-compression heat pumps for producing energy-efficient heating and cooling. In a sorption heat pump, the refrigerant is adsorbed and desorbed by the sorbent material, and the thermal effect of the sorption process and the refrigerant phase change can be used to extract heat from a cold environment and supply heat to a warm environment. Compare with vapor-compression heat pumps that use high global warming potential (GWP) and ozone depletion potential (ODP) refrigerants, sorption heat pumps usually use environmentally friendly refrigerants such as water, ammonia, methanol, and others. Ammonia is suitable as the refrigerant for cold-climate heating applications because it is chemically stable, has a high vaporization heat, and has an above-atmospheric saturation pressure at temperature down to −34 °C [11,12]. On the other hand, ammonia is both toxic and flammable and is classified as Group B2 refrigerant in ANSI/ASHRAE Standard 34 [13]. ANSI/ASHRAE Standard 15 [14] establishes the requirement for safely applying ammonia in refrigeration systems. The safe handling of ammonia can also draw lessons from the experience and understanding of using ammonia in the industrial refrigeration field for over 100 years [15].

Sorption heat pumps can be categorized into liquid–gas absorption and solid–gas adsorption systems based on the phase of the sorbent material. Absorption heat pumps with ammonia refrigerant usually use water as the sorbent and can produce high-capacity heating under cold ambient conditions [16,17]; however, rectification, i.e. the process to condense and separate the water content from the vapor after desorption is required to maintain ammonia vapor purity, and a specialized ammonia solution pump is needed to circulate liquid solution [18]. In contrast, ammonia-based adsorption systems have simpler configurations, do not need rectification, and require little parasitic energy input and special components for pumping [19,20]. Ammonia-based adsorption systems can be further divided into two categories: physical adsorption using the van der Waals force to bond ammonia in sorbents such as activated carbon, and chemical adsorption (chemisorption) using the reversible chemical reactions to bond ammonia in metal halide salt sorbents. Compared with the 0.1 kg–0.3 kg ammonia sorption per kg sorbent of the physical adsorption [11,21], as much as 1 kg of ammonia per kg can be bonded in the chemisorption sorbent [11,22]. The unique advantages of high sorption capacity and the ability to extract heat at very low temperatures make chemisorption technology the subject of multiple studies of refrigeration using renewable energy [23–27] and of effective heating in cold climates [28,29].

The chemisorption heat pumps (CSHP) operate among three temperature levels: low, medium, and high; and they can be categorized into two types. The type-I heat pumps are driven by high-temperature heat to amplify and supply heat at the medium temperature with extra heat extracted from the low-temperature environment. Type-II heat pumps, often referred to as heat transformers, are driven by medium-temperature heat to upgrade and supply heat at the high temperature while also rejecting heat to the low-temperature environment. Therefore, type-I CSHP can efficiently utilize heat from fuel combustion and amplifies heat production at the medium temperature with heat drawn from the cold ambient. Most type-II CSHP operate to upgrade heat from the medium temperature for high-temperature end uses such as steam generation, which is not typically suitable for cold climate heat pumping. However, one innovative example of a type-II CSHP is suitable for cold-climate heating applications, as described by [30–32]. This type-II CSHP takes advantage of two ambient temperatures (for example, above-freezing ground water and below-freezing air) to upgrade medium-temperature ambient heat to the space heating temperature while rejecting heat to low-temperature ambient.

With the extra heat drawn from cold ambient, gas-driven CSHP can provide heating with much higher effectiveness of energy utilization than gas boilers. Meanwhile, similar to vapor compression heat pumps, extracting heat from cold ambient can lead to frosting on the outdoor heat exchanger and deteriorate the heat transfer. The frosting can be resolved by temporarily heating the heat exchanger with an electric heater or by reversing the heat pump cycles [10,33], which could lead to a reduction of the heating coefficient of performance (COP). Different aspects of chemisorption technology have been included in existing reviews, which provide excellent summaries of chemisorption technology from their specific perspectives. Wongsuwan et al. [34] presented an overview of the chemical heat pump using various chemical reactions in the early 2000s. Dieng and Wang [23] and Yu et al.

[35] focused on solar-powered adsorption technology. Chan et al. [36] summarized chemical heat pump and energy storage technology for low-grade heat use. Li et al. [37] provided a detailed review of cycle configurations of adsorption systems. Wang et al. [38] summarized designs to improve heat transfer in adsorption refrigeration systems. Wang et al. [11] reviewed the working pairs used in physical and chemical adsorption refrigeration applications. Jiang and Roskilly [39] summarized thermophysical characteristic enhancement for solid sorbents in adsorption systems using ammonia as the refrigerant. Cabeza et al. [40] conducted a broad review of absorption and adsorption technologies used in heat pump and thermal storage applications. Some recent reviews on thermal energy storage applications also include chemisorption technology for its high energy density [41,42].

Meanwhile, a few review works were found in the literature including discussions of chemisorption technology for heating applications. Dias and Costa [43] reviewed the state-of-the-art of adsorption heat pumps for heating applications. However, the review is mostly centered on water- and alcohol-based physical adsorption technology and systems, with only brief discussions of chemisorption working pairs and systems. Oliveira [44] introduced the principles and published performances of various chemisorption cycles. The commonly used water- and ammonia-based working pairs and the methods to address the swelling and agglomeration of salts were introduced, along with a discussion on the technical and economic feasibility of the technology. However, the review of sorbent material and system cycle was not comprehensive, and it didn't include the development and challenges on the component level.

Different from the existing reviews focusing on the general chemisorption technology, its use in cooling/refrigeration applications, or only some aspects for heating applications, this paper provides a comprehensive review on using the chemisorption technology specifically for space and water heating in cold-climates. Furthermore, chemisorption technology as well as cold-climate heating technologies have been intensively studied with funding from national and international agencies such as the US Department of Energy, National Science Foundation of China, Engineering and Physical Science Research Council of UK, and the International Energy Agency. Therefore, a review dedicated to the chemisorption heating technology for cold climates is greatly needed.

The scope of this review is CSHP for heat production under cold-climate conditions. Most such systems found in the literature are type-I heat pumps, with a few recent ones using type-II configurations. This paper begins by briefly introducing the basic principles of CSHP. It then summarizes the latest studies and developments on sorbent materials and the design and cycle configurations of CSHP systems. Finally, it concludes with discussions on future research needed to improve the performance of CSHP systems for cold-climate heating applications.

2. Basics of ammonia-based chemisorption heat pumps

In an ammonia-based CSHP system, the thermal effects of chemisorption reaction and ammonia phase change are applied to produce useful heating in sorbent- and ammonia-containing heat exchangers under different temperatures and pressures. Fig. 1 illustrates the schematic and working procedure of a basic CSHP cycle with a sorbent-containing adsorber and a heat exchanger acting as a condenser or an evaporator. The CSHP cycles between the desorption and adsorption modes. In the desorption mode, heat from a high-temperature source, Q_{des}, is supplied to the adsorber. The ammonia-salt compound is heated and starts to decompose, releasing ammonia vapor. The ammonia vapor flows into the condenser to be cooled by the medium-temperature heat sink and condense, releasing heat, Q_{cond}. The desorption mode ends with the sorbent in the adsorber exhausted of ammonia and the ammonia accumulating in liquid phase in the condenser. The adsorption mode then starts by cooling the dry sorbent in the adsorber. The adsorber pressure decreases to below the ammonia-containing heat exchanger (acting as evaporator) and drives evaporation of the liquid ammonia, which continuously extracts heat, Q_{evap}, from the low-temperature heat source. The ammonia vapor flows into the adsorber and bonds with the sorbent, releasing heat, Q_{ads}, to the medium-temperature heat sink. The adsorption mode ends upon exhaustion of ammonia in the evaporator, and the system switches back to the desorption mode for continued operation.

In the basic chemisorption heat pump cycle, the heat input to the system (Q_{in}) is the desorption heat (i.e. Q_{des}), and the useful heat output (Q_{ht}) is the heat output in the condenser and adsorber at the heat supply temperature (i.e., Q_{cond} and Q_{ads}). The system performance of the CSHP can be evaluated by two parameters: (1) the COP as the ratio of useful heating produced over the high-temperature heat input in (1), and (2) the specific heating power (SHP) as the ratio of heating output over the system mass (m_{sys}) averaged over the time lapse of a complete desorption-adsorption cycle (t_{cyc}) in (2).

$$COP_{ht} = \frac{Q_{ht}}{Q_{in}} = \frac{Q_{cond} + Q_{ads}}{Q_{des}}. \quad (1)$$

$$SHP = \frac{1}{t_{cyc}} \cdot \frac{Q_{ht}}{m_{sys}}. \quad (2)$$

The performances of CSHP systems are significantly influenced by the sorbent material, component design, and the system configuration. To achieve a high COP and SHP, the CSHP system needs to use sorbents with high sorption capacity, an adsorber that supports high heat and mass transfer rate, and system cycles that fully use energy input to

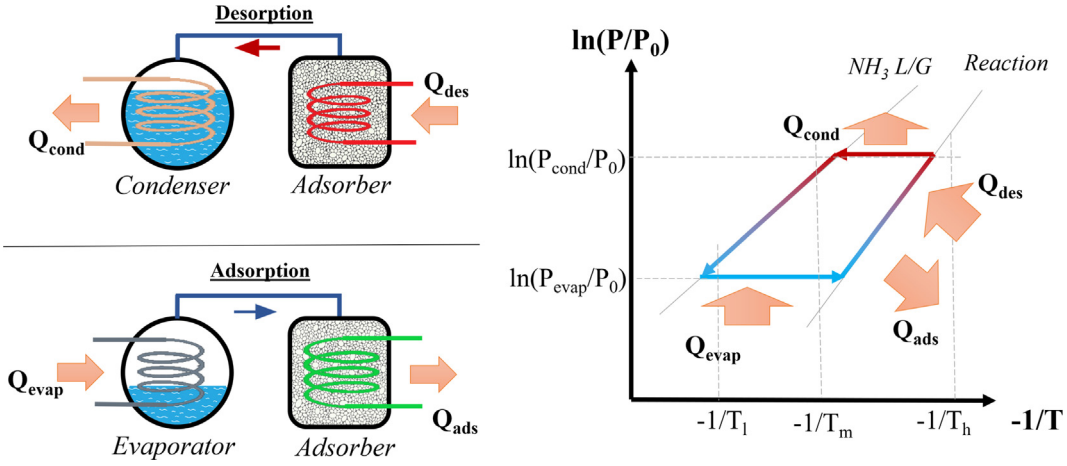

Fig. 1. System schematic (left) and operation on the Clapeyron diagram (right) of a basic chemisorption heat pump cycle.

produce useful heating. Meanwhile, since the heat flow, sorbent mass, and cycle time in Eqs. (1) and (2) are related to multiple parameters of material, component, and system design and operation, the changes that improves the COP might not necessarily increase the SHP. The state of the art of these critical aspects for high-performance CSHP cold-climate heating systems are reviewed in the following sections.

3. Sorbent materials

The viability and performance of the CSHPs are largely determined by the properties of the sorbent salt, where a suitable equilibrium and large sorption capacity are preferred. A sorption material has suitable equilibrium means that when the material is at the driving heat temperature, the saturation temperature corresponding to the equilibrium vapor pressure of the material is above the heat rejection temperature; meanwhile, when the material is at the heat rejection temperature, the saturation temperature corresponding to the equilibrium vapor pressure of the material is below the cold ambient temperature. As the result, the sorption material is able to support continuous ammonia condensation and evaporation. An ideal chemisorption reaction adsorbs a large amount of ammonia to extract heat under freezing temperatures and reject heat at a high temperature through ammonia condensation and adsorption reaction.

In practical operations, the CSHP performance is also significantly affected by the heat and mass transfer rate in the sorbent, as well as the extent of reaction completion. Therefore, the sorbent salts in CSHP systems were often combined with thermally conductive porous matrix materials to enhance heat and mass transfer performance. This section summarizes the sorbent salt and matrix materials commonly used in published studies.

3.1. Sorbent salts and chemisorption reactions

In an ammonia-based chemisorption reaction, a neutral ammonia molecule is adsorbed by the sorbent salt by donating a pair of electrons to the metal ion in the sorbent salt and forming a complex compound with coordinate covalent bond while releasing the bonding energy as heat. On the other hand, when the compound is heated at a high temperature, the bond is broken and ammonia is desorbed from the sorbent [45]. A generic reaction formula between ammonia and metal chloride (MCl_x) can be written as Eq. (3) [46]. In the reaction formula, M is the metal in the sorbent salt capable of bonding with ammonia molecules and forming complex compounds. $MCl_x{\cdot}n_1NH_3$ and $MCl_x{\cdot}(n_1-n_2)NH_3$ are both solid-phase ammoniate compounds. n_2 is the mole of ammonia that reacts with each mole of ammoniate salt. The reaction can be simply denoted as $MCl_x{\cdot}n_1/(n_1-n_2)$. The reaction in the forward direction, i.e. decomposition of $MCl_x{\cdot}n_1NH_3$ requires heat input; on the other hand, the reaction in the backward direction, i.e. the synthesis of $MCl_x{\cdot}n_1NH_3$ releases heat.

$$MCl_x{\cdot}n_1NH_3(s) \leftrightarrow MCl_x{\cdot}(n_1-n_2)NH_3(s) + n_2NH_3(g). \quad (3)$$

Ammonia molecules can form complex compounds with salts of both main group metals (e.g., Li, Ca, and Na) and transition metals (e.g., Co, Mn, and Ni) [47], and metal halide salts (e.g., $CaCl_2$ and NaBr) are the most commonly used sorbent for ammonia-based chemisorption reactions. The number of ammonia molecules bonded to one metal ion is determined by the type of metal ion, as well as the chemisorption reaction equilibrium, which also leads to different sorption capacities between salts. For example, one mole Ni^{2+} and Ca^{2+} in $NiCl_2$ and $CaCl_2$ can bond with six and eight moles of NH_3, which corresponds on a mass basis to maximum sorption capacities of 0.79 kg/kg and 1.22 kg/kg of salt, respectively. Some salts have only one stable complex compound corresponding to one reaction, such as $BaCl_2$-8/0; other salts can form multiple stable compounds at different temperatures and pressures, such as $CaCl_2$-8/4 and $CaCl_2$-4/2.

The equilibrium vapor pressure of a chemisorption reaction is usually considered mono-variant as a function of the sorbent temperature expressed by the van 't Hoff equation (Eq. (4)). The coefficients in Eq. (4), ΔH and ΔS, are often associated to the reaction enthalpy and entropy per mole of NH_3 under the standard state, albeit they are usually derived from the linear equilibrium curve (e.g. in [48–50]) instead of directly measured. R is the gas constant of 8.314 J/(mol·K), T_s is the sorbent temperature in Kelvin, K_p is the equilibrium constant of the reaction, P_{eq} is the equilibrium vapor pressure in Pascal. The reference pressure P_0 in chemical reactions is usually defined as 1 bar, 1 atm, or 100 kPa [51–54]. However, the reference pressure was assumed to be 1 Pa for the equilibrium of ammonia chemisorption reactions reported in [55,56] and listed in Table 1. The different values adopted for the reference pressure will not affect the value of the reaction enthalpy obtained from linear fitting, but will lead to an offset to the value of the reaction entropy.

$$\ln\left(\frac{P_{eq}}{P_0}\right) = \ln(K_p) = \frac{-\Delta H}{R{\cdot}T_s} + \frac{\Delta S}{R} \quad (4)$$

The reaction equilibrium can be illustrated as straight lines on the Clapeyron diagram, as shown in Fig. 2. The vapor–liquid equilibrium of pure ammonia is shown in the left of the chart, and the lines to the right of the ammonia equilibrium represent the vapor–solid equilibria of 66 chemisorption reactions between ammonia and halide salts/compounds. The reaction enthalpy and entropy of these reaction were

Table 1
Summary of chemisorption reactions between ammonia and metal halide salts ordered by the equilibrium temperature when the pressure is 40 kPa. The labels correspond to the order of the equilibrium lines on Fig. 2 from left to right. Data from [37,55,56].

Label	Reaction	Label	Reaction	Label	Reaction	Label	Reaction
1	$CuCl_2$-10/6	18	NaI-4.5/0	35	LiCl-1/0	52	$NiBr_2$-6/2
2	$ZnCl_2$-10/6	19	$SrCl_2$-8/1	36	$FeCl_2$-6/2	53	$CaCl_2$-1/0
3	$SnCl_2$-9/4	20	$BaBr_2$-8/4	37	SrI_2-6/2	54	NiI_2-6/2
4	KI-4/1	21	$CaCl_2$-4/2	38	$MnBr_2$-6/2	55	$MnCl_2$-2/1
5	LiBr-5/4	22	$BaBr_2$-4/2	39	$CuCl_2$-3.3/2	56	$MgCl_2$-2/1
6	NH_4Cl-3/0	23	$ZnCl_2$-6/4	40	BaI_2-2/0	57	$FeCl_2$-2/1
7	$PbCl_2$-8/3.25	24	LiCl-3/2	41	$CoCl_2$-6/2	58	$CoCl_2$-2/1
8	CaI_2-8/6	25	$PbCl_2$-2/1.5	42	$PbCl_2$-1/0	59	$NiCl_2$-2/1
9	NaBr-5.25/0	26	$SrBr_2$-8/2	43	$MgCl_2$-6/2	60	$ZnCl_2$-2/1
10	$PbBr_2$-5.5/3	27	BaI_2-6/4	44	$FeBr_2$-6/2	61	$MnCl_2$-1/0
11	LiCl-4/3	28	$PbCl_2$-1.5/1	45	CaI_2-6/2	62	$FeCl_2$-1/0
12	$SnCl_2$-4/2.5	29	BaI_2-4/2	46	$CoBr_2$-6/2	63	$MgCl_2$-1/0
13	$BaCl_2$-8/0	30	LiCl-2/1	47	$CaCl_2$-2/1	64	$CoCl_2$-1/0
14	$PbCl_2$-3.25/2	31	$MnCl_2$-6/2	48	$NiCl_2$-6/2	65	$NiCl_2$-1/0
15	$PbBr_2$-3/2	32	$CaBr_2$-6/2	49	MnI_2-6/2	66	$ZnCl_2$-1/0
16	PbI_2-5/2	33	$ZnCl_2$-4/2	50	FeI_2-6/2		
17	$CaCl_2$-8/4	34	$CuCl_2$-5/3.3	51	$MgBr_2$-6/2		

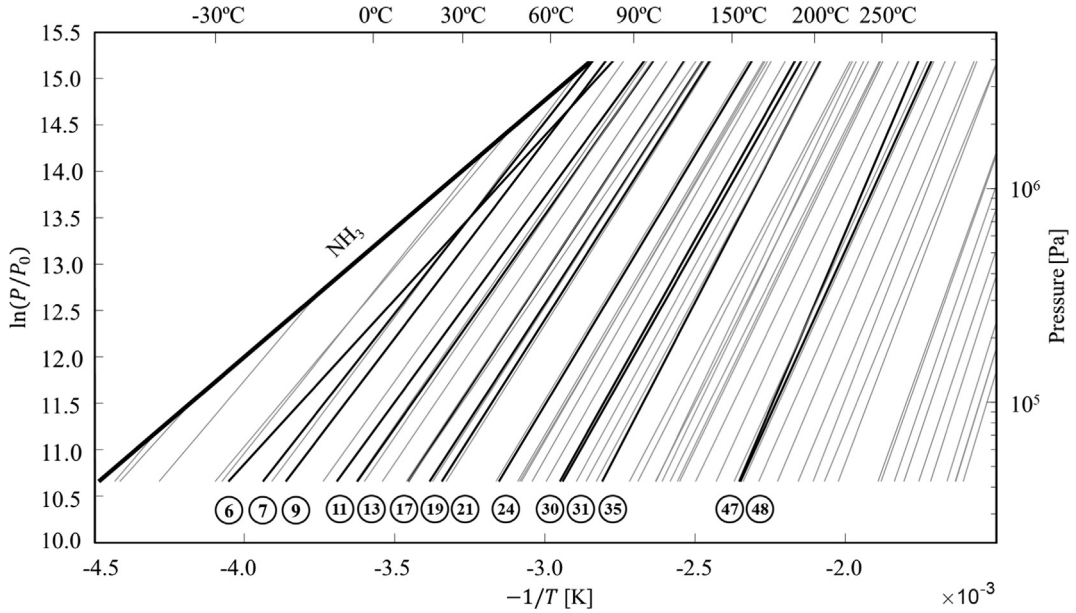

Fig. 2. Ammonia-based chemisorption reaction equilibrium on the Clapeyron chart. The labels of all lines from left to right are listed in Table 1. Commonly used reaction are shown in bold: (6) NH_4Cl-3/0, (7) $PbCl_2$-8/3, (9) NaBr-5.25/0, (11) LiCl-4/3, (13) $BaCl_2$-8/0, (17) $CaCl_2$-8/4, (19) $SrCl_2$-8/1, (21) $CaCl_2$-4/2, (24) LiCl-3/2, (30) LiCl-2/1, (31) $MnCl_2$-6/2, (35) LiCl-1/0, (47) $CaCl_2$-2/1, (48) $NiCl_2$-6/2. Data from [37,55,56].

collected from [37,55,56]. 14 commonly used reactions are highlighted with bold lines in Fig. 2 including $CaCl_2$-8/4 [57], $BaCl_2$-8/0 [16,57], $MnCl_2$-6/2 [16,58], $SrCl_2$-8/1 [16], $NiCl_2$-6/2 [16,57], NH_4Cl-3/0 [58], LiCl [59], and NaBr-5.25/0 [60]. These reactions are popular choices in chemisorption systems [11,39,55,61] for cold-climate heating applications.

The complete list of the 66 reaction in the left–right order in Fig. 2 is in Table 1 ordered by the equilibrium temperature when the pressure is 40 kPa. The reaction enthalpy and entropy from [37,55,56] are listed in Table 2. The specific sorption capacity of a reaction in Table 2 is determined by the reaction stoichiometry and the molar mass of the salt.

The reactions shown in Table 2 are used in CSHP systems in two different arrangements: (1) conventional adsorption coupling the adsorption/desorption reactions with evaporation and condensation of pure ammonia such as the basic cycle in Fig. 1, and (2) resorption [62,63] where two different ammoniate compounds are coupled to extract heat with the desorption reaction of the low-temperature salt and supply heat with the adsorption reaction of both the high-temperature and low-temperature salts.

The viability of a reaction for the cold-climate heating application is determined by its equilibrium pressure relative to the ammonia pressure under the cold ambient and the hot heat source. The low-temperature heat extraction—either through ammonia evaporation or desorption reaction—happens toward the left of Fig. 2 with a low vapor pressure; on the other hand, the heat rejection through ammonia condensation or adsorption reaction needs to happen at a sufficiently high temperature toward the right of Fig. 2 with a high vapor pressure. Moreover, a deviation from the equilibrium is necessary for the chemical reaction to occur [55,61]; therefore, the desorption equilibrium pressure needs to be higher than the pressure around the ammoniate compound, and vice versa for adsorption. Such temperature or pressure deviation is often referred to as the equilibrium drop and indicates the driving force of the chemisorption reactions [55].

3.1.1. Reactions for conventional adsorption configuration

In the adsorption configuration, heat extraction is accomplished by ammonia evaporation at low temperature, and heating output is from ammonia condensation and adsorption reaction. Therefore, suitable chemisorption reactions under this configuration need to adsorb ammonia at low pressure but high temperature to supply heat during adsorption.

The reactions with low desorption and adsorption temperatures are located toward the left in Fig. 2. Driven by low-temperature heat sources such as solar heat, these reactions include $BaCl_2$-8/0 [64–68], NaBr-5.25/0 [67], NH_4Cl-3/0 [60], and LiCl-4/3 [69]. However, the adsorption temperatures of these reactions corresponding to freezing evaporation temperatures are usually around 20–30 °C, which is much lower than the required temperature for typical heating applications (40–55 °C) [16].

Higher heat source temperatures enable reactions toward the middle of Fig. 2 with higher adsorption temperatures. Reactions based on $CaCl_2$ have been used in many deep-freezing applications [67,68,70–73], and they are also capable of generating heat at high temperatures. With a heat source temperature of 120 °C, $CaCl_2$-8/4 was used by Vasiliev et al. [57] to produce heating at 50 °C while extracting heat at below freezing temperatures. As the heat source temperature gets higher, $SrCl_2$-8/1 becomes available and is used for heating at 55 °C in research from Pons [16]. The reaction equilibrium of $MnCl_2$-6/2 and $NiCl_2$-6/2 are located toward the right of Fig. 2; therefore, they can adsorb ammonia and produce heating under quite low vapor pressures. On the other hand, they require higher driving temperatures (> 240 °C), as simulated by Pons [16] for high-COP heating under −15 °C ambient temperature.

3.1.2. Salts for resorption arrangement

In resorption, heat extraction from the cold ambient is accomplished by the desorption reaction of the low-temperature salt (LTS) at low vapor pressures. The equilibrium pressures of the LTSs need to be high enough to provide the necessary equilibrium drop between the LTS desorption and the high-temperature salt (HTS) adsorption. Therefore, reactions located on the bottom left of Fig. 2 are often selected as the LTS in resorption systems to operate at low-temperature and low-pressure conditions.

NH_4Cl-3/0, NaBr-5.25/0, and $BaCl_2$-8/0 are the most commonly used LTSs with high sorption capacities in chemisorption systems. $BaCl_2$-8/0 was used in the Pons et al. simulation of a resorption heat pump [16] as the LTS for heat production under 5 °C ambient temperatures. Vasiliev et al. [57] built and tested a resorption system using

Table 2
Summary of the sorption capacity, reaction enthalpy and entropy of chemisorption reactions between ammonia and metal halide salts. Data from [37,55,56]

Salt	Molar mass [g/mol]	Reaction	Specific sorption cap. [kg/kg salt]	Reaction enthalpy [J/mol]	Reaction entropy [J/(mol·K)]	Reaction	Specific sorption cap. [kg/kg salt]	Reaction enthalpy [J/mol]	Reaction entropy [J/(mol·K)]
LiCl	42.3	4–3	0.401	36,828	224.6	2–1	0.401	48,128	230.6
		3–2	0.401	44,780	229.8	1–0	0.401	51,894	234.4
NH_4Cl	53.4	3–0	0.955	29,433	207.9	—	—	—	—
$CoCl_2$	94.3	6–2	0.721	53,987	228.1	1–0	0.18	88,303	232.8
		2–1	0.18	78,134	232.17	—	—	—	—
$MgCl_2$	95.1	6–2	0.715	55,661	230.63	1–0	0.179	87,048	230.88
		2–1	0.179	74,911	230.3	—	—	—	—
$CaCl_2$	110.8	8–4	0.614	41,013	230.3	2–1	0.153	63,193	237.34
		4–2	0.307	42,269	229.92	1–0	0.153	69,052	234.14
$MnCl_2$	125.7	6–2	0.541	47,416	228.07	1–0	0.135	84,202	233.18
		2–1	0.135	71,019	232.35	—	—	—	—
$FeCl_2$	126.6	6–2	0.537	51,266	227.99	1–0	0.134	86,880	233.01
		2–1	0.134	76,167	231.91	—	—	—	—
$NiCl_2$	129.5	6–2	0.525	59,218	227.75	1–0	0.131	89,810	233.01
		2–1	0.131	79,515	232.17	—	—	—	—
$CuCl_2$	134.5	10–6	0.506	31,387	227.72	3.3–2	0.164	56,497	237.22
		5–3.3	0.215	50,241	230.75	—	—	—	—
$ZnCl_2$	136.2	10–6	0.499	29,588	219.23	2–1	0.125	80,352	229.72
		6–4	0.25	44,779	230.24	1–0	0.125	104,625	227.79
		4–2	0.25	49,467	230.24	—	—	—	—
$SrCl_2$	158.4	8–1	0.751	41,432	228.8	—	—	—	—
$SnCl_2$	189.6	9–4	0.448	31,806	224.86	4–2.5	0.134	38,920	229.82
$BaCl_2$	208.2	8–0	0.653	38,250	227.25	—	—	—	—
$PbCl_2$	278	8–3.25	0.29	34,317	223.76	1.5–1	0.031	47,290	232.5
		3.25–2	0.076	39,339	230.27	1–0	0.061	55,660	231.04
		2–1.5	0.031	46,035	230.89	—	—	—	—
LiBr	86.8	5–4	0.196	33,689	225.9	—	—	—	—
NaBr	102.9	5.25–0	0.867	35,363	225.2	—	—	—	—
$MgBr_2$	184.1	6–2	0.369	63,612	230.2	—	—	—	—
$CaBr_2$	199.8	6–2	0.34	48,965	230.4	—	—	—	—
$MnBr_2$	214.7	6–2	0.317	53,066	228.3	—	—	—	—
$FeBr_2$	215.6	6–2	0.315	55,828	228.1	—	—	—	—
$NiBr_2$	218.5	6–2	0.311	64,240	227.2	—	—	—	—
$CoBr_2$	218.7	6–2	0.311	58,590	227.5	—	—	—	—
$SrBr_2$	247.4	8–2	0.412	45,617	229.3	—	—	—	—
$BaBr_2$	297.1	8–4	0.229	41,850	229.8	4–2	0.114	42,687	230.7
$PbBr_2$	367	5.5–3	0.116	37,665	229.4	3–2	0.046	39,758	229.4
NaI	149.9	4.5–0	0.51	39,339	224.5	—	—	—	—
KI	166	4–1	0.307	32,015	219.8	—	—	—	—
CaI_2	293.8	8–6	0.115	35,991	229.3	6–2	0.231	58,590	231
MnI_2	308.7	6–2	0.22	59,301	227.4	—	—	—	—
FeI_2	309.6	6–2	0.22	60,683	227.5	—	—	—	—
NiI_2	312.5	6–2	0.218	65,453	224.1	—	—	—	—
SrI_2	341.4	6–2	0.2	52,731	230.5	—	—	—	—
BaI_2	391.1	6–4	0.087	46,454	231.6	4–2	0.087	47,291	230.3
		2–0	0.087	56,079	235	—	—	—	—
PbI_2	461	5–2	0.111	40,595	229.1	—	—	—	—

$BaCl_2$-8/0 as the LTS to produce 50 °C heating while cooling at 0 °C. NH_4Cl was used as the LTS in a resorption system for simultaneous heating and cooling by Xu et al. [58] where the LTS extracts heat at −5 to 0 °C and rejected heat at 70–80 °C with a cycle time of 6 h. NaBr-5.25/0 was used in a resorption system for combined heating and cooling from Oliveira [60], where the combined heating and cooling performance saw a significant increase from cooling at −5 °C and heating at 50 °C to cooling at 10 °C and heating at 70 °C. The HTS in resorption needs to adsorb ammonia at a very low pressure and reject heat at a high temperature; therefore, it often has a relatively high operation temperature toward the right in Fig. 2. $NiCl_2$-6/2 and $MnCl_2$-6/2 are used in [16,57,58,60] as HTS in resorption systems.

3.1.3. Challenges in chemisorption reaction and sorbent salt

- *Resorption Low-Operating-Pressure Limit*

A heating system based on the resorption configuration theoretically has a higher COP than the adsorption configuration under the same operating conditions as simulated by Goetz et al. and Wang et al. [61,70]. Meanwhile, unlike the adsorption configuration that nearly always operates above atmospheric pressure, the pressure during the LTS desorption in resorption is usually below atmospheric pressure. Such low pressure was found to limit the sorption reaction rate in some studies [70,74]. Wang et al. [70] tested a $BaCl_2$-$MnCl_2$ resorption system cooling at −5 °C, and only 0.33 kg/kg sorption capacity was observed in 20 min of adsorption compared with the theoretical sorption capacity of 0.65 kg/kg. The difference was attributed to the very low pressure (< 0.03 MPa) during LTS desorption, which limited the vapor transfer in the sorbent and slowed down the reaction rate. A similar conclusion was drawn by Goetz et al. from detailed simulation that the vapor diffusion in the sorbent at low operating pressures was very limited, reducing the equilibrium drop and the reaction rate [61]. Bao et al. [75] tested a resorption cold box with NH_4Cl/$MnCl_2$ cooling to −25 °C. After 3 h, the adsorption reaction progressed to only 31% with 0.29 kg/kg sorption capacity compared with the theoretical 0.9 kg/kg. In contrast, Bao et al. [76] tested resorption refrigeration using the same $MnCl_2$-NH_4Cl pair cooling at −5 °C and rejecting heat at 30 °C, and a sorption capacity of more than 80% was observed. On the other hand, resorption systems operating around 0.1 MPa were

reported by Xu et al. and Jiang et al. [58,73] with relatively high completion. Goetz et al. [61] set a pressure limit of 0.1 bar for resorption cycle models.

- *Hysteresis*

As described in the van 't Hoff equation (4), the equilibrium vapor pressure of chemisorption reactions is generally considered monovariant as the function of only the sorbent temperature. However, the bivariant behavior, or hysteresis, of the equilibrium of some ammonia-metal halide chemisorption working pairs was identified by Goetz and Marty [77], where the decomposition of ammoniate $MnCl_2$ took a higher temperature to occur than the synthesis reaction under the same pressure. The hysteresis effect of ammonia-halide salt reactions was also reported for $MnCl_2$ [78], $CoCl_2$ [79,80], $BaCl_2$ [81], LiCl [59], $CaCl_2$ [82], NH_4Cl [82], and $FeCl_2$ [83].

Wu et al. [84] measured the hysteresis of ammoniate $SrCl_2$ adsorption and desorption, where the $SrCl_2$ salt was embedded in porous expanded graphite and kept at 0.615 MPa while its temperature varied between 65 °C and 90 °C to trigger desorption and adsorption reactions. As shown in Fig. 3, when the temperature increases from 65 °C, the reactions of $SrCl_2$-8/2 and $SrCl_2$-2/1 start in the desorption direction at ~73 °C and 92 °C, respectively. However, when the temperature decreases from 95 °C, the adsorption-direction reactions start at ~74 °C and 70 °C, respectively. As highlighted in the figure, there is a 3 °C and 18 °C difference between equilibrium of the adsorption and desorption of the same reaction.

Trudel et al. [85] observed a similar behavior when measuring the equilibrium of $CoCl_2$-6/2 reaction. Both Zhong et al. and Trudel et al. attributed the hysteresis to the solid phase change and expansion–contraction of the salt crystal during synthesis-decomposition reactions. The additional energy required for desorption was connected to the work of expansion of the crystal lattice during adsorption.

Though the hysteresis phenomenon is not yet fully understood, studies have been carried out to model [82] and mitigate [86,87] the hysteresis effect using a mixture of sorbents NH_4Cl, $CaCl_2$, and $MnCl_2$ with an identified optimal mixing portion for refrigeration operation.

Table 3 lists the reactions used in cold-climate CSHP heating systems in the literature.

3.2. Porous matrix material

Besides the salt's adsorption capacity and feasible operating temperature and pressure, the performance of the chemisorption system is also significantly influenced by the heat and mass transfer within the sorbent. Conventional pure halide salts are usually available in granular form with limited heat and mass transfer rates. For example, the thermal conductivity of granular $CaCl_2$ and its ammoniates ranges between 0.0065 W/(m·K) and 0.145 W/(m·K) [39,88]. Moreover, the swelling and agglomeration of the bulk salt during adsorption deteriorates the sorption capacity and vapor transfer across the sorbent [22]. Therefore, composite sorbent materials were developed that consist of salt and highly conductive porous materials such as activated carbon (AC) and graphite. The composite sorbents demonstrated significant improvement of the sorbent heat and mass transfer performance (e.g., 1.7–17.4 W/(m·K) for expanded graphite-$CaCl_2$ composite sorbent [67,89]) while also eliminating the mass transfer deterioration due to agglomeration.

Under proper temperatures and pressures, the sorbent salts can react with ammonia vapor upon contact. However, the salt grains have very poor heat and mass transfer performances, and they tend to agglomerate together and create a large nonporous bulk during adsorption, preventing the center salts from reacting with ammonia and reducing the adsorption capacity [20,90]. The salt grains also swell during adsorption, which could potentially damage the confinement of the heat exchanger.

Porous matrix materials were thus introduced to overcome the aforementioned issues of the salt grain. The porous matrix materials offer large surface area to host sorbent salts as sites for the vapor–solid reaction. Matrix materials such as expanded graphite have a high thermal conductivity that allows fast heat propagation through the bulk sorbent. The porous matrix also helps mitigate the performance deterioration of ammoniate salt agglomeration and swelling. The composites of the porous matrix and salt during adsorption/desorption reactions are illustrated in Fig. 4.

The key parameters for a matrix material are therefore its porosity, permeability, and thermal conductivity. The most common porous matrix materials studied and applied in chemisorption systems are expanded graphite (EG) [60,64,67,68,74–76,89–104], AC [22,72,105–107], AC fiber (ACF) [57,108–112], and other materials including multiwall carbon nanotube (MWCNT) [42,113] and expanded vermiculite (EVM) [81]. The proper mass ratio between the salt and matrix material, the composite density, and the direction of consolidation also affect the heat and mass transfer performance of the porous matrix.

3.2.1. Expanded graphite

EG, also referred to as expanded natural graphite (ENG), is prepared by electrochemically and chemically treating (oxidizing) natural graphite to force apart the crystal lattice and create abundant micropores for salt impregnation and channels for vapor transfer. The salt can be embedded into the pores of EG by (1) mixing EG with a salty solution, (2) drying the composite, and (3) compressing the composite as shown in Fig. 5. This impregnation procedure is also used in graphite [67,94] and other composite sorbent preparations.

The interconnected flake structure of EG provides high thermal conductivity (4–40 W/m·K) and high gas permeability (10^{-14}–10^{-12} m^2) [114] while the creases of the flakes provide a large surface area to host ammoniate salt. Wang et al. [100] also measured the thermal conductivity of EG without salt to be ~1.7 to 4 W/(m·K).

One of the early EG-based composites, IMPEX, was developed at CNRS-IMP in France and has thermal conductivities as high as 4–40 W/(m·K) [90,91]. The thermal conductivity of the EG-salt composite sorbent is strongly related to the EG/salt ratio and its density after consolidation. Han et al. [92] reported that the effective thermal conductivity of $CaCl_2$ ammoniates increased with a higher EG ratio, higher density, and more ammonia in the compound. Jiang et al. [93] measured the thermal conductivity of the $SrCl_2$-EG compound ranging from 0.44 W/m·K (500 kg/m^3) to almost 2.94 W/m·K (800 kg/m^3). Wang et al. [94] measured the thermal conductivity of $CaCl_2$-EG composite to be ~7.02–9.2 W/(m·K) at densities of 1100–1300 kg/m^3.

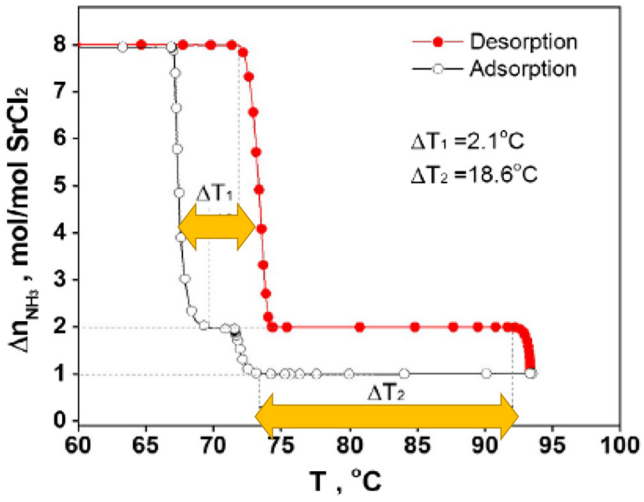

Fig. 3. Hysteresis of ammoniate $SrCl_2$ plotted by Wu et al. [84].

Table 3
Summary of chemisorption reactions used in existing cold-climate chemisorption heat pump heating systems. LTS = low-temperature salt; HTS = high-temperature salt.

Salt	Reaction	Max. sorption capacity [kg/kg salt]	Actual sorption capacity [kg/kg salt]	Operating temperatures [°C]	Reference
$CaCl_2$	8/2	0.919	0.6	120/50/−18	Vasiliev 2001 (exp) [57]
$SrCl_2$	8/1	0.751	—	135/55/5	Pons 1999 (sim) [16]
			—	180/55/−15	Pons 1999 (sim) [16]
$MnCl_2$	6/2	0.541	—	240/55/−15	Pons 1999 (sim) [16]
$NiCl_2$	6/2	0.525	—	300/55/−15	Pons 1999 (sim) [16]
NH_4Cl (LTS)	3/0	0.953	0.743	140/70–80/−5–5	Xu 2011 (exp) [58]
$BaCl_2$ (LTS)	8/0	0.654	—	231/50/0	Vasiliev 2001 (exp) [57]
NaBr (LTS)	5.25/0	0.866	—	165/50/−5	Oliveira 2009 (exp) [60]
$MnCl_2$ (HTS)	6/2	0.541	0.332	140/80/−	Xu 2011 (exp) [58]
			—	150/55/5	Pons 1999 (sim) [16]
			—	245/55/5	Pons 1999 (sim) [16]
			—	165/50/−5	Oliveira 2009 (exp) [60]
$NiCl_2$ (HTS)	6/2	0.525	—	240/50/0	Vasiliev 2001 (exp) [57]

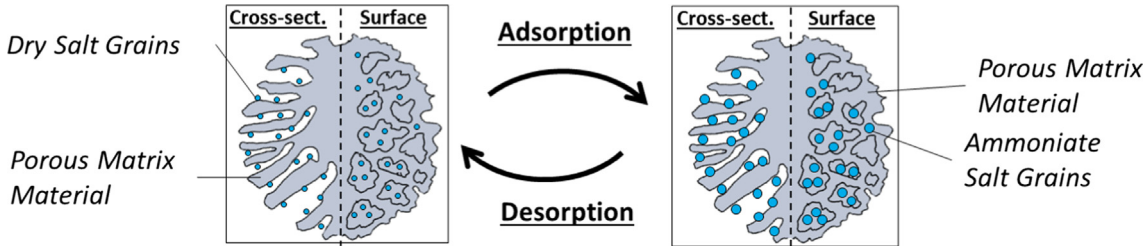

Fig. 4. Salt-matrix composite in adsorption and desorption reactions.

Gas permeability, on the other hand, declines with increasing density. Tian et al. [89] reported a decrease of permeability of $CaCl_2$-EG compound from 3.16×10^{-11} m^2 to 8.61×10^{-13} m^2 when the density increased from 400 kg/m^3 to 550 kg/m^3. Han and Lee. [115] measured the permeability of EG composites of $CaCl_2$, $MnCl_2$, and $BaCl_2$ at different densities, EG/salt ratios, and ammoniate states and found a similar trend.

Because EG is inexpensive and the process to embed salt into it is mature, it has been widely used as the matrix material for a variety of sorbent salts in numerous chemisorption systems [60,64,67,68,74–76,89,93,95–100].

To further enhance the heat transfer performance of ENG, Wang et al. [101] introduced ENG treated with sulfuric acid (ENG-TSA): the sulfuric acid is first intercalated in the graphite flakes; then, the graphite is exfoliated by heating in a flame to form ENG with densities as low as 5–6 kg/m^3 compared with the normal ENG density of 20–50 kg/m^3 [89]. The sulfuric acid treatment improved the thermal conductivity of the ENG-TSA up to 15.4 W/(m·K) for Jiang et al. [67], and 337 W/(m·K) for Wang et al. [101]. ENG-TSA was further used by Jiang et al. [102,103] in several experimental tests in which the effect of higher heat transfer capacity was investigated. Zhao et al. [104] reported 45 times higher conductivity and 50% volumetric cooling power enhancement by using the ENG-TSA composite over granular AC for the ammonia-AC physical adsorption system.

Fig. 6 shows the scanning electron microscopy (SEM) picture of EG and ENG-TSA from Zhao et al. [104].

For both EG and ENG-TSA, the direction of consolidation compression in the matrix-salt composite significant influences the composite heat and mass transfer performance. The thermal conductivity and permeability of EG [100] and ENG-TSA [101] parallel (disk) and

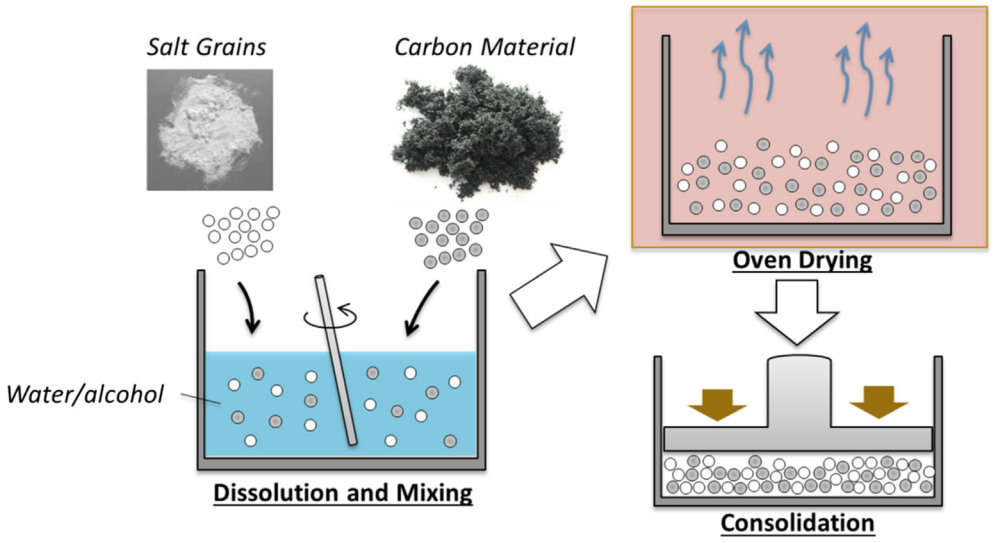

Fig. 5. Steps of preparing consolidated salt composite sorbent.

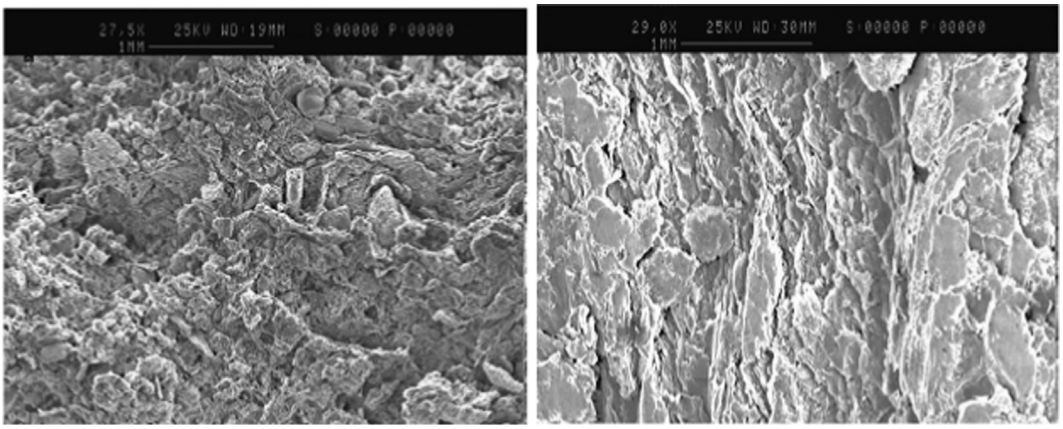

Fig. 6. Scanning electron microscopy of expanded graphite (left) and expanded graphite treated with sulfuric acid (right) [104].

perpendicular (plate) to the direction of compression were measured. Both studies used consolidated graphite without salt embedment, and the results are shown in Table 4. The disk thermal conductivity has a plateau with the increasing density after compression compared with the monotonic increase in plates. The plates of both matrices showed higher thermal conductivity than the disks at similar densities as the microlayers after compression in the plates follow the heat transfer direction [101]. The permeability decreased with higher density as compression reduced pore size and interconnection of pores [100]. As the result, compression perpendicular to the heat and mass transfer direction led to a higher transfer rate, while a higher compression density generally improved thermal conduction but reduced mass diffusion in the sorbent.

The limitation of a chemisorption reaction under low operation pressures presented in Section 3.1.2 was also discussed in the studies of the EG-salt composite sorbents from the matrix material perspective. Lu et al. [91] analyzed the reaction progression of $MnCl_2$ in an EG composite with a validated detailed model and concluded that when constraint pressure gets below 1 bar (0.1 MPa), the sorbent permeability great influences the reaction completion. Because the sorbent permeability decreases with higher density after consolidation, Han et al. [115] suggested using a sorbent with a density below 200 kg/m^3 for low-pressure (i.e., low-temperature) applications to avoid a significantly reduced mass transfer rate. Moreover, Lu and Mazet [116] compared the modeled and measured reaction progression and suggested that the composite permeability varies with the progression of the chemisorption reaction.

3.2.2. Activated carbon

AC is produced from natural materials such as acorn and coconut shells. A typical preparation process starts with crushing and sieving the raw material to control the particle dimension; then, the particles are chemically activated by immersion in salt solutions before being heat-treated at high temperatures; finally, the remaining salt in the particles are rinsed off with acid and distilled water and dried [117]. Such preparation procedure results in a highly porous surface structure, as shown in Fig. 7 from Saka [117]. The AC can then be impregnated with sorbent salt to form a consolidated composite through a similar process as described for EG-salt composites.

The AC-salt composites were used in a series of studies on a chemisorption ice making system [72,105,106] and a refrigeration system [107] and demonstrated improved sorption performance. Because AC can physically adsorb vapor ammonia as well, using AC as the matrix material for composite sorbent can increase the sorption capacity [22]. However, the thermal conductivity of AC (0.35–0.4 W/(mK) for granular AC [118]) is considerably lower than EG because of the lack of interconnected plate structure; therefore, composite sorbents using AC are less seen in recent literatures.

Fig. 7 illustrates the SEM picture of the microstructure of AC from Saka [117].

3.2.3. Activated carbon fiber

Carbon fibers (CFs) are fiber-shaped materials containing more than 92% carbon content in a non-graphitic state with a diameter of 5–10 μm [119]. ACFs are prepared from general-purpose CFs by heat treatment to achieve high porosity and well-defined porous structure [120,121]. The specific surface area of ACFs can be ~2000 m^2/g [119], making them good candidates to host large amounts of salt for composite sorbent materials.

A single CF has a very high thermal conductivity of 150–1100 W/m·K [108]. Dellero et al. [108] developed and tested an ACF-$MnCl_2$ composite of the impregnated carbon fiber (ICF) and the graphite fiber intercalation (GFIC). The ICF was prepared by immersing CF in an alcoholic solution of $MnCl_2$ before heating and vaporizing the alcohol to let the salt adhere to the fiber surface. The GFIC was prepared by intercalation of $MnCl_2$ salt into the graphitized fibers. The intercalation process involves impregnating sulfuric and nitric acid in graphite fiber and heating it to a high temperature before impregnating the $MnCl_2$ salt in between the graphite layers. Both ACF-$MnCl_2$ composite sorbents improved in reaction kinetics compared with granular $MnCl_2$. However, it was found that the salt in ICF adhered less to the fiber after a few cycles, and the preparation time was quite long.

Table 4
Anisotropic conductivity and permeability test; illustration generated according to [100,101].

Sample	Compression direction*	Dominant micro-layer direction*	Expanded graphite [100]		Expanded natural graphite treated with sulfuric acid [101]	
			Thermal conductivity [W/(m·K)]	Permeability [$\times 10^{-12}$ m^2]	Thermal conductivity [W/(m·K)]	Permeability [$\times 10^{-16}$ m^2]
Disk	Parallel	Perpendicular	1.2–1.8	1.9–2.1	< 8.9	0.15–11.2
Plate	Perpendicular	Parallel	1.5–4.1	4.5–8.8	< 337	1.64–117

* Directions relative to the heat/mass transfer direction.

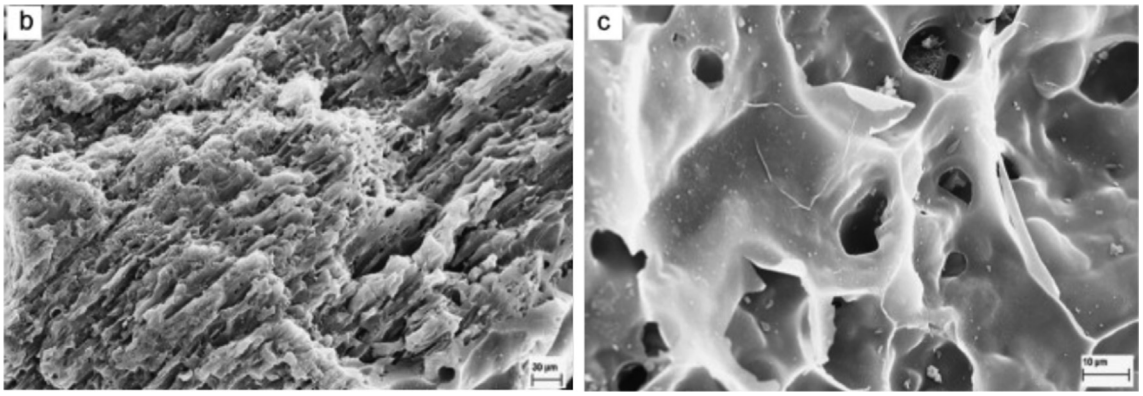

Fig. 7. Scanning electron microscopy picture of activated carbon at a scale of 30 μm (left) and 10 μm (right) [117].

The ICF, which has a simpler preparation, was further studied by Dellero and Touzain [109] to improve the transfer performance through compression and fiber arrangement in the adsorber. By balancing the thermal conductivity and permeability, an optimal composite density of ~700 kg/m^3 was identified to achieve the shortest reaction time. Furthermore, because the thermal conductivity along the fiber is 10 times higher than that across the fiber, the influence of fiber disposition on the reaction rate was studied. The long (30 cm) fibers winding around the adsorber led to a slower reaction compared with short (3 cm) fibers lying radially in the direction of heat transfer.

Vasiliev et al. introduced a $CaCl_2$-ACF composite sorbent using a special type of CF named "Busofit" that has a thermal conductivity of 0.2 W/(m·K) [110]. Later, Vasiliev et al. developed ACF-$NiCl_2$ and ACF-$BaCl_2$ for a multi-salt space cooling system [57]. The ACF provided a uniform distribution of thin (2–3 μm) films of salt on the porous host material surface [111]. Aristov et al. developed a $CaCl_2$-ACF Busofit composite for cooling applications and reported a composite thermal conductivity of 0.2–0.4 W/(m·K) [112]. Fig. 8 shows the scanning eletron microscopy of ACF and ACF-$CaCl_2$ composite from [122].

3.2.4. Other matrix materials

Other matrix materials include carbon nanotubes (CNTs) and expanded vermiculite (EVM). CNTs are molecules of carbon with a cylindrical nanostructure. The high thermal conductivity (W/(m·K)) of CNT makes it a good candidate for composite matrix material with enhanced heat transfer performance. Yan et al. [42,113] prepared a composite sorbent made of $CaCl_2$ and multi-wall carbon nanotubes (MWCNT) for its macro-porous structure. The MWCNT had an average diameter of 10 nm and length of 10 μm and a specific surface area of 200 m^2/g. The thermal conductivity of MWCNT was 750 W/(m·K) in array form and 15–25 W/(m·K) in film form. The composite was prepared by impregnating the salt into the MWCNT in aqueous solution before drying in the oven. The thermal conductivity of the composite was 1.52 W/(m·K) compared with the granular $CaCl_2$ thermal conductivity of 0.17 W/(m·K). Moreover, the MWCNT proved to prevent salt agglomeration during adsorption. SEM pictures of the MWCNT from Yan et al. [113] are shown in Fig. 9.

EVM is made by heat-treatment of natural vermiculite, a hydrous phyllosilicate mineral. EVM has a flake structure similar to expanded graphite, but its thermal conductivity is considerably lower. Zhong et al. [81] prepared EVM with grain sizes of 2–3 mm by immersing EVM with aqueous solution of $BaCl_2$ before drying it under 200 °C for 5 h. The composite was then used to test an isothermal adsorption and desorption process. SEM pictures of EVM from Zhang et al. [123] are shown in Fig. 10.

Table 5 compare the thermal conductivity and permeability of granular salt, AC, and composite sorbents using EG and ENG-TSA matrixes. Because of the lack of thermal conductivity and permeability data reported in the literature, ACF, CNT, and EVM composites are not plotted in Fig. 11. The granular salt in Fig. 11 was measured by Jiang et al. [103] for $CaCl_2$, which demonstrated very low permeability due to agglomeration. The only known AC data with both thermal conductivity and permeability measurements is from Critoph et al. for consolidated AC sorbent without salt embedment [124].

Compared with granular salt, AC had a higher permeability but lower thermal conductivity. Most data points in Fig. 11 and Table 5 are EG and ENG-TSA since they have been extensively investigated with both the thermal conductivity and permeability reported in multiple papers. The permeability of a composite sorbent using EG was measured to be one to four orders of magnitude higher than granular salt [89,93,115,125]. The thermal conductivity of EG composites was about 1–3 W/(m·K) [89,93,115] and 10–26 W/(m·K) [125]. The ENG-TSA

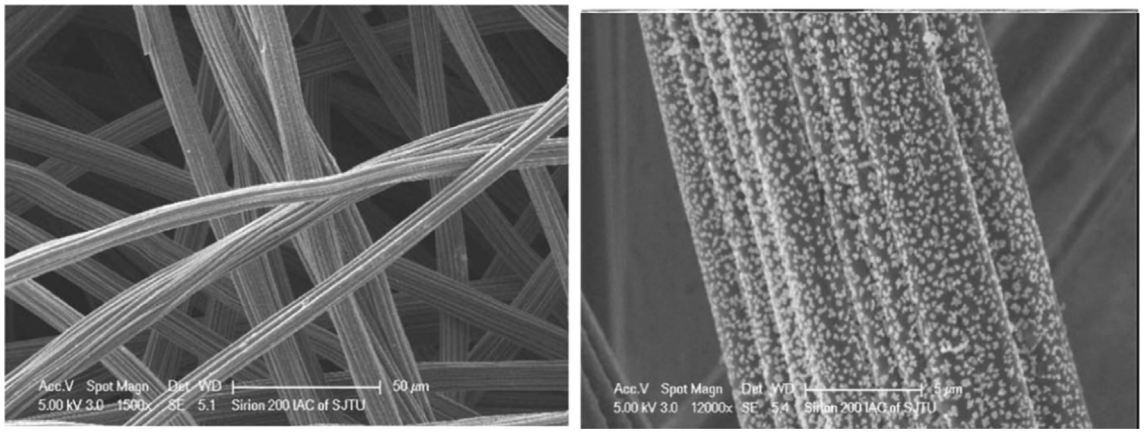

Fig. 8. Scanning electron microscopy of activated carbon fiber (left) and activated carbon fiber–$CaCl_2$ composite sorbent (right) [122].

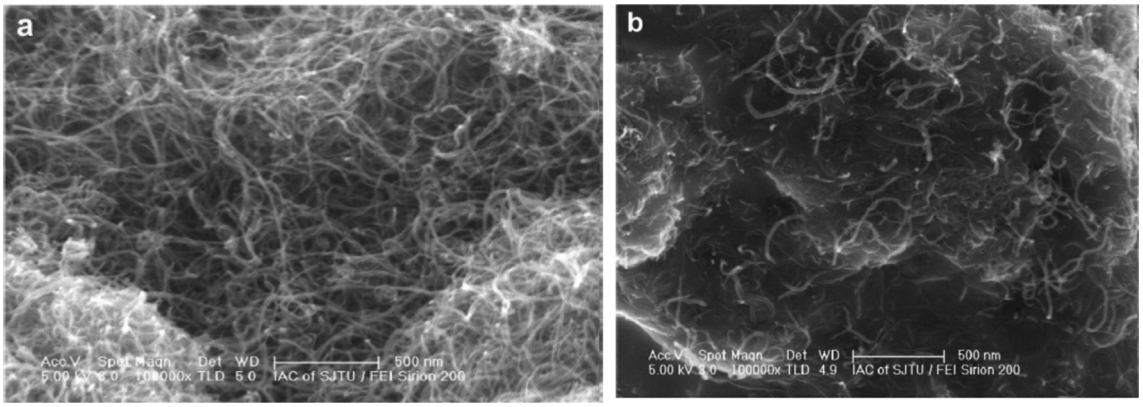

Fig. 9. Scanning electron microscopy of multiwall carbon nanotube (left) and multiwall carbon nanotube–$CaCl_2$ composite sorbent (right) [113].

composites generally have thermal conductivities of more than 10 W/(m·K) and slightly lower permeabilities than EG [102,103].

Table 5 shows that the thermal conductivities and permeabilities of the graphite composites are related to their density, salt/matrix mass ratio, sorption quantity, and the consolidation direction. Though the thermal conductivity generally improves with the density as shown by Tian et al., Jiang et al., and Han et al. [89,103,125], the permeability suffers with increasing density with narrower vapor transfer channels shown in the same literature. Unlike granular salt where the agglomeration improves thermal conduction, more salt in the composite leads to lower conductivity and slightly higher permeability [89,102,103,125]. As reported by Han et al. [125], the sorption capacity affects the permeability considerably because of the significant change in molecular volume during the chemisorption reaction, while it has little influence on the thermal conductivity.

4. Components

The major components in CSHP systems are heat-exchanging vessels, including adsorbers, condensers, and evaporators. An adsorber is a sorbent-containing heat exchanger that allows heat to be transferred between the sorbent and an external heat transfer fluid (HTF) such as water, steam, oil, and others. The condenser and evaporator provide a heat exchange surface for the condensation or evaporation of ammonia and transfer the phase-change heat to the external HTF. The heating/cooling power of the CSHP system depends on effectively providing heat to or extracting heat from the sorbent or the refrigerant. Furthermore, as suggested by Li et al. and Zhu et al. [126,127], the extra heat associated with the thermal mass of the heat exchangers has significant impact on the CSHP system COP. Therefore, numerous studies have been carried out to improve the design of the adsorber and condenser/evaporator (C/E) to enhance heat transfer performance and reduce the mass of metallic heat exchangers.

4.1. Adsorber

In a CSHP system, the sorbent-containing adsorber is the most important component, as it provides heat exchange surfaces for the solid sorbent and heat transfer fluid. The design of the adsorber also determines the length of the ammonia vapor transfer path and the subsequent vapor mass flow rate. Fig. 12 is a schematic of general heat and mass transfer in the adsorber. Heat from the HTF transfers through the heat exchanger wall that is in contact with the sorbent block. Meanwhile, ammonia vapor diffuses in the sorbent and flows in and out of the block across openings not in contact with the heat exchanger wall.

The overall heat transfer resistance between the external HTF and the sorbent can be expressed in (5) as the sum of resistance between the heat exchanger wall and the HTF and the sorbent, the conduction resistance across the heat exchanger wall, and the conduction resistance within the sorbent block.

$$\frac{1}{(UA)_{overall}} = \frac{1}{h_{fw} \cdot A_{fw}} + \frac{1}{h_{ws} \cdot A_{ws}} + \frac{x_w}{\lambda_w \cdot A_w} + \frac{x_s}{\lambda_s \cdot A_s}. \quad (5)$$

In (5), $(UA)_{overall}$ is the overall thermal conductance between the HTF and the sorbent, h_{fw} and h_{ws} are the heat transfer coefficients on the HTF-wall and sorbent-wall surface, A_{fw} and A_{ws} are the heat exchange surfaces on each side, and x_w and λ_w are the thickness and thermal conductivity of the heat exchanger wall, λ_s is the thermal conductivity, x_s is the mean heat transfer path length (average distance of sorbent to the heat exchanger wall), and A_s is the mean heat transfer cross section area (the average cross-sectional area perpendicular to the heat transfer direction). Based on Eq. (5), the heat transfer through the adsorber heat exchanger can be improve with larger heat exchange areas, higher heat transfer coefficients, and thinner wall and sorbent

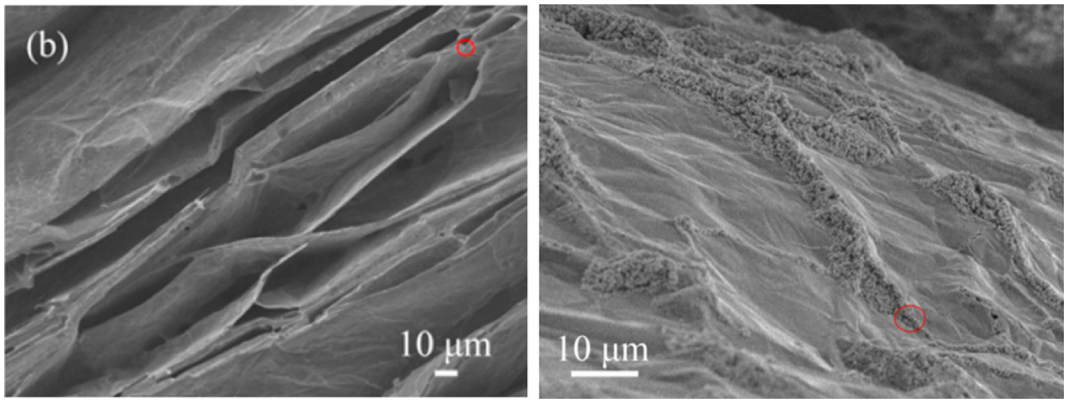

Fig. 10. Scanning electron microscopy of expanded vermiculite (left) and expanded vermiculite impregnated with $SrBr_2$ salt (right) [123].

Table 5
Thermal conductivity and permeability of composite sorbents. AC = activated carbon; EG = expanded graphite; ENG–TSA = expanded natural graphite treated with sulfuric acid.

Reference	Salt/matrix	Salt mass ratio	Density [kg/m^3]	Sorption quantity [mol/mol]	Conductivity [W/(m·K)]	Permeability [m^2]
Jiang 2014 [103]	$CaCl_2$ granular	—	—	1	0.47	7.78×10^{-15}
			—	2	0.66	6.55×10^{-15}
			—	3	0.8	9.26×10^{-16}
			—	4	0.82	8.18×10^{-16}
			—	5	0.8	5.87×10^{-16}
			—	6	0.81	5.78×10^{-16}
			—	7	0.82	3.65×10^{-16}
			—	8	0.83	1.56×10^{-16}
Critoph 2004 [124]	AC	—	—	—	0.44	3.60×10^{-14}
Tian 2012 [89]	$CaCl_2$ EG	50%	450	—	1.66	2.73×10^{-12}
		67%		—	1.23	7.85×10^{-12}
		75%		—	1.09	1.02×10^{-11}
		80%		—	1.01	1.76×10^{-11}
		83%		—	0.85	3.16×10^{-11}
		50%	550	—	1.7	8.61×10^{-13}
		67%		—	1.51	1.36×10^{-12}
		75%		—	1.36	1.90×10^{-12}
		80%		—	1.28	3.58×10^{-12}
		83%		—	1.08	1.19×10^{-11}
Han 2000 [125]	$MnCl_2$ EG	50%	100	6	14.8	2.50×10^{-13}
		50%		2	13.9	8.60×10^{-13}
		30%		6	11.7	8.00×10^{-14}
		30%		2	10.9	2.50×10^{-13}
		50%	150	6	16.1	4.00×10^{-14}
		50%		2	15.5	1.20×10^{-13}
		50%		6	14	1.50×10^{-14}
		50%		2	12.8	4.30×10^{-14}
		50%	200	6	21.9	1.30×10^{-14}
		50%		2	20.8	3.00×10^{-14}
		50%	250	6	25.6	8.10×10^{-15}
		50%		2	24.7	1.80×10^{-14}
Jiang 2016 [102][a]	NH_4Cl ENG-TSA	50%	400	—	34.9	5.14×10^{-14}
		67%		—	27.4	2.87×10^{-14}
		75%		—	18.7	6.45×10^{-14}
		80%		—	14.7	8.00×10^{-14}
		83%		—	12.4	8.67×10^{-14}
	$MnCl_2$ ENG-TSA	50%		—	36.6	6.47×10^{-15}
		67%		—	24.8	4.25×10^{-14}
		75%		—	18.3	5.95×10^{-14}
		80%		—	14.5	8.94×10^{-14}
		83%		—	11.9	8.96×10^{-14}
	$CaCl_2$ ENG-TSA	50%		—	31.7	1.63×10^{-14}
		67%		—	23.3	4.24×10^{-14}
		75%		—	17.4	6.45×10^{-14}
		80%		—	14.2	8.94×10^{-14}
		83%		—	12.2	8.96×10^{-14}
Jiang 2014 [103][a]	$CaCl_2$ ENG-TSA	50%	300	—	23.2	7.34×10^{-14}
			350	—	27.1	5.96×10^{-14}
			400	—	31.5	5.20×10^{-14}
			450	—	40	4.23×10^{-14}
			500	—	47.5	3.05×10^{-14}
		67%	300	—	15	6.34×10^{-13}
			350	—	18	5.54×10^{-13}
			400	—	23	4.52×10^{-13}
			450	—	27	3.14×10^{-13}
			500	—	32	2.05×10^{-13}
		75%	300	—	12	8.05×10^{-13}
			350	—	13.3	6.64×10^{-12}
			400	—	16.1	5.20×10^{-12}
			450	—	20	9.66×10^{-13}
			500	—	26.3	7.34×10^{-13}
		80%	300	—	10.5	9.25×10^{-11}
			350	—	12	7.32×10^{-11}
			400	—	14	5.52×10^{-11}
			450	—	17.4	9.84×10^{-12}
			500	—	22.6	7.34×10^{-12}
		83%	300	—	7.6	9.31×10^{-10}
			350	—	9.2	8.51×10^{-10}
			400	—	11.5	7.52×10^{-11}
			450	—	14.3	6.56×10^{-11}
			500	—	18.5	5.42×10^{-11}

[a] Data digitized from plot.

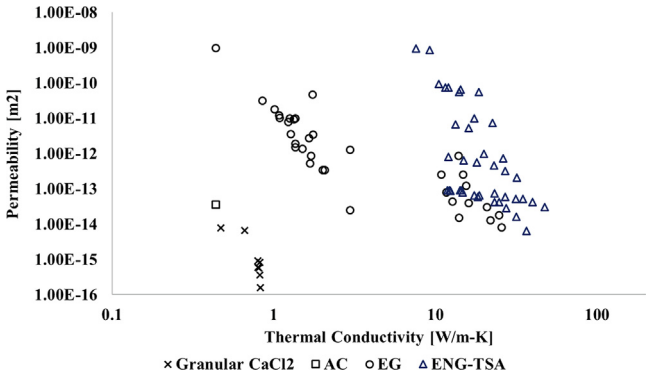

Fig. 11. Comparison of thermal conductivity and permeability of composite sorbents. AC = activated carbon; EG = expanded graphite; ENG-TSA = expanded natural graphite treated with sulfuric acid.

mean thicknesses. The increase of the heat exchange area could lead to a decrease of the sorbent thickness and an increase of sorbent cross section area, reducing the heat transfer path length and also could affect the mass transfer path length.

To accommodate the incompatibility of ammonia refrigerant with copper, adsorbers and ammonia piping are usually built with stainless steel [63,128] or aluminum [72]. The salt stays in solid phase in the matrix during operation and therefore poses no corrosion threat to the component materials. The heat transfer resistance across the heat exchanger wall is usually small, and the reduction of metal mass by using thinner heat exchanger walls is limited because the walls need to sustain the pressure difference between the ammonia and HTF loop.

This section presents the designs to improve the heat and mass transfer in the chemisorption adsorbers. Since the consolidated composite sorbents do not experience swelling and expansion during adsorption, the enhancement designs proposed in physical adsorption adsorbers using adsorbents of similar form factors (e.g. consolidated porous material such as activate carbon) in [124,129–131] are also included. These physisorption adsorber designs could provide beneficial reference for designing high-performance chemisorption adsorbers, but they have not been proven on chemisorption systems. In general, two approaches have been followed to enhance adsorber heat transfer in the literature: (1) increase the heat transfer area (A_{fw} and A_{ws}) by using an extended exchange surface such as a finned tube and flat plate, and (2) improve the heat transfer coefficients (h_{fw} and h_{ws}) at the heat exchanger surface by using heat pipe.

4.1.1. Increasing adsorber heat exchanger surface area

- *Chemisorption adsorbers*

Adsorbers in early CSHP studies [77,132] used a simple annular design in which the sorbent is molded into an annular shape and placed in a cylindrical adsorber shell as in. The sorbent transfers heat with the external HTF through the adsorber shell, and the ammonia vapor flows across the sorbent to the vapor channel in the center. Wrapped electric heating coil [77] and a water/oil bath [63,67] were used to maintain the sorbent temperature.

Finned tube heat exchangers are inexpensive to manufacture and provide a large heat exchange surface area; therefore, they are also popular choices for adsorbers, usually with a cylindrical pressure vessel as the shell with multiple tube-and-fin heat exchangers inside, as shown in Fig. 13. Thin fins are crossed by several tubes or welded on individual tubes to increase the heat transfer surface. The sorbent material is filled around the tube and between the fins, and the heat transfer fluid flows in the tube. This type of adsorber was used in a few experimental studies [71,133–135], and the systems using the shell-and-tube adsorbers achieved 115–245 W/kg system specific cooling power (SCP). The chemical adsorbent needs to be filled between the fins and often covered with wire mesh to secure the sorbent while allowing the ammonia vapor to pass through [133].

- *Physisorption adsorbers*

Improvement of the annular design was proposed in physical adsorption systems. To increase the heat transfer area of the annular adsorbers, fins were added inside the adsorber. Critoph et al. built and tested an annular adsorber where the monolithic carbon powder and thin aluminum plates were compressed to form a compact plate-fin structure in close contact with the stainless steel cylinder wall for enhanced heat transfer (Fig. 13) [136,137]. SCP of 218 W/kg based on the carbon adsorbent mass was achieved using this type of adsorber. Tube-fin heat exchanger design was also used in physical adsorption systems such as [138]. Plate heat exchangers were used in a few physical adsorption systems. A serpentine-shaped plate heat exchanger was built by Tchernev et al. [131,139] from folded 0.1 mm thin metal foil with pumped heat transfer fluid flowing inside the plates for a high heat transfer rate (Fig. 15, left). Critoph and Metcalf [124] developed a detailed simulation model for a plate-type adsorber (Fig. 15, right). Thin carbon plates were bonded on the space between stainless steel heat exchanger plates, with small gaps between the carbon plates to allow free flow of ammonia vapor. The thickness and dimensions of the carbon plates were optimized using the model for a high SCP and COP (see Fig. 14).

4.1.2. Enhancing adsorber heat transfer

Apart from increasing the heat transfer surface area of the adsorber heat exchanger, heat pipes using two-phase heat transfer principles were also used in CSHP adsorbers to provide high heat transfer capacity. Critoph [140] discussed the pros and cons of using heat pipe versus pumped HTF in the adsorber. The benefit of using pumped HTF is that the pumping pressure can be controlled to equalize the pressure on both sides of the heat exchanger, allowing thin heat exchanger walls. On the other hand, adding a pump reduces the system's reliability and simplicity. In contrast, a thermosyphon heat pipe can operate without a pump and achieve a high heat transfer rate. The major drawback of a heat pipe in an adsorber is that the large pressure difference usually

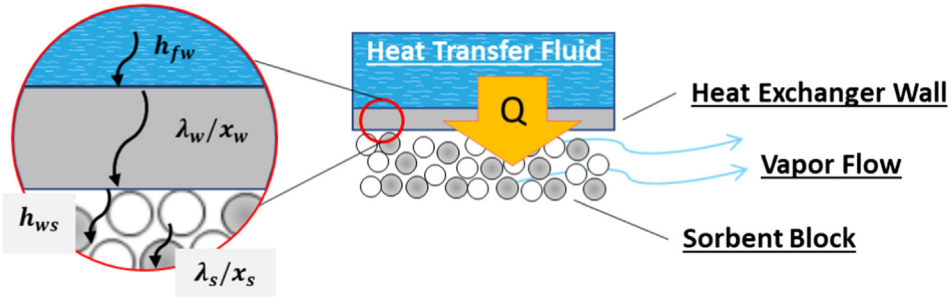

Fig. 12. General heat and mass transfer in the adsorber.

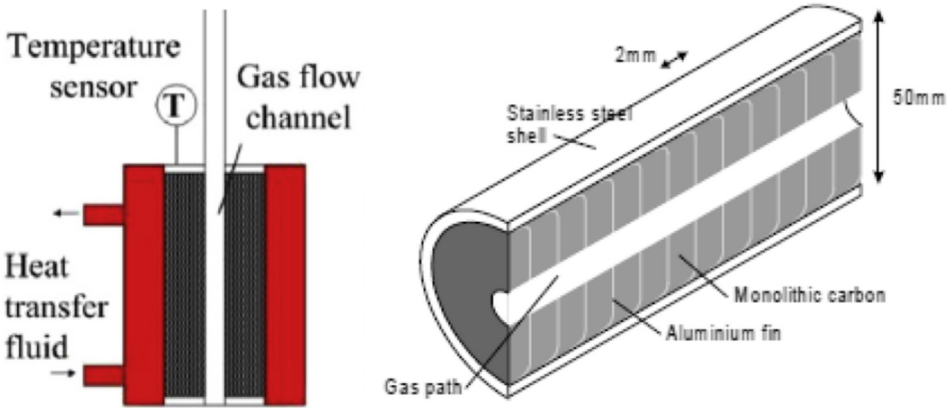

Fig. 13. Annular adsorbers without fins (left [67]) and with fins (right [137]).

leads to thick heat pipe walls and thus, large thermal mass. Since the adsorber needs to be heated during desorption and cooled during adsorption, different heat pipe designs were implemented to provide the alternating heating and cooling: reversable heat pipe, hybrid heat pipe/HTF, and multiple heat pipe designs.

- *Chemisorption adsorber*

The design of reversable heat pipes switching the hot and cold ends of the heat pipe was used in several CSHP systems. Vasiliev et al. [111] built a heat pipe adsorber with horizontally installed heat pipes to allow two-way heat transfer. Heating elements at the outer end of the heat pipe generated steam to heat the adsorber in the heating phase; in the cooling phase, cold water passes through the outer end of the heat pipe and the induced evaporative cooling in the adsorber. Split-type heat pipes were used in a series of studies using CSHP to make ice for a fishing boat [22,105,107,141,142]. The steam heat pipes were used to transfer heat from the diesel engine exhaust gas to the sorbent for desorption with an average heat transfer coefficient of 155.8 W/m^2·K. Finned tube adsorbers in these systems were then cooled by evaporating liquid water in the heat pipe at low pressure during adsorption. The liquid level and pressure in the heat pipe between two operating modes was controlled by a pump. Depending on the temperatures of the available heat and selected sorbent salt, the use of methanol and water as the heat pipe medium was discussed [128].

The hybrid heat pipe/HTF design uses the heat pipe effect for heating and a circulating HTF for cooling the adsorber. Li et al. [71] pointed out that the split-type heat pipes involved significant steam pressure difference between heating and cooling modes and that the heat pipe pressure was very low during cooling. Instead, pumped water was proposed for cooling to operate at more stable pressures. The hybrid heat pipe/circulated HTF design was also used by Alyousef et al. [143] with a valved heat pipe for transferring solar heat to the adsorbers for desorption, and circulating cooling water in a separate loop for cooling the adsorber.

In addition to heat pipe designs, Lu et al. [72] used heat exchange tubes with internal 3-D fins as shown in Fig. 13 to further enhance the heat transfer between the HTF and the heat exchanger wall. On the other side of the heat exchanger wall, the chemisorption sorbents need to be prefabricated into disks or blocks and inserted into the heat exchanger. Therefore, good contact is needed to reduce the heat resistance on the sorbent-metal surface. Even though the consolidated composite sorbent is considered to eliminate the swelling effect during adsorption, Lu et al. [116] reported that the heat transfer coefficients at the sorbent heat exchanger varied between 40 W/m^2·K and 3,000 W/m^2·K during adsorption and attributed it to the expansion and contraction of the sorbent block.

- *Physisorption adsorber*

In addition to the two heat pipe designs, multiple heat pipe design using separate heat pipes operating at different temperature ranges for heating and cooling was proposed for physical adsorption systems. Critoph et al. [144] contrived an adsorption refrigerator using two sets of heat pipes with water and pentane outside a circular adsorber to transfer heat from the heat source to support desorption. In a different design, Critoph built an aluminum circular adsorber with a steam heat pipe in the center for heating and an R22 heat pipe surrounding the sorbent for cooling [145].

To enhance the heat transfer between the sorbent and the heat exchanger walls in the physical adsorption systems, sorbents such as zeolites were directly coated on the surface of the heat exchanger

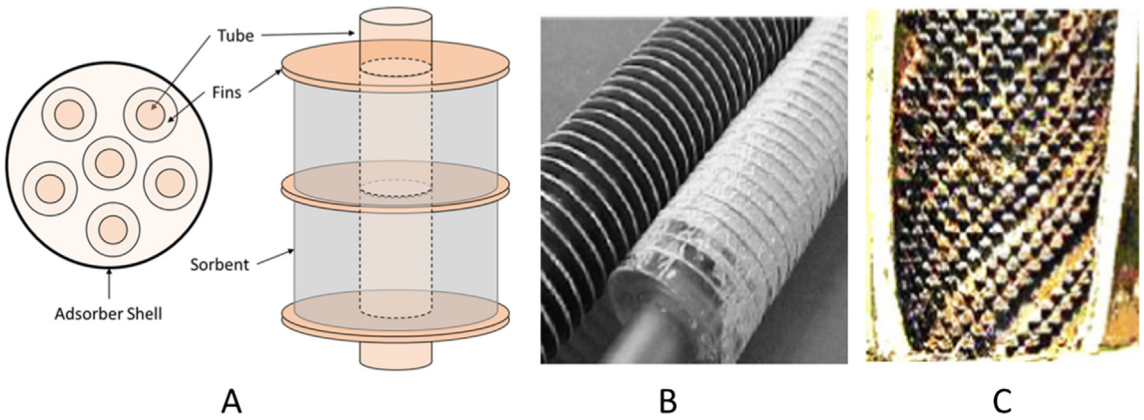

Fig. 14. Tube-fin-type adsorber. A—schematic; B—sorbent-filled tube-fin heat exchanger [138]; C—3D fins inside tube (Lu et al. [72]).

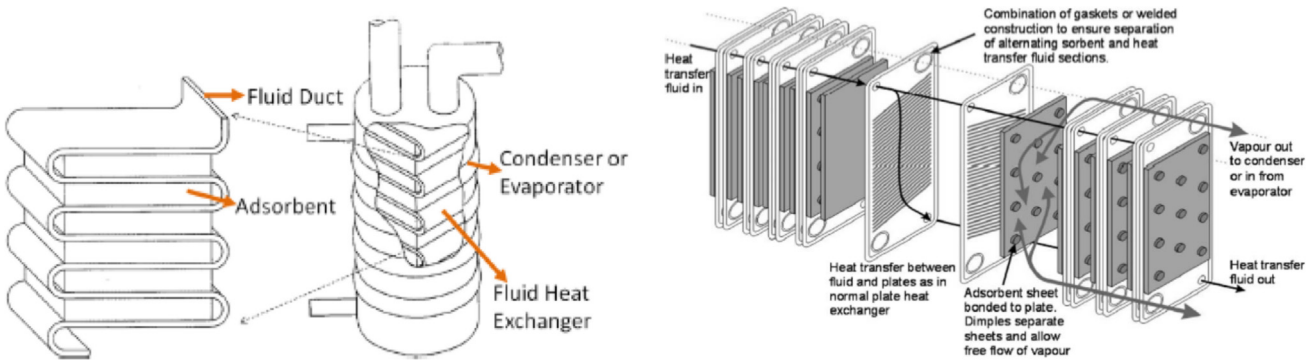

Fig. 15. Flat-plate adsorber design by Tchernev et al. (left [131,139]) and Critoph and Metcalf (right [124]).

[146–148] to reduce the contact heat resistance between the sorbent and the heat exchanger walls.

Table 6 provides a summary of different adsorber designs in literature.

4.2. Condenser/evaporator and integrated component design

Compared with the adsorbers in which design considerations encompass the sorbent and the external heat source, the C/E operates under a simpler premise. With adequate heat transfer surface between the ammonia phase change and the pumped HTF, the novel designs of the C/E focus on reducing the thermal mass and vapor transfer path. Furthermore, integrated designs combining the adsorber and C/E into a single vessel for a modular system capable of continuous operation have also been investigated.

The separate condenser and evaporator from Li et al. [71] were integrated into a connected component with the condensate flowing from the top condenser down into the evaporator/reservoir and the ammonia vapor in and out of the component sharing one passage, reducing the thermal mass compared with using two separate vessels.

Further integration of the C/E combines it with the adsorber to create an even more compact component with less thermal mass and a short vapor transfer path between the sorbent and the condensing/evaporating surface. Iammak et al. [149] integrated the adsorber, condenser, evaporator, and liquid refrigerant reservoir in one annular tube, as shown in Fig. 16. The refrigerant vapor condensed when cooled in the condenser, and the condensate accumulated in the evaporator/reservoir at the bottom. When the adsorber section was cooled, the liquid refrigerant vaporized and flowed upward into the adsorber.

Jaehnig et al. [150] integrated the C/E under the adsorber by separating the cylindrical vessel into two compartments. The whole system was packed in a single pressure vessel in which the water–silica gel working pair was used for thermal storage. The liquid level in the C/E was controlled to avoid emersion of the heat exchanger and improve heat transfer.

Tchernev et al. [131,139] integrated the adsorber with the C/E by using the cylindrical wall of the adsorber as the heat transfer surface of refrigerant condensation to reduce the vapor transport resistance between the adsorbent and the C/E, as well as to eliminate the need for a separate C/E component.

5. Cycle and system

Although enhancing the heat and mass transfer in the sorbent material and heat-exchanging components can improve system performance with faster and more complete reactions, the thermodynamic performance of a CSHP system is largely determined by its cycle configuration. Based on the heat source of the chemisorption reactions in the systems, CSHP cycles can be categorized into single-effect, double-effect, and other configurations. By arranging the chemisorption reactions in adsorption or resorption arrangements, numerous cycle configurations have been investigated for CSHP applications by simulation [16] and experiment [57,58,60]. This section summarizes the configuration and performance of these CSHP cycles and systems.

5.1. Single-effect cycles

Single-effect CSHP cycles take external high-temperature heat directly for desorption heat in all adsorbers. Depending on the how the chemisorption reactions in the adsorber(s) are arranged, single-effect systems can be further categorized into combined condenser-evaporator (SCCE), separate condenser and evaporator (SSCE), and resorption (SRES). Fig. 17 shows the generic operation of single-effect cycles. For SCCE and SSCE cycles, pure ammonia is the low-temperature (LT) material and salt is the medium-temperature (MT) material. Similarly, for SRES cycles, the LT is the LTS, and MT is the HTS. At high pressure, MT takes in high-temperature heat from the heat source and desorbs to give off ammonia. The high-pressure ammonia vapor is condensed (in SCCE/SSCE) or adsorbed (in SRES) and rejects useful heat. Once the system gets to low pressure, useful heat is extracted from the MT and

Table 6
Summary of adsorber designs and performances. H = heating; C = cooling.

Reference	Adsorption type	Heat exchanger	Heat transfer method	Average heat transfer coefficient [W/m^2·K]	
				Heating	Cooling
[63]	Chemical	Tubular shell	Circulated oil	—	—
[106]	Chemical	Finned tube	Reversable steam heat pipe	150–200 [38]	
[128]	Chemical	Finned tube	Reversable steam heat pipe	109.3	105.1
[128]	Chemical	Finned tube	Reversable methanol heat pipe	90.1	84.8
[111]	Chemical	Finned tube	Reversable steam/HFC heat pipe	—	
[72]	Chemical	Finned tube with inner 3D fins	Steam heat pipe	204.9	208.8
[71]	Chemical	Finned tube	Hybrid steam heat pipe (H)/pumped water (C)	745.4 [38]	832.6 [38]
[143]	Chemical	Finned tube	Hybrid steam heat pipe (H)/pumped water (C)	—	—
[145]	Physical	Finned tubular shell	Separate steam (H)/R22 (C) heat pipe	—	—

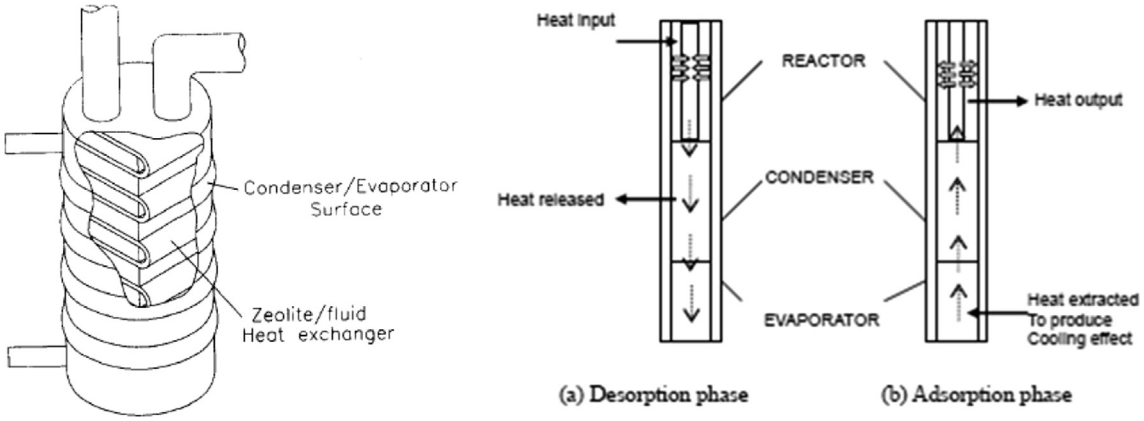

Fig. 16. Compact condenser/evaporator design (left [131], right [149]).

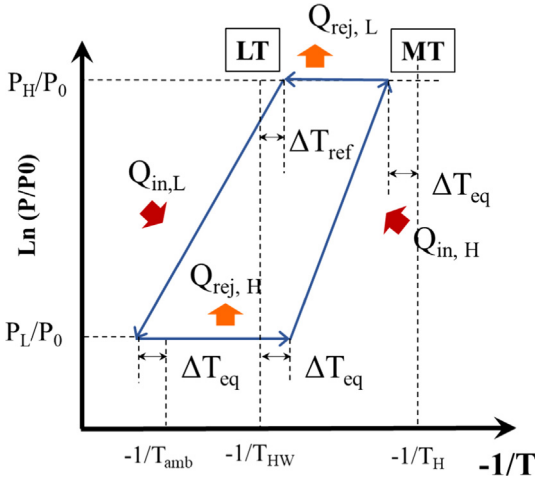

Fig. 17. Clapeyron chart of typical single-effect cycles.

the system starts to adsorb vapor ammonia. The ammonia in LT is released, taking in LT heat from the cold ambient.

5.1.1. Single-effect combined condenser-evaporator and single-effect separate condenser and evaporator cycles

SCCE is the most basic chemisorption cycle, described in Fig. 1 as an adsorber coupling with a single phase-change heat exchanger alternately acting as the condenser and the evaporator under high and low pressures. SCCE has been studied for chemisorption cooling applications [60,61,65,71,99] with a cooling COP of ~0.3. The low COP was attributed to the heat loss caused by the temperature swing of the sorbent and the heat exchanger metal, which reduced the COP by 10–20% [55]. Therefore, few SCCE cycles were used for cold-climate heating in which the temperature swing heat loss could be exacerbated by the large temperature lift.

The SSCE configuration, as shown in Fig. 18, avoids repeated heating and cooling of the combined C/E during the operating cycle switches by using separate and dedicated heat exchangers for condensation and evaporation. Although the two adsorbers are alternately heated and cooled by external heat, the hot ammonia vapor always condenses in the condenser, and the liquid ammonia always vaporizes to take in LT heat in the evaporator. Thus, the SSCE cycle avoids the heat losses and the associated COP reduction in the repeated heating and cooling of the condenser and evaporator.

The ideal COP of SCCE and SSCE cycles according to (1) are shown in Eq. (6) assuming $Q_{des} = Q_{ads}$ [127]. Since the reaction heat of desorption and adsorption reactions are similar, and both are about twice the vaporization heat of ammonia [55,61], the ideal heating COP of SSCE and SCCE is 1.5 [61].

$$COP_{ht,SSCE/SCCE} = \frac{Q_{ht}}{Q_{in}} \approx \frac{Q_{cond} + Q_{ads}}{Q_{des}} = 1 + \frac{H_{fg,NH3}}{\Delta H_{reaction}}. \quad (6)$$

Pons et al. used an analytical model developed by Stitou et al. [46] that was verified against an established phenomenological model and validated with experimental data to simulate CSHP heating systems in an SSCE configuration based on a $SrCl_2$-8/1 reaction [16]. The heating

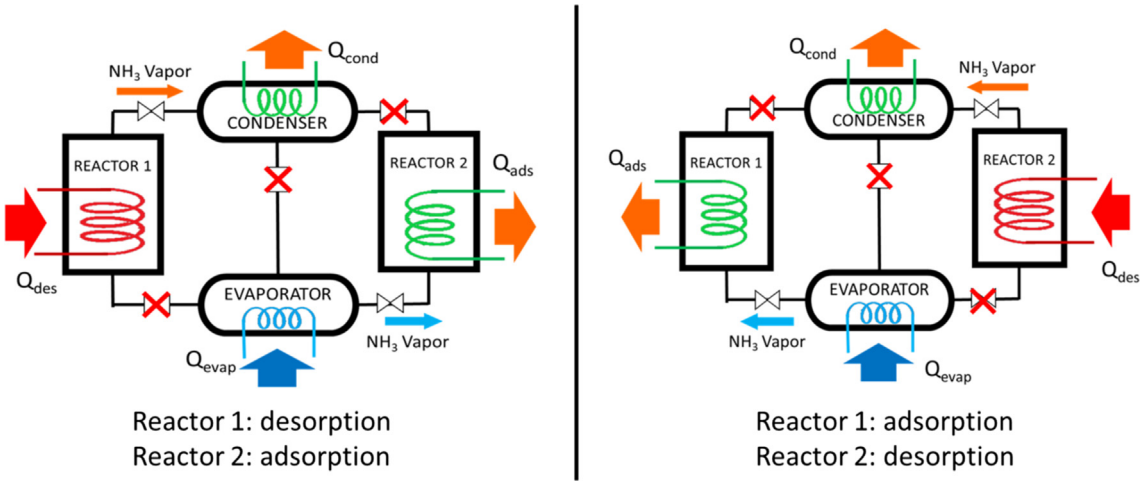

Fig. 18. Typical configuration and operating modes of a single-effect separate condenser-evaporator cycle.

COP was between 1.31 and 1.35 at a heating temperature of 40 °C and between 1.21 and 1.23 at a heating temperature of 55 °C. The SHP at 40 °C was ~450 W/kg and below 300 W/kg at 55 °C. The low ambient temperature of −15 °C required a high heat input temperature of 170–185 °C, compared with a 135 °C heat source for 5 °C ambient. Vasiliev et al. [57] built and tested an SSCE system based on $CaCl_2$ reactions and an ACF Busofit matrix and reported heating COP of 1.43 under 50 °C heating and −18 °C evaporation.

It is worth mentioning that type-II heat pump (heat transformers) can also be assembled in SCCE [31] and SSCE [30] configurations and used for heating in cold climate. The "Heat from Cold" cycles introduced in uses methanol instead of ammonia as the refrigerant, and elevates heat from the ambient of 2–20 °C up to 35–50 °C with typical COPs below 1.0 [30,31]. These new cycles have the potential to be applied using ammonia as the refrigerant.

5.1.2. Single-effect resorption cycle

The SRES direct couples two different chemisorption reactions where the system extracts heat from the LT ambient through the desorption reaction of LTS and supplies heat via the adsorption reactions of both LTS and HTS at high temperatures (Fig. 19). The ideal COP of a SRES cycle according to (1) is calculated in Eq. (7) with all heat input and output based on chemisorption reaction heat [55,61 127]; the ideal heating COP of SRES is 2.0 [61].

$$COP_{ht,SRES} = \frac{Q_{ht}}{Q_{in}} = \frac{Q_{ads,HTS} + Q_{ads,LTS}}{Q_{des,HTS}} \approx 1 + \frac{\Delta H_{LTS}}{\Delta H_{HTS}}. \quad (7)$$

SRES cycles have been studied to produce high-temperature heating under subfreezing ambient conditions. However, because of the temperature and operating pressure limits on LTS, the minimum ambient temperature for resorption systems is usually above −10 °C. Oliveira [44] calculated the heating COP of SRES using thermodynamic property data of several working pairs. For $CaCl_2$-$MgCl_2$ and $ZnCl_2$-$NiCl_2$ pairs, the heating COP was 1.75 and 1.79, respectively. For $CaCl_2$-$CoCl_2$ working pair with simultaneous cooling at 5 °C and heating at 65–75 °C, the calculated cooling COP was 1.0 and heating COP was 2.9 ~3.3 depending on the heat source temperature.

Pons et al. [16] simulated an SRES system using $MnCl_2$-$BaCl_2$ as the working pair, and the system supplying 40–55 °C heat under 5 °C ambient achieved a COP above 1.52 and an SHP of 370 W/kg. Vasiliev et al. [57] tested a resorption system using $NiCl_2$ as the HTS and $MnCl_2$ as the LTS. The system produced 50 °C heating and cooling at 0 °C with a heating COP of 1.44 and an SHP of 350 W/kg. Xu et al. [58] tested $MnCl_2$-NH_4Cl resorption systems for heating above 70 °C with only the HTS adsorption reaction, while the LTS desorption took heat from the 0 °C ambient. With cycle times of more than 6 h, the chemisorption reactions approached completion, and the heating COPs with only HTS adsorption heat were above 0.92. Oliveira et al. [60] conducted similar tests with an $MnCl_2$-NaBr pair with HTS adsorption producing heat at 55 °C, and the heating COP was 0.9.

5.2. Double-effect cycles

When salts with different operating temperatures are used with ammonia condensing and evaporating, a double-effect system can be formed by directing the adsorption heat of HTS to drive the desorption reaction of the medium-temperature salt (MTS), thereby reducing the heat demand from a high-temperature heat source and improving system COP. Double-effect cycles involve three different reactive materials; thus, their generic operations can be described on the Clapeyron chart, as in Fig. 20, with LT representing the ammonia in adsorption cycles and the LTS in resorption cycles, with the other two equilibrium lines representing two different salts.

Fig. 20 illustrates the generic operation of double-effect cycles. The HTS and MTS in double-effect cycles operate in opposite phases; that is, when the HTS desorbs ammonia by the heat from a high-temperature heat source, the MTS absorbs ammonia either from evaporation or desorption of LTS. Once the operating modes of the two salts are switched, the adsorption heat of the HTS, which is at higher temperature than the desorption threshold of the MTS, is used to directly drive ammonia out of the MTS.

Therefore, with the same HTS desorption heat input from the heat source, double-effect cycles are capable of producing heating with condensation and adsorption in multiple components, leading to an elevated thermal COP. The ideal heating COP of the double-effect separate condenser-evaporator (DSCE) and double-effect resorption (DRES) are calculated in Eq. (8) and Eq. (9) [127]:

$$COP_{ht,DSCE} = \frac{Q_{ht}}{Q_{in}} = \frac{Q_{cond,HTS} + Q_{cond,MTS} + Q_{ads,MTS}}{Q_{des,HTS}} \approx 1 + \frac{2 \cdot H_{fg}}{\Delta H_{HTS}}. \quad (8)$$

$$COP_{ht,DRES} = \frac{Q_{ht}}{Q_{in}} = \frac{Q_{ads,MTS} + Q_{ads,LTS-HTS} + Q_{ads,LTS-MTS}}{Q_{des,HTS}} \approx 1 + \frac{2 \cdot \Delta H_{LTS}}{\Delta H_{HTS}}. \quad (9)$$

However, because of the added system complexity, the majority of studies on multiple-effect cycles are via the simulation approach, with only a few physical systems constructed and tested. The configuration of the double-effect corresponding cycles of DSCE and DRES are shown in Fig. 21.

Oliveira [44]calculated the heating COP of 2.27 for a DSCE system based on thermodynamic properties of CaCl2-FeCl2 working pair under supplying heat of 75–90 °C and ambient of 25 °C. Pons et al. [16] simulated the performance of a DSCE heat pump system using $MnCl_2$ as the MTS and $NiCl_2$ as the HTS. The system required a heat source above 280 °C and achieved heating COP above 1.43. The temperatures of the heat rejection and cold ambient had little impact on the heating COP, while the colder ambient of −15 °C compared with 5 °C reduced the SHP from above 300 W/kg to 140 W/kg. The SHP is about half of the SSCE system simulated under the −15 °C ambient conditions.

A DRES heat pump was also simulated by Pons et al. [16] for producing heating under 5 °C ambient temperature. The DRES heat pump used $NiCl_2$, $MnCl_2$, and $BaCl_2$ as the HTS, MTS, and LTS and achieved a heating COP of above 1.9. The SHP was also about half compared with SRES systems operating under similar conditions.

The simulation and experimental studies on the CSHP heating systems are listed in Tables 7 and 8.

The comparisons of COP and SHP in different studies are shown in Fig. 22. For ambient temperatures below −10 °C, only conventional adsorption configurations (i.e., SSCE and DSCE) are viable, with

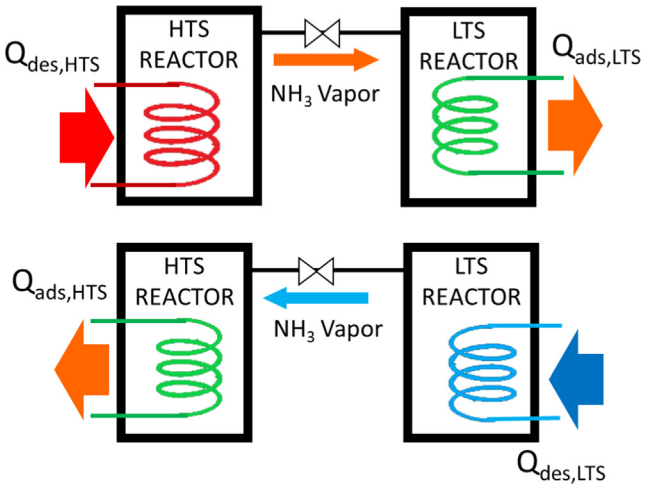

Fig. 19. Single-effect resorption cycle.

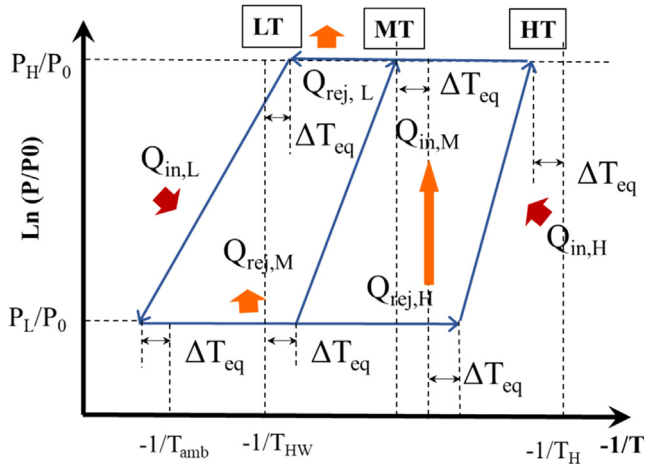

Fig. 20. Clapeyron chart of typical double-effect cycles.

Table 7
Simulation studies of chemisorption heat pump heating systems by Pons et al. [16]. SSCE = single-effect combined condenser-evaporator; SRES = single-effect resorption; DSCE = double-effect separate condenser-evaporator; DRES = double-effect resorption; COP = coefficient of performance; SHP = specific heating power.

Configuration	Salt	Temp [°C]	Temp lift [°C]	COP	SHP [W/kg]
SSCE	$SrCl_2$	135/40/5	35	1.35	450
		170/40/−15	55	1.23	290
		135/55/5	60	1.31	430
		185/55/−15	70	1.21	290
SRES	$MnCl_2/BaCl_2$	130/40/5	35	1.55	380
		150/55/5	60	1.52	370
DSCE	$MnCl_2$-$NiCl_2$	280/40/5	35	1.45	350
		285/40/−15	55	1.44	140
		295/55/5	60	1.45	320
		290/55/−15	70	1.43	140
DRES	$MnCl_2$-$NiCl_2$/$BaCl_2$	230/40/5	35	1.92	220
		250/55/5	60	1.90	210

double-effect systems having a higher COP. At a higher ambient temperature around 0 °C, resorption configurations (i.e., SRES and DRES) become available and achieve higher COP than adsorption configurations. The SHP, on the other hand, is affected by the temperature lift defined as the temperature difference between heat rejection and cold ambient. Generally, single-effect systems have higher SHPs than double-effect systems. The two adsorption systems (SSCE and DSCE) with a dip in SHP at 55 °C and 70 °C were simulated under −15 °C, indicating that the SHP was also affected by the ambient temperature.

6. Conclusions and future research

Ammonia-based chemisorption is a promising technology to provide energy-efficient heating, especially for residential applications in cold climates. Recently, the chemisorption technology has received increasing interest, and significant research and development efforts have been invested to overcome the critical drawbacks of chemisorption systems such as heat and mass transfer limits in the sorbent material.

This paper reviews the state of the art of the chemisorption technology specifically for cold-climate heating applications. Existing studies on the sorbent material, component, and cycle system levels are summarized and reviewed. With the recent progress made in the technology, more research is needed to overcome the challenges, including the following:

- Material—salt
  - o The low equilibrium pressure of LTSs limits the use of the high-COP resorption configuration. To ensure mass transfer in the LTS, the minimum ambient temperature has been limited to above −10 °C; however, the adsorption temperatures of the LTS are not high enough to produce heating, as in the experimental studies of Xu et al. [58] and Oliveira et al. [60]. Therefore, salts beyond the existing metal halide salts with a more preferable equilibrium as LTS are desired. One candidate, $ZnSO_4$, is introduced by Goetz et al. [61].
  - o Hysteresis of sorbent salts is an important phenomenon that can significantly affect the performance or even viability of the chemisorption system. Vapor equilibrium is the key factor when determining the working pair and designing the system for a particular application. However, with hysteresis, the operational chemical reaction equilibrium could deviate from the design and result in reduced capacity and COP. Therefore, both the physiochemical principle behind the phenomenon and the means to prevent or mitigate the effect require further study, especially for salts suitable for cold-climate heating applications such as LiCl, $SrCl_2$, and others.
  - o Although a few salts have been investigated for cold-climate heating applications, there are other candidates with theoretically more favorable properties. Fig. 23 illustrates the sorption capacity and desorption temperature of salts in the adsorption configuration with a heat rejection temperature of 50 °C and an evaporation temperature of 0 °C and −15 °C based on the equilibrium and molar mass properties. The commonly used salts mentioned previously all have above 0.5 kg/kg sorption capacity. Meanwhile, reactions such as LiCl-4/0 and LiCl-3/1 also have high theoretical sorption capacity under the typical cold-climate heating conditions but have not yet been investigated for heating applications.

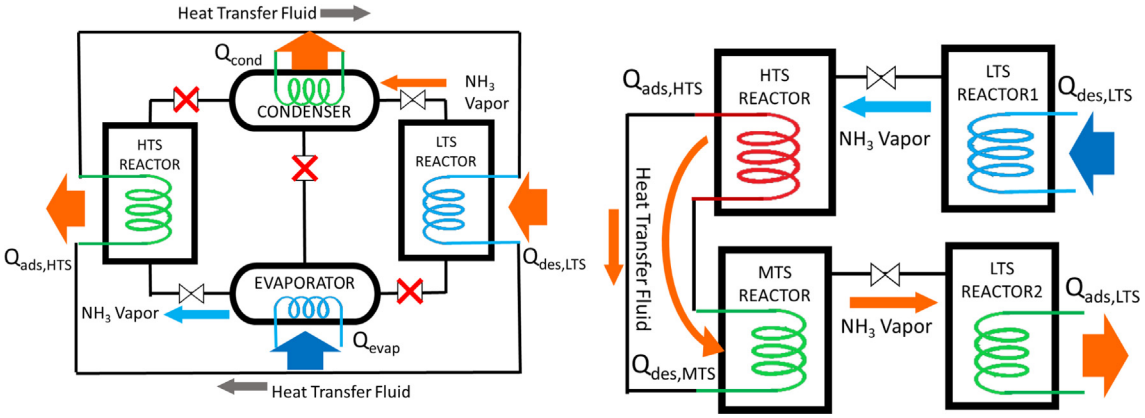

Fig. 21. Configuration and operation of double-effect separate condenser-evaporator (left) and double-effect resorption (right).

Table 8
Experimental studies of chemisorption heat pump heating systems. SSCE = single-effect combined condenser-evaporator; SRES = single-effect resorption; COP = coefficient of performance; SHP = specific heating power.

Reference	Configuration	Salt	Temp [°C]	Temp lift [°C]	COP	SHP [W/kg]
Vasiliev 2001 [57]	SSCE	$CaCl_2$	120/50/−18	68	1.43	850
	SRES	$NiCl_2/BaCl_2$	140/50/0	50	1.44	—
Xu 2011 [58]	SRES	$MnCl_2/NH_4Cl$	140/75/0	75	0.95[a]	35
			145/75/0	75	0.95[a]	36
			140/80/0	80	0.92[a]	24
			140/70/−5	75	0.95[a]	29
			145/80/5	85	0.95[a]	35
			140/80/0	80 (11 h)	0.96[a]	16
			140/70/−5	75 (10 h)	0.95[a]	18
Oliveira 2009 [60]	SRES	$MnCl_2$/NaBr	165/50/−5	55	0.90[a]	—

[a] Considering only high-temperature salt adsorption heat.

In addition, the mixture of different salts demonstrated deviation of the "effective equilibrium" from the equilibrium of single-salt ingredients as studied in [82,86,87] for mitigation of hysteresis. However, it also suggests the possibility to tailor the equilibrium of the sorbents to the target application by mixing salts.

- o The system COP is also strongly affected by the reaction heat of the working pair as discussed in [151,152]. With the step-like equilibrium of the chemisorption processes, the equilibrium vapor pressure of a high-reaction-heat salt is lower under the same temperature, and therefore allows heat extraction from colder ambient or utilization of lower temperature heat sources. Meanwhile, the reduction of system COP can be derived from Eqs. (6)–(9) where a higher reaction heat would reduce the extra heat from cold ambient relative to the heat input. The trade-off of operating temperatures and the system COP should also be considered when designing the system.

- Material—matrix:
  - o Expanded graphite has proved to be a superior matrix material providing high thermal conductivity and permeability. However, the enhancement of heat and mass transfer must be balanced by adjusting the consolidated density, conductivity, and permeability of the matrix materials, which is especially important to ensure sufficient mass transfer within the sorbent under low-pressure operating conditions during refrigeration or in cold climates. The effect of matrix material, matrix-salt ratio, compression method, and the resulting thermophysical characteristics of commonly used sorbent salt and matrix types needs to be comprehensively studied.
  - o The change of thermal conductivity and permeability related to the reaction progression needs more theoretical and experimental study. As suggested by Lu et al. [91,116], such change could be significant and therefore needs to be accurately considered during modeling and design of the system.
- Component
  - o Reducing the thermal mass of components with innovative integrated component design is desirable. The thermal mass of components can hurt system COP with unrecovered heat loss and limit system power density by slowing down heat transfer. Because the main vessels of chemisorption systems need to withstand varying pressures during operation, the most effective approach to reducing thermal mass is to integrate components adjunct in functionalities. Meanwhile, such integration would bring up challenges such as unwanted heat loss between integrated functional parts. Therefore, innovative design and engineering are greatly needed.
  - o Heat pipe adsorbers have high heat transfer rates, but their heating and cooling rate is not directly controlled as pumped HTF. Therefore, future research should work toward improving heat pipe adsorbers with accurate control of heat flow. To regulate the system under varying heating output and mitigate maintenance risks, a robust and controllable heat pipe adsorber design is desired.
  - o Optimizing adsorber design while considering the properties of the composite sorbent is another area of future work. As argued by Critoph and Metcalf [124], an optimal combination of conductivity and heat transfer path length, as well as permeability and mass transfer path length, are more desirable for high overall system performance.
- System
  - o More experimental and theoretical studies are greatly desired to confirm the heating performance of CSHP systems under cold ambient. So far, only one simulation and less than five experimental studies have been found by the authors during literature searches. The information provided in these publications is far

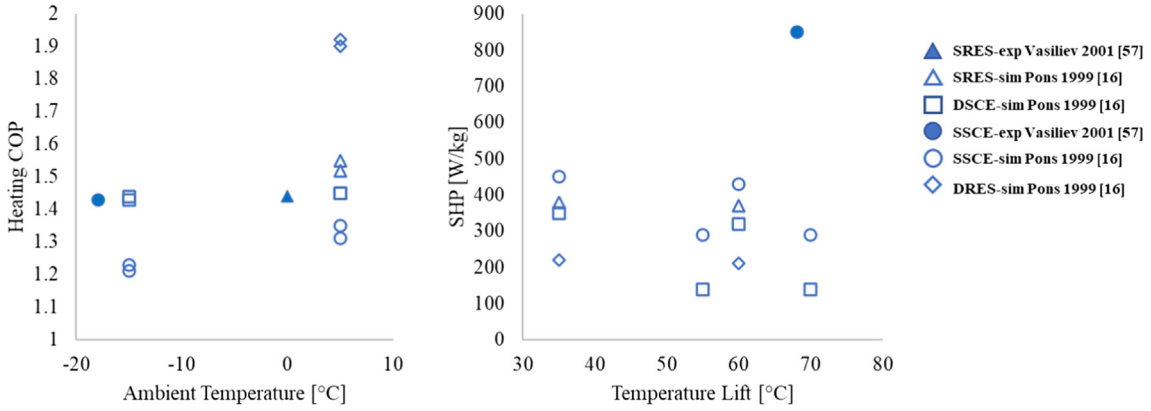

Fig. 22. Coefficient of performance (COP; left) and specific heating power (SHP; right) of chemisorption heat pump heating systems under different ambient temperatures and temperature lifts. SRES = single-effect resorption; DSCE = double-effect separate condenser-evaporator; DRES = double-effect resorption.

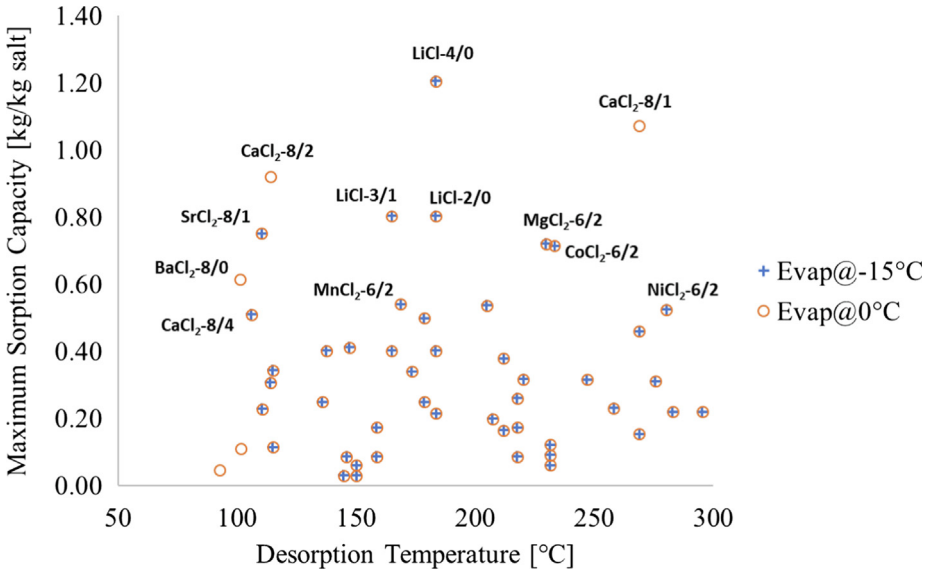

Fig. 23. Sorption capacity and desorption temperature of salts in adsorption configuration with a heat rejection of 50 °C.

from sufficient to confirm the potential high COP of the technology.

- Applying performance enhancement cycles to heating applications needs to be studied. Heat and mass recovery have improved the performance of chemisorption refrigeration systems [106,107], but no such mechanism has been studied for heating applications in which the positive effect can be even more pronounced because of the large temperature lift.
- The type-II heat pump configurations have been recently proposed to elevate ambient-temperature heat to the heat production temperature using methanol as the refrigerant [32]. Therefore, although type-II heat pump systems traditionally were not considered for space heating applications, further study of them using ammonia for space heating is warranted.

The aforementioned challenges indicate that chemisorption systems still require significant research and development to meet their full potential of effectively generating heating and refrigeration driven by renewable energy sources and under extreme climate conditions. The challenges also point to the improvement needed for the technology to play a more significant role in wider applications in the future: research and development in materials, components, systems, and methodologies for system design and evaluation.

CRediT authorship contribution statement

Zhiyao Yang: Conceptualization, Methodology, Software, Formal analysis, Investigation, Data curation, Writing - original draft, Visualization. **Ming Qu:** Conceptualization, Methodology, Resources, Writing - review & editing, Supervision. **Kyle R. Gluesenkamp:** Conceptualization, Resources, Writing - review & editing, Visualization, Funding acquisition.

Declaration of Competing Interest

The authors declare that they have no known competing financial interests or personal relationships that could have appeared to influence the work reported in this paper.

Acknowledgments

This work was sponsored by the US Department of Energy's Building Technologies Office under contract DE-AC05-00OR22725 with UT-Battelle, LLC. The authors would also like to acknowledge Mr. Antonio Bouza, Technology Manager–HVAC&R, Water Heating, and Appliance, US Department of Energy Building Technologies Office.

The authors would also like to thank Charlie Horak for technical language editing.

References

[1] D. Bosseboeuf, L. Gynther, B. Lapillonne, K. Pollier, Energy efficiency trends and policies in the household and tertiary sectors; an analysis based on the ODYSSEE and MURE databases, ODYSSEE-MURE project, (2015).
[2] P. Beiter, M. Elchinger, T. Tian, 2016 renewable energy data book, in, National Renewable Energy Lab.(NREL), Golden, CO (United States), 2017.
[3] X. Cao, X. Dai, J. Liu, Building energy-consumption status worldwide and the state-of-the-art technologies for zero-energy buildings during the past decade, Energy Build. 128 (2016) 198–213.
[4] E.I.A. (EIA), Residential Energy Consumption Survey (RECS), vol. 2019, 2019.
[5] K.J. Chua, S.K. Chou, W.M. Yang, Advances in heat pump systems: A review, Appl. Energy 87 (2010) 3611–3624.
[6] L. Yang, H. Yuan, J.-W. Peng, C.-L. Zhang, Performance modeling of air cycle heat pump water heater in cold climate, Renew. Energy 87 (2016) 1067–1075.
[7] M. Guoyuan, C. Qinhu, J. Yi, Experimental investigation of air-source heat pump for cold regions, Int. J. Refrig. 26 (2003) 12–18.
[8] S. Ramaraj, J.E. Braun, E.A. Groll, W.T. Horton, Performance analysis of liquid flooded compression with regeneration for cold climate heat pumps, Int. J. Refrig. 68 (2016) 50–58.
[9] L. Zhang, Y. Jiang, J. Dong, Y. Yao, Advances in vapor compression air source heat pump system in cold regions: A review, Renew. Sustain. Energy Rev. 81 (2018) 353–365.
[10] S.L. Caskey, Cold climate field test analysis of an air-source heat pump with two-stage compression and economizing, vol. PhD, Purdue University, 2013.
[11] L.W. Wang, R.Z. Wang, R.G. Oliveira, A review on adsorption working pairs for refrigeration, Renew. Sustain. Energy Rev. 13 (2009) 518–534.
[12] R.E. Critoph, Activated carbon adsorption cycles for refrigeration and heat pumping, Carbon 27 (1989) 63–70.
[13] ASHRAE, Standard 34-2010, Designation safety classification of refrigerants, 2010.
[14] ASHRAE, Standard 15-2010, Safety Standard for Refrigeration Systems, 2010.
[15] A. Pearson, Refrigeration with ammonia, Int. J. Refrig. 31 (2008) 545–551.
[16] M. Pons, F. Meunier, G. Cacciola, R.E. Critoph, M. Groll, L. Puigjaner, B. Spinner, F. Ziegler, Thermodynamic based comparison of sorption systems for cooling and heat pumping: Comparaison des performances thermodynamique des systèmes de pompes à chaleur à sorption dans des applications de refroidissement et de chauffage, Int. J. Refrig. 22 (1999) 5–17.
[17] M. Garrabrant, R. Stout, C. Keinath, P. Glanville, Experimental Evaluation of Low-Cost Gas Heat Pump Prototypes for Building Space Heating (2016).
[18] K.E. Herold, R. Radermacher, S.A. Klein, Absorption Chillers and Heat Pumps, CRC Press, 2016.
[19] R.Z. Wang, Adsorption refrigeration research in Shanghai Jiao Tong University, Renew. Sustain. Energy Rev. 5 (2001) 1–37.
[20] R. Wang, L. Wang, J. Wu, Adsorption Refrigeration Technology: Theory and Application, John Wiley & Sons, 2014.

[21] L.W. Wang, R.Z. Wang, Z.S. Lu, C.J. Chen, K. Wang, J.Y. Wu, The performance of two adsorption ice making test units using activated carbon and a carbon composite as adsorbents, Carbon 44 (2006) 2671–2680.
[22] L.W. Wang, R.Z. Wang, J.Y. Wu, K. Wang, Compound adsorbent for adsorption ice maker on fishing boats, Int. J. Refrig. 27 (2004) 401–408.
[23] A.O. Dieng, R.Z. Wang, Literature review on solar adsorption technologies for ice-making and air-conditioning purposes and recent developments in solar technology, Renew. Sustain. Energy Rev. 5 (2001) 313–342.
[24] Y. Fan, L. Luo, B. Souyri, Review of solar sorption refrigeration technologies: Development and applications, Renew. Sustain. Energy Rev. 11 (2007) 1758–1775.
[25] O. Afshar, R. Saidur, M. Hasanuzzaman, M. Jameel, A review of thermodynamics and heat transfer in solar refrigeration system, Renew. Sustain. Energy Rev. 16 (2012) 5639–5648.
[26] K.R. Ullah, R. Saidur, H.W. Ping, R.K. Akikur, N.H. Shuvo, A review of solar thermal refrigeration and cooling methods, Renew. Sustain. Energy Rev. 24 (2013) 499–513.
[27] M.S. Fernandes, G.J.V.N. Brites, J.J. Costa, A.R. Gaspar, V.A.F. Costa, Review and future trends of solar adsorption refrigeration systems, Renew. Sustain. Energy Rev. 39 (2014) 102–123.
[28] Z. Yang, M. Qu, K.R. Gluesenkamp, Model-Based Performance Comparison of Ammonia Chemisorption Heat Pumps for Cold Climate with Different Working Pairs and Cycle Configurations, Oak Ridge National Lab. (ORNL), Oak Ridge, TN (United States), 2018.
[29] C. Blackman, K.R. Gluesenkamp, M. Malhotra, Z. Yang, Study of optimal sizing for residential sorption heat pump system, Appl. Therm. Eng. 150 (2019) 421–432.
[30] L. Gordeeva, Y.I. Aristov, Adsorptive heat storage and amplification: New cycles and adsorbents, Energy 167 (2019) 440–453.
[31] M.M. Tokarev, L.G. Gordeeva, A.D. Grekova, Y.I. Aristov, Adsorption cycle “heat from cold” for upgrading the ambient heat: The testing a lab-scale prototype with the composite sorbent CaClBr/silica, Appl. Energy 211 (2018) 136–145.
[32] Y.I. Aristov, Adsorptive transformation of ambient heat: a new cycle, Appl. Therm. Eng. 124 (2017) 521–524.
[33] M. Amer, C.-C. Wang, Review of defrosting methods, Renew. Sustain. Energy Rev. 73 (2017) 53–74.
[34] W. Wongsuwan, S. Kumar, P. Neveu, F. Meunier, A review of chemical heat pump technology and applications, Appl. Therm. Eng. 21 (2001) 1489–1519.
[35] N. Yu, R. Wang, L. Wang, Sorption thermal storage for solar energy, Progr. Energy Combust. Sci. 39 (2013) 489–514.
[36] C.W. Chan, J. Ling-Chin, A.P. Roskilly, A review of chemical heat pumps, thermodynamic cycles and thermal energy storage technologies for low grade heat utilisation, Appl. Therm. Eng. 50 (2013) 1257–1273.
[37] T. Li, R. Wang, H. Li, Progress in the development of solid–gas sorption refrigeration thermodynamic cycle driven by low-grade thermal energy, Prog. Energy Combust. Sci. 40 (2014) 1–58.
[38] R.Z. Wang, Z.Z. Xia, L.W. Wang, Z.S. Lu, S.L. Li, T.X. Li, J.Y. Wu, S. He, Heat transfer design in adsorption refrigeration systems for efficient use of low-grade thermal energy, Energy 36 (2011) 5425–5439.
[39] L. Jiang, A.P. Roskilly, Thermal conductivity, permeability and reaction characteristic enhancement of ammonia solid sorbents: A review, Int. J. Heat Mass Transf. 130 (2019) 1206–1225.
[40] L.F. Cabeza, A. Solé, C. Barreneche, Review on sorption materials and technologies for heat pumps and thermal energy storage, Renew. Energy 110 (2017) 3–39.
[41] D. Lefebvre, F.H. Tezel, A review of energy storage technologies with a focus on adsorption thermal energy storage processes for heating applications, Renew. Sustain. Energy Rev. 67 (2017) 116–125.
[42] T. Yan, R.Z. Wang, T.X. Li, L.W. Wang, I.T. Fred, A review of promising candidate reactions for chemical heat storage, Renew. Sustain. Energy Rev. 43 (2015) 13–31.
[43] J.M. Dias, V.A. Costa, Adsorption heat pumps for heating applications: A review of current state, literature gaps and development challenges, Renew. Sustain. Energy Rev. 98 (2018) 317–327.
[44] R.G. de Oliveira, Chemisorption Heat Pumps for Water Heating and Steam Production, in: J.D.F. Barbin, V. Silveira (Eds.), Novel Concepts for Energy-Efficient Water Heating Systems, Nova Science Publishers, Inc, 2013.
[45] G.L. Miessler, P.J. Fischer, D.A. Tarr, Inorganic Chemistry, fifth ed., Pearson Education, 2013.
[46] D. Stitou, V. Goetz, B. Spinner, A new analytical model for solid-gas thermochemical reactors based on thermophysical properties of the reactive medium, Chem. Eng. Process. Process Intensif. 36 (1997) 29–43.
[47] F.A. Cotton, G. Wilkinson, C.A. Murillo, M. Bochmann, R. Grimes, Advanced Inorganic Chemistry, Wiley, New York, 1988.
[48] M. van der Pal, J. Veldhuis, Thermodynamic properties of lithium chloride ammonia complexes under heat pump type II working conditions, Energy Research Centre of the Netherlands, 2010 Report nr ECN-M–10-076.
[49] E. Bevers, P. van Ekeren, W. Haije, H. Oonk, Thermodynamic properties of lithium chloride ammonia complexes for application inahigh-lifthigh temperature chemical heat pump, J. Therm. Anal. Calorimet. 86 (2006) 825–832.
[50] R. Sharma, E.A. Kumar, Measurement of thermodynamic properties of ammoniated salts and thermodynamic simulation of resorption cooling system, Int. J. Refrig. 67 (2016) 54–68.
[51] D.E. Winterbone, A. Turan, Chapter 12 - Chemical Equilibrium and Dissociation, in: D.E. Winterbone, A. Turan (Eds.), Advanced Thermodynamics for Engineers (second ed.), Butterworth-Heinemann, Boston, 2015, pp. 247–294.
[52] P.W. Atkins, J. De Paula, J. Keeler, Atkins' Physical Chemistry, Oxford University Press, 2018.
[53] W.G. Don, H.P. Robert, Perry's Chemical Engineers' Handbook, 8th ed., McGraw-Hill Education, New York, 2008.
[54] B. Michel, P. Neveu, N. Mazet, Comparison of closed and open thermochemical processes, for long-term thermal energy storage applications, Energy 72 (2014) 702–716.
[55] P. Neveu, J. Castaing, Solid-gas chemical heat pumps: field of application and performance of the internal heat of reaction recovery process, Heat Recovery Syst. CHP 13 (1993) 233–251.
[56] T. Li, R. Wang, J.K. Kiplagat, A target-oriented solid-gas thermochemical sorption heat transformer for integrated energy storage and energy upgrade, AIChE J. 59 (2013) 1334–1347.
[57] L. Vasiliev, D. Mishkinis, A. Antukh, Solar-gas solid sorption refrigerator, Adsorption 7 (2001) 149–161.
[58] J. Xu, R.G. Oliveira, R.Z. Wang, Resorption system with simultaneous heat and cold production, Int. J. Refrig. 34 (2011) 1262–1267.
[59] M. Pal, J. Veldhuis, Thermodynamic properties of lithium chloride ammonia complexes under heat pump type II working conditions, Innov. Mater. Process. Energy Syst. (2010).
[60] R.G. Oliveira, R.Z. Wang, J.K. Kiplagat, C.Y. Wang, Novel composite sorbent for resorption systems and for chemisorption air conditioners driven by low generation temperature, Renew. Energy 34 (2009) 2757–2764.
[61] V. Goetz, F. Elie, B. Spinner, The structure and performance of single effect solid-gas chemical heat pumps, Heat Recovery Syst. CHP 13 (1993) 79–96.
[62] J. Castaing-Lasvignottes, P. Neveu, Development of a numerical sizing tool applied to a solid-gas thermochemical transformer—II. Influence of external couplings on the dynamic behaviour of a solid-gas thermochemical transformer, Appl. Therm. Eng. 17 (1997) 519–536.
[63] T.X. Li, R.Z. Wang, J.K. Kiplagat, H. Chen, Experimental study and comparison of thermochemical resorption refrigeration cycle and adsorption refrigeration cycle, Chem. Eng. Sci. 65 (2010) 4222–4230.
[64] N. Le Pierrès, N. Mazet, D. Stitou, Experimental results of a solar powered cooling system at low temperature, Int. J. Refrig. 30 (2007) 1050–1058.
[65] T.X. Li, R.Z. Wang, L.W. Wang, J.K. Kiplagat, Study on the heat transfer and sorption characteristics of a consolidated composite sorbent for solar-powered thermochemical cooling systems, Sol. Energy 83 (2009) 1742–1755.
[66] C. Rivera, I. Pilatowsky, E. Méndez, W. Rivera, Experimental study of a thermochemical refrigerator using the barium chloride–ammonia reaction, Int. J. Hydrogen Energy 32 (2007) 3154–3158.
[67] L. Jiang, L.W. Wang, W.L. Luo, R.Z. Wang, Experimental study on working pairs for two-stage chemisorption freezing cycle, Renew. Energy 74 (2015) 287–297.
[68] Y. Hu, L. Wang, L. Xu, R. Wang, J. Kiplagat, J. Wang, A two-stage deep freezing chemisorption cycle driven by low-temperature heat source, Front. Energy 5 (2011) 263.
[69] J.K. Kiplagat, R.Z. Wang, R.G. Oliveira, T.X. Li, Lithium chloride – Expanded graphite composite sorbent for solar powered ice maker, Sol. Energy 84 (2010) 1587–1594.
[70] L. Wang, H. Bao, R. Wang, A comparison of the performances of adsorption and resorption refrigeration systems powered by the low grade heat, Renew. Energy 34 (2009) 2373–2379.
[71] S.L. Li, Z.Z. Xia, J.Y. Wu, J. Li, R.Z. Wang, L.W. Wang, Experimental study of a novel CaCl2/expanded graphite-NH3 adsorption refrigerator, Int. J. Refrig. 33 (2010) 61–69.
[72] Z.S. Lu, R.Z. Wang, T.X. Li, L.W. Wang, C.J. Chen, Experimental investigation of a novel multifunction heat pipe solid sorption icemaker for fishing boats using CaCl2/activated carbon compound–ammonia, Int. J. Refrig. 30 (2007) 76–85.
[73] L. Jiang, L.W. Wang, C.Z. Liu, R.Z. Wang, Experimental study on a resorption system for power and refrigeration cogeneration, Energy 97 (2016) 182–190.
[74] V. Goetz, B. Spinner, E. Lepinasse, A solid-gas thermochemical cooling system using BaCl2 and NiCl2, Energy 22 (1997) 49–58.
[75] H.S. Bao, R.Z. Wang, L.W. Wang, A resorption refrigerator driven by low grade thermal energy, Energy Convers. Manage. 52 (2011) 2339–2344.
[76] H. Bao, R. Oliveira, R. Wang, L. Wang, Z. Ma, Working pairs for resorption refrigerator, Appl. Therm. Eng. 31 (2011) 3015–3021.
[77] V. Goetz, A. Marty, A model for reversible solid-gas reactions submitted to temperature and pressure constraints: simulation of the rate of reaction in solid-gas reactor used as chemical heat pump, Chem. Eng. Sci. 47 (1992) 4445–4454.
[78] E. Lépinasse, M. Marion, V. Goetz, Cooling storage with a resorption process. Application to a box temperature control, Appl. Therm. Eng. 21 (2001) 1251–1263.
[79] Z. Aidoun, M. Ternan, Pseudo-stable transitions and instability in chemical heat pumps: the NH3–CoCl2 system, Appl. Therm. Eng. 21 (2001) 1019–1034.
[80] Z. Aidoun, M. Ternan, The synthesis reaction in a chemical heat pump reactor filled with chloride salt impregnated carbon fibres: the NH3–CoCl2 system, Appl. Therm. Eng. 22 (2002) 1943–1954.
[81] Y. Zhong, R.E. Critoph, R. Thorpe, Z. Tamainot-Telto, Y.I. Aristov, Isothermal sorption characteristics of the BaCl 2–NH 3 pair in a vermiculite host matrix, Appl. Therm. Eng. 27 (2007) 2455–2462.
[82] Z.S. Zhou, L.W. Wang, L. Jiang, P. Gao, R.Z. Wang, Non-equilibrium sorption performances for composite sorbents of chlorides–ammonia working pairs for refrigeration, Int. J. Refrig. 65 (2016) 60–68.
[83] R. Sharma, E. Anil Kumar, Performance evaluation of simple and heat recovery adsorption cooling system using measured NH3 sorption characteristics of halide salts, Appl. Therm. Eng. 119 (2017) 459–471.
[84] S. Wu, T.X. Li, R.Z. Wang, Experimental identification and thermodynamic analysis of ammonia sorption equilibrium characteristics on halide salts, Energy 161 (2018) 955–962.
[85] J. Trudel, S. Hosatte, M. Ternan, Solid–gas equilibrium in chemical heat pumps:

the NH3–CoCl2 system, Appl. Therm. Eng. 19 (1999) 495–511.
[86] J. Gao, L.W. Wang, R.Z. Wang, Z.S. Zhou, Solution to the sorption hysteresis by novel compact composite multi-salt sorbents, Appl. Therm. Eng. 111 (2017) 580–585.
[87] J. Gao, L.W. Wang, G.L. An, J.Y. Liu, S.Z. Xu, Performance analysis of multi-salt sorbents without sorption hysteresis for low-grade heat recovery, Renew. Energy 118 (2018) 718–726.
[88] F.R.S. Hosatte, Kinetics and modelling of CaCl2-NH3 reactions, in: Proceeding of the Symposium of Solid Sorption Refrigeration, LIMSI, Paris, 1992, pp. 245–252.
[89] B. Tian, Z.Q. Jin, L.W. Wang, R.Z. Wang, Permeability and thermal conductivity of compact chemical and physical adsorbents with expanded natural graphite as host matrix, Int. J. Heat Mass Transf. 55 (2012) 4453–4459.
[90] S. Mauran, P. Prades, F. L'Haridon, Heat and mass transfer in consolidated reacting beds for thermochemical systems, Heat Recovery Syst. CHP 13 (1993) 315–319.
[91] H.-B. Lu, N. Mazet, B. Spinner, Modelling of gas-solid reaction—Coupling of heat and mass transfer with chemical reaction, Chem. Eng. Sci. 51 (1996) 3829–3845.
[92] J.H. Han, K.-H. Lee, H. Kim, Effective thermal conductivity of graphite-metallic salt complex for chemical heat pumps, J. Thermophys. Heat Transfer 13 (1999) 481–488.
[93] L. Jiang, Y.J. Lu, K. Tang, Y.D. Wang, R. Wang, A.P. Roskilly, L. Wang, Investigation on heat and mass transfer performance of novel composite strontium chloride for sorption reactors, Appl. Therm. Eng. 121 (2017) 410–418.
[94] K. Wang, J.Y. Wu, R.Z. Wang, L.W. Wang, Effective thermal conductivity of expanded graphite–CaCl2 composite adsorbent for chemical adsorption chillers, Energy Convers. Manage. 47 (2006) 1902–1912.
[95] L. Xu, R.Z. Wang, T.X. Li, L.W. Wang, Experimental study on a combined double-way chemisorption refrigeration system, Int. J. Refrig. 34 (2011) 914–921.
[96] R.G. Oliveira, R.Z. Wang, A consolidated calcium chloride-expanded graphite compound for use in sorption refrigeration systems, Carbon 45 (2007) 390–396.
[97] C. Wang, P. Zhang, R.Z. Wang, Investigation of solid–gas reaction heat transformer system with the consideration of multistep reactions, AIChE J. 54 (2008) 2464–2478.
[98] R. Oliveira, R. Wang, C. Wang, Evaluation of the cooling performance of a consolidated expanded graphite–calcium chloride reactive bed for chemisorption icemaker, Int. J. Refrig. 30 (2007) 103–112.
[99] T.X. Li, R.Z. Wang, J.K. Kiplagat, L.W. Wang, Performance study of a consolidated manganese chloride–expanded graphite compound for sorption deep-freezing processes, Appl. Energy 86 (2009) 1201–1209.
[100] L.W. Wang, Z. Tamainot-Telto, S.J. Metcalf, R.E. Critoph, R.Z. Wang, Anisotropic thermal conductivity and permeability of compacted expanded natural graphite, Appl. Therm. Eng. 30 (2010) 1805–1811.
[101] L.W. Wang, S.J. Metcalf, R.E. Critoph, R. Thorpe, Z. Tamainot-Telto, Thermal conductivity and permeability of consolidated expanded natural graphite treated with sulphuric acid, Carbon 49 (2011) 4812–4819.
[102] L. Jiang, L.W. Wang, Z.S. Zhou, F.Q. Zhu, R.Z. Wang, Investigation on non-equilibrium performance of composite adsorbent for resorption refrigeration, Energy Convers. Manage. 119 (2016) 67–74.
[103] L. Jiang, L.W. Wang, R.Z. Wang, Investigation on thermal conductive consolidated composite CaCl2 for adsorption refrigeration, Int. J. Therm. Sci. 81 (2014) 68–75.
[104] Y.J. Zhao, L.W. Wang, R.Z. Wang, K.Q. Ma, L. Jiang, Study on consolidated activated carbon: Choice of optimal adsorbent for refrigeration application, Int. J. Heat Mass Transf. 67 (2013) 867–876.
[105] T.X. Li, R.Z. Wang, L.W. Wang, Z.S. Lu, C.J. Chen, Performance study of a high efficient multifunction heat pipe type adsorption ice making system with novel mass and heat recovery processes (This work was supported by National Science Fund for Distinguished Young Scholars of China under the contract No. 50225621, Shanghai Shuguang Training Program for the Talents under the contract No. 02GG03, the Natural Science Fund of Shanghai City under the contract No. 05ZR14072), Int. J. Therm. Sci. 46 (2007) 1267–1274.
[106] Z.S. Lu, R.Z. Wang, L.W. Wang, C.J. Chen, Performance analysis of an adsorption refrigerator using activated carbon in a compound adsorbent, Carbon 44 (2006) 747–752.
[107] T.X. Li, R.Z. Wang, L.W. Wang, Z.S. Lu, Experimental investigation of an innovative dual-mode chemisorption refrigeration system based on multifunction heat pipes, Int. J. Refrig. 31 (2008) 1104–1112.
[108] T. Dellero, D. Sarmeo, P. Touzain, A chemical heat pump using carbon fibers as additive. Part I: enhancement of thermal conduction, Appl. Therm. Eng. 19 (1999) 991–1000.
[109] T. Dellero, P. Touzain, A chemical heat pump using carbon fibers as additive. Part II: study of constraint parameters, Appl. Therm. Eng. 19 (1999) 1001–1011.
[110] L.L. Vasiliev, L.E. Kanonchik, A.A. Antuh, A.G. Kulakov, NaX zeolite, carbon fibre and CaCl2 ammonia reactors for heat pumps and refrigerators, Adsorption 2 (1996) 311–316.
[111] L. Vasil'ev, D. Nikanpour, A. Antukh, K. Snelson, A. Lebru, Multisalt-carbon chemical cooler for space applications, J. Eng. Phys. Thermophys. 72 (1999) 572–577.
[112] Y.I. Aristov, L.L. Vasiliev, New composite sorbents of water and ammonia for chemical and adsorption heat pumps, J. Eng. Phys. Thermophys. 79 (2006) 1214–1229.
[113] T. Yan, T.X. Li, H. Li, R.Z. Wang, Experimental study of the ammonia adsorption characteristics on the composite sorbent of CaCl2 and multi-walled carbon nanotubes, Int. J. Refrig. 46 (2014) 165–172.
[114] J.H. Han, K.W. Cho, K.H. Lee, H. Kim, Porous graphite matrix for chemical heat pumps, Carbon 36 (1998) 1801–1810.
[115] J.H. Han, K.-H. Lee, Gas permeability of expanded graphite–metallic salt composite, Appl. Therm. Eng. 21 (2001) 453–463.
[116] H.B. Lu, N. Mazet, Mass-transfer parameters in gas-solid reactive media to identify permeability of IMPEX, AIChE J. 45 (1999) 2444–2453.
[117] C. Saka, BET, TG–DTG, FT-IR, SEM, iodine number analysis and preparation of activated carbon from acorn shell by chemical activation with ZnCl2, J. Anal. Appl. Pyrol. 95 (2012) 21–24.
[118] Z. Jin, B. Tian, L. Wang, R. Wang, Comparison on thermal conductivity and permeability of granular and consolidated activated carbon for refrigeration, Chin. J. Chem. Eng. 21 (2013) 676–682.
[119] T. Lee, C.-H. Ooi, R. Othman, F.-Y. Yeoh, Activated carbon fiber-the hybrid of carbon fiber and activated carbon, Rev. Adv. Mater. Sci 36 (2014) 118–136.
[120] Y. Xu, D. Chung, Silane-treated carbon fiber for reinforcing cement, Carbon 39 (2001) 1995–2001.
[121] M. Suzuki, Activated carbon fiber: Fundamentals and applications, Carbon 32 (1994) 577–586.
[122] J.Y. Wang, R.Z. Wang, L.W. Wang, Water vapor sorption performance of ACF-CaCl2 and silica gel-CaCl2 composite adsorbents, Appl. Therm. Eng. 100 (2016) 893–901.
[123] Y.N. Zhang, R.Z. Wang, Y.J. Zhao, T.X. Li, S.B. Riffat, N.M. Wajid, Development and thermochemical characterizations of vermiculite/SrBr 2 composite sorbents for low-temperature heat storage, Energy 115 (2016) 120–128.
[124] R.E. Critoph, S.J. Metcalf, Specific cooling power intensification limits in ammonia–carbon adsorption refrigeration systems, Appl. Therm. Eng. 24 (2004) 661–678.
[125] J.H. Han, K.H. Lee, D.H. Kim, H. Kim, Transformation analysis of thermochemical reactor based on thermophysical properties of graphite-MnCl 2 complex, Ind. Eng. Chem. Res. 39 (2000) 4127–4139.
[126] T.X. Li, R.Z. Wang, J.K. Kiplagat, L.W. Wang, R.G. Oliveira, A conceptual design and performance analysis of a triple-effect solid–gas thermochemical sorption refrigeration system with internal heat recovery, Chem. Eng. Sci. 64 (2009) 3376–3384.
[127] C. Zhu, K.R. Gluesenkamp, Z. Yang, C. Blackman, Unified thermodynamic model to calculate COP of diverse sorption heat pump cycles: Adsorption, absorption, resorption, and multistep crystalline reactions, Int. J. Refrig. 99 (2019) 382–392.
[128] L.W. Wang, R.Z. Wang, Z.S. Lu, C.J. Chen, Studies on split heat pipe type adsorption ice-making test unit for fishing boats: Choice of heat pipe medium and experiments under unsteady heating sources, Energy Convers. Manage. 47 (2006) 2081–2091.
[129] G. Cacciola, G. Restuccia, Progress on adsorption heat pumps, Heat Recovery Syst. CHP 14 (1994) 409–420.
[130] R. Critoph, Y. Zhong, Review of trends in solid sorption refrigeration and heat pumping technology, Proc. Instit. Mech. Engineers, Part E: J. Process Mech. Eng. 219 (2005) 285–300.
[131] D. Tchernev, High-efficiency regenerative zeolite heat pump, ASHRAE Trans. 2 (1988) 2024–2032.
[132] N. Mazet, M. Amouroux, B. Spinner, Analysis and experimental study of the transformation of a non-isothermal solid/gas reacting medium, Chem. Eng. Commun. 99 (1991) 155–174.
[133] S. Wu, T.X. Li, T. Yan, R.Z. Wang, Experimental investigation on a thermochemical sorption refrigeration prototype using EG/SrCl2–NH3 working pair, Int. J. Refrig. 88 (2018) 8–15.
[134] L. Xu, R.Z. Wang, T.X. Li, L.W. Wang, Experimental study on the performance of double-effect and double-way thermochemical sorption refrigeration cycle, Appl. Therm. Eng. 31 (2011) 3658–3663.
[135] Y.B. Gui, R.Z. Wang, W. Wang, J.Y. Wu, Y.X. Xu, Performance modeling and testing on a heat-regenerative adsorptive reversible heat pump, Appl. Therm. Eng. 22 (2002) 309–320.
[136] R.E. Critoph, Rapid cycling solar/biomass powered adsorption refrigeration system, Renew. Energy 16 (1999) 673–678.
[137] R.E. Critoph, Z. Tamainot-Telto, G.N.L. Davies, A prototype of a fast cycle adsorption refrigerator utilizing a novel carbon—aluminium laminate, Proc. Instit. Mech. Engineers, Part A: J. Power Energy 214 (2000) 439–448.
[138] G. Restuccia, Vasta, S., Freni, A., Russo, F., Aristov, Y. I., An advanced solid sorption chiller using SWS-1L: performance analysis and hydrothermal cycling stability of the sorbent bed, in: International Sorption Heat Pump Conference, Broomfield, Colorado, USA, 2005, pp. 22–24.
[139] D.I. Tchernev, J.M. Clinch, Closed cycle zeolite regenerative heat pump, in: eleventh annual ASME Solar Energy Conference, San Diego, California, 1989, pp. 347-351.
[140] R. Critoph, Towards a one tonne per day solar ice maker, Renew. Energy 9 (1996) 626–631.
[141] K. Wang, J. Wu, R. Wang, L. Wang, Composite adsorbent of CaCl2 and expanded graphite for adsorption ice maker on fishing boats, Int. J. Refrig. 29 (2006) 199–210.
[142] L.W. Wang, R.Z. Wang, Z.S. Lu, Y.X. Xu, J.Y. Wu, Split heat pipe type compound adsorption ice making test unit for fishing boats, Int. J. Refrig. 29 (2006) 456–468.
[143] Y. Alyousef, A.A. Antukh, A.P. Tsitovich, L.L. Vasiliev, Three adsorbers solar cooler with composite sorbent bed and heat pipe thermal control, Appl. Therm. Eng. 38 (2012) 124–130.
[144] R. Critoph, The use of thermosyphon heat pipes to improve the performance of a carbon–ammonia adsorption refrigerator, in: Proc. of the IV Minsk Int. Seminar-Heat Pipes, Heat Pumps, Refrigerators, Citeseer, 2000.
[145] R.E. Critoph, Performance estimation of convective thermal wave adsorption cycles, Appl. Therm. Eng. 16 (1996) 429–437.
[146] M. Tatlıer, B. Tantekin-Ersolmaz, A. Erdem-Şenatalar, A novel approach to enhance heat and mass transfer in adsorption heat pumps using the zeolite–water pair, Microporous Mesoporous Mater. 27 (1999) 1–10.
[147] G. Restuccia, A. Freni, G. Maggio, A zeolite-coated bed for air conditioning

adsorption systems: parametric study of heat and mass transfer by dynamic simulation, Appl. Therm. Eng. 22 (2002) 619–630.
[148] L. Bonaccorsi, A. Freni, E. Proverbio, G. Restuccia, F. Russo, Zeolite coated copper foams for heat pumping applications, Microporous Mesoporous Mater. 91 (2006) 7–14.
[149] K. Iammak, W. Wongsuwan, T. Kiatsiriroj, Investigation of modular chemical energy storage performance, in: The joint international conference on sustainable energy and environment (SEE), 2004.
[150] D.H. Jaehnig, W.R. Wagner, C.W. Isaksson, Thermo-Chemical Storage for Solar Space Heating in Single-Family House, in: Proceedings of Ecostock, Galloway, New Jersey, 2006.
[151] Y. Jiang, M.H. Bagheri, R.T. Loibl, S.N. Schiffres, Thermodynamic limits of adsorption heat pumps: A facile method of comparing adsorption pairs, Appl. Therm. Eng. 160 (2019) 113906.
[152] M.H. Bagheri, S.N. Schiffres, Ideal adsorption isotherm behavior for cooling applications, Langmuir 34 (2018) 1908–1915.

Energy 207 (2020) 118213

Contents lists available at ScienceDirect

Energy

journal homepage: www.elsevier.com/locate/energy

Design screening and analysis of gas-fired ammonia-based chemisorption heat pumps for space heating in cold climate

Zhiyao Yang [a, b, *, 1], Ming Qu [a], Kyle R. Gluesenkamp [b, 1]

[a] Purdue University, Lyle School of Civil Engineering, West Lafayette, IN, USA
[b] Oak Ridge National Laboratory, Building Equipment Research Group, Oak Ridge, TN, USA

ARTICLE INFO

Article history:
Received 18 February 2020
Received in revised form
29 May 2020
Accepted 22 June 2020
Available online 28 June 2020

Keywords:
chemisorption
Heat pump
Cold climate
Ammoniate salt
Thermodynamic analysis

ABSTRACT

Thermally-driven ammonia-based chemisorption heat pumps (CSHP) have the potential to provide high-efficiency space heating in cold climates. Using the reversible chemical bond between sorbent salt and ammonia, CSHP thermochemically pumps heat from the cold ambient to the end-uses of space heating at 50 °C. The heating coefficient of performance (COP) of a CSHP is largely dependent on the selection of the sorbent salts, cycle configuration, and the system operation. This study uses a thermodynamic model to investigate the performance of six CSHP system configurations, including four single-effect and two double-effect cycles. The feasibility and performance of 121 available NH_3/salt reactions are studied for each configuration. The thermal COP of the cycles and the primary energy COP of the gas-fired CSHP systems are evaluated assuming 50 °C supply temperature for building space heating and the optimal system designs are identified. The highest thermal COP for single-effect and double-effect cycles under −25 °C ambient temperatures are predicted to be 1.22 and 1.57, respectively. The corresponding primary energy COPs are above 1.0 and 1.15, which are 30% higher than condensing furnaces and is sustained into the same cold temperatures.

1. Introduction

Space heating accounts for over 2.35 quadrillion BTU, or 45% of total residential site energy consumption in the U.S [1]. This percentage is even higher for households in the heating-dominated cold-climate zones. According to the 2015 EIA residential energy consumption survey, almost 90% of the heating system in cold-climate residential buildings in the U.S. are either fuel-combusting or electric-resistance based, and 5–6% are electric heat pumps [2]. The fuel-combustion systems have efficiencies of 82–95% regardless of the ambient temperature, which have already approached the ideal thermodynamic efficiency of 100%. Electric furnaces and electric resistance heaters have an electric coefficient of performance (COP_e) below 1.0, which corresponds to a primary energy COP (COP_{pe}) even lower than the fuel-combusting heating systems. The electric heat pump can produce heating with COP_e of 4–5 under moderate ambient temperatures. However, as demonstrated in Ref. [3–6], both the capacity and energy efficiencies of electric heat pump heating systems decrease drastically below 2.5 as the ambient temperature drops below 0 °C·As a result, cold-climate electric heat pumps have COP_{pe} comparable to that of the conventional fuel-combusting systems. With the low energy efficiency of existing cold-climates heating systems, there is a strong need for systems capable of producing heat at higher efficiency under low ambient temperatures.

Thermally-driven chemisorption heat pumps (CSHP) is one of the potential technologies to address the challenge of high-efficiency space heating in cold climates. A CSHP uses reversible chemical reactions between solid sorbent material and gaseous refrigerants to pump heat from a cold environment to space-heating temperatures. The COP of a CSHP system is largely determined by the selection of working pairs and cycle configurations, as

* Corresponding author. Purdue University, Lyle School of Civil Engineering, West Lafayette, IN, USA.
E-mail address: yang573@purdue.edu (Z. Yang).

[1] This manuscript has been authored by UT-Battelle, LLC under Contract No. DE-AC05-00OR22725 with the U.S. Department of Energy. The United States Government retains and the publisher, by accepting the article for publication, acknowledges that the United States Government retains a non-exclusive, paid-up, irrevocable, world-wide license to publish or reproduce the published form of this manuscript, or allow others to do so, for United States Government purposes. The Department of Energy will provide public access to these results of federally sponsored research in accordance with the DOE Public Access Plan (http://energy.gov/downloads/doe-public-access-plan).

https://doi.org/10.1016/j.energy.2020.118213
0360-5442/

Nomenclature

COP	Coefficient of performance
CSHP	Chemisorption heat pump
DRES	Double-effect resorption system
DENE	Double-effect system with NH_3 evaporator
h_{fg}	Vaporization heat [kJ/kg]
HTF	Heat transfer fluid
HTS	High-temperature salt
HR	Heat recovery
LTS	Low-temperature salt
M	Molar mass [kg/mol]
MTS	Medium-temperature salt
P	Pressure [Pa]
Q	Heat [kJ]
R	Gas constant [kJ/kg·K]
SRES	Single-effect resorption system
STM	Specific thermal mass [KJ/K-kg sorbent]
SENE	Single-effect system with NH_3 evaporator
TM	Thermal mass [kJ/K]
T	Temperature [K]
ΔH_r	Reaction enthalpy [J/mol NH_3]
ε	Heat recovery effectiveness

Subscripts

ads	Adsorption
condHX	Flue gas condensing heat exchanger
cl	Cooling
e	Electricity
eq	Equilibrium
H	High
ht	Heating
pe	Primary energy
M_aX_b	Generic chemical formula of metal halide salt
ΔS_r	Reaction entropy [J/K-mol NH_3]
η	Heat exchange effectiveness
amb	Ambient
cond	Condensation
des	Desorption
evap	Evaporation
$E \rightarrow PE$	Conversion from electricity to primary energy
HW	Hot water supply
L	Low
rej	Heat rejection

well as the system operation. Therefore, model-based performance analysis and comparison of the CSHP systems with different salts and cycle configurations are necessary to achieve a higher energy efficiency than the existing heating systems.

There are several such studies in the literature on the COP of chemisorption systems using different designs. The majority of model-based comparative studies on chemisorption systems focused on refrigeration applications [7–10]. Neveu and Castaing [7] developed a thermodynamic model for a chemisorption heat pump with internal heat recovery to study 16 possible ammoniate salts for refrigeration application. They correlated system COP to the heat source temperature and the evaporation temperature and generated a domain of application for each of the salt. Goetz et al. [8] mapped the performance of chemisorption refrigeration and thermo-transformation systems for 26 ammoniate salts and single-effect configurations. Li et al. [9] compared the performance of chemisorption refrigeration systems using single-effect, double-effect, and triple-effect cycle configurations. Pons et al. [10] modeled five thermally-driven chemisorption systems (four salts and four cycle-configurations) for not only refrigeration but also heat pumping applications. Experimental tests were also used for comparison. Wang et al. [11] experimentally compared the performance of the resorption and the ammonia-evaporation configurations in deep freezing applications using three different salts. Most existing studies focused on refrigeration application with heat rejection temperatures too low to provide heating;

There are a few comparative studies on using chemisorption for heating applications [12,13]. Zhu et al. [12] developed a unified thermodynamic model to evaluate the COP of sorption systems, and the model was used to analyze the heating performance of three single-effect chemisorption systems. Yang et al. [13] conducted a comparative study of chemisorption reactions and cycles for cold climate heat pumping, where the heating COP of CSHP using 66 single-stage ammoniate reactions and six cycle configurations were evaluated and compared. Despite the comparative studies in the literature, the performance of chemisorption systems under the low-ambient and high-supply temperatures typical for cold-climate heat pumping applications has not been sufficiently explored: a very limited number of salts and configurations were considered compared to the vast candidate pool of salts and cycles. The study conducted by Yang et al. did not consider double-effect cycles or the multiple-stage reactions of the same salt that could potentially lead to higher performance than the single-stage reactions.

This study fills the gap by providing a comprehensive thermodynamic performance study on the ammonia-based CSHP for cold-climate heating applications to facilitate proper system design. The paper first introduces the basic principle of CSHP followed by research methods to evaluate the thermodynamic performance of the CSHP systems with six cycles configurations and different the ammonia-based chemisorption reactions under the cold-climate conditions. Finally, the designs with optimal performance are highlighted and compared with existing technologies.

2. Basic principles of chemisorption heat pump

In an ammonia-based CSHP system, the thermal effects of chemisorption reaction and ammonia phase change are applied to produce useful heating in sorbent- and ammonia-containing heat exchangers under different temperatures and pressures. A general expression of the reversible chemical reactions between ammonia vapor and sorbent salt in a CSHP system is as equation (1). Metal-halide such as $CaCl_2$ and NaBr are the most commonly used sorbent salt in ammonia chemisorption system, and in equation (1) the salt is generically referred to as M_aX_b, where M is the metal atom and X is the non-metal atom that together make up the sorbent salt capable of bonding with ammonia molecules and forming complex compounds.

$$M_aX_b \cdot n_1NH_3(s) + n_2\Delta H_r \leftrightarrow M_aX_b \cdot (n_1 - n_2)NH_3(s) + n_2NH_3(g) \quad (1)$$

When external energy ($n_2\Delta H_r$) is provided to heat the reactants the reaction occurs in the forward direction where the ammoniate complex ($M_aX_b \cdot n_1NH_3$) is decomposed, releasing gaseous ammonia. When heat is extracted the reaction occurs in the backward direction with the "dry" sorbent ($M_aX_b \cdot (n_1 - n_2)NH_3$) absorbs gaseous ammonia and synthesize into ammonia-rich compounds

($M_aX_b \cdot n_1 NH_3$).

Fig. 1 illustrates the schematic and working procedure of a basic CSHP cycle with a sorbent-containing adsorber and a heat exchanger acting as a condenser or an evaporator. The CSHP cycles between the desorption and adsorption modes. In the desorption mode, heat from a high-temperature source, Q_{des}, is supplied to the adsorber to decompose the ammoniate salt and release ammonia vapor. The ammonia vapor flows into the condenser to be cooled by the medium-temperature heat sink and condense, releasing heat, Q_{cond}. The desorption mode ends with the sorbent in the adsorber exhausted of ammonia and the ammonia accumulating in the liquid phase in the condenser. The adsorption mode then starts by cooling the hot and dry sorbent in the adsorber. The cooler sorbent absorbs vapor and reduces the pressure to drive evaporation of the liquid ammonia to extract heat, Q_{evap}, from the cold ambient. The synthesis of ammonia and the sorbent releases heat, Q_{ads}, to the medium-temperature heat sink. The adsorption mode ends upon exhaustion of ammonia in the evaporator, and the system switches back to the desorption mode for continued operation.

The performances of CSHP systems are significantly influenced by the sorbent material and the system configuration. To achieve a high COP, the CSHP system needs to use sorbents with high sorption capacity and system cycles that fully use energy input to produce useful heating.

3. Research methodology

The investigation of CSHP system performance starts with the identification of the CSHP system designs that are feasible under the cold-climate heating conditions. The system design includes the selection of cycle configuration and the sorbent material. First, the method to identify chemisorption reactions that can operate under the cold-climate heating conditions is described. Then the six cycle configurations included in this study and the method to calculate their thermal COPs are introduced. For each combination of material and cycle configuration, the cycle thermal COP and the gas-fired system's primary energy COP are calculated, and the latter is compared with the efficiencies of the existing technologies.

3.1. Screening procedure to identify chemisorption reactions for cold-climate space heating

A cold-climate heat pump typically needs to extract heat from ambient at below 0 °C, while also rejecting heat to the end-use at temperatures as high as 50 °C. Therefore, the sorbent materials need to be carefully selected so that the desorption or adsorption reactions can happen under such an operating condition. The sorption capacity of a reaction is the mass of ammonia change associated with a reaction. The specific sorption capacity of the reaction is defined as the mass of ammonia change per unit mass of the pure salt. Reactions with high specific sorption capacities require less salt per unit capacity and typically enable a more compact system with high energy and power density, and therefore they are generally preferred in the screening.

The pressure-temperature equilibrium of such reactions is described by the van't Hoff equation as equation (2). In the van't Hoff equation, ΔH_r and ΔS_r are the enthalpy and entropy change associated with the reaction per mole of ammonia change, R is the ideal gas constant, T is the temperature of the sorbent salt in Kelvin, P_{eq} is the corresponding equilibrium vapor pressure of ammonia in Pascal, and P_0 is a reference pressure of 1 Pa.

$$\ln\left(\frac{P_{eq}}{P_0}\right) = -\frac{\Delta H_r}{RT} + \frac{\Delta S_r}{R} \tag{2}$$

Using to the enthalpy and entropy of 66 ammonia-based chemisorption reactions reported in Ref. [7,14], the pressure-temperature equilibrium lines of these reactions are illustrated on the Clapeyron Chart as in Fig. 4. The procedure for screening feasible chemisorption reactions based on the operating temperatures is illustrated in the flow chart in Fig. 2 and the Clapeyron chart in Fig. 4.

Fig. 2 shows the screening procedure for the available reactions by the low-temperature and high-temperature materials of the working pair. The procedure starts with a decision of whether a resorption configuration is used. In a non-resorption configuration such as the basic CSHP in Fig. 1, the desorption and sorption processes in the salt are coupled with ammonia condensation and evaporation. However, in a resorption configuration, the condenser-evaporator of the basic CSHP system is replaced with another adsorber containing a different type of salt. The desorption of the high-temperature-salt (HTS) leads to sorption reaction and heat rejection in the low-temperature-salt (LTS), while on the other hand, the sorption process of the HTS drives the LTS to absorb heat and desorb ammonia.

The low operating pressure (P_L) is the ammonia pressure when the system is extracting heat from the cold ambient. In non-resorption cycles, it is the saturation pressure of ammonia during evaporation; in resorption cycles, it is the desorption equilibrium pressure of the LTS during desorption. The high operating pressure (P_H) is the ammonia pressure when system is taking heat from the high-temperature heat source. In non-resorption cycles, it is the saturation pressure of ammonia during condensation; in resorption cycles, it is the sorption equilibrium pressure of the LTS. The minimum operating pressure (P_{min}) is the lower pressure boundary of P_L for a cycle to be considered feasible. The P_{min} limit is imposed to avoid the significant reduction of vapor transfer in the sorbent under very low pressures as pointed out in Ref. [8,11,15].

The screening procedure is further illustrated in Fig. 3 for non-resorption systems and Fig. 4 for resorption systems. In a non-resorption system, ammonia is the low-temperature material in the working pair. The first step of screening is to determine the P_H and P_L as the ammonia saturation pressure at the temperatures of heat rejection (T_{rej}) and the ambient (T_{amb}). In Fig. 3 (1) the

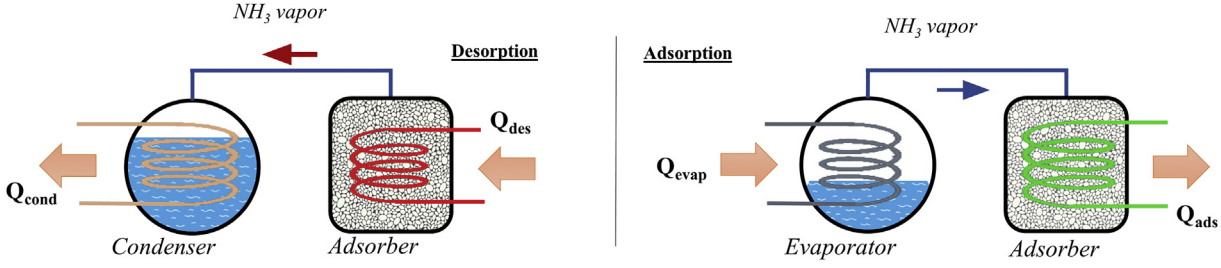

Fig. 1. Basic CSHP configuration and operating modes.

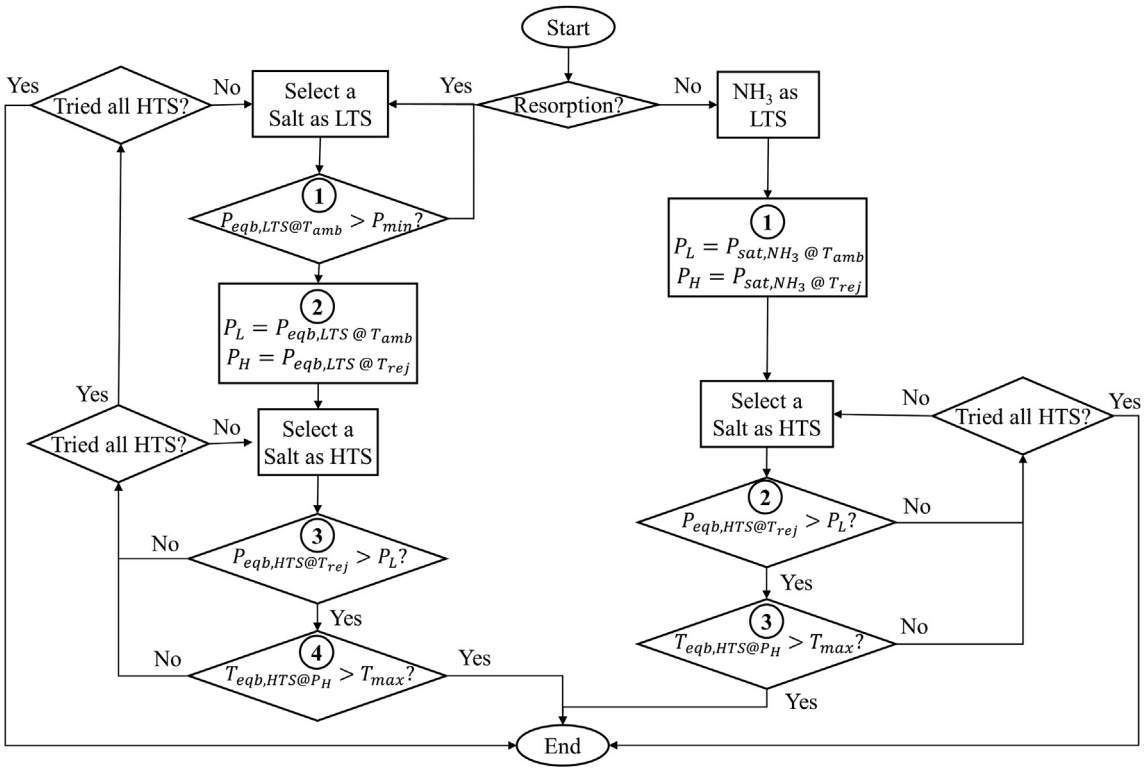

Fig. 2. Flow chart for the working pair screening procedure.

pressures are determined by the intersection point of the temperature lines and the vapor-liquid line of ammonia. The second step is to determine the lower temperature and pressure boundaries for the feasible HTS: the equilibrium vapor pressure of a feasible HTS at T_{rej} needs to be lower than P_L so that ammonia evaporation in the evaporator and the ammonia sorption in the adsorber can occur under the pressure difference. In Fig. 3 (2) the corresponding area is below the P_L line and to the right of the T_{rej} line. The third step is to determine the upper temperature and pressure boundaries: the equilibrium vapor pressure of the HTS needs to be above P_H to continuously drive ammonia out of the salt to condense in the condenser. Meanwhile, the corresponding equilibrium temperature of the salt needs to be below the maximum source temperature (T_{max}) to utilize the available heat source. In Fig. 3 (3) the area is bounded above the P_H line and to the left of the T_{max} line. By applying these three steps, the range of feasible salts are identified as the overlapping highlighted areas in Fig. 3 (4).

In a resorption system, two different salts need to be identified as the LTS and the HTS. The first step of screening is to identify the feasible LTS by comparing the equilibrium vapor pressure of each salt with the minimum ammonia pressure (P_{min}) at the ambient temperature as in Fig. 4 (1). The equilibrium vapor pressure of the LTS at T_{amb} needs to be above P_{min}. Then for a feasible LTS, the P_H and P_L of the system is determined based on the ambient temperature and the heat rejection temperature as in Fig. 4 (2). Then the feasible range of the HTS can be identified following the same approach as non-sorption configurations based on the operating pressures.

Single-stage reactions that fall within the feasible region such as $MnCl_2$-6/2 in Fig. 4 (3) can operate under the desired conditions. In addition, multiple reactions of the same salt such as $CaCl_2$-4/2 and $CaCl_2$-2/1 can all fall within the feasible region as in Fig. 4 (4), and they can operate sequentially as a multiple-stage reaction (designated as $CaCl_2$-4/1) under the operating temperatures to achieve a high total sorption capacity. The combination of multiple reactions that are based on the same salt can act as one integral reaction, as illustrated in Fig. 4 (4) with the three $CaCl_2$-based reactions occurring sequentially. These multiple-stage reactions correspond to a wider temperature span and offer a sorption capacity higher than their single-stage components. In total there are 121 single-stage and multiple-stage reactions to choose from for any chemisorption systems.

As shown in Fig. 4 (1), the feasible range of LTS in the resorption system is identified to the left of the Clapeyron chart near the ammonia vapor-liquid line. Based on the P_H and P_L determined by the LTS, the feasible range of the HTS is determined to the right of the chart. The example LTS operating under low temperature is NH_4Cl-3/0, and an HTS that falls in the feasible range for this LTS is $MnCl_2$-6/2.

In real CSHP systems, the sorbent salts are often impregnated in porous matrix materials such as expanded graphite to enhance the heat and mass transfer performance and mitigate the detrimental effect of salt swell and agglomeration during adsorption [16,17]. The interaction between the matrix material and ammonia is negligible. Therefore, as long as the operating pressure is sufficiently high as not to limit the mass transfer within the porous composite as suggested in Refs. [8,11,15], the temperature-pressure equilibrium of the reactions is not affected by the inclusion of the porous matrix material, and thus the sorbent and reaction screening results still apply to such composite sorbents.

3.2. CSHP cycle configurations

Based on the basic CSHP configuration with a salt-containing adsorber and an integrated condenser-evaporator shown in Fig. 1, more complex cycles are developed in the literature to improve the utilization of the heat input and increase the system thermal efficiency [14]. This study limits the number of heat exchangers to no

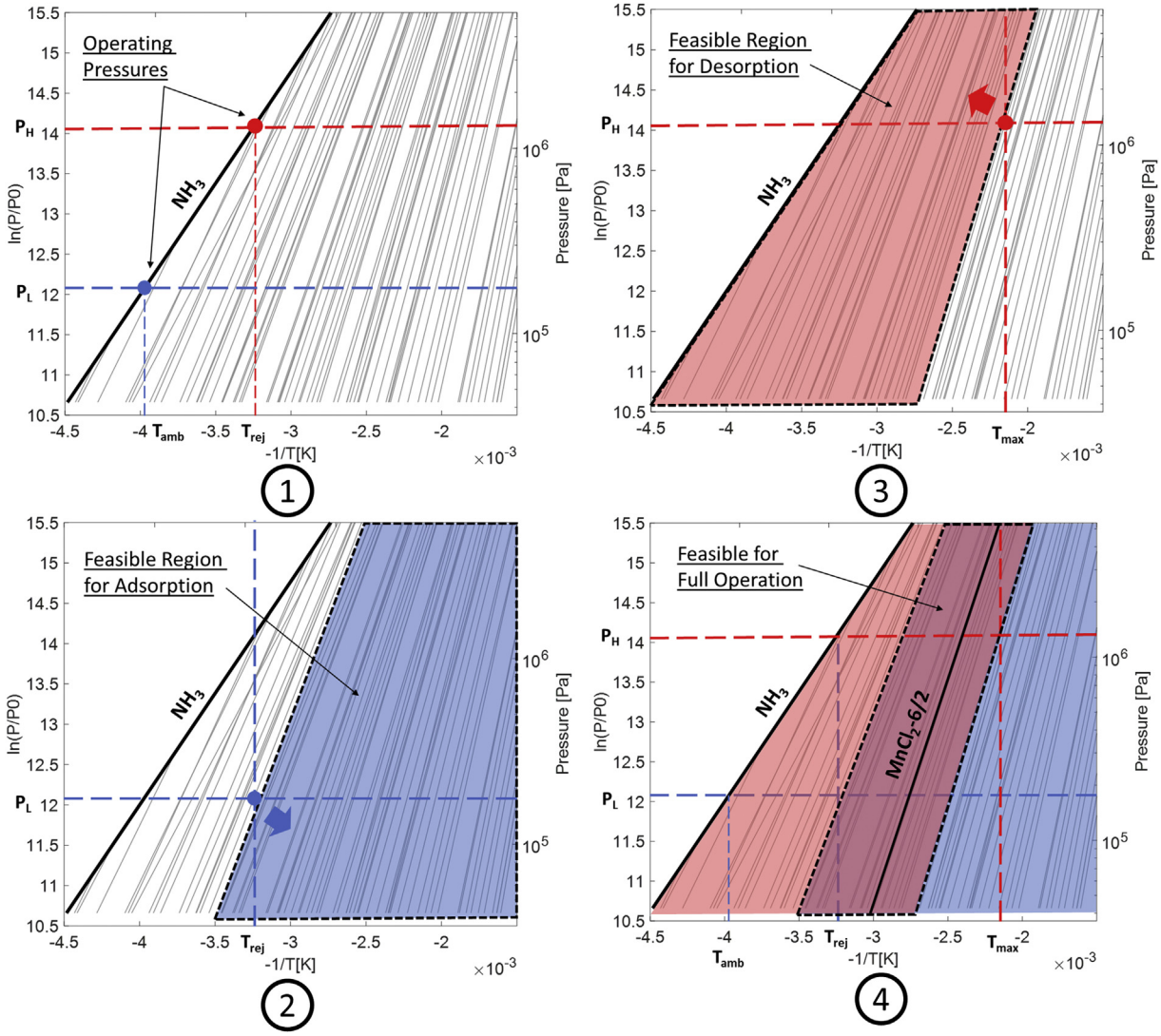

Fig. 3. Reaction screening for non-resorption configurations. (1) determine the high (condensing) and low (evaporating) operating pressures based on the ammonia saturation pressures at the ambient and heat rejection temperatures; (2) at the heat rejection temperature, the equilibrium pressure of the feasible salts should be below the ammonia evaporating pressure to drive evaporation; (3) at the maximum heat source temperature, the equilibrium pressure of the feasible salts should be above the ammonia condensing pressure to drive condensation; (4) salts falling in the overlapping area of (2) and (3) are suitable for the given operating condition. In the figure, P_H and P_L are the operating pressures during desorption-condensing and adsorption-evaporating processes. T_{amb}, T_{rej} and T_{max} are the temperature of the ambient, heat rejection, and heat source.

more than 4. Within such limitation, single-effect and double-effect cycles can be assembled with adsorbers, condensers, and evaporators as listed in Table 1.

The two most basic configurations are single-effect with NH_3 evaporator (SENE) and single-effect resorption (SRES) as described in Ref. [8]. SENE consists of a salt-containing adsorber connected to a condenser and an evaporator operating in alternating desorption-adsorption half-cycles. SRES consists of two adsorbers containing the LTS and the high-temperature-salt (HTS). SRES also operates in alternating half-cycles where the HTS is heated and desorbs ammonia to be adsorbed by the LTS and release heat, or the HTS is cooled and adsorbs ammonia from the LTS.

More complex cycle configurations are developed based on the SENE and SRES cycles. For these two single-effect cycles, heat-recovery (HR) mechanism can be implemented to exchange heat between two opposite half-cycle adsorbers to recover some heat required to pre-heat the adsorber before desorption, an example of which is the SENE-HR system investigated by Wang et al. [18]. Double-effect cycles are assembled by channeling the adsorption heat of HTS to supply the desorption heat of reactions at lower temperatures, such as the DRES cycle built and studied by Oliveira et al. [19] and the double-effect cycle with NH_3 evaporator (DENE) investigated by Neveu et al. [7]. Table 1 lists the six cycle configurations included in this study.

These cycles can be illustrated on the Clapeyron chart with the equilibrium lines of the materials in the system as in Fig. 5. The single-effect cycles involve two materials—either ammonia and salt, or two different salts. Thus, they can be illustrated in Fig. 5 (a). For SENE and SENE-HR cycles, ammonia is the low-temperature (LT) material that extracts heat from cold ambient, and the sorbent salt is the high-temperature (HT) material that is heated by the external energy source in Fig. 5 (a). For SRES and SRES-HR cycles, the LTS is the LT and the HTS is the HT in Fig. 5 (a). During the desorption half-cycle of the single-effect cycles, the high-temperature heat from the energy source ($Q_{in,H}$) enters the system by heating and driving the desorption of the HT. Ammonia is released by HT and then gets condensed or adsorbed in LT, releasing useful heat at the medium temperature ($Q_{rej,L}$). In the adsorption

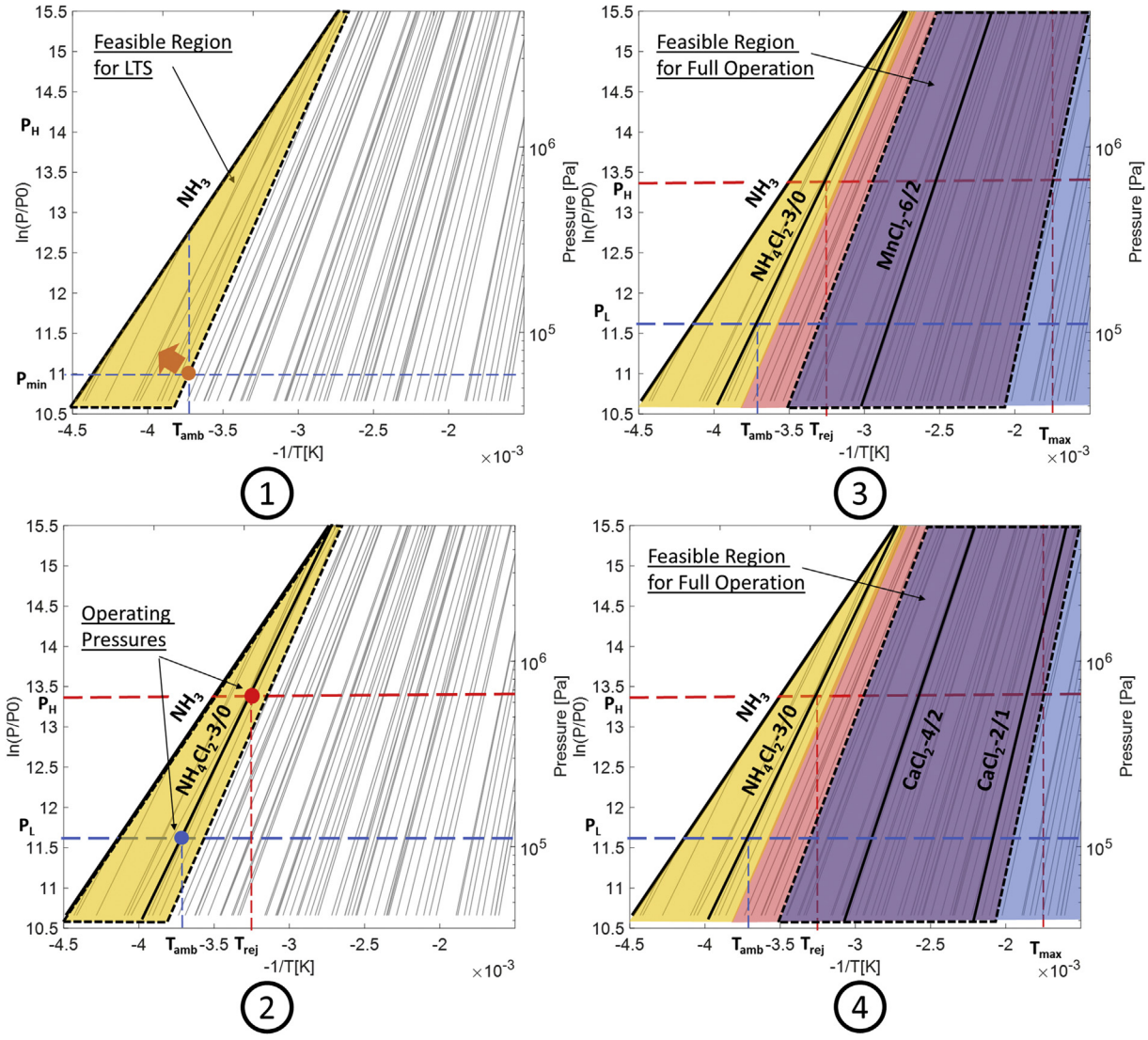

Fig. 4. Reaction screening for resorption configurations: (1) at the ambient temperature, the equilibrium pressure of the feasible LTSshould be above the lower limit of the system operating pressure to avoid mass transfer limitations; (2) determine the high and low operating pressures based on the equilibrium pressures of a selected LTS at the ambient and heat rejection temperatures; (3) determine the HTS using the high and low operating pressures and following the same procedure as non-resorption reactions; (4) for both resorption and non-resorption configurations, multiple-stage reactions of the same salt within the feasible region are available. In the figure, P_H and P_L are the operating pressures during desorption-condensing and adsorption-evaporating processes. T_{amb}, T_{rej} and T_{max} are the temperature of the ambient, heat rejection, and heat source.

half-cycle, useful heat is extracted from the HT ($Q_{rej,H}$), driving the exothermic adsorption process leading to the endothermic evaporation or desorption of ammonia in LT ($Q_{in,L}$).

The DENE and DRES cycles involve three different materials, and their operations can be described in Fig. 5 (b). The LT represents ammonia in DENE and the LTS in DRES. The MT and HT represent the medium-temperature and high-temperature salts in the double-effect cycles. High-temperature heat entering the system by heating the HT ($Q_{in,H}$). The desorbed ammonia from HT is condensed or adsorbed by LT, releasing useful heat ($Q_{rej,L}$). Later ammonia is evaporated or desorbed from LT to be adsorbed in HT, and the adsorption heat ($Q_{rej,H}$) is supplied to drive the desorption of MT ($Q_{in,M}$). The ammonia desorbed from MT also gets condensed or adsorbed in LT, releasing another useful heat ($Q_{rej,L}$). When this ammonia gets adsorbed by MT, the released heat ($Q_{rej,M}$) is supplied to the end-use as well. In order to drive the chemical reaction and phase change, the operating temperatures need to deviate from the equilibrium. These "equilibrium drop" are illustrated in Fig. 5 as ΔT_{eq}.

The operation of a chemisorption system is always transient with varying temperatures and progression of the chemisorption reaction. Nevertheless, the performance of chemisorption systems can still be analyzed using thermodynamic models based on the overall change of state over an entire cycle under simplifying assumptions [7,8,11]. The thermodynamic model is generic for each specific cycle configuration and is not affected by the sorbent salt selection. Therefore, such models can be used to evaluate and compare the performance of different system designs.

3.3. Thermodynamic performance

The heating COP of a system is defined as the ratio of heat produced over the heat consumption. For single-effect CSHP cycles the useful heat ($Q_{out,HW}$) produced at the heat rejection temperature (T_{HW}) includes the adsorption heat ($Q_{rej,H}$) in adsorbers and the condensation heat ($Q_{rej,L}$) in the condenser. The heat input from

Table 1
Summary of cycle configurations included in this study.

Config.	Heat recovery	Single-effect	Double-effect
NH_3 Evaporator	Non-HR	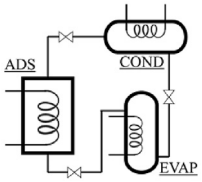	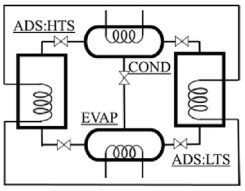
	HR	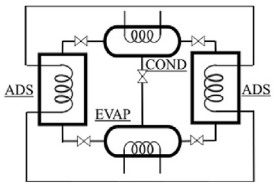	N/A
Resorption	Non-HR	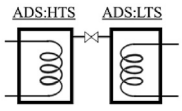	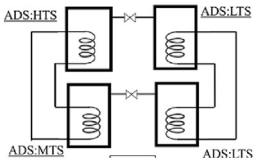
	HR	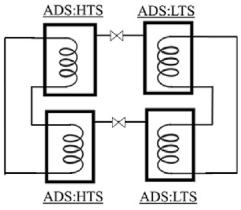	N/A

*ADS = adsorber, COND = condenser, EVAP = evaporator.

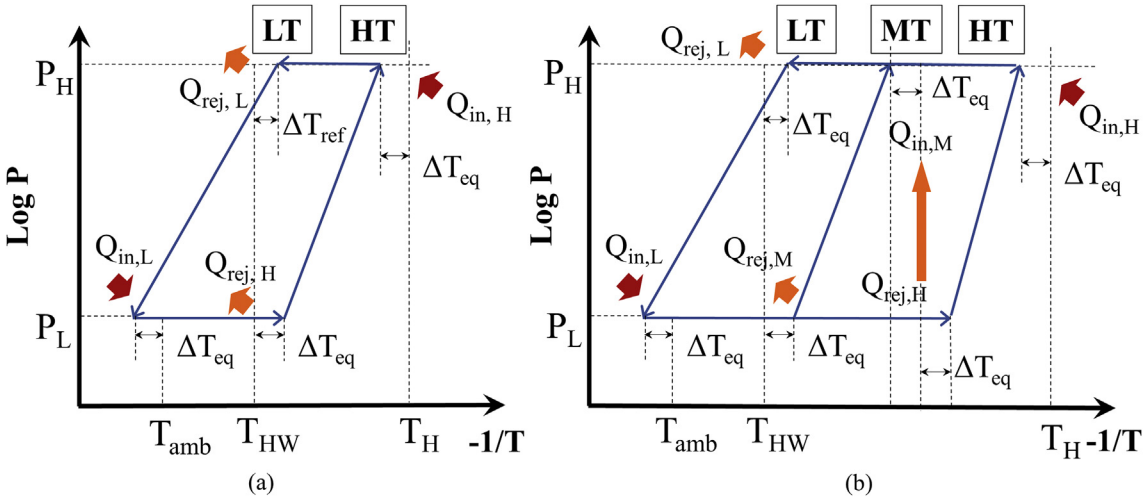

Fig. 5. Chemisorption cycles on Clapeyron chart: (a) single-effect cycles and (b) double-effect cycles.

the energy source ($Q_{in,H}$) is the heat input at high temperature (T_H) into the adsorber. With energy balance the total heat production ($Q_{rej,H} + Q_{rej,L}$) equals to the total heat input from both the high-temperature energy source ($Q_{in,H}$) and the cold ambient ($Q_{in,L}$). Thus, heating COP can be written as one plus the ratio of heat extraction ($Q_{in,L}$) at low temperature (T_{amb}) over the driving heat as in equation (3), that is, one plus the cooling COP had it been used as a chiller.

$$COP_{ht} = \frac{Q_{out,\,T_{HW}}}{Q_{in,\,T_H}} = 1 + \frac{Q_{in,L}}{Q_{in,\,H}} = 1 + COP_{cl} \tag{3}$$

Without considering the thermal mass of any material in the operation process, the theoretical heat input and rejection in the adsorber is only associated with the reaction enthalpy (ΔH_r), and the theoretical heat production in the condenser is proportional to

the ammonia evaporation enthalpy (H_{fg}). The expressions of the cycle heating COP are listed in Table 2. For single-stage reactions the reaction enthalpy is directly used to calculate COP; for multiple-stage reaction, an average reaction enthalpy per mole of ammonia is used.

However, in real system operations, part of the high-temperature heat is consumed to repeatedly heat the thermal masses in the HTS adsorber from the previous adsorption temperature to the high desorption temperature. The thermal masses of the adsorber include the salt, binder-matrix, sorbed ammonia, heat transfer fluid, and the metal of heat exchangers. In the resorption configuration, part of the adsorption heat of the LTS is also lost to pre-heating the thermal masses of the LTS adsorber from below ambient temperature up to the heat supply temperature. Dead thermal mass (TM), therefore, was introduced by Gluesenkamp [20] to reflect these losses. The TM, which is the product of the mass and specific heat, summed for all masses in the heat exchangers. In the unified thermodynamic model developed by Zhu et al. [12] the effect of TM is accounted for using the ratio of heat loss associated with the TM and the reaction or latent heat, which varies between 0.14 and 0.76 according to the experimental data in the literature. Li et al. [21] used the mass ratio of 5 between the heat exchanger metal and the sorbent as a rule-of-the-thumb estimation of the amount of TM in a well-designed adsorption system, and the same method was used in Yang et al. [22] as well. The impact of TM on the adsorption system performance was further discussed in Refs. [12,22] where the TM was categorized into two parts: inherent TM and design TM as in equation (4). In this study, the design thermal mass includes that of the adsorber heat exchanger metal and the heat transfer fluid (HTF) as in equation (5). The inherent thermal mass includes that of the salt, the binder-matrix such as expanded graphite, and the sorbed refrigerant as in equation (6). The thermal mass of the sorbed refrigerant is estimated using the liquid phase heat capacity.

$$TM = TM_{inherent} + TM_{design} \quad \left[\frac{kJ}{K}\right] \tag{4}$$

$$TM_{design} = \rho_{HTF} V_{HTF} c_{HTF} + \rho_{metal} V_{metal} c_{metal} \quad \left[\frac{kJ}{K}\right] \tag{5}$$

$$TM_{inherent} = m_{salt} c_{salt} + m_{binder-matrix} c_{binder-matrix} + m_{NH3} c_{NH3} \quad \left[\frac{kJ}{K}\right] \tag{6}$$

$$STM = specific\ thermal\ mass = \frac{TM}{m_{salt}} \quad \left[\frac{kJ}{K \cdot kg_{salt}}\right] \tag{7}$$

A specific thermal mass (STM) metric, as expressed in equation (7), was defined in Ref. [23] as the ratio of the total thermal mass (excluding the retained refrigerant) to the salt mass. STMs of experimentally tested adsorbers in Ref. [24–29] were calculated to be ranging from 2.46 to 19.58. An STM of 6 kJ/kg·K is used in this study as a typical value for adsorbers, and the impact of different STMs on the system performance is investigated later in this study.

The internal heat recovery mechanisms can reduce the negative effect of TM on the system performance by recovering heat between the heat exchangers at the opposite half-cycles. For heat recovery on the heat source side and ambient side, heat recovery effectiveness ε_H and ε_L are defined respectively as in equations (8) and (9) with T_{rec} as the temperature of the initially hotter thermal mass after heat recovery. Pre-heating the cold heat exchanger from the T_{amb} with the sensible heat of the heat exchanger at T_{HW} can only heat the cold heat exchanger up to the average temperature of T_{amb} and T_{HW}. Therefore, the maximum value of ε_L is 0.5. The same limit goes with ε_H and the heat recovery at the high-temperature side. Table 2 lists the COP expressions of the six cycle configurations with and without consideration of TM.

$$\varepsilon_L = \frac{T_{rec} - T_{amb}}{T_{HW} - T_{amb}} \tag{8}$$

$$\varepsilon_H = \frac{T_{rec} - T_{HW}}{T_H - T_{HW}} \tag{9}$$

The expressions listed in Table 2 use the mass and specific heat of various materials to calculate the thermal masses of different components. Based on the mass of ammonia transferred during the operation, the mass of salt can be calculated using the stoichiometric ratio of salt and ammonia in equation (1). Then using the STM and the mass of salt, the thermal mass of all other components in the system can be directly estimated.

The maximum amount of ammonia transferred in the operation is determined by the difference of ammonia content in the sorbent between desorption and adsorption phases. Only a fraction of the maximum is reached depending on factors such as reaction rate and cycle time. A realistic reaction completion fraction of 85% was used by Li et al. [21] in chemisorption refrigeration system models, and the same value was used in this study. Wang et al. [11] studied a resorption cycle and pointed out pressure below 30 kPa during LTS desorption would limit the mass transfer and significantly reduce

Table 2
Expression for COP of the 6 cycles with and without considering thermal mass.

Cycle	Heating COP without Thermal Mass	Heating COP Considering Thermal Mass
SENE	$1+\frac{M_{NH_3}\cdot h_{fg}}{\Delta H_{r,salt}}$	$1+\frac{m_{NH3}\cdot\left(h_{fg}-(T_{HW}-T_{amb})\cdot c_{NH_3}\right)}{m_{NH3}\cdot\Delta H_{r,salt}/M_{NH_3}+m_{salt}\cdot(T_H-T_{HW})\cdot STM_{ads}}$
SENE-HR	$1+\frac{M_{NH_3}\cdot h_{fg}}{\Delta H_{r,salt}}$	$1+\frac{m_{NH3}\cdot\left(h_{fg}-(T_{HW}-T_{amb})\cdot c_{NH_3}\right)}{m_{NH3}\cdot\Delta H_{r,salt}/M_{NH_3}+(1-\varepsilon_H)\cdot m_{salt}\cdot(T_H-T_{HW})\cdot STM_{ads}}$
SRES	$1+\frac{\Delta H_{r,\ LTS}}{\Delta H_{r,HTS}}$	$1+\frac{m_{NH3}\cdot\Delta H_{r,LTS}/M_{NH_3}+m_{LTS}\cdot(T_{HW}-T_{amb})\cdot STM_{ads,LTS}}{m_{NH3}\cdot\Delta H_{r,HTS}/M_{NH_3}+m_{HTS}\cdot(T_H-T_{HW})\cdot STM_{ads,HTS}}$
SRES-HR	$1+\frac{\Delta H_{r,\ LTS}}{\Delta H_{r,HTS}}$	$1+\frac{m_{NH3}\cdot\Delta H_{r,LTS}/M_{NH_3}+(1-\varepsilon_L)\cdot m_{LTS}\cdot(T_{HW}-T_{amb})\cdot STM_{ads,HTS}}{m_{NH3}\cdot\Delta H_{r,HTS}/M_{NH_3}+(1-\varepsilon_H)\cdot m_{HTS}\cdot(T_H-T_{HW})\cdot STM_{ads,HTS}}$
DENE	$1+\frac{2\cdot M_{NH_3}\cdot h_{fg}}{\Delta H_{r,HTS}}$	$1+\frac{2\cdot m_{NH3}\cdot\left(h_{fg}-(T_{HW}-T_{amb})\cdot c_{NH_3}\right)}{m_{NH3}\cdot\Delta H_{r,HTS}/M_{NH_3}+m_{HTS}\cdot(T_H-T_{HW})\cdot STM_{ads,HTS}}$
DRES	$1+\frac{2\cdot\Delta H_{r,LTS}}{\Delta H_{r,HTS}}$	$1+\frac{2\cdot m_{NH3}\cdot\Delta H_{r,LTS}/M_{NH_3}+m_{LTS}\cdot(T_{HW}-T_{amb})\cdot STM_{ads,LTS}}{m_{NH3}\cdot\Delta H_{r,HTS}/M_{NH_3}+m_{HTS}\cdot(T_H-T_{HW})\cdot STM_{ads,HTS}}$

the cycle capacity. Therefore, a low-pressure limit of 50 kPa is applied in this study. Additionally, the equilibrium temperature drop from the external heat source or sink is assumed to be 5 °C at the refrigerant side, e.g. in condenser/evaporator, and 10 °C on the sorbent side, e.g. in the adsorber.

3.4. Primary energy efficiencies

The primary energy COP of gas-fired CSHP systems can be calculated using equation (10) based on the cycle thermal COP ($COP_{cycle,ht}$), the gas-combustion efficiency (η_{burner}), the flue gas condensing heat exchanger efficiency (η_{condHX}), and the parasitic electricity consumption compared with the gas consumption ($\frac{P_{electricity}}{Q_{gas}}$). Evaluating the primary energy COP allows the energy efficiency of CSHP to be compared with other heating technologies.

$$COP_{pe} = \frac{Q_{supply}}{Q_{gas} + C_{E\to PE}\cdot P_{electricity}} = \frac{COP_{cycle,\ ht}\cdot\eta_{burner} + \eta_{condHX}}{1 + C_{E\to P}\cdot P_{electricity}\big/Q_{gas}} \quad (10)$$

In equation (10), the conversion ratio ($C_{E\to PE}$) of 3.365 is used for the conversion of electricity to primary energy based on the national power production data [30]. The total supplied heat of a gas-fired CSHP includes the heat from the heat exchangers in the heat pump cycle and the recovered flue gas heat in the condensing heat exchanger $Q_{condHX} = Q_{gas}\cdot\eta_{condHX}$. Following typical thermal efficiencies of 80% and 95% based on higher heating value for non-condensing and condensing furnaces, respectively. Therefore, in equation (10), the burner efficiency η_{burner} is 0.8, and the condensing heat exchanger efficiency η_{condHX} is 0.15. According to Garrabrant et al. [31], the ratio of parasitic electricity consumption to gas input is about 4% for condensing furnaces and 6% for the gas-fired absorption heat pump. Since CSHP requires less pump work compared with absorption heat pumps, a parasitic power ratio of 5% was assumed in this work.

The operating conditions and assumptions in this study are listed in Table 3. The temperature approach between the external heat source and the refrigerant is assumed to be 5 °C in the condenser and evaporator, and the temperature approach between the external heat source and the salt in the adsorber is assumed to be 10 °C due to the higher resistance in the solid-solid heat transfer.

4. Results and discussion

4.1. Screening of feasible reactions

The screening methodology was applied to all the 121 available reactions under the typical gas-fired cold-climate heating conditions: (1) <0 °C ambient, (2) 50 °C heat rejection, and (3) <300 °C heat source limited by the safety temperature of most heat transfer oil. Based on the cycle configuration, the feasible boundaries of the eligible reactions are different. When coupled with ammonia evaporation and condensation in SENE and DENE configurations, the eligible reactions have an equilibrium that (1) remains at above 50 °C at the pressure corresponding to 0 °C ammonia saturation; and (2) is below 300 °C at the pressure corresponding to 50 °C ammonia saturation. Under below 0 °C ambient temperatures, the selection of LTS in resorption configurations is limited to only NaBr-5.25/0 and NH_4Cl-3/0. The pressure constraints in resorption configurations are thus corresponding to the equilibrium pressures of NaBr-5.25/0 and NH_4Cl-3/0 at 0 °C and 50 °C, respectively. The MTS in double-effect cycles need to utilize the adsorption heat of HTS for its desorption, and therefore its equilibrium at high pressure needs to be cooler than the equilibrium of the HTS at low pressure, as corresponds to the process in Fig. 5 (b).

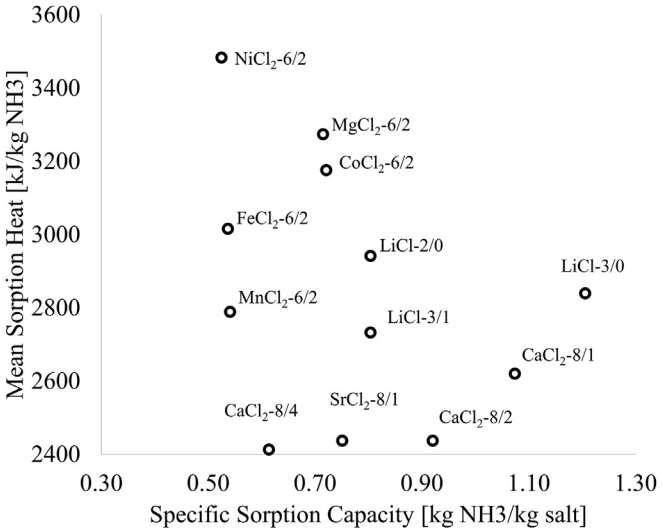

Fig. 6. Sorption capacity and sorption heat of high-capacity reactions.

Among the feasible reactions, a high sorption capacity is preferred as it implies more compact components with less salt required for the same ammonia transfer, therefore reducing the thermal mass and improving the system COP. Fig. 6 show the feasible reactions with the specific sorption capacity above 0.3 kg/kg. The high-capacity reactions with over 0.5 kg/kg are located in the right side of the plot and annotated.

Based on the expressions to calculate system COP in Table 2, the system COP generally benefits from a lower HTS sorption heat, as less heat is required from the energy source to drive the same amount of ammonia transfer and heat pumping effect. These

Table 3
Operating conditions and model assumptions used in this work.

T_{HW}, heat rejection temperature	50 °C
T_{amb}, ambient temperature range	−35 °C–0 °C
Temperature approach at refrigerant side (e.g. $T_{amb} - T_{NH3,eq}$)	5 °C
Temperature approach at sorbent side (e.g. $T_{amb} - T_{salt,eq}$)	10 °C
Ammonia pressure limits	>50 kPa; <5000 kPa
Specific thermal mass (STM) (TM_{total}/m_{salt})	6.0 $kJ^1K^{-1}kg^{-1}$ salt
Heat recovery effectiveness (ϵ_L and ϵ_H)	80%
Reaction completion fraction (fraction of maximum ammonia transfer)	85%
η_{burner}, natural gas burner efficiency (Q_{output}/Q_{gas})	0.80
η_{condHX}, condensing heat exchanger efficiency (Q_{cond}/Q_{gas})	0.15
Primary energy conversion ratio of electricity ($C_{E\to PE}$)	3.365
$P_{electricity}/Q_{gas}$, ratio of CSHP electricity consumption to gas input	0.05

Table 4
High-capacity reaction feasible for cold-climate heating applications.

Reaction	Specific Sorption Capacity [kg NH_3/kg salt]	Mean Reaction Heat [kJ/kg NH_3]	Desorption Temperature [°C]	Evaporation Temperature [°C]
LiCl-3/0	1.21	2839	193.4	< −30
$CaCl_2$-8/1	1.07	2620	278.8	−13
$CaCl_2$-8/2	0.92	2437	124.0	−13
LiCl-3/1	0.80	2733	175.0	< −30
LiCl-2/0	0.80	2942	193.4	< −30
$SrCl_2$-8/1	0.75	2437	120.3	−21
$CoCl_2$-6/2	0.72	3176	239.7	< −30
$MgCl_2$-6/2	0.72	3274	243.4	< −30
$CaCl_2$-8/4	0.61	2413	111.2	−13
$MnCl_2$-6/2	0.54	2789	178.6	−21
$FeCl_2$-6/2	0.54	3016	214.9	< −30
$NiCl_2$-6/2	0.53	3483	290.2	< −30
NaI-4.5/0	0.51	2314	116.0	−15

reactions are located at the bottom in Fig. 6. The specific sorption capacity and sorption heat of these high-capacity reactions are listed in Table 4. The reactions involving $CaCl_2$ and $SrCl_2$ have both high sorption capacity and low reaction heat, thus they are used in existing experimental studies of chemisorption heat pumps [10,32]. The reactions of $CoCl_2$, $MgCl_2$, $NiCl_2$ also have high sorption capacities, and their high equilibrium temperature makes them good candidates as the HTS in resorption and double-effect systems [10,32−34]. It is worth noting that some of these salts (especially LiCl and $CaCl_2$) are commonly used in aqueous solutions for liquid absorption cycles. Since this paper focuses on chemisorption systems, the values shown in Table 4 are for the synthesis or decomposition reactions of the ammoniate complexes of each salt.

In addition to the sorption capacity and reaction heat, the cost of the salt should also be taken into account when selecting the working pair for practical applications and commercialization. Liu et al. compared the prices of water-absorbing salts for seasonal thermal storage and found the prices of expensive sorbents such as LiCl and LiBr are over 14 times higher than cheap salts such as $CaCl_2$ [35]. Generally, the salts consisting of abundant and highly accessible elements such as $CaCl_2$ and $MgCl_2$ are usually less expensive compared with those with rare earth and other less common elements such as $CoCl_2$ and $SrCl_2$.

4.2. Comparison of cycle performance

Once the reactions feasible under cold-climate heating conditions are identified for each cycle configuration, the cycle heating COP can be determined. For each cycle configuration, the heating COP was calculated using the corresponding expression in Table 2 with the equilibrium of the selected chemisorption reaction and the properties of the sorbent material. The effect of the thermal mass as well as the “equilibrium drop” temperature difference are included in the calculation.

Fig. 7 shows the cycle COP of the best-performing reactions for each cycle configuration. The temperature-pressure equilibrium of chemisorption as described in equation (2) are discrete lines each corresponding to a fixed stoichiometric ratio of salt-ammonia in the chemical reaction. Therefore, the theoretical sorption capacities of chemisorption reactions are agnostic to the change of operating temperatures compared with the diminishing capacity of physical adsorption and absorption under decreasing ambient temperatures. Only the heat loss associated with thermal masses is affected by varying the ambient temperature. As a result, the trends of COP in Fig. 7 are linear, and the slope of the trendlines represents the effect of TM. Implementing heat recovery mechanism in the single-effect cycles reduces the TM heat losses and improves COP. The heat recovery mechanism also flattens the slope of COP against ambient temperature, indicating less performance sensitivity to temperature change. On the other hand, resorption cycles use more salt and subsequently more heat exchanger metal compared to cycles with NH3 evaporator, therefore they have more TM, leading to a higher COP sensitivity to the temperature lift.

The limited temperature ranges of some systems in Fig. 7 result from the limited feasibility of the selected reaction under low ambient temperatures: for SENE operating at below −5 °C ambient, LiCl-3/1NH3 is the optimal reaction with COP of 1.22 at −29 °C and 1.26 at 10 °C; at temperature above −5 °C, SrCl2-8/1NH3 becomes feasible and provides higher COP of above 1.32. For SRES cycles, the NaBr−LiCl reaction combination provides higher COP than NH4Cl−LiCl, but the former is only feasible with ambient warmer than −1 °C, while the latter can operate under −13 °C. Implementing heat recovery in the single-effect cycles can improve the heating COP from 1.15 to 1.35 up to 1.29−1.42. For DENE cycles the best-performing working pairs both use LiCl-3/2 as the medium temperature reaction, as it has a relatively low equilibrium temperature. Based on the process described in Fig. 5 (b), this allows high-capacity reactions such as $MgCl_2$-6/2 and $NiCl_2$-6/2 to be used as the HTS to lead to better performance. The combination of LiCl-3/2 and $NiCl_2$-6/2 can operate at below −30 °C with COP of 1.51−1.64. At ambient of −10 °C and above, $MgCl_2$-6/2 becomes feasible as the HTS with a higher COP of 1.61−1.67. The heating COP of SENE and DENE systems at −15 °C evaporation temperatures are around 1.2 and 1.55, which are slightly higher than the reported values from previously published work by Pons et al. [10].

The performance of DRES appears to be very limited both in terms of the temperature range and the COP. The best-performing working pairs can only use NH_4Cl-3/0 as the LTS and operate at above −1 °C ambient, with COP of around 1.48. Such low performance can be attributed to the limited selection of feasible HTS under the limitation of the heat source temperature below 300 °C. The ammonia vapor pressure of the LTS at low temperatures is lower than the corresponding ammonia saturation pressure, i.e. P_L in Fig. 5 (b) is quite low, requiring the HTS equilibrium pressure to be even lower to drive the adsorption process. Meanwhile, the adsorption temperature of the HTS needs to be higher than the MTS to supply the heat for MTS desorption.

Table 5 lists the minimum operating temperatures and cycle COP under different TM assumptions for the optimal system designs. The required heat source temperatures to drive single-effect cycles are below 200 °C compared to the almost 300 °C requirement for double-effect cycles. The effect of heat loss and COP reduction associated with thermal masses is much more pronounced in double-effect cycles as well, with an ideal COP of

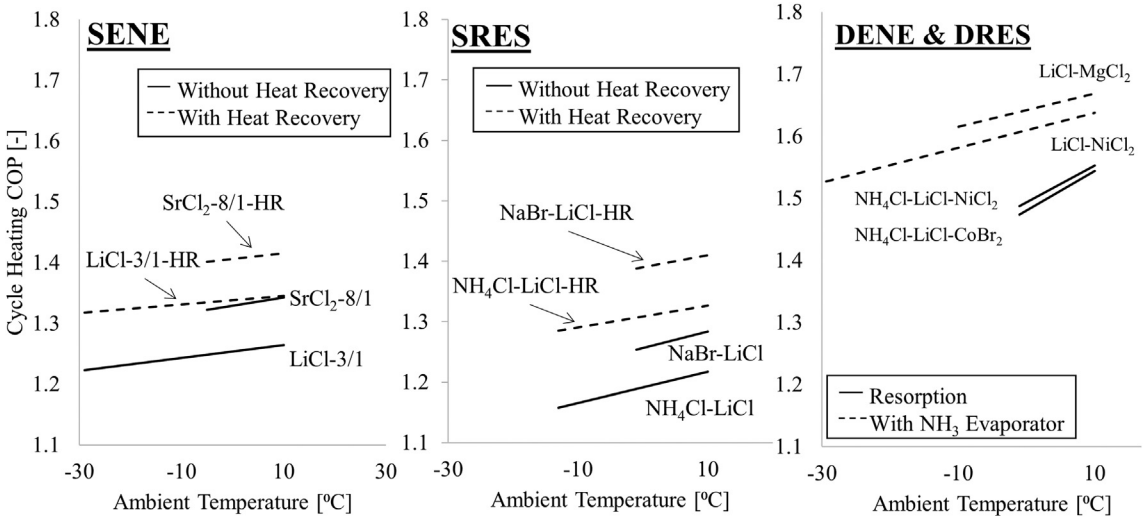

Fig. 7. Heating COP of the best-performing reactions under each cycle configuration assuming STM of 6 kJ/kg salt-K.

Table 5
Best-performing reactions for each configuration at its minimum ambient temperature.

Cycle	Reaction	Min. Ambient Temp. [ºC]	Heat Source Temp. [ºC]	COP without TM	COP with only inherent TM	COP with full TM	COP with HR
SENE	LiCl-3/0	−29	179	1.502	1.264	1.223	1.318
	$SrCl_2$-8/1	−5	124	1.563	1.381	1.322	1.401
SRES	NH_4Cl−LiCl	−13	188	1.589	1.276	1.158	1.286
	NaBr−LiCl	−1	186	1.701	1.408	1.254	1.388
DENE	LiCl−$MgCl_2$	−15	248	1.839	1.628	1.615	N/A
	LiCl−$NiCl_2$	−29	295	1.788	1.529	1.514	N/A
DRES	NH_4Cl−LiCl−$NiCl_2$	−1	284	1.994	1.643	1.487	N/A
	NH_4Cl−LiCl−$CoBr_2$	−1	279	2.005	1.697	1.474	N/A

around 2.0 of DRES drop to around 1.5. Meanwhile, the TM in single-effect cycles also reduces their heating COP, but the effect can be considerably mitigated by heat recovery. The COP with only inherent TM (salt and refrigerant) represents the efficiency limit of the optimal design to minimize TM without heat recovery. Since the sensible heat of the high-temperature adsorber thermal masses in double-effect systems is used to drive the desorption in the low-temperature adsorber, recovery of this heat is not feasible. Therefore, the COP with HR in Table 5 are marked N/A.

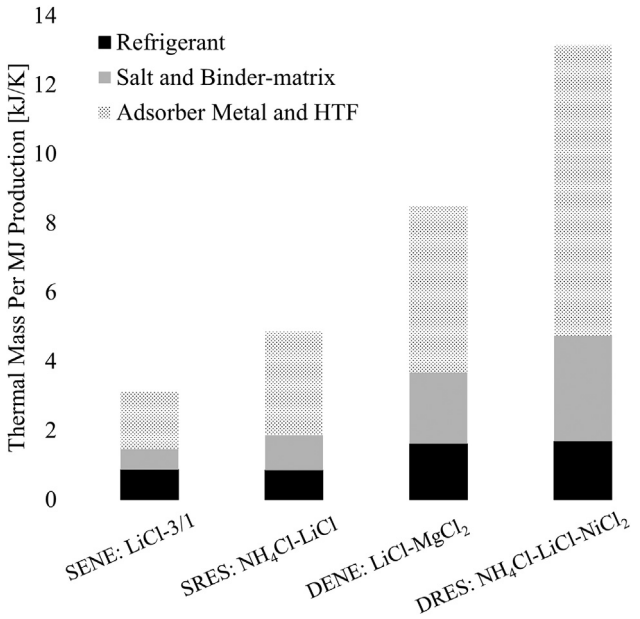

Fig. 8. Thermal mass of each configuration per MJ of heat production assuming STM = 6 kJ/kg_{salt}·K.

Fig. 8 compares the amount of thermal mass corresponding to 1 MJ of heat production over a complete desorption-adsorption cycle. The thermal masses in a cycle is 6 kJ/K per kg of salt and are broken down into salt and binder-matrix, refrigerant, and the adsorber heat exchanger metals and heat transfer fluid (HTF). For all cycle types, the thermal mass associated with metal and HTF is the dominant thermal mass.

The thermal masses of resorption and non-resorption cycles are also compared in the figure. The resorption cycles replace the ammonia condenser and evaporator with salt-containing adsorbers, which introduces more salt and binder-matrix masses into the system while also making the metal and HTF in the substitute adsorbers operate under the alternating temperatures. Therefore, for the same STM, the thermal masses of the salt and non-active components per unit heat produced in resorption cycles are much higher than their non-resorption counterparts. This explains the higher sensitivity of resorption cycle COPs to ambient temperatures in Fig. 7.

Furthermore, the required thermal masses to generate the same amount of heat of single-effect cycles are less than double-effect cycles. Therefore, despite their lower COP, the single-effect cycles could have higher specific heating capacities than the double-effect cycles. Moreover, as illustrated in Table 5, the higher-effect cycle operates over wider temperature ranges, which further adds to the heat loss associated with the thermal masses. This helps explain the

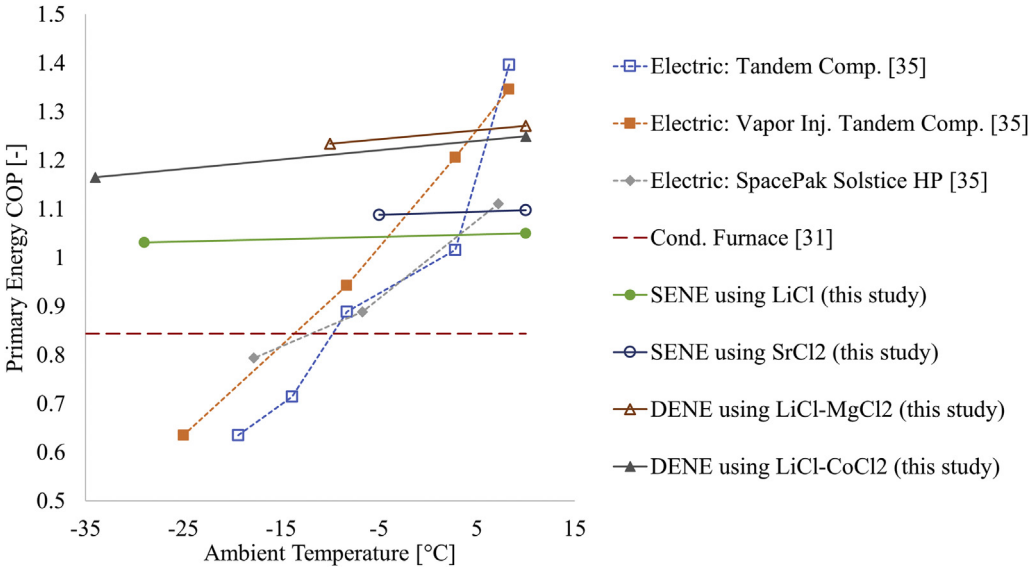

Fig. 9. Primary energy COP of conventional heating technologies and four CSHP configurations.

diminishing benefit of going for higher-effect systems when comparing the COP without thermal masses and with full thermal masses in Table 5.

4.3. Comparison of primary energy with conventional technologies

With the cycle heating COP calculated, the primary energy COP of gas-fired CSHP system using these selected cycles can be evaluated using equation (10). Fig. 9 shows the calculated primary energy COP of the gas-fired CSHP under cold-climate operating temperatures. The CSHP system COPs are compared with the efficiencies of conventional heating technologies from the literature. The performance of specially designed cold-climate electric heat pumps supplying hot water at 48.8 °C were from Ref. [36]. The COP_{pe} of 0.85 for condensing furnace is calculated from the gas efficiency of 92% and electricity energy consumption 4% of gas energy consumption [31].

The best-performing single-effect CSHP with heat recovery mechanisms can maintain a primary energy COP >1.0 under the ambient temperature of as low as −29 °C. Double-effect CSHP can achieve primary energy COP >1.15 at −25 °C ambient. Compared with the condensing furnaces, the COP_{pe} of CSHP is 18−35% higher. Compared with the drastic decline of efficiency electric vapor compression heat pumps at below −20 °C ambient temperature, the selected gas-fired CSHP systems can maintain a high efficiency into the deeply freezing temperatures.

5. Conclusions

Chemisorption heat pumps (CSHP) offer a promising solution to the challenge of high-efficiency heating in cold climates. The performance of CSHP largely depends on the system design. This study screened the available NH_3/salt chemisorption reactions for space heating applications and investigated the performance of various CSHP designs under cold-climate heating conditions to facilitate proper selection of the working pair and the cycle configuration. The method to screening for feasible working pairs based on the operating conditions is first described. Then six single- and double-effect cycle configurations are introduced and the method to calculate their heating COP is described. These methodologies are carried out to identify feasible candidates from the 121 available ammonia/salt reactions for each cycle configuration. The heating COPs of the feasible systems are evaluated and analyzed, and the best-performing system designs are identified. The results show that at below −25 °C ambient temperatures, the single-effect and double-effect cycles can achieve heating COP of 1.22 and 1.51, respectively. Meanwhile, due to the significant influence of the thermal masses on the system performance, the resorption cycles with high ideal COP ends up with lower performance when the thermal masses are considered, while also having a narrower temperature range. The primary energy COPs of the gas-fired CSHP system are calculated based on the cycle COPs and assumptions of combustion and parasitic power consumption. The gas-fire CSHP system demonstrated 30% higher primary COP than condensing furnaces, and the high efficiency is well sustained at below −25 °C.

CRediT authorship contribution statement

Zhiyao Yang: Conceptualization, Visualization, Methodology, Investigation, Writing - original draft, Software. **Ming Qu:** Conceptualization, Methodology, Data curation, Supervision, Writing - review & editing. **Kyle R. Gluesenkamp:** Visualization, Methodology, Data curation, Funding acquisition, Writing - review & editing.

Declaration of competing interest

The authors declare that they have no known competing financial interests or personal relationships that could have appeared to influence the work reported in this paper.

Acknowledgment

This work was sponsored by the U. S. Department of Energy's Building Technologies Office (BTO) under Contract No. DE-AC05-00OR22725 with UT-Battelle, LLC. The authors also acknowledge Mr. Antonio Bouza, Technology Manager for HVAC&R, Water Heating, and Appliance, U.S. Department of Energy BTO.

References

[1] Building Energy Data Book. Office of energy efficiency & renewable energy.

2011.
[2] (EIA) EIA. Residential energy consumption survey (RECS). 2019.
[3] Yang L, Yuan H, Peng J-W, Zhang C-L. Performance modeling of air cycle heat pump water heater in cold climate. Renew Energy 2016;87:1067–75.
[4] Guoyuan M, Qinhu C, Yi J. Experimental investigation of air-source heat pump for cold regions. Int J Refrig 2003;26(1):12–8.
[5] Ramaraj S, Braun JE, Groll EA, Horton WT. Performance analysis of liquid flooded compression with regeneration for cold climate heat pumps. Int J Refrig 2016;68:50–8.
[6] Zhang L, Jiang Y, Dong J, Yao Y. Advances in vapor compression air source heat pump system in cold regions: a review. Renew Sustain Energy Rev 2018;81:353–65.
[7] Neveu P, Castaing J. Solid-gas chemical heat pumps: field of application and performance of the internal heat of reaction recovery process. Heat Recovery Syst CHP 1993;13(3):233–51.
[8] Goetz V, Elie F, Spinner B. The structure and performance of single effect solid-gas chemical heat pumps. Heat Recovery Syst CHP 1993;13(1):79–96.
[9] Li TX, Wang RZ, Kiplagat JK, Wang LW. Performance study of a consolidated manganese chloride–expanded graphite compound for sorption deep-freezing processes. Appl Energy 2009;86(7):1201–9.
[10] Pons M, Meunier F, Cacciola G, Critoph RE, Groll M, Puigjaner L, et al. Thermodynamic based comparison of sorption systems for cooling and heat pumping: comparaison des performances thermodynamique des systèmes de pompes à chaleur à sorption dans des applications de refroidissement et de chauffage. Int J Refrig 1999;22(1):5–17.
[11] Wang L, Bao H, Wang R. A comparison of the performances of adsorption and resorption refrigeration systems powered by the low grade heat. Renew Energy 2009;34(11):2373–9.
[12] Zhu C, Gluesenkamp KR, Yang Z, Blackman C. Unified thermodynamic model to calculate COP of diverse sorption heat pump cycles: adsorption, absorption, resorption, and multistep crystalline reactions. Int J Refrig 2019;99:382–92.
[13] Yang Z, Qu M, Gluesenkamp K. Model-based performance comparison of ammonia chemisorption heat pumps for cold climate with different working pairs and cycle configurations. Conference model-based performance comparison of ammonia chemisorption heat pumps for cold climate with different working pairs and cycle configurations, West Lafayette, IN.
[14] Li T, Wang R, Li H. Progress in the development of solid–gas sorption refrigeration thermodynamic cycle driven by low-grade thermal energy. Prog Energy Combust Sci 2014;40:1–58.
[15] Goetz V, Spinner B, Lepinasse E. A solid-gas thermochemical cooling system using BaCl2 and NiCl2. Energy 1997;22(1):49–58.
[16] Wang LW, Wang RZ, Oliveira RG. A review on adsorption working pairs for refrigeration. Renew Sustain Energy Rev 2009;13(3):518–34.
[17] Jiang L, Roskilly AP. Thermal conductivity, permeability and reaction characteristic enhancement of ammonia solid sorbents: a review. Int J Heat Mass Tran 2019;130:1206–25.
[18] Wang R, Xu Y, Wu J, Wang W. Experiments on heat-regenerative adsorption refrigerator and heat pump. Int J Energy Res 1998;22(11):935–41.
[19] Oliveira RG, Wang RZ, Li TX. Transient analysis of a chemisorption air conditioning system operating under different kinds of cycle. Ind Eng Chem Res 2008;47(4):1102–10.
[20] Gluesenkamp K. Development and analysis of micro-polygeneration systems and adsorption chillers. College Park: University of Maryland; 2012.
[21] Li TX, Wang RZ, Kiplagat JK, Wang LW, Oliveira RG. A conceptual design and performance analysis of a triple-effect solid–gas thermochemical sorption refrigeration system with internal heat recovery. Chem Eng Sci 2009;64(14):3376–84.
[22] Yang Z, Qu M, Gluesenkamp KR. Model-based performance comparison of ammonia chemisorption heat pumps for cold climate with different working pairs and cycle configurations. Oak Ridge, TN (United States): Oak Ridge National Lab.(ORNL); 2018.
[23] Gluesenkamp KR, Frazzica A, Velte A, Metcalf S, Yang Z, Rouhani M, et al. Experimentally measured thermal masses of adsorption heat exchangers. Energies 2020;13(5):1150.
[24] Sapienza A, Santamaria S, Frazzica A, Freni A. Influence of the management strategy and operating conditions on the performance of an adsorption chiller. Energy 2011;36(9):5532–8.
[25] Frazzica A, Palomba V, Dawoud B, Gullì G, Brancato V, Sapienza A, et al. Design, realization and testing of an adsorption refrigerator based on activated carbon/ethanol working pair. Appl Energy 2016;174:15–24.
[26] Freni A, Bonaccorsi L, Calabrese L, Caprì A, Frazzica A, Sapienza A. SAPO-34 coated adsorbent heat exchanger for adsorption chillers. Appl Therm Eng 2015;82:1–7.
[27] Bendix P, Füldner G, Möllers M, Kummer H, Schnabel L, Henninger S, et al. Optimization of power density and metal-to-adsorbent weight ratio in coated adsorbers for adsorptive heat transformation applications. Appl Therm Eng 2017;124:83–90.
[28] Sharafian A, Mehr SMN, Thimmaiah PC, Huttema W, Bahrami M. Effects of adsorbent mass and number of adsorber beds on the performance of a waste heat-driven adsorption cooling system for vehicle air conditioning applications. Energy 2016;112:481–93.
[29] Tamainot-Telto Z, Critoph R. Advanced solid sorption air conditioning modules using monolithic carbon–ammonia pair. Appl Therm Eng 2003;23(6):659–74.
[30] Deru MP, Torcellini PA. Source energy and emission factors for energy use in buildings. National Renewable Energy Laboratory Golden, CO; 2007.
[31] Garrabrant M, Stout R, Keinath C, Glanville P. Experimental evaluation of low-cost gas heat pump prototypes for building space heating. 2016.
[32] Vasiliev L, Mishkinis D, Antukh A. Solar-gas solid sorption refrigerator. Adsorption 2001;7(2):149–61.
[33] Xu J, Oliveira RG, Wang RZ. Resorption system with simultaneous heat and cold production. Int J Refrig 2011;34(5):1262–7.
[34] Oliveira RG, Wang RZ, Kiplagat JK, Wang CY. Novel composite sorbent for resorption systems and for chemisorption air conditioners driven by low generation temperature. Renew Energy 2009;34(12):2757–64.
[35] Hui L, N'Tsoukpoe KE, Lingai L. Evaluation of a seasonal storage system of solar energy for house heating using different absorption couples. Energy Convers Manag 2011;52(6):2427–36.
[36] Shen B, Abdelaziz O, Rice CK, Baxter VD. Cold climate heat pumps using tandem compressors. Oak ridge national laboratory (ORNL), oak ridge, TN (United States). Building technologies research and integration center. BTRIC); 2016.

energies

MDPI

Article

Experimentally Measured Thermal Masses of Adsorption Heat Exchangers

Kyle R. Gluesenkamp [1,*], Andrea Frazzica [2], Andreas Velte [3], Steven Metcalf [4], Zhiyao Yang [1,5], Mina Rouhani [6], Corey Blackman [7,8,9], Ming Qu [5], Eric Laurenz [3], Angeles Rivero-Pacho [4], Sam Hinmers [4], Robert Critoph [4], Majid Bahrami [6], Gerrit Füldner [3] and Ingemar Hallin [10]

[1] Oak Ridge National Laboratory, Oak Ridge, TN 37830, USA
[2] Consiglio Nazionale delle Ricerche (CNR), Istituto di Tecnologie Avanzate per l'Energia "Nicola Giordano" (ITAE), 98126 Messina, Italy; andrea.frazzica@itae.cnr.it
[3] Fraunhofer Institute for Solar Energy Systems ISE, 79110 Freiburg, Germany; gerrit.fueldner@ise.fraunhofer.de (G.F.); eric.laurenz@ise.fraunhofer.de (E.L.); andreas.velte@ise.fraunhofer.de (A.V.)
[4] School of Engineering, University of Warwick, Coventry CV47AL, UK; Steven.Metcalf@warwick.ac.uk (S.M.); A.Rivero-Pacho@warwick.ac.uk (A.R.P.); S.Hinmers@warwick.ac.uk (S.H.); R.E.Critoph@warwick.ac.uk (R.C.)
[5] Lyles School of Civil Engineering, Purdue University, West Lafayette, IN 47907, USA; yang573@purdue.edu (Z.Y.), mqu@purdue.edu (M.Q.)
[6] Laboratory for Alternative Energy Conversion, School of Mechatronic Systems Engineering, Simon Fraser University, Surrey, BC V3T0A3, Canada, mrouhani@sfu.ca (M.R.), mbahrami@sfu.ca (M.B.)
[7] SaltX Technology AB, Västertorpsvägen 135, Hägersten 12944, Sweden, Corey.Blackman@saltxtechnology.com
[8] School of Technology and Business Studies, Dalarna University, Borlänge 78170, Sweden
[9] School of Business, Society & Engineering, Mälardalens University, Västerås 72123, Sweden
[10] HeatAmp Sweden AB, Stockholm 11332, Sweden, ingemar.hallin@heatamp.com
* Correspondence: gluesenkampk@ornl.gov

Received: 17 January 2020; Accepted: 26 February 2020; Published: 3 March 2020

Abstract: The thermal masses of components influence the performance of many adsorption heat pump systems. However, typically when experimental adsorption systems are reported, data on thermal mass are missing or incomplete. This work provides original measurements of the thermal masses for experimental sorption heat exchanger hardware. Much of this hardware was previously reported in the literature, but without detailed thermal mass data. The data reported in this work are the first values reported in the literature to thoroughly account for all thermal masses, including heat transfer fluid. The impact of thermal mass on system performance is also discussed, with detailed calculation left for future work. The degree to which heat transfer fluid contributes to overall effective thermal mass is also discussed, with detailed calculation left for future work. This work provides a framework for future reporting of experimental thermal masses. The utilization of this framework will enrich the data available for model validation and provide a more thorough accounting of adsorption heat pumps.

Keywords: adsorption; thermal mass; mass ratio; inactive mass; specific thermal mass; resorption

1. Introduction

Many adsorption systems (including chemisorption systems) are operated with intermittent heating and cooling of components. Thus, the thermal mass (*TM*; the product of mass and specific heat capacity in units of kJ/K) of the components influences performance. For example, Ziegler (2002) [1] concluded from an overview of existing studies that a key challenge for adsorption systems is the

temperature cycling of *TM* that negatively affects efficiency. Wittstadt et al. (2017) [2] reviewed the recent development for adsorption heat exchangers and pointed out that *TM* affects efficiency and power density within the cyclic operation of adsorption heat pumps. Furthermore, modeling of such systems requires an accounting of the *TM*. However, limited experimental data are available that provide a full accounting of the full *TM* of sorption components.

An inherent tradeoff exists between the thermal cooling or heating capacity of a system and its *TM*. The most efficient cyclic adsorption heat exchanger (HX) will tend toward zero *TM*, but at the expense of reduced heat transfer surface area, thereby leading to longer cycle times, larger size, and lower power density than a less efficient design with higher *TM*. Metcalf and Critoph (2004) [3] investigated the heat and mass transfer intensification limits for carbon—ammonia heat pumps but found that the problem is largely in what can be manufactured.

The link between *TM* and performance has been discussed in the literature. Goetz et al. (1993) [4] studied the effect of the *TM* of the reactive salts and the exchanger and suggested that, based on the experimental results from Neveu (1990) and Douss (1988) [5,6], the drop in the coefficient of performance (COP) due to the *TM* was expected to be around 5–10%.

Li et al. (2009) [7] investigated the impact of the mass ratio between the metallic part of the reactor and the reactive salt in thermochemical refrigeration systems using a thermodynamic model. The mass ratio for an optimally designed solid–gas sorption system was estimated to be around 5:1. Under a higher mass ratio, the added reactor *TM* increased both desorption heat consumption and adsorption heat production without affecting the cold production, which reduced the cooling COP.

Demir et al. (2008) [8] identified *TM* as a critical parameter for cycle times. Paul et al. (2018) [9] studied how to improve efficiency by reducing *TM* by implementing microchannel HXs.

There are several terms known for *TM* in the literature and the research community; Table 1 summarizes the common terms. Heat exchanger materials are commonly divided into two categories, one representing the sorbent material itself and the other representing all other materials, with analogy to a colloquially familiar dichotomy such as living/dead, host/guest, or simply active/inactive. Identifying the active (adsorbent) mass and inactive (non-adsorbent) mass is relatively straightforward. However, identifying the inactive *TM* is more complicated. Among the terms for *TM*, perhaps the primary one is "dead thermal mass." Little was found in the literature for ratios of *TMs*, although "dead thermal mass ratio" was used by Gluesenkamp (2012) and Zhu et al. (2019) [10,11].

The sorbent material itself has *TM*. Thus, while it is logical to distinguish between live and dead mass, a distinction between live and dead *TM* is not very useful. For this reason, this paper uses "thermal mass" and does not use "dead thermal mass."

Table 1. Common terms relating to adsorption heat exchanger thermal mass.

Sorbent Material Mass (kg)	Non-Sorbent Material Mass (kg)
Live mass	Dead mass
Active mass	Inactive mass
Active mass	Inert mass
Host or active mass	Guest material

There are three metrics utilized in this paper: mass ratio, specific *TM* (*STM*), and effective specific heat, as defined in detail in Section 2. Only mass ratio is commonly reported in existing literature.

In the following sections, mass ratios and *TMs* in the literature are summarized.

1.1. Mass Ratios of Heat Exchangers

The mass ratio of adsorber metallic masses to adsorbent material was referred to as the "adsorber bed to adsorbent mass ratio (AAMR)" by Sharafian et al. (2016) [12]. This concept is referred to as simply "mass ratio" in the present work.

The mass ratio of adsorber bed metal to adsorbent mass for 18 fin and tube adsorber bed systems reported in the literature is summarized by Sharafian et al. (2016) [12]. Reported values range from

as low as 0.654 to as high as 20.9 kg/kg, with 88% of values being between 1.4 and 7.9 kg/kg. These reported values are strictly mass ratios and do not account for *TM*.

Additional mass ratios reported in the literature are summarized by Sharafian and Bahrami (2014) [13]. This list includes ten finned tube adsorbers that are also reported by Sharafian et al. (2016) [12], plus 16 more adsorbers of other types including plate, plate–fin, shell–tube, hairpin, and annulus tube. The mass ratio values for the non-finned tube types reported by Sharafian and Bahrami (2014) [13] ranged from as low as 2.0 to as high as 13.3 kg/kg.

1.2. Thermal Masses of Heat Exchangers

The literature was surveyed for reporting of *TM*, as summarized in Table 2. The authors found that only mass ratio is commonly reported in the existing literature, although some cases were identified from which *TM* can be extracted.

Table 2 reports the *TM* of HXs reported in the literature. Two normalizations were calculated: *TM* normalized against the sorbent mass (TM/m_{sorb}; specific thermal mass [*STM*]) and *TM* normalized against the total HX mass (TM/m_{HX}; effective specific heat [$c_{effective}$]). Each of these terms is described in more detail in Section 2. The numerical values of *STM* and $c_{effective}$ were not reported in the original reference, but were computed in this work based on the geometry reported in the original reference.

Only two experimental systems were found in the literature that reported all of the data required to calculate a full accounting of HX *TM*. From Gluesenkamp (2019) and Qian et al. (2013) [10,14], full geometric details were provided for an adsorption HX adsorber/desorber with water as refrigerant and FAM-Z02 as adsorbent, including heat transfer fluid (HTF). From Sharafian et al. (2016) and Rouhani (2019) [12,15], full geometric details were also provided for a water/FAM-Z02 adsorber, including HTF. The component described by Sharafian et al. (2016) and Rouhani (2019) [12,15] was investigated in both coated and packed configurations. The packed configuration was packed with two quantities of sorbent, 0.5 and 1.5 kg. All three studies (coated, 0.5 kg packed, and 1.5 kg packed) are shown in Table 2.

In three additional studies from Xu et al. (2011), Bao et al. (2011), and Lepinasse et al. (1994) [16–18], a nearly complete dataset has been provided to calculate *TM* for resorption HXs; however, the HTF data were not provided (Table 2). Had the HTF been included, the reported *STM* would have been higher for these HXs.

Table 2. Studies in the literature that provide all or some data needed to calculate heat exchanger (HX) thermal mass (*TM*). HTS, high-temperature salt; LTS, low-temperature salt.

System and Working Pair	HX	HTF	Specific Thermal Mass: TM/m_{sorb} ($kJ^1K^{-1}kg_{sorb}^{-1}$)	$c_{effective}$: TM/m_{HX} ($kJ^1K^{-1}kg_{HX}^{-1}$)	Reference
Adsorption: water/ FAM-Z02	Coated round tube–plain fin	Water	5.62*	1.64*	[10,14]
Adsorption: water/ FAM-Z02	Coated round tube–corrugated fin	Silicon oil Water	4.17* 7.01*	0.77* 1.28*	[15]
Adsorption: water/ FAM-Z02	Packed round tube–corrugated fin	Silicon oil	5.96*[1] 2.53*[2]	0.77*[1] 0.78*[2]	[12,15]
		Water	10.30*[1] 3.98*[2]	1.31*[1] 1.21*[2]	
Resorption: ammonia/ $MnCl_2$ (HTS)/ $BaCl_2$ (LTS)	Packed shell–tube	Not reported	2.34† (HTS) 2.18† (LTS)	0.49† (HTS) 0.47† (LTS)	[18]
Resorption: ammonia/ $MnCl_2$ (HTS)/ NH_4Cl (LTS)	Coated annular tube	Not reported	4.77† (HTS) 3.85† (LTS)	0.47† (HTS) 0.48† (LTS)	[16]
Resorption: ammonia/ $MnCl_2$ (HTS)/ NaBr (LTS)	Packed fin–tube	Not reported	4.55† (HTS) 5.00† (LTS)	0.47† (HTS) 0.47† (LTS)	[17]

* Includes HTF; † HTF data not provided and cannot be directly compared to other values in this work; [1] m_{sorb} = 0.5 kg; [2] m_{sorb} = 1.5 kg.

This work aims to cover the gap in knowledge regarding adsorption HX *TM* by reporting new experimental data for several pieces of experimental hardware from several research laboratories

around the world. This research provides new experimental data to the literature with a full accounting of *TM* for fabricated experimental adsorption components. By describing the experimental data in terms of *STM* and $c_{effective}$, the authors also provide a useful correlation between the easily-measured mass ratio and the difficult-to-measure *STM*. Mass ratio is easily measured in the laboratory but not directly useful to system simulation or performance prediction. *STM* is useful to modeling and performance prediction. This work focuses only on experimental measurements and does not attempt to quantify any correlation between *STM* and system performance.

2. Methodology

2.1. The Definition of Heat Exchanger Thermal Mass

In general, *TM* is the product of mass and specific heat capacity in units of kJ/K. This work only examines the *TM* of adsorption HXs. In adsorption HXs, both the sorbent (the live mass) and the dead mass have *TM*. The *TM* of live mass is inherent to the sorbent material and is thus called $TM_{inherent}$. The amount of dead mass depends on the HX design, and, thus, the *TM* of non-sorbent materials is called TM_{design}. The sum of these *TMs* is the total *TM*, TM_{total}, as shown in Equation (1).

$$TM_{total} = TM_{inherent} + TM_{design} \quad \left(\frac{\text{kJ}}{\text{K}}\right) \tag{1}$$ (1)

The TM_{design} can be written as in Equation (2). It is the sum of the heat transfer fluid (HTF) thermal mass and the thermal masses of *N* number of materials of construction ("materials" or "mat"). In this work, binders or other materials integrated with the sorbent material are considered as part of the sorbent (unless otherwise noted), and are thus not explicit in Equation (2). The role of HTF is addressed in detail in the next section. Since many material types can be used in HX construction (e.g., copper, aluminum, polymers, and steel), each with their own properties, the materials are written as a sum of $i = 1$ to $i = \text{N}$ material types.

$$TM_{design} = \rho_{\text{HTF}} V_{\text{HTF}} c_{\text{HTF}} + \sum_{i=1}^{N} (\rho_{mat,i} V_{mat,i} c_{mat,i}) \quad \left(\frac{\text{kJ}}{\text{K}}\right) \tag{2}$$ (2)

The $TM_{inherent}$ can be written as in Equation (3), where Y is the mass ratio refrigerant sorbed in the sorbent ($\text{kg}_{\text{ref}}/\text{kg}_{\text{sorbent}}$), which varies over time. The product $m_{sorbent} Y C_{p,ref,adsorbed}$ is the thermal mass of the refrigerant sorbed in the sorbent. This thermal mass will be lower during heating (from $T_{adsorption}$ to $T_{desorption}$) than during cooling (from $T_{desorption}$ to $T_{adsorption}$) since less refrigerant is retained in the sorbent after completing desorption.

$$TM_{inherent} = m_{sorbent}\left(c_{sorbent} + Y c_{ref,sorbed}\right) \quad \left(\frac{\text{kJ}}{\text{K}}\right) \tag{3}$$ (3)

Neglecting the sorbed refrigerant would simplify the calculation of $TM_{inherent}$ in two significant ways: (1) the calculated thermal mass no longer involves the equilibrium composition of the sorbent; and (2) the thermal mass can be treated as constant in both sorption and desorption processes. For many adsorption HXs, neglecting the *TM* of sorbed refrigerant will have only a small impact on TM_{total} (even though it may be a significant portion of $TM_{inherent}$). In these cases, Equation (3) simplifies significantly to Equation (4).

$$TM_{inherent} = m_{sorbent} c_{sorbent} \quad \left(\frac{\text{kJ}}{\text{K}}\right) \tag{4}$$ (4)

The approach of neglecting sorbed refrigerant thermal mass (i.e., Equation (4)) is utilized throughout this work. Quantification of the impact of neglecting sorbed refrigerant, and the expected dependence on working pair or HX design, is left for future studies. For the present study, this choice of scope allows the focus to be on providing a dataset of experimental values. It is important to note that this represents a limitation of the present study, and it may not be relevant for working pairs

with a large quantity of retained refrigerant, or for very low thermal mass HX designs where TM_{design} is small compared to $TM_{inherent}$ and $m_{sorbent}YC_{p,ref,sorbed}$ is a significant fraction of TM_{total}.

To summarize, the definition of TM_{total} used in this work is shown in Equation (5). This definition of TM_{total} does not depend on sorbent composition, under the assumption that the sorbate's thermal mass is neglected. All TM_{totals} were evaluated using the material properties specified in Table 3. Any temperature-dependence of these properties was neglected and the fixed values in Table 3 were used.

$$TM_{total} = \rho_{\mathrm{HTF}} V_{\mathrm{HTF}} c_{\mathrm{HTF}} + \sum_{i=1}^{N} (\rho_{mat,i} V_{mat,i} c_{mat,i}) + m_{sorbent} c_{sorbent} \qquad \left(\frac{\mathrm{kJ}}{\mathrm{K}}\right) \qquad (5) \quad (5)$$

Additional terms used in this work are expressed in Equations (6)–(9). Equation (6) defines the HX mass (m_{HX} [kg]) as the sum of sorbent, HTF, and materials of construction. Equation (7) defines the mass ratio (*MR*, [kg/kg]) as the ratio of m_{HX} to mass of sorbent (m_{sorb}). Equation (8) defines specific thermal mass *STM* ($\mathrm{kJ^1K^{-1}kg_{sorb}^{-1}}$) as the TM_{total} per unit sorbent mass. Equation (9) defines the effective specific heat ($c_{effective}$, $\mathrm{[kJ^1K^{-1}kg_{HX}^{-1}]}$) as the TM_{total} per unit HX mass.

The utility in defining $c_{effective}$ this way is that it provides a path to a straightforward translation between an easily measured quantity (component *MR*) and a less easily measured one (component TM_{total}). In other words, if one seeks to know the TM_{total} of an HX for which a detailed measurement of TM_{total} has not been made, the mass of the unknown component can be multiplied by a relevant $c_{effective}$ to obtain an estimated TM_{total}.

This translation requires knowledge of typical values of $c_{effective}$. If the $c_{effective}$ is reported for many similar components, a statistical expectation can be established for the typical $c_{effective}$ for that type of component. The work in this paper is the first step to such a catalog of data.

$$m_{\mathrm{HX}} = m_{sorb} + m_{\mathrm{HTF}} + m_{mat} \qquad (kg_{\mathrm{HX}}) \qquad () \quad (6)$$

$$MR = \frac{m_{\mathrm{HX}}}{m_{sorb}} \qquad \left(\frac{kg_{\mathrm{HX}}}{kg_{sorbent}}\right) \qquad (7)$$

$$STM = \frac{TM}{m_{sorb}} \qquad \left(\frac{\mathrm{kJ}}{\mathrm{K} \cdot kg_{sorbent}}\right) \qquad (8)$$

$$c_{effective} = \frac{TM}{m_{\mathrm{HX}}} \qquad \left(\frac{\mathrm{kJ}}{\mathrm{K} \cdot kg_{\mathrm{HX}}}\right) \qquad (9)$$

A useful property of these definitions is that *STM*, *MR*, and $c_{effective}$ are related, as shown in Equation (10). Since *MR* is much easier to measure than *STM*, Equation (10) can be used to predict *STM* based on an expected value of $c_{effective}$.

$$STM = c_{effective} MR \qquad \left(\frac{\mathrm{kJ}}{\mathrm{K} \cdot kg_{sorbent}}\right) \qquad (10)$$

Table 3. Thermophysical data.

Material	Specific Heat Capacity ($\mathrm{kJ^1kg^{-1}K^{-1}}$)	Density ($\mathrm{kg^1m^{-3}}$)	Reference
Activated carbon (monolithic)	1.05	750	[19]
Aluminum (purity > 99%)	0.91	2700	[20]
Ammonia (liquid)	4.60	639	[21]
Binder SilRes MP50 E	1.27	Not used	Measured
TiAPSO SCT-323	0.90	Not used	Estimated value
Adsorbent SAPO-34 directly crystallized	0.90	1500	[22]
Copper	0.385	8.96	[23]
Water	4.19	1,000	[20]
AQSOA FAM Z02 grains	0.69	Not used	[24]
AQSOA FAM Z02 powder	0.822	600–700	[24,25]

Silicon oil (HL80, Julabo)	1.726	910	[26]
Siogel	0.62	Not used	[24]
Activated carbon	1.1	Not used	[27]
Silane binder	1.3	Not used	[28]
Stainless steel (316)	0.49	7954	[29]
$MnCl_2$–graphite 1:2 mixture	1.24	470	[16]
NH_4Cl–graphite 1:2 mixture	0.61[1]	470	[16]
$MnCl_2$–graphite 13:7 mixture	0.6[1]	495	[17,18]
$BaCl_2$–graphite 13:7 mixture	0.5[1]	507	[17,18]
$MnCl_2$–graphite 13:7 mixture	0.61[1]	310	[17]
NaBr–graphite 13:7 mixture	0.54[1]	300	[17]

[1] Calculated based on weighted average of c_{binder} and c_{salt}, and mass ratio of binder/salt provided in the reference.

2.2. Definition of a Relevant Control Volume

To apply these definitions to an adsorption HX, a control volume must be chosen. Three possible control volumes are depicted in Figure 1a,c for three classes of HX. The comprehensive control volume has the advantage of including all thermal masses expected to undergo a temperature change with each adsorption/desorption cycle, including HTF and plumbing between the HX and the switching valves, which is relevant to whole-system performance. However, the system is highly dependent on any particular implementation of an HX. In addition, many laboratory/experimental systems are not relevant to full systems because they are small-scale and lack a header or include instrumentation and other components within the comprehensive control volume, which would not be present in a commercial system.

Treating the comprehensive control volume is complicated because significant spatial temperature variations can exist within the control volume, and can vary with number of cycles. For example, if the sorbent is cycled between 25 and 100 °C in adsorption and desorption phases, the enclosure might experience minimum and maximum temperatures of 25 and 35 °C in the first cycle, and stabilize to minimum and maximum temperatures of 40 and 60 °C after several cycles. In contrast, the "HX-only" control volume can usually be characterized by a single set of minimum and maximum temperatures.

For simplicity, values in this work are reported for the HX-only control volume. The HX-only control volume includes the sorbent, metal, and HTF within the core and headers. It excludes the enclosure and any plumbing between the headers and the switching valves. In the case of a shell–tube or plate–shell HX, the headers and shell are typically inextricable, and have been excluded from the HX-only control volume.

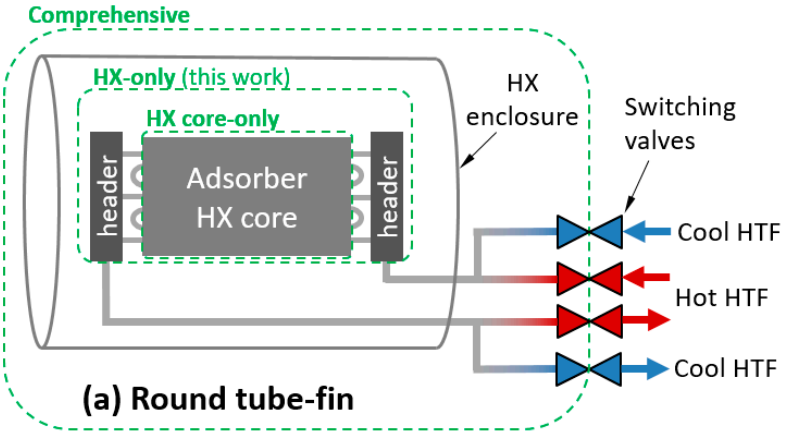

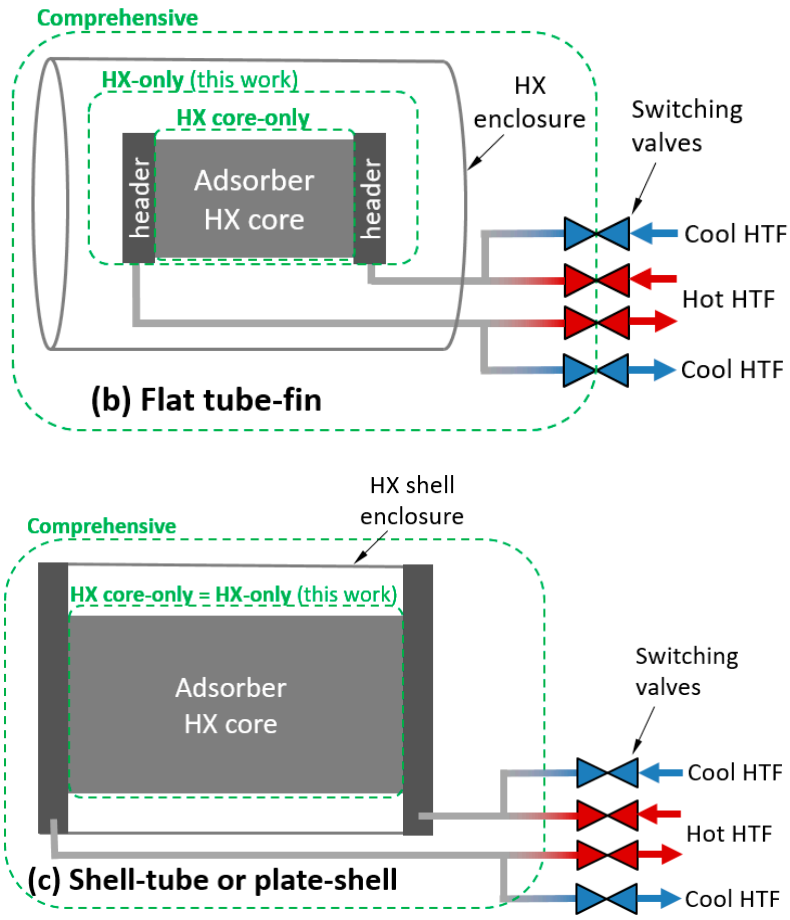

Figure 1. Illustration of control volumes and heat transfer fluid (HTF) relevant to thermal mass for: (**a**) round tube–fin; (**b**) flat tube–fin; and (**c**) shell–tube or plate–shell HXs.

2.3. The Role of Heat Transfer Fluid

An emphasis is placed here on HTF because it is the most commonly neglected parameter in reported data for computing thermal mass.

In typical designs, the HTF is a full participant in the thermal cycling behavior of the component. In other words, all the HTF retained in the HX must be fully heated and cooled with each cycle. There may be system-level options to minimize the impact of the HTF thermal mass, but in all cases, the HTF thermal mass contributes to the heat that must be added and removed from the component with each cycle.

The HTF can be accounted for in various control volumes, as illustrated in Figure 1. In this work, the HX-only control volume was used.

2.4. The Role of Heat Exchanger Enclosures

The enclosure (or shell) of an HX does not fully participate in the temperature swings experienced by the sorbent and heat exchange materials inside. Thus, the thermal mass of the shell has reduced importance compared with the HX core. The degree of participation depends on factors including the switching duration, the thermal diffusivity of the shell, the effectiveness of heat transfer between the shell and the core (radiation, convection, and conduction mechanisms), and the degree of insulation on the exterior of the shell.

In this work, this complexity is treated by ignoring the thermal mass of the HX shell. A rigorous treatment would require that shell or enclosure thermal mass be considered.

3. Experimental Results for Specific Thermal Mass

In this section, experimentally measured masses (and their corresponding TM_{totals}) are presented for several sorption HXs. Flat tube–fin HX are investigated, including packed adsorber beds (Sections 3.1 and 3.2) and coated HXs (Sections 3.3 and 3.4). Round tube–corrugated fins are investigated in Section 3.5 (both coated and packed), a modular finned tube in Section 3.6, shell–tube in Section 3.7, plate–shell in Section 3.8, and a fiber HX in Section 3.9.

3.1. Flat Tube–Fin—Packed (Water as Refrigerant)

Two packed HX components are described here: one packed with silica gel, and one with zeolite. Different adsorber configurations based on a defined aluminum flat tube–fin HX, shown in Figure 2, were realized and tested by means of a laboratory-scale test rig (cooling capacity up to 1 kW) described by Frazzica et al. (2016) [30]. The HX was characterized by an aluminum mass of 0.51 kg and an HTF volume of 300 cm^3 with an HX core-only volume of approximately 1000 cm^3. The overall heat transfer area, comprising the fins, accounted for 0.94 m^2. As a packed adsorber bed, it was tested using the zeotype material (i.e., grains of AQSOA-Z02) and later with silica gel (grains of Siogel). The mass of AQSOA-Z02 was 0.26 kg, while the mass of Siogel was 0.31 kg. In both cases, the grain size distribution was 0.6–0.8 mm; thus, the mass difference was related to the different density of the material, as well as the shape of the grains. Being characterized by an irregular shape, Siogel had a higher packing density. The specific heat for the two adsorbent materials was derived from the work by Santori et al. (2013) [24]. In particular, average values of 0.75 and 0.72 kJ/kg K were used for AQSOA-Z02 and Siogel, respectively. The experimental characterization of the adsorbers, carried out in a dedicated test rig described by Sapienza et al. (2011) [30], showed an average cooling power of 0.30 and 0.20 kW for the AQSOA-Z02 and Siogel configurations, respectively. No effect of the inert mass of the vacuum chamber was considered in the performance evaluation.

Figure 2. Small-scale aluminum heat exchanger [30].

3.2. Flat Tube–Fin—Packed (Ethanol as Refrigerant)

A concept similar to that of Section 3.1 was developed for a laboratory-scale activated carbon-ethanol refrigerator, whose nominal cooling capacity was 0.5 kW [31]. For each adsorber, four tube–fin aluminum HXs were employed, such as the one presented in Figure 3, working in parallel. Each adsorption HX had about 1.9 kg of aluminum and hosted 0.6 kg of activated carbon. The internal volume for HTF was 550 cm^3. The considered specific heat of the activated carbon was 1.1 kJ/kg K, as reported by Brancato et al. (2015) [27]. In the experimental tests reported by Palomba et al. (2017) [32], the inert mass due to the adsorber vacuum chamber was also considered. Particularly, the thermal cycling of the flanges on top of the chamber and the whole shell was monitored during the testing. The results allowed estimating that the thermal energy input allocated to heating the flanges and shell accounted for about 15% of the total thermal energy used to drive the prototype.

Figure 3. Tube–fin aluminum heat exchanger filled with activated carbon for a small-scale adsorption refrigerator, employing ethanol as the refrigerant [31].

3.3. Flat Tube–Fin—Coated

An innovative binder-based coating was developed and applied to the HX shown in Figure 4. It employed 90 wt % of AQSOA-Z02 and 10 wt % of silane as the binder, which had a specific heat of 1.3 kJ/kg K [28]. The amount of adsorbent material loaded inside the HX was much lower than that of the packed bed because the coating thickness of 0.12 mm maximizes the heat and mass transfer efficiency, thus achieving a specific power as high as possible.

Figure 4. Flat tube–fin coated adsorber [28].

3.4. Flat Tube–Fin—Coated

Figure 5 shows a series of the flat tube–fin HXs coated with TiAPSO SCT-323 from Clariant AG, Bitterfeld, with binder SILRES MP 50 E from Wacker Chemie AG [33]. The HX without coating and flanges had a weight of 0.465 kg and was completely made of aluminum. The mass of the HTF (water) inside the flat tubes was 0.1 kg, and in the headers and the additional tubes was 0.15 kg.

Five variants with different coating thicknesses were manufactured and measured by Bendix et al. (2017) [33]. The measurements revealed that variant HX-4 with an adsorbent mass of 0.445 kg was a good compromise between efficiency and power density. If the coating thickness (or filling factor) was increased further, heat and mass transfer limitations led to significantly lower power output.

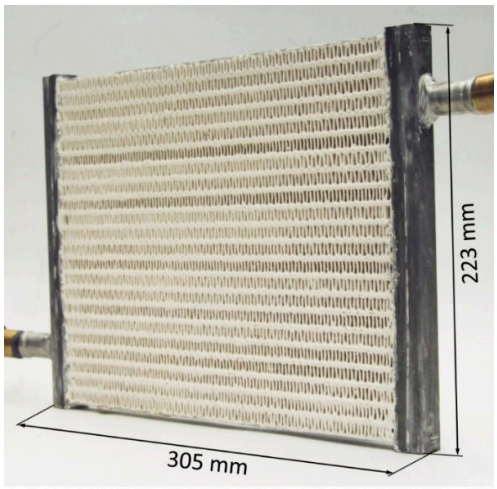

Figure 5. Coated flat tube–fin heat exchanger [33].

3.5. Round Tube–Corrugated Fin—Coated and Packed (Water as Refrigerant)

A custom-built sorption heat pump testbed was designed and used to study the performance of FAM-Z02-coated and -packed adsorber beds [12,15]. As shown in Figure 6, round tube–corrugated fin HXs, manufactured by Hayden Automotive, were chosen as the adsorber beds. The weight of the bare HX (m_{mat}) was about 2.6 kg, consisting of 2.1 kg of copper tubes and 0.5 kg of aluminum fins. The internal volume of the HTF was 837 cm^3, equivalent to 0.762 kg of silicon oil with density of 910 kg/m^3 (at 30°C) and heat capacity of 1.726 $kJ^1kg^{-1}K^{-1}$ (at 30°C). The volume of the adsorber bed loaded with sorbent was 4079 cm^3, while the total volume of the adsorber bed was 5,521 cm^3.

In the packed configuration, the HX was filled with 0.5 or 1.5 kg of 2 mm diameter FAM-Z02 particles. In the coated configuration, the identical HX was coated with 0.766 kg of FAM-Z02 in coating thickness of 0.3 mm, fabricated by Mitsubishi Plastics. The overall heat transfer area of the coated bed was 2.8 m^2.

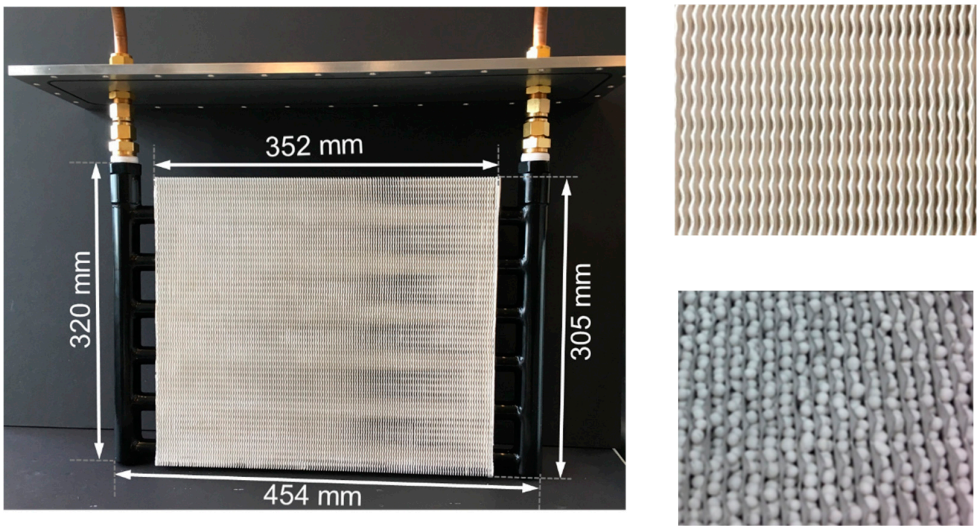

Figure 6. Round tube–corrugated fin adsorber bed with FAM-Z02-coated and -packed configurations [12,15].

3.6. Modular Finned Tube

Figure 7 shows a modular generator design for a carbon-ammonia heat pump [34]. The modules were heated and cooled by air and were arranged in a rotating bank to allow regeneration

approaching counter-flow heat transfer. The thermal mass of the HTF (air) was negligible. However, a significant mass of aluminum fins was required for effective heat transfer. The central 12.7 mm diameter stainless steel tubes contained active carbon and were 600 mm long and had a wall thickness of 0.25 mm and a mass of 93 g. The aluminum fins were 0.3 mm thick on a 1 mm pitch, with a total mass of 543 g. Since the modules rotated, the outer ducting for the air flow was at a constant temperature and thus its thermal mass could be neglected. The highly regenerative cycle allowed for a relatively high COP despite the high thermal mass of aluminum fins, but came at the expense of long cycle time and low power density.

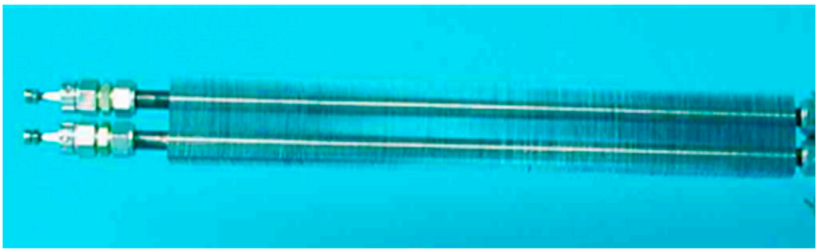

Figure 7. Modular finned tube carbon-ammonia adsorber [34].

3.7. Shell–Tube

Figure 8 shows the core of a shell–microtube HX developed for a carbon-ammonia adsorption heat pump [35]. The unit was made from nickel-brazed stainless steel, with approximately 800 tubes that were 300 mm long, 1.2 mm in diameter, and 0.2 mm in wall thickness. The unit contained 1.12 kg of active carbon with a density of 750 kg m^{-3}. The microtube design gave a good trade-off between short conduction path length in the active carbon for high power density and low TM_{total} for high COP. The HX contained 1.71 kg of stainless steel (1.46 kg in the core and 0.25 kg in the headers) and 0.22 kg of water (0.12 kg in the tubes and 0.1 kg in the headers). The outer shell did not undergo thermal cycling and thus was excluded from the mass of the unit.

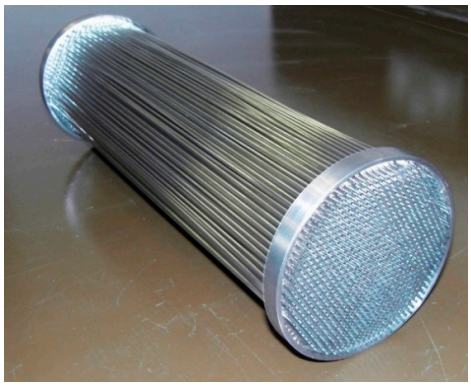

Figure 8. Heat exchanger core of ammonia/carbon heat pump generator [35].

3.8. Plate–Shell

Figure 9 shows a core of a plate–shell HX for a halide salt-ammonia adsorption heat pump [36]. The HX incorporated a heat pipe, enabling high heat flux and full utilization of the contacting surface area with condensation heat transfer during heating desorption, and convection heat transfer during cooling adsorption.

The unit was made from 56 plates of 316 stainless steel with 3 mm thickness and 10 mm spacing. The HX contained 7.8 kg of stainless steel and 2.36 kg of HTF (water) inside the stacked plates and HX tubes between the inlet and outlet. The unit contained 2.4 kg of nanocoated halide salt and carbon-based matrix materials as the sorbent. The density of the composite sorbent was 520 kg m^{-3}.

Additionally, the shell of the HX was 24.9 kg of 316 stainless steel. The summary in Table 4 does not include this mass. Experimentally, the shell mass was found to undergo 40% of the temperature change experienced by the halide salt sorbent and active HX surfaces.

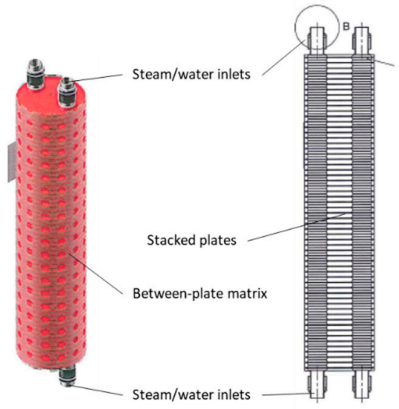

Figure 9. Plate–shell heat exchanger.

3.9. Fiber Heat Exchangers

Figure 10 shows an HX with flat tubes and fibrous aluminum structures between the flat tubes. The fibrous structures are directly crystallized with SAPO-34 with the partial support transformation (PST) technique [37]. The fibrous structures are made of aluminum fibers sintered together, brazed onto the aluminum flat tubes and finally coated with adsorbent crystals [38]. The first experimental results for directly crystallized fibrous structures showed the potential of this approach to massively increase power density [39]. These findings were confirmed later at the scale of a complete adsorption module including a fiber HX [40]. The fibers had a mean diameter of approximately 130 µm. The mean thickness of the SAPO-34 crystallite layer was around 50 µm. The fibrous structures had a large volume-specific surface area, more than 7000 m^2/m^3. The total surface area of the fibers of this HX was approximately 41 m^2.

The mass of HTF (water) inside the flat tubes was 1.07 kg, and in the header and the additional tubes was 0.83 kg. The measurements of the module indicated that the *TM* of the housing also plays a role since heat is transferred from the adsorber and the combined evaporator–condenser to the housing.

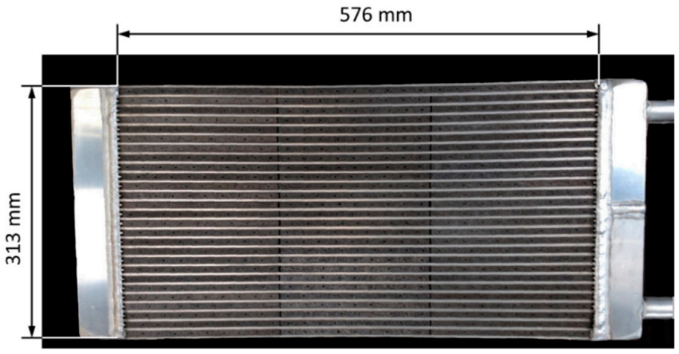

Figure 10. Fiber heat exchanger developed and tested by Wittstadt et al. (2017) [40].

3.10. Summary of Experimental Results

The main results of the original measurements made for this paper are summarized in Table 4. For each HX, the TM_{total}, sorbent mass, and total heat exchange mass are reported. From these three

raw measured values, the *MR*, *STM*, and $c_{effective}$ were calculated according to their definitions in Equations (7)–(9).

Representative propagated measurement uncertainties in TM_{total}, *STM*, and $c_{effective}$ were computed for one case. For the plate–shell HX described in Section 3.8, the propagated uncertainties were 2.3% in TM_{total}, 2.7% in *STM*, and 2.2% in $c_{effective}$. These were based on measurement uncertainties of 5% in m_{HTF}, 2% in m_{matrix} and m_{sorb}, and 1% in m_{HX}, and property uncertainties of 0.3% in c_{HTF}, 1% in c_{HX}, and 4% in c_{matrix} and c_{sorb}. Other cases are expected to be similar.

Repeatability of measurements was not addressed in this work.

Table 4. Measured mass ratios (*MR*), specific thermal masses (*STM*), and $c_{effective}$, excluding shells and enclosures for HX-only control volume of adsorber heat exchangers (HXs).

Component (Section)	Working Pair (refr./ Sorbent)	HTF	TM_{total} (kJ^1K^{-1})	Sorbent Mass m_{sorb} (kg_{sorb})	HX Mass* m_{HX} (kg_{HX})	MR, m_{HX}/m_{sorb} ($kg_{HX}{}^1$ $kg_{sorb}{}^{-1}$)	STM, TM/m_{sorb} ($kJ^1K^{-1}kg_{sorb}{}^{-1}$)	$c_{effective}$ TM/m_{HX} (kJ^1K^{-1} $kg_{HX}{}^{-1}$)
Flat tube–fin, packed (Section 3.1)	Water/ silica gel	Water	1.92	0.31	1.12	3.58	6.10	1.70
Flat tube–fin, packed (Section 3.1)	Water/ zeolite	Water	1.90	0.26	1.07	4.12	7.31	1.78
Flat tube–fin, packed (Section 3.2)	Ethanol/ AC	Water	4.66	0.60	3.05	5.08	7.77	1.53
Flat tube–fin, coated (Section 3.3)	Water/ zeolite	Water	1.80	0.092	0.90	9.80	19.58	2.00
Flat tube–fin, coated (Section 3.4)	Water/ zeolite	Water	1.97	0.45	1.24	2.77	4.40	1.59
Round tube–fin, packed (Section 3.5)	Water/ FAM-Z02	Silicon oil	2.98	0.5	3.86	7.72	5.96	0.77
			3.80	1.5	4.86	3.24	2.53	0.78
Round tube–fin, packed (Section 3.5)	Water/ FAM-Z02	Water	5.15	0.5	3.94	7.87	10.30	1.31
			5.97	1.5	4.94	3.29	3.98	1.21
Round tube–fin, coated (Section 3.5)	Water/ FAM-Z02	Silicon oil	3.20	0.766	4.12	5.39	4.17	0.77
Round tube–fin, coated (Section 3.5)	Water/ FAM-Z02	Water	5.37	0.766	4.20	5.49	7.01	1.28
Round tube–fin, coated (1.2)	Water/ zeolite	Water	14.1	2.82	9.68	1.84	5.00	1.46
Modular finned tube (Section 3.6)	NH_3/A	Water	0.6	0.078	0.71	9.1	7.7	0.85
Shell–tube (Section 3.7)	NH_3/ AC	Water	2.75	1.12	3.05	2.72	2.46	0.9
Plate–shell (Section 3.8)	NH_3/ nanocoated halide salt	Water	20.8	3.4	13.56	3.99	6.12	1.53
Flat tube–fiber (Section 3.9)	Water/ zeolite	Water	18.58	3.30	13.69	4.15	5.63	1.36

* Heat exchanger mass includes sorbent mass and HTF mass, per Equation (6). In this table, the HX-only control volume has been used. refr., refrigerant

Table 5 provides additional details for each HX studied in this work. This table provides the individual contributions to mass and thermal mass of the three main components: HTF, metal, and sorbent. In most cases, the HTF is the largest contributor to thermal mass.

Table 5. Details of measured masses and thermal masses, excluding shells and enclosures for HX-only control volume of adsorber heat exchangers.

Component (Section)	Masses			Thermal Masses		
	HTF (kg)	Metal (kg)	Sorbent m_{sorb} (kg_{sorb})	HTF (kJ^1K^{-1})	Metal (kJ^1K^{-1})	Sorbent (kJ^1K^{-1})
Flat tube–fin, packed (Section 3.1)	0.3 (water)	0.51	0.31	1.25	0.46	0.226
Flat tube–fin, packed (Section 3.1)	0.3 (water)	0.51	0.26	1.25	0.46	0.195
Flat tube–fin, packed (Section 3.2)	0.55 (water)	1.9	0.60	2.30	1.73	0.66
Flat tube–fin, coated (Section 3.3)	0.3 (water)	0.51	0.084 (sorbent) 0.009 (binder)	1.25	0.46	0.074
Flat tube–fin, coated (Section 3.4)	0.25 (water)	0.47 (Al)	0.45	1.05	0.42	0.50[1]
Round tube–fin, packed (Section 3.5)	0.76 (silicon oil) 0.83 (water)	2.1 (copper) 0.5 (Al)	0.5 1.5	1.31 3.49	1.25	0.41 1.23
Round tube–fin, coated (Section 3.5)	0.76 (silicon oil) 0.83 (water)	2.1 (copper) 0.5 (Al)	0.766	1.31 3.49	1.25	0.63
Round tube–fin, coated (1.2)	1.66 (water)	5.20	2.82	6.96	4.68	4.23
Modular finned tube (Section 3.6)	5e-4 (air)	0.636	0.078	5e-4	0.53	0.07
Shell–tube (Section 3.7)	0.222 (water)	1.71	1.12	0.92	0.86	1
Plate–shell (Section 3.8)	2.36 (water)	7.8 (stainless steel)	3.4	9.86	3.82	5.44
Fiber heat exchanger (Section 3.9)	1.9 (water)	8.5 (Al)	3.3	7.94	7.65	2.97

[1] Includes 0.10 for binder.

4. Discussion

The data for the 16 adsorber cases compiled in Table 4 are plotted in Figures 11 and 12. The data are the 15 measurements presented in Section 3, plus one measurement from the literature (described in Section 1.2).

Figure 11a plots the *MR* as a function of sorbent mass. Sorbent mass here is a proxy for HX size. In general, for larger HXs, the *MR* declines. Figure 11b plots the *STM* as a function of sorbent mass. In general, similar to the trend for *MR*, the *STM* declines for larger HXs.

Figure 12 plots *STM* as a function of *MR*. This relationship between *STM* and *MR* has a reduced dependence on HX size. Two linear fit lines are shown: one considering the five flat tube–fin adsorbers (all of which used water as the HTF), and another considering all 13 adsorbers with water as the HTF.

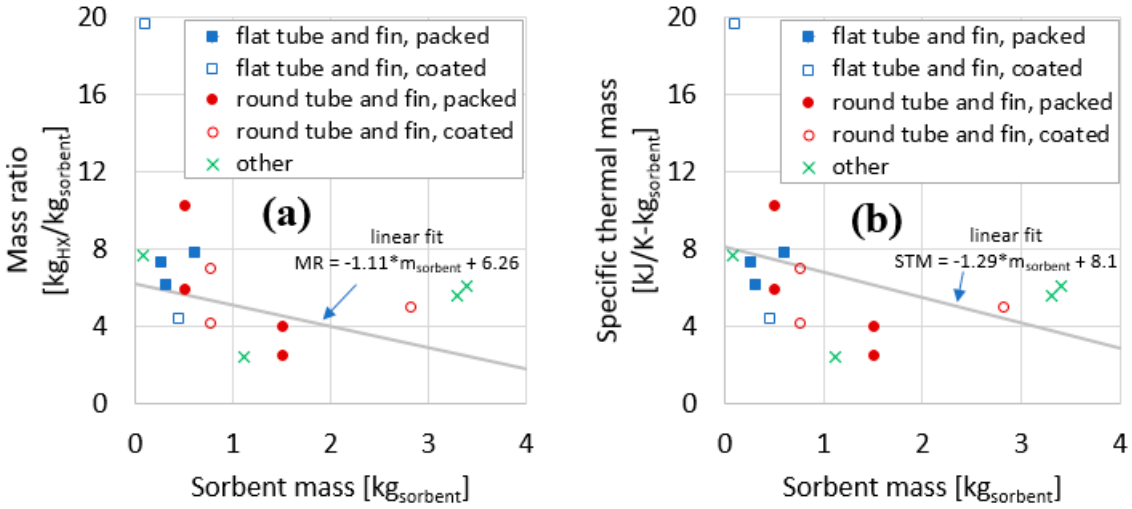

Figure 11. Mass ratio (**a**) and specific thermal mass (**b**) plotted against sorbent mass for the components evaluated in this work.

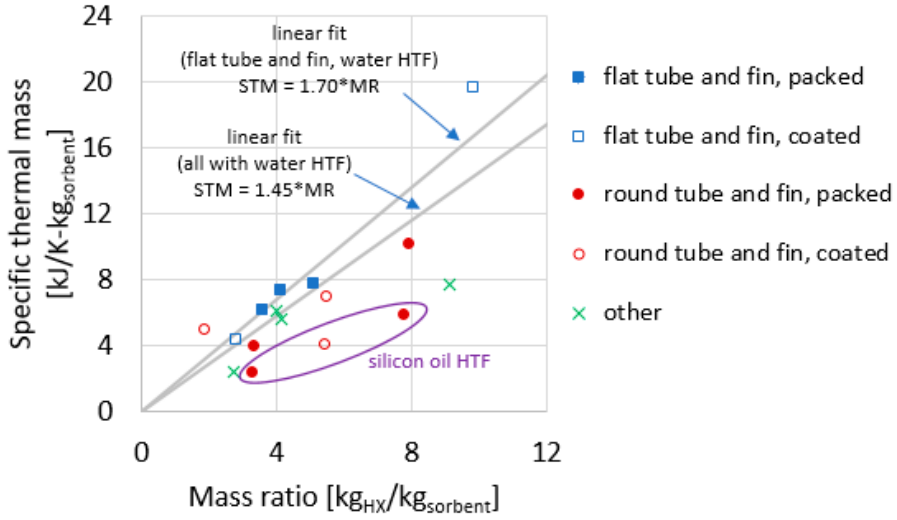

Figure 12. Specific thermal mass plotted against the mass ratio for the heat exchangers reported in this study.

One observation based on Figure 12 is the *STM* can often be predicted fairly well using a simple linear fit to the data. Considering only those adsorbers with water as HTF, $STM = 1.45 \times MR$, where 1.45 is a $c_{effective}$ ($kJ^1K^{-1}kg_{HX}^{-1}$) obtained empirically to fit the data compiled in this work, with the fitted line forced to traverse the origin of the plot (0,0), as required by Equation (10). Specifically, using this fit, the root mean-square error (RMSE) of the prediction relative errors was 32%. The correlations predict the *STM* for 10 of the 13 reported HXs within −28%/+19% maximum relative error. The outliers are the coated round tube–fin from Section 1.2 (−47% prediction error), the modular finned tube from Section 3.6 (+71% prediction error), and the shell–tube from Section 3.7 (+60% prediction error).

Restricting consideration to the flat tube–fin HX (including packed and coated), a separate fit can be determined, in which the $c_{effective} = 1.70$ ($kJ^1K^{-1}kg_{HX}^{-1}$) (in other words, $STM = 1.70 \times MR$). The fit for this geometry is such that all five data points are predicted fit within −15% to +10% prediction error, and the RMSE of the relative errors was 9%.

The three HXs that use silicon oil as the HTF appear as outliers because HTF has a large influence on TM_{total}, and changing from high specific heat water (c = 4.19 $kJ^1kg^{-1}K^{-1}$) to low specific heat oil (c = 1.73 $kJ^1kg^{-1}K^{-1}$) has a large influence on *STM*, but a much smaller influence on *MR*.

This study focused on TM_{total} within the HX-only control volume, and Table 6 compares the "HX core-only" to the HX-only control volume for some of the components reported in this study. Data for the HX core-only control volume was only compiled for five of the evaluated adsorbers. By comparing the last two columns in Table 6, it is apparent that significant differences exist between these two control volumes, with the header (also called "collector") contributing an additional 23–63% to the TM_{total} of the core-only control volume. In other words, the header is critical to the adsorber TM_{total} and should not be neglected.

Future work should consider the effect of additional thermal masses that are included in the "comprehensive" control volume.

Table 6. Comparison of thermal mass in header with HX core.

Component (Section)	Header Mass (Mass Difference between HX-Only and HX Core-Only)		Header Thermal Mass (Difference between HX-Only and HX Core-Only)	Thermal Mass, HX Core-Only
	HTF (kg)	Metal (kg)	(kJ^1K^{-1})	(kJ^1K^{-1})
Adsorber, flat tube–fin, coated (Section 3.4)	0.15	0.13	0.76	1.21
Adsorber, round tube–fin, packed (Section 3.5) [1] HTF: silicon oil	0.30	1.49	1.08	1.90 (0.5 kg packed) 2.12 (0.766 kg coated)
Adsorber, round tube–fin, packed (Section 3.5) [3] HTF: water	0.33	1.49	1.93	3.22 (0.5 kg packed) 3.44 (0.766 kg coated)
Adsorber, shell–tube (Section 3.7)	0.1	0.25	0.52	2.23
Adsorber, fiber heat exchanger (Section 3.9)	0.83	2.23	5.48	13.08

[1] Values in this row are estimates since exact geometrical information on the header was not available.

To further illustrate the importance of HTF to TM_{total} and *STM*, consider the case of a single round tube–fin packed adsorber (Section 3.5) that was used with two different HTFs: water and silicon oil. The silicon oil had a slightly lower density (910 vs. 1000 kg^1m^{-3}) and a much lower specific heat (1.73 vs. 4.19 $kJ^1kg^{-1}K^{-1}$). As a result, referring to Table 4, the TM_{total} reduced from 5.15 to 2.98 kJ^1K^{-1} (42% lower), with a corresponding drop in *STM* from 10.30 to 5.96 $kJ^1K^{-1}kg_{sorb}^{-1}$ (also 42%). This occurred with only a minor change in *MR*, from 7.87 to 7.72 $kg_{HX}{}^1 kg_{sorb}^{-1}$ (2% lower).

5. Conclusions

TM_{total} and *STM* are useful to the analysis of sorption systems by providing measures of the thermal mass of sorption components. New experimental data for the thermal masses of nine sorption HXs are presented. The thermal mass of the shell or enclosure was not included. The overall *STM* varied from 2.46 to 19.51 $kJ^1K^{-1}kg_{sorb}^{-1}$.

The reported $c_{effective}$ ranged from 0.77 to 2.00 $kJ^1K^{-1}kg_{HX}^{-1}$. Because of this wide range of values, the *STM* is not generally accurately predictable for a generic adsorption HX. A $c_{effective}$ of 1.45 can serve as a general rule of thumb for attaining the TM_{total} for a flat tube–fin adsorber from the readily calculated *MR*.

However, the accuracy of $c_{effective}$ is much better when consideration is restricted to flat tube–fin type geometry (either packed or coated adsorbent) with water as HTF. With these constraints, the *STM* was predicted with an RMSE of 9% and a worst-case prediction error of 15% by multiplying the simple *MR* (m_{HX}/m_{sorb}) by an empirically fitted $c_{effective}$ of 1.70 $kJ^1K^{-1}kg_{HX}^{-1}$.

This rule of thumb can be useful for estimating the TM_{total} of a flat tube–fin HX when only its *MR* is readily obtainable. As more data are compiled in the literature, it may become possible to develop additional guidelines for $c_{effective}$ for different HX types.

Nomenclature

A	area (m^2)
AC	activated carbon
AT	approach temperature (K)
c	specific heat capacity ($kJ^1kg^{-1}K^{-1}$)
$c_{effective}$	effective specific heat
HTS	high temperature salt
HX	heat exchanger
LTS	low temperature salt
m	mass (kg)
MR	mass ratio ($kg_{HX}/kg_{sorbent}$)
STM	specific thermal mass
TM	thermal mass (kJ/kg)
V	volume (m^3)
Y	ratio of refrigerant (sorbate) mass to sorbent mass ($kg_{ref}/kg_{sorbent}$)
Greek	
$\boldsymbol{\rho}$	density (kg/m^3)
ω	humidity ratio (kg_w/kg_{da})
Subscripts	
0	initial
HTF	heat transfer fluid
liq	liquid
mat	material (non-HTF, non-sorbent), typically metals, comprising the heat exchanger
total	total (thermal mass)
ref	refrigerant (sorbate)
sorb	sorbent

Author Contributions: Conceptualization, K.R.G.; Data curation, K.R.G.; Investigation, A.F., A.V., S.M., Z.Y., M.R., and C.B.; Methodology, K.R.G., A.V., S.M., and M.R.; Visualization, K.R.G.; Writing—original draft, K.R.G., A.F., A.V., S.M., Z.Y., and M.R.; and Writing—review and editing, K.R.G., A.F., A.V., S.M., Z.Y., M.R., C.B., M.Q., E.L., A.R., S.H., R.C., M.B., G.F. and I.H. All authors have read and agreed to the published version of the manuscript.

Funding: This work was partially sponsored by the US Department of Energy's Building Technologies Office under Contract No. DE-AC05-00OR22725 with UT-Battelle, LLC. The authors would like to acknowledge Mr. Antonio Bouza, Technology Manager HVAC&R, Water Heating, and Appliance, US Department of Energy Building Technologies Office. Funding of the German Ministry of Economics and Energy within the project "ADOSO" (FKZ 03ET1127) for the work on the fiber adsorber is gratefully acknowledged. The work on binder coated adsorbers was supported by the Fraunhofer Zukunftsstiftung under grant HARVEST and by the German Federal Ministry of Education and Research (BMBF) under grant 03SF0441B. Funding is acknowledged from UK EPSRC Grant EP/K011847/1 i-STUTE. Funding is acknowledged from Natural Sciences and Engineering Research Council of Canada (NSERC) through the Automotive Partnership Canada Grant No. APCPJ 401826-10.

Acknowledgments: The authors would like to acknowledge the IEA Heat Pump Program Annex 43 "Fuel Driven Sorption Heat Pumps" for motivation and establishing working relationships among institutions, Kathy Jones for formatting, and Olivia Shafer for technical editing.

Conflicts of Interest: The authors declare no conflict of interest.

References

1. Ziegler, F. State of the art in sorption heat pumping and cooling technologies. *Int. J. Refrig.* **2002**, *25*, 450–459, doi:10.1016/S0140-7007(01)00036-6.
2. Wittstadt, U.; Füldner, G.; Vasta, S.; Volmer, R.; Bendix, P.; Schnabel, L.; Mittelbach, W. Adsorption heat pumps and chillers: Recent developments for materials and components. In Proceedings of the 12th

International Energy Agency Heat Pump Conference, Rotterdam, The Netherlands, 15–18 May 2017.
3. Critoph, R.E.; Metcalf, S.J. Specific cooling power intensification limits in ammonia–carbon adsorption refrigeration systems. *Appl. Therm. Eng.* **2004**, *24*, 661–678, doi:10.1016/j.applthermaleng.2003.11.004.
4. Goetz, V.; Elie, F.; Spinner, B. The structure and performance of single effect solid-gas chemical heat pumps. *Heat Recover. Syst. CHP* **1993**, *13*, 79–96, doi:10.1016/0890-4332(93)90027-S.
5. Neveu, P. Performances d'un pilote de pompe à chaleur chimique solide/gaz de 20/50 Kw : analyse des flux engendrés par la thermicité de telles réactions. PhD dissertation, Université Perpignan, France, 1990.
6. Douss, N.; Meunier, F.E.; Sun, L.M. Predictive model and experimental results for a two-adsorber solid adsorption heat pump. *Ind. Eng. Chem. Res.* **1988**, *27*, 310–316, doi:10.1021/ie00074a017.
7. Li, T.X.; Wang, R.Z.; Kiplagat, J.K.; Wang, L.W.; Oliveira, R.G. A conceptual design and performance analysis of a triple-effect solid-gas thermochemical sorption refrigeration system with internal heat recovery. *Chem. Eng. Sci.* **2009**, *64*, 3376–3384, doi:10.1016/j.ces.2009.04.021.
8. Demir, H.; Mobedi, M.; Ülkü, S. A review on adsorption heat pump: Problems and solutions. *Renew. Sustain. Energy Rev.* **2008**, *12*, 2381–2403, doi:10.1016/j.rser.2007.06.005.
9. Paul, B.K.; Lee, K.; Wang, H. Improving the Energy Efficiency of Adsorption Chillers by Intensifying Thermal Management Systems in Sorbent Beds. *J. Manuf. Sci. Eng. Trans. ASME* **2018**, *140*, doi:10.1115/1.4037606.
10. Gluesenkamp, K.R. Development and Analysis of Micro Polygeneration Systems and Adsorption Chillers. Ph.D. Thesis, University of Maryland, College Park, MD, USA, 2012.
11. Zhu, C.; Gluesenkamp, K.R.; Yang, Z.; Blackman, C. Unified thermodynamic model to calculate COP of diverse sorption heat pump cycles: Adsorption, absorption, resorption, and multistep crystalline reactions. *Int. J. Refrig.* **2019**, *99*, 382–392, doi:10.1016/j.ijrefrig.2018.12.021.
12. Sharafian, A.; Mahdi, S.; Mehr, N.; Thimmaiah, C.; Huttema, W.; Bahrami, M. Effects of adsorbent mass and number of adsorber beds on the performance of a waste heat-driven adsorption cooling system for vehicle air conditioning applications. *Energy* **2016**, doi:10.1016/j.energy.2016.06.099.
13. Sharafian, A.; Bahrami, M. Assessment of adsorber bed designs in waste-heat driven adsorption cooling systems for vehicle air conditioning and refrigeration. *Renew. Sustain. Energy Rev.* **2014**, *30*, 440–451, doi:10.1016/j.rser.2013.10.031.
14. Qian, S.; Gluesenkamp, K.; Hwang, Y.; Radermacher, R.; Chun, H.-H. Cyclic steady state performance of adsorption chiller with low regeneration temperature zeolite. *Energy* **2013**, *60*, doi:10.1016/j.energy.2013.08.041.
15. Rouhani, M. Sorption Thermal Energy Storage for Sustainable Heating and Cooling. Ph.D. Thesis, 2019, Simon Fraser University, Vancouver, Canada.
16. Xu, J.; Oliveira, R.G.; Wang, R.Z. Resorption system with simultaneous heat and cold production. *Int. J. Refrig.* **2011**, *34*, 1262–1267, doi:10.1016/j.ijrefrig.2011.03.012.
17. Bao, H.S.; Oliveira, R.G.; Wang, R.Z.; Wang, L.W.; Ma, Z.W. Working pairs for resorption refrigerator. *Appl. Therm. Eng.* **2011**, *31*, 3015–3021, doi:10.1016/J.APPLTHERMALENG.2011.05.035.
18. Lepinasse, E.; Goetz, V.; Crosat, G. Modelling and experimental investigation of a new type of thermochemical transformer based on the coupling of two solid-gas reactions. *Chem. Eng. Process.* **1994**, *33*, 125–134, doi:10.1016/0255-2701(94)90002-7.
19. Tamainot-Telto, Z.; Critoph, R.E. Thermophysical properties of monolithic carbon. *Int. J. Heat Mass Transf.* **2000**, *43*, 2053–2058, doi:10.1016/S0017-9310(99)00266-5.
20. Perry, R.H.; Green, D.W.; Maloney, J.O. *Perry's Chemical Engineers'*; Handbook; McGraw-Hill: New York, NY, USA, 1997.
21. Ullmann, F. *Ullmann's Encyclopedia of Industrial Chemistry*, 6th ed.; Wiley: Hoboken, NJ, USA, 2001.
22. Füldner, G. Stofftransport und Adsorptionskinetik in Porösen Adsorbenskompositen für Wärmetransformationsanwendungen. Ph.D. Thesis, University of Freiburg, Breisgau ,Germany, 2015.
23. Domalski, E.S.; Hearing, E.D. Condensed Phase Heat Capacity Data. In *NIST Chemistry WebBook, NIST Standard Reference Database Number 69*; Linstrom, P.J., Mallard, W.G., Eds.; National Institute of Standards and Technology: Gaithersburg MD, USA, 20899.
24. Santori, G.; Frazzica, A.; Freni, A.; Galieni, M.; Bonaccorsi, L.; Polonara, F.; Restuccia, G. Optimization and testing on an adsorption dishwasher. *Energy* **2013**, *50*, 170–176, doi:10.1016/j.energy.2012.11.031.
25. Kakiuchi, H.; Iwade, M.; Shimooka, S.; Ooshima, K.; Yamazaki, M.; Takewaki, T. Novel zeolite adsorbents and their application for AHP and Desiccant system. *lEA-Annex* **2004**, *17*, 6.

26. Julabo. *The Thermal Bath Fluids*; Julabo: Seelbach, Germany, 2015.
27. Brancato, V.; Frazzica, A.; Sapienza, A.; Gordeeva, L.; Freni, A. Ethanol adsorption onto carbonaceous and composite adsorbents for adsorptive cooling system. *Energy* **2015**, *84*, 177–185, doi:10.1016/j.energy.2015.02.077.
28. Freni, A.; Bonaccorsi, L.; Calabrese, L.; Caprì, A.; Frazzica, A.; Sapienza, A. SAPO-34 coated adsorbent heat exchanger for adsorption chillers. *Appl. Therm. Eng.* **2016**, *82*, 1–7, doi:10.1016/j.applthermaleng.2015.02.052.
29. Kim, C.S. *Thermophysical Properties of Stainless Steels*; Argonne National Laboratory No. ANL-75-55; Argonne National Laboratory: Lemont, IL, USA, 1975.
30. Sapienza, A.; Santamaria, S.; Frazzica, A.; Freni, A. Influence of the management strategy and operating conditions on the performance of an adsorption chiller. *Energy* **2011**, *36*, 5532–5538, doi:10.1016/j.energy.2011.07.020.
31. Frazzica, A.; Palomba, V.; Dawoud, B.; Gullì, G.; Brancato, V.; Sapienza, A.; Vasta, S.; Freni, A.; Costa, F.; Restuccia, G. Design, realization and testing of an adsorption refrigerator based on activated carbon/ethanol working pair. *Appl. Energy* **2016**, *174*, 15–24, doi:10.1016/j.apenergy.2016.04.080.
32. Palomba, V.; Dawoud, B.; Sapienza, A.; Vasta, S.; Frazzica, A. On the impact of different management strategies on the performance of a two-bed activated carbon/ethanol refrigerator: An experimental study. *Energy Convers. Manag.* **2017**, *142*, 322–333, doi:10.1016/j.enconman.2017.03.055.
33. Bendix, P.; Füldner, G.; Möllers, M.; Kummer, H.; Schnabel, L.; Henninger, S.; Henning, H.M. Optimization of power density and metal-to-adsorbent weight ratio in coated adsorbers for adsorptive heat transformation applications. *Appl. Therm. Eng.* **2017**, *124*, 83–90, doi:10.1016/j.applthermaleng.2017.05.165.
34. Tamainot-Telto, Z.; Critoph, R.E. Advanced solid sorption air conditioning modules using monolithic carbon–ammonia pair. *Appl. Therm. Eng.* **2003**, *23*, 659–674, doi:10.1016/S1359-4311(02)00238-7.
35. Rivero-Pacho, A.M.; Critoph, R.E.; Metcalf, S.J. Alternative monolithic/composite carbons for adsorption generators and simulation for optimal performance. *Appl. Therm. Eng.* **2017**, *126*, 350–357, doi:10.1016/j.applthermaleng.2017.07.177.
36. Blackman, C.; Bales, C.; Thorin, E. Experimental evaluation and concept demonstration of a novel modular gas-driven sorption heat pump, in *Proceedings of 12th IEA Heat Pump Conference*, Rotterdam, Netherlands, May 15–18, 2017.
37. Bauer, J.; Herrmann, R.; Mittelbach, W.; Schwieger, W. Zeolite/aluminum composite adsorbents for application in adsorption refrigeration. *Int. J. Energy Res.* **2009**, *33*, 1233–1249, doi:10.1002/er.1611.
38. Fink, M.; Andersen, O.; Seidel, T.; Schlott, A. Strongly Orthotropic Open Cell Porous Metal Structures for Heat Transfer Applications. *Metals* **2018**, *8*, 554, doi:10.3390/met8070554.
39. Wittstadt, U.; Füldner, G.; Andersen, O.; Herrmann, R.; Schmidt, F. A new adsorbent composite material based on metal fiber technology and its application in adsorption heat exchangers. *Energies* **2015**, *8*, 8431–8446, doi:10.3390/en8088431.
40. Wittstadt, U.; Füldner, G.; Laurenz, E.; Warlo, A.; Große, A.; Herrmann, R.; Schnabel, L.; Mittelbach, W. A novel adsorption module with fiber heat exchangers: Performance analysis based on driving temperature differences. *Renew. Energy* **2017**, *110*, 154–161, doi:10.1016/j.renene.2016.08.061.

International Journal of Refrigeration 99 (2019) 382–392

Contents lists available at ScienceDirect

International Journal of Refrigeration

journal homepage: www.elsevier.com/locate/ijrefrig

Unified thermodynamic model to calculate COP of diverse sorption heat pump cycles: Adsorption, absorption, resorption, and multistep crystalline reactions☆

Chaoyi Zhu[a,b], Kyle R. Gluesenkamp[b,*], Zhiyao Yang[c], Corey Blackman[d,e,f]

[a] Building Energy Research Center, Department of Building Science, Tsinghua University, Beijing 100084, China
[b] Oak Ridge National Laboratory, Building Equipment Research, Energy & Transportation Science Division, Oak Ridge, TN 37831, USA
[c] Lyle School of Civil Engineering, Purdue University, West Lafayette, IN 47906, USA
[d] SaltX Technology AB, Västertorpsvägen 135, 12944 Stockholm, Sweden
[e] Dalarna University, Borlänge, Sweden
[f] School of Business, Society & Engineering, Mälardalens University, Västerås, Sweden

ARTICLE INFO

Article history:
Received 15 January 2018
Revised 13 November 2018
Accepted 21 December 2018
Available online 24 December 2018

Keywords:
Resorption
Ammonia
Sorption heat pump
Dead thermal mass
Analytical
Heat recovery

ABSTRACT

A straightforward thermodynamic model is developed in this work to analyze the efficiency limit of diverse sorption systems. A method is presented to quantify the dead thermal mass of heat exchangers. Solid and liquid sorbents based on chemisorption or physical adsorption are accommodated. Four possible single-effect configurations are considered: basic absorption or adsorption (separate desorber, absorber, condenser, and evaporator); separate condenser/evaporator (two identical sorbent-containing reactors with a condenser and a separate direct expansion evaporator); combined condenser/evaporator (one salt-containing reactor with a combined condenser/evaporator module); and resorption (two sorbent-containing reactors, each with a different sorbent). The analytical model was verified against an empirical heat and mass transfer model derived from component experimental results. It was then used to evaluate and determine the optimal design for an ammoniate salt-based solid/gas sorption heat pump for a space heating application. The effects on system performance were evaluated with respect to different working pairs, dead thermal mass factors, and system operating temperatures. The effect of reactor dead mass as well as heat recovery on system performance was also studied for each configuration. Based on the analysis in this work, an ammonia resorption cycle using LiCl/NaBr as the working pair was found to be the most suitable single-effect cycle for space heating applications. The maximum cycle heating coefficient of performance for the design conditions was 1.50 with 50% heat recovery and 1.34 without heat recovery.

Modèle thermodynamique unifié pour calculer le COP de divers cycles de pompe à chaleur à sorption: adsorption, absorption, résorption, et réactions cristallines en plusieurs étapes

Mots-clés: Résorption; Ammoniac; Pompe à chaleur à sorption; Masse thermique morte; Analytique; Récupération de chaleur

1. Introduction

A natural gas–driven sorption heat pump for space heating applications was proposed and studied by Blackman et al. (2017) with the goal of reducing primary energy consumption and energy cost compared with conventional fuel-fired boilers and furnaces. The heat pump uses ammoniated salt or a salt pair to absorb ammonia refrigerant with three configuration options:

* Corresponding author.
E-mail address: gluesenkampk@ornl.gov (K.R. Gluesenkamp).

https://doi.org/10.1016/j.ijrefrig.2018.12.021
0140-7007/

Nomenclature

ADS	adsorption system
ABS	absorption system
COP	coefficient of performance
DTMR	dead thermal mass ratio, kJ kJ^{-1}
L	latent heat, kJ kg^{-1}
Y	loading, kg kg^{-1}
Q	heat per unit of refrigerant, kJ kg^{-1}
T	temperature, ^{0}C
m	mass, kg
ρ	density, kg m^{-3}
V	volume, m^3
ΔH	reaction heat, kJ kg^{-1}
ΔT	temperature difference, K
ΔY	differential loading, kg kg^{-1}
C_p	specific heat, kJ kg^{-1} K^{-1}
x	vapor quality
ε	heat exchange effectiveness
ψ	maximum cooling COP (ratio of latent heats defined in Table 1)
HTS	high temperature salt
LTS	low temperature salt
DTM	dead thermal mass, kJ K^{-1}
DTMR	dead thermal mass ratio
RES	resorption cycle
SCE	ammoniate adsorption cycle with separate condenser/evaporator
CCE	ammoniate adsorption cycle with combined condenser/evaporator
θ_1	Parameter associated with the dead thermal mass of the ΔT_L-coupled heat exchangers
θ_2	Parameter associated with the dead thermal mass of the ΔT_D-coupled heat exchangers
ε_1	sensible heat recovery fraction for ΔT_L-coupled heat exchangers
ε_2	sensible heat recovery fraction for ΔT_D-coupled heat exchangers
λ	COP approach factor
C/E	condenser/evaporator

Subscripts

0	low temperature heat source
1	medium temperature heat sink
2	high temperature heat source
D	desorber/difference
E	evaporator
L	lift
des	desorbing
cond	condensing
comp	ammonia complex
abs	absorbing
ads	adsorbing
evap	evaporating
ht	heating
cl	cooling
i	inlet
sol	solution
max	maximum
min	minimum
ref	refrigerant
ret	retained
liq	liquid
mat	material
HTF	heat transfer fluid
HTR	high temperature reactor
LTR	low temperature reactor
SHX	solution heat exchanger

the ammoniate adsorption cycle with separate condenser and evaporator (SCE), the ammoniate cycle with combined condenser/evaporator (CCE), and the resorption cycle (RES). These configurations are the basic sorption cycle configurations in solid/gas chemisorption heat pump studies (Li et al., 2014; Wang et al., 2014; Wongsuwan et al., 2001). They are the foundation for various advanced cycles. Compared with the more advanced configurations of each type, they require the fewest components to develop a prototype machine (Blackman et al., 2017). To reveal the major characteristics of different cycle configurations, this study focused on these three basic configurations instead of other advanced ones.

The SCE cycle shown in Fig. 1a consists of two identical solid/gas reactors, a condenser, and an evaporator; the CCE cycle shown in Fig. 1b consists of a solid/gas reactor and a combined condenser/evaporator; and the RES cycle shown in Fig. 1c consists of two solid/gas reactors. In the first half-cycle of operation, the heat pump is driven by natural gas where the heat evolving from a natural gas burner is used to desorb ammonia from the reactor to the condenser (SCE and CCE) or the reactor B (RES). The condensation (SCE and CCE) or reaction heat (RES) is used for space heating purposes. In the second half-cycle, the heat of adsorption from the reactor is used for heating purposes while an outdoor fan coil is thermally connected to the evaporator (SCE and CCE) or reactor B (RES) to absorb low-temperature thermal energy from outdoor air. It should be noted that the SCE studied in this work has two identical reactors running out of phase and simultaneously. One reactor is connected to the condenser, and the other is connected to the evaporator every half cycle. The condenser and evaporator run continuously.

Performance analysis and comparison of different configurations using various working pairs are necessary to determine the optimal design for prototype development. Moreover, the effect of dead thermal mass (or DTM, defined here as the sensible heat load [kJ K^{-1}] due to the cyclic temperature swing of the sorbent, retained refrigerant, heat transfer fluid, and bed material) and different operating conditions should also be considered. In literature, the performance of various sorption cycles was analyzed by modeling and test approaches (Goetz et al., 1997; Zhu et al., 2016). Modeling is the faster and cheaper approach to evaluate a design. Three types of model are usually considered: thermodynamic model, lumped-parameter model, and distributed-parameter model (Pesaran et al., 2016). The thermodynamic model is the fastest and most straightforward model with acceptable error. It is always applied for fast preliminary analysis of sorption systems in many studies.

Thermodynamic studies of absorption cycle started from Carnot heat engine-heat pump model (Herold et al., 2016). Zebbar et al. (2012) applied exergy analysis to find irreversibility of a cycle. Optimizations were made based on that. Herold (1999) provided a zero-order model and compared calculated COP with real machine data. The model showed a more realistic result than the reversible model. Xie and Jiang (2015) proposed a new absorption heat pump model based on ideal solution circulation. A temperature lift coefficient was connected to COP to illustrate basic performance of absorption heat pump.

Cacciola and Restuccia (1995) applied thermodynamic model based on first law analysis to calculate and compare the COP and cooling capacity of adsorption cycle with three different working pairs. Zeolite/water was concluded to be the most suitable

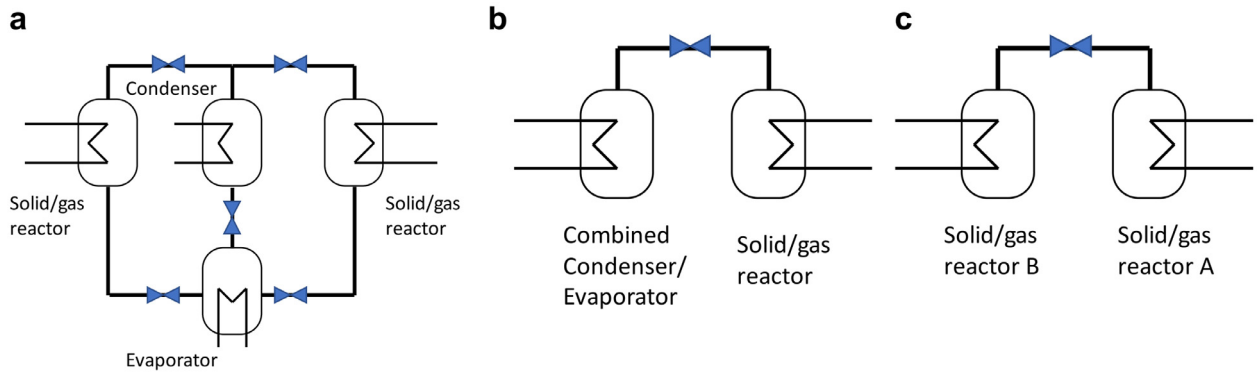

Fig. 1. Three possible sorption cycle configurations: (a) SCE, sorption with separate (dedicated) evaporator/condenser; (b) CCE, sorption with combined condenser/evaporator; and (c) RES, resorption.

pair for domestic applications in southern Europe. Meunier et al. (1998) defined entropic temperature and introduced an equivalent Carnot cycle for thermodynamic modeling of sorption systems. Difference between liquid absorption and solid adsorption technologies was compared by internal entropy production calculation. Pons and Poyelle (1999) applied similar analysis to study two types of vapor recovery cycles. Dead thermal mass was not considered in the model. Douss and Meunier (1988) investigated the effect of operating temperatures on the COP of activated-carbon-methanol adsorption cooling systems with experimental test and a thermodynamic model. The model considered the extra sensible heat requirement of sorbent, refrigerant, and reactor metal under the desorption mode. Freni et al. (2015) developed a thermodynamic model to evaluate adsorption heat pump cycle with combined condenser-evaporator. Dead mass was considered in calculation of desorption and evaporation heat.

Li et al. (2014) provided a uniformed thermodynamic model to calculate performance of solid/gas sorption cycles. Sensible heat consumption was considered as a factor to improve cycle COP. However, the expression of sensible heat was too general and was unable to present key difference between cycles. Neveu and Castaing (1993) used a thermodynamic model to compare performance of different solid/gas recovery cycles upgraded from SCE. Dead mass of material and heat transfer fluid were not considered. They also provided a three temperature model from first and second law of thermodynamics (Neveu, & Castaing, 1996). Sharma and Kumar (2017, 2018) applied a thermodynamic model in metal hydride based sorption systems to choose suitable metal hydride pair. Material dead mass was considered. The author also considered mass transfer kinetics at different working pressures when selecting working pair candidates.

Present studies established a thermodynamic model for very specific cycles. It is hard to compare key differences between various cycles clearly. For simplification, some studies ignored dead thermal mass effect that would over estimate the performance of the system. Dead thermal mass is influenced by both design ability and inherent salt mass and should be discussed separately to better understand the improvement potential of the system. For fast preliminary analysis of sorption systems with many configurations and working pair options, and to facilitate qualitative comparison among such options, a thermodynamic model that is accurate, computationally efficient, and transparent in its technical meaning is needed.

In this work, a unified thermodynamic model for system COP of sorption cycles was developed to enable rapid performance comparison between, and analysis of, various cycle configurations and working pairs. A simple expression that accommodates ammoniate salt-based chemisorption and many other sorption cycle types was provided. A table was provided to clearly compare key differences between systems: cycle configuration, working pair selection, and system design. Meanwhile, dead mass was considered in a new way that: (a) has separate terms for design-related and inherent mass, (b) is more relevant to cycle performance, and (c) is easier to compute.

2. Analytical model

An analytical model is developed in this section to evaluate the heating COP of various sorption cycle configurations. The following assumptions are made to simplify the model:

a. *Single effect cycles*: Only single effect cycles are considered, in order to reveal the major characteristics of different cycle configurations.
b. *Cyclic steady state*: The parameters (temperatures and refrigerant loading) at the end of a whole cycle are the same as those at the beginning of the cycle.
c. *Mass transfer temperature*: The desorption process happens only at T_{des}, the absorption/adsorption process happens only at T_{abs}/T_{ads}, and the evaporation process happens only at T_{evap}.
d. *Thermodynamic equilibrium*: Cycle time is not considered; it is assumed that processes reach equilibrium with no mass transfer limitations (solution leaves the desorber and absorber in equilibrium).
e. *No heat losses*: Losses through pipes and walls are neglected.
f. *Sorbent temperature*: References are made only to the sorbent bed temperatures (temperatures of external heat transfer fluids are not considered).
g. *Lumped capacitance*: The sorbent temperature is assumed to be spatially uniform.

2.1. COP expression for conventional absorption and adsorption cycles

In this work, the conventional absorption cycle is the basic single stage single effect absorption cycle that consists of a desorber, an absorber, a condenser, an evaporator, and optionally a solution heat exchanger (Herold et al., 2016). The conventional adsorption cycle refers to the basic adsorption cycle with a condenser, an evaporator, and one (or two) adsorption bed(s) as described by Wang et al. (2014). The conventional adsorption cycle is only differs from the SCE in Fig. 1 because the conventional adsorption cycle uses physical adsorption instead of chemisorption.

Analytical models for the cooling or heating COP of absorption and adsorption cycles have been proposed numerous times before; for example in Gluesenkamp (2012) and Freni et al. (2015) The heating COP of a sorption cycle is defined as the ratio between

useful heat Q_1 and driving heat Q_2, as shown in Eq. (1). It can also be expressed in terms of low temperature source heat Q_0 and driving heat Q_2.

$$COP_{ht} = \frac{Q_1}{Q_2} = 1 + \frac{Q_0}{Q_2} = 1 + COP_{cl} \tag{1}$$

For a sorption heat pump, the useful heat usually includes heat from both the absorber/adsorber and the condenser, and the driving heat is the heat into the desorber. Based on energy balance, the heating COP of a sorption heat pump can be expressed as one plus the ratio of evaporator heat to desorber heat—that is, one plus the cooling COP, had it been used as a chiller. Therefore, the following derivations will focus only on the evaporator heat and the desorber heat, which are defined as heat per unit mass flow of refrigerant.

For both absorption and adsorption cycles, the evaporator heat per unit mass flow of refrigerant can be expressed as Eq. (2). During cyclic steady state operation, only the latent heat of evaporation is considered. In the equation, $x_{evap,\,i}$ is the inlet vapor quality to evaporator, which depends on temperature lift $\Delta T_L = T_{cond} - T_{evap}$ and choice of refrigerant, as shown in Eq. (3).

$$Q_E = L_{evap}\left(1 - x_{evap,i}\right) \tag{2}$$

$$x_{evap,i} = \frac{C_{p,ref,liq}\Delta T_L}{L_{evap}} \tag{3}$$

The desorber heat is composed of the latent heat and the sensible heat. The latent heat is the main part of the heat requirement in desorber and is the same for absorption and adsorption cycles. The sensible heat is slightly different between absorption and adsorption cycles. For an absorption cycle, the sensible heating of the solution through the desorber is considered. The desorber heat is shown in Eq. (4). Note that Eq. (4) uses loading Y (i.e., the mass ratio of refrigerant to sorbent) instead of the convention more common for absorption systems (i.e., the mass fraction refrigerant for ammonia/water, or mass fraction sorbent for water/LiBr). The sensible heat depends on the inlet solution mass flow per unit mass flow of refrigerant, the driving temperature difference $\Delta T_D = T_{des} - T_{abs}$, the maximum loading in the desorber Y_{max}, the differential loading $\Delta Y = Y_{max} - Y_{min}$, and the effectiveness of the solution heat exchanger ε_{SHX}. The solution temperature difference can be calculated from $\Delta T_{sol} = (1 - \varepsilon_{SHX})\Delta T_D$, and the mass flow of solution per unit mass flow of refrigerant is $\frac{(1+Y_{max})}{\Delta Y}$. Then, by combining Eqs. (1)–(4), the heating COP for absorption cycle can be expressed as Eq. (5). Note that the use of Y_{max} is due to assumption c, which states that all desorption occurs at T_{des}. Thus all refrigerant in the sorbent at the end of sorption (associated with Y_{max}) must be sensibly heated in the transition from sorption to desorption.

$$Q_D = L_{des} + C_{p,sol}(1 - \varepsilon_{SHX})\Delta T_D \frac{(1 + Y_{max})}{\Delta Y} \tag{4}$$

$$COP_{ht} = 1 + \frac{L_{evap} - C_{p,ref,liq}\Delta T_L}{L_{des} + C_{p,sol}(1 - \varepsilon_{SHX})\Delta T_D \frac{(1+Y_{max})}{\Delta Y}} \tag{5}$$

For an adsorption cycle, the desorption and adsorption processes occur separately in the same reactor. The sensible heat should include heating of the adsorbent, retained refrigerant, heat transfer fluid (HTF), bed material, and other possible "dead thermal masses" in the adsorber/desorber. Gluesenkamp (2012) defined a term dead thermal mass ratio (DTMR) to capture the relative size of these dead thermal masses. In this framework, the dead thermal mass (DTM), defined in Eq. (6a) is the aggregate of all thermal masses that must be heated and cooled each cycle. The DTMR is defined in Eq. (6b) as a dimensionless ratio of sensible heat to latent heat per cycle, including heat transfer fluid, heat exchanger materials, and the sensible heat of the sorbent and refrigerant. The sensible heat per cycle is DTM [kJ K^{-1}] multiplied by ΔT_D [K], and the latent heat per cycle is the latent heat of desorption [kJ] per cycle. Note that the product of ΔY and m_{ads} give the mass of refrigerant transferred per half-cycle (also referred to as the active mass).

Using the DTMR, we can derive the heating COP for a typical adsorption cycle without heat recovery in Eq. (7). A more detailed expression that accounts for heat recovery is included in the work of Gluesenkamp (2012). Note that DTM is strictly a function of the geometry of the physical sorbent heat exchanger. As will be shown later, the impact of DTM on the cycle efficiency is mediated by DTMR, which also includes operating parameters (temperatures and working fluid properties).

$$DTM = \rho_{HTF}V_{HTF}C_{p,HTF} + \rho_{mat}V_{mat}C_{p,mat} + m_{ads}(C_{p,ads} + Y_{max}C_{p,ref,liq}) \tag{6a}$$

$$DTMR = \frac{\Delta T_D DTM}{\Delta Y m_{ads} L_{des}} \tag{6b}$$

$$COP_{ht} = 1 + \frac{L_{evap} - C_{p,ref,liq}\Delta T_L}{L_{des}(1 + DTMR)} \tag{7}$$

2.2. COP expression for ammoniate sorption with separate dedicated condenser and evaporator

In this section, the heating COP of an ammoniate sorption cycle with separate dedicated condenser and evaporator is derived. The expression for evaporator heat is the same compared with the conventional adsorption cycle. The desorber heat consists of both reaction heat and sensible heat. The reaction heat ΔH_{des} depends on the working pair and reaction process. The sensible heat is like that of the conventional adsorption cycle except that ammoniate composite instead of refrigerant is retained in the desorber. The DTMR and heating COP for ammoniate sorption cycle are shown in Eqs. (8) and (9).

$$DTMR = \frac{\Delta T_D}{\Delta Y m_{ads}\Delta H_{des}}(\rho_{HTF}V_{HTF}C_{p,HTF} + \rho_{mat}V_{mat}C_{p,mat} + (1 + Y_{max})m_{ads}C_{p,comp}) \tag{8}$$

$$COP_{ht} = 1 + \frac{L_{evap} - C_{p,ref,liq}\Delta T_L}{\Delta H_{des}(1 + DTMR)} \tag{9}$$

2.3. COP expression for cycle with combined condenser/evaporator

The combined condenser/evaporator configuration can be used for both physical adsorption (such as water/silica gel) and chemical sorption (such as ammonia/ammoniated salts). The distinguishing characteristic of the CCE cycle is that a single chamber is used as the condenser in one half cycle and as the evaporator in the other half-cycle. This leads to two main differences compared with the conventional cycle. Firstly, the refrigerant will not go through an expansion process; therefore, the vapor fraction of the refrigerant at the beginning of evaporation is zero. Secondly, the dead thermal masses in the combined condenser/evaporator are cooled from T_{cond} to T_{evap} during the evaporation process, which reduces the evaporator heat and undermines the COP. The DTMR for evaporator and evaporator heat is shown in Eqs. (10) and (11). The $m_{ref,\,ret}$ is the retained mass of refrigerant at the end of the condensing process.

$$DTMR_E = \frac{\Delta T_L}{\Delta Y m_{ads} L_{evap}}(\rho_{HTF,E}V_{HTF,E}C_{p,HTF,E} + \rho_{mat,E}V_{mat,E}C_{p,mat,E} + m_{ref,ret}C_{p,ref,liq}) \tag{10}$$

Table 1
Expressions for characters in different systems.

System configuration	Abbr.	ψ	θ_1	θ_2
Absorption cycle	ABS	$\frac{L_{evap}}{L_{des}}$	$\frac{C_{p,ref,liq}\Delta T_L}{L_{evap}}$	$C_{p,sol}\Delta T_D\frac{(1+Y_{min})}{\Delta Y L_{des}}$
Adsorption cycle	ADS	$\frac{L_{evap}}{L_{des}}$	$\frac{C_{p,ref,liq}\Delta T_L}{L_{evap}}$	$DTMR$
Separate condenser/ evaporator cycle	SCE	$\frac{L_{evap}}{\Delta H_{des}}$	$\frac{C_{p,ref,liq}\Delta T_L}{L_{evap}}$	$DTMR$
Combined condenser/ evaporator cycle	CCE	$\frac{L_{evap}}{\Delta H_{des}}$	$DTMR_E$	$DTMR_D$
Resorption cycle	RES	$\frac{\Delta H_{LTS}}{\Delta H_{HTS}}$	$DTMR_{LTR}$	$DTMR_{HTR}$

$$Q_E = L_{evap}(1 - DTMR_E) \tag{11}$$

The desorber DTMR in Eq. (6) for conventional adsorption desorber or in Eq. (8) for ammoniate sorption desorber can be used for COP calculation for the combined condenser/evaporator cycle depending on the sorption process. The heating COP for this combined condenser/evaporator cycle with ammoniate sorption desorber is shown in Eq. (12). For CCE cycle with conventional adsorption desorber, latent heat L_{des} should be used instead of reaction heat ΔH_{des}.

$$COP_{ht} = 1 + \frac{L_{evap}(1 - DTMR_E)}{\triangle H_{des}(1 + DTMR_D)} \tag{12}$$

2.4. COP expression for resorption cycle with two reactors and two adsorbents

For the resorption cycle with two reactors (a high temperature reactor (HTR) and a low temperature reactor (LTR) and two adsorbents (high/low temperature salt [HTS and LTS]), the cooling COP is defined as the heat absorbed by the LTR divided by heat required by the HTR. Correspondingly, heating COP is cooling COP plus one. Like the combined condenser/evaporator cycle, DTM should be considered in both reactors. Eqs. (13) and (14) illustrate the DTMR for low and high temperature reactors. The heating COP is expressed in Eq. (15). The temperature lift ΔT_L is defined as the difference between the adsorption and desorption temperature of LTS ($T_{ads,\,LTS} - T_{des,\,LTS}$); the temperature difference ΔT_D is defined as the difference between the desorption and adsorption temperature of HTS ($T_{des,\,HTS} - T_{ads,\,HTS}$). When there are multiple steps of reactions for LTS or HTS, the COP should combine all the reactions together as shown in Eq. (16).

$$\begin{aligned} DTMR_{LTR} = \frac{\Delta T_L}{\Delta Y_{HTS} m_{HTS} \Delta H_{LTS}} & (\rho_{HTF,LTR} V_{HTF,LTR} C_{p,HTF,LTR} \\ & + \rho_{mat,LTR} V_{mat,LTR} C_{p,mat,LTR} \\ & + (1 + Y_{max,LTS}) m_{LTS} C_{p,LTS,comp}) \end{aligned} \tag{13}$$

$$\begin{aligned} DTMR_{HTR} = \frac{\Delta T_D}{\Delta Y_{HTS} m_{HTS} \Delta H_{HTS}} & (\rho_{HTF,HTR} V_{HTF,HTR} C_{p,HTF,HTR} \\ & + \rho_{mat,HTR} V_{mat,HTR} C_{p,mat,HTR} \\ & + (1 + Y_{max,HTS}) m_{HTS} C_{p,HTS,comp}) \end{aligned} \tag{14}$$

$$COP_{ht} = 1 + \frac{\Delta H_{LTS}(1 - DTMR_{LTR})}{\Delta H_{HTS}(1 + DTMR_{HTR})} \tag{15}$$

$$COP_{ht} = 1 + \frac{\sum_{i=1}^{n} \frac{\Delta Y_{LTS,i} \Delta H_{LTS,i}}{\Delta Y_{LTS}} (1 - DTMR_{LTR})}{\sum_{j=1}^{m} \frac{\Delta Y_{HTS,j} \Delta H_{HTS,j}}{\Delta Y_{HTS}} (1 + DTMR_{HTR})} \tag{16}$$

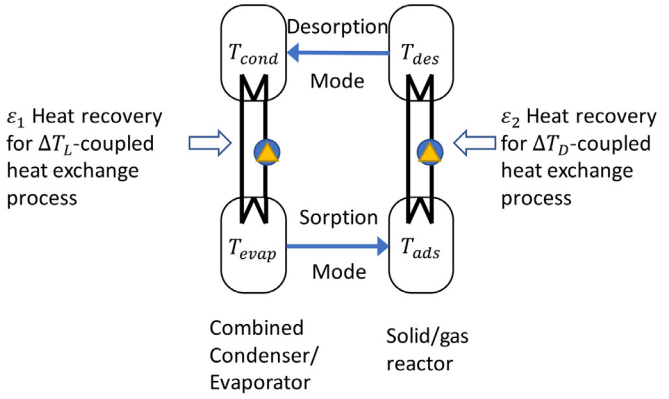

Fig. 2. System with heat recovery (using a combined condenser/evaporator as an example).

2.5. Unified expression for all configuration types

Based on Eqs. (1), (5), (7), (9), (12), and (15) or (16), the universal expression of heating COP for a sorption system is shown in Eq. (17), and the meaning of each term is explained in Table 1. The systems related to ammoniate sorption are SCE, CCE, and RES.

$$COP_{ht} = 1 + \psi \frac{1 - \theta_1}{1 + \theta_2} \tag{17}$$

Any one of these configurations is generally capable of incorporating heat recovery, according to the following considerations.

Heat recovery can be accomplished from the ΔT_L-coupled heat exchange process, where at least two discrete heat exchangers are used for heat exchange with T_{cond} and T_{evap}. The fraction of sensible heat recovered from the ΔT_L-coupled heat exchangers is denoted here as ε_1, as shown in Fig. 2.

Similarly, any one of these configurations is capable of incorporating heat recovery from the ΔT_D-coupled heat exchange process, when at least two discrete heat exchangers are used for heat exchange with T_{des} and T_{ads}. The fraction of sensible heat recovered from the ΔT_D-coupled heat exchangers is denoted here as ε_2, as also shown in Fig. 2.

To accommodate heat recovery, Eq. (17), which assumes no heat recovery, can be modified as shown in Eq. (18). Note that heat recovery ε_1 is always zero for cycles not considering dead thermal mass in the low temperature heat source–driven reactor.

Note that the effectivenesses ε_1 and ε_2 act only on the sensible heat. This can be observed by inspection of Eq. (18) and the definition of θ_1 and θ_2, by evaluating these expressions with values of $\varepsilon_1 = \varepsilon_2 = 0$ and $\varepsilon_1 = \varepsilon_2 = 1$. In other words, in this work, heat recovery effectiveness is the fraction of sensible heat that can be recovered. A scheme that recovers latent heat as well (such as the well-known generator-absorber exchange or GAX cycle) would have an effectiveness greater than one since latent heat is recov-

Table 2
Comparison of DTM_{design} and $DTM_{inherent}$ for each configuration and heat exchanger type.

Type[a]	DTM_{design}	$DTM_{inherent}$
ABS	0	$(1-\varepsilon_{SHX})(1+Y_{max})m_{abs}C_{p,sol}$
ADS	$\rho_{HTF}V_{HTF}C_{p,HTF}+\rho_{mat}V_{mat}C_{p,mat}$	$m_{ads}(C_{p,ads}+Y_{max}C_{p,ref.liq})$
SCE	$\rho_{HTF}V_{HTF}C_{p,HTF}+\rho_{mat}V_{mat}C_{p,mat}$	$(1+Y_{max})m_{ads}C_{p,comp}$
CCE—Evaporator	$\rho_{HTF,E}V_{HTF,E}C_{p,HTF,E}+\rho_{mat,E}V_{mat,E}C_{p,mat,E}$	$m_{ref,\ ret}C_{p,\ ref,\ liq}$
CCE—Desorber	$\rho_{HTF,D}V_{HTF,D}C_{p,HTF,D}+\rho_{mat,D}V_{mat,D}C_{p,mat,D}$	$(1+Y_{max})m_{ads}C_{p,comp}$
RES—LTR	$\rho_{HTF,LTR}V_{HTF,LTR}C_{p,HTF,LTR}+\rho_{mat,LTR}V_{mat,LTR}C_{p,mat,LTR}$	$(1+Y_{max,LTS})m_{LTS}C_{p,LTS,comp}$
RES—HTR	$\rho_{HTF,HTR}V_{HTF,HTR}C_{p,HTF,HTR}+\rho_{mat,HTR}V_{mat,HTR}C_{p,mat,HTR}$	$(1+Y_{max,HTS})m_{HTS}C_{p,HTS,comp}$

[a] ABS = absorption cycle; ADS = adsorption cycle; DTM = dead thermal mass; SCE = separate condenser and evaporator; CCE = combined condenser/evaporator; RES = resorption cycle; LTR = low temperature reactor; HTR = high temperature reactor.

ered in addition to sensible heat.

$$COP_{ht}=1+\psi\frac{1-(1-\varepsilon_1)\theta_1}{1+(1-\varepsilon_2)\theta_2} \tag{18}$$

In Eqs. (17) and (18), the ratio expression after ψ shows the gap between real cooling COP and maximum single effect cooling COP because of the effects of dead thermal mass and other penalties. We name this ratio as the COP approach factor (λ), as shown in Eq. (19). A higher λ means the COP is closer to maximum COP. When λ equals 1, the real COP is equal to maximum COP.

$$\lambda=\frac{1-(1-\varepsilon_1)\theta_1}{1+(1-\varepsilon_2)\theta_2} \tag{19}$$

Combining this definition with Eq. (18) yields Eq. (20).

$$COP_{ht}=1+\psi\lambda \tag{20}$$

In Eqs. (6), (8), (10), (13), and (14), the DTM can be defined as the sum of two parts as shown in Eq. (21). For each heat exchanger type, the definitions of DTM_{design} and $DTM_{inherent}$ change slightly, as shown in Table 2.

$$DTM=DTM_{design}+DTM_{inherent} \tag{21}$$

The DTM_{design} represents the dead thermal mass of HTF and heat exchanger material. Clearly, this has a very strong dependence on reactor dimensions and design. This is generally the primary source of dead thermal mass, and it can be optimized.

The $DTM_{inherent}$ represents the dead thermal mass of salt and refrigerant. These depend primarily on inherent thermophysical properties. However, it is also important to note that, since the quantity of refrigerant may vary with cycle time and other operating conditions, the $DTM_{inherent}$ does have some slight dependence on operating conditions.

For reactor design, the ideal condition is when DTM_{design} equals zero. With a given working pair, working condition, mass of salt, and mass of refrigerant vapor, a better design usually means a lower DTM_{design} and higher performance.

3. Model verification and validation

In this section, we focus on the cooling COP because it is the most widely available in existing literature. The heating COP model is considered verified and validated at the same time because of its connection with cooling COP (as expressed in Eq. (1)).

Most published literature on experimental and modeled performance of sorption systems does not include sufficient information to determine the dead thermal mass of the system in question. A few examples were found. For all of these examples that included sufficient information about dead thermal mass, we performed validation against experimental studies and verification with numerical studies, as described in Sections 3.1 and 3.2.

3.1. Conventional absorption and adsorption cycles

For conventional absorption and adsorption cycles, the COP expression used in this work is identical to those used by the two previous references, as follows.

The COP expression for a conventional absorption heat pump was verified previously by Gluesenkamp (2012) by comparing the analytical model of cooling COP with the result from a numerical model for single effect absorption chiller in Herold et al. (2016). The analytical model COP was 0.735, and the COP from the detailed numerical model was 0.720.

The COP expression for a conventional adsorption heat pump was verified previously by Qian et al. (2013). The cooling COP analytical model was compared with experiment data of 170 test points for a synthetic zeolite-based adsorption system. The difference was within a ± 10% range.

3.2. Resorption cycle with two reactors and two adsorbents

Two sources, both using ammoniate sorption, were used to confirm the analytical model for the resorption cycle with two reactors and two adsorbents. The sensible heat of both reactors was considered.

The analytical model in this work was verified against the numerical model for the resorption cycle using two solid–gas reactors studied by Lepinasse et al. (1994). $MnCl_2$ and $BaCl_2$ were used as HTS and LTS, respectively. Lepinasse et al. (1994) validated their numerical model against experimental results. The input parameters for the model calculation are shown in Table 3.

Lepinasse et al. (1994) used their numerical model to calculate the COP under three different dead thermal mass scenarios: considering DTM of adsorbent only; considering DTM of adsorbent and material; and considering DTM of adsorbent, material, and HTF. The authors did not provide information about the type of HTF used. Therefore, we cannot verify our result against theirs for the case of including DTM of HTF. We used the analytical model from this work to calculate COP assuming DTM of HTF is zero, and the comparison between our result and literature's result is shown in Table 4. The COP calculated by two models had less than ± 0.02 difference. The analytical model in this work showed good agreement with the classical numerical model and required less calculation time.

Secondly, the analytical model in this work was validated by experimental results from two classical experiments of the resorption cycle. One used $MnCl_2$ as HTS and NH_4Cl as LTS (Xu et al., 2011), and the other used the same HTS with NaBr as LTS (Bao et al., 2011). The parameters provided by these studies are listed in Table 5 as calculation input. The result is shown in Table 6. The COP difference between calculation and experiment result is less than 0.04. Therefore, the analytical model demonstrates a good agreement with experimental result.

Table 3
Parameters used in coefficient of performance verification[a].

	Value		Unit
$T_{des,HTS}$	150		°C
$T_{ads,HTS}$	30		°C
$T_{des,LTS}$	5		°C
$T_{ads,LTS}$	30		°C
ΔT_D	120		K
ΔT_L	25		K
Properties of reactors	HTS	LTS	
Mass of salt	2.57	2.125	kg
Mass of expanded graphite	1.385	1.145	kg
Mass of heat exchange material	15	12	kg
Volume of HTF	9	7.8	L
Density of HTF	N/A[b]	N/A[b]	kg L^{-1}
Specific heat of HTF	N/A[b]	N/A[b]	kJ kg^{-1} K^{-1}
Specific heat of salt[b]	0.6	0.44	kJ kg^{-1} K^{-1}
Specific heat of expanded graphite[c]	0.61	0.61	kJ kg^{-1} K^{-1}
Specific heat of liquid refrigerant[c]	4.59	4.59	kJ kg^{-1} K^{-1}
Specific heat of stainless steel[c]	0.46	0.46	kJ kg^{-1} K^{-1}
Maximum loading	0.486	0.710	$kg^{-1}{}_{salt}$
Differential loading	0.432	–	$kg^{-1}{}_{salt}$
Reaction heat[d]	2789	2250	kJ $kg^{-1}{}_{ref}$

Notes: HTS = high temperature salt; LTS = low temperature salt; HTF = heat transfer fluid.

[a] Source: Lepinasse et al. (1994). Modelling and experimental investigation of a new type of thermochemical transformer based on the coupling of two solid–gas reactions. *Chemical Engineering and Processing: Process Intensification*, 33 (3), 125–134.

[b] Values were not provided in the original source.

[c] Specific heat comes from: Bao et al. (2011). Working pairs for resorption refrigerator. *Applied Thermal Engineering*, 31 (14), 3015–3021.

[d] Reaction heat comes from: Li et al. (2014). Progress in the development of solid–gas sorption refrigeration thermodynamic cycle driven by low-grade thermal energy. *Progress in Energy and Combustion Science*, 40, 1–58.

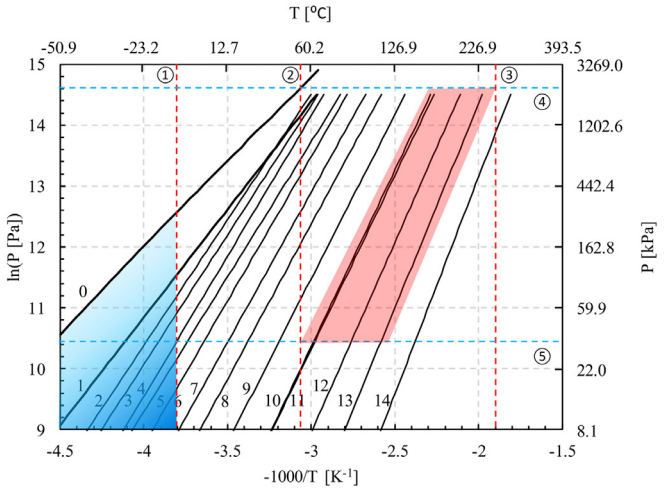

Fig. 3. The Clapeyron diagram of different reaction steps. [Notes: 0-NH_3; 1-NH_4Cl (3/0); 2-$PbCl_2$ (8/3.25); 3-NaBr (5.25/0); 4-$BaCl_2$ (8/0); 5-LiCl (4/3); 6-$PbCl_2$ (3.25/2); 7-$CaCl_2$ (8/4); 8-$CaCl_2$ (4/2); 9-LiCl (3/2); 10-LiCl (2/1); 11-$MnCl_2$ (6/2); 12-LiCl (1/0); 13-$MgCl_2$ (6/2); 14-$NiCl_2$ (6/2). ①—ambient temperature; ②—hot water supply temperature; ③—heat source temperature; ④—assumed highest feasible pressure; ⑤—assumed lowest feasible pressure. Reaction enthalpy and entropy come from Li et al. (2014)].

In this section, the analytical model of cooling COP was verified against numerical model results in the literature and was validated against experimental results in the literature. The maximum cooling COP deviation was less than 0.04. Based on Eq. (1), the heating COP model was also verified and validated, and the relative difference in COP would be lower for heating COP.

4. Using the model to choose the best cycle for an example application

In this section, the verified analytical model is used to evaluate and determine the optimal cycle configuration and working pairs for a sorption heat pump used in a space heating application. In this example application, the assumed design target of the sorption heat pump for space heating is to produce 10 kW of 50 °C hot water at an ambient of −10 °C and with a heat source temperature of 250 °C.

4.1. Selection of working pair

To select optimal working pairs for the sorption heat pump, equilibrium lines of potential ammoniates are illustrated on a Clapeyron diagram in Fig. 3. The operating temperatures and pressures are also shown in Fig. 3. The choices of LTS shown in the blue area on Fig. 3 are constrained by the ambient temperature. However, the operating pressure should also be considered, as in practice high vacuum conditions (i.e., low ammonia vapor pressures) usually lead to a limited mass transfer rate and subsequently low heating power. Therefore, the LTSs operating at higher pressure (lighter blue area) are better options than those that operate at low pressure (darker blue area). The choices of HTS are shown in the red area of Fig. 3. In the case of the HTS selection, the constraints are imposed by the hot water supply and heat source temperatures as well as the working pressure.

For the resorption cycle, comprising two reactors with two adsorbents, the potential LTSs include NH_4Cl, $PbCl_2$, NaBr, and $BaCl_2$, whereas the potential HTSs include LiCl, $MnCl_2$, and $MgCl_2$. In considering sorption cycles with only one adsorbent, the candidates include LiCl, $MnCl_2$, and $MgCl_2$. Based on Eqs. (7), (9), (12), and (15), the maximum cooling COP (assuming DTMR = 0), regardless of system configuration and dead thermal mass factors, has been calculated and is shown in Table 7. The term ψ is the ratio of reaction heats, which also corresponds to the maximum single effect cooling COP. The reaction heat ψ discussed here is defined as the amount of heat rejected or absorbed in the chemical reaction with one unit of ammonia vapor adsorbed by or desorbed from the salt sorbent; it is defined for each system type in Table 1.

With the selected working pairs, the resorption cycles in general demonstrate better maximum COP than sorption cycles demonstrate because the reaction heat of LTS is larger than the

Table 4
Comparison of coefficient of performance (COP) calculation result between analytical and numerical models.

	With dead thermal mass of adsorbent	With dead thermal mass of adsorbent + heat exchange material
$DTMR_{HTR}$	0.31	0.58
$DTMR_{LTR}$	0.09	0.14
$COP_{analytical}$ (this work)	0.56	0.44
$COP_{numerical}$[a]	0.54	0.45

Note: DTMR = dead thermal mass ratio; LTR = low temperature reactor; HTR = high temperature reactor.

[a] Lepinasse et al. (1994). Modelling and experimental investigation of a new type of thermochemical transformer based on the coupling of two solid–gas reactions. *Chemical Engineering and Processing: Process Intensification* 33 (3), 125–134.

Table 5
Parameters used in coefficient of performance validation[a].

		Working pair			
		$MnCl_2/NH_4Cl$		$MnCl_2/NaBr$	
ΔT_D	K	65		120	
ΔT_L	K	30		30	
		HTS	LTS	HTS	LTS
Mass of salt	g	100.09	55.35	55.5	34.59
Mass of expanded graphite	g	50.06	27.51	29.88	18.63
Mass of heat exchange material	g	774.38	582.89	732.42	515.98
Specific heat of salt	kJ kg^{-1} K^{-1}	0.61	1.55	0.6	0.505
Specific heat of expanded graphite	kJ kg^{-1} K^{-1}	0.61	0.61	0.61	0.61
Specific heat of refrigerant	kJ kg^{-1} K^{-1}	4.59	4.59	4.59	4.59
Specific heat of stainless steel	kJ kg^{-1} K^{-1}	0.46	0.46	0.46	0.46
Maximum loading	kg^{-1}_{salt}	0.486	0.812	0.518	0.781
Differential loading	kg^{-1}_{salt}	0.432	–	0.507	–
Reaction heat	kJ kg^{-1}_{ref}	2740	1630	2924	1790

Notes: HTS = high temperature salt; LTS = low temperature salt.
[a] *Source:* Xu et al., (2011). Resorption system with simultaneous heat and cold production. *International Journal of Refrigeration* 34 (5), 1262–1267.

Table 6
Comparison of coefficient of performance (COP) between analytical model and experiment result.

	Working pair	
	$MnCl_2/NH_4Cl$	$MnCl_2/NaBr$
$DTMR_{HTR}$	0.368	0.759
$DTMR_{LTR}$	0.246	0.232
$COP_{analytical}$ (this work)	0.33	0.27
$COP_{experiment}$[a]	0.35	0.31

Notes: DTMR = dead thermal mass ratio; LTR = low temperature reactor; HTR = high temperature reactor.
[a] *Source:* Xu et al., (2011). Resorption system with simultaneous heat and cold production. *International Journal of Refrigeration* 34 (5), 1262–1267.

Table 7
Heating coefficient of performance and sorbent mass for different working pairs.

Resorption		ψ	Sorbent mass [g kJ^{-1}]	
HTS	LTS		HTS	LTS
$MnCl_2$ (6/2)	NH_4Cl (3/0)	1.62	0.66	0.60
LiCl (3/0)	NH_4Cl (3/0)	1.61	0.29	0.60
$MgCl_2$ (6/2)	NH_4Cl (3/0)	1.53	0.43	0.60
$MnCl_2$ (6/2)	$PbCl_2$ (8/3.25)	1.72	0.66	1.71
LiCl (3/0)	$PbCl_2$ (8/3.25)	1.71	0.29	1.71
$MgCl_2$ (6/2)	$PbCl_2$ (8/3.25)	1.62	0.43	1.71
$MnCl_2$ (6/2)	NaBr (5.25/0)	1.75	0.66	0.55
LiCl (3/0)	NaBr (5.25/0)	1.73	0.29	0.55
$MgCl_2$ (6/2)	NaBr (5.25/0)	1.64	0.43	0.55
$MnCl_2$ (6/2)	$BaCl_2$ (8/0)	1.81	0.66	0.68
LiCl (3/0)	$BaCl_2$ (8/0)	1.79	0.29	0.68
$MgCl_2$ (6/2)	$BaCl_2$ (8/0)	1.69	0.43	0.68
Sorption		ψ	**Sorbent mass** [g kJ^{-1}]	
$MnCl_2$ (6/2)		1.43	0.66	
LiCl (3/0)		1.42	0.29	
$MgCl_2$ (6/2)		1.37	0.43	

Notes: HTS = high temperature salt; LTS = low temperature salt.

ammonia latent heat. The working pair of $MnCl_2/BaCl_2$ has the highest ψ (see Table 7); however, the extremely low operating pressure of $BaCl_2$ as the LTS is a major concern because of low power density. In practice, lower power density tends toward a larger (and thus more expensive) system for a given heating capacity. NaBr and $PbCl_2$ as LTS have similar ψ and higher operating pressure, but $PbCl_2$ has much lower energy density (Li et al., 2013) manifested as an elevated sorbent mass per unit of reaction heat in one desorption or sorption mode (g kJ). As shown in Table 7, using $MnCl_2$ or LiCl as the HTS leads to higher COPs compared with using $MgCl_2$ as the HTS. However, again LiCl has higher energy density and lower sorbent mass per unit of reaction heat than that of $MnCl_2$.

The best candidates for the resorption cycle are NaBr (5.25/0) as LTS and LiCl (3/0) as HTS because this working pair has demonstrated a good ψ and a low sorbent mass per unit of refrigerant latent heat. Correspondingly, in the case of the SCE and CCE sorption cycles, LiCl as HTS is considered the best option.

4.2. Selection of system configuration

The aim of this section is to find a suitable system configuration to realize a higher COP more easily. This is determined by both ψ (defined in Section 4.1) and the COP approach factor λ (defined in Eq. (20)).

We defined DTM as the sum of design-related DTM_{design} and fluid-related $DTM_{inherent}$ (see Eq. (21)). In Fig. 5, the effect of DTM_{design} on θ_1, θ_2, and λ for each working pair and configuration is illustrated. Generally systems are easier to build with a higher allowance for DTM_{design}, but the performance is limited; with low DTM_{design} and higher theoretical performance, realizing the design becomes increasingly challenging. We plot the figure applying LiCl/NaBr for RES cycle and LiCl for SCE and CCE cycles to illustrate the main trends. We also plot two of the most commonly used working pairs for RES as reference of how much the DTM_{design} and λ can be in common practice; oil is assumed to be the HTF with density of 890 (kg m^{-3}) and specific heat of 1.8 (kJ kg^{-1} K^{-1}).

To make the DTM_{design} for different applications comparable, we use the ratio of DTM_{design} divided by active mass of refrigerant (ΔYm_{ads}) to represent DTM_{design} level of one application. The active mass of refrigerant means the total mass of refrigerant vapor adsorbed for heating in sorption mode. For simplicity, we assume that DTM_{design} of LTR equals DTM_{design} of HTR for the RES configuration and that DTM_{design} of the salt reactor is twice the DTM_{design} of the C/E for the CCE cycle. These assumptions are deemed reasonable for the authors' current application but might be different for other exchanger designs and heat transfer fluid flow network designs. With the present model the system designer can change the relation between DTM_{design} of HTR, LTR, and C/E according to their own design level and draw a similar figure for comparison.

According to Fig. 4, the SCE and CCE cycles using LiCl salt have the same θ_1, θ_2, and λ when $DTM_{design} = 0$. As the DTM_{design} level increases, the CCE has a lower λ than SCE cycle. The λ difference between the CCE and SCE cycles increases because the CCE cycle

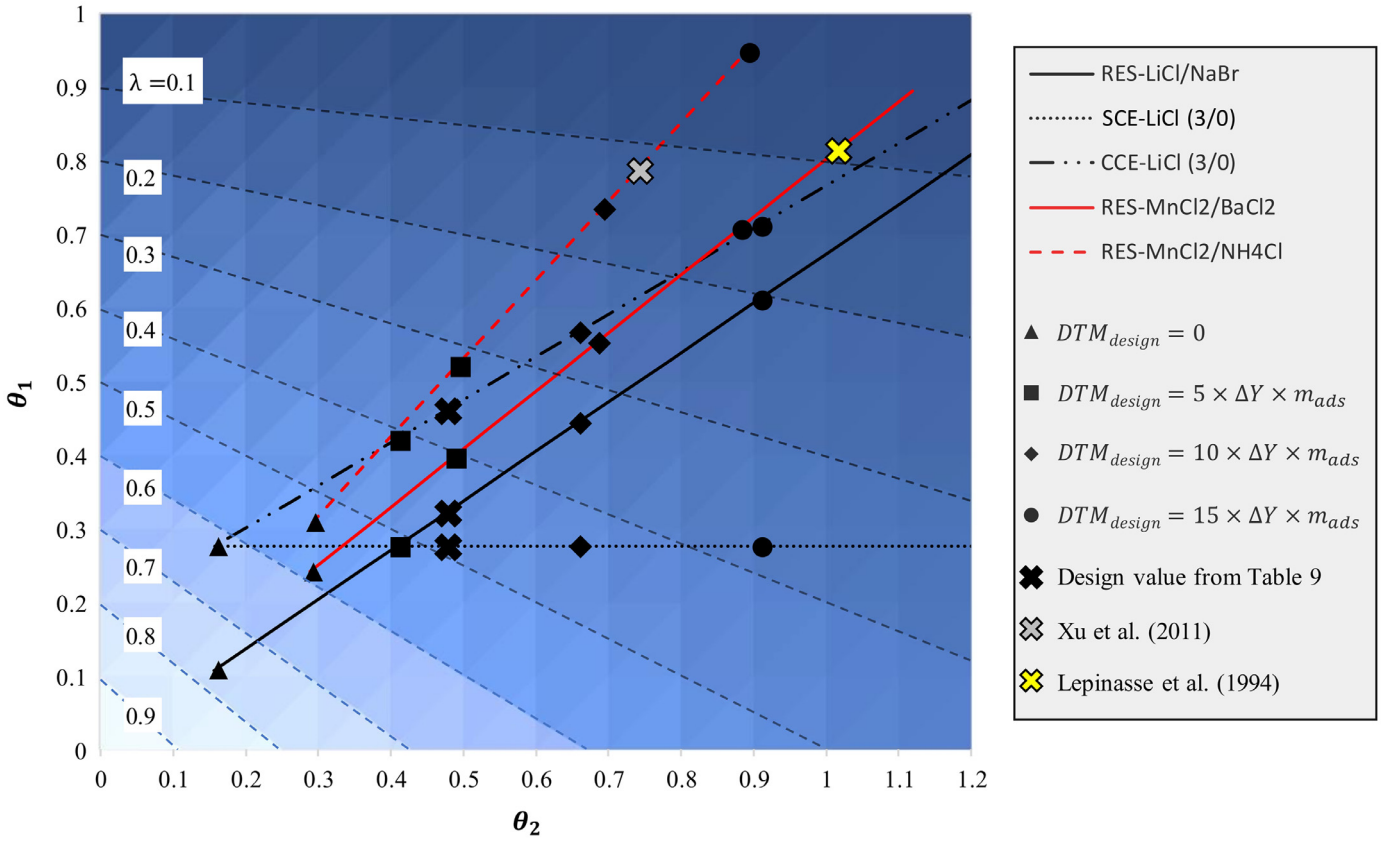

Fig. 4. Effect of dead thermal mass (DTM), θ_1, and θ_2 on λ. The relative dead thermal mass of the low-temperature-coupled component(s) are denoted θ_1; and θ_2 for the high-temperature coupled components. These combine to form the penalty factor λ as defined in Eq. (19).

Table 8
Comparison of different system configurations.

Configuration	Working pair	ψ	θ_1	θ_2	COP_{ht}, $\varepsilon_1=\varepsilon_2=0$	COP_{ht}, $\varepsilon_1=\varepsilon_2=0.5$
SCE	LiCl (3/0)	0.42	0.27	0.48	1.21	1.29
CCE	LiCl (3/0)	0.42	0.44	0.48	1.16	1.27
RES	LiCl/NaBr	0.73	0.32	0.48	1.34	1.50

Notes: COP = coefficient of performance; SCE = separate condenser and evaporator; CCE = combined condenser/evaporator; RES = resorption cycle.

has to consider the DTM_{design} of C/E HTF and materials. Comparing λ of SCE using LiCl and RES using LiCl/NaBr, the λ of the RES cycle is higher than that of the SCE cycle when the DTM_{design} level is low; the λ of the SCE cycle is higher than that of the RES cycle when the DTM_{design} level is high. Given reactor design properties like mass of HTF and mass of material, the DTM_{design} level can be calculated, and the performance of different cycles can be compared easily. For example, the DTM_{design} levels of design calculated according to Table 9 for SCE, CCE, and RES configurations are shown as black "X" mark points in Fig. 4. The SCE cycle has slightly better λ than the RES cycle. However, the difference of λ is small so that the RES cycle using LiCl/NaBr may still have higher COP than the SCE cycle because RES has higher ψ according to the working pair property advantage in Table 7.

Table 8 provides the analytical performance parameters of different configurations. Configurations without heat recovery ($\varepsilon_1=\varepsilon_2=0$) and with 50% heat recovery were considered. Since heat recovery in this work only involves sensible heat recovery, a value of 50% corresponds to equilibration of the temperatures of two relevant heat exchangers before switching phases, and thus represents an upper limit for many systems.

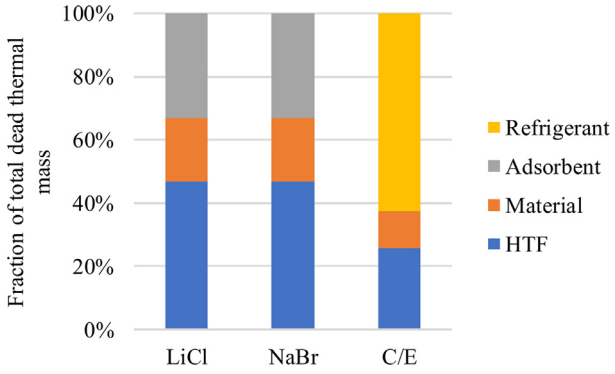

Fig. 5. Contribution of each dead thermal mass factor to DTMR for the LiCl/NaBr RES and CCE cycles (Notes: HTF = heat transfer fluid; C/E = condenser/evaporator; DTMR = dead thermal mass ratio; RES = resorption cycle; CCE = combined condenser evaporator cycle).

The LiCl/NaBr resorption cycle has the highest heating COP of 1.34 without sensible heat recovery. And this number can be improved to 1.50 when 50% sensible heat recovery is applied.

Table 9
Dead mass for LiCl/NaBr reactor and condenser/evaporator (C/E) reactor.

		LiCl	NaBr	C/E
Mass of heat transfer fluid	kg	15.1	15.1	7.9
Mass of salt	kg	20.7	43.8	–
Mass of heat exchange material	kg	60	60	27

This section illustrated the use of the analytical model in the selection of working pairs and configurations, the analysis of each dead thermal mass factor effect on performance, and the influence of working condition on performance. The analytical model is also applied to study the effect of reactor design on performance for each configuration and the effect of sensible heat recovery on performance.

5. Discussion

5.1. Dead thermal mass

In this section, the influence of dead thermal mass ratio DTMR on the performance of the sorption and resorption cycles is discussed for the working pairs selected in Section 4.1. Note that the salt LiCl will go through three reaction steps: 3/2, 2/1, and 1/0. In this work, the dead masses shown in Table 9 are assumed for each component. Based on the experience of the authors in development of the system described in Blackman et al. (2017), these masses are considered reasonable for a system producing 10 kW of 50 °C hot water at an ambient of −10 °C and with a heat source temperature of 250 °C.

The contribution of each component of dead thermal mass to the DTMR of each reactor is calculated based on the geometry of the novel sorption heat pump reactor; the results are shown in Fig. 5. In the resorption cycle with the LiCl reactor and NaBr reactor, the dead thermal mass of the HTF contributes to almost half of the DTMR; in the CCE sorption cycle, DTMR of the C/E is influenced mainly by the retained refrigerant at the end of the condensation process. In the SCE sorption cycle, the DTMR of condenser and evaporator is zero.

5.2. Model response to working temperatures

As ambient temperature changes from the design point temperature, the temperature lift $\Delta T_L (i.e., T_{cond} - T_{evap})$ is influenced more than the temperature difference $\Delta T_D (i.e., T_{des} - T_{abs})$; therefore, the DTMR of a LiCl reactor (HTS) remains almost the same. However, the DTMR of a NaBr reactor (LTS) and C/E are reduced for higher ambient temperature and increased for lower ambient temperature; therefore, the heating COP increases at temperatures higher than design point and decreases at lower temperatures. For simplicity, we assume that differential loading ΔY is constant. In reality, this would require varying cycle time, with complex impacts on cycle power and ΔY. However, such an analysis is beyond the scope of the present study. A wider temperature range is considered here to predict cycle performance under extreme cold and warmer condition. As evaluated using Eq. (20), the heating COP of the RES, CCE, and SCE cycles increases from 1.31 to 1.37, 1.14 to 1.19, and 1.19 to 1.22, respectively, when the ambient temperature rises from −23 °C to 5 °C.

6. Conclusion

In this study, a unified analytical model to calculate heating COP and enable rapid comparison of five different sorption cycles (ABS, ADS, SCE, CCE, and RES) was derived. This conceptual model allows direct comparison of diverse cycle types. The term DTMR was used to describe the effect of dead thermal mass on COP. The COP approach factor λ was defined based on the dead thermal mass for ammoniate sorption with separate condenser/evaporator, combined condenser/evaporator, and resorption cycles to allow direct comparison among these cycle types.

Using available numerical and experimental results in the literature, the analytical model was verified by a classical numerical model and validated by experiment results. The model was used along with a Clapeyron diagram to select a suitable working pair for an ammoniate sorption heat pump for space heating. LiCl/NH_3 was selected for the RES cycle, and LiCl was selected for the SCE and CCE cycles.

The contribution of different dead thermal mass factors to the DTMR was studied based on the working pair selection. For salt reactors, the main contribution comes from HTF; for the C/E, the main contribution comes from retained refrigerant.

The model was also applied to predict the performance change under different working conditions. The heating COP of the RES, CCE, and SCE cycles increases from 1.31 to 1.37, 1.14 to 1.19, and 1.19 to 1.22, respectively, when the ambient temperature rises from −23 °C to 5 °C.

The comparison of different system configurations applying selected working pairs was carried out using the analytical model. The effect of dead thermal mass of HTF and reactor material on λ was studied. The CCE cycle has lower λ than the other two cycles. In a practical range of DTM_{design}, LiCl/NaBr RES cycle and LiCl SCE cycles have very similar λ. Therefore, the LiCl/NaBr RES cycle will have better COP because of the benefit of higher ψ.

Based on a simple analytical model calculation, for space heating applications at ambient temperature −10 °C, heat delivery temperature of 50 °C and up to 250 °C driving heat source temperature, without heat recovery the highest efficiency is obtained with the LiCl/NaBr resorption cycle, with a COP 11–15% higher than that of the competing options. With 50% recovery of sensible heat, LiCl/NaBr still has the highest COP, 16–18% higher than that of the competing options. The LiCl/NaBr RES cycle is shown to be a good option for the sorption cycle in space heating applications.

Acknowledgments

This work was sponsored by the US Department of Energy's Building Technologies Office under Contract No. DE-AC05-00OR22725 with UT-Battelle, LLC. The authors would also like to acknowledge Mr. Antonio Bouza, Technology Manager—HVAC&R, Water Heating, and Appliance, US Department of Energy Building Technologies Office.

The authors also gratefully acknowledge support from the National Natural Science Foundation of China (grant numbers 51306098, 51138005), the innovative Research Groups of National Natural Science Foundation of China (grant number 51521005), and the Independent Research Program from Ministry of Education of China (No. 20151080470).

References

Bao, H.S., Oliveira, R.G., Wang, R.Z., Wang, L.W., Ma, Z.W., 2011. Working pairs for resorption refrigerator. Appl. Therm. Eng. 31 (14), 3015–3021.
Blackman, C., Gluesenkamp, K., Malhotra, M., Yang, Z., 2017. Study of optimal sizing for residential sorption heat pump system. In: Proceedings of the ISHPC. Tokyo, Japan.
Blackman, C., Bales, C., Thorin, E., 2017. Experimental evaluation and concept demonstration of a novel modular gas-driven sorption heat pump. In: Proceedings of the Twelfth IEA Heat Pump Conference. Rotterdam, The Netherlands June 2017 ISBN 978-90-9030412-0.
Cacciola, G., Restuccia, G., 1995. Reversible adsorption heat pump: a thermodynamic model. Int. J. Refrig. 18 (2), 100–106.
Douss, N, Meunier, F, 1988. Effect of operating temperature on the coefficient of performance of active-carbon methanol systems. Heat Recover. Syst. 8 (5), 383–392.

Freni, A., Dawoud, B., Bonaccorsi, L., Chmielewski, S., Frazzica, A., Calabrese, L., Restuccia, G., 2015. Characterization of zeolite-based coatings for adsorption heat pumps. SpringerBriefs in Applied Sciences and Technology, 2015. Springer ISBN 9783319093260.

Goetz, V., Spinner, B., Lepinasse, E., 1997. A solid–gas thermochemical cooling system using $BaCl_2$ and $NiCl_2$. Energy 22 (1), 49–58.

Gluesenkamp, K., 2012. Development and analysis of micro polygeneration systems and adsorption chillers. Department of Mechanical Engineering, University of Maryland, College Park, MD, USA Doctoral dissertation.

Herold, K., Radermacher, R., Klein, S., 2016. Absorption Chillers and Heat Pumps. CRC Press, Boca Raton.

Herold, K., 1999. Performance predictions of absorption cycles using an Endo-Reversible model. In: Proceedings of the International Sorption Heat Pump Conference. Munich, Germany.

Lepinasse, E., Goetz, V., Crosat, G., 1994. Modelling and experimental investigation of a new type of thermochemical transformer based on the coupling of two solid–gas reactions. *Chem. Eng. Process. Process Intensif.* 33 (3), 125–134.

Li, T., Wang, R., Kiplagat, J.K., 2013. A target-oriented solid–gas thermochemical sorption heat transformer for integrated energy storage and energy upgrade. AIChE J. 59 (4), 1334–1347.

Li, T.X., Wang, R.Z., Li, H., 2014. Progress in the development of solid–gas sorption refrigeration thermodynamic cycle driven by low-grade thermal energy. Prog. Energy Combust. Sci. 40, 1–58.

Meunier, F., Neveu, P., Castaing, J., 1998. Equivalent Carnot cycles for sorption refrigeration. Int. J. Refrig. 21 (6), 472–489.

Neveu, P., Castaing, J., 1993. Solid–gas chemical heat pumps: field of application and performance of the internal heat of reaction recovery process. Heat Recover. Syst. CHP 13 (3), 233–251.

Neveu, P., Castaing, J., 1996. Analyse thermodynamique des transformateurs thermochimique solide/gaz. In: Proceedings of the International Sorption Heat Pump Conference. Montreal, Canada.

Pesaran, A., Lee, H., Hwang, Y., Radermacher, R., Chun, H.H., 2016. Review article: numerical simulation of adsorption heat pumps. Energy 100, 310–320.

Pons, M., Poyelle, F., 1999. Adsorptive machines with advanced cycles for heat pumping or cooling applications. Int. J. Refrig. 22, 27–37.

Qian, S., Gluesenkamp, K., Hwang, Y., Radermacher, R., Chun, H.H., 2013. Cyclic steady state performance of adsorption chiller with low regeneration temperature zeolite. Energy 60, 517–526.

Sharma, V.K., Kumar, E.A., 2017. Thermodynamic analysis of novel multi stage multi effect metal hydride based thermodynamic system for simultaneous cooling heat pumping and heat transformation. Int. J. Hydrog. Energy 42, 437–447.

Sharma, V.K., Kumar, E.A., 2018. Thermodynamic simulation of hydrogen based solid sorption heat transformer. Int. J. Therm. Sci. 125, 74–80.

Wang, R., Wang, L., Wu, J., 2014. Adsorption Refrigeration Technology: Theory and Application. John Wiley & Sons, Inc.

Wongsuwan, W., Kumar, S., Neveu, P., Meunier, F., 2001. A review of chemical heat pump technology and applications. Appl. Therm. Eng. 21 (15), 1489–1519.

Xie, X., Jiang, Y., 2015. An ideal model of absorption heat pump with ideal solution circulation. J. Refrig. 36 (1), 1–12.

Xu, J., Oliveira, R.G., Wang, R.Z., 2011. Resorption system with simultaneous heat and cold production. Int. J. Refrig. 34 (5), 1262–1267.

Zebbar, D., Kherris, S., Zebbar, S., Mostefa, K., 2012. Thermodynamic optimization of an absorption heat transformer. Int. J. Refrig. 35 (5), 1393–1401.

Zhu, C., Xie, X., Jiang, Y., 2016. A multi-section vertical absorption heat exchanger for district heating systems. Int. J. Refrig. 71, 69–84.

Applied Thermal Engineering 150 (2019) 421–432

Contents lists available at ScienceDirect

Applied Thermal Engineering

journal homepage: www.elsevier.com/locate/apthermeng

Research Paper

Study of optimal sizing for residential sorption heat pump system☆

Corey Blackman[a,b,c], Kyle R. Gluesenkamp[d,*], Mini Malhotra[d], Zhiyao Yang[d,e]

[a] SaltX Technology, Hägersten, Stockholm, Sweden
[b] Dalarna University, Borlänge, Sweden
[c] Mälardalen University, Västerås, Sweden
[d] Oak Ridge National Laboratory, Oak Ridge, TN, USA
[e] Purdue University, West Lafayette, IN, USA

HIGHLIGHTS

- The optimum design heating capacity of the sorption heat pump ranges between 22 and 44% of peak capacity.
- Two climates, two energy price scenarios, and two sorption system types were evaluated.
- A detailed building model was used to calculate hourly building loads.

ARTICLE INFO

Keywords:
Sorption heat pump
Sizing
Residential
Bivalent

ABSTRACT

Gas-driven sorption heat pumps (GDSHP) show significant potential to reduce primary energy use, associated emissions and energy costs for space heating and domestic hot water production in residential applications. This study considered a bivalent heating system consisting of a sorption heat pump and a condensing boiler, and focuses on the optimal heating capacity of each of these components relative to each other. Two bivalent systems were considered: one based on a solid chemisorption cycle (GDSHPA), and one based on a resorption cycle (GDSHPB). Simulations of year-round space heating loads for two single-family houses, one in New York and the other Minnesota, were carried out and the seasonal gas coefficient of performance (SGCOP) calculated. The sorption heat pump's design heating capacity as a fraction of the bivalent system's total heating capacity was varied from 0 to 100%. Results show that SGCOP was effectively constant for sorption heat pump design capacity greater than 41% of the peak bivalent GDSHPA design capacity in Minnesota, and 32% for GDSHPB. In New York, these values were 42% and 34% for GDSHPA and GDSHPB respectively. The payback period was also evaluated based on postulated sorption heat pump component costs. The fastest payback was achieved with sorption heat pump design capacity between 22 and 44%.

1. Introduction

Sorption heat pumps may use the combustion of natural gas as a heat source to drive a sorption cycle. This cycle effectively pumps heat from a low temperature source to a sink of a higher temperature allowing for more effective gas utilisation for space and domestic water heating. Cycle heating efficiencies as high as 140% (i.e. COP 1.4) for gas-driven sorption heat pumps (GDSHP) are not uncommon [1].

A bivalent heat pump system consists of a heat pump unit and a supplemental heating source. This study considers a GDSHP integrated with a supplementary condensing boiler. Since, in general, the peak building demand conditions occur for relatively few hours of the year, the more costly sorption module should be dimensioned to avoid inefficient operation at low part loads, whilst cost effectively maximising the seasonal efficiency defined by the seasonal gas coefficient of performance (SGCOP). Additionally, this approach opens the possibility of

☆ This manuscript has been authored by UT-Battelle, LLC under Contract No. DE-AC05-00OR22725 with the U.S. Department of Energy. The United States Government retains and the publisher, by accepting the article for publication, acknowledges that the United States Government retains a non-exclusive, paid-up, irrevocable, world-wide license to publish or reproduce the published form of this manuscript, or allow others to do so, for United States Government purposes. The Department of Energy will provide public access to these results of federally sponsored research in accordance with the DOE Public Access Plan (http://energy.gov/downloads/doe-public-access-plan).

* Corresponding author.
E-mail address: gluesenkampk@ornl.gov (K.R. Gluesenkamp).

https://doi.org/10.1016/j.applthermaleng.2018.12.151
Received 17 August 2018; Received in revised form 28 December 2018; Accepted 29 December 2018
Available online 04 January 2019
1359-4311/

Nomenclature

ACH	air changes per hour ventilation rate
AHU	air handling unit
CE	combined condenser-evaporator vessel
f	function
f_2	function
GCOP	gas coefficient of performance
GDSHP	gas driven sorption heat pump with boiler and sorption module
GDSHPA	gas driven sorption heat pump with boiler and type "A" chemisorption module
GDSHPB	gas driven sorption heat pump with boiler and type "B" resorption module
HTS	high temperature salt
LTS	low temperature salt
Q	heating capacity of GDSHP system
R	reactor vessel containing low temperature salt (in chemisorption type sorption module)
RA	reactor vessel A containing high temperature salt (in resorption type sorption module)
RB	reactor vessel B containing low temperature salt (in resorption type sorption module)
SCOP	seasonal coefficient of performance
SGCOP	seasonal gas coefficient of performance
SM	sorption module
SMA	sorption module Type A (chemisorption-based)
SMB	sorption module Type B (resorption-based)
T_{out}	outdoor ambient temperature
T_{supply}	temperature heat transfer fluid supplied to air handling unit
ΔT_{lift}	temperature lift of sorption module (supply temperature minus outdoor temperature)
η	thermal efficiency (energy out as fraction of energy into a component)

cost-effective GDSHPs tailor-sized for specific climates.

Based on the working principle, heat pumps can be categorized as vapor-compression (including electric-driven and gas-driven) or vapor-absorption heat pumps [2]. The majority of heat pumps deployed today, and the majority covered in the literature, are of the vapor-compression type. The most common bivalent heat pump system for residential and small commercial applications is the air-to-air vapor compression heat pump with electric resistance as the supplemental heat source, using electricity from the grid. However, other configurations have been investigated. These include various heat pump heat sources (ground-source, solar thermal, and combinations), supplemental heating type (gas-fired condensing boiler, solar thermal), and electricity source (solar PV, fuel cell) [3–5]. A large number of studies are available on vapor compression heat pumps; while vapor-absorption heat pumps, having a low environmental impact, have gained considerable attention in recent years [6].

For lower installed costs, heat pump systems are configured with the heat pump unit (higher cost and higher efficiency) sized for less than peak building loads and the supplemental heating source (typically, lower cost and lower efficiency) sized to meet the peak heating demand. It is widely known that, when sized carefully and strategically operated and controlled, the use of supplemental heating source can also improve annual efficiency and lower annual operating cost. This is because heat pump efficiency can suffer at very low part loads, and using a supplemental heating source avoids over-sizing of the heat pump component [7,8].

Various studies have investigated the sizing and operation strategies for heat pump systems. In these studies, the key sizing and/or operating parameters investigated include: (a) the *capacity of heat pump* with respect to the building load, expressed in relation to the *bivalent temperature* — the ambient temperature at which the heat pump output matches the building load [7–10]; (b) the bivalent operation mode: either *bivalent-parallel* when the heat pump continues to operate in parallel with the auxiliary heat source or *bivalent-alternative* when only the auxiliary heat source would operate at temperatures below the bivalent temperature [10]; (c) the *cut off temperature*—the ambient temperature below which the heat pump unit is switched off, thus only running the auxiliary heat source [10]; (d) heat pump control—on-off versus modulating control [8–11]; (e) sizing of thermal storage [7,11].

Several studies analyzed different heat pump types in different climates with different sets of operating parameters. Most importantly, the system performance is most sensitive to the sizing of the heat pump (thus, the bivalent temperature). Additionally, improved system performance results from bivalent-parallel operation over bivalent-alternative operation [11], and from modulating control over on-off control [8–10]. For larger sized heat pump systems (that is, low bivalent temperatures), the performance improvement from a lower cut-off temperature relative to bivalent temperature is negligible [11]. Similarly, the performance change from varying the size of thermal storage in case of systems with water as the heat sink was marginal to none [7]. The analysis in this study assumes bivalent parallel operation, no cycling losses associated with the on-off operation, and no thermal storage (such as a condensing boiler tank).

In most studies that have evaluated the sizing or operation strategy of a specific heat pump system, the evaluation criteria typically include the annual or seasonal system efficiency, and/or the operating cost (especially for systems using two different fuels). Only a few studies have factored in the installed cost of the system in terms of total cost of ownership [12] and levelized cost of energy [13]. Installed costs of the system are accounted for in studies which compared different types of heat pump systems, for example, Busato et al. [14] compared net present worth and payback period for an electric heat pump, a natural gas engine-driven heat pump, and a natural gas boiler, and Aste et al. [15] compared net present costs for air-to-air heat pumps, air-to-water heat pumps, ground-source heat pumps, and ground-water heat pumps.

In the present study, due to the modular nature of the sorption component, which is the costlier component in the system, the sizing of the sorption heat pump system (i.e., the sorption modules vs auxiliary heat source—the condensing boiler) requires the optimization criteria to also account for the capital cost. Therefore, this paper seeks to fill a gap by exploring the optimal sizing of sorption heat pump and backup heating systems, since literature review yielded few studies on residential-scale sorption heat pump systems and no sizing studies for sorption heat pumps. This work aims to develop a sizing strategy for bivalent sorption heat pumps considering the similarities to the sizing of bivalent electric heat pumps.

The present study considers a parallel bivalent system, in which both the heat pump and boiler components are capable of simultaneously providing heat at temperatures between the heat pump cut-off temperature and the bivalent temperature. Furthermore, two modular sorption unit types are considered with two different sorption cycle principles. One sorption module (SM) based on the solid chemisorption cycle principle (type A) and the other a resorption cycle (type B), both employing ammonia as the working fluid. For this study, simplified performance correlations for each SM type were used to determine the optimum capacity of the SM implemented in a bivalent GDSHP. Optimum capacity was determined based on both cost and performance indicators. Two climate zones in the USA were studied, representative of a cold (Minnesota) and a moderate (New York) climate.

2. Sorption modules

This study considers a sorption module, defined as a fully modular sorption heat pump device. The sorption module can operate based on an absorption or adsorption cycle principle as described by Blackman et al. [16]. It is modular because it can be combined with a backup boiler, and the sorption heat pump sizing is continuously variable: by virtue of its design, it can be sized and/or coupled together with another sorption module without the need for significant re-design. This allows it to be readily designed for any capacity. These modules can be employed for heating and/or cooling purposes and operate at ambient temperatures below 0 °C due to the use of ammonia as a refrigerant [17,18].

2.1. Basic sorption module component (Type A)

The sorption component referred to in this work as "Type A" is a sorption heat pump module component comprising two cylindrical vessels, the reactor (R) and the combined condenser-evaporator (CE). The vessels each house a heat exchanger made up of disc-shaped steel plates engineered in such a way as to allow a heat transfer fluid to flow within the discs. The heat exchanger of the reactor provides thermal energy to, or removes thermal energy from, a matrix material infused with a salt (alkali halide) which reversibly absorbs ammonia. The matrix is housed, in good thermal contact, between the heat exchanger discs (see Fig. 1). The CE is identical to the R except that the matrix material between the heat exchanger discs does not contain salt. The R and CE vessels have an opening at the top to allow ammonia to flow back and forth via a connecting pipe.

The Type A sorption module (SMA) operates in a batch process with two main modes of operation; absorption and desorption [19]. In absorption mode, the difference in vapor pressure between the salt and the ammonia causes ammonia to evaporate from the CE (operating as an evaporator) and form a salt ammoniate in the reactor. The reaction between salt and ammonia creates heat which is removed via a flow of heat transfer fluid in the heat exchanger discs. This heat can then be transferred to the building's heat distribution system. Upon completion of absorption (when all the ammonia has reacted with the salt), the SM switches to desorption mode. The desorption mode is characterised by the heating of the reactor via high temperature heat transfer fluid heated by a natural gas burner. The heating of the reactor forces the desorption of ammonia from the salt in the reactor matrix. This desorbed ammonia condenses in the CE where the condensation heat produced in the CE is removed via the heat transfer fluid flowing in the CE's heat exchanger and this heat is also transferred to the heat distribution system. The SMA is characterised by high temperature lift and high heating capacity with a moderate coefficient of performance (COP) [17].

2.2. Resorption module component (Type B)

The resorption module component (referred to in this work as Type B) operates under the resorption principle where two different salts (alkali halides) are employed, each having a different chemical affinity for ammonia. The salt with the higher affinity is known as the high temperature salt (HTS), and the salt with lower affinity for ammonia is referred to as the low temperature salt (LTS) [20]. In desorption mode, the fluid from the high temperature heat transfer fluid source (from the natural gas burner) drives the flow of ammonia from the HTS which is housed in the primary reactor (R1) to the LTS housed in the secondary reactor (R2). In absorption mode, the refrigerant flows from the LTS to the HTS, while the LTS absorbs low temperature (below ambient temperature) thermal energy and expels the ammonia. The ammonia reacts with the HTS, generating heat that is removed with the heat transfer fluid and transferred to the building's heat distribution system [21]. SMB is characterised by moderate temperature lift and low heating capacity with high COP [17].

2.3. Sorption heat pump module

To adequately perform as a heat pump unit, the sorption module components should be outfitted with hydronic connections, a natural gas burner, pumps, and valves. In addition, an outdoor fan coil is used to capture low temperature ambient heat during the absorption mode of operation. Fig. 2 shows the sorption module system concept for operation as a heat pump [17].

3. Gas-driven sorption heat pump

This work evaluates bivalent GDSHPs comprised of a sorption heat pump module (SM) and a condensing boiler as described in [17]. Two variants of SM are considered to investigate their performance and optimal sizing under different climatic conditions. The bivalent GDSHP operates using the bivalent parallel operation strategy presented in

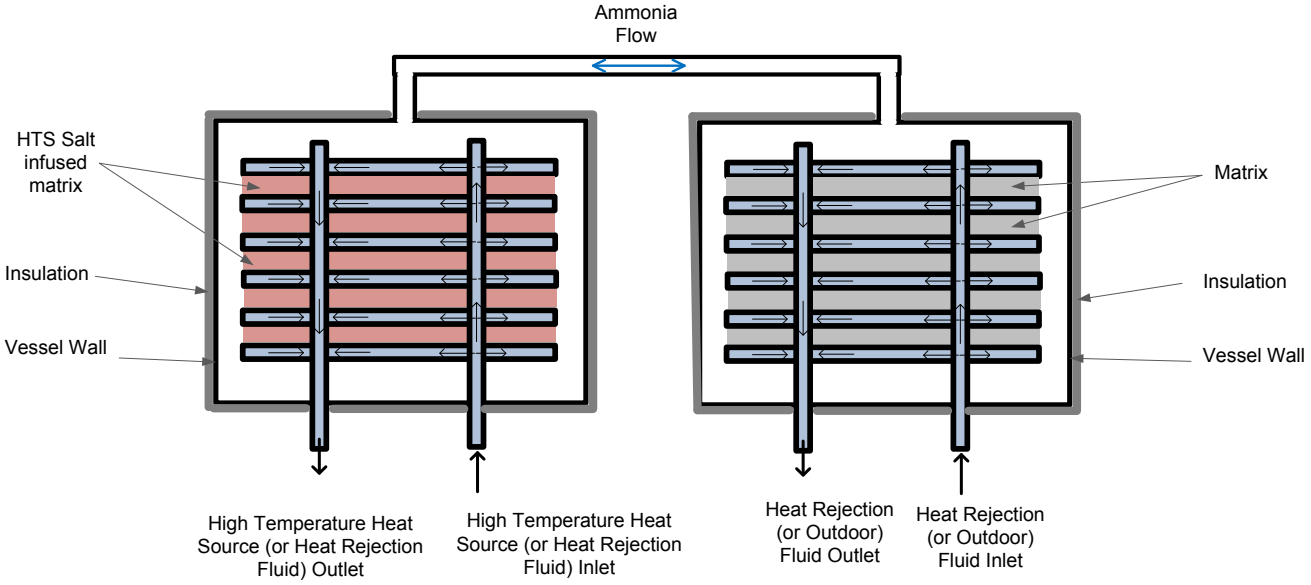

Fig. 1. Schematic diagram of main components of basic sorption module Type A (SMA).

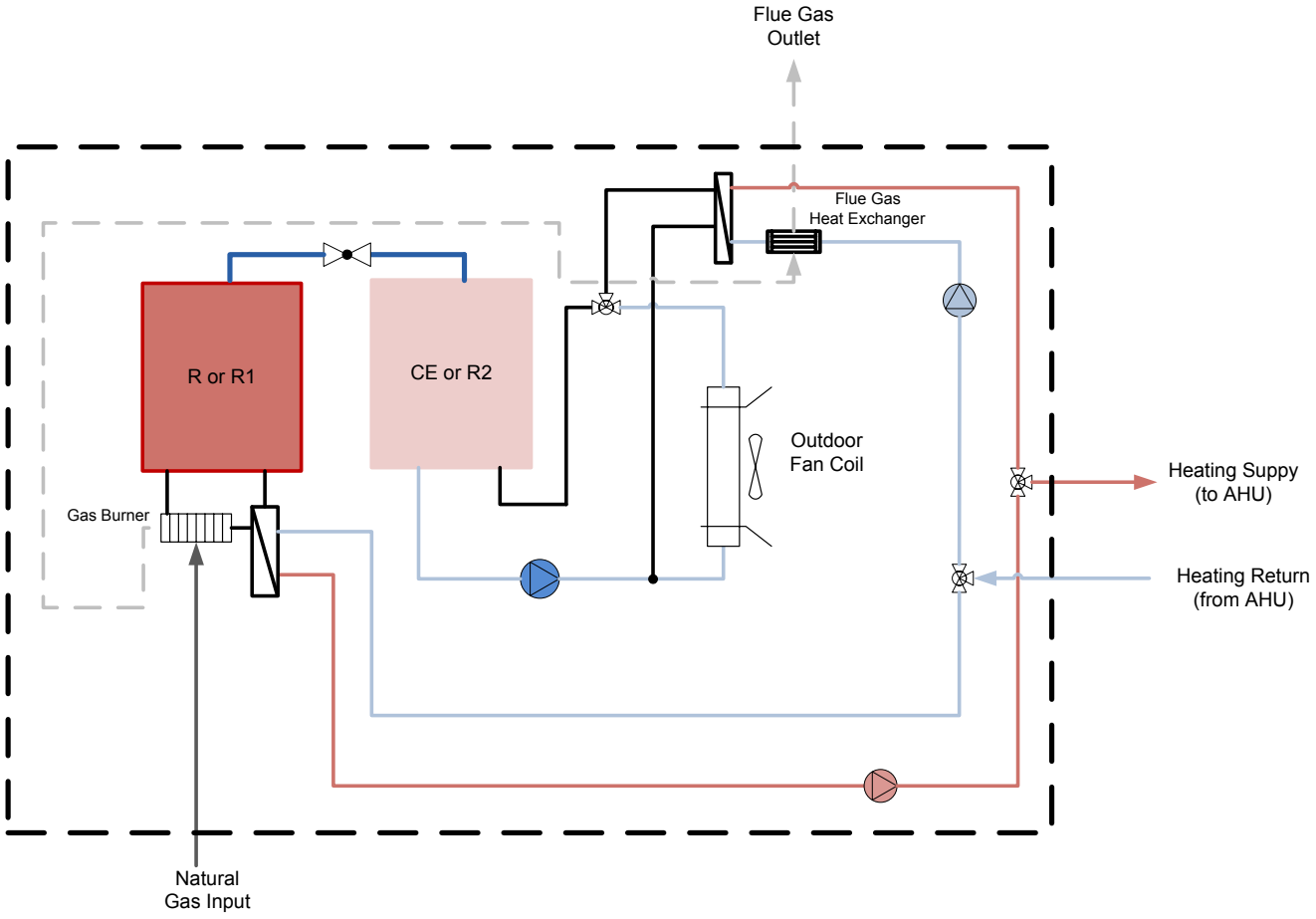

Fig. 2. Schematic drawing of sorption module with complementary components for heat pump operation.

[11]: the SMs provide 100% of the building load when ambient temperatures are at or above the bivalent temperature. At temperatures below the bivalent temperature both the SM and the condensing boiler operate simultaneously to meet the required heating demand. At even lower ambient temperatures, below the cut-off operation temperature for the SM, the SM operates in a non-heat pumping mode in which it operates with condensing boiler efficiency. The bivalent GDSHP unit was considered to be connected to a hydronic air handling unit (AHU) (see Fig. 3).

A Type A gas-driven sorption heat pump (GDSHPA) consists of the SMA coupled with an auxiliary condensing boiler. Similarly, the Type B gas-driven sorption heat pump (GDSHPB) consists of the SMB coupled with an auxiliary condensing boiler.

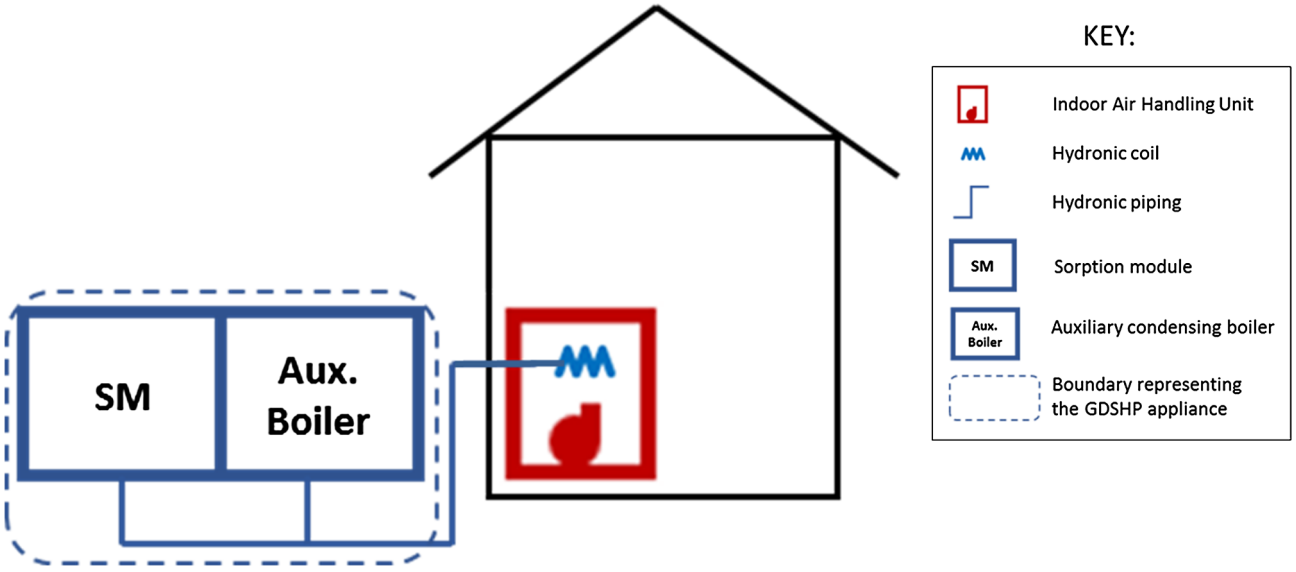

Fig. 3. Schematic of bivalent gas-driven sorption heat pump concept in a house with centrally ducted heating.

3.1. Auxiliary condensing boiler

The GDSHPA and GDSHPB systems include an auxiliary condensing boiler that complements the SM when the SM alone cannot meet the required heating demand. Well-dimensioned natural gas-fired condensing boilers typically have efficiencies between 90% and 96% [22–24]. For the purposes of this study, a generic condensing boiler with a constant efficiency (η_{boiler}) of 92% was assumed for both GDSHPA and GDSHPB.

4. Methodology

To investigate the impact of the SM capacity sizing for different SM types in different climatic conditions, space heating load simulations for two single-family houses were carried out. These hourly building space heating load data were generated via simulations with a 2006 International Energy Conservation Code (IECC) [25] compliant EnergyPlus residential prototype model for New York and Minnesota. The prototype building models were representative of typical construction in these regions. The SM size was defined by the normalised parameter "Design capacity ratio of SM". Where:

$$Design\ \ capacity\ \ ratio\ \ of\ \ SM = \frac{design\ \ heating\ \ capacity\ \ of\ \ SM}{peak\ \ heating\ \ capacity\ \ of\ \ system} \quad (1)$$

From the simulated space heating demand of the building, the hourly outdoor temperatures and the required heating supply temperatures were determined.

The specific heating capacity of each SM type at different outdoor temperatures was employed in the sizing of the SM, while the required auxiliary condensing boiler capacity and thus overall system size, were calculated. The seasonal gas coefficient of performance (SGCOP) for each GDSHP system type was also calculated.

Evaluations were done for GDSHPA and GDSHPB for 4 scenarios: 1 – low fuel prices and cold climate, 2 – low fuel prices and moderate climate, 3 – high fuel prices and cold climate, 4 – high fuel prices and moderate climate.

To investigate the applicability of each bivalent GDSHP system variant, the systems were evaluated using two metrics: SGCOP and simple payback period for varying sizes of the sorption module (SM). The analysis was conducted for a given design capacity ratio of each SM type. From this design capacity ratio, SGCOP, operating costs and total system costs, were calculated. For the operating cost, the fraction of heating provided by the SM and the load covered by the auxiliary condensing boiler were calculated for each hour. The system cost was calculated based on the design capacity of the SM and the capacity of the auxiliary condensing boiler. This calculation process was repeated for various SM sizes.

4.1. Simulation of building and climate

In order to account for the influence of different climates on the energy performance of the system, two climate locations are considered:

- New York City, NY (40.7°N, 73.8°W), representative of mixed-humid climate characterized by $CDD_{10°C} \leq 2500$ and $HDD_{18°C} \leq 3000$, and
- Minneapolis, MN (44.9°N, 93.2°W), representative of a cold-humid climate characterized by $4000 < HDD_{18°C} \leq 5000$; according to ASHRAE Standard 169-2006 [26].

Table 1 shows the climate characteristics of these locations including the heating design conditions. The outdoor air temperature bin trends for these locations are plotted in Fig. 4 based on the Typical Meteorological Year, version 3 (TMY3) weather data [27].

To model residential space heating loads for a typical existing house in these locations, the 2006 IECC version of the publicly available residential prototype building models developed by Pacific Northwest National Laboratory (PNNL) were used for the analysis. These models are used extensively for developing and evaluating residential energy codes in the US and are available for all climate zones in all states in the US, different foundation types and heating systems, and successive versions of IECC [28]. The model represents a two-story, 223 m^2 (2400 ft^2) single-family detached house with a vented attic and a crawlspace. The house has wood-frame construction with insulation properties as required by 2006 IECC for the respective climate zones. Table 2 lists the general characteristics and climate-specific requirements of the building. The space heating loads were modelled in EnergyPlus 8.4.0 using TMY3 climatic data for New York City and Minneapolis, Minnesota (see Fig. 5). Table 3 shows the building peak and annual space heating loads.

Table 1
Climate characteristics of locations used in heat load simulations.

	New York City, NY	Minneapolis, Minnesota
ASHRAE climate zone	4A (Mixed-Humid)	6A (Cold-Humid)
TMY3 degree-days	1984 $CDD_{10°C}$ 2627 $HDD_{18°C}$	1532 $CDD_{10°C}$ 4202 $HDD_{18°C}$
99.6% heating dry-bulb temperature	−10.7 °C	−25.2 °C
Cities with similar climate zone	Paris, France Seoul, South Korea	Oslo, Norway Moscow, Russia

For each hour with space heating load, the required heating fluid supply temperature (T_{supply}) to the AHU is calculated according to an outdoor temperature reset schedule. Where:

$$T_{supply} = linear\ \ interpoloation \begin{vmatrix} 57.2°C@ - 23.3°C T_{out} \\ 37.8°C@ + 15.6°C T_{out} \end{vmatrix} \quad (2)$$

4.2. Sorption module performance

In this work, we adopt experimental measurements of SMs performance as carried out in [17]. Experimental evaluations as described in [17] were conducted for two sorption module prototypes; Type A and Type B, where one cycle constituted a desorption phase immediately followed by an absorption phase. Each sorption module prototype was connected to two hydronic circuits, heated by steam generated from an electric heater. Several test sequences were carried out comprising at least 40 cycles for each sorption module prototype [17]. The average heating capacity and COP of the sorption modules were measured at various temperature lifts. Temperature lift was defined as the temperature difference between the heat delivery temperature and heat transfer fluid leaving the CE or RB during absorption mode [17].

It was observed that for both SM prototypes type A and type B, the average heating capacity was inversely proportional to the temperature lift. Given that the sorption modules are designed to be totally modular, the number of heat exchanger discs, that is, the heat transfer area of the heat exchangers, determines the heating capacity of the module [17]. Thus, SM heating capacity is given in units of power per square metre of heat transfer area (i.e. as a heat flux). The sorption module capacity was linear with respect to temperature lift (Eq. (3a) for SMA; Eq. (3b) SMB), and the SM COP was second-order with respect to temperature lift (Eq. (4a) for SMA; Eq. (4b) for SMB).

$$Q_A = -46.95 \times \Delta T_{lift} + 5629.7 [W/m^2] \quad (3a)$$

$$Q_B = -38.29 \times \Delta T_{lift} + 3018.9 [W/m^2] \quad (3b)$$

$$COP_A = -0.0001(\Delta T_{lift})^2 + 0.0088(\Delta T_{lift}) + 1.1596 \quad (4a)$$

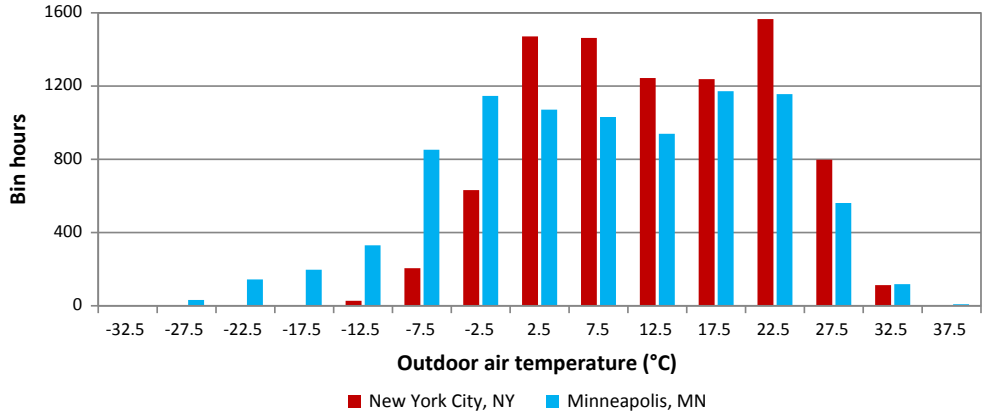

Fig. 4. Outdoor air temperature bins for New York City, NY and Minneapolis, MN.

Table 2
Summary of the general and climate-specific characteristics of the building.

General building characteristics		
Building type	Single-family detached house	
Construction	Wood-frame construction, vented attic, crawlspace foundation	
Conditioned floor area	223 m^2	
Conditioned volume	476 m^3	
Gross wall area	221.2 m^2	
Window-to-wall ratio	15%	
Internal heat loads	Lighting: 2.57 W/m^2, Plug loads: 6.53 W/m^2, Occupants: 3	
Thermostat set points	Heating: 22.2 °C, Cooling: 23.9 °C	
Climate-specific thermal properties of building	New York City, NY	Minneapolis, MN
Wall U-factor	0.495 $W\,m^{-2}\,K^{-1}$	0.356 $W\,m^{-2}\,K^{-1}$
Ceiling U-factor	0.186 $W\,m^{-2}\,K^{-1}$	0.186 $W\,m^{-2}\,K^{-1}$
Floor U-factor	0.277 $W\,m^{-2}\,K^{-1}$	0.180 $W\,m^{-2}\,K^{-1}$
Window U-factor	2.273 $W\,m^{-2}\,K^{-1}$	1.988 $W\,m^{-2}\,K^{-1}$
Window SHGC	0.394	0.394
Infiltration rate	0.721 ACH	0.162 ACH

$$COP_B = -0.0004(\Delta T_{lift})^2 + 0.0268(\Delta T_{lift}) + 0.9817 \quad (4b)$$

In [17], the experimental evaluations of the SMs were carried out with fixed cycle times of 75 min which allowed for full desorption and absorption under all conditions tested. Additionally, since Eqs. (3a) and (3b) only account for the temperature lift across the SMs, for the total temperature lift of the GDSHP appliance (including the various heat exchangers), in this work an additional 15 °C 'penalty' is applied.

Table 3
Energy simulation results.

	New York City, NY	Minneapolis, MN
Peak space heating load	13.4 kW	10.3 kW
Annual space heating load	20,898 kWh	16,435 kWh

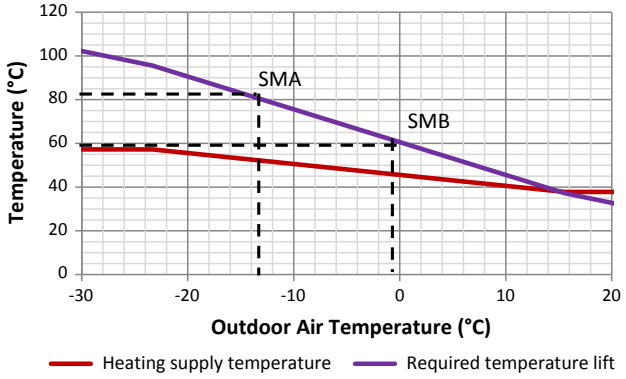

Fig. 6. Supply temperature and required temperature lift across the sorption module at varying outdoor air temperature.

Therefore, for the GDSHPA and GDSHPB systems:

$$\Delta T_{lift,required} = (T_{supply} - T_{out}) + 15\hat{A}°C \quad (3)$$

Fig. 6 shows the supply temperature and the required temperature lift ($\Delta T_{lift,required}$) corresponding to the outdoor air temperature. As

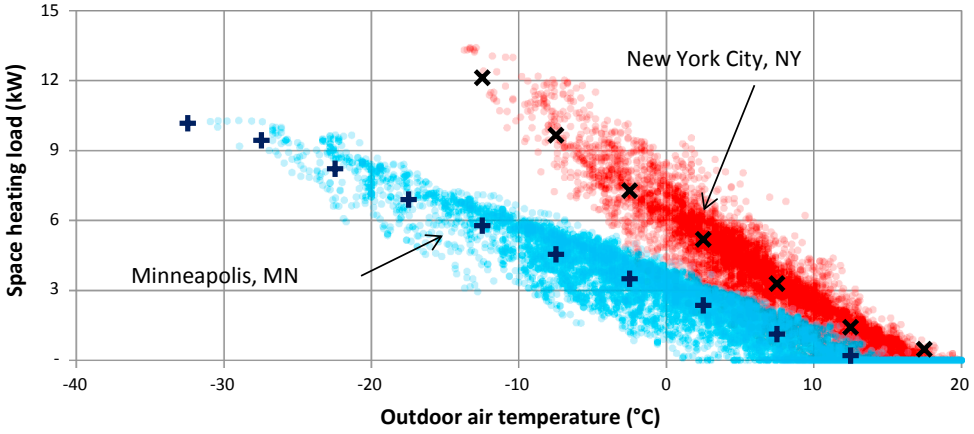

Fig. 5. Hourly and bin-average space heating loads for Minneapolis, MN and New York City, NY.

Table 4
Maximum temperature and sorption module cut-off temperature.

	Maximum temperature lift	Sorption module cut-off temperature
SMA	80 °C	−13 °C
SMB	60 °C	0.4 °C

Table 5
Energy prices used the two energy price scenarios; low energy price case and high energy price case.

	Low energy price scenario	High energy price scenario
Natural gas	0.034 USD/kWh$_{thermal}$ (10 USD/MMBtu)	0.068 USD/kWh$_{thermal}$ (20 USD/MMBtu)
Electricity	0.12 USD/kWh	0.22 USD/kWh

reported in [17] the maximum temperature lift of the prototype A and prototype B were 80 °C and 60 °C respectively. Considering the required temperature lift, Table 4 summarises the cut-off temperatures of the SMs, that is, the temperature below which the SMs run in non-heat-pumping mode.

Based on calculations of the required temperature lift for each hour, the heat flux (in kW/m^2) of SM is calculated as:

$$\phi = \frac{Q}{A_{measured}} = \frac{f_1(\Delta T_{lift,required})}{A_{measured}} \quad (4)$$

Then, the capacity of the SM and the fraction of space heating load provided by the SM of given area A [m^2] is calculated as

$$Capacity_{SM}(kW) = \frac{\phi \times A}{1000} \quad (5)$$

$$f\dot{Q}_{SM} = \max\left(\frac{Capacity_{SM}}{\dot{Q}}, 1\right) \quad (6)$$

The fraction of space heating load to be provided by the auxiliary condensing boiler is given by:

$$f\dot{Q}_{boiler} = (1 - f\dot{Q}_{SM}) \quad (7)$$

Thus, the space heating loads met by the SM and the boiler will be given by Eqs. (8) and (9) respectively:

$$\dot{Q}_{SM} = \dot{Q} * f\dot{Q}_{SM} \quad (8)$$

$$\dot{Q}_{boiler} = \dot{Q} - \dot{Q}_{SM} \quad (9)$$

The natural gas consumption was given by:

$$NGuse = \frac{\dot{Q}_{SM}}{GCOP} + \frac{\dot{Q}_{boiler}}{\eta_{boiler}} \quad (10)$$

In addition to the consumption of natural gas, the SMs, as well as the auxiliary burner utilise electricity. A condensing boiler used for hydronic heating systems as presented in [29] was considered. For a system configuration similar to that expected for the GDSHP and hydronic AHU, the condensing boiler delivers 68 kWh of thermal energy per kWh of electricity consumed. That is, the condensing boiler had an electrical coefficient of performance (ECOP) of 68. Additionally, for the purposes of this study, it was assumed that the ECOP of the sorption module is 25% lower than that of the condensing boiler due to additional electrical components. Therefore, the electricity consumption of the GDSHP was given by:

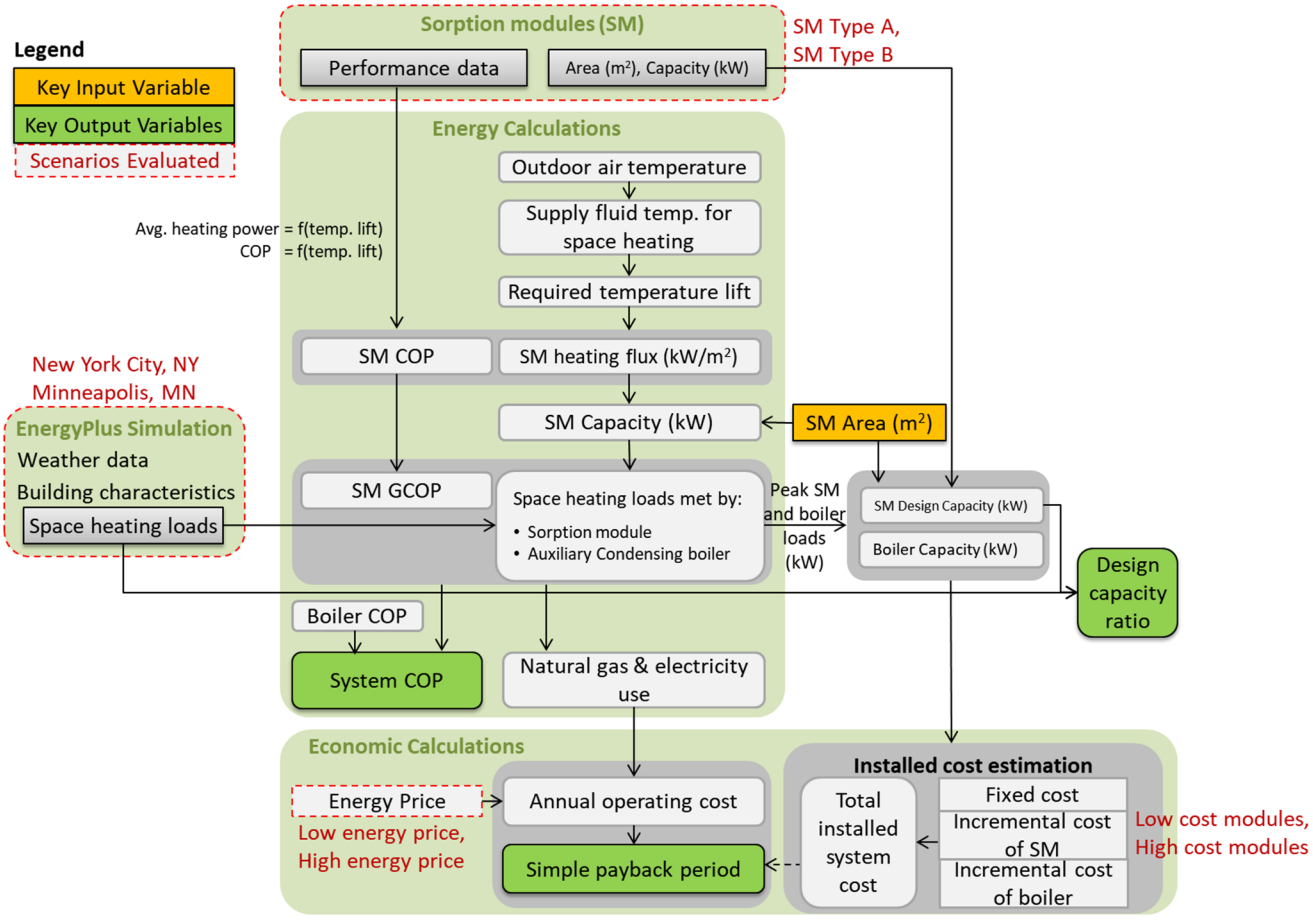

Fig. 7. Analysis methodology.

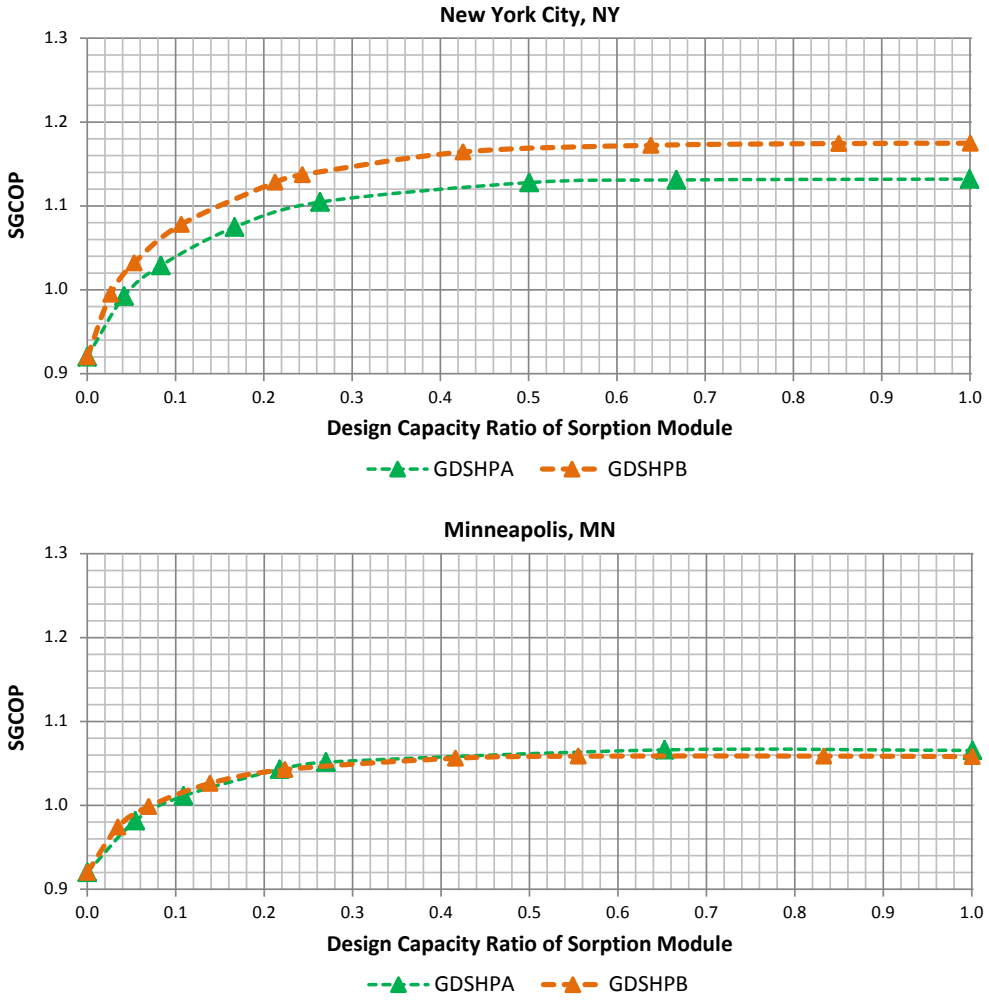

Fig. 8. System SGCOP versus SM design heating capacity ratio for New York City and Minneapolis, MN.

$$Elec_{use} = \frac{\dot{Q}_{boiler}}{ECOP_{boiler}} + \frac{\dot{Q}_{SM}}{ECOP_{SM}} \quad (11)$$

4.2.1. Calculation of COP

Knowing the required temperature lift for each hour, the COP of SM is calculated as:

$$COP = f_2(\Delta T_{lift,required}) \quad (12)$$

The efficiency of the main burner and post burner (i.e. flue gas) heat recovery of the SM are estimated as $\eta_{post\ \ burner} = 0.10$ and $\eta_{main\ \ burner} = 0.84$ [23]. The gas coefficient of performance of SM was calculated as below:

$$GCOP = \eta_{post\ \ burner} + \eta_{main\ \ burner} \times COP,\ if\ \Delta T_{lift,required} \leq \Delta T_{lift,max};\ else\ \ 0 \quad (13)$$

The SGCOP is given by:

$$SGCOP = f\dot{Q}_{SM} * GCOP + f\dot{Q}_{boiler} * \eta_{boiler} \quad (14)$$

4.3. Economic calculations

The economic analysis was performed using the following considerations for energy prices and system costs.

4.3.1. Energy prices

Two energy price scenarios were evaluated: the low energy price case with \$10/MMBtu for natural gas and \$0.12/kWh for electricity and high energy price case with \$20/MMBtu for natural gas and \$0.22/kWh for electricity (see Table 5). The low and high energy prices were determined from the current US average and highest state average residential energy prices, respectively [30,31].

From natural gas and electricity prices, the annual operating cost of the GDSHP system was calculated by:

$$Annual\ \ operating\ \ cost = \sum NGuse * NGprice + \sum Elecuse * Elecprice \quad (15)$$

4.3.2. System costs and payback period

For gas-driven absorption and adsorption heat pumps, the current installed costs vary from €315 (\$335) per kW to €1300 (\$ 1383) per kW according to [32,33]. Given that the SM based bivalent GDSHP is a novel development, cost estimates are employed within the range found in the literature. For the SMA, a low installed cost scenario of €315/kW and high-cost scenario of €1300/kW were assumed. The SMB, working on the resorption principle, is expected to have a higher cost than the respective SMA due to the lower thermal capacity per unit heat transfer area as well as the increased complexity of the resorption system [17,34,35]. Therefore, for the SMB, in each scenario, the installed cost was considered to be 25% higher than for SMA. For the purposes of this study, an assumed fixed cost of 10% was used to account for electrics, control system and other components that are predetermined irrespective of the SM size. The installed cost of the auxiliary condensing boiler unit integrated with both GDSHPA and GDSHPB was estimated to

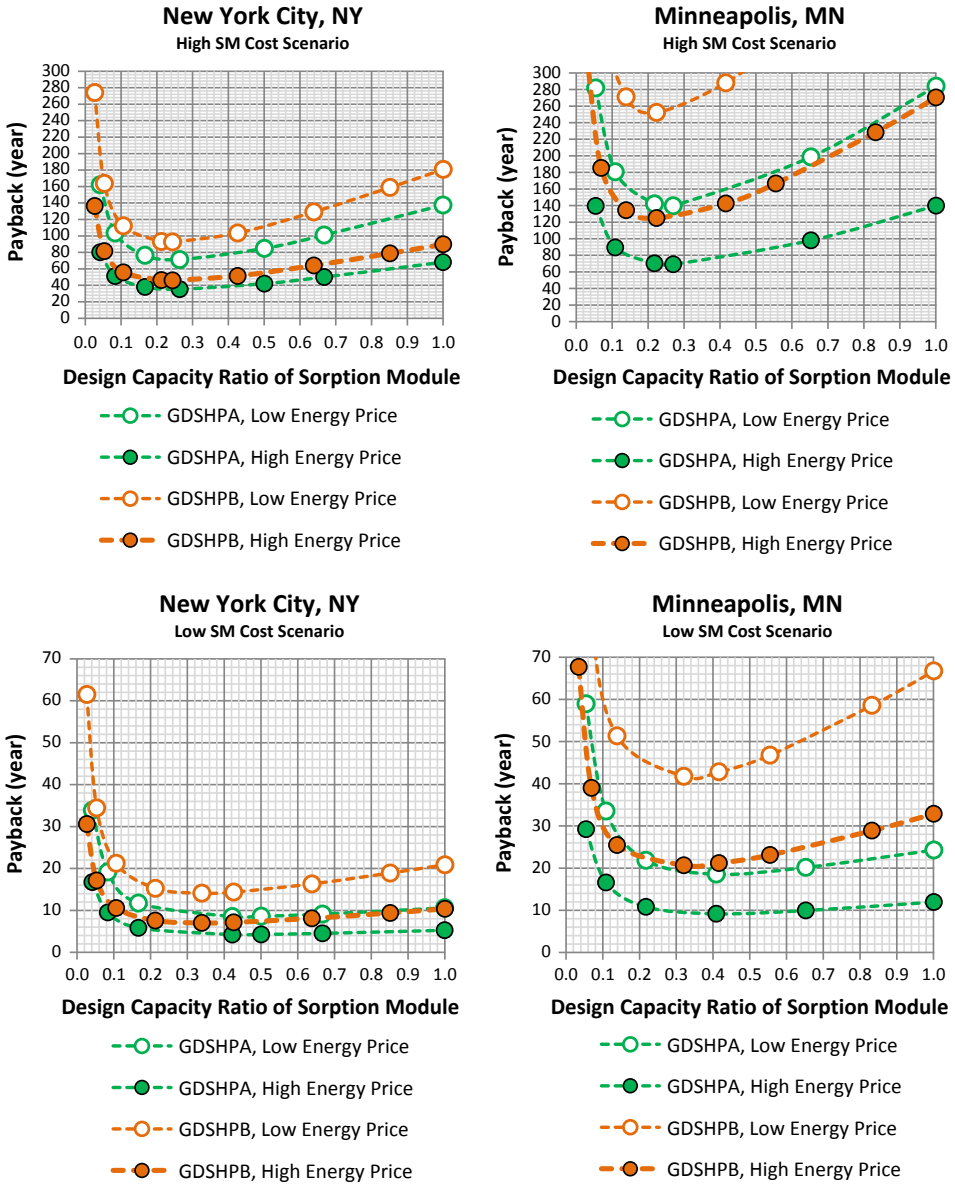

Fig. 9. Simple payback period versus SM design heating capacity ratio for New York City and Minneapolis, MN for high (upper graphs) and low (lower graphs) sorption module cost scenarios.

be $260 per kW heating capacity [36]. Thus:

$$\begin{aligned} Total\ \ installed\ \ cost\ \ GDSHP(\$) = Fixed\ \ cost\ \ (\$) \\ + \left[Incremental\ \ Cost_{SM}\left(\frac{\$}{kW}\right) * Size_{SM}(kW) \right] \\ + \left[Incremental\ \ Cost_{boiler}\left(\frac{\$}{kW}\right) * Size_{boiler}(kW) \right] \end{aligned} \quad (16)$$

The capacity of the sorption module used in the determination of the installed system cost was based on measured capacity and heat transfer area from evaluations carried out in [17], where:

$$Capacity_{SM}(kW) = A_{SM} * \frac{Capacity_{SM,measured}}{A_{SM,measured}} \quad (17)$$

The simple payback time of the GDSHP is calculated taking a condensing boiler as the baseline heating system, where:

$$\begin{aligned} Payback\ \ period \\ = \frac{Total\ \ installed\ \ cost\ \ GDSHP - Total\ \ installed\ \ cost\ \ condensing\ \ boiler}{Annual\ \ operating\ \ cost\ \ condensing\ \ boiler - Annual\ \ operating\ \ cost\ \ GDSHP} \end{aligned} \quad (18)$$

The methodology used for the full analysis is summarised in Fig. 7. Energy and economic calculations were carried out in Microsoft Excel based on exported hourly data from the EnergyPlus simulations and the equations defined in this work.

5. Results and discussion

5.1. Influence of design capacity ratio on SGCOP

Analyses were carried out to determine the system SGCOP for various design capacity ratios of the SMs for GDSHPA and GDSHPB and the results shown in Fig. 8. In the case of New York City, the GDSHPB exhibits higher SGCOP than GDSHPA this is attributed to the higher

COP and thus GCOP of the SMB. However, in the case of Minneapolis, GDSHPA marginally outperforms GDSHPB at higher design capacity ratios. This observation is due to the fact that the Minneapolis climate is characterised by a higher proportion of the heating demand occurring at low ambient temperatures. The GDSHPA's lower SM cut-off temperature allows it to run as a heat pump at lower outdoor temperatures and thus with a higher GCOP (see Fig. 9).

Although SGCOP increases with increasing SM design capacity ratio for both GDSHPA and GDSHPB, little improvement in SGCOP was observed at high design capacity ratios. In New York city SM design capacity ratios greater than 0.40 and in Minneapolis ratios greater than 0.30, for both GDSHPA and GDSHPB, show only a very small increase in SGCOP.

5.2. Influence of design capacity ratio on the payback period

Interestingly, for all scenarios, lower energy savings and thus longer payback periods are observed for the GDSHPB compared to GDSHPA in both climates. This can be attributed to the higher expected cost of the SMB. Additionally, despite SMB having higher COPs than SMA at ambient temperatures above 5 °C, the GDSHPB had a lower SGCOP due to its limited range of operation. The limited running of the SMB in heat pump mode is even more pronounced for Minneapolis due to the larger portion of hours with low outdoor temperatures.

As might be expected, for both GDSHPA and GDSHPB the higher energy price scenario gives lower payback time since energy cost savings are higher. Conversely, the lower the cost of the SM the lower the overall installed cost and the shorter the payback period (see Fig. 9).

5.3. Optimum sorption module design capacity ratio

For each scenario, that is, for each GDSHP type, SM cost and location, there was an optimum SM design capacity ratio which provides the minimum payback period. These optima are summarised in Table 6.

In all scenarios, the optimum design capacity of the SM was below 50% of the peak capacity of the GDSHP, with design capacity ratio of the SMs ranging from 0.22 to 0.42. Energy savings for New York City were between 11.1% and 14.4% compared to a condensing boiler, while in the case of Minneapolis savings ranged from 4.5% to 8.1%. The milder New York climate coupled with higher heating energy demand compared to Minneapolis means that the SM module operates in heat pump mode for more hours of the year producing higher energy savings and thus energy cost savings.

Additionally, a link is observed between SM cost and energy savings: the lower the cost of the SM, the more cost-effective it is to incorporate a higher capacity SM, leading to higher energy savings.

Payback times at optimum SM design capacity ratios varied between 4.2 and 92 years in the case of New York City. In the case of Minneapolis, payback times were longer ranging between 9.2 years and 252 years.

For each location, further analyses were carried at the optimum SM design capacity ratio under the most favourable scenarios, i.e. GDSHPA, high energy prices and low SM cost. Analyses yielded the following:

- In New York the GDSHPA with a SM design capacity ratio of 0.42 gave rise to energy savings of 14.4% and a payback time of 4.2 years compared to a standard condensing boiler. The SMA covered over the course of a year 86.6% of the space heating load.
- In Minnesota with a SM design capacity ratio of 0.41 the GDSHPA provided 8.1% energy savings over a baseline condensing boiler. That provided a payback time of 9.2 years whilst covering 74.1% of the space heating load.

Fig. 10, shows the results of the operation characteristics from annual hourly simulations carried out for each location under the best scenario. By inspection of Fig. 10, for the building in New York City, the

Table 6
Optimum sorption module design capacity ratio for each climate.

Climate/Location	System type	Low SM cost scenario		High SM cost scenario	
		Optimum SM design capacity ratio	Energy savings	Optimum SM design capacity ratio	Energy savings
New York	GDSHPA	0.42	14.4%	0.26	11.8%
	GDSHPB	0.34	13.0%	0.24	11.1%
Minnesota	GDSHPA	0.41	8.1%	0.27	7.0%
	GDSHPB	0.32	5.1%	0.22	4.5%

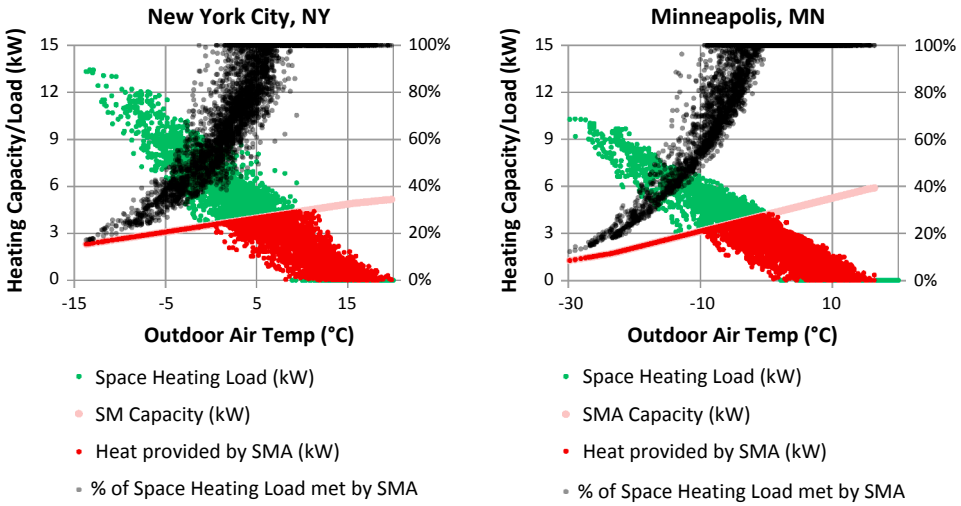

Fig. 10. Annual simulation hourly results at optimum SM design capacity ratio for New York City, NY (left) and Minneapolis, MN (right).

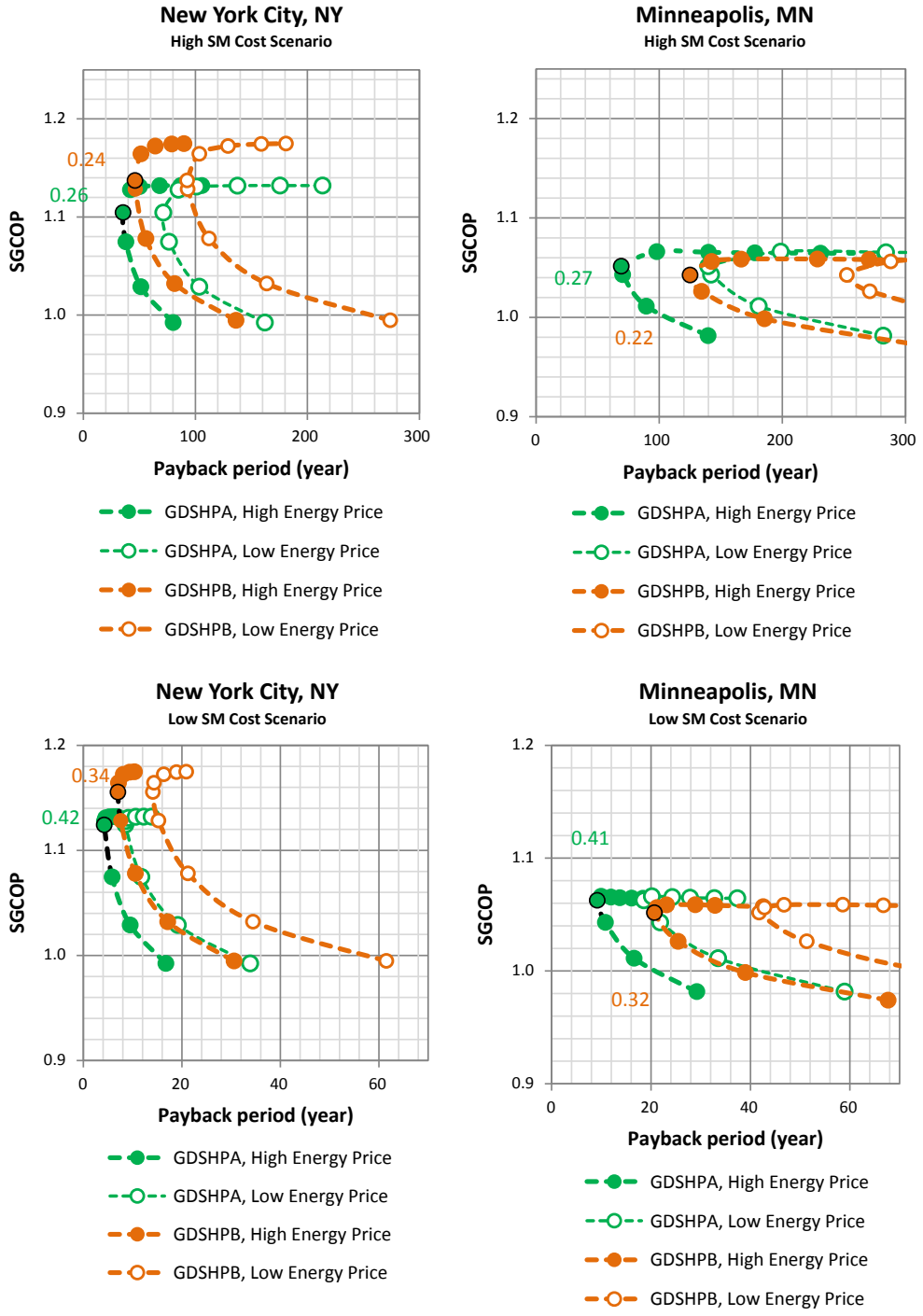

Fig. 11. Seasonal COP versus simple payback period for New York City, NY and Minneapolis, MN.

bivalent temperature is 2–6 °C. This is the range of ambient temperature at which the SM is no longer able to meet the entire building load. It varies across a range due to variations in solar insolation and internal loads. For the building in Minneapolis, the bivalent temperature is −8 to −1°C. In both locations, the SM continues to operate in non-heat-pumping mode at temperatures below the cut-off temperature, leading to parallel bivalent operation at all temperatures below the bivalent temperature.

5.4. GDSHP design considerations

In the present study of a bivalent GDSHP system there are several optimisation parameters, principally; SM module type, SM design capacity ratio, heat load, climate, energy prices and SM cost.

The SM type has a significant impact on the achievable energy savings within a given climate, for colder climates, an SM with a low cut-out temperature is required to maximise energy savings. For both climates, SMA proved the superior sorption module type due to its comparatively low cut-out temperature and lower cost, however, for warmer climates, SMB with its superior COPs at higher outdoor temperatures, might have an advantage.

The optimum design capacity ratio did not vary significantly based on climate for either SM sorption module type suggesting that this parameter is more sensitive to energy and system costs.

An additional consideration is acceptable payback periods for a given application. Considerations beyond cost might be applicable, for instance, reduction of emissions or regulations on minimum renewable energy mix in the heating system. Fig. 11 shows Pareto fronts for New York and Minnesota. Here it is observed that especially in the case of GDSHPB, in New York moderately higher SGCOP would be achievable if slightly longer payback periods are allowed.

6. Conclusions and perspectives

In this study, a method for the optimum sizing of a bivalent gas-driven sorption heat pump (GDSHP) incorporating a sorption module (SM) and an auxiliary condensing boiler was presented. Two different sorption module types were investigated; one operating under the basic chemisorption cycle (Type A) and the other under the resorption process (Type B).

The GDSHP systems were evaluated based on several scenarios based on SM type (Type A vs. Type B), climate (New York vs. Minnesota), natural gas prices (3.4 US cents/kWh vs. 6.8 US cents/kWh), electricity prices (12 US cents/kWh vs. 22 US cents/kWh) and SM cost ($335/kW vs. $1383/kW).

The results of the evaluation indicated that the sorption module design heating capacity ratio that results in the shortest payback period was 0.42 and 0.34 for GDSHPA and GDSHPB respectively, for systems installed in New York with a sorption module cost of $335/kW. In the case of Minnesota, the corresponding optimum capacity ratios were 0.41 for GDSHPA and 0.32 for GDSHPB.

In New York, a GDSHPA, with SM capacity ratio of 0.42 had expected payback periods of 4.2 years and 8.5 years for the high energy cost and low energy cost scenarios respectively. However, the GDSHPB system, even at optimum SM capacity ratios, exhibited higher payback periods 7.0 and 14.1 years for the high energy cost and low energy cost scenarios respectively.

The optimum design capacity ratio did not vary significantly based on climate for either SM sorption module type but was more sensitive to energy and system costs. However, the SM type had a significant impact on the achievable energy savings and thus minimum payback times for a given climate. Even though SMB had higher COP than SMA at higher ambient temperatures, its relatively high cut-out temperature, and lower heating capacity at low outdoor temperatures meant it performed less favourably than SMA. Therefore, SMA is more suitable for both cold-humid (Minnesota) and mixed-humid (New York) climates. SMB might however be more applicable to warmer climate zones.

Based on the study carried out, the optimum sizing of the bivalent GDSHP can be determined from studying cost, performance, and climate. Thus allowing for an evaluation of the techno-economic feasibility of modular residential sorption heat pumps from a design perspective. Optimisation or trade-offs beyond achieving the lowest payback time are also relevant to be explored considering desired savings level, reduction of emissions or other important considerations at the time of design.

Acknowledgments

This work was sponsored by the U. S. Department of Energy's Building Technologies (BTO) Office under Contract No. DE-AC05-00OR22725 with UT-Battelle, LLC. This work was also carried out under the auspices of the industrial post-graduate school REESBE (Resource Efficient Energy Systems for the Built Environment), which is financed by the Swedish Knowledge Foundation (KK-stiftelsen). The authors also acknowledge Mr. Antonio Bouza, Technology Manager for HVAC&R, Water Heating, and Appliance, U.S. Department of Energy BTO.

References

[1] M. Aprile, R. Scoccia, T. Toppi, M. Guerra, M. Motta, Modelling and experimental analysis of a GAX NH3-H2O gas-driven absorption heat pump, Int. J. Refrig. 66 (2016) 145–155.
[2] E. Elgendy, J. Schmidt, Experimental study of gas engine driven air to water heat pump in cooling mode, Energy 35 (6) (2010) 2461–2467.
[3] U. Lucia, M. Simonetti, G. Chiesa, G. Grisolia, Ground-source pump system for heating and cooling: review and thermodynamic approach, Renew. Sustain. Energy Rev. 70 (2017) 867–874.
[4] S. Poppi, N. Sommerfeldt, C. Bales, H. Madani, P. Lundqvist, Techno-economic review of solar heat pump systems for residential heating applications, Renew. Sustain. Energy Rev. 81 (1) (2018) 22–32.
[5] S. Nižetić, A.M. Papadopoulos, G.M. Tina, M. Rosa-Clot, Hybrid energy scenarios for residential applications based on the heat pump split air-conditioning units for operation in the Mediterranean climate conditions, Energy Build. 140 (2017) 110–120.
[6] W. Wu, B. Wang, W. Shi, X. Li, Absorption heating technologies: a review and perspective, Appl. Energy 130 (2014) 51–71.
[7] C. Naldi, G.L. Morini, E. Zanchini, A method for the choice of the optimal balance-point temperature of air-to-water heat pumps for heating, Sustain. Cities Soc. 12 (2014) 85–91.
[8] M. Dongellini, C. Naldi, G.L. Morini, Seasonal performance evaluation of electric air-to-water heat pump systems, Appl. Therm. Eng. 90 (2015) 1072–1081.
[9] M. Dongellini, C. Naldi, G.L. Morini, Sizing effects on the energy performance of reversible air-source heat pumps for office buildings, Appl. Therm. Eng. 114 (2017) 1073–1081.
[10] G. Bagarella, R. Lazzarin, M. Noro, Sizing strategy of on-off and modulating heat pump systems based on annual energy analysis, Int. J. Refrig. 65 (2016) 183–193.
[11] G. Bagarella, R. Lazzarin, M. Noro, Annual simulation, energy and economic analysis of hybrid heat pump systems for residential buildings, Appl. Therm. Eng. 99 (2016) 485–494.
[12] G. Mader, H. Madani, Capacity control in air-water heat pumps: total cost of ownership analysis, Energy Build. 81 (2014) 296–304.
[13] S. Nižetić, N. Duić, A.M. Papadopulos, G.M. Tina, F. Grubišić-Čabo, Energy efficiency evaluation of a hybrid energy system for building applications in a Mediterranean climate and its feasibility aspect, Energy 90 (1) (2015) 1171–1179.
[14] F. Busato, R.M. Lazzarin, M. Noro, Energy and economic analysis of different heat pump systems for space heating, Int J Low-Carbon Technol. 7 (2) (2012) 104–112.
[15] N. Aste, R.S. Adhikari, M. Manfren, Cost optimal analysis of heat pump technology adoption in residential reference buildings, Renew. Energy 60 (2013) 615–624.
[16] C. Blackman, C. Bales, Experimental evaluation of a novel absorption heat pump module for solar cooling applications, Sci. Technol. Built. Environ. 21 (3) (2015) 323–331.
[17] C. Blackman, C. Bales, E. Thorin, Experimental evaluation and concept demonstration of a novel modular gas-driven sorption heat pump, 12th IEA Heat Pump Conference, (2017).
[18] Z. Tamainot-Telto, R.E. Critoph, Advanced solid sorption air conditioning modules using monolithic carbon-ammonia pair, Appl. Therm. Eng. 23 (6) (2003) 659–674.
[19] A. Rosato, S. Sibilio, Preliminary experimental characterization of a three-phase absorption heat pump, Int. J. Refrig. 36 (3) (2013) 717–729.
[20] H.S. Bao, R.G. Oliveira, R.Z. Wang, L.W. Wang, Z.W. Ma, Working pairs for resorption refrigerator, Appl. Therm. Eng. 31 (14–15) (2011) 3015–3021.
[21] S. Spoelstra, W.G. Haije, J.W. Dijkstra, Techno-economic feasibility of high-temperature high-lift chemical heat pumps for upgrading industrial waste heat, Appl. Therm. Eng. 22 (14) (2002) 1619–1630.
[22] W.M. Barcellos, L.C.E.O. Souza, A.V. Saveliev, L.A. Kennedy, Ultra-low-emission steam boiler constituted of reciprocal flow porous burner, Exp Therm Fluid Sci 35 (3) (2011) 570–580.
[23] R.M. Lazzarin, Condensing boilers in buildings and plants refurbishment, Energy Build. 47 (2012) 61–67.
[24] J. Anesi, DOW proposes national 92% AFUE standard. Air Conditioning, Heating & Refrigeration News, Troy: BNP Media (2015) 1.
[25] International Code Council, International Energy Conservation Code (2006).
[26] ANSI, ASHRAE, ANSI/ASHRAE Standard 169-2013 – Climatic Data for Building Design Standards, 2013.
[27] S. Wilcox, W. Marion, Users Manual for TMY3 Data Sets, Report No. NREL/TP-581-43156, Revised May 2008. Available from: https://www.nrel.gov/docs/fy08osti/43156.pdf.
[28] US Department of Energy, Residential Prototype Building Models [Internet], Available from: https://www.energycodes.gov/development/residential/iecc_models.
[29] L. Arena, O. Faakye, Optimizing Hydronic System Performance in Residential Applications, Report No. DOE/GO-102013-4108, 2013 (October).
[30] US Energy Information Administration, Electricity Data Browser [Internet], 2017, Available from: https://www.eia.gov/electricity/data/browser/.
[31] US Energy Information Administration, Natural Gas Prices [Internet], 2017, Available from: https://www.eia.gov/dnav/ng/ng_pri_sum_dcu_nus_m.htm.
[32] B. Winiewska, B. Oschatz, Erarbeitung eines Verfahrens zur energetischen Bewertung von Sorptions-Gaswärmepumpen innerhalb der Systemnormung [Internet], (2014) Available from: https://www.irbnet.de/daten/rswb/14109021128.pdf.
[33] HEAT4U – project no. 285158, New efficient solutions for energy generation, storage and use related to space heating and domestic hot water in existing buildings [Internet], 2014, Available from: http://cordis.europa.eu/project/rcn/101431_en.html.
[34] L. Jiang, L.W. Wang, Z.S. Zhou, F.Q. Zhu, R.Z. Wang, Investigation on non-equilibrium performance of composite adsorbent for resorption refrigeration, Energy Convers. Manag. 119 (2016) 67–74.
[35] L.W. Wang, C.Z. Liu, L. Jiang, Y.J. Zhao, R.Z. Wang, Performance of a resorption cycle for recovering the waste heat from vehicles, Sci. Technol. Built. Environ. 21 (3) (2015) 280–289.
[36] US Department of Energy, Technical Support Document: Energy Efficiency Program for Consumer Products and Commercial and Industrial Equipment: Residential Boilers [Internet], 2015. Available from: https://energy.mo.gov/sites/energy/files/technical-support-document—residential-boilers_doe.pdf.

REFERENCES

1. DOE, U., *Buildings Energy Data Book, 2011*. 2012: https://openei.org/doe-opendata/dataset/buildings-energy-data-book.
2. (EIA), E.I.A. *Residential Energy Consumption Survey (RECS)*. 2019 [cited 2019 July 21]; Available from: https://www.eia.gov/consumption/residential/.
3. (AGA), A.G.A. *American Gas Association: Natural Gas Furnace Efficiency Rule* 2017 [cited 2019 July 21]; Available from: https://www.aga.org/sites/default/files/2017_furnace_efficiency_rule.pdf.
4. Energy, D.o. *Furnaces and Boilers*. 2019 [cited 2019 July 21]; Available from: https://www.energy.gov/energysaver/home-heating-systems/furnaces-and-boilers.
5. Garrabrant, M., et al., *Experimental Evaluation of Low-Cost Gas Heat Pump Prototypes for Building Space Heating.* 2016.
6. Chua, K.J., S.K. Chou, and W.M. Yang, *Advances in heat pump systems: A review.* Applied Energy, 2010. **87**(12): p. 3611-3624.
7. Gschwend, A., et al., *Energy consumption of cold climate heat pumps in different climates – Comparison of single-stage and two-stage systems.* International Journal of Refrigeration, 2016. **62**: p. 193-206.
8. Bertsch, S.S. and E.A. Groll, *Two-stage air-source heat pump for residential heating and cooling applications in northern U.S. climates.* International Journal of Refrigeration, 2008. **31**(7): p. 1282-1292.
9. Caskey, S.L., et al., *Simulation of an air-source heat pump with two-stage compression and economizing for cold climates*, in *14th International Refrigeration and Air Conditioning Conference at Purdue*. 2012: West Lafayette, USA.
10. Ma, G.-Y. and H.-X. Zhao, *Experimental study of a heat pump system with flash-tank coupled with scroll compressor.* Energy and Buildings, 2008. **40**(5): p. 697-701.
11. Bach, C.K., et al., *Experimental Investigation of Vapor Injected Compression for Cold Climate Heat Pumps*, in *International Refrigeration and Air Conditioning Conference*. 2014: West Lafayette, USA.
12. Shen, B., et al., *Field Investigation of an Air-Source Cold Climate Heat Pump*, in *IEA Heat Pump Conference*. 2017, Oak Ridge, TN: ORNL. http://hpc2017.org/wpcontent/uploads/2017/05/P: Rotterdam, NL.
13. Shen, B., et al., *Cold Climate Heat Pumps Using Tandem Compressors*. 2016, Oak Ridge National Laboratory (ORNL), Oak Ridge, TN (United States). Building Technologies Research and Integration Center (BTRIC).
14. Hakkaki-Fard, A., Z. Aidoun, and M. Ouzzane, *Improving cold climate air-source heat pump performance with refrigerant mixtures.* Applied Thermal Engineering, 2015. **78**: p. 695-703.

15. Sarbu, I. and C. Sebarchievici, *General review of ground-source heat pump systems for heating and cooling of buildings.* Energy and Buildings, 2014. **70**: p. 441-454.

16. Mustafa Omer, A., *Ground-source heat pumps systems and applications.* Renewable and Sustainable Energy Reviews, 2008. **12**(2): p. 344-371.

17. Self, S.J., B.V. Reddy, and M.A. Rosen, *Geothermal heat pump systems: Status review and comparison with other heating options.* Applied Energy, 2013. **101**: p. 341-348.

18. Hu, B., et al., *Thermal modeling and experimental research of a gas engine-driven heat pump in variable condition.* Applied Thermal Engineering, 2017. **123**: p. 1504-1513.

19. Shah, N.N., M.J. Huang, and N.J. Hewitt, *Experimental study of a diesel engine heat pump in heating mode for domestic retrofit application.* Applied Thermal Engineering, 2016. **98**: p. 522-531.

20. Shah, N.N., M.J. Huang, and N.J. Hewitt, *Performance analysis of diesel engine heat pump incorporated with heat recovery.* Applied Thermal Engineering, 2016. **108**: p. 181-191.

21. Yang, L., et al., *Performance modeling of air cycle heat pump water heater in cold climate.* Renewable Energy, 2016. **87**: p. 1067-1075.

22. Deru, M.P. and P.A. Torcellini, *Source energy and emission factors for energy use in buildings*. 2007: National Renewable Energy Laboratory Golden, CO.

23. Mauran, S., P. Prades, and F. L'Haridon, *Heat and mass transfer in consolidated reacting beds for thermochemical systems.* Heat Recovery Systems and CHP, 1993. **13**(4): p. 315-319.

24. Pons, M., et al., *Thermodynamic based comparison of sorption systems for cooling and heat pumping: Comparaison des performances thermodynamique des systèmes de pompes à chaleur à sorption dans des applications de refroidissement et de chauffage.* International Journal of Refrigeration, 1999. **22**(1): p. 5-17.

25. Yang, Z., M. Qu, and K.R. Gluesenkamp, *Model-Based Performance Comparison of Ammonia Chemisorption Heat Pumps for Cold Climate with Different Working Pairs and Cycle Configurations*. 2018, Oak Ridge National Lab.(ORNL), Oak Ridge, TN (United States).

26. Vasiliev, L., O. Filatova, and A. Tsitovich, *Application of sorption heat pumps for increasing of new power sources efficiency.* Archives of Thermodynamics, 2010. **31**(2): p. 21-43.

27. Yang, Z., M. Qu, and K.R. Gluesenkamp, *Ammonia-Based Chemisorption Heat Pumps for Cold-Climate Heating Applications: A Comprehensive Review*. Applied Thermal Engineering, 2020: p. 115674.

28. Yang, Z., M. Qu, and K.R. Gluesenkamp, *Design screening and analysis of gas-fired ammonia-based chemisorption heat pumps for space heating in cold climate.* Energy, 2020: p. 118213.

29. Miessler, G.L., P.J. Fischer, and D.A. Tarr, *Inorganic Chemistry*. Fifth Edition ed. 2013: Pearson Education.

30. Cotton, F.A., et al., *Advanced inorganic chemistry*. Vol. 6. 1988: Wiley New York.

31. Jiang, L. and A. Roskilly, *Thermal conductivity, permeability and reaction characteristic enhancement of ammonia solid sorbents: A review.* International Journal of Heat

Mass Transfer

2019. **130**: p. 1206-1225.

32. S. Hosatte, F.R. *Kinetics and Modelling of CaCl2-NH3 Reactions*. in *Proceeding of the Symposium of Solid Sorption Refrigeration*. 1992. LIMSI, Paris.

33. Wang, L.W., et al., *Compound adsorbent for adsorption ice maker on fishing boats.* International Journal of Refrigeration, 2004. **27**(4): p. 401-408.

34. Tian, B., et al., *Permeability and thermal conductivity of compact chemical and physical adsorbents with expanded natural graphite as host matrix.* International Journal of Heat and Mass Transfer, 2012. **55**(15): p. 4453-4459.

35. Jiang, L., et al., *Experimental study on working pairs for two-stage chemisorption freezing cycle.* Renewable Energy, 2015. **74**(Supplement C): p. 287-297.

36. Stitou, D., V. Goetz, and B. Spinner, *A new analytical model for solid-gas thermochemical reactors based on thermophysical properties of the reactive medium.* Chemical Engineering and Processing: Process Intensification, 1997. **36**(1): p. 29-43.

37. van der Pal, M. and J. Veldhuis, *Thermodynamic properties of lithium chloride ammonia complexes under heat pump type II working conditions.* Energy Research Centre of the Netherlands . Report nr ECN-M–10-076, 2010.

38. Bevers, E., et al., *Thermodynamic properties of lithium chloride ammonia complexes for application inahigh-lifthigh temperature chemical heat pump.* Journal of Thermal Analysis Calorimetry, 2006. **86**(3): p. 825-832.

39. Sharma, R. and E.A. Kumar, *Measurement of thermodynamic properties of ammoniated salts and thermodynamic simulation of resorption cooling system.* International Journal of Refrigeration, 2016. **67**: p. 54-68.

40. Winterbone, D.E. and A. Turan, *Chapter 12 - Chemical Equilibrium and Dissociation*, in *Advanced Thermodynamics for Engineers (Second Edition)*, D.E. Winterbone and A. Turan, Editors. 2015, Butterworth-Heinemann: Boston. p. 247-294.

41. Atkins, P.W., J. De Paula, and J. Keeler, *Atkins' physical chemistry*. 2018: Oxford university press.

42. Don, W.G. and H.P. Robert, *Perry's Chemical Engineers' Handbook, Eighth Edition*. 8th ed. / ed. 2008, New York: McGraw-Hill Education.

43. Michel, B., P. Neveu, and N. Mazet, *Comparison of closed and open thermochemical processes, for long-term thermal energy storage applications.* Energy, 2014. **72**: p. 702-716.

44. Neveu, P. and J. Castaing, *Solid-gas chemical heat pumps: field of application and performance of the internal heat of reaction recovery process.* Heat Recovery Systems & Chp, 1993. **13**(3): p. 233-251.

45. Li, T., R. Wang, and J.K. Kiplagat, *A target-oriented solid-gas thermochemical sorption heat transformer for integrated energy storage and energy upgrade.* AIChE Journal, 2013. **59**(4): p. 1334-1347.

46. Li, T., R. Wang, and H. Li, *Progress in the development of solid–gas sorption refrigeration thermodynamic cycle driven by low-grade thermal energy*. Progress in Energy and Combustion Science, 2014. **40**: p. 1-58.

47. Vasiliev, L., D. Mishkinis, and A. Antukh, *Solar-gas solid sorption refrigerator*. Adsorption, 2001. **7**(2): p. 149-161.

48. Xu, J., R.G. Oliveira, and R.Z. Wang, *Resorption system with simultaneous heat and cold production.* International Journal of Refrigeration, 2011. **34**(5): p. 1262-1267.

49. Pal, M. and J. Veldhuis, *Thermodynamic properties of lithium chloride ammonia complexes under heat pump type II working conditions*. 2010, Innovative Materials for Processes in Energy Systems.

50. Oliveira, R.G., et al., *Novel composite sorbent for resorption systems and for chemisorption air conditioners driven by low generation temperature.* Renewable Energy, 2009. **34**(12): p. 2757-2764.

51. Goetz, V., F. Elie, and B. Spinner, *The structure and performance of single effect solid-gas chemical heat pumps.* Heat Recovery Systems and CHP, 1993. **13**(1): p. 79-96.

52. Wang, L.W., R.Z. Wang, and R.G. Oliveira, *A review on adsorption working pairs for refrigeration.* Renewable & Sustainable Energy Reviews, 2009. **13**(3): p. 518-534.

53. Jiang, L. and A.P. Roskilly, *Thermal conductivity, permeability and reaction characteristic enhancement of ammonia solid sorbents: A review.* International Journal of Heat and Mass Transfer, 2019. **130**: p. 1206-1225.

54. Castaing-Lasvignottes, J. and P. Neveu, *Development of a numerical sizing tool applied to a solid-gas thermochemical transformer—II. Influence of external couplings on the dynamic behaviour of a solid-gas thermochemical transformer.* Applied thermal engineering, 1997. **17**(6): p. 519-536.

55. Li, T.X., et al., *Experimental study and comparison of thermochemical resorption refrigeration cycle and adsorption refrigeration cycle.* Chemical Engineering Science, 2010. **65**(14): p. 4222-4230.

56. Le Pierrès, N., N. Mazet, and D. Stitou, *Experimental results of a solar powered cooling system at low temperature.* International Journal of Refrigeration, 2007. **30**(6): p. 1050-1058.

57. Li, T.X., et al., *Study on the heat transfer and sorption characteristics of a consolidated composite sorbent for solar-powered thermochemical cooling systems.* Solar Energy, 2009. **83**(9): p. 1742-1755.

58. Rivera, C., et al., *Experimental study of a thermo-chemical refrigerator using the barium chloride–ammonia reaction.* International Journal of Hydrogen Energy, 2007. **32**(15): p. 3154-3158.

59. Hu, Y., et al., *A two-stage deep freezing chemisorption cycle driven by low-temperature heat source.* Frontiers in Energy, 2011. **5**(3): p. 263.

60. Kiplagat, J.K., et al., *Lithium chloride – Expanded graphite composite sorbent for solar powered ice maker.* Solar Energy, 2010. **84**(9): p. 1587-1594.

61. Wu, S., et al., *Experimental investigation on a thermochemical sorption refrigeration prototype using EG/SrCl2–NH3 working pair.* International Journal of Refrigeration, 2018. **88**: p. 8-15.

62. Oliveira, R., R. Wang, and C. Wang, *Evaluation of the cooling performance of a consolidated expanded graphite–calcium chloride reactive bed for chemisorption icemaker.* International Journal of Refrigeration, 2007. **30**(1): p. 103-112.

63. Oliveira, R.G. and R.Z. Wang, *A consolidated calcium chloride-expanded graphite compound for use in sorption refrigeration systems.* Carbon, 2007. **45**(2): p. 390-396.

64. Lu, Z.S., et al., *Performance analysis of an adsorption refrigerator using activated carbon in a compound adsorbent.* Carbon, 2006. **44**(4): p. 747-752.

65. Wang, L., H. Bao, and R. Wang, *A comparison of the performances of adsorption and resorption refrigeration systems powered by the low grade heat.* Renewable Energy, 2009. **34**(11): p. 2373-2379.

66. Wang, L.W., et al., *Split heat pipe type compound adsorption ice making test unit for fishing boats.* International Journal of Refrigeration, 2006. **29**(3): p. 456-468.

67. Wang, L.W., et al., *The performance of two adsorption ice making test units using activated carbon and a carbon composite as adsorbents.* Carbon, 2006. **44**(13): p. 2671-2680.

68. Li, S.L., et al., *Experimental study of a novel CaCl2/expanded graphite-NH3 adsorption refrigerator.* International Journal of Refrigeration, 2010. **33**(1): p. 61-69.

69. Lu, Z.S., et al., *Experimental investigation of a novel multifunction heat pipe solid sorption icemaker for fishing boats using CaCl2/activated carbon compound–ammonia.* International Journal of Refrigeration, 2007. **30**(1): p. 76-85.

70. Jiang, L., et al., *Experimental study on a resorption system for power and refrigeration cogeneration.* Energy, 2016. **97**(Supplement C): p. 182-190.

71. Li, T.X., et al., *Performance study of a high efficient multifunction heat pipe type adsorption ice making system with novel mass and heat recovery processes ☆☆This work was supported by National Science Fund for Distinguished Young Scholars of China under the contract No. 50225621, Shanghai Shuguang Training Program for the Talents under the contract No. 02GG03, the Natural Science Fund of Shanghai City under the contract No. 05ZR14072.* International Journal of Thermal Sciences, 2007. **46**(12): p. 1267-1274.

72. Li, T.X., et al., *Experimental investigation of an innovative dual-mode chemisorption refrigeration system based on multifunction heat pipes.* International Journal of Refrigeration, 2008. **31**(6): p. 1104-1112.

73. Li, T.X., et al., *Performance study of a consolidated manganese chloride–expanded graphite compound for sorption deep-freezing processes.* Applied Energy, 2009. **86**(7): p. 1201-1209.

74. Bao, H., Y. Wang, and A.P. Roskilly, *Modelling of a chemisorption refrigeration and power cogeneration system.* Applied Energy, 2014. **119**: p. 351-362.

75. Bao, H.S., R.Z. Wang, and L.W. Wang, *A resorption refrigerator driven by low grade thermal energy.* Energy Conversion and Management, 2011. **52**(6): p. 2339-2344.

76. Goetz, V., B. Spinner, and E. Lepinasse, *A solid-gas thermochemical cooling system using BaCl2 and NiCl2.* Energy, 1997. **22**(1): p. 49-58.

77. Lépinasse, E., M. Marion, and V. Goetz, *Cooling storage with a resorption process. Application to a box temperature control.* Applied Thermal Engineering, 2001. **21**(12): p. 1251-1263.

78. Bao, H., et al., *Working pairs for resorption refrigerator.* Applied Thermal Engineering, 2011. **31**(14-15): p. 3015-3021.

79. Goetz, V. and A. Marty, *A model for reversible solid-gas reactions submitted to temperature and pressure constraints: simulation of the rate of reaction in solid-gas reactor used as chemical heat pump.* Chemical Engineering Science, 1992. **47**(17-18): p. 4445-4454.

80. Aidoun, Z. and M. Ternan, *Pseudo-stable transitions and instability in chemical heat pumps: the NH3–CoCl2 system.* Applied Thermal Engineering, 2001. **21**(10): p. 1019-1034.

81. Aidoun, Z. and M. Ternan, *The synthesis reaction in a chemical heat pump reactor filled with chloride salt impregnated carbon fibres: the NH3–CoCl2 system.* Applied Thermal Engineering, 2002. **22**(17): p. 1943-1954.

82. Zhong, Y., et al., *Isothermal sorption characteristics of the BaCl 2–NH 3 pair in a vermiculite host matrix.* Applied Thermal Engineering, 2007. **27**(14): p. 2455-2462.

83. Zhou, Z.S., et al., *Non-equilibrium sorption performances for composite sorbents of chlorides–ammonia working pairs for refrigeration.* International Journal of Refrigeration, 2016. **65**(Supplement C): p. 60-68.

84. Sharma, R. and E. Anil Kumar, *Performance evaluation of simple and heat recovery adsorption cooling system using measured NH3 sorption characteristics of halide salts.* Applied Thermal Engineering, 2017. **119**: p. 459-471.

85. Wu, S., T.X. Li, and R.Z. Wang, *Experimental identification and thermodynamic analysis of ammonia sorption equilibrium characteristics on halide salts.* Energy, 2018. **161**: p. 955-962.

86. Trudel, J., S. Hosatte, and M. Ternan, *Solid–gas equilibrium in chemical heat pumps: the NH3–CoCl2 system.* Applied Thermal Engineering, 1999. **19**(5): p. 495-511.

87. Gao, J., et al., *Solution to the sorption hysteresis by novel compact composite multi-salt sorbents.* Applied Thermal Engineering, 2017. **111**: p. 580-585.

88. Gao, J., et al., *Performance analysis of multi-salt sorbents without sorption hysteresis for low-grade heat recovery.* Renewable Energy, 2018. **118**: p. 718-726.

89. Wang, R., L. Wang, and J. Wu, *Adsorption refrigeration technology: theory and application*. 2014: John Wiley & Sons.

90. Lu, H.-B., N. Mazet, and B. Spinner, *Modelling of gas-solid reaction—Coupling of heat and mass transfer with chemical reaction.* Chemical Engineering Science, 1996. **51**(15): p. 3829-3845.

91. Han, J.H., K.-H. Lee, and H. Kim, *Effective thermal conductivity of graphite-metallic salt complex for chemical heat pumps.* Journal of thermophysics and heat transfer, 1999. **13**(4): p. 481-488.

92. Jiang, L., et al., *Investigation on heat and mass transfer performance of novel composite strontium chloride for sorption reactors.* Applied Thermal Engineering, 2017. **121**: p. 410-418.

93. Wang, K., et al., *Effective thermal conductivity of expanded graphite–CaCl2 composite adsorbent for chemical adsorption chillers.* Energy Conversion and Management, 2006. **47**(13): p. 1902-1912.

94. Xu, L., et al., *Experimental study on a combined double-way chemisorption refrigeration system.* International Journal of Refrigeration, 2011. **34**(4): p. 914-921.

95. Wang, C., P. Zhang, and R.Z. Wang, *Investigation of solid–gas reaction heat transformer system with the consideration of multistep reactions.* AIChE Journal, 2008. **54**(9): p. 2464-2478.

96. Wang, L.W., et al., *Anisotropic thermal conductivity and permeability of compacted expanded natural graphite.* Applied Thermal Engineering, 2010. **30**(13): p. 1805-1811.

97. Wang, L.W., et al., *Thermal conductivity and permeability of consolidated expanded natural graphite treated with sulphuric acid.* Carbon, 2011. **49**(14): p. 4812-4819.

98. Jiang, L., et al., *Investigation on non-equilibrium performance of composite adsorbent for resorption refrigeration.* Energy Conversion and Management, 2016. **119**(Supplement C): p. 67-74.

99. Jiang, L., L.W. Wang, and R.Z. Wang, *Investigation on thermal conductive consolidated composite CaCl2 for adsorption refrigeration.* International Journal of Thermal Sciences, 2014. **81**(Supplement C): p. 68-75.

100. Zhao, Y.J., et al., *Study on consolidated activated carbon: Choice of optimal adsorbent for refrigeration application.* International Journal of Heat and Mass Transfer, 2013. **67**: p. 867-876.

101. Dellero, T., D. Sarmeo, and P. Touzain, *A chemical heat pump using carbon fibers as additive. Part I: enhancement of thermal conduction.* Applied Thermal Engineering, 1999. **19**(9): p. 991-1000.

102. Dellero, T. and P. Touzain, *A chemical heat pump using carbon fibers as additive. Part II: study of constraint parameters.* Applied Thermal Engineering, 1999. **19**(9): p. 1001-1011.

103. Vasiliev, L.L., et al., *NaX zeolite, carbon fibre and CaCl2 ammonia reactors for heat pumps and refrigerators.* Adsorption, 1996. **2**(4): p. 311-316.

104. Vasil'ev, L., et al., *Multisalt-carbon chemical cooler for space applications.* Journal of Engineering Physics and Thermophysics, 1999. **72**(3): p. 572-577.

105. Aristov, Y.I. and L.L. Vasiliev, *New composite sorbents of water and ammonia for chemical and adsorption heat pumps.* Journal of Engineering Physics and Thermophysics, 2006. **79**(6): p. 1214-1229.

106. Yan, T., et al., *Experimental study of the ammonia adsorption characteristics on the composite sorbent of CaCl2 and multi-walled carbon nanotubes.* International Journal of Refrigeration, 2014. **46**(Supplement C): p. 165-172.

107. Yan, T., et al., *A review of promising candidate reactions for chemical heat storage.* Renewable and Sustainable Energy Reviews, 2015. **43**(Supplement C): p. 13-31.

108. Han, J.H., et al., *Porous graphite matrix for chemical heat pumps.* Carbon, 1998. **36**(12): p. 1801-1810.

109. Han, J.H. and K.-H. Lee, *Gas permeability of expanded graphite–metallic salt composite.* Applied Thermal Engineering, 2001. **21**(4): p. 453-463.

110. Lu, H.B. and N. Mazet, *Mass-transfer parameters in gas-solid reactive media to identify permeability of IMPEX.* AIChE journal, 1999. **45**(11): p. 2444-2453.

111. Saka, C., *BET, TG–DTG, FT-IR, SEM, iodine number analysis and preparation of activated carbon from acorn shell by chemical activation with ZnCl2.* Journal of Analytical and Applied Pyrolysis, 2012. **95**: p. 21-24.

112. Jin, Z., et al., *Comparison on Thermal Conductivity and Permeability of Granular and Consolidated Activated Carbon for Refrigeration.* Chinese Journal of Chemical Engineering, 2013. **21**(6): p. 676-682.

113. Lee, T., et al., *Activated carbon fiber-the hybrid of carbon fiber and activated carbon.* Rev. Adv. Mater. Sci, 2014. **36**(2): p. 118-136.

114. Xu, Y. and D. Chung, *Silane-treated carbon fiber for reinforcing cement.* Carbon, 2001. **39**(13): p. 1995-2001.

115. Suzuki, M., *Activated carbon fiber: Fundamentals and applications.* Carbon, 1994. **32**(4): p. 577-586.

116. Wang, J.Y., R.Z. Wang, and L.W. Wang, *Water vapor sorption performance of ACF-CaCl2 and silica gel-CaCl2 composite adsorbents.* Applied Thermal Engineering, 2016. **100**: p. 893-901.

117. Zhang, Y.N., et al., *Development and thermochemical characterizations of vermiculite/SrBr2 composite sorbents for low-temperature heat storage.* Energy, 2016. **115**: p. 120-128.

118. Critoph, R.E. and S.J. Metcalf, *Specific cooling power intensification limits in ammonia–carbon adsorption refrigeration systems.* Applied Thermal Engineering, 2004. **24**(5): p. 661-678.

119. Han, J.H., et al., *Transformation analysis of thermochemical reactor based on thermophysical properties of graphite-MnCl 2 complex.* Industrial and Engineering Chemistry Research, 2000. **39**(11): p. 4127-4139.

120. Li, T.X., et al., *A conceptual design and performance analysis of a triple-effect solid–gas thermochemical sorption refrigeration system with internal heat recovery.* Chemical Engineering Science, 2009. **64**(14): p. 3376-3384.

121. Zhu, C., et al., *Unified thermodynamic model to calculate COP of diverse sorption heat pump cycles: Adsorption, absorption, resorption, and multistep crystalline reactions.* International Journal of Refrigeration, 2019. **99**: p. 382-392.

122. Wang, L.W., et al., *Studies on split heat pipe type adsorption ice-making test unit for fishing boats: Choice of heat pipe medium and experiments under unsteady heating sources.* Energy Conversion and Management, 2006. **47**(15): p. 2081-2091.

123. Cacciola, G. and G. Restuccia, *Progress on adsorption heat pumps.* Heat Recovery Systems and CHP, 1994. **14**(4): p. 409-420.

124. Critoph, R. and Y. Zhong, *Review of trends in solid sorption refrigeration and heat pumping technology.* Proceedings of the Institution of Mechanical Engineers, Part E: Journal of Process Mechanical Engineering, 2005. **219**(3): p. 285-300.

125. Tchernev, D., *High-efficiency regenerative zeolite heat pump.* ASHRAE transactions, 1988. **2**: p. 2024-2032.

126. Mazet, N., M. Amouroux, and B. Spinner, *Analysis and experimental study of the transformation of a non-isothermal solid/gas reacting medium.* Chemical engineering communications, 1991. **99**(1): p. 155-174.

127. Xu, L., et al., *Experimental study on the performance of double-effect and double-way thermochemical sorption refrigeration cycle.* Applied Thermal Engineering, 2011. **31**(17): p. 3658-3663.

128. Gui, Y.B., et al., *Performance modeling and testing on a heat-regenerative adsorptive reversible heat pump.* Applied Thermal Engineering, 2002. **22**(3): p. 309-320.

129. Critoph, R.E., *Rapid cycling solar/biomass powered adsorption refrigeration system.* Renewable Energy, 1999. **16**(1): p. 673-678.

130. Critoph, R.E., Z. Tamainot-Telto, and G.N.L. Davies, *A prototype of a fast cycle adsorption refrigerator utilizing a novel carbon—aluminium laminate.* Proceedings of the Institution of Mechanical Engineers, Part A: Journal of Power and Energy, 2000. **214**(5): p. 439-448.

131. Restuccia, G., Vasta, S., Freni, A., Russo, F., Aristov, Y. I. *An Advanced Solid Sorption Chiller Using SWS-1L: Performance Analysis and Hydrothermal Cycling Stability of the Sorbent Bed*. in *International Sorption Heat Pump Conference*. 2005. Broomfield, Colorado, USA.

132. Tchernev, D.I. and J.M. Clinch. *Closed cycle zeolite regenerative heat pump*. in *eleventh annual ASME Solar Energy Conference*. 1989. San Diego, California.

133. Critoph, R., *Towards a one tonne per day solar ice maker.* Renewable Energy, 1996. **9**(1-4): p. 626-631.

134. Wang, K., et al., *Composite adsorbent of CaCl 2 and expanded graphite for adsorption ice maker on fishing boats.* International Journal of Refrigeration, 2006. **29**(2): p. 199-210.

135. Alyousef, Y., et al., *Three adsorbers solar cooler with composite sorbent bed and heat pipe thermal control.* Applied Thermal Engineering, 2012. **38**: p. 124-130.

136. Critoph, R. *The use of thermosyphon heat pipes to improve the performance of a carbon–ammonia adsorption refrigerator*. in *Proc. of the IV Minsk Int. Seminar-Heat Pipes, Heat Pumps, Refrigerators*. 2000. Citeseer.

137. Critoph, R.E., *Performance estimation of convective thermal wave adsorption cycles.* Applied Thermal Engineering, 1996. **16**(5): p. 429-437.

138. Tatlıer, M., B. Tantekin-Ersolmaz, and A. Erdem-Şenatalar, *A novel approach to enhance heat and mass transfer in adsorption heat pumps using the zeolite–water pair.* Microporous and Mesoporous Materials, 1999. **27**(1): p. 1-10.

139. Restuccia, G., A. Freni, and G. Maggio, *A zeolite-coated bed for air conditioning adsorption systems: parametric study of heat and mass transfer by dynamic simulation.* Applied Thermal Engineering, 2002. **22**(6): p. 619-630.

140. Bonaccorsi, L., et al., *Zeolite coated copper foams for heat pumping applications.* Microporous and Mesoporous Materials, 2006. **91**(1): p. 7-14.

141. Wang, R.Z., et al., *Heat transfer design in adsorption refrigeration systems for efficient use of low-grade thermal energy.* Energy, 2011. **36**(9): p. 5425-5439.

142. Iammak, K., W. Wongsuwan, and T. Kiatsiriroj. *Investigation of modular chemical energy storage performance*. in *The joint international conference on sustainable energy and environment (SEE)*. 2004.

143. Jaehnig, D.H., R.; Wagner, W.;Isaksson, C. *Thermo-Chemical Storage for Solar Space Heating in Single-Family House*. in *Proceedings of Ecostock*. 2006. Galloway, New Jersey.

144. Tokarev, M.M., et al., *Adsorption cycle "heat from cold" for upgrading the ambient heat: The testing a lab-scale prototype with the composite sorbent CaClBr/silica.* Applied energy, 2018. **211**: p. 136-145.

145. Gordeeva, L. and Y.I. Aristov, *Adsorptive heat storage and amplification: New cycles and adsorbents.* Energy, 2019. **167**: p. 440-453.

146. de Oliveira, R.G., *Chemisorption Heat Pumps for Water Heating and Steam Production*, in*: Novel Concepts for Energy-Efficient Water Heating Systems*, J. D. F. Barbin and V. Silveira, Editor. 2013, Nova Science Publishers, Inc

147. ANSI/AHRI, *Standard 210/240: Performance rating of unitary A/C and air-source heat pump equipment*. 2008.

148. Gschwend, A., et al., *Energy consumption of cold climate heat pumps in different climates–Comparison of single-stage and two-stage systems.* International Journal of Refrigeration, 2016. **62**: p. 193-206.

149. Patankar, S., *Numerical heat transfer and fluid flow*. 2018: CRC press.

150. Bejan, A., *Film condensation on an upward facing plate with free edges.* International journal of heat mass transfer, 1991. **34**(2): p. 578-582.

151. Gerstmann, J. and P. Griffith, *Laminar film condensation on the underside of horizontal and inclined surfaces.* International Journal of Heat Mass Transfer, 1967. **10**(5): p. 567-580.

152. Collins, S. and F. Cameron, *Lithium Chloride and Ammonia Complexes.* The Journal of Physical Chemistry A, 2002. **32**(11): p. 1705-1716.

153. van der Pal, M. and J. Veldhuis, *Thermodynamic properties of lithium chloride ammonia complexes under heat pump type II working conditions*, in *Energy Research Centre of the Netherlands . Report nr ECN-M–10-076*. 2010.

154. Berthiaud, J., *A solid-gas sorption process for the long distance transport of heat and cold*. 2007, PhD thesis. PROMES, Perpignan, France.

155. Spinner, B. and F. Rheault. *Kinetics models in solid/gas reactions under imposed pressure and temperature constraints*. in *Proc of International Workshop on Heat Transformation and Storage. ISPRA*. 1985.

156. Tykodi, R.J., *Thermodynamics of steady states*. 1967: New York: Macmillan Company.

157. Tykodi, R., *Thermodynamics of steady states:"resistance change" transitions in steady-state systems.* Bulletin of the Chemical Society of Japan, 1979. **52**(2): p. 564-570.

158. Lebrun, M. and B. Spinner, *Simulation for the development of solid—gas chemical heat pump pilot plants Part I. simulation and dimensioning.* Chemical Engineering & Processing: Process Intensification, 1990. **28**(2): p. 55-66.

159. An, G., et al., *Wide applicability of analogical models coupled with hysteresis effect for halide/ammonia working pairs.* Chemical Engineering Journal, 2020: p. 125020.

160. ANSI/CGA, *Performance Testing and Rating of Gas-Fired, Air Conditioning and Heat Pump Appliances*. 2017, CSA America, Inc.: Cleveland, OH.

161. Gluesenkamp, K.R., et al., *Experimentally Measured Thermal Masses of Adsorption Heat Exchangers.* Energies, 2020. **13**(5): p. 1150.

162. Blackman, C., et al., *Study of optimal sizing for residential sorption heat pump system.* Applied Thermal Engineering, 2019. **150**: p. 421-432.

163. Qu, M., et al., *Energy-saving technologies for building heating, ventilation, and air conditioning systems.* Annual Review of Heat Transfer, 2018. **21**.